Studying Turbulence Using Numerical Simulation Databases – II

Proceedings of the 1988 Summer Program

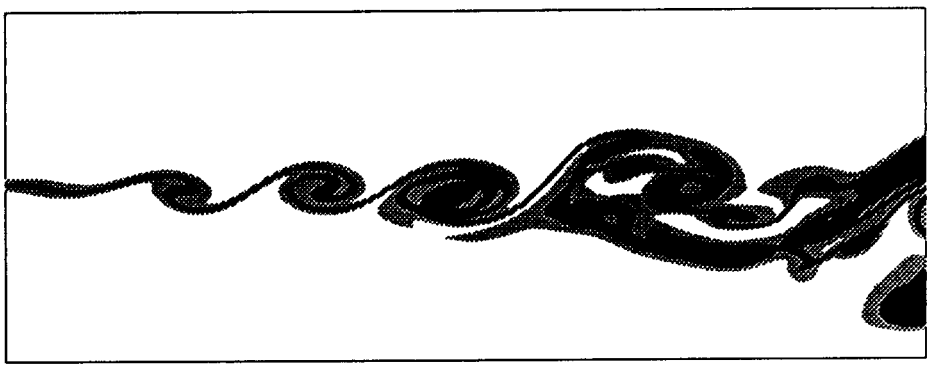

Center for Turbulence Research

Report CTR-S88

December 1988

NASA

Ames Research Center

Stanford University

Studying Turbulence Using Numerical Simulation Databases – II

Proceedings of the 1988 Summer Program

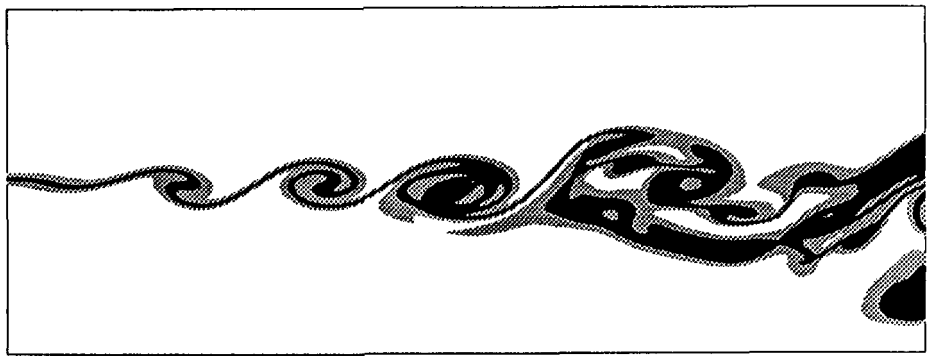

Center for Turbulence Research

Report CTR-S88

December 1988

NASA

Ames Research Center

Stanford University

ORIGINAL PAGE
BLACK AND WHITE PHOTOGRAPH

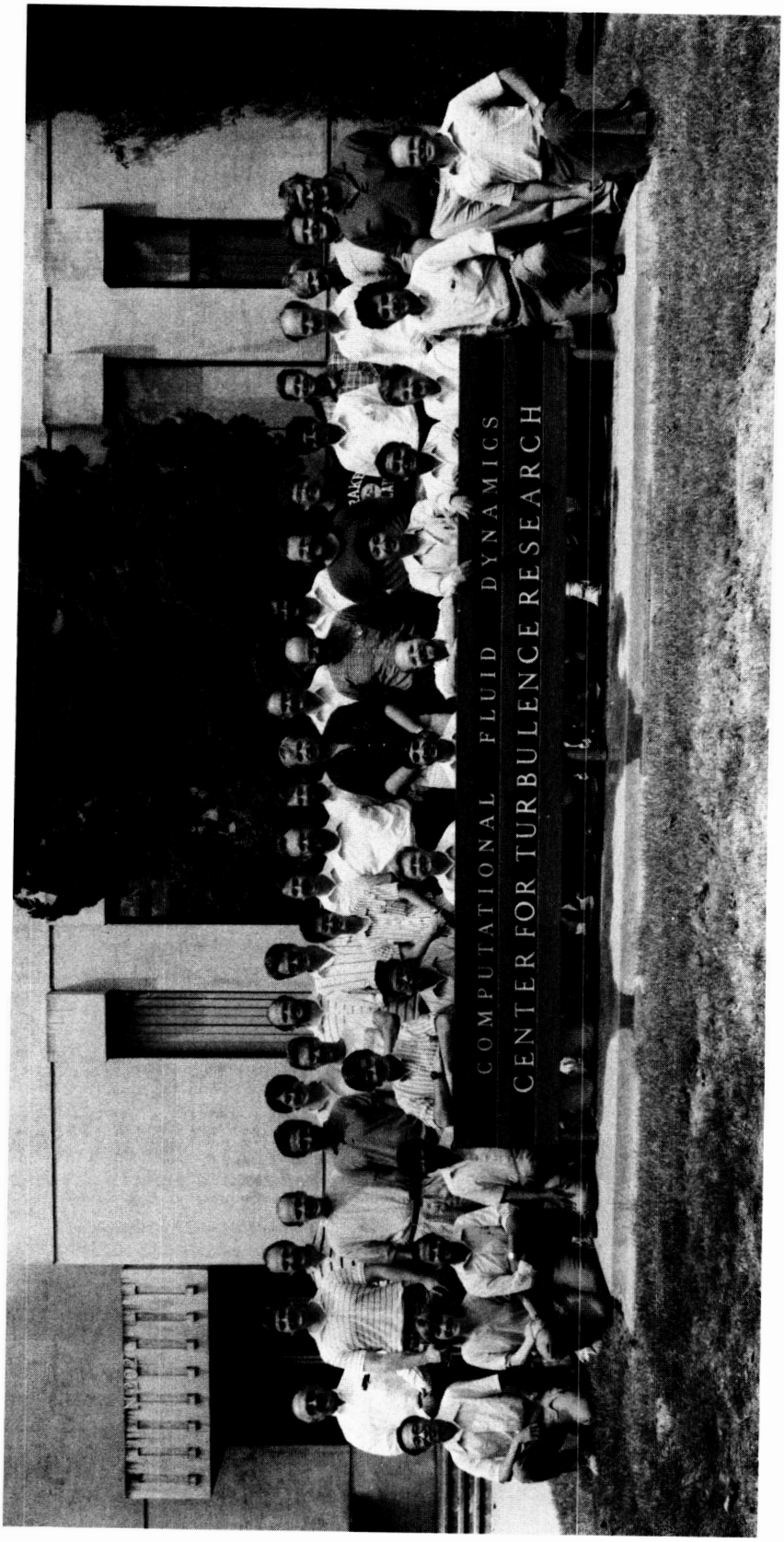

CONTENTS

Preface

The second Summer Program of the Center for Turbulence Research was held during the four week period June 27-July 22, 1988. As in the summer of 1987 the program focused on the use of direct numerical simulations of turbulent flows for study of turbulence physics and modeling. The main differences were the absence of distinct thematic groups, and a special emphasis on turbulent mixing layers; about a third of the research projects were concerned with turbulent mixing layers. The required data for these investigations were generated from four newly developed codes for simulation of time and spatially developing incompressible and compressible mixing layers.

The remaining projects covered a wide range of topics in turbulence research. These included, the structure of wall bounded turbulent and transitional flows, evaluation of diagnostic techniques for detection of organized motions, energy transfer in isotropic turbulence, optical propagation through turbulent media, and detailed analysis of the interaction of vortical structures. Some of these projects were a continuation of the efforts started in the 1987 Summer Program. A significant fraction of the research conducted during the Summer program used new simulations rather than existing databases. This allowed exploration of different parameter regimes and boundary conditions.

As part of the program, four review tutorials were given on topics related to turbulent mixing: Convective and absolute instability (P. Huerre), Concepts for mixing layer control (C. M. Ho), Dynamical systems and mixing (J. Ottino), Mixing and Chemical reactions (J. C. Hill). There were also four special lectures on recent numerical simulations and databases.

This volume begins with the nine papers on turbulent mixing layers arranged in alphabetical order by the first author followed by the remaining papers also arranged in alphabetical order. The volume is an account of a short but intense period of research activity; therefore, the results should be considered as preliminary. Many of the studies that began during the summer are being continued, and it is hoped that in due course the results will be submitted to the appropriate journals by the authors. Early reporting of virtually all of the projects occurred at the Forty-First Meeting of the Fluid Dynamics Division of the American Physical Society in Buffalo, New York, November 20-22, 1988. Twenty two abstracts based on the work accomplished during the summer program were presented at this meeting.

Parviz Moin
William C. Reynolds
John Kim

Center for Turbulence Research
Proceedings of the Summer Program 1988

Chaos in a Spatially-Developing Plane Mixing Layer

By J. G. Broze[1], F. Hussain[1] and J. C. Buell[2]

A spatially-developing plane mixing layer has been analyzed for chaotic behavior. A direct numerical simulation of the Navier-Stokes equations in a two-dimensional domain infinite in y and having inflow-outflow boundary conditions in x was used for data. Spectra, correlation dimension and the largest Lyapunov exponent have been computed as functions of downstream distance x, over the range $0 \leq x/\delta_\omega \leq 250$, from velocity time series in an Eulerian reference frame. When forced at a single (fundamental) frequency with maximum amplitude $v'_e/\Delta U = 0.01$, the flow is periodic at the inflow but becomes aperiodic with increasing x. The aperiodic behavior is caused by the presence of a "noisy" subharmonic caused by the feedback between the necessarily nonphysical inflow and outflow boundary conditions. In order to overshadow this noise the flow was also studied with the same fundamental forcing and added random forcing of amplitude $v'_r/\Delta U = 0.01$ at the inlet. Results were qualitatively the same in both cases: for small x, spectral peaks were sharp and dimension was nearly 1, but as x increased a narrowband spectral peak grew, spectra decayed exponentially at high frequencies and dimension increased to greater than 3. Based on these results, the flow appears to exhibit deterministic chaos. However, at no location was the largest Lyapunov exponent found to be significantly greater than zero. Moderate forcing with both fundamental at $v'_e/\Delta U = 0.01$ and subharmonic at $v'_e/\Delta U = 0.01$ and 0.002 caused the flow to be periodic throughout the computational domain.

1. Introduction

The discovery of deterministic chaos in dynamical systems has opened the possibility of understanding and modelling transitional and turbulent flows, which previously could only be described statistically. Complementary to this concept, the discovery and measurement in these flows of large-scale organized vortical motions, called "coherent structures", add evidence that there is order underlying the apparent randomness of turbulence. To couple these two concepts – chaos and coherent structures – might yield working models of turbulence which do not require solution of the full Navier-Stokes equations but which may predict flow statistics and dynamics with useful accuracy. In order to do this, it must be established that chaos and coherent structures are present in flows of interest and relevant measurements must be made. It is the existence of deterministic chaos in a mixing layer which is

1 University of Houston
2 NASA Ames Research Center

the object of this study; coherent structures in mixing layers have been studied in detail previously.

Prior studies of flow chaos have been almost exclusively in closed flows, in particular, Rayleigh-Bénard convection and Taylor-Couette flow. However, most flows of interest are open flows: jets, wakes, mixing layers and boundary layers. Finding deterministic chaos in open flows is complicated by a number of factors. Most open flows, including jets, plane Poiseuille flow and spatially developing mixing layers, are convectively unstable (Bechert 1985), *i.e.*, perturbation wave packets do not remain at the point of their origin but move downstream as they grow. It might be relevant to make measurements in a reference frame moving with the disturbance; for example, Deissler & Kaneko (1987) found that solutions of the time-dependent generalized Ginzburg-Landau equation gave the appearance of being chaotic, but had no positive Lyapunov exponents until they were measured in a moving frame. However, measurements in a moving frame are quite difficult to make; laboratory techniques such as hot-wire, hot-film, or laser-Doppler anemometry are best suited to collecting time series at a single location, or in a few locations simultaneously. New techniques, such as particle displacement velocimetry, can give more spatial detail but have reduced accuracy. Numerical simulations have both spatial detail and accuracy, but an advecting probe would leave the computational domain after only about a thousand time steps, compared to tens of thousands needed for standard analysis techniques. It might also be useful to analyze instantaneous spatial data for spatial chaos. Methods for analysis of spatial data are not well established, although it is possible to apply techniques to a "space series" rather than a time series, if those data are available (Sauliere & Huerre 1988). Even so, the same obstacles to data collection apply in the spatial case as they do to the moving probe.

The flow investigated was a two-dimensional, two-stream mixing layer with $Re = (U_1 - U_2)\delta_\omega/\nu = 100$ and velocity ratio $U_2/U_1 = 0.2$. U_1 and U_2 are the velocities of the two streams, δ_ω is the inflow vorticity thickness and ν is the kinematic viscosity. All lengths and coordinates are normalized by δ_ω, and velocities by $(U_1 - U_2)$. In order to minimize the streamwise pressure gradient, entrainment velocities $v(y=-\infty) = 0.0115$ and $v(y=\infty) = -0.0044$ were imposed. The inflow profile for the streamwise velocity u was calculated from the Blasius self-similarity equation. The corresponding vertical velocity v could not be used since the self-similarity solution has vorticity at infinity. Instead, a somewhat arbitrary profile consistent with the entrainment velocities and containing a small amount of downwash was imposed at the inflow. Both velocity components were required to satisfy a "convective" outflow boundary condition of the form $\partial\phi/\partial t = -c\partial\phi/\partial x$, where $c = (U_1 + U_2)/2$. See figure 2 of Buell & Huerre (1988) for a schematic of the geometry.

Data for analysis were obtained from direct numerical simulations using a recently developed code. The two-dimensional Navier-Stokes equations are solved on a domain that is infinite in the vertical (y) direction and finite in the streamwise (x) direction. Pressure is eliminated by taking the curl of the momentum equations

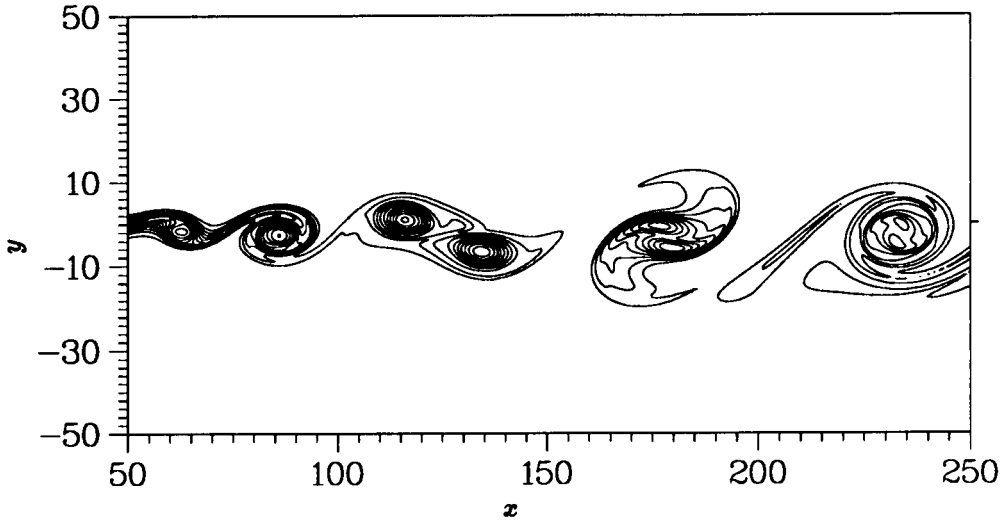

FIGURE 1. Contours of vorticity for $a = 0.01$, $b = 0.01$, $c = 0$.

twice and retaining only the x-component of the result. This yields a fourth-order equation for the streamwise velocity u which is advanced in time explicitly using a compact third-order Runge-Kutta scheme (Wray 1988). Since the Laplacian is contained in the time-derivative term, a Poisson equation must be solved during each substep. The vertical velocity v is recovered directly from the continuity equation. The numerical algorithm is based on a Fourier method with a cotangent mapping in the y direction (a modification of the method of Cain *et al.* 1984), and high-order accurate Padé approximations in the x direction. The first x-derivatives in the continuity equation and in the advection terms are approximated with modified Padé finite differencing (S. Lele, private communication). The particular approximation used here yields sixth-order accuracy for the low to moderate wavenumber components of the solution, and significantly lower dispersion errors for high wavenumbers. The second and fourth-order x-derivatives are approximated with classical fourth-order accurate Padé formulas. In order to avoid the inversion of very large sparse matrices for the solution of the Poisson equation for u, the effective wavenumber concept (Kim & Moin 1985) is applied in the x-direction so that the y-direction matrices are decoupled. The mesh used here was 384×192 in (x, y), and the domain length in the x-direction was 250. Perturbations were introduced in v at the inflow; the perturbation amplitude was tapered by a Gaussian shape over a small region near $y = 0$.

The primary instability in mixing layers is a fundamental wave which grows exponentially from its initial (linear) amplitude at the inflow, becomes nonlinear and saturates at some x, forming a rolled-up vortex. The secondary instability is the subharmonic of the fundamental which grows and saturates, resulting in vortex pairing. Both the fundamental and subharmonic are receptive to disturbances over

a band of frequencies; the initial amplitudes and phase difference control the evolution of the mixing layer. For more details, see Monkewitz (1988). The frequencies, amplitudes and phases from which these grow depend on extrinsic perturbations: controlled excitation, feedback and ambient noise. A sample vorticity plot is shown in figure 1 for a simulation with both fundamental and subharmonic perturbations. This plot shows all stages of 2-D mixing layer dynamics up through pairing. The vortex entering at $x = 60$ has not yet fully rolled up; the structure at $x = 80$ is fully formed and will eventually pair with the one at $x = 60$. Two structures near $x = 120$ are in the process of pairing, while the structures at $x = 180$ and $x = 230$ are fully paired structures.

Coflowing two stream mixing layers have been shown theoretically to be convectively unstable. However, the upstream flow can be perturbed by feedback from somewhere downstream. In experiments, this feedback may be provided by impingement on a solid body, causing pressure fluctuations which propagate upstream to the inflow, or perhaps by velocity fluctuations at the splitter plate induced by downstream vortex rollup. In numerical experiments with solid surfaces absent, this cannot occur except as boundary condition reflections. In the present numerical simulation, it was established that boundary condition reflection did exist (Buell & Huerre 1988), causing vortex rollup to occur in a nontransient manner for the conditions being simulated.

2. Approach

It is not clear whether the flow in question, a two-stream transitional mixing layer, is temporally or spatially chaotic. The flow develops in x and is obviously not spatially periodic, but it is not possible to examine the exact nature of its spatial behavior in the current framework. The flow looks somewhat more periodic in time, but closer examination reveals definite aperiodicity. It is entirely possible that the flow is both temporally and spatially chaotic. Given the inability to follow disturbances spatially for great distances, we wanted to focus more closely on temporal aspects of the flow and to exclude possible spatial dynamics. To do this, we chose to analyze time series collected in an Eulerian frame at selected flow locations and to treat streamwise distance x as a flow parameter. Since the disturbance at a given x originates upstream and convects past our "probe", we perturbed the flow by imposing a sinusoidal fluctuation (with a fundamental and/or subharmonic frequency) at the inflow boundary. This way, we imposed a periodicity on the dynamics and observed how it deviated from periodicity with increasing x. We still must rely on the presence of other disturbances to initiate this deviation, but what is of interest is how the flow organizes itself in the presence of these disturbances.

3. Excitation Case Studies

The inlet profile of the mixing layer had the form $U(y)\mathbf{i} + [V(y) + v_e(y,t)]\mathbf{j}$, where $U(y)$ is the Blasius similarity solution for a 2-D mixing layer and $v_e(y,t)$ is the perturbation. The inlet was excited with fundamental and subharmonic

perturbations and random noise with several combinations of amplitudes:

$$v_e(y,t) = f(y)\left[a\cos(\omega t) + b\cos(\omega t/2 + \phi) + c\,r(t)\right]$$

where $f(y)$ has a Gaussian shape centered at $y = 0$ and is zero elsewhere and $r(t)$ is a uniform random variable distributed on the interval (-1,1). We isolated a few key cases:

Case (i): no forcing ($a = b = c = 0$),
Case (ii): (a) fundamental only ($a = 0.01$; $b = c = 0$),
(b) fundamental plus random forcing ($a = 0.01$; $b = 0$; $c = 0.01$),
Case (iii): fundamental and subharmonic ($a = 0.01$; $b = 0.01$, 0.002, 0.0005; $c = 0$).

In case (i), fundamental and subharmonic waves grow due to unknown perturbations arising from boundary condition reflections; low-dimensional behavior is not expected in general. In case (ii(a)), the fundamental is driven by periodic forcing, but the subharmonic is subject to background perturbation by reflections. Case (ii(b)) was used to study the difference between the subharmonic driven by background perturbation and by a random inlet forcing. In case (iii), both fundamental and subharmonic are driven by the imposed periodic perturbation. The phase angle ϕ was chosen to be 100 degrees, in the range where subharmonic enhancement is expected (Monkewitz 1988, Husain & Hussain 1988).

4. Analysis Techniques

4.1. Time Series Analysis

Power spectra, correlation dimension and largest Lyapunov exponent were calculated from time series collected at selected locations in the flow domain. To establish the existence of chaos from (numerical or laboratory) experimental data is tricky, at best; several pieces of supporting evidence must be assembled and analyzed for trends as parameters are varied. Taken together, continuous spectra, noninteger correlation dimension and positive Lyapunov exponent are strong indicators of deterministic chaos.

4.1.1. Power spectra

Spectra can provide insight into flow dynamics. There are two obvious extremes: a discrete spectrum indicates periodicity or quasi-periodicity, whereas a continuous spectrum with no peaks suggests nonperiodic, random behavior. In contrast, other spectra which are intermediate cases, such as sharp peaks on broadband background noise or a combination of sharp and narrowband peaks, indicate possible low-dimensional, chaotic dynamics. The behavior of spectra at high frequencies can be used to separate deterministic chaos from randomness. In particular, the idea that exponential decay of spectra is indicative of deterministic chaos, while power-law behavior is indicative of randomness, is argued by Sigeti & Horsthemke (1987) and utilized in several studies, *e.g.*, Brandstater & Swinney (1987).

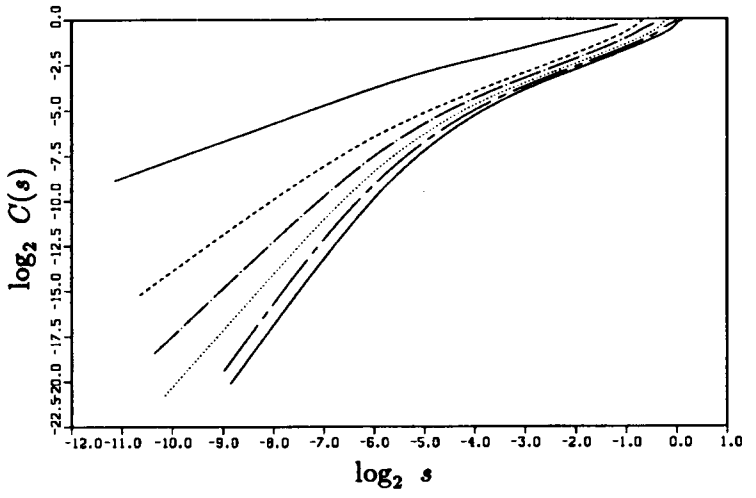

(a)

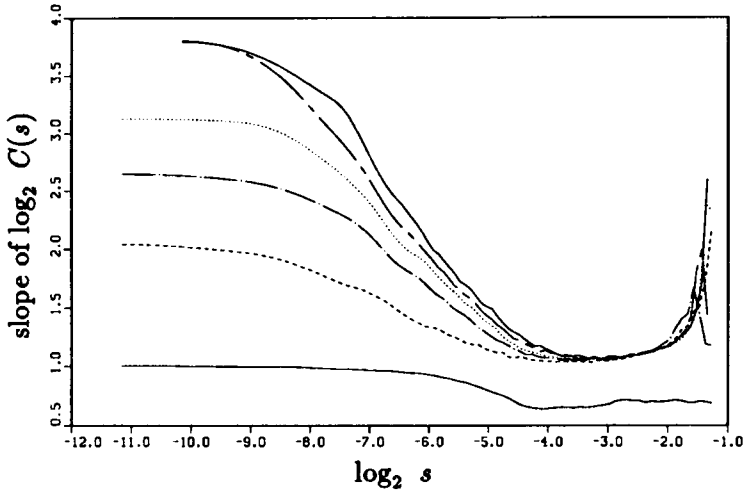

(b)

FIGURE 2. (a) Correlation integral for case (ii(a)), $a = 0.01$, $b = c = 0$, $m = 1, \ldots, 7$ from top; (b) Slope of correlation integral, $m = 1, \ldots, 7$ from bottom.

4.1.2. Correlation dimension

The trajectories in phase space are reconstructed from a single dynamic variable using time-series-delay embedding (Takens 1980). Time delays were chosen using the first minimum of the mutual information (Fraser & Swinney 1986) and checked visually by making two-dimensional phase portraits. Correlation dimension was calculated using the algorithm of Grassberger & Procaccia (1983) (modified to use 1000 randomly chosen reference points). The correlation integral $C(s)$, where s is phase space distance, was computed for a range of embedding dimensions and fit with a cubic spline polynomial (figure 2a). Each line in the figure represents a

different embedding dimension m, increasing from top to bottom. Notice that, near the region where the $\log_2 s = -3$, all curves have approximately the same slope. The slope of C versus s was computed analytically in log-log coordinates from the spline coefficients (figure 2b). The slope is typically quite high (possibly as high as m) at the smallest distances due to the presence of noise. At larger distances, the slope drops off sharply and may flatten out; this occurs near $\log_2 s = -3$ in the example. The correlation integral is said to "scale" when the slope is constant over some range of distances and said to "saturate" when this constant slope converges as m increases. This saturated slope is called the correlation dimension ν, and is an estimate of the Hausdorff dimension. The distances over which the slope is constant is called the scaling region, since it implies that the correlation integral scales exponentially, *i.e.*, $C \sim s^{\nu}$. The scaling region is computed by finding the scales over which the slope does not deviate more than a given bound, typically 5%. In the example shown in figure (2b), for $m = 3$, $\nu = 1.07$ over a scaling region from $s = 0.045$ to $s = 0.20$, where s in this case is v. The actual value computed from this algorithm cannot be used to determine n very accurately; *e.g.*, it can not discriminate between 1.0 and 1.05 and therefore can not be used to "prove" that an object is fractal. It can be used to estimate dimension roughly and to measure increasing complexity as a parameter is varied. Unfortunately, data length required for the correlation dimension algorithm is large and increases roughly as k^m, where k is the some constant (Brandstater & Swinney 1987). Since higher embedding dimensions are required to reveal higher dimensional attractors, data requirements quickly get very large as dimension increases.

4.1.3. Lyapunov exponent

The largest Lyapunov exponent is a measure of the maximum rate of exponential divergence of trajectories in phase space and is indicative of chaos when positive. We calculated it using the method of Wolf *et al.* (1985). The exact value of the exponent is not crucial and should not be expected from this algorithm, although it does give results within a few percent for time series from model systems of ordinary differential equations, such as the Lorenz system. It is an important indicator of chaotic behavior, and it is important to be sure whether or not it is positive. Since the calculated exponent can vary significantly depending on input parameters (*viz.*, time delay, embedding dimension, maximum and minimum scales, evolution time), care was taken to select consistent values. The results of the correlation dimension calculation form natural choices for several of these parameters. In particular, the time delay was chosen from mutual information (the same delay was used for correlation dimension and Lyapunov exponent), embedding dimension was chosen to be the minimum m for which saturation was observed in the correlation integral, the minimum and maximum scales were taken from the limits of the flat scaling region, and the evolution time was chosen as the time delay. Several tests of these parameters were conducted. Small differences in time delay and embedding dimension had little effect on the computed exponent. However, since the algorithm follows the distance between nearby trajectories in the reconstructed phase space, minimum and maximum scales are quite important. These scale parameters sets the

range of distances between trajectories which will be considered. A distance which is too small would include the random noise at the smallest scales and might give a positive exponent even when the large-scale flow is not chaotic, while measuring at very large distances might yield a negative or zero exponent even for a chaotic attractor. The limits of the scaling region of the correlation exponent were chosen for these parameters since those are the scales over which the flow behaves as an attractor. Small variations about these values had little effect on the computed value. The choice of evolution time has some effect on the magnitude, but not on the sign, of the exponent. In summary, the exponents we calculated seem to give a good indication of the sign of the largest Lyapunov exponent.

4.1.4. Flow variable

The choice of flow variable, in principle, should make very little difference in the results using these methods. Three variables were tested: u, v, and $G = \int \omega_z dy$, where ω_z is the vorticity. The v component had a smoother profile with a peak at $y \simeq 0$ while u had sharp peaks near $y \simeq 0$. The variable G was generated as a means of tracking passage of vortex peaks for use in the analysis of discrete sequences (see next section). Results were in good agreement: dimension and Lyapunov exponent using v and G were quite similar, while u tended to give slightly higher values and smaller scaling regions. After these tests, v was chosen as the variable to be used.

4.2. Analysis of Discrete Sequences

Two goals of open-flow studies using nonlinear dynamics techniques are low-dimensional modeling and prediction. One way to do this is to extract from the data a discrete sequence of significant events, such as vortex passage periods T, vortex strengths or any other significant dynamic measure. From this sequence, first-return maps (T_n versus T_{n+1}) can be constructed which give information about what the next period will be based on the previous period. If these maps are highly ordered, a curve fit might give a useful predictive model. If the maps are less structured, it may still be possible to quantify how much information is "stored" by the flow system – about the future based on the past – by computing "stored information" (Shaw 1984). We constructed first-return maps from periods between zero-crossings of v and computed stored information:

$$\mathbf{I}(T_{n+1}|T_n) = \int P(T_n) \int P(T_{n+1}|T_n) \log(P(T_{n+1}|T_n)/P(T_n)) dT_{n+1} dT_n$$

where $\mathbf{I}(T_{n+1}|T_n)$ is the stored information, $P(T_n)$ is the probability density function (pdf) of T_n, and $P(T_{n+1}|T_n)$ is the pdf of T_{n+1} conditional on T_n. Unfortunately, to construct a convergent pdf estimate requires a large number of points, particularly when one wishes to construct conditional pdfs from some subset of the data set. As a result, we were unable to get useful results from our data, which had less than 200 structure passages (when we needed of the order of thousands). The pdfs and stored information were quite sensitive to number of bins used in the pdf estimate. The stored information fluctuated significantly as number of bins was changed. We were unable to establish reliably even an approximate value which could reveal trends in $\mathbf{I}(T_{n+1}|T_n)$ as location was changed.

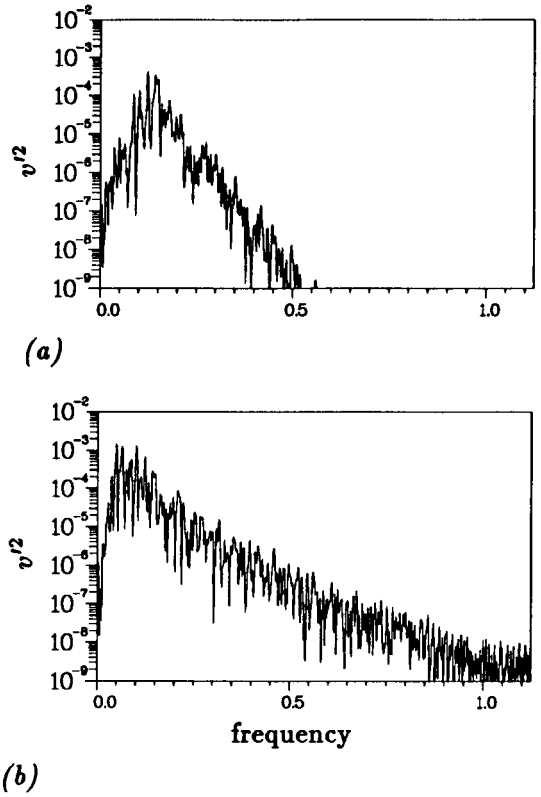

FIGURE 3. Spectrum of v for case (i), $a = b = c = 0$; (a) $x = 140$, (b) $x = 230$.

5. Results and Discussion

Case (i): $(a = b = c = 0)$

Velocity spectra in the unforced case showed no sharp peaks: a broadband fundamental peak appeared at small x (figure 3a) and was replaced at larger x by a broadband subharmonic peak (figure 3b). Computation of the correlation integral revealed no scaling region. This is not unexpected; the instability is driven by ambient perturbations only, which are almost entirely boundary condition reflections at the outflow. For the computational domain chosen, the reflection was weak and aperiodic (Buell & Huerre 1988). Since the reflections are not periodic, the fluctuations passing the "probe" are necessarily not. Due to the lack of scaling, no parameters could be extracted to compute Lyapunov exponent.

Case (ii(a)): $(a = 0.01;\ b = c = 0)$

The fundamental was forced at $\omega = 0.18$. Traces of v velocity at four different x locations (figure 4) show how the flow is periodic at $x = 100$ and becomes more disordered with increasing x. At $x = 140$, the emergence of the subharmonic component can be seen in the alternating higher and lower peaks at some times. At $x = 170$ and 200, events can be seen with twice the period of the fundamental; this is the footprint of paired vortices. Spectra of v velocity (figures 5a-d) at the same

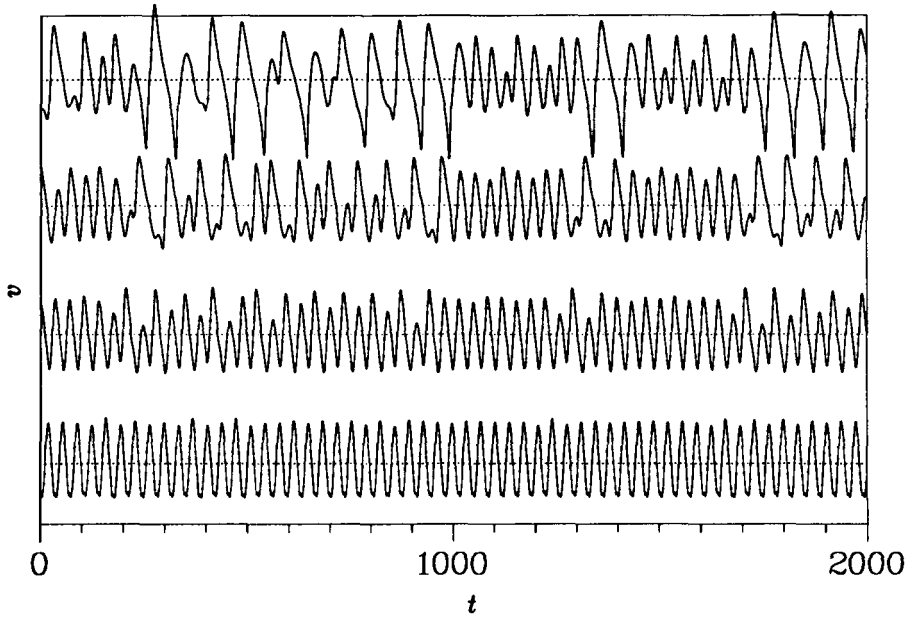

FIGURE 4. Time traces of v for case (ii(a)), $a = b = 0.01$, $c = 0$; from bottom to top, $x = 100, 140, 170, 200$.

locations reveal sharp peaks at the fundamental frequency and its harmonics which slowly diminish with x. The peak of the subharmonic is not sharp, however; it forms a noisy narrowband peak at about $\omega = 0.09$. This peak is initially quite low: at $x = 100$ (figure 5a), the fundamental is almost 4 orders of magnitude higher; at $x = 140$ (figure 5b), the fundamental is 2 decades higher; at $x = 170$ (figure 5c), the peaks are only a decade apart; and at $x = 200$ (figure 5d), the noisy subharmonic clearly dominates the spectrum. At this point, the spectrum looks quite similar to the spectrum in the unforced case (figure 3b). This is not surprising, since the subharmonic was unforced in both cases.

In contrast with case (i), correlation integral calculations worked quite well in this case. Results for cases (ii(a)) and (ii(b)) are shown in figure 6. For case (ii(a)), correlation dimension was near 1 for $x < 100$ and increased monotonically to a value between 3 and 4 by $x = 170$. For locations $x > 170$, the correlation integral did not truly scale. An oscillation in the slope sometimes appears at high embedding dimensions which obscures any flat slope; in other cases the slope is flat but still rises a few percent with each higher embedding dimension. In all cases, at large x, the scaling region is quite small, extending over a factor of two or less in distance. This is quite likely due to a lack of long time series, as discussed above in Analysis Techniques. Time series of only 9000 points (188 orbits) were used. The values shown in figure 6 for $x > 170$ are estimates from the time series available; the true dimension is likely to be higher.

Calculation of the largest Lyapunov exponent over the domain $100 \leq x \leq 200$ did

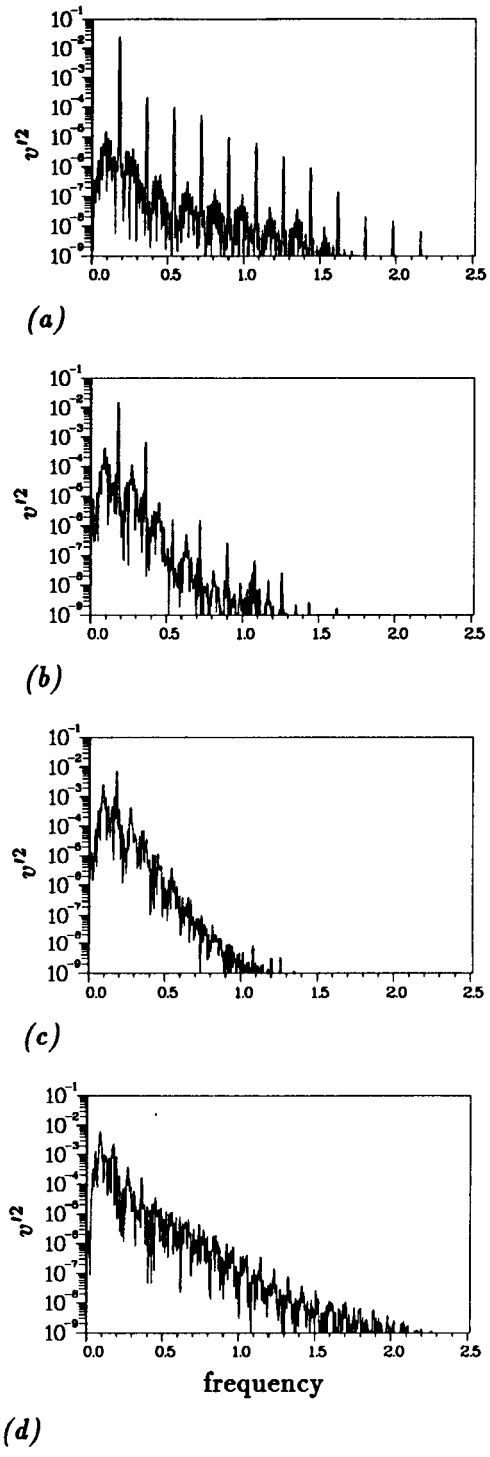

FIGURE 5. Spectra of v corresponding to figure 4; (a) $x = 100$, (b) $x = 140$, (c) $x = 170$, (d) $x = 200$.

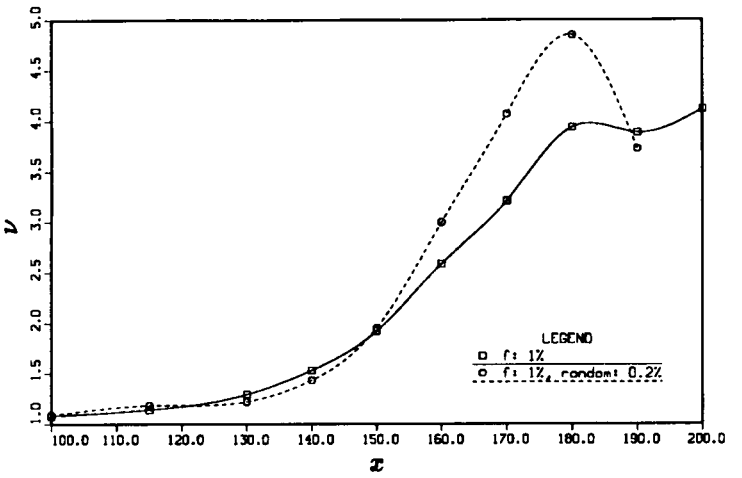

FIGURE 6. Correlation dimension as a function of location for cases (ii(a)) and (ii(b)).

not show an appreciable positive value at any location. Values ranged from -0.0083 bits/orbit (-0.00023 bits/time unit) to 0.072 bits/orbit (0.002 bits/time unit), showing a general, though not monotonic, increase with x. While the largest value found might indicate chaos, this possibility is not certain. These exponents can be interpreted as the average rate at which information is lost or gained about the initial condition of a phase space trajectory; a positive value represents a loss of information and therefore sensitive dependence on initial condition. The largest calculated value can be compared loosely with values reported by Wolf *et al.* (1985) for the Lorenz attractor (2.16 bits/time unit, 1.08 bits/orbit) and the Rossler attractor (0.13 bits/time unit, 0.78 bits/orbit) for typical parameter values.

Case (ii(b)): ($a = 0.01$; $b = 0$; $c = 0.01$)

Since the boundary condition reflection was difficult to quantify but was clearly not periodic, we imposed a random perturbation on the inlet in addition to the fundamental perturbation. This perturbation was designed to be of lower amplitude than the fundamental but higher than the background. At the first x station ($x = 0.7$), the fundamental amplitude of the v spectrum was 10^{-5}, while the white noise amplitude was 10^{-10} (figure 7). For the case with no random input, the background amplitude was less than 10^{-11}. Spectral development is quite similar to that of the case with no random forcing, as was that of dimension (figure 6) and Lyapunov exponent. The two dimensions begin to deviate after $x = 160$; exact values at larger x are unreliable, but the trend seems to indicate that the system under random forcing may have higher dimension. The drop in dimension for the randomly forced case at $x = 190$ is clearly not physical; it is most likely due to the lack of data records of adequate length.

Case (iii): ($a = 0.01$; $b = 0.01$, $b = 0.002$, 0.0005; $c = 0$)

This case yielded both expected and unusual results. Intuition suggests that the

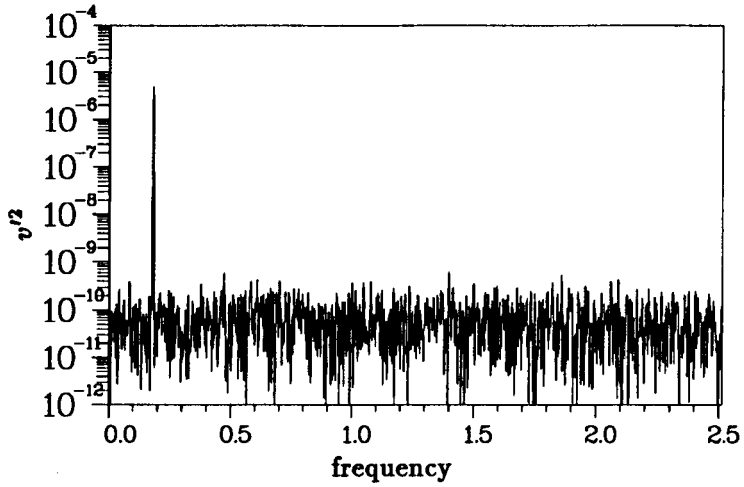

FIGURE 7. Spectrum of v at first x station for case (ii(b)), $a = 0.01$, $b = 0$, $c = 0.01$.

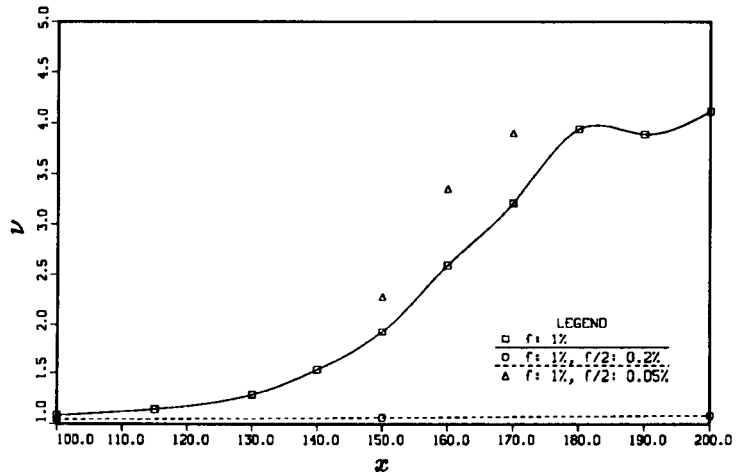

FIGURE 8. Correlation dimension as a function of location for cases (ii(a)) and (iii).

presence of sinusoidal fundamental and subharmonic should make the flow periodic for a larger streamwise distance. When the subharmonic amplitude was 1% and 0.2%, this was the case; in fact, the flow was periodic and dimension was 1 throughout the domain (figure 8). When the subharmonic was very low (0.05%), however, the flow was not periodic, and had higher dimension than with no subharmonic forcing at all. This is contrary to intuition, since we expect that even a low amplitude subharmonic would organize the flow more than no subharmonic at all. As a check, spectra with and without this forcing were compared, and they revealed that the noisy subharmonic had higher amplitude with the forcing. Further investigation showed that the forcing amplitude was of the order of reflection noise. We speculate

that superposition of subharmonic forcing with the boundary condition reflections creates higher subharmonic amplitude which is still noisy.

The results of cases (ii(a)) and (ii(b)) seem to indicate chaotic behavior. The growth of narrowband noise in the spectrum, exponential falloff of spectra at high frequencies for large x and the increase from unity of correlation dimension all point to the presence of low dimensional chaos in this system. By comparing the development in x of the spectrum with correlation dimension, one sees the connection between dimension and the growth of the subharmonic. The fundamental excitation has caused the flow to be periodic for small x, but the subharmonic does not grow from a pure sinusoid and its contribution to the dynamics is necessarily aperiodic. As the subharmonic grows, the flow becomes less organized; however, this disorganization appears to be low dimensional chaos.

The similarity between cases (ii(a)) and (ii(b)) is quite significant. The boundary condition reflection can not be entirely random; reflections will peak as large structures pass out of the computational window, yielding a broadband reflection centered at the subharmonic frequency, as there is only one pairing within the computational domain. The random forcing is white (figure 7). But the flow driven by weak internal reflections and the flow driven by white noise are similar: these perturbations are organized by the secondary instability into a low-dimensional chaotic flow rather than a random flow. However, this low-dimensional behavior is observed only in forced cases with periodic roll up; the unforced case showed no scaling at all. Why is this? Perhaps the answer lies with the subharmonic resonance phenomenon, which has been investigated both theoretically (Monkewitz 1988) and experimentally (Husain & Hussain 1986). Comparing spectra in cases (i) and (ii(a)), the bandwidth of the unforced flow (figure 3a) is significantly broader than that of the subharmonic component in the forced flow (*e.g.*, figure 5b). Because we have supplied a single fundamental frequency ω, it resonates most strongly with the frequency $\omega/2$. Other frequencies near $\omega/2$ will resonate because of detuning, but their amplitudes will be lower. However, if the fundamental is narrowband rather than a sharp peak, resonance will occur over a wider range of frequencies, giving a wider subharmonic bandwidth. Thus, the flow with no forcing has a wider spectral band in both the fundamental and subharmonic. This lack of organization must result in higher dimension, too high to be measured with the record length available. The linear falloff at high frequencies in case (i) and in cases (ii(a,b)) points to deterministic chaos in this flow (Sigeti & Horsthemke 1987), although we could not measure its dimension.

6. Concluding Remarks

A numerically generated, two-stream mixing layer has been studied as a function of position in an Eulerian frame for evidence of temporal chaos. The most interesting result was for cases in which a single, periodic perturbation was imposed at the inlet. With increasing x, narrowband peaks developed in the spectra, dimension increased from 1, and spectra at high frequencies fall exponentially, indicating that the flow had become chaotic.

The absence of a positive Lyapunov exponent is puzzling in light of other indicators of chaos. The recent work of Deissler and Kaneko (1987) shows, using the Ginzburg-Landau equation and coupled logistic maps, that convectively unstable systems which appear chaotic may nonetheless have zero Lyapunov exponent when measured in a stationary frame. However, positive Lyapunov exponents were measured in a frame moving with the disturbance. The mixing layer is a convectively unstable flow and may exhibit the same behavior. Additional study will be focused on this possibility.

The development of chaos in the singly forced case can be seen as the result of resonance between the periodic fundamental and its subharmonic. Since the ambient fluctuations are broadband, the subharmonic develops as a narrow band rather than a single frequency due to detuning. The layer shows qualitatively the same behavior when forced with fundamental alone as when forced with fundamental and random noise. This is quite interesting because the perturbation sources are quite different: in one case the source is reflections which are due to downstream flow conditions, whereas in the other case it is imposed random perturbations. More investigation is necessary to determine whether this similarity is superficial or there is some universality to the dynamics regardless of the extrinsic perturbation.

Laboratory experiments will serve as an important test of these results. Will the flow evolve similarly in the laboratory, or will the low-dimensional dynamics be overcome by three-dimensional phenomena? Three-dimensional mixing layers should behave quite differently. The onset of the spanwise secondary instability, the development of ribs, the possibility of vortex cut-and-connect and the breakdown of the mixing layer are important dynamic events which are not possible in two dimensions. In addition, 3-D spatially developing simulations and simulations of temporally developing flows will be quite important to study these phenomena as low-dimensional dynamical systems under carefully controlled conditions.

REFERENCES

BECHERT, D. 1985 *Z. Flugwiss. Weltraumforschung* **9**, 356.

BRANDSTATER, A. & SWINNEY, H.L. 1987 *Phys. Rev. A* **35**, 2207.

BUELL, J. & HUERRE, P. 1988, elsewhere in the volume.

CAIN, A. B., FERZIGER, J. H. & REYNOLDS, W. C. 1984 *J. Comp. Phys.* **56**, 272-286.

DEISSLER, R.J. & KANEKO, K. 1987 *Physics Letters A* **119**, 397.

FRASER, A.M. & SWINNEY, H.L. 1986 *Phys. Rev. A* **33**, 1134.

GRASSBERGER, P. & PROCACCIA, I. 1983 *Phys. Rev. Lett.* **50** , 346; 1983 *Physica* **9D**, 189.

HUSAIN, H.S. & HUSSAIN, A.K.M.F. 1986 *Bull. Am. Phys. Soc.* **31**, 1696.

HUSAIN, H.S. & HUSSAIN, F. 1988 Subharmonic Resonance in a Shear Layer, presented at the 2nd European Turbulence Conference, Berlin.

KIM, J. & MOIN, P. 1985 *J. Comp. Phys.* **59**, 308-323.

MONKEWITZ, P. A. 1988 *J. Fluid Mech.* **188**, 223.

SAULIERE & HUERRE, P. 1988, private communication from Patrick Huerre.

SHAW, R. 1984 *The Dripping Faucet as a Model Chaotic System.* Aerial Press.

SIGETI, D. & HORSTHEMKE, W. 1987 *Phys. Rev. A* **35**, 276.

TAKENS, F. 1980 in: Proc. Warwick Symp., D. Rand and B. S. Young, eds, *Lecture Notes in Math.* **898** (Springer, Berlin, 1981).

WOLF, A., SWIFT, J., SWINNEY, H.L & VASTANO, J.A. 1985 *Physica* **16D**, 285.

WRAY, A. A. 1988 submitted to *J. Comp. Phys.*

Center for Turbulence Research
Proceedings of the Summer Program 1988

Inflow/Outflow Boundary Conditions and Global Dynamics of Spatial Mixing Layers

By J. C. Buell[1] AND P. Huerre[2]

1. Introduction

The numerical simulation of incompressible spatially-developing shear flows poses a special challenge to computational fluid dynamicists. The Navier-Stokes equations are elliptic and boundary equations need to be specified at the inflow and outflow boundaries in order to compute the fluid properties within the region of interest. It is, however, difficult to choose inflow and outflow conditions corresponding to a given experimental situation. Furthermore the effects that changes in the boundary conditions or in the size of the computational domain may induce on the global dynamics of the flow are presently unknown. The purpose of this study is to examine these issues in light of recent developments in hydrodynamic stability theory. The particular flow to be considered is the spatial mixing layer but it is expected that similar phenomena are bound to occur in other cases such as channel flow, the boundary layer, etc. A short summary of local/global and absolute/convective instability concepts is given in section 2. In section 3 we present the results of numerical simulations which strongly suggest that global resonances may be triggered in domains of finite streamwise extent although the evolution of the perturbation vorticity field is everywhere locally convective. In the last section, we discuss a relationship between finite domains and pressure sources which might help in devising a scheme to eliminate these difficulties.

2. Local/Global, Absolute/Convective Instabilities

Rigorous definitions of absolute and convective instability have been given in the context of plasma physics by Briggs (1964) and Bers (1983). Similar ideas have recently been applied to inviscid instabilities in free shear layers by Huerre & Monkewitz (1985), Koch (1985) and Monkewitz (1988), among others. For a review, the reader is referred to Huerre (1987).

A parallel flow (*i.e.*, independent of the streamwise coordinate x) is said to be convectively unstable if its linear response to a delta function impulse in space and time decays to zero everywhere as time increases to infinity, but increases along certain rays in the downstream direction (Figure 1b). Conversely, a parallel flow is absolutely unstable if its impulse response becomes unbounded everywhere for infinite time (Figure 1a). These notions are particularly relevant in spatially-evolving flows, as long as the streamwise variations of the basic velocity profile are

1 NASA Ames Research Center

2 Department of Aerospace Engineering, University of Southern California

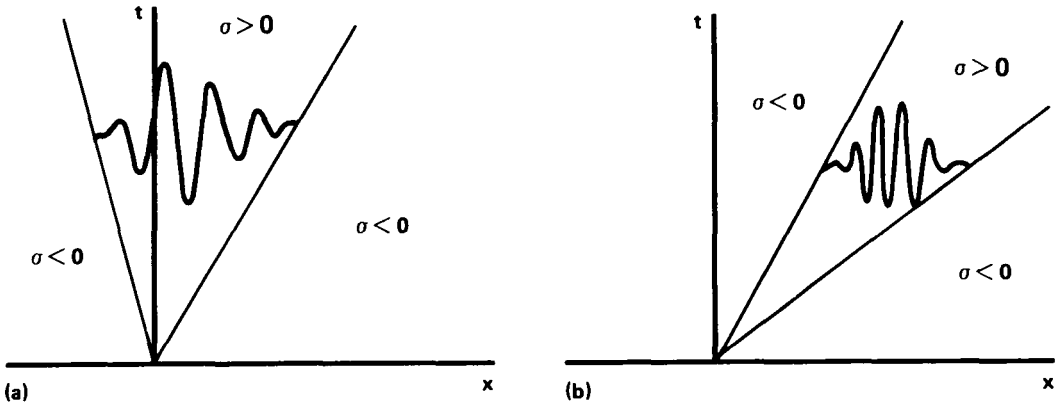

FIGURE 1. Sketch of a typical impulse response: *(a)* absolutely unstable flow; *(b)* convectively unstable flow.

small over a characteristic instability wavelength. One then says that the flow is *locally* absolutely unstable or *locally* convectively unstable at a given streamwise station. For instance, it has been demonstrated (Huerre & Monkewitz 1985) that the hyperbolic tangent mixing layer is convectively unstable for values of the velocity ratio $R = (U_1 - U_2)/(U_1 + U_2)$ smaller than one (*i.e.*, for coflowing streams), U_1 and U_2 being the respective velocities of each stream. Since this model is a good approximation to experimentally measured local mean velocity profiles, one may safely conclude that spatially-developing shear layers are locally convectively unstable everywhere: any initial vortical disturbance is advected downstream as it is amplified and the flow is extremely sensitive to external forcing (Ho & Huerre 1984). It is important to note that this locally convective behavior strictly pertains to *vortical* fluctuations in the shear zone and not to pressure fluctuations in the outer potential flow.

Since there is no region of absolute instability, one cannot have a self-sustained *global* response (*i.e.*, a finely tuned oscillation with the streamwise coordinate as an eigenfunction direction) involving temporally amplified upstream and downstream propagating *vorticity* waves (Chomaz *et al.* 1988). In the absence of a splitter plate, a downstream body, or a "non-transparent" outflow or inflow boundary, one therefore does not expect a self-sustained fluctuation field unless the flow is continuously forced from the outside.

3. Effects of Boundary Conditions on Spatially-developing Simulations

A two-dimensional numerical code of the spatial mixing layer developed by the first author was used to conduct the present investigation. The boundary conditions applied to the perturbation quantities are indicated on Figure 2. The reference length and velocity scales are the inflow vorticity thickness and the velocity difference, respectively. In all cases there was no external forcing at the inflow boundary and no splitter plate was inserted into the flow. At a velocity ratio $R = 2/3$ and for a computational domain of streamwise extent $Lx = 250$, one obtains throughout the flow a self-sustained noisy dynamical state characterized by a broad power

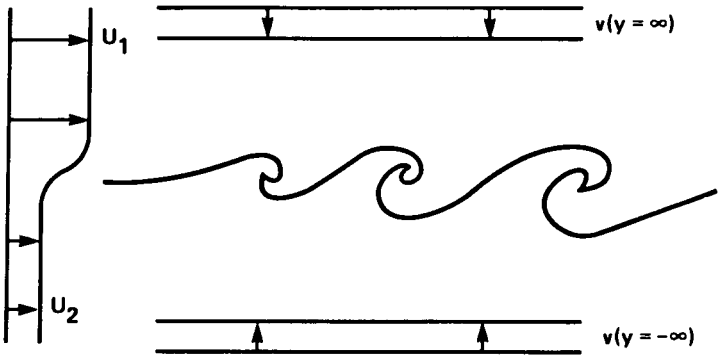

FIGURE 2. Geometry and boundary conditions.

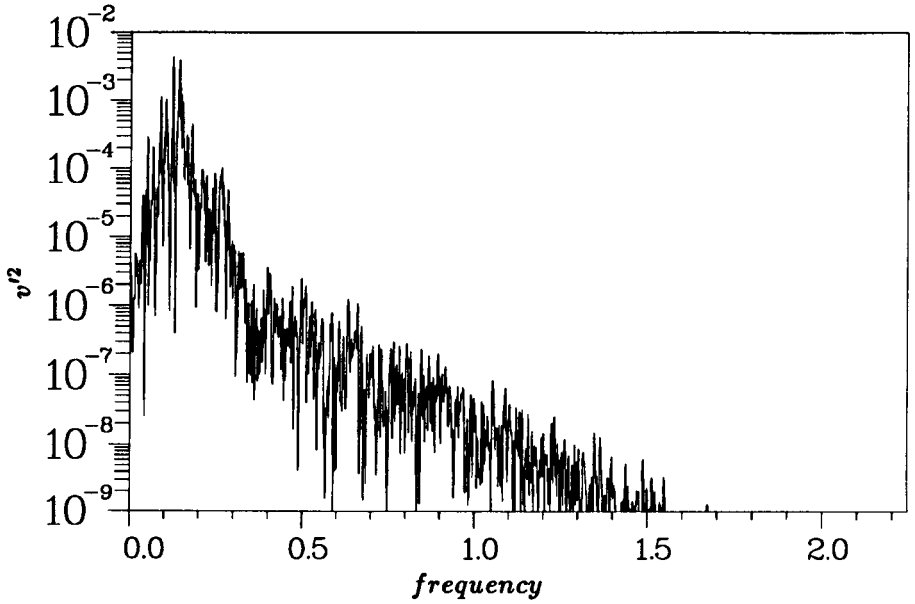

FIGURE 3. Power spectrum of v velocity at $x = 170$, $y = 0$.

spectrum, as shown in Figure 3. The spatial evolution of the vorticity field presents all the usual features of laboratory experiments, namely: spatial amplification of instability waves, roll-up, pairing of vortices, etc. The temporal behavior, however, appears to contradict the reasoning of the previous section: a convectively unstable flow should not be able to give rise to a "natural" self-excited state.

Time series of the cross-stream perturbation velocity v taken at different streamwise stations during the transient regime proved to be enlightening (see Figure 4). The discontinuity in slope generated at time $t = 0$ at the inflow boundary produces a wavepacket which propagates downstream. This discontinuity is induced by a mismatch between the initial conditions and the boundary condition at $x = 0$ (this

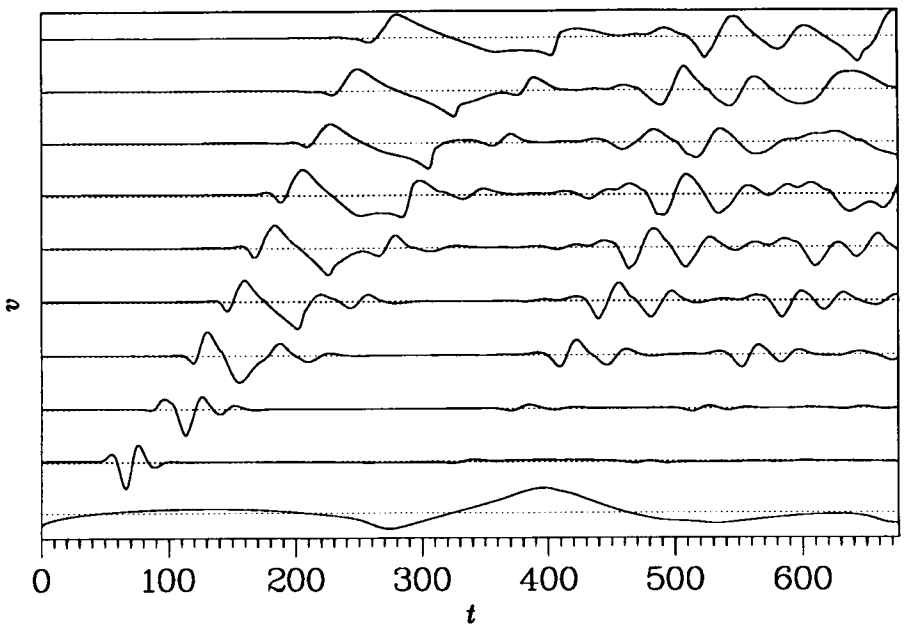

FIGURE 4. Time traces of v-velocity at $x = 1$, 50, 85, 115, 140, 160, 180, 200, 220, 249 (from bottom to top). Each trace is scaled with its maximum amplitude.

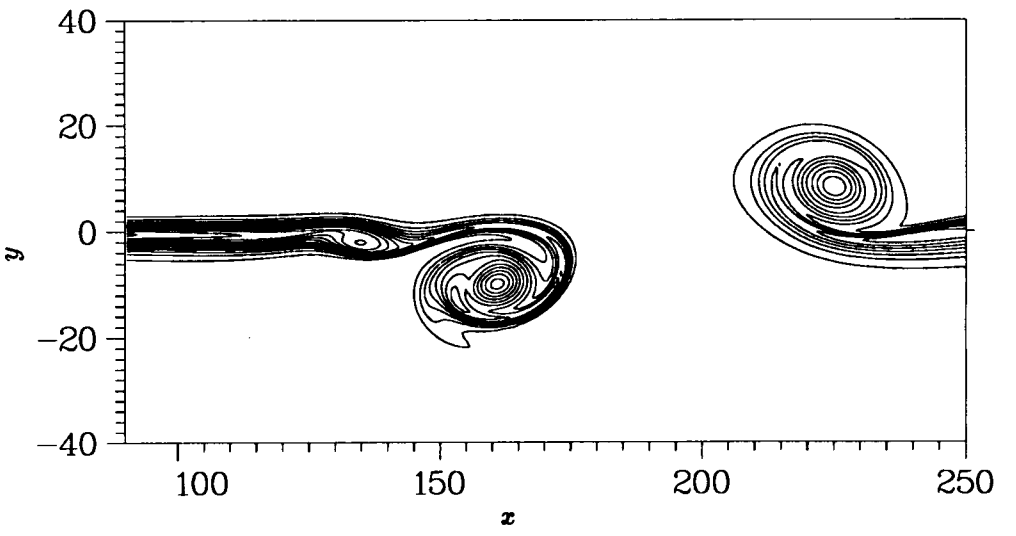

FIGURE 5. Contours of vorticity during the initial transient, showing the startup vortex pair.

appears to be unavoidable). The wavepacket is associated with the start-up vortex clearly seen in the downstream part of Figure 5. One can therefore conclude that the numerically generated velocity profile is indeed *convectively* unstable, the start-up transient being effectively a convolution of the initial state and the impulse response. Furthermore, one notes that, as soon as the wavepacket hits the downstream boundary, a sharp variation instantaneously takes place in the signal measured at the inflow. This local inhomogeneity in turn generates, after suitable filtering by the mean flow, a second wavepacket which also propagates downstream. It appears that the self-excited noisy state is induced by multiple reflections at the inflow and outflow boundaries of the computational domain. But temporally amplified vorticity waves cannot propagate upstream since the flow is convectively unstable!

Such is not the case for the pressure fluctuations prevailing outside the shear layer: Figure 6 presents statistical averages of various fluctuating variables plotted as a function of the cross-stream coordinate y. Two distinct regions are clearly in evidence: an exponential decay (linear on the semi-log plot) region followed by a much slower decay rate in the farfield region. The transition between the two regions is well-defined. The velocity in the second region might be associated with algebraically decaying pressure fluctuations generated by spatial inhomogeneities of the vorticity field due to modulations (Crighton & Huerre 1984) or pairing events (Gutmark & Ho 1985). Another likely candidate is the pressure field generated by multiple reflections at the inflow and outflow boundaries (strictly speaking, such a terminology is not legitimate: the potential flow is governed by an elliptic Poisson equation and information is transmitted instantaneously everywhere). Levels of constant mean-square v velocity are displayed in Figure 7. Levels are equally distributed on a log scale (two levels per decade). One observes a strong maximum at the outflow boundary, with equally separated contours in the downstream portion of the domain. Slower decay takes place in the upstream region, as indicated by increasing separation between neighboring contours. One may therefore infer that the v fluctuations in that region are due to pressure waves "radiating" towards the inflow boundary.

The following scenario emerges: the flow is locally convectively unstable from the point of view of vorticity fluctuations, but the global dynamics of the flow is dominated by a feedback loop (Laufer & Monkewitz 1980, Ho & Huerre 1984). The downstream branch consists of rotational instability waves rolling up into vortices. The interaction between the vortical structures and the downstream boundary then generates global irrotational pressure disturbances which are immediately transmitted to the inflow boundary. These are in turn converted into hydrodynamic instability waves by the inflow boundary condition. The noisy state is due to the relatively long streamwise extent of the computational domain which does not allow for stable periodic behavior. In a sense, the numerical experiment simulates a closed flow which, at this particular value of Lx, is in a highly chaotic dynamical state. This is consistent with a closer examination of Figure 3. The power spectrum is not just a continuous broadband one, but exhibits in addition closely spaced peaks.

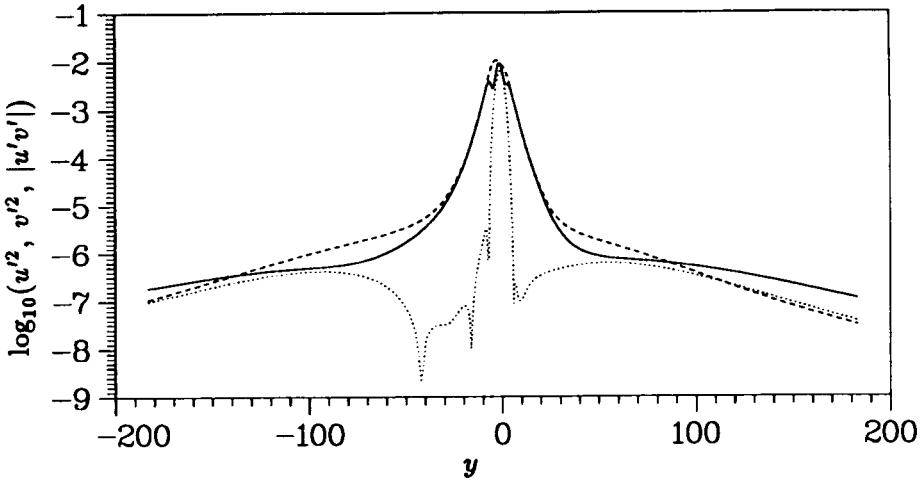

FIGURE 6. y-profiles of time-averaged statistics at $x = 125$: u'^2 (solid), v'^2 (dashed), $|u'v'|$ (dots).

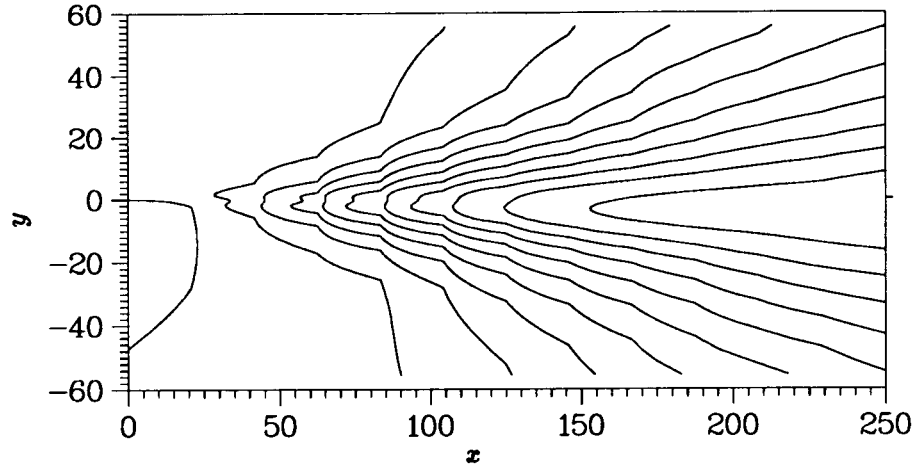

FIGURE 7. Contours of time-averaged v'^2.

Between frequencies 0.1 and 0.2 (for example) these peaks are equally spaced with the separation equal to the "box frequency", $(2\pi)\frac{1}{2}(U_1 + U_2)/Lx$. Thus the effect of the feedback appears directly in the spectrum.

The above scenario is further supported by the observed behavior of the system as the domain length Lx is varied. As mentioned previously, one sees a chaotic state when Lx is sufficiently large. For small Lx (*i.e.*, less than 100), the system approaches a steady state. For Lx not too much above 100, a periodic state is obtained (albeit after a long transient in some cases). Thus, one can think of Lx as a bifurcation parameter. Figure 8 shows the variation in amplitude of the fluctuation v velocity at two x locations as Lx increases from 100. The trend is consistent

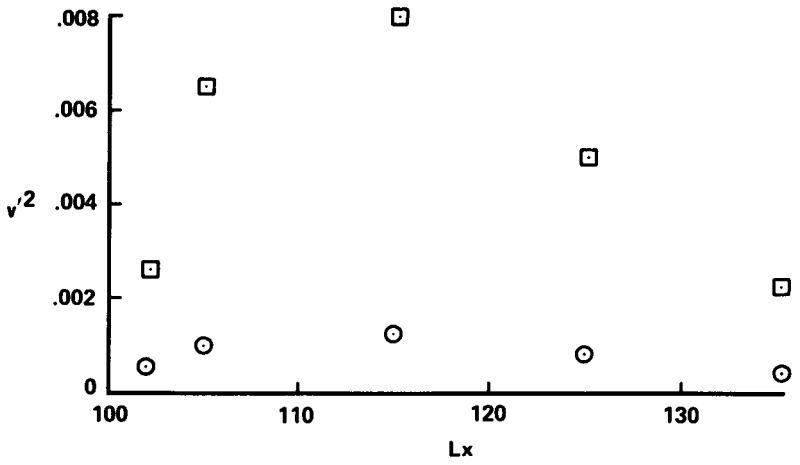

FIGURE 8. Maximum amplitude (in y) of v'^2 as a function of Lx at $x = 85$ (circles) and $x = 100$ (squares).

with a supercritical Hopf bifurcation from a steady state to a periodic orbit at approximately $Lx = 100$. A distinctive feature of all the periodic solutions obtained is that an exact integral number of instability wavelengths λ fit in the domain. For $102 \leq Lx \leq 125$, we found $\lambda = \frac{1}{4}Lx$, and for $Lx = 135$, $\lambda = \frac{1}{5}Lx$. Thus, the perturbations at the inflow and outflow boundaries are exactly in phase, indicating instantaneous communication through global pressure fluctuations. The decrease in amplitude for $Lx > 115$ is due to the largest fluctuations being associated with the outflow boundary (in these simulations, at most only one rollup is obtained). For sufficiently large Lx (in the chaotic regime), the fluctuation amplitudes at a given x become independent of Lx.

4. Finite Domains and Pressure Sources

The results of the previous section indicate that self-sustained oscillations are due to global pressure fluctuations being instantaneously transmitted between the inflow and outflow boundaries. In other words, the imposed boundary conditions do not correspond to those appropriate for an infinite (streamwise) domain. To cure this problem, one might try, in some way, to adapt the boundary conditions on the finite domain to simulate more accurately those of the infinite domain. We do not have an explicit scheme to suggest but only a very preliminary analysis.

For instance, we may consider the boundary-value problem

$$\nabla^2 p = Q, \qquad p = 0 \text{ on } S.$$

for the pressure p within a finite volume V bounded by a surface S. (Nuemann instead of Dirichlet boundary conditions may be imposed with little change in the following analysis). The source distribution $Q(\mathbf{x})$ is contained within V and takes the form

$$Q(\mathbf{x}) \equiv \frac{\partial^2 (u_i u_j)}{\partial x_i \partial x_j}.$$

Let $G(\mathbf{x}|\mathbf{x}_0)$ denote the *free space* Green's function such that

$$\nabla^2 G = \delta(\mathbf{x} - \mathbf{x}_0).$$

The function $G(\mathbf{x}|\mathbf{x}_0)$ gives the pressure field generated by a point source located at $\mathbf{x}_0$ and "radiating" in free space. From Green's theorem, one may show that $p(\mathbf{x}, t)$ satisfies the *integral* equation

$$p(\mathbf{x},t) = \int_V G(\mathbf{x}|\mathbf{x}_0) Q(\mathbf{x}_0) dV_0 + \int_S \left[p(\mathbf{x}_0) \frac{dG}{dn_0}(\mathbf{x}|\mathbf{x}_0) - G(\mathbf{x}|\mathbf{x}_0) \frac{dp}{dn_0}(\mathbf{x}_0) \right] dS_0. \quad (1)$$

The volume integral corresponds to the pressure field in *free space* due to the source distribution Q within the field. The surface integral is associated with finite domain effects. Since $p = 0$ on S, only the pressure gradient dp/dn_0 remains. The surface integral is then the pseudo-sound field generated by a source distribution of strength $-dp/dn_0$ on the surface S. It is precisely this term that is responsible for the "reflections" observed in the numerical simulations. Whether active control methods can be used to cancel such surface integral terms remains to be determined. It might also be possible to obtain approximate expressions for these terms in the case of large computational domains. One must also point out that similar source distributions can also be obtained for the Navier-Stokes equations as derived in Ffowcs Williams & Hawkins (1969).

A possible use of equation (1) might involve minimizing the component of the pressure field at the inflow ($x = 0$) due to surface sources at the outflow ($x_0 = Lx$), by adjusting the outflow boundary conditions on u and v. If dp/dn_0 is known (from the u-momentum equation), then this will require an estimate of how p at the exit plane depends on the outflow velocity boundary conditions. Whether this can be done without actually solving the Poisson equation for pressure is not presently known.

Acknowledgments

We have benefitted from stimulating discussions with Chih-Ming Ho, Sanjiva Lele, Parviz Moin and Jim Riley. In addition to support of the C.T.R. Summer Program, P. Huerre would like to acknowledge support from a Joint NASA/USC Research Interchange. This work was done while J. Buell held a National Research Council-NASA Ames Research Associateship.

REFERENCES

BERS, A. 1975 in *Physique des Plasmas* (ed. C. DeWitt & J. Peyrand), pp. 117-213. New York: Gordon-Breach.

BRIGGS, R.J. 1964 Research Monograph No. 29. Cambridge, Mass.: M.I.T. Press.

CHOMAZ, J.M., HUERRE, P. & REDEKOPP, L.G. 1988 *Phys. Rev. Lett.* **60**, 25-28.

CRIGHTON, D.G. & HUERRE., P. 1984 AIAA Paper 84-2295.

FFOWCS WILLIAMS, J.E. & HAWKINGS, D.L. 1969 *Phil. Trans. R. Soc. Lond.* **A264**, 321-342.

GUTMARK, E. & HO, C.M. 1985 *AIAA J.* **23**, 354-358.

HO, C.M. & HUERRE, P. 1984 *Ann. Rev. Fluid Mech.* **16**, 365-424.

HUERRE, P. 1987 in *Instabilities and Nonequilibrium Structures* (ed. E. Tirapegui & D. Villaroel), pp. 141-177. Dordrecht: Reidel.

HUERRE, P. & MONKEWITZ, P.A. 1985 *J. Fluid Mech.* **159**, 151-168.

KOCH, W. 1985 *J. Sound and Vib.* **99**, 53-83.

LAUFER, J. & MONKEWITZ, P.A. 1980 AIAA Paper 80-0962.

MONKEWITZ, P.A. 1988 *Phys. Fluids* **31**, 999-1006.

Page intentionally left blank

Phase decorrelation, streamwise vortices and acoustic radiation in mixing layers

By C. M. Ho[1], Y. Zohar[1], R.D. Moser[2], M.M. Rogers[2], S.K. Lele[3] AND J.C. Buell[2]

Several direct numerical simulations have been performed and analyzed to study various aspects of the early development of mixing layers. Included are (1) the phase jitter of the large-scale eddies, which was studied using a two-dimensional spatially-evolving mixing layer simulation; (2) the response of a time-developing mixing layer to various spanwise disturbances; and (3) the sound radiation from a two-dimensional compressible time-developing mixing layer.

1. Phase decorrelation in a spatially-developing mixing layer

Since the realization that spanwise coherent structures (rolls) dominate the dynamics of free shear flows, much effort has been focused on the control of these rolls in an effort to manipulate shear layers (Ho & Huerre 1984). When low-level periodic excitation is applied to force a mixing layer, the vortex formation becomes phase-locked with the forcing signal. However, experiments by Zohar et al. (1988) show that a short distance from the splitter-plate trailing-edge, the phase jitter increases abruptly indicating the loss of phase correlation. To achieve better control of the mixing layer it is important to understand the cause of this phase jitter.

The phase decorrelation of the spanwise rolls was studied using a 2-D numerical code written for spatially-developing free shear flows. The code is based on a spectral method in the vertical direction (which extends to infinity) and high-order compact finite differencing in the streamwise direction. The advantage of numerical simulations over experiments is that some possible causes of the phase decorrelation, such as 3-D effects or small-scale transition, can be isolated. A simulation was performed at a Reynolds number of 100, with 1% forcing of the inlet vertical velocity at a frequency of 0.18. (The length and velocity scales are the initial vorticity thickness and free stream velocity difference.) The velocity ratio is $R = (U_1 - U_2)/(U_1 + U_2) = 2/3$. As documented elsewhere, the inflow and outflow boundary conditions lead to feedback from the latter to the former through the pressure. This has the net effect of introducing a small amount of noise into the

1 University of Southern California
2 NASA Ames Research Center
3 Center for Turbulence Research

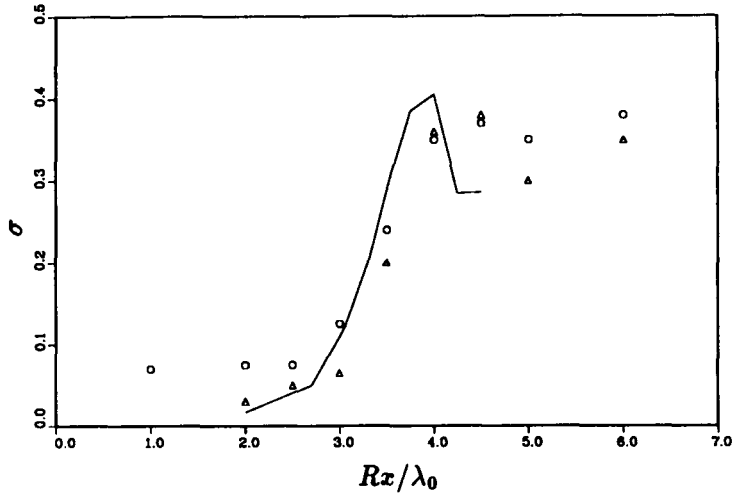

FIGURE 1. Standard deviation of the difference between successive zero crossing (σ) as a function of down-stream distance. Current results, ——— ; Experiments of Zohar *et al.*, △ , forced, o natural.

system at the inflow boundary. We believe the results should be independent of the origin of the noise, although in the present case the noise is not random.

The numerical results quantitatively confirm the experimental data, as shown in figure 1. The standard deviation of the difference between successive zero crossings of the v-velocity is plotted as a function of the downstream distance. The phase jitter of the passing coherent rolls increases sharply around the first vortex merging. Therefore, the phase jitter is primarily a 2-D phenomenon, and neither phase instability nor small-scale transition is the cause of it. The frequency spectrum of the velocity fluctuations, shown in figure 2, indicates that the contamination of the subharmonic mode by background noise is responsible for the loss of the phase information. The subharmonic mode is amplified as an unstable mode from the noise via energy transfer from the fundamental. Consequently, the resulting paired rolls are not phase-locked with the forcing signal.

2. Three-dimensional temporally-evolving mixing layers

Plan-view shadowgraph pictures taken by Konrad (1976) clearly reveal the existence of periodically distributed streamwise streaks, positioned in the braid region between the large coherent spanwise rollers of their mixing layer. These streaks are a result of counterrotating pairs of streamwise vortices (Bernal & Roshko 1986) that arise from a secondary instability of the plane mixing layer. Pierrehumbert & Widnall (1982) have used linear stability analysis to show that the most amplified spanwise wavelength is about 2/3 of the streamwise wavelength of the large coherent rollers for a class of Stuart (1967) vortices with a vorticity distribution similar to that of experimental mixing layers. They also found that the growth-rate curve is fairly flat around this most amplified wavelength. This wavelength ratio is in good

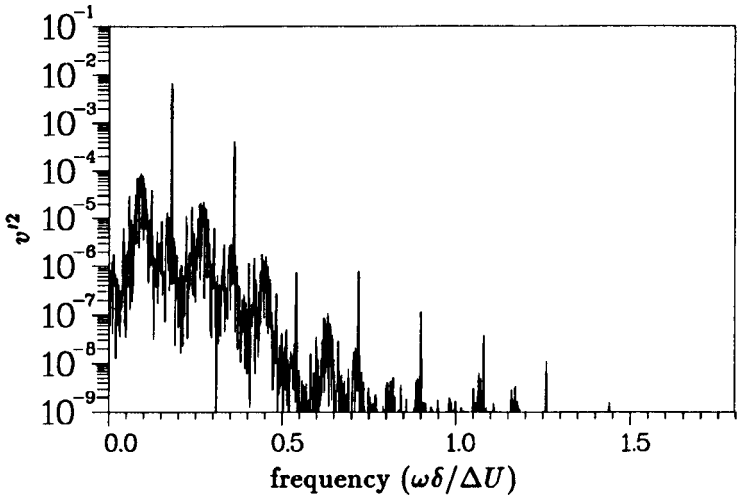

FIGURE 2. Spectrum of the cross-stream velocity (v) at $x/\delta = 140$ and $y = 0$.

agreement with that of experimentally observed structures and was also found to remain constant after the merging or pairing of the coherent rolls (Huang & Ho 1988). The mechanism by which this ratio remains constant during a pairing (i.e., how the spacing of the streamwise vortices doubles) is not understood.

A three-dimensional temporally-evolving shear layer code was used to study the development of mixing layers in the presence of spanwise disturbances. The temporal nature of the simulation permits the direct use of spectral methods in the periodic streamwise and spanwise directions. The cross-stream direction is mapped onto a uniform grid in a finite domain using a cotangent mapping and the spatial dependence of each dependent variable in this direction is represented by a Fourier series in the mapped domain (see Cain, Ferziger & Reynolds 1984).

In order to estimate the most unstable spanwise wavelength of a mixing layer during both roll up and pairing the code was modified to ensure that the three-dimensional disturbances remained small (and thus could be treated as linear). This rescaling of the disturbance in no way affects the development of the two-dimensional base flow. The spanwise periodic boundary condition requires that all spanwise disturbances must have an integral number of wavelengths in the computational domain. In order to permit a "natural" wavelength selection it is thus necessary to use a very large spanwise computational domain compared to the expected most unstable spanwise wavelength. This will ensure that the flow can select the wavelength of its choice rather than one imposed by the computational box. Each spanwise wavenumber is initialized with a small disturbance and the growth (or decay) rate of the disturbance in each wavenumber is recorded as the two-dimensional mixing layer undergoes first a roll up and then a pairing. The initial streamwise disturbances used were eigenfunctions determined from inviscid linear theory (Rayleigh eigenfunctions).

Plots of the growth rate of each spanwise wavenumber at two times in the mixing

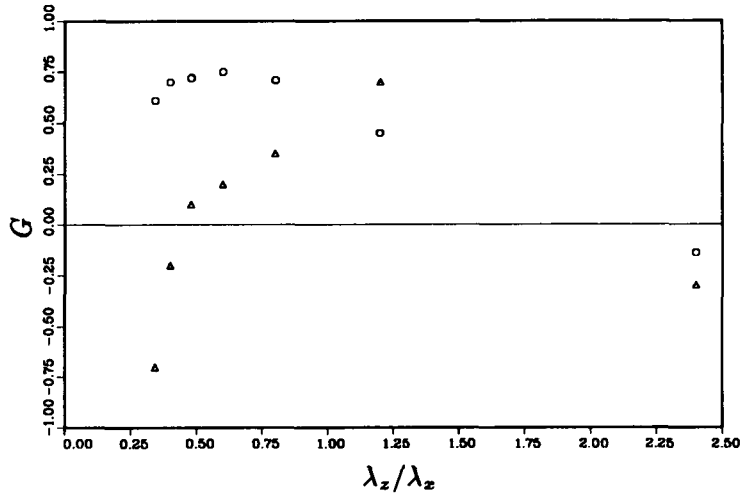

FIGURE 3. Growth rates (G) of Fourier modes of with spanwise wave-length λ_z at two times: o , roll up ($t = 16\delta/U$) and $\triangle$, pairing ($t = 25.5\delta/U$).

layer development are shown in figure 3. At early time, when the layer has rolled up but not yet paired, the most unstable wavelength is about 60% of the streamwise wavelength. When vortex pairing occurs, the amplified band of streamwise vortex disturbances shifts toward longer wavelengths, as can be seen in figure 3. The most amplified wavelength is then about twice the wavelength before pairing. Thus the most amplified wavelength of the streamwise vortices remains proportional to the local wavelength of the coherent structures, in agreement with the experimental observations.

This analysis suggests a mechanism by which the experimentally observed spanwise scale change could occur at a pairing; that is, the longer wavelength modes begin to grow faster than the mode at the originally dominant scale. However, there are two major shortcomings of the analysis. The first is that it is linear, and there may be important non-linear effects. The second is that only local (in time) growth rates are considered, whereas the observed strength of a given Fourier mode depends on the time-integral of the growth.

To address these difficulties, a fully non-linear computation was performed. This simulation was done using an improved numerical method based on a hyperbolic tangent mapping of the cross-stream (y) coordinate. The simulation was initialized with an array of weak streamwise vortices corresponding to the most unstable spanwise wavelength (60% of the streamwise wavelength). The subharmonic in the spanwise direction was also excited but at half the amplitude. It is this subharmonic which should grow to become dominant if there is to be a scale change after a pairing. Energies in four of the Fourier modes in the simulation are shown as a function of time in figure 4. The fundamental and subharmonic of the main Kelvin-Helmholtz roll up ($k_z = 0$) are shown indicating the time at which roll up (when the fundamental is maximum) and pairing (when the subharmonic is maximum)

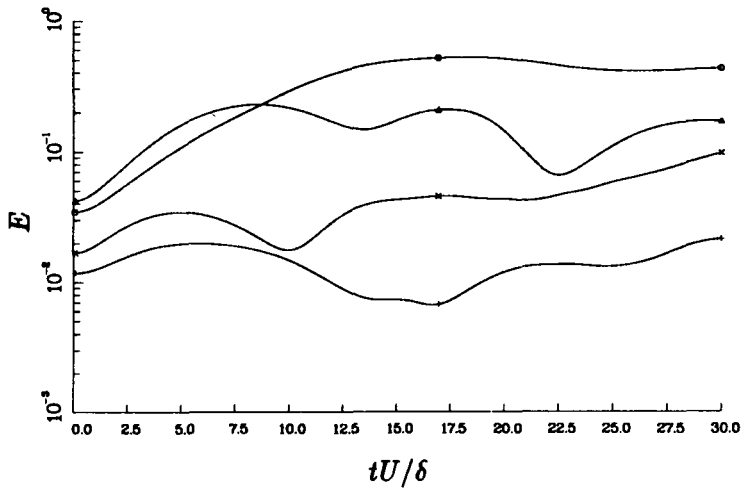

FIGURE 4. Evolution of the energy in four Fourier modes: △ , fundamental Kelvin-Helmholtz mode, ○ subharmonic Kelvin-Helmholtz mode, × fundamental streamwise vortex mode, + , subharmonic streamwise vortex mode.

occur. Note that the subharmonic of the mode representing the streamwise vortices ($k_x = 0$), does not grow or become dominant after the pairing. Thus there is no indication of a spanwise scale change in this simulation. The reason for the discrepancy between the fully non-linear simulation and both the experimental observations and linear analysis is not known. This is a problem for future research.

Another form of spanwise disturbance that was studied consists of a spanwise variation of the vorticity thickness. Such flows could be difficult to realize in the laboratory and numerical simulation provides a good means to study their behavior.

Several simulations were made using an initially sinusoidal spanwise variation (one period in the computational domain) of vorticity thickness with a maximum to minimum thickness ratio of two. As before, initial streamwise disturbances were determined from inviscid stability theory. The spanwise extent of the computational box was five times the wavelength of the most unstable mode in the initially thin region of the layer. When forced by the eigenfunction associated with the most unstable frequency of the layer at its thinnest point, roll up was observed to occur only in this region. Further simulations were made with the addition of an eigenfunction at the subharmonic frequency at various phases relative to the fundamental. In these cases the layer rolled up and paired at the thin location while a roll up occurred at the thick location, ultimately leading to one spanwise vortex (figure 5). Figure 6 shows the behavior at an earlier time. At the thin location (figure 6a) two well-defined rollers have developed in a manner similar to a two-dimensional layer with the same streamwise disturbances. At the thick location (figure 6b) a weak roll up of two vortices has started. Intermediate locations show intermediate behavior (figure 6c). Slightly later the pairing at the thin location is nearing completion as it does in the two-dimensional case. At the thick location the forward

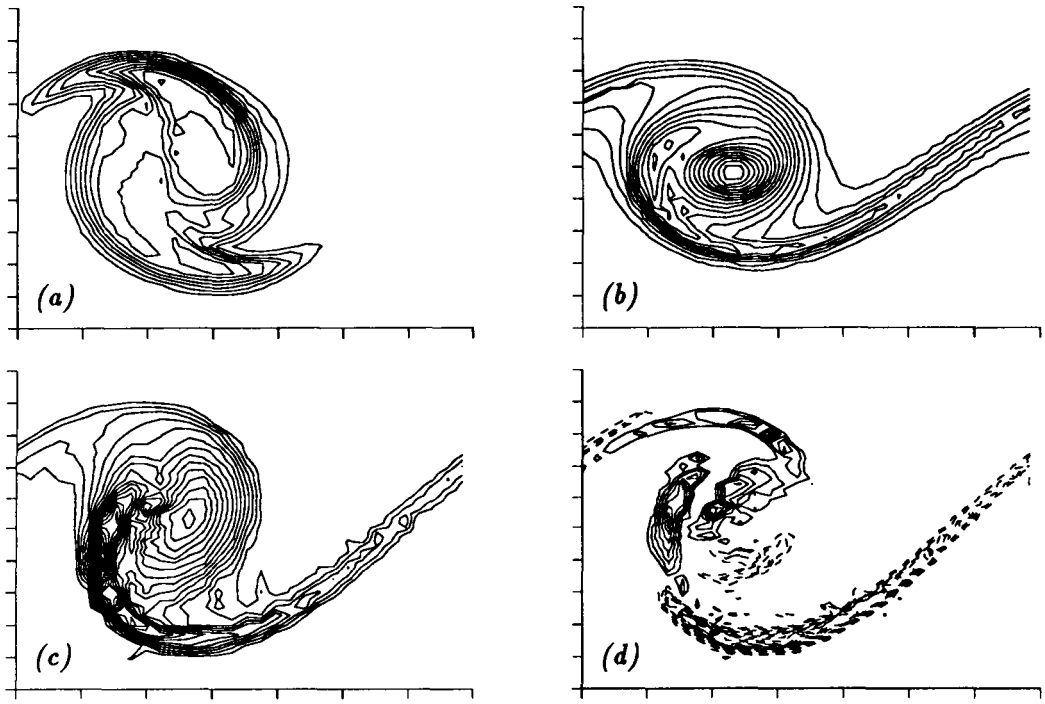

FIGURE 5. Vorticity distribution in x-y planes at a late time, $t = 19.9\delta/U$. (a) spanwise vorticity, ω_z, at the initially thin location (peak level -1.2); (b) spanwise vorticity, ω_z, at the initially thick location (peak level -1.9); (c) spanwise vorticity, ω_z, at location half way between (a) and (b) (peak level -1.8); (d) streamwise vorticity, ω_x, at same location as (c) (levels ranging from -0.7 to 0.4, dashed contours correspond to negative contour levels).

vortex lump has been almost completely absorbed by the rear vortex lump as the full roll up of figure 5b is being approached (this stage bears some resemblance to the two-dimensional "shredding" behavior observed when the fundamental and subharmonic disturbance have a relative phase that inhibits pairing). Intermediate locations are again intermediate in behavior.

During this process the blending of rollers at different locations is associated with the development of streamwise vorticity. Initially there is no streamwise vorticity anywhere in the domain and by symmetry none ever forms at the thinnest and thickest spanwise sections of the layer. In the intermediate regions, however, significant streamwise vorticity does develop. Figure 6d illustrates its form at a section half way between the thickest and thinnest locations. From this section the streamwise vorticity structure appears to resemble the streamwise vortices typical of the secondary instability described earlier. However, a three-dimensional surface plot shows that, rather than roughly axisymmetric streamwise vortices, this section represents a cut through a slab-like structure of streamwise vorticity that extends the entire width from the thinnest to thickest point of the layer. As the roll up

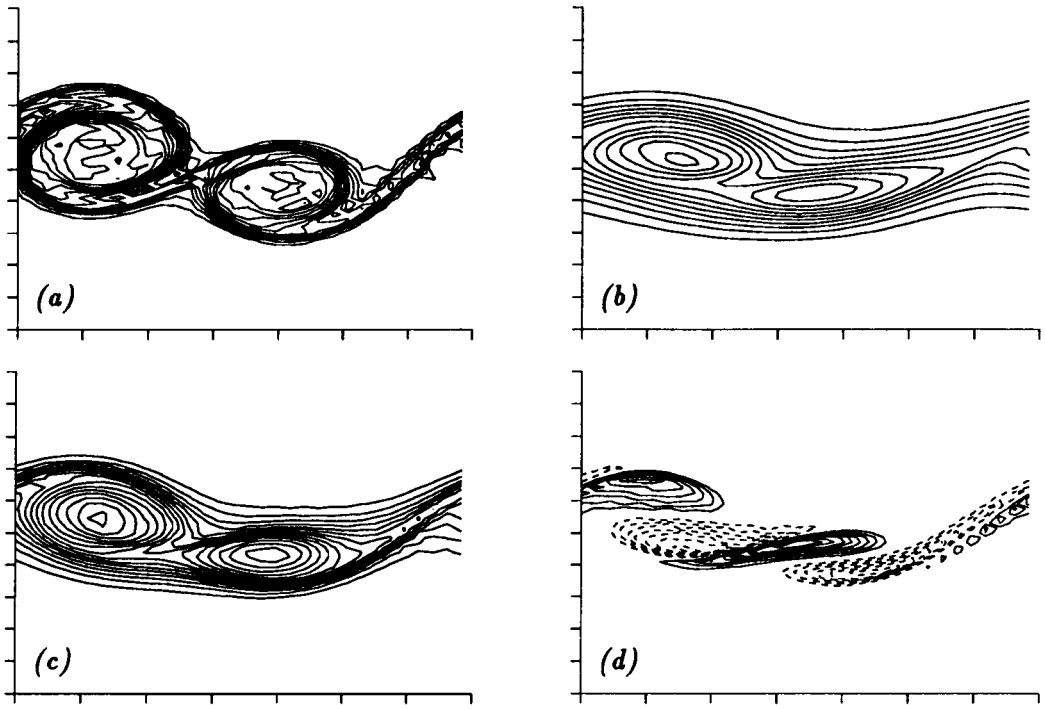

FIGURE 6. Vorticity distribution in x-y planes at an early time, $t = 12.0\delta/U$. (a) spanwise vorticity, ω_z, at the initially thin location (peak level -1.4); (b) spanwise vorticity, ω_z, at the initially thick location (peak level -1.2); (c) spanwise vorticity, ω_z, at location half way between (a) and (b) (peak level -1.5); (d) streamwise vorticity, ω_x, at same location as (c) (levels ranging from -0.45 to 0.6, dashed contours correspond to negative contour levels).

progresses at the thick location the magnitude of the streamwise vorticity increases (up to ± 1.6) but ultimately, when the layer approaches one large two-dimensional roller it decays to the moderate levels observed in figure 5d.

Future plans include the study of the more interesting case where the ratio of the vorticity thickness of the thick to the thin region is not an integer number.

3. Acoustic radiation from vortex roll up and pairing

In low Mach number shear layers, the energy radiated by sound is a small portion of that generated by turbulence production. At higher Mach numbers the sound radiation can be a major energy sink. It was suggested by Laufer (1974) that the merging of the spanwise rolls was the dominant sound generation mechanism; however, the detailed process has never been clarified. A compressible temporally-developing shear layer code was used to study this problem. The code used high-order accurate compact finite differencing. The calculation domain contained the entire region with significant pressure fluctuations, from the near-field of shear layer vortices to the far-field region. The process of noise generation was identified by

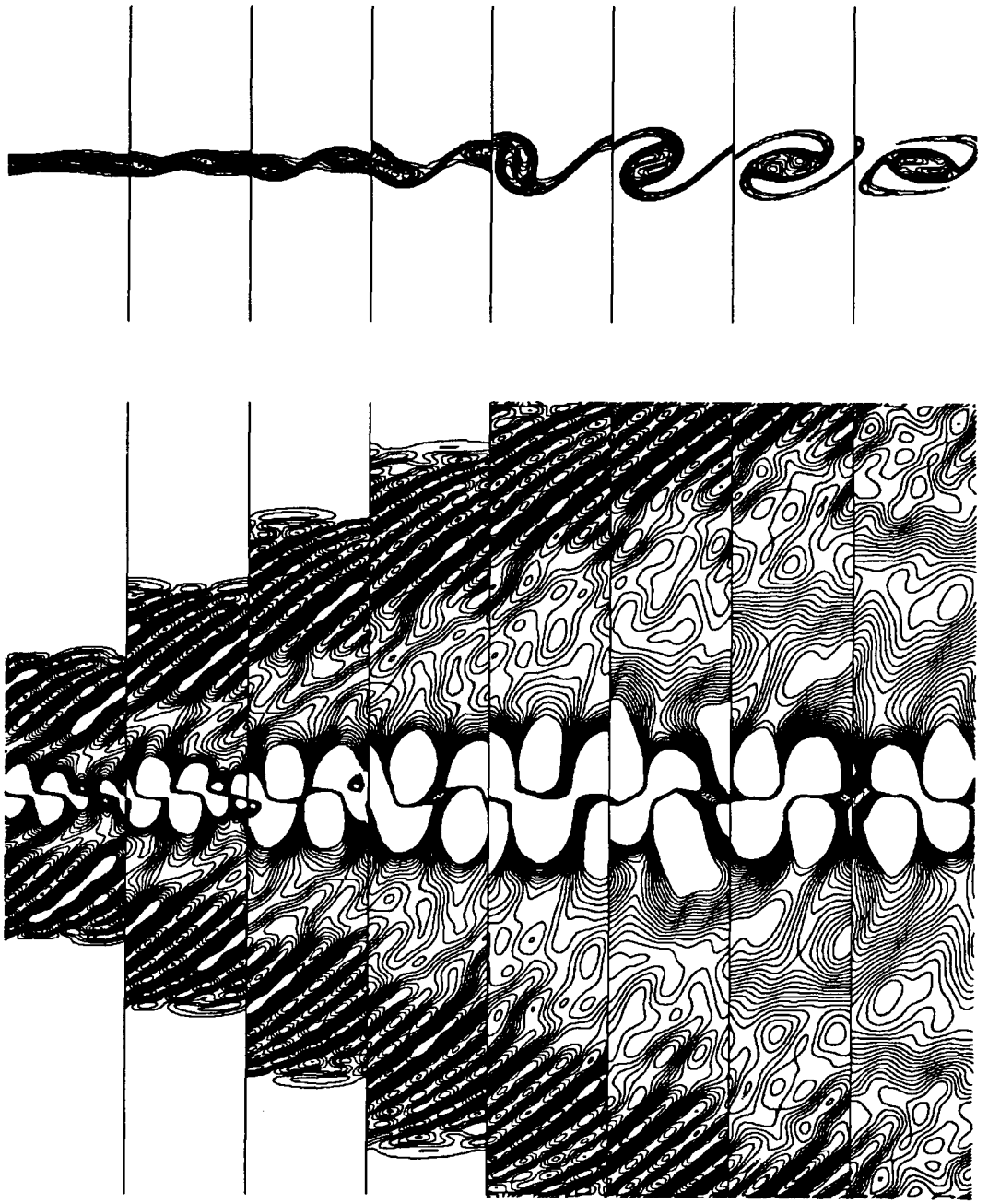

FIGURE 7. Contours of vorticity and dilatation fields. Snapshots from eight equally spaced times are arranged from left to right. The vorticity contours (shown only in a part of the domain) provide a visualization of the flow generating the acoustic waves radiating to the far-field. The plotted dilatation contours are chosen to show the waves in the far-field. Waves generated by the roll up and pairing are preceded by an initial transient.

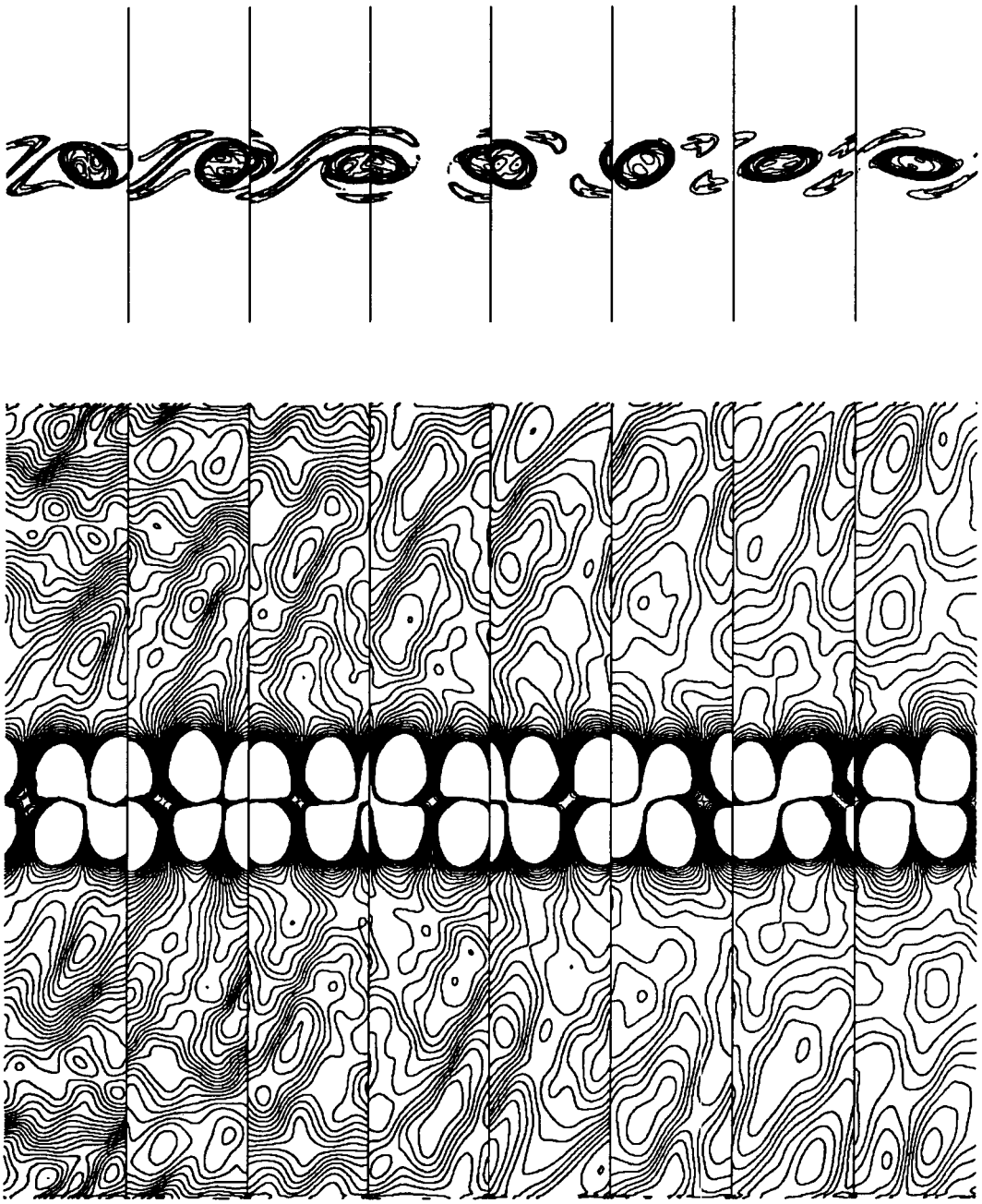

FIGURE 8. Contours of vorticity and dilatation fields. Continuation of the time series in the figures on left. Sound waves generated by the vortex unsteadiness after a vortex merger are shown. Almost two cycles of this unsteadiness are shown.

following the time evolution of vorticity, dilatation and pressure fields during the roll up and pairing events. The roll up process generated a compression wave, while the pairing event generated a compression and an expansion wave. The acoustic power emitted during a pairing was 5-6 times stronger than the emission from a roll up of the fundamental disturbance.

Examples of the time evolution of the vorticity and dilatation fields are shown in figures 7 and 8, respectively. For this case, the velocity ratio $\frac{U_2}{U_1}$ is 0.2 and $T_2 = T_1$, where the subscripts refer to the high and low speed streams. The two streams have Mach numbers of $M_1 = 1.0$ and $M_2 = 0.2$ which corresponds to a convective Mach number (as defined by Papamoschou and Roshko 1986) of $M_c = 0.4$. The calculations are performed in a frame of reference moving with $\frac{U_f}{U_1}$ of 0.4. Note that this reference speed is different from the propagation speed of the vortices, $\frac{U_c}{U_1}$ of 0.6. It was verified that the reference speed had no effect on the results described here. The panels in these figures correspond to 8 different snapshots of the flow as it evolves. The roll up and pairing is evident from the vorticity contours. The dilatation pattern associated with each vortex is a quadrupole, and the acoustic waves radiate during the roll up and vortex merging stage. The vortex merging process generates first a compression wave while the Reynolds stresses extract work from the mean flow. Later in time the Reynolds stress is negative in the shear layer, indicating that energy is being transferred from the shear region back to the mean flow. At the same time, sound is radiated to the surroundings in the form of an expansion wave.

In the far-field the density, pressure and velocity fluctuations were computed. The acoustic energy flux radiated to the far-field was also monitored. It was found that the far-field fluctuations satisfied plane wave acoustic relations exceedingly well. The fluctuations in the near-field (pressure and velocity) were found to decay exponentially away from the shear layer. This near-field region was found to scale with the hydrodynamic instability wavelength.

In the future the Mach number dependence of the radiated acoustic flux will be studied, and acoustic radiation from spatially-evolving mixing layers will be studied.

Acknowledgement

The first two authors (C.M.H. & Y.Z.) wish to acknowledge the generous support of the Center for Turbulence Research for making this work possible. This work was partially supported by ONR.

REFERENCES

BERNAL, L. P. & ROSHKO, A. 1986 Streamwise Vortex Structure in Plane Mixing Layers. *J. Fluid Mech.* **170**, 499–525.

CAIN, A. B., FERZIGER, J. H. & REYNOLDS, W. C. 1984 Discrete Orthogonal Function Expansions for Non-uniform Grids Using the Fast Fourier Transform. *J. Comp. Phys.* **56**, 272–286.

HO, C. M. & HUERRE, P. 1984 Perturbed Free Shear Layers. *Ann. Rev. Fluid Mech.* **16**, 365–424.

HUANG, L. S. & HO, C. M. 1988 Small-Scale Transition in Plane Mixing Layers. *in preparation.*

KONRAD, J. H. 1976 An Experimental Investigation of Mixing in Two-Dimensional Turbulent Shear Flows with Applications to Diffusion-Limited Chemical Reactions. *Intern. Rep. CIT-8-PU,* Calif. Inst. Tech., Pasadena.

LAUFER, J. 1974 On the Mechanism of Noise Generation by Turbulence. In *Omaggio a Carlo Ferrari*p. 451, Libreria Editrice Universitaria Levrotto and Bella, Torino.

PAPAMOSCHOU, D.& ROSHKO, A. 1986 Observations of Supersonic Free Shear Layers. *AIAA Paper 86-0162.*

PIERREHUMBERT, R. T. & WIDNALL, S. E. 1982 The Two- and Three-Dimensional Instabilities of a Spatially Periodic Shear Layer. *J. Fluid Mech.* **114**, 59-82.

STUART, J. T. 1967 On Finite Amplitude Oscillations in Laminar Mixing Layers. *J. Fluid Mech.* **29**, 417-440.

ZOHAR, Y., FOSS, J. K., HO, C. M. & BUELL, J. C. 1988 Phase De-correlation in Plane Mixing Layers. in preparation.

Page intentionally left blank

A numerical study of bifurcations in a barotropic shear flow

By P. Huerre[1], L. R. Keefe[2], G. Meunier[1], M. M. Rogers[3], L. G. Redekopp[1], and P. R. Spalart[3]

1. Introduction

In the last few years, more and more evidence has emerged suggesting that transition to turbulence may be viewed as a succession of bifurcations to deterministic chaos. Most experimental and numerical observations have, for the most part, been restricted to Rayleigh-Benard convection and Taylor-Couette flow between concentric cylinders. The goal of the present study is to accurately describe the bifurcation sequence leading to chaos in a two-dimensional temporal free shear layer on the β-plane.

The β-plane is a locally-Cartesian reduction of the equations describing the dynamics of a shallow layer of fluid on a rotating spherical planet. It is a valid model for large-scale flows of interest in meteorology and oceanography. The mathematical formulation involves the following vorticity equation

$$\left(\frac{\partial}{\partial t} + U(y)\frac{\partial}{\partial x}\right)\nabla^2\Psi + J(\nabla^2\Psi, \Psi) + \left(\beta - U''(y)\right)\Psi_x = \frac{1}{Re}\nabla^4\Psi,$$

where $U(y)$ is the basic hyperbolic-tangent velocity profile, Ψ is the perturbation stream function, and Re is the Reynolds number. The symbol β denotes the gradient of the planetary vorticity. Inviscid linearized stability analyses (Dickinson and Clare 1973) reveal that the flow is unstable within a neutral curve in the $\beta - k$ plane as sketched in Figure 1 (from Burns & Maslowe 1983), k denoting the streamwise wavenumber. Thus β is a convenient control parameter with which one can bring about qualitative changes in the attractor as a function of the supercriticality $|\beta - \beta_c|$. The limit of the classical mixing layer is approached as β goes to zero.

2. Numerical approach

The three-dimensional code developed by M. Rogers has been adapted to the present problem by adding the appropriate β terms in the equations. The basic velocity profile has been changed to $U(y) = \tanh(y)$ (a body force is applied to hold that velocity profile against viscous diffusion). We recall that periodic boundary conditions are chosen in the streamwise direction and that a Cain mapping is used in

1 Department of Aerospace Engineering, University of Southern California
2 Center for Turbulence Research
3 NASA/Ames Research Center

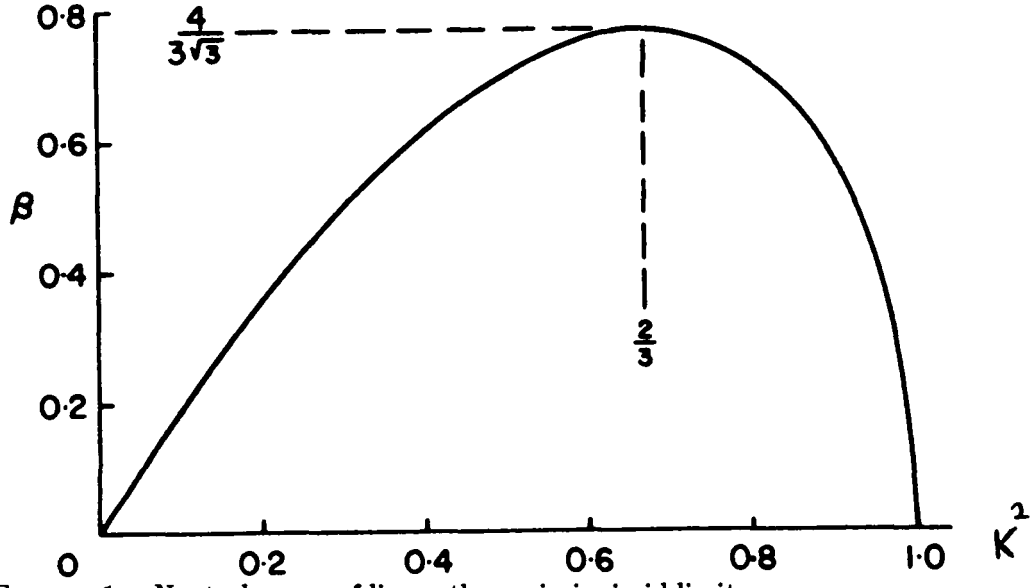

FIGURE 1. Neutral curve of linear theory in inviscid limit.

the cross-stream direction. The exponential tails in y for the perturbation variables are known to decay more slowly than in the $\beta = 0$ case and the value of the B stretching factor in y had to be increased up to 10 (typical values are around 2) to properly account for this phenomenon. The numerical code is well-behaved with 16 by 96 grids, but the execution is slow (8 Mflops on the Cray 2) due to the small length of the vectors.

3. The first Hopf bifurcation

Numerical simulations were conducted at $Re = 1000$ and a streamwise box length corresponding to the critical wavenumber $k_c = \sqrt{2/3}$. The critical value $\beta_c = 4/(3\sqrt{3})$ was well approximated and linear growth rates were also found to be consistent with inviscid stability theory.

As β decreases below β_c, the basic flow bifurcates to a finite-amplitude *traveling-wave state* which takes the form of a vortex as shown on Figure 2. As a result of the β effect, the Kelvin's cat's-eye pattern is shifted off the axis $y = 0$. The traveling wave is characterized by a circular frequency ω and normalized amplitude

$$|A| \equiv \max_y \hat{v}(y, k_c).$$

The normal form pertaining to a supercritical Hopf bifurcation is known to be

$$\frac{dA}{dt} = -i[\omega_c + \omega_\beta(\beta - \beta_c)]A - \Gamma|A|^2 A, \tag{1}$$

where A is the complex amplitude of the wave and ω_c the frequency at $k = k_c$, $\beta = \beta_c$. Other quantities appearing in (1) are $\omega_\beta \equiv \partial\omega/\partial\beta|_c$ and the Landau

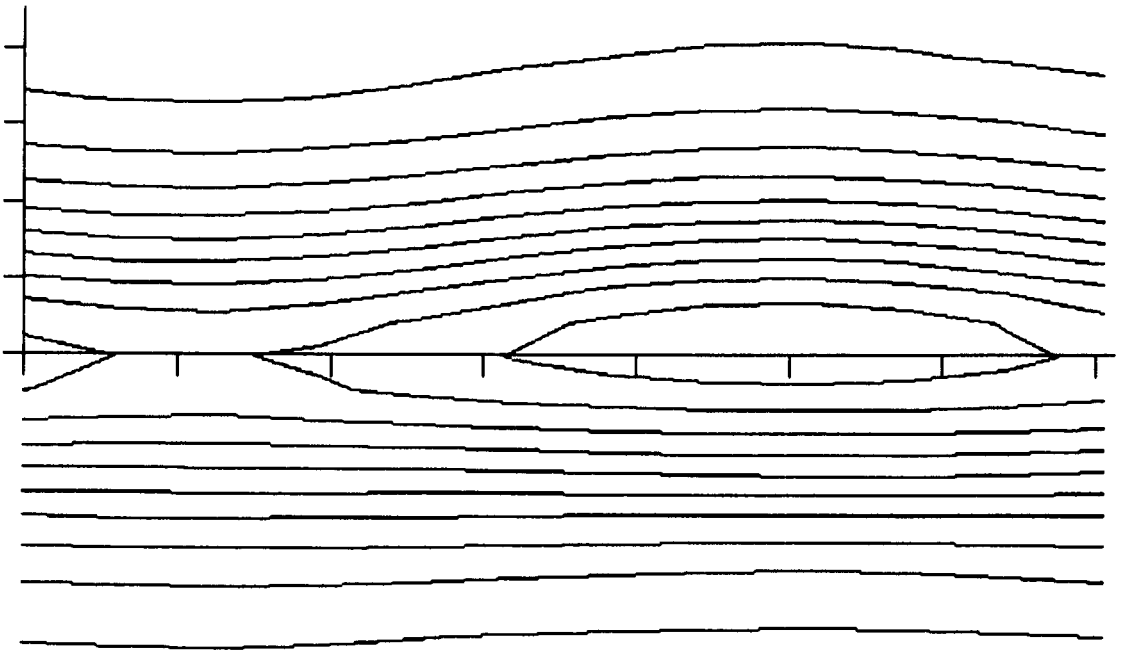

FIGURE 2. Isovorticity contours at $\beta = 0.7$, $Re = 1000$, $k = k_c$.

constant $\Gamma = \Gamma_r + i\Gamma_i$. An elementary analysis of (1) indicates that as β decreases below β_c, the solution of (1) bifurcates from the basic flow $A = 0$ to a limit cycle of amplitude

$$|A|^2 \propto \beta_c - \beta \tag{2}$$

and frequency

$$\omega - \omega_c \propto \beta_c - \beta. \tag{3}$$

The quantities $|A|^2$ and ω are represented as a function of β on Figures 3 and 4 respectively. The exact linear value of ω has also been plotted on Figure 4. One notes that $|A|^2$ and ω do vary linearly with decreasing β in the vicinity of β_c, in agreement with (2) and (3). The value of ω at $\beta = \beta_c$ is indeed equal to $\omega_c = \sqrt{2}/3$. Finally one notes a nonlinear frequency shift in the value of ω when compared to linear estimates.

We attempted to compare the values of the slopes of these curves with the analytical results obtained by Churilov (1988), Churilov and Shukhman (1986, 1987), and Lipps (1965). There were large discrepancies and we suspect that the critical-layer structure is not satisfactorily resolved with the present distribution of points in the y direction.

4. A preliminary look at pairing in the presence of dispersion

To test the validity of the code, numerical simulations of the evolution of 3 vortices were conducted in a computational domain of length $6\pi/k_c$ at $\beta = 0.2$. The

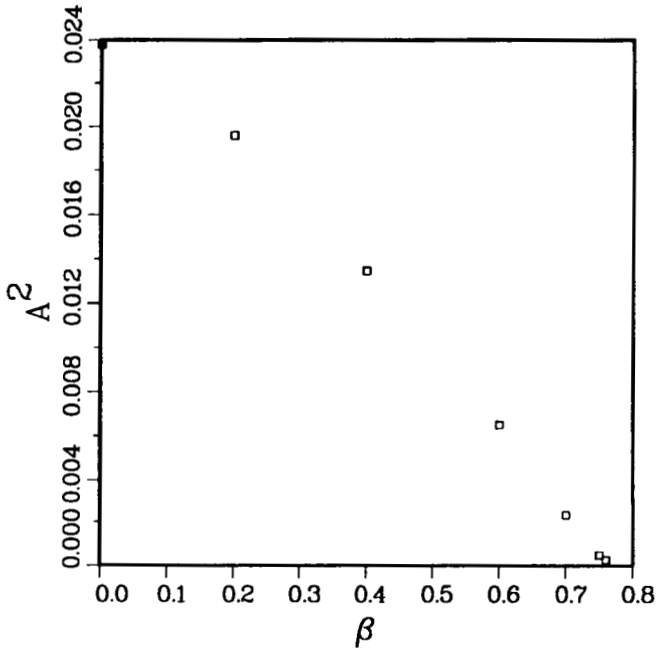

FIGURE 3. $|A|^2$ versus β at $Re = 1000$, $k = k_c$.

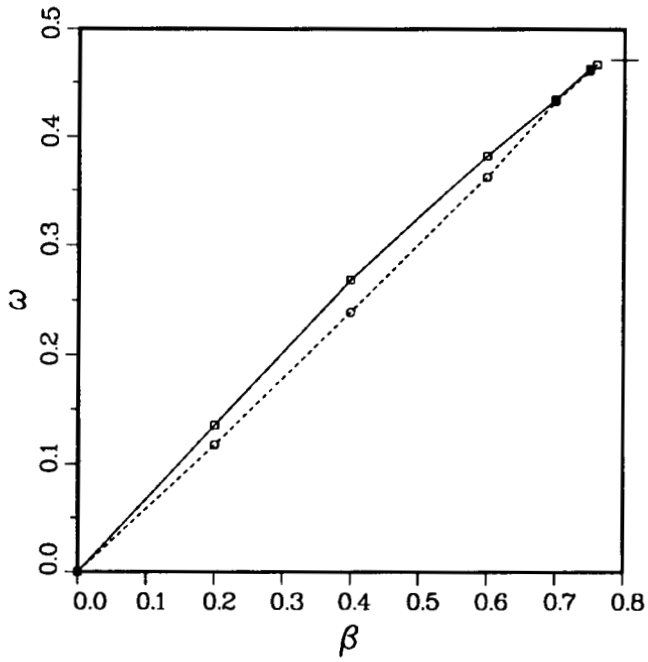

FIGURE 4. ω versus β at $Re = 1000$, $k = k_c$. —, nonlinear frequency; - - -, linear frequency.

fundamental k_c was given a finite energy level at $t = 0$, the 2 subharmonics at $k_c/3$ and $2k_c/3$ being initialized to low levels. Figures 5 a, b, c show the resulting evolution. One notes the nutation of the vortical structures in the course of time, indicated by a tilting motion. Pairing eventually takes place between 490 and 500 time steps with a corresponding energy transfer from the k_c to the $2k_c/3$ component. At $\beta = 0.2$, the $k_c/3$ component lies in the linearly stable domain and it is not triggered by nonlinear interactions. Thus, no further pairing events are observed and the asymptotic state consists of 2 vortices. This is distinctly different from the homogeneous mixing layer case where pairings take place until one observes a triple vortex condition in the computational domain.

5. Future work

The results obtained so far, namely the fact that a Hopf bifurcation takes place at $\beta = \beta_c$, suggest that nontrivial chaotic dynamics are likely to occur within subregions of the neutral curve. To back up this claim, we note that in the vicinity of β_c, the streamwise modulations of the complex amplitude $A(x,t)$ are governed by the p.d.e. equivalent of (1), i.e.:

$$\frac{\partial A}{\partial t} = -i\left[\omega_c + \omega_\beta(\beta - \beta_c)\right]A - \omega_k \frac{\partial A}{\partial x} + \frac{i}{2}\omega_{kk}\frac{\partial^2 A}{\partial x^2} - \Gamma|A^2|A.$$

This Ginzburg-Landau equation is known to give rise to chaos via a modulational instability mechanism [Keefe (1985)]. In the present context, we therefore suspect that amplitude and phase modulations applied to a row of vortices would induce a disordered evolution as the streamwise extent of the computational domain is increased.

To test this hypothesis, we need to considerably increase the reliability and speed of the numerical code for low-wavenumber simulations.

Acknowledgements

P. Huerre and G. Meunier would like to acknowledge support from the Summer Program at the Center for Turbulence Research and a Joint NASA/USC Research Interchange.

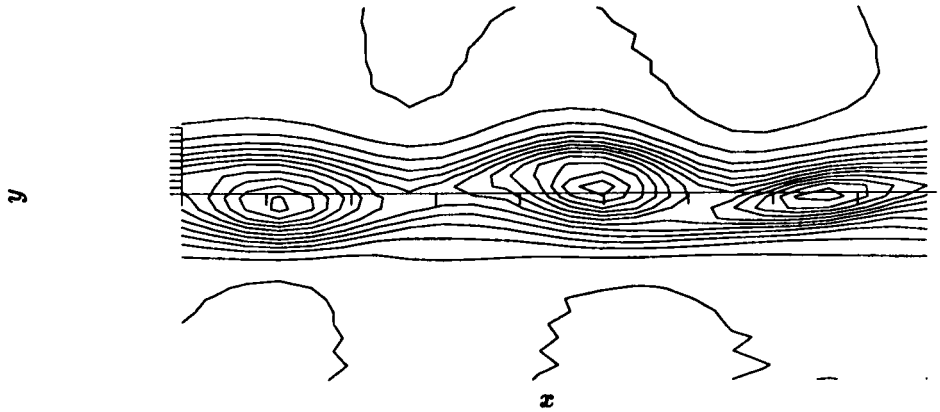

(A)

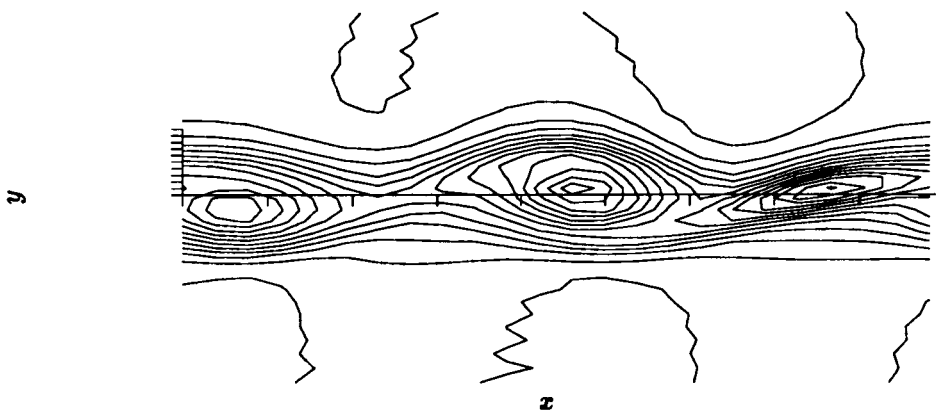

(B)

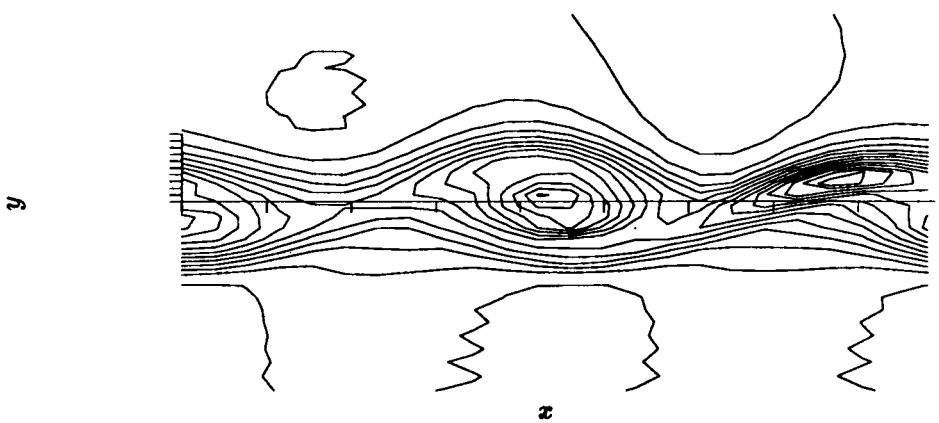

(C)

FIGURE 5A, B, C. Evolution of 3 vortices in a domain of size $6\pi/k_c$ at $\beta = 0.2$, $Re = 200$.

REFERENCES

BURNS, A. G. & MASLOWE, S. A. 1983 . *J. Atmos. Sci.* **40, 1,** 3.

CHURILOV, S. M. 1988 The nonlinear stabilization of a zonal shear flow instability, preprint.

CHURILOV, S. M. AND SHUKHMAN, I. G. 1986 . *Geophys. Astrophys. Fluid Dyn.* **36,** 31-52.

CHURILOV, S. M. AND SHUKHMAN, S. G. 1982 . *Geophys. Astrophys. Fluid Dyn.* **38,** 145-175.

DICKINSON, R. E. AND CLARE, F. J. 1973 . *J. Atm. Sci.* **30,** 1035-1049.

KEEFE, L. R. 1985 . *Stud. Appl. Math.* **73,** 91-153.

LIPPS, F. B. 1965 . *J. Fluid Mech.* **21,** 225-239.

Page intentionally left blank

Center for Turbulence Research
Proceedings of the Summer Program 1988

Dynamics of coherent structures in a plane mixing layer

By F. Hussain[1], R. Moser[2], T. Colonius[3], P. Moin[2,3] AND M. M. Rogers[2]

An incompressible, time-developing three-dimensional mixing layer with idealized initial conditions has been simulated numerically. Consistent with the suggestions from experimental measurements, the braid region between the dominant spanwise vortices or rolls develops longitudinal vortices or ribs, which are aligned upstream and downstream of a roll and produce spanwise distortion of the rolls. The process by which this distortion occurs has been explained by studying a variety of quantities of dynamic importance (*e.g.* production of enstrophy, vortex stretching). Other quantities of interest (dissipation, helicity density) have also been computed and are discussed. The currently available simulation only allows the study of the early evolution (before pairing) of the mixing layer. New simulations in progress will relieve this restriction.

Introduction

While there is no doubt about the occurrence of large-scale coherent structures in turbulent shear flows, there is doubt about their role and dynamical significance. Unfortunately, a mathematical definition of coherent structures or a theory of turbulence based on coherent structures has not yet been developed, nor is there any in sight. Until the development of a theoretical framework , or even to formulate one, we must continue to improve our understanding of coherent structures. Studies of coherent structures in shear flows, in particular the mixing layer, have focused on the geometric form of the structures (morphology) and the relationship of the structures to topological features of the flow (*e.g.* the stagnation line and saddle between rolls in the mixing layer); also of interest are quantitative measures of dynamical quantities such as coherent Reynolds stress and coherent production. Experimental observations of coherent structures in the mixing layer have relied on flow visualization techniques (which suffer from the indirect relationship of flow markers to the hydrodynamics) and quantitative point-wise measurements (which are unable to measure the full three-dimensional flow field). Such measurements strongly suggest the complex morphology of the coherent structures in mixing layers, in particular the counter-rotating longitudinal vortices (ribs) in the braid region between the rolls (Bernal & Roshko, 1986, Hussain, 1983). However, the details of these structures are not currently accessible from experimental data. Fortunately,

1 University of Houston
2 NASA Ames Research Center
3 Stanford University

direct numerical simulation of turbulent flows can provide the 3D flow field with adequate resolution, albeit at low Re (Metcalf *et al.*, 1987, Hussain 1986).

Several numerical simulations were performed to study the details of the coherent structures observed experimentally in mixing layers. A three-dimensional time-developing mixing layer with prescribed initial conditions was simulated. The initial conditions were chosen to produce structures similar to those observed experimentally. These simulations are different from the experiments they are meant to mimic in several important ways. First, the experimental flows are spatially developing, whereas the simulations are time developing. The time-developing simulation approximates the evolution of a structure in the spatially-developing flow as it travels downstream. Second the initial conditions do not necessarily reflect the conditions present in an experiment. In the simulations the initial conditions are very smooth and simple, there is no small-scale random motion, thus the resulting flow fields are not turbulent. These simple conditions are used so that the coherent structures can be studied in their simplest form. The question of how the observed structures evolve from conditions actually present in experiments, and how they respond to small-scale random disturbances is left to future work. Finally, the Reynolds number in the simulations is quite low compared to experiments.

The simulations were performed using a numerical method similar to that discussed by Cain, Ferziger & Reynolds (1984). In this method periodic boundary conditions are applied in the streamwise (x) and spanwise (z) directions, and Fourier series are used in these directions. An infinite domain in the cross-stream direction (y) is treated by using a coordinate transformation which maps the domain into a finite interval. Fourier series are then used in the finite interval. In the particular simulation to be discussed below, 32 Fourier modes were used in the x and z directions and 64 modes were used in the y direction. The length of the computational domain in the x direction was $4.48\pi\delta$, and in the z direction it was $2.7\pi\delta$ where δ is the initial vorticity thickness of the layer. The initial velocity field consisted of an error function velocity profile and a pair of three-dimensional disturbances. The first disturbance leads to the two-dimensional Kelvin-Helmholtz roll-up of the mixing layer and ultimately pairing, the initial spanwise vorticity in this disturbance is given by

$$\omega_z = 0.1 f_1(y)\cos(\frac{x}{1.12\delta}) + 0.05 f_2(y)\cos(\frac{x}{2.24\delta}).$$

where the functions f_1 and f_2 are Rayleigh eigenfunctions and the wave-lengths are chosen to be the most unstable and its subharmonic. The second disturbance leads to the longitudinal vortices in the braid region between the Kelvin-Helmholtz rolls. This disturbance initially consists of an array of streamwise vortices described by

$$\omega_x = 0.05 g_1(y) sin(\frac{z}{0.675\delta}) + 0.025 g_2(y) sin(\frac{z}{1.35\delta})$$

where the functions g_1 and g_2 were chosen to represent streamwise vortices and the wave-lengths were chosen to be the most unstable and its subharmonic. A Reynolds number of 1000 based on initial vorticity thickness and velocity difference was used in this simulation.

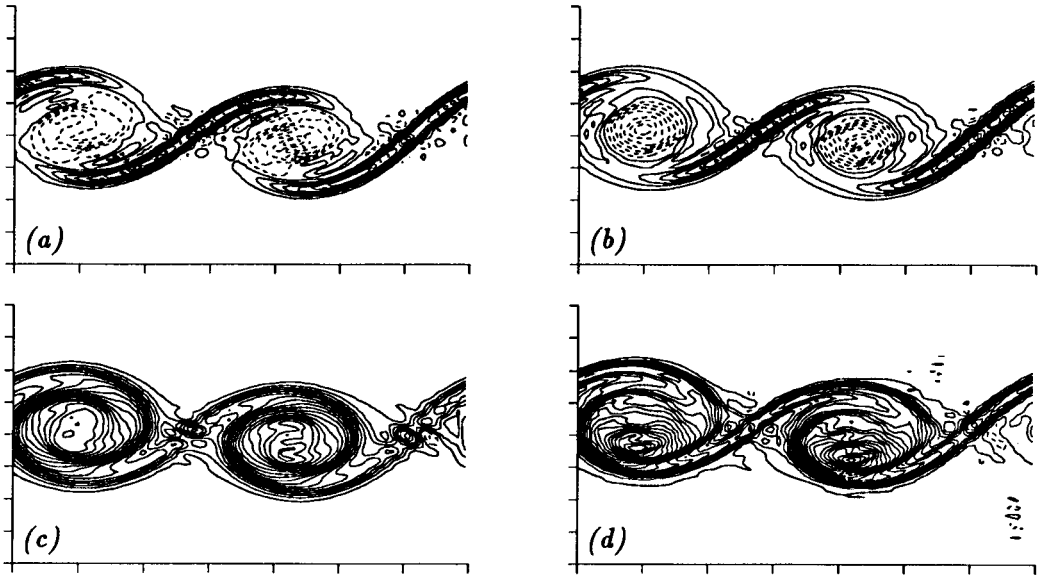

FIGURE 1. Vorticity contours in plane 1; (a), ω_x, (b), ω_y and (c), ω_z, and plane 2; (d), ω_z at time I. Contour increment is $0.1U/\delta$. Negative contours are dashed in $(a)$and (b), positive contours are dashed in $(c)$and (d). Streamwise (x) direction is horizontal; cross stream (y) direction is vertical.

Results and Discussion

For the current discussion we have selected two instants in the simulation described above: time I ($t = 26.4\delta/\Delta U$) is when the initial Kelvin-Helmholtz roll-up is saturating and the two rolls are nearly identical, and time II ($t = 35\delta/\Delta U$) is a short time later when the pairing interaction has started. To study the pairing process, a much later time is required; however, the current simulation was stopped at $t = 17.5$ because of lack of resolution. Higher resolution simulations are being performed to address questions of pairing. In the discussion to follow, two dimensional contour plots of various quantities will be presented in two planes in the flow field. The first plane (plane 1) is an x-y plane (plane of constant z) which passes through the center of the longitudinal vortices (location of maximum streamwise vorticity). The second plane (plane 2) is also an x-y plane, and it passes halfway between the longitudinal vortices (streamwise vorticity is zero in this plane).

Contours of the three components of vorticity in both planes at time I are shown in figure 1 (ω_x and ω_y are identically zero in plane 2). The role-up of the shear-layer resulting in the concentration of spanwise vorticity in two large rolls is clearly evident. Note that there is substantial spanwise vorticity in the braid region between the rolls (as much as -0.55) compared to the initial maximum spanwise vorticity (-2) As the roll-up continues, spanwise vorticity continues to be swept from the braid region; at time II (figure 2) the spanwise vorticity in the braid region has been reduced to -0.25. The streamwise and cross-stream vorticity (ω_x and ω_y in figures $1(a,b)$ are concentrated in the braid region as expected; these are the longitudinal

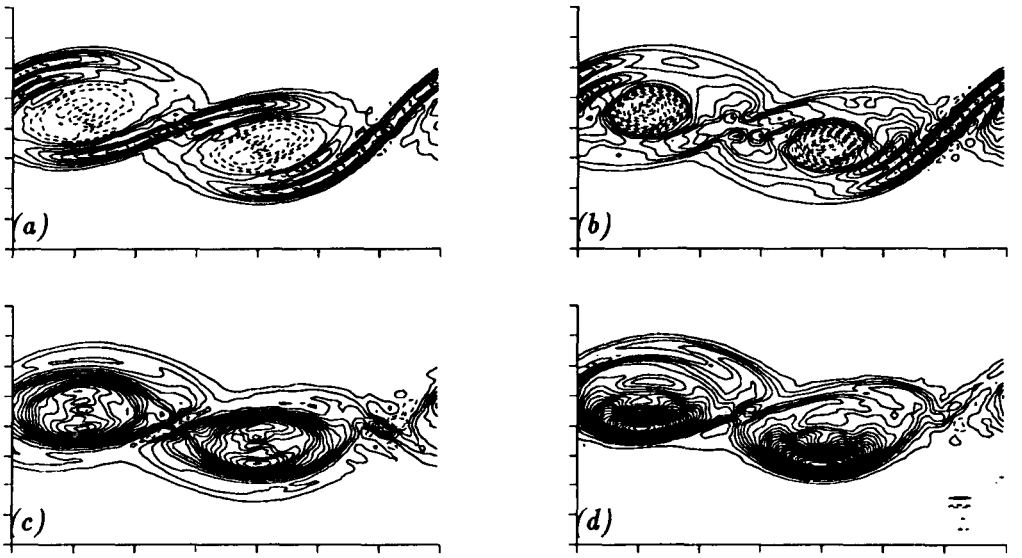

FIGURE 2. Vorticity contours in plane 1; (*a*), ω_x, (*b*), ω_y and (*c*), ω_z, and plane 2; (*d*), ω_z at time II. Contour increment is (*a*), $0.15U/\delta$, (*b,c,d*), $0.1U/\delta$. Negative contours are dashed in (*a*)and (*b*), positive contours are dashed in (*c*)and (*d*). Streamwise (x) direction is horizontal; cross stream (y) direction is vertical.

(or rib) vortices. They include both ω_x and ω_y because they are inclined. There are, of course, an array of counter-rotating rib vortices, the ones in this plane have positive vorticity but in other planes the vorticity would be negative. The rib vortices lie along the diverging separatrix of the stagnation point between the two main rolls. Therefore they are subjected to a plane strain which stretches them along the separatrix. The result is an increase in the vorticity magnitude with time ($\omega_x = 0.65$ at time I, and 0.98 at time II, see figures 1 and 2).

In the rolls there is a somewhat weaker region of streamwise and cross-stream vorticity of opposite sign to that in the ribs ($\omega_x = -0.35$ at time I). This is apparently a result of the three-dimensional distortion of the rolls by the ribs. This distortion is most apparent at time II where there is a marked difference in the spanwise vorticity contours in planes 1 and 2 (figures 2(*c,d*)). In plane 2, the spanwise vorticity is concentrated near the bottom of the rolls and is very strong there (-3.05) compared to the initial maximum spanwise vorticity (-2.0). In plane 1, the vorticity is more evenly distributed through the roll and has a maximum value of -1.85. The mechanism by which the ribs produce three-dimensionality in the rolls can be understood by examining the rate of production of enstrophy ($\omega_i S_{ij} \omega_j$, where $S_{ij} = \frac{1}{2}(\partial u_i/\partial x_j + \partial u_j/\partial x_i)$) at time II (figure 3). In plane 2 there is a region of strong enstrophy production coinciding with the concentrated region of spanwise vorticity. Above it there is also a region of negative enstrophy production. The strong production is a consequence of the stretching of the spanwise vorticity. This stretching occurs in the region between the counter-rotating rib vortices where

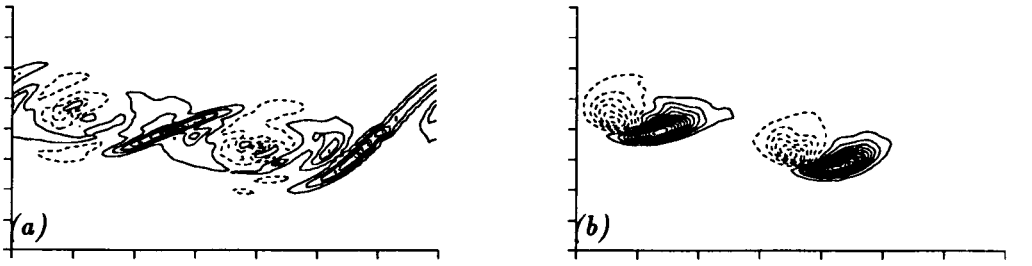

FIGURE 3. Rate of enstrophy production in (a), plane 1 and (b), plane 2 at time II. Contour increment is $0.2U^3/\delta^3$. Negative contours are dashed. Streamwise (x) direction is horizontal; cross stream (y) direction is vertical.

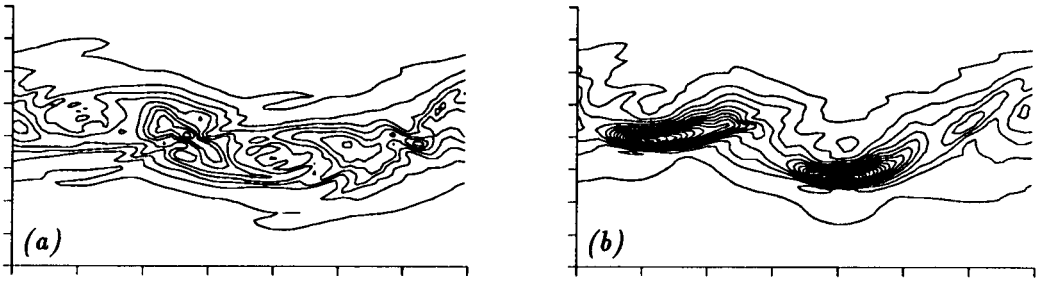

FIGURE 4. Dissipation of kinetic energy in (a) plane 1 and (b) plane 2 at time II. Contour increment is $0.0005U^3/\delta$. Streamwise (x) direction is horizontal; cross stream (y) direction is vertical.

the strain $\partial w/\partial z$ is large and negative. Between rib vortices where $\partial w/\partial z$ is positive compression occurs resulting in the negative enstrophy production mentioned above. In plane 1, which is through the center of the rib vortices ($\partial w/\partial z = 0$), the enstrophy production in the rolls is small. There is however enstrophy production in the braid region, corresponding to the stretching of the rib vortices.

Another quantity of interest is the dissipation of kinetic energy, which is shown at time II in figure 4. The dissipation is rather weak in plane 1 (0.003) compared to plane 2 (0.009). In particular, the dissipation in plane 2 is concentrated in the region of large ω_z and large enstrophy production discussed in the previous paragraph. Thus the three dimensional distortion of the rolls results in significant dissipation of kinetic energy. The work of Moffatt (1985) on inviscid flows suggests that dissipation and helicity density ($u_i\omega_i$) should be spatially exclusive; however, Hussain (1986) suggests that this may not be the case. Helicity density and dissipation contours in plane 1 at time I are shown in figure 5. Helicity density is identically zero in plane 2. The helicity density is concentrated in the region where the ribs meet the rolls and is zero near the stagnation point between the rolls; this is as suggested by Hussain (1986). We note that there is also a concentration of dissipation in the braid region, thus at this time the dissipation and helicity density are not spatially exclusive. This may be a consequence of low Reynolds number or the early stage of

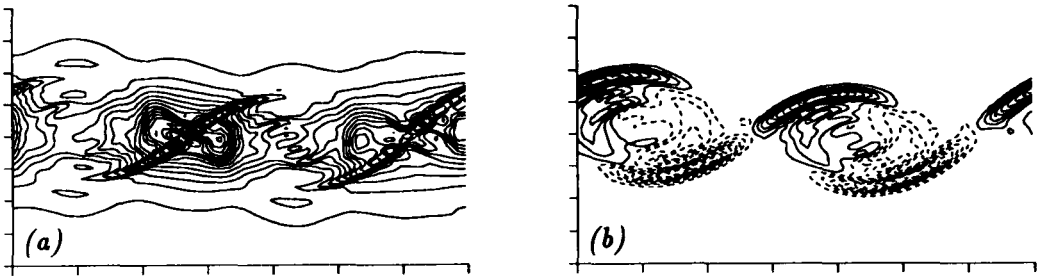

FIGURE 5. Dissipation of kinetic energy (a) and helicity density (b) in plane 1 at time I. Contour increment is (a), $0.00025U^3/\delta$ and (b), $0.1U^2/\delta$. Negative contours are dashed. Streamwise (x) direction is horizontal; cross stream (y) direction is vertical.

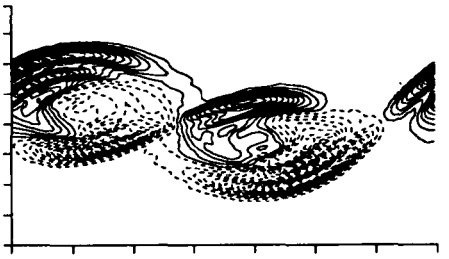

FIGURE 6. Helicity density in plane 1 at time II. Contour increment is $0.1U^2/\delta$. Streamwise (x) direction is horizontal; cross stream (y) direction is vertical.

development of the flow. At time II the dissipation is not significantly concentrated in the braid region (see figure 4), whereas the helicity density is nearly the same as the earlier time (figure 6). Thus at time II the peak of dissipation occurs in plane 2, where the helicity density is zero, and the peak of the helicity density occurs in plane 1 where the dissipation is minimum.

Summary

A simulation of a time-developing mixing layer with idealized initial conditions has produced flow structures which are at least qualitatively similar to those observed in experimental mixing layers. With the availability of the three-dimensional flow field, it is possible to investigate a variety of structural and dynamical questions by computing any number of flow quantities (*e.g.* vorticity, production of enstrophy, dissipation etc.). For example, in this brief study we were able to observe and explain the three-dimensional distortion of the Kelvin-Helmholtz rolls by the rib vortices, and we were able to study the relationship of helicity density and dissipation. A more complete study of higher-resolution simulations should provide great insight into the dynamics and topology of coherent structures in the mixing layer. This is the focus of our ongoing research.

REFERENCES

BERNAL, L. P. & ROSHKO, A. 1986 Streamwise vortex structure in plane mixing layers. *J. Fluid Mech.* **170**, 499-525.

CAIN, A. B., FERZIGER, J. H. & REYNOLDS, W. C. 1984 Discrete orthogonal function for non-uniform grids using the fast Fourier transform. *J. Comp. Phys.* **56**, 272-286.

HUSSAIN, A. K. M. F. 1983 *Turbulence and Chaotic Phenomena in Fluids* (ed. T. Tatsumi), p.453.

HUSSAIN, A. K. M. F. 1986 Coherent structures and turbulence. *J. Fluid Mech.* **173**, 303-356.

MOFFATT, H. K. 1985 Magnetostatic equilibria and analogous Euler flows of arbitrarily complex topology. Part 1. Fundamentals. *J. Fluid Mech.* **159**, 359-378.

METCALF, R. W., ORSZAG, S. A., BRACHET, M. E., MENON, S. & RILEY, J. J. 1987 Secondary instability of temporally growing mixing layer. *J. Fluid Mech.* **184**, 207-243.

Page intentionally left blank

Center for Turbulence Research
Proceedings of the Summer Program 1988

Subharmonic Resonance in a Mixing Layer

By N. N. Mansour [1], F. Hussain [2], and J. C. Buell[1]

The subharmonic resonance phenomenon in a spatially-evolving mixing layer is studied using direct simulations of the two-dimensional Navier-Stokes equations. The computational domain extends to $\pm\infty$ in the cross-stream direction with $U_1 = 1.25$ and $U_2 = 0.25$ imposed at $+\infty$ and $-\infty$ respectively. The domain is finite in the streamwise direction with inflow and outflow boundary conditions imposed at $x/\delta_w = 0$ and $x/\delta_w = 100$, respectively. A hyperbolic-tangent mean velocity profile is assumed at the inlet and the Reynolds number based on the inlet vorticity thickness and velocity difference is $Re = 600$. It is observed that the phase angle between the fundamental and its subharmonic plays a key role in the spatial development of these modes. Contour plots of vorticity show that varying the phase will have a dramatic effect on the dynamics of the vortices. Pairing or shredding is observed depending on the phase. Fourier decomposition of the time traces show that the fundamental grows, saturates and decays with the downstream distance. The subharmonic has a similar behavior. However, the level at which the modes will saturate is affected by the phase. At 0° phase, we find that as the fundamental saturates, the growth rate of the subharmonic is enhanced. At 90° phase, we find that as the fundamental saturates, the growth rate of the subharmonic is inhibited. In the later case, the growth rate of the subharmonic recovers after saturation of the fundamental. These results are in qualitative agreement with experimental data.

1. Introduction

While the occurrence of large-scale, vortical coherent structures (CS) in turbulent shear flows is not in question, what role they play, how this role is affected by the interaction of these CS and how this role can be enhanced or suppressed through manipulation of CS are still open questions. The initiation, growth, interaction, breakdown and regeneration of coherent structures are manifestations of a hierarchy of instability mechanisms in both transitional and turbulent flows. In a turbulent flow the interaction of coherent structures is complex and three-dimensional. The interaction of 2D coherent structures in a mixing layer should be addressed first as the simpler case. Following the 2D roll-up of an initially laminar layer into discrete structures, the most common, and dynamically significant, event observed is the growth of the subharmonic which manifests itself as pairings. The pairing process, i.e., the growth of the subharmonic, is a consequence of what has come to be known as *subharmonic resonance* - a simple consequence of nonlinear interaction between a

1 NASA Ames Research Center
2 University of Houston

wave of angular-frequency ω and its subharmonic wave (of angular-frequency $\omega/2$). Under suitable conditions (say proper choices of relative phase and amplitudes of ω and $\omega/2$ components) the fundamental component that results from nonlinear interaction can reinforce the subharmonic. The resulting growth of the subharmonic, causing merger of the vortices, is one of the most striking features of turbulent shear flows because it provides a direct mechanism for large-scale mixing and other phenomena such as aerodynamic noise.

The subharmonic resonance mechanism was first analyzed by Kelly (1967) using a weakly nonlinear temporal formulation for a parallel flow. He showed that the mean together with a fundamental wave component can reinforce the growth of the subharmonic of that fundamental. Monkewitz (1988) extended Kelly's analysis to spatially evolving mixing layers and addressed some interesting features: effect of the phase angle between the fundamental and subharmonic, the critical fundamental amplitude required for resonance and the effect of detuning. The phenomenon has been studied numerically by Patnaik et al. (1976) and Riley & Metcalfe (1980) for the time-developing mixing layer. In this work the spatial mixing layer is investigated.

The computational scheme uses high-order approximations to the two-dimensional Navier-Stokes equations. A spatially evolving mixing layer is studied by forcing the inlet flow with the eigenfunction solutions to the Rayleigh equation at the desired frequencies. The boundary conditions used are described in section 2. Vorticity contours, time spectra and the spatial development of the modes are discussed in section 3.

2. The computational parameters

The numerical scheme approximates the Navier-Stokes equations by using a spectral method in the vertical direction, high-order Padé finite differencing in the streamwise direction and third-order Runge-Kutta in time. The mean inlet streamwise velocity is forced to be a tanh profile,

$$U_{inlet} = \frac{1}{2}\left(\frac{1+r}{1-r} + \tanh(2y)\right) \tag{1}$$

where $r = U_1/U_2$ is the velocity ratio of the low-speed side over the high-speed side. All lengths are nondimensionalized with the vorticity thickness, δ_w, of the inlet mean flow, all velocities are nondimensionalized with the velocity difference, $\Delta U = U_1 - U_2$. To correspond with the experiment of Husain & Hussain (1986) we want $r = 0$; however, computationally the exit boundary conditions for this case are harder to prescribe. At the exit the structures are assumed to convect out of the domain at a constant convection speed (c),

$$\frac{\partial}{\partial t}u_i + c\frac{\partial}{\partial x}u_i = 0$$

for both the streamwise and cross-stream velocity. If the velocity at the low speed side is too low there will be intermittent backflow at the exit boundary which

Case	α_1	α_2	ϕ	Summary
1	0.005	0.	0°	Forcing only the fundamental.
2	0.	0.005	0°	Forcing only the subharmonic.
3	0.005	0.005	0°	Forcing both the fund. and its sub. with 0° phase.
4	0.005	0.005	90°	Forcing both the fund. and its sub. with 90° phase.

Table 1. Summary of computed cases

will violate our "convection out of the domain" assumption. We chose $r = 0.2$. Proper prescription of the exit boundary condition is still an unsolved problem. Buell & Huerre (this proceeding) found that the exit boundary condition causes global potential fluctuations which interact with the inflow boundary and create small-amplitude noise at the inlet. In our study we will force the inlet flow at one frequency and its subharmonic. The amplitude of the forcing (0.005 of the velocity difference) is much larger than the feedback amplitude. It is found that the growth rate of the forced frequency is not affected by the boundary feedback problem.

The boundary condition at $\pm\infty$ is imposed so that the streamwise velocity is constant and equal to $U_1 = 1.25$ and $U_2 = 0.25$ at $+\infty$ and $-\infty$ respectively. The cross stream velocity can be defined arbitrarily at these boundaries. Numerical experimentation with $r = 0.2$ suggest the values $V_1 = -0.002$ and $V_2 = 0.005$ at $+\infty$ and $-\infty$ respectively. These entrainment velocities were selected to minimize the streamwise pressure gradient. Numerical experimentation with these boundary conditions show that the level of the cross-stream velocity will not affect the vorticity thickness of the layer but has a direct effect on the momentum thickness.

The inlet profile is forced as follows:

$$\begin{aligned} u_1 &= U_{inlet} + \alpha_1 \mathrm{Real}(\hat{u}_f \exp(-i\omega t)) + \alpha_2 \mathrm{Real}(\hat{u}_{f/2} \exp(-i(\omega t/2 + \phi))) \\ u_2 &= \alpha_1 \mathrm{Real}(\hat{v}_f \exp(-i\omega t)) + \alpha_2 \mathrm{Real}(\hat{v}_{f/2} \exp(-i(\omega t/2 + \phi))) \end{aligned} \tag{2}$$

where ω is a fundamental frequency, $\hat{u}_f$, $\hat{v}_f$, ..., are the eigenfunctions of the Rayleigh equation corresponding to the forced frequencies, and ϕ is the phase difference between the fundamental and its subharmonic. α_1 and α_2 are arbitrary constants that were set equal to $\alpha_1 = \alpha_2 = 0.005$.

3. Basic measured quantities

Numerical integration of the Rayleigh equation show that the most unstable angular frequency is about $\omega = 0.65$ for the mean profile given by Eq. (1). We will choose this frequency as our fundamental frequency. The objective of this work is to study the effect of the phase difference between the fundamental and its subharmonic on the development of the layer. We know that mixing layers develop by the interaction of vortices and that the layer grows by the amalgamation of these vortices.

3.1 Vorticity Contours

Figures 1a-d show characteristic vorticity contours after the layer has developed for the four cases that are summarized in Table 1. Case 1 corresponds to forcing the fundamental without forcing the subharmonic. Case 2 corresponds to the case

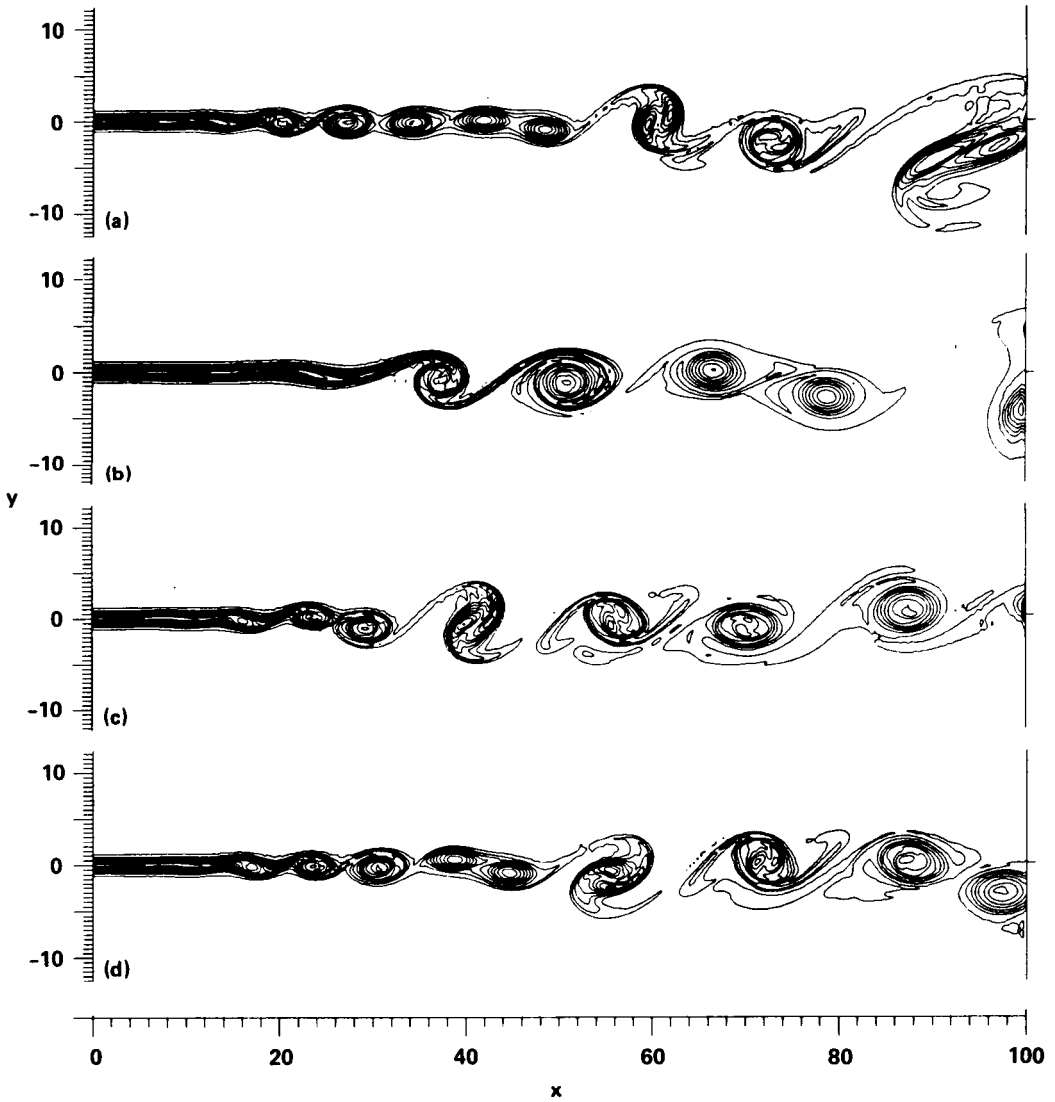

FIGURE 1. Contour plots of vorticity. a) Case 1, forcing the fundamental only. b) Case 2, forcing the subharmonic only. c) Case 3, forcing the fundamental and its subharmonic with $\phi = 0°$. d) Case 4, forcing the fundamental and its subharmonic with $\phi = 90°$.

where only the subharmonic is forced. In case 3 both the fundamental and the subharmonic are forced with $\phi = 0°$ phase difference between them. In case 4 the fundamental and subharmonic are forced with $\phi = 90°$ phase difference between them. One can notice that in all cases the layer breaks into vortices corresponding

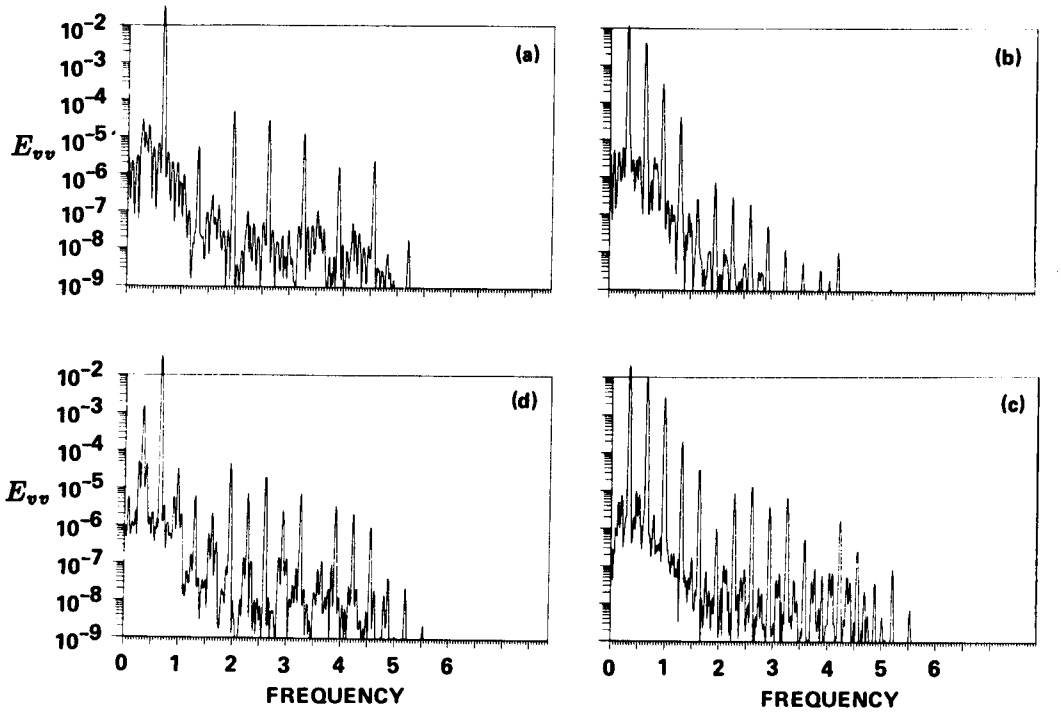

FIGURE 2. Time spectra at $x = 28.1$ and $y = 0$. a) Case 1, forcing the fundamental only. b) Case 2, forcing the subharmonic only. c) Case 3, forcing the fundamental and its subharmonic with $\phi = 0°$. d) Case 4, forcing the fundamental and its subharmonic with $\phi = 90°$.

to the forced frequency. These vortices subsequently pair. The growth of the subharmonic (pairing of the forced frequency) that occurs in case 1 is due to the effect of the downstream boundary condition on the layer. In our reference frame the mixing layer should be convectively unstable, therefore, no subharmonic can be generated unless it is forced from the upstream. Because the inlet for cases 1 and 2 is forced at one frequency only, the appearance of the subharmonic as detected by the pairing can only come from the effect of the downstream boundary condition on the upstream. Comparing the four cases, we find that the earliest pairing occurs in case 3 where the subharmonic was forced with $\phi = 0°$.

The layer is thicker (at $x = 40$) for this case as compared to the other cases. By changing the phase to 90° the location of the pairing is shifted downstream. Comparing the case of $\phi = 90°$ phase difference (Figure 1d) with the case of forcing only the fundamental (Figure 1a), we find that the two layers are similar. This is an indication that the subharmonic is being inhibited for $\phi = 90°$. The suppression is not complete since pairing in case 4 still occurs earlier than in case 1.

Vorticity contours yield a qualitative picture on the development of the layer. A series of contour plots as a sequence in time or a movie will yield a better picture of the dynamics of the layer, but the information they will yield is still qualitative.

3.2 Time spectra

An effective tool for the study of unsteady data is to analyze the time signal using Fourier transforms in time. Given the time trace of the velocity component at a location in space, the signal is windowed, and then expanded in a Fourier series in time,

$$v = \sum_{\omega} \hat{v}(\omega) \exp(i\omega t)$$

The spectrum of the velocity is defined as,

$$E_{vv}(\omega) = \hat{v}(\omega)\hat{v}^*(\omega).$$

Figures 2a and 2b show the spectra of the v-velocity component at $x = 28.1$, and $y = 0$ for the four cases. We can see clearly that modes other than the forced modes and their harmonics have developed. The development of a broad spectrum is due to the interaction of the downstream boundary condition with the inlet flow. This interaction is forcing a background noise which is unavoidable in experiments. Since we are forcing a given frequency and are interested in the early development of the layer, we expect that the effect of the downstream boundary condition on our results and conclusion should be small. This is supported by the fact that the forced frequencies and their harmonics are still the dominant frequencies at $x < 30$. Comparison of Figures 2c and 2d show that the subharmonic is much larger for case 3 as compared to case 2. This is an indication that the growth rate of the subharmonic is larger for $\phi = 0°$. Comparing the amplitude of the fundamental for the three cases (1, 3 and 4), we find that the magnitude of the fundamental is comparable for cases 1 and 4; for case 3, the growth of the subharmonic has inhibited the fundamental. In case 2, the fundamental is a harmonic of the forced frequency and is expected to be lower than the forced cases. To properly compare the growth rate of the different modes we need to examine the development of the modes in space.

3.3 Contour plots of Fourier modes.

In our discussion on the development of the layer (§3.1) we implicitly decomposed the flow field into its Fourier components. In the present study we are interested in the spatial distribution of the forced modes. Figures 3 and 4 show contour plots of $|\hat{u}_{f/2}|$ and $|\hat{v}_{f/2}|$ for cases 3 and 4. From these figures we find that $|\hat{u}_{f/2}|$ will grow in the downstream direction and develop a double peak. Contour plots of $|\hat{v}_{f/2}|$ (see Figure 3) show that in the early stages $|\hat{v}_{f/2}|$ has one peak close to the centerline. The effect of the phase difference is manifested by the shift in the downstream direction of the peak. For case 3, the subharmonic saturates at around $x = 40$, while for case 4 the peak occurs at around $x = 50$. Comparing the contour plots for the two cases, we find general similarities. Both $|\hat{u}_{f/2}|$ contours exhibit a region

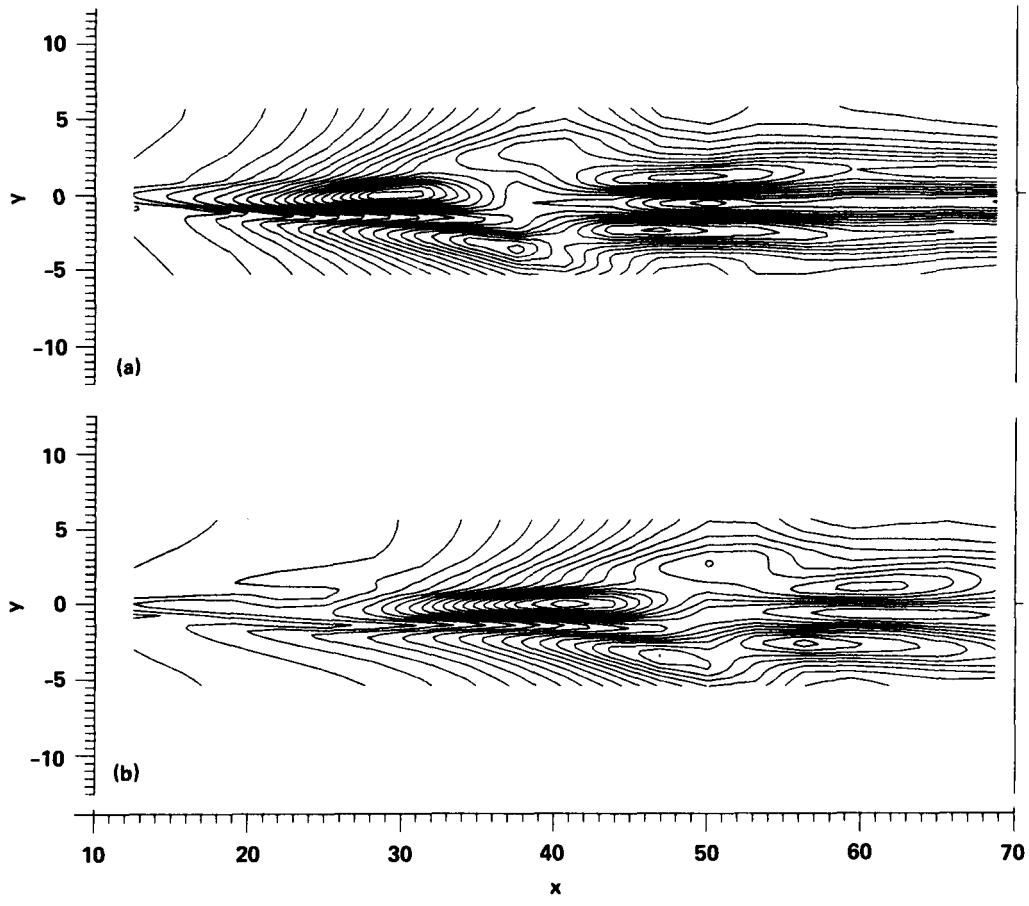

FIGURE 3. Contour plots of $|\hat{u}_{f/2}|$. a) Case 3, forcing the fundamental and its subharmonic with $\phi = 0°$. b) Case 4, forcing the fundamental and its subharmonic with $\phi = 90°$.

with double peaks, then a region of decay, followed again by a region with double peaks. Quantifying the $|\hat{u}_{f/2}|$ by plots of the intensity at one y location will not yield a proper norm since this component varies rapidly across the layer.

In general, the $|\hat{v}|$ component is simpler to quantify . Contour plots of $|\hat{v}|$ show a peak around $y = 0$ for both cases. The two plots are similar; however, shifting the coordinate so that the peaks will coincide shows that the distribution of the modes in space is different. The distance between contour levels in case 3 is shorter, indicating that the subharmonic is growing at a faster rate.

3.4 Growth of the fundamental and Subharmonic

While contour plots show the distribution of the mode in space, it is not simple to compare the data for the different cases. For simplicity, we assume that a proper

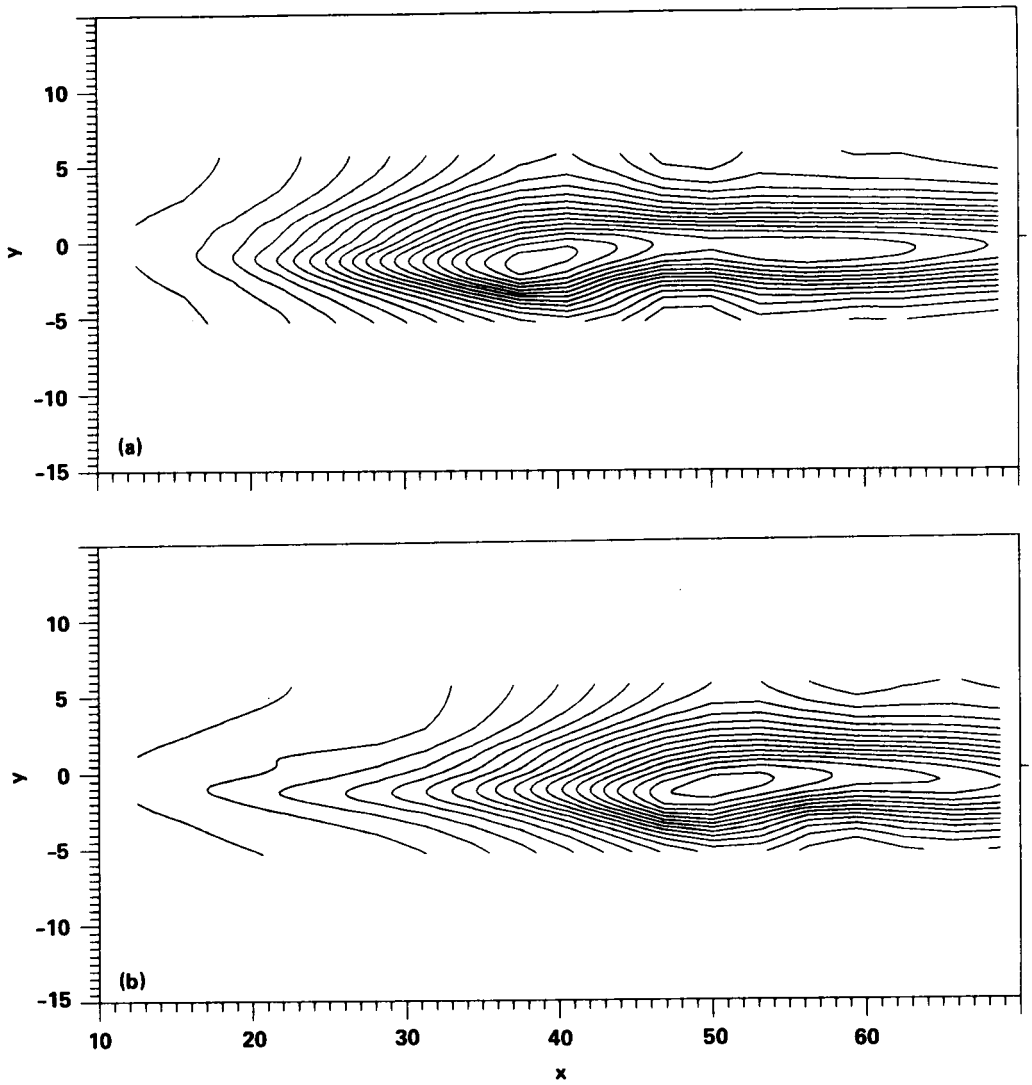

FIGURE 4. Contour plots of $|\hat{v}_{f/2}|$. a) Case 3, forcing the fundamental and its subharmonic with $\phi = 0°$. b) Case 4, forcing the fundamental and its subharmonic with $\phi = 90°$.

norm for the distribution is well represented by the development of $|\hat{v}|$ along $y = 0$, and study the development of the fundamental and subharmonic along that line.

3.4.1 Effect of the Reynolds number.

At the early stages of the development of the modes and at high Reynolds numbers we expect linear theory to be a good approximation. At low Reynolds numbers the viscous growth of the layer will be important and will affect the growth rate of the

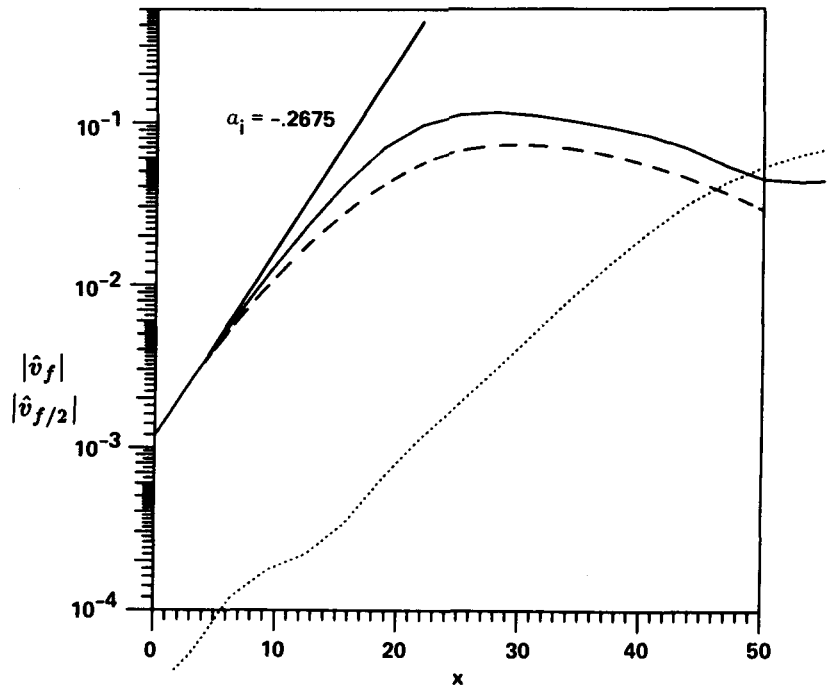

FIGURE 5. Effect of the Reynolds number on the development of the fundamental. ——— $|\hat{v}_f|$ with $Re = 600$. ---- $|\hat{v}_f|$ with $Re = 300$. ····· $|\hat{v}_{f/2}|$ with $Re = 600$.

modes. Figures 5 and 6 compare the development of $\hat{v}_f$ at $Re = 300$ and $Re = 600$ for cases 1 and 2 where only the fundamental and only the subharmonic is forced. We find that the effect of the Reynolds number is to reduce the growth rate in the downstream direction. This effect is less severe for the subharmonic mode. In addition, exponential growth is valid for significantly larger amplitudes of the subharmonic mode as compared to the fundamental mode. Note that in the case of forcing at only the fundamental, the subharmonic will develop because of feedback from the downstream boundary condition.

3.4.2 Effect of the phase difference on $|\hat{v}|$.

The development of the magnitude of the fundamental and its subharmonic with the downstream distance is shown in Figures 7a and 7b for $\phi = 0°$ and $\phi = 90°$ respectively. We find that the growth rate of the fundamental is only slightly affected by the presence of the subharmonic. However, the saturation level is higher for $\phi = 90°$ as compared to $\phi = 0°$. This is an indication that there is an interaction between the fundamental and its subharmonic. On the other hand the level at

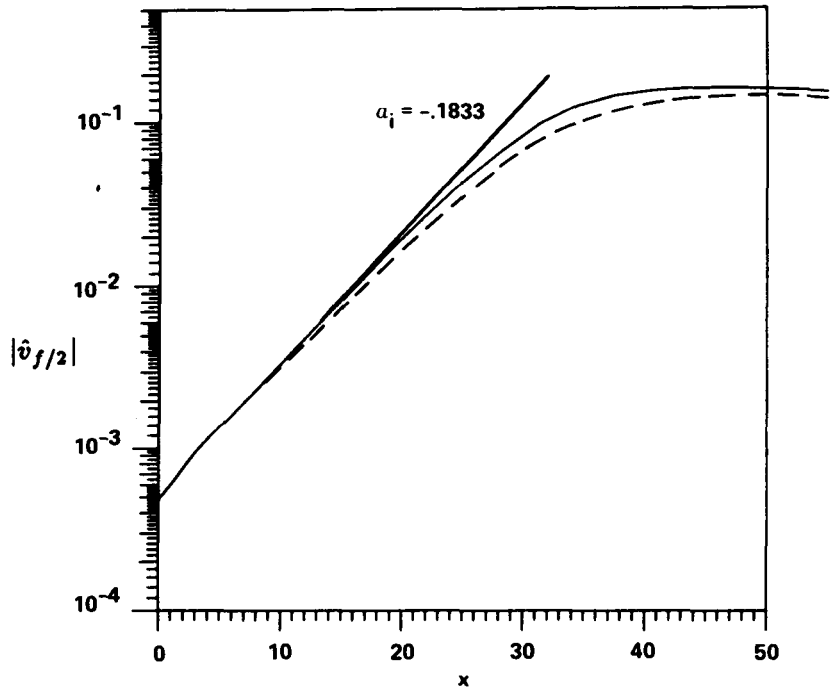

FIGURE 6. Effect of the Reynolds number on the development of the subharmonic. —— $|\hat{v}_{f/2}|$ with $Re = 600$. ---- $|\hat{v}_{f/2}|$ with $Re = 300$.

which the subharmonic saturates seems independent of the phase angle. But the location of the peak is dramatically affected by the phase angle. Comparison of the growth rate of the subharmonic with linear theory and case 2 (forcing only the subharmonic) shows that with $\phi = 0°$ the subharmonic grows faster than predicted by linear theory. On the other hand for $\phi = 90°$ its growth rate is suppressed as the fundamental saturates. After saturation the subharmonic recovers and starts growing. This is a clear indication that the phase between the fundamental and the subharmonic plays a critical role on the development of the layer. In agreement with Monkewitz's analysis we find that the amplitude of the fundamental has to reach a critical level before it can modify the growth rate of the subharmonic.

3.4.3 Effect of the phase difference on $|\hat{u}|$.

The effect of the phase difference on $|\hat{u}|$ is more dramatic that the effect on $|\hat{v}|$. Figures 8a and b show the development of $|\hat{u}_f|$ and $|\hat{u}_{f/2}|$ with the downstream direction at $y = 0$. We find that at $\phi = 90°$, $|\hat{u}_{f/2}|$ actually decreases as the fundamental saturates. After saturation the subharmonic grows at a faster rate than

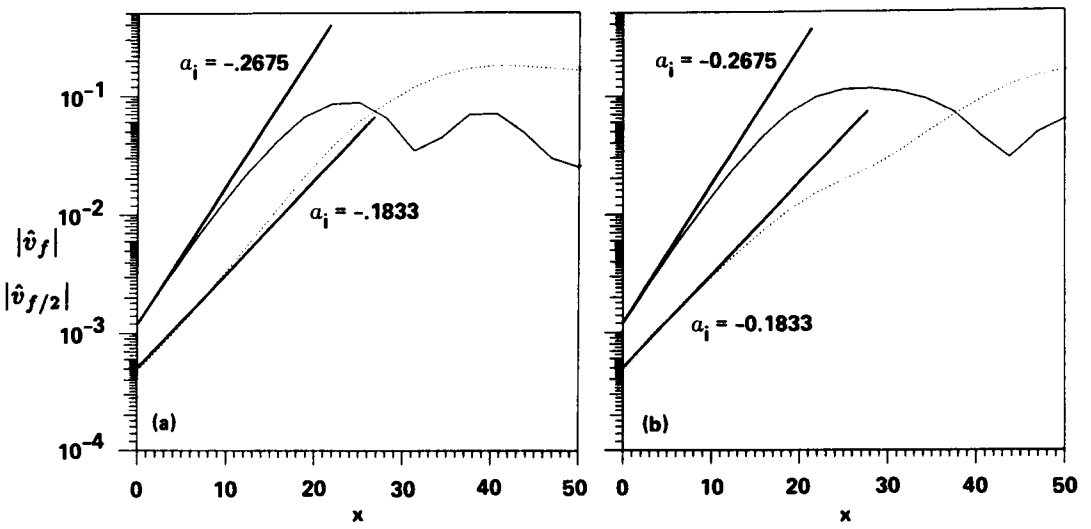

FIGURE 7. Development of $|\hat{v}_f|$ and $|\hat{v}_{f/2}|$ in the downstream direction at $y = 0$. a) Case 3, forcing the fundamental and its subharmonic with $\phi = 0°$. b) Case 4, forcing the fundamental and its subharmonic with $\phi = 90°$. ——— $|\hat{v}_f|$. ····· $|\hat{v}_{f/2}|$.

expected from linear theory. These observations are in qualitative agreement with the experimental measurements of Husain & Hussain (1986), but give a different pictures than Figure 7 on the development of the modes after saturation of the fundamental. This is an indication that results based on one component of the velocity should be interpreted with caution.

4. Future extensions

We have studied the effect of the phase angle between a fundamental and its subharmonic for one frequency, namely the most unstable frequency as predicted from linear theory. Two phases 90° apart were considered. In future work, the phase range $0° \leq \phi \leq 180°$ will be investigated. Early results indicate that the maximum suppression occurs at $\phi = 97°$. Also, in agreement with experimental observation, the maximum suppression occurs in a narrow phase range. This is an indication that suppression of mixing may be difficult to achieve in practical applications. Simulations at various frequencies will also be carried out to investigate the effect of Strouhal number on the phase difference between maximum enhancement and suppression. Finally, evaluation of different nonlinear theories on subharmonic resonance will be carried out by comparing the numerical results with the theoretical predictions and by evaluating the assumptions made by the theories.

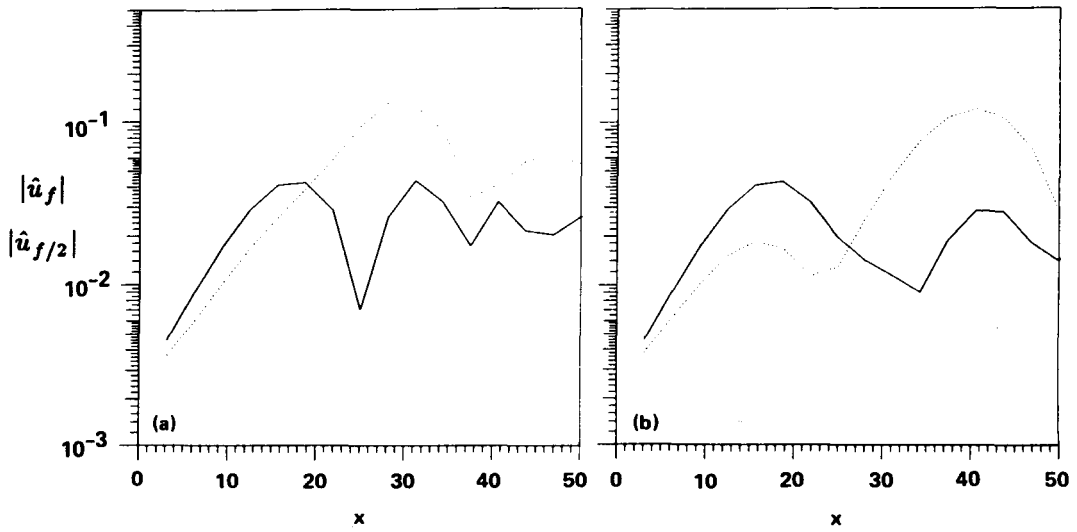

FIGURE 8. Development of $|\hat{u}_f|$ and $|\hat{u}_{f/2}|$ in the downstream direction at $y = 0$. a) Case 3, forcing the fundamental and its subharmonic with $\phi = 0°$. b) Case 4, forcing the fundamental and its subharmonic with $\phi = 90°$. —— $|\hat{u}_f|$. ····· $|\hat{u}_{f/2}|$.

REFERENCES

BUELL, J. C., AND HUERRE, P. 1988 . *Proceedings of the Summer Program 1988, Center for Turbulence Research, Ames Research Center.*

HUSAIN, H. S., AND HUSSAIN, F. 1986 . *Bull. of the Am. Phys. Soc.* **31**, 1696.

KELLY, R. E. 1967 . *J. Fluid Mech.* **27**, 657-689.

MONKEWETIZ, P. A. 1988 . *J. Fluid Mech.* **188**, 223-252.

PATNAIK, P. C., SHERMAN, F. S., AND CORCOS, G. M. 1976 . *J. Fluid Mech.* **73**, 215-240.

RILEY, J. J., AND METCALFE, R. W. 1980 . *AIAA paper 80-0274, Reno.*

Center for Turbulence Research
Proceedings of the Summer Program 1988

Scalar Entrainment in the Mixing Layer

By N. D. Sandham[1], M. G. Mungal[1],
J. E. Broadwell[2] and W. C. Reynolds[1]

New definitions of entrainment and mixing based on the passive scalar field in the plane mixing layer are proposed. The definitions distinguish clearly between three fluid states – (a) unmixed fluid (b) fluid 'engulfed' in the mixing layer, trapped between two scalar contours, and (c) mixed fluid. The difference between (b) and (c) is the amount of fluid which has been engulfed during the pairing process, but has not yet mixed. Trends are identified from direct numerical simulations and extensions to high Reynolds number mixing layers are made in terms of the Broadwell-Breidenthal mixing model. In the limit of high Peclet number ($Pe = ReSc$) it is speculated that engulfed fluid rises in steps associated with pairings, introducing unmixed fluid into the large scale structures, where it is eventually mixed at the Kolmogorov scale. From this viewpoint pairing is a prerequisite for mixing in the turbulent plane mixing layer.

1. Introduction

Existing definitions of entrained fluid are not specific about the state of the fluid (whether mixed or unmixed) that is carried by large scale structures. Corcos & Sherman [1984] used the instantaneous streamlines in the moving reference frame to identify a cat's-eye structure boundary. Similarly Hernan & Jimenez [1982] in their digital analysis of movies of the mixing layer, used a best-fit ellipse to frame each structure, and measured the area within the ellipses to estimate entrainment. Neither definition distinguishes between entrained fluid that is mixed, entrained fluid that is doomed to be mixed, and appear to allow for the possibility of 'entrained' fluid subsequently leaving the ellipse.

In this paper we use insights from direct numerical simulations to provide ideas on how the large-scale structure dynamics affect scalar transport in the mixing layer. For this purpose a two-dimensional time-developing code was used to solve the compressible Navier-Stokes equations (Sandham [1988]). The simulations were made at low convective Mach number ($M_c = 0.4$) so that the results can be applied to the low-speed mixing layer. The simulations are of course limited by two-dimensionality and the low Reynolds and Schmidt numbers that can be handled numerically. However some basic trends emerge clearly in the simulations and by using the Broadwell-Breidenthal model of the post-mixing-transition layer we are able to make some qualitative statements about the influence of pairing on mixing in the high Reynolds number mixing layer.

1 Stanford University
2 California Institute of Technology

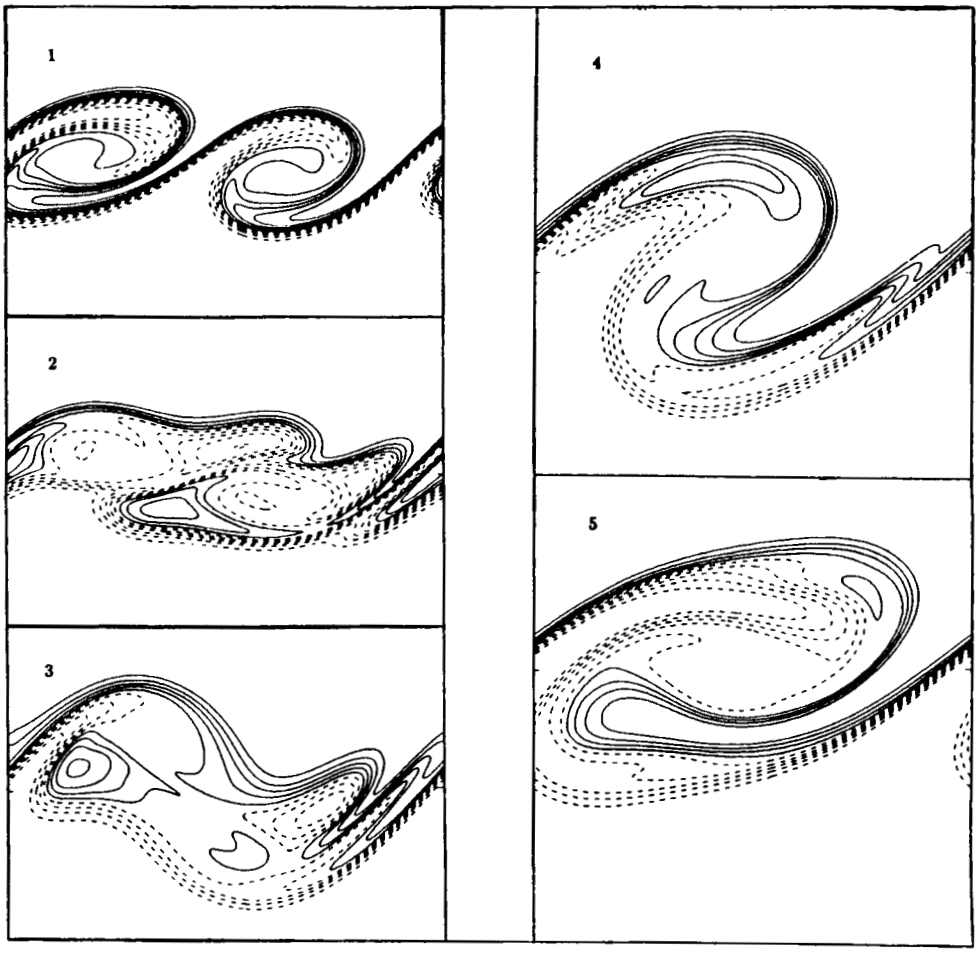

FIGURE 1. Time series of a pairing cycle.

2. Observations From Direct Simulations

From flow visualisations it is apparent that the pairing process is the dominant mechanism for local adjustment of the mixing layer eddy length scale to allow growth in the streamwise direction. To investigate this basic process we consider the simple case of the numerically-simulated time-developing mixing layer undergoing a pairing, shown in Figure 1. The mixing layer is viewed at approximately equal time steps in the cycle. At the first step shown it has already undergone one pairing and by the last (5th) time step the structure has filled its periodic box and is unable to grow or pair any further. The Reynolds number based on vorticity thickness was initially 200 and rose to 2000 by the end of the simulation. The Schmidt number was 1, and a 300×300 grid was used.

If the structure is assumed to maintain self-similarity from the first time step to the last, then the area must rise by a factor of 4. Two vortices have paired; so in the final structure half the fluid came from the original two structures and

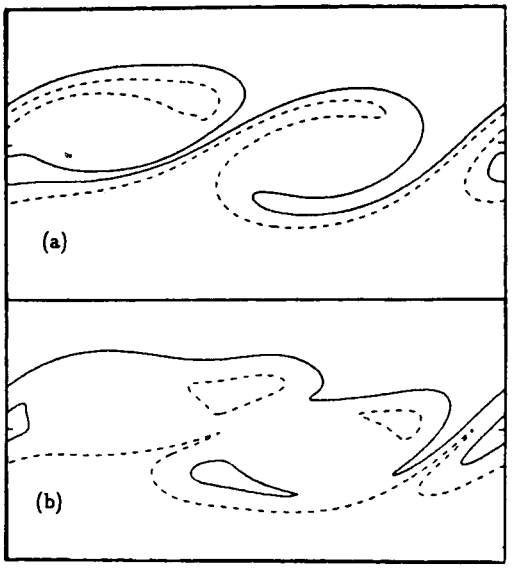

FIGURE 2. Scalar cut-and-connect process showing the 0.1 and 0.9 scalar contours (a) before (b) after.

the other half was introduced during the pairing cycle. Mixing by diffusion is one mechanism for the growth of the structure. A second mechanism can be identified from the scalar contour plots as a scalar cut-and-connect, which has the effect of trapping nearly-unmixed fluid within the structure. This is shown in more detail in Figure 2. Unmixed fluid is wrapped around the structure at time 1 (see Figure 1), with mixing only occurring by diffusion. Then, between times 1 and 2 this fluid is cut off from the outside and becomes trapped in the structure. Between times 3 and 5 mixing is occurring in two places – diffusion from the outside, and diffusion of the fluid inside the structure which was captured by the pairing.

This observation suggested new definitions of fluid state based on the scalar contours. *Engulfed fluid* (E) is that fluid contained between the outermost scalar contours, for example fluid between the levels 0.1 and 0.9, where 0 and 1 represent the free-stream values. *Mixed fluid* (M) is that fluid throughout the mixing layer which is molecularly mixed between two levels (*e.g.* 0.1 and 0.9). The difference $E - M$ is the fluid that has been engulfed, but is yet to mix.

The effect of Peclet number on the process was investigated by running 150×150 simulations at a Reynolds number of 200 and Schmidt numbers of 0.25 and 1.0. The results are shown in Figures 3(a) for $Sc = 0.25$ and 3(b) for $Sc = 1.0$. Engulfed fluid E was found by integrating around scalar contours, while mixed fluid M was calculated by scanning the computational domain for mixed fluid and adding area increments. The two measures are equal so long as all the fluid within the newly defined structure is mixed. It is seen from Figure 3(a) that at low Schmidt number molecular diffusion is very strong, and fluid is essentially diffusion-mixed before it is engulfed. The plots are shown for various scalar cutoff levels $0.1 - 0.9$ (containing

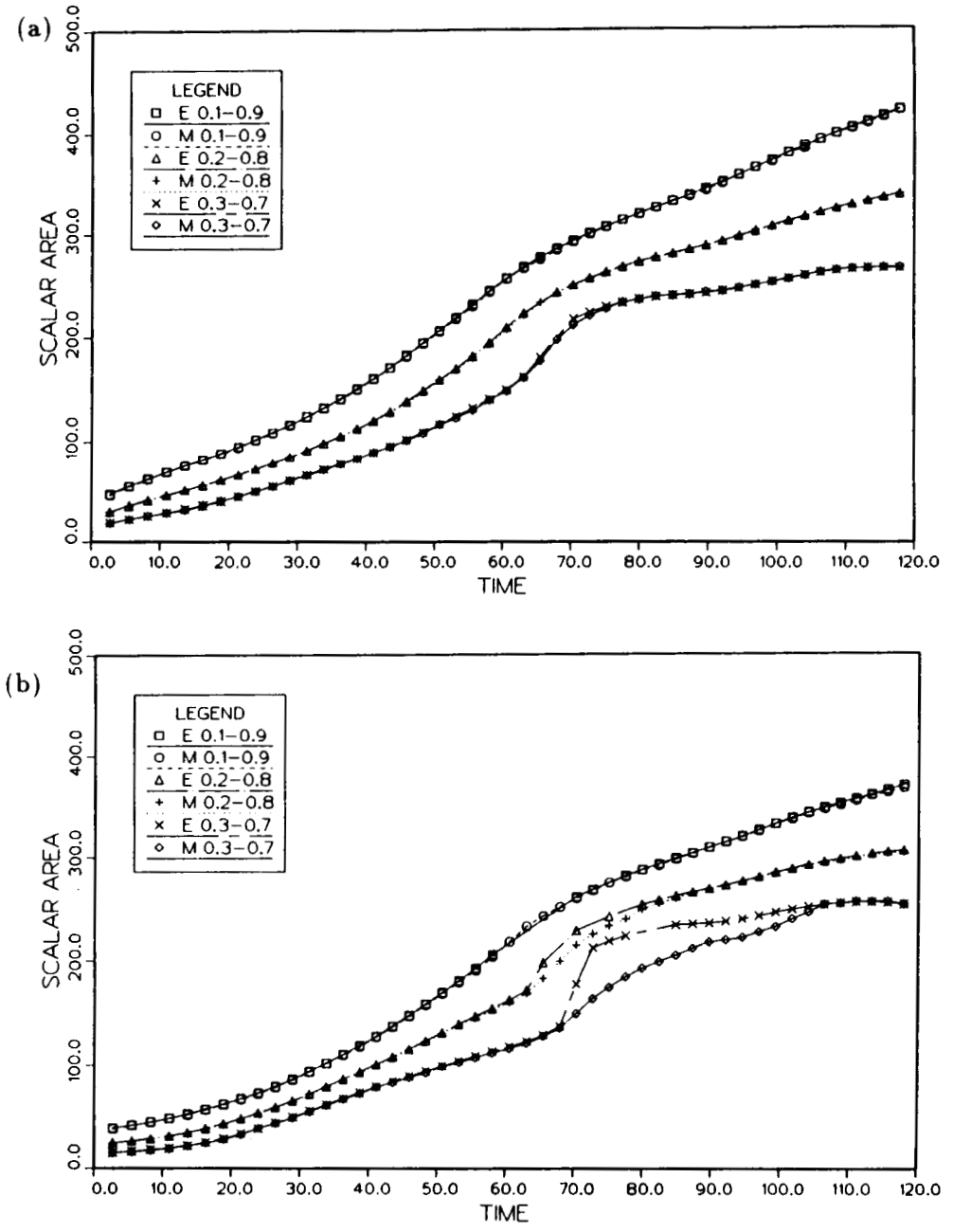

FIGURE 3. Growth of engulfed and mixed fluid at Sc = (a) 0.25 and (b) 1.0.

80% of the mixed fluid), 0.2 – 0.8 (60%), and 0.3 – 0.7 (40%). The effect of lowering the limits on the cutoff is to exclude some of the diffusion effects and give some indication of how a higher Schmidt number flow would behave. At $Sc = 1.0$ (Figure 3(b)) and taking the 40% and 60% limits there is a clear trend emerging. The E

curve shows a sharp jump at the moment of the scalar cut-and-connect, trapping fluid within the structure, which later mixes. By extrapolating these results we speculate that in the limit of infinite Pe, for simulations with Re fixed below the mixing transition, the function E would be a step function, while the function M would remain essentially zero since the computations have no three-dimensional small scales to increase the interfacial area for mixing.

In the following section we use the Broadwell-Breidenthal picture of the mixing layer past the mixing-transition to include the small scales of the vortex core in our model pairing event, and to make some predictions about the influence of pairing on the mixing process.

3. Extension of Ideas to High Reynolds Numbers

A simplified model of mixing in the plane mixing layer was proposed by Broadwell & Breidenthal [1982] and has been extended to include chemical reactions of arbitrary rate by Broadwell & Mungal [1988]. In the model, fluid is viewed as mixing (1) in laminar strained-flame regions between the two free-stream fluids, and (2) inside the structure at the Kolmogorov scale. In the former process the amount of product that is formed has Reynolds and Schmidt number dependence, while in the latter process it does not. The model correctly predicts many features of the mixing layer experiments, including the differences between liquid and gas experiments and the variation of product formation with equivalence ratio, that cannot be explained with conventional gradient-diffusion models.

In the limit of high Peclet number, such as occurs in liquid mixing layers and in gases at very high Reynolds numbers, mixing in the laminar strained flame regions is reduced to zero and we need only consider mixing at the Kolmogorov scale. The ideas from the previous section show that the pairing is responsible for introducing unmixed fluid into the structures in a discrete manner. Immediately after the scalar cut-and-connect process the structure contains one-half old fluid and one-half new, unmixed fluid. The vorticity field at this stage consists of the two pairing vortices, plus their associated streamwise vortices and small scales. It is assumed that a cascade in scales occurrs and that mixing finally occurs at the Kolmogorov scale when the interfacial area of fluid has increased dramatically. Schematically the proposed process is given in Figure 4. From the Broadwell-Breidenthal model the time scale for mixing to occur after engulfment would be given by $T_M - T_E \sim L/\Delta U$, where L is a characteristic length scale at the start of the cascade.

Some experimental results of Roberts and Roshko [1985] can be interpreted in the light of the above ideas. Roberts performed chemical reactions in a liquid mixing layer ($Pe \rightarrow \infty$) at high Reynolds number and found that, when the layer was forced, new product formation dropped to zero. We can now postulate that the effect of forcing is to lock the mixing layer, stopping pairing and hence preventing new fluid being engulfed, which in turn prevents any new product being formed.

In reaching the above conclusions for $Pe \rightarrow \infty$ it has been assumed that the increase in interfacial area due to the presence of streamwise vortices in the flow is not sufficient to outweigh the reduction in diffusion coefficient. At lower Peclet

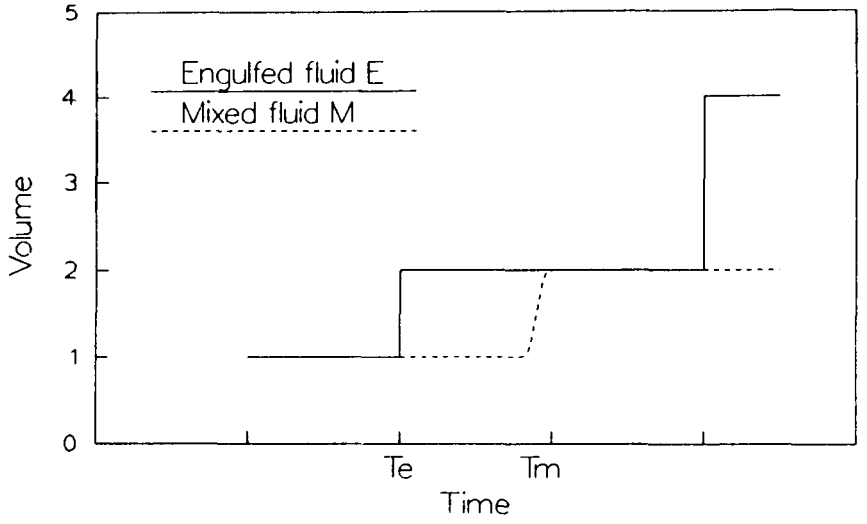

FIGURE 4. Prediction of growth in engulfed and mixed fluid for $Pe \to \infty$.

numbers, for example in the gaseous mixing layer, these streamwise vortices will be important, and have been invoked by Mungal & Dimotakis [1985] to explain some features of 'ramping' in the temperature time traces of a reacting mixing layer. Finite Peclet numbers will have the effect of reducing the jump in engulfed fluid and giving the E and M curves a positive slope between pairings, due to mixing in the strained laminar diffusion layers. At the Reynolds number used by Mungal & Dimotakis (6.8×10^4 based on visual thickness) it was estimated that about half the mixing occurred in these diffusion layers, and we would expect the jump in E to be reduced by approximately a factor of two.

The method used by Hernan & Jimenez [1982] to estimate entrainment in a gaseous mixing layer at high Reynolds number (but finite Pe) involved framing each structure with a best-fit ellipse. Figure 5 shows how this might work for the structure at time 5 in the pairing cycle. For times 2 and 3 (see Figure 1) it was more difficult to fit any meaningful ellipse to the structures. This method evidently includes unmixed fluid that is not contained in our engulfed fluid definition, and may exclude some mixed fluid. The amount of extra fluid included is a function of the particular structure orientation, so that the area of the ellipse may change even if no mixing is taking place. The conclusion of Hernan & Jimenez that entrainment mostly occurs between pairings should therefore be viewed with caution, since it may be influenced by the method that they used to measure entrainment. Also, we should not interpret their measurements of entrainment as giving any information about mixing. The model proposed here for finite Pe is that mixed fluid rises steadily in between discrete jumps which are associated with the mixing of fluid that was engulfed during pairing and has reached the Kolmogorov scale. The size of each jump is speculated to be Reynolds number dependent, reducing as Reynolds number is reduced.

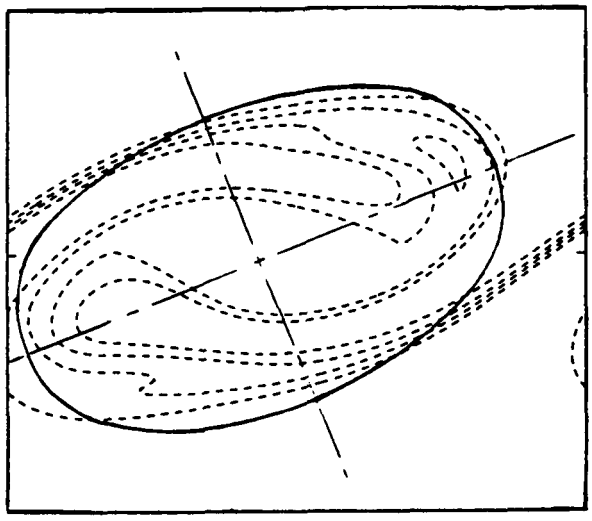

FIGURE 5. Result of fitting an ellipse to a structure.

4. Conclusions

Definitions of entrainment and mixing based on the scalar field of a numerically simulated plane mixing layer have been used to study the fundamental effects of pairing on the mixing process. It was found that pairing is responsible for the process of 'engulfment', bringing unmixed fluid into the structure, while actual mixing lagged behind. Use of the Broadwell-Breidenthal mixing model allowed the results from two-dimensional simulations to be extended to the high Reynolds number mixing layer, leading to a model picture of pairing for $Pe \rightarrow \infty$ as a step function doubling in fluid contained in a structure, followed by molecular mixing after a time lag for the cascade in scales to reach the Kolmogorov scale. It is concluded that for $Pe \rightarrow \infty$ pairing is necessary for mixing, helping to explain some experimental findings of Roberts & Roshko [1985].

REFERENCES

BROADWELL, J. E. & BREIDENTHAL, R. E. 1982 A simple model of mixing and chemical reaction in a turbulent shear layer . *J. Fluid Mech.* **125**, 397-410.

BROADWELL, J. E. & MUNGAL, M. G. 1988 Molecular mixing and chemical reactions in turbulent shear layers. *Twenty-Second International Symposium on Combustion, Seattle, August 1988.*

CORCOS, G. M. & SHERMAN, F. S. 1984 The mixing layer : deterministic models of a turbulent flow. Part 1. Introduction and the two-dimensional flow . *J. Fluid Mech.* **139**, 29-65.

HERNAN, A. H. & JIMENEZ, J. 1982 Computer analysis of a high-speed film of the plane turbulent mixing layer . *J. Fluid Mech.* **119**, 323-345.

MUNGAL, M. G. & DIMOTAKIS, P. E. 1984 Mixing and combustion with low heat release in a turbulent shear layer . *J. Fluid Mech.* **148**, 349-382.

ROBERTS, F. A. & ROSHKO, A. 1985 Effects of periodic forcing on mixing in turbulent shear layers and wakes . *AIAA-85-0570.*

SANDHAM, N. D. 1988 Ph. D. Thesis, Stanford University. In preparation.

Center for Turbulence Research
Proceedings of the Summer Program 1988

Use of Passive Scalar Tagging for the Study of Coherent Structures in the Plane Mixing Layer

By B. R. Ramaprian[1], N. D. Sandham[2], M. G. Mungal[2] and W. C. Reynolds[2]

Data obtained from the numerical simulation of a two-dimensional mixing layer have been used to study the feasibility of using the instantaneous concentration of a passive scalar for detecting the typical coherent structures in the flow. The study has shown that this technique works quite satisfactorily and yields results similar to those that can be obtained by using the instantaneous vorticity for structure detection. Using the coherent events educed by the scalar conditioning technique, the contribution of the coherent events to the total turbulent momentum and scalar transport has been estimated. It is found that the contribution from the typical coherent events is of the same order as that of the time-mean value. However, the individual contributions become very large during the pairing of these structures. The increase is particularly spectacular in the case of the Reynolds shear stress.

1. Introduction

Several techniques have been used in the past to educe and study organized structures in turbulent shear flows. These vary from simple level detection of the velocity signal to the use of various types of short-time averages of the flow properties. A relatively simple technique which proved to be very successful in a recent study of the two-dimensional wake of a flat plate (Jovic and Ramaprian [1986]) consisted of using heat as a passive scalar to tag the flow. In this experiment one side of the wake was maintained at a uniformly higher temperature relative to the other side. The resulting instantaneous temperature levels in the flow were found to provide a convenient and simple means of detecting the arrival of organized structures at the probe. In fact, with this technique, it was possible to isolate and study organized structures in the flow even at distances of the order of 250 momentum thicknesses downstream of the trailing edge using only single point measurements. The results of this study are in good agreement with the recent findings of other researchers (Browne *et al.*[1986], Hussain and Hayakawa [1987]) who have used more sophisticated techniques for the eduction and analysis of the organized structures.

The success of the heat tagging technique in detecting organized large-scale structures suggests that there is a strong correlation between passive scalar transport and the large scale structure and that presumably the former is predominantly brought

1 Washington State University
2 Stanford University

about by the latter. It seems also that the manner of introduction of the scalar (uniformly over the entire side of the wake, as opposed to introduction at the trailing edge) contributed to the success of the method. This is apparent from the experiments of Cimbala [1985] in the two-dimensional wake of a cylinder, which clearly showed that the flow field inferred from visualization of the passive scalar depends critically on the location of the point of introduction of the scalar contaminant (and the Schmidt number).

Some of the above issues can be better understood if the scalar tagging technique is tested under conditions when the available flow information is not limited to single-point measurements. It was therefore proposed to apply this technique to study the large scale organized structure of a numerically generated two-dimensional mixing layer, in which case, information on the entire flow field is available at all instants of time. Such a test would enable one not only to determine the power and limitations of the scalar tagging technique as a means of identifying large-scale organized structures but also to understand role of these structures in the process of turbulent transport in the mixing layer. The present paper describes the results of such a numerical study.

2. Flow Studied

The flow studied is a two-dimensional mixing layer. The database was produced by Sandham & Reynolds [1987], using a random-walk on the phase of the forcing eigenfunctions to simulate the natural mixing layer. The computations are made for the mixing layer between two streams with scalar concentrations $G_1 = 1$ ('high scalar' side) and $G_2 = -1$ ('low scalar' side), and moving at velocities $U_1 = 2$ and $U_2 = 1$ respectively. The code is two-dimensional, i.e., the two-dimensional instantaneous Navier-Stokes equations are solved. The computational domain extends from $x = 0$ to $x = 200$ initial vorticity thicknesses in the streamwise direction and $y = -\infty$ to $y = +\infty$ in the normal direction. The flow development within this domain is computed from the initial time $t = 0$ to a time corresponding to 640 vorticity time units. At $x = 0$, velocity perturbations of a frequency corresponding to the fundamental and subharmonic instability modes of the mixing layer but with a randomly walked phase are introduced. A hyperbolic tangent distribution across the mixing layer is assumed for the scalar. The numerical simulation corresponds to a Reynolds number (based on the initial vorticity thickness) of 100. The simulated mixing layer has been found to agree reasonably well with experimental measurements with respect to growth rate, and distributions of mean velocity and turbulent stresses. Hence, in spite of the rather low Reynolds number and two-dimensionality of the simulation, the numerical data can be considered to be adequate for the purpose of the present studies. In order to avoid the effects of the initial conditions, data corresponding to $t > 240$ only have been used in the study. Likewise, data corresponding to only two locations, namely $x = 78$ and $x = 137$ have been used in the present study. These locations are sufficiently far away from the boundaries to be directly influenced by the specified boundary conditions.

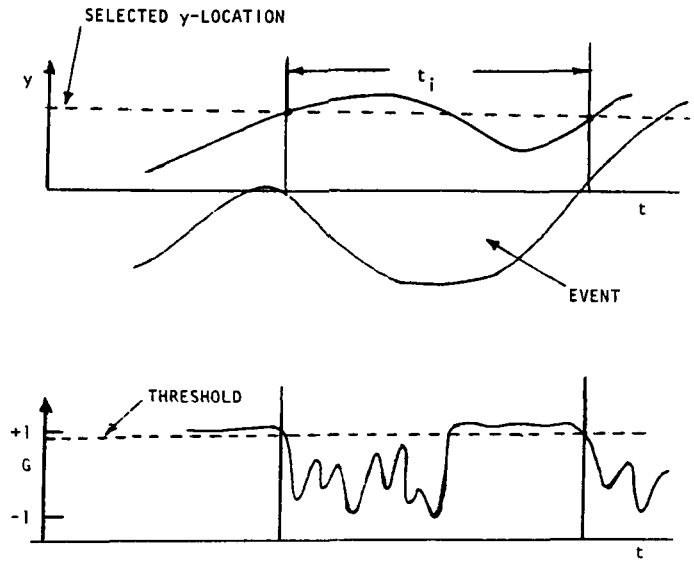

FIGURE 1. Schematic of the eduction procedure

3. Eduction Procedure and Results

It was decided to study the organization in the flow in terms of coherent *events* in time rather than coherent *structures* in space. The study thus simulated the experimental situation in which fixed probes measure flow properties as a function of time. Furthermore, averages taken over the events have direct significance since they represent the contribution by the coherent activity to the 'conventional' time-averaged properties. The procedure used for the eduction of the organized structure in the flow was, in principle, similar to that used in the experiments described in Jovic and Ramaprian [1986] and briefly, is as follows. First, a given x-location is selected for the study. The instantaneous velocity, vorticity and scalar values at this station are each organized in the form of a time series for each y-location. A y-location in the 'high scalar' side sufficiently away from the $y = 0$ line is selected (arbitrarily to begin with). Based on the reasoning that a scalar value of less than 1 at this location indicates contamination with fluid from the 'low scalar' side brought in by the large eddies, the scalar time-series is scanned to detect the time instants when the scalar level crosses a prescribed threshold (say 0.95). The interval between two such crossings from 1 to 0.95 is defined as a large 'event' (see Fig.1). All such events are collected and a histogram of the duration t_i of these events is generated. Also, the mean duration of the events and the standard deviation are evaluated. The y-location and the threshold level are optimized so as to minimize the standard deviation of the durations. The resulting normalized histogram is shown in Figure 2 for the station $x = 78$, along with the lognormal distribution predicted by Bernal [1988]. The agreement indicates that the random-walk phase model used in the simulation algorithm yields a realistic description of the mixing layer.

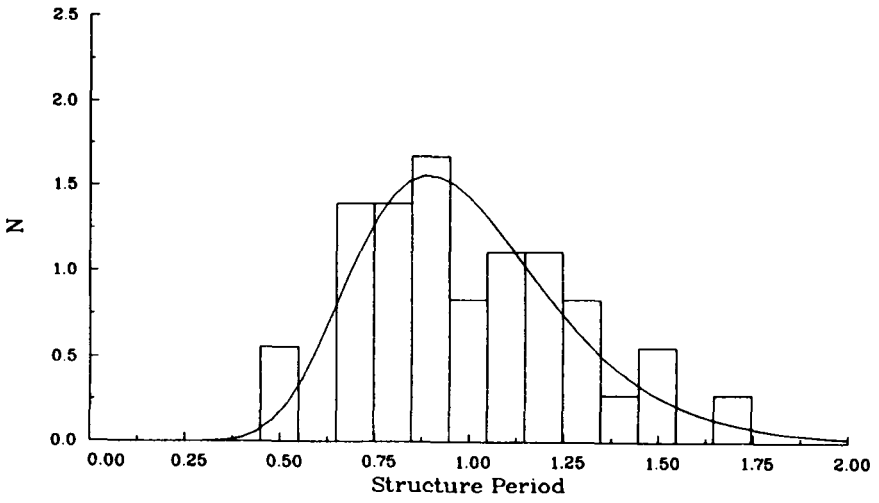

FIGURE 2. Normalized histogram of event durations. Station $x = 78$, $y = 19$, scalar threshold=0.95. Mean duration=10.3 $\sigma = 0.315$. The solid line is the Bernal model.

The next step in the analysis consists of obtaining at all y-locations, ensemble-averaged values of the velocity components U, V, the vorticity ω and the scalar concentration G at several instants during the event. For this purpose, the time coordinate τ is measured relative to the beginning ('front') of the event and is normalized with respect to the duration of the event. Ensemble averages over the several realizations are obtained at ten equally spaced intervals of τ/t_i, separately for each duration t_i. From these ensemble averages, contours of these properties within the event are constructed. Results from this study indicated that not only were realistic contours obtained in each case but also that the contours were nearly the same for *all* the durations in the range $9 \leq t_i \leq 12$ suggesting thereby that these typical events are indeed coherent. As a final step, the contours are averaged over these different durations to obtain the ensemble-averaged contours for the typical coherent event.

Figures 3 and 4 show typically the results for the scalar concentration G and the vorticity ω. The contours are drawn for equal intervals. These contours are analogous to those that would be obtained in an experiment from the instantaneous outputs of a multitude of probes located across the mixing layer at the given x-station, as a coherent event passes by the station. The figures clearly show that the scalar conditioning technique has been successful in educing the typical coherent events in the flow. A secondary observation that can be made from the figures is that while details within the event may differ, there is a strong overall correlation between the scalar field and the vorticity field associated with the coherent event. This close correlation perhaps explains why the scalar conditioning technique is successful in educing the coherent (vortical) events in the flow. It is, however,

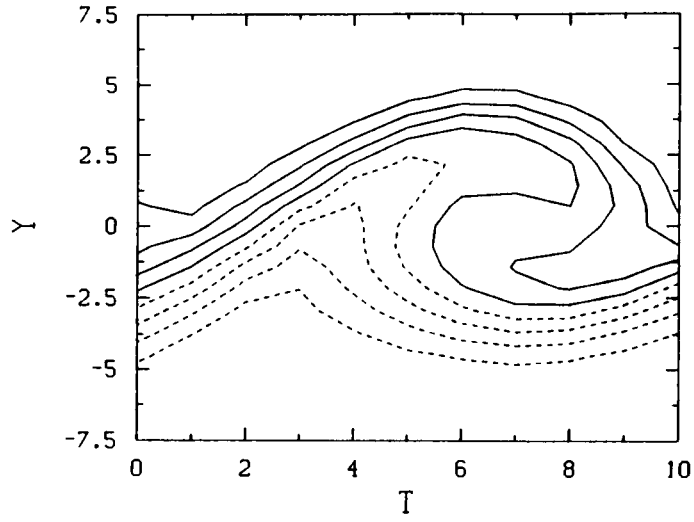

FIGURE 3. Contours of ensemble-averaged scalar concentration in the typical coherent event at station $x = 78$.

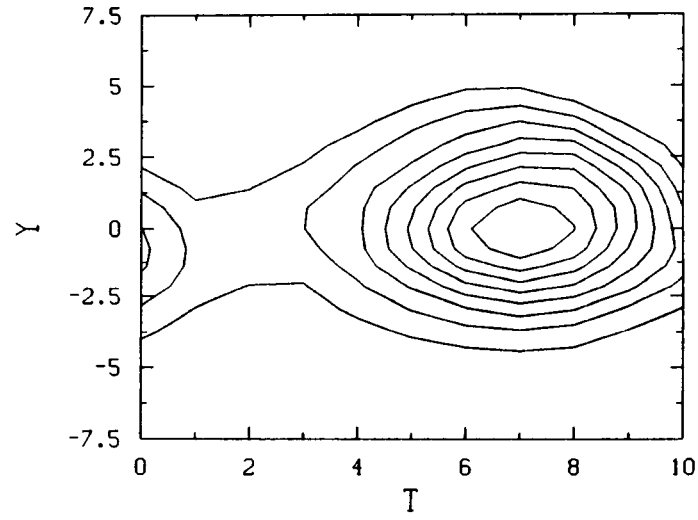

FIGURE 4. Contours of ensemble averaged vorticity in the typical coherent event.

important to note that in this case the Schmidt number of the passive scalar is of the order 1 and that the scalar is 'introduced' at all y-locations. It is also important to note that there are differences in detail between the scalar and vorticity fields. For example, it is very clearly seen that the scalar gradients are very strong within the braid but there is hardly any spanwise vorticity carried by the braid.

4. Contribution from Coherent Events to Turbulent Transport

The availability of information on the instantaneous flow field in this case, provides an opportunity to study the detailed structure of these typical coherent events and their contribution to the overall turbulent transport. One can estimate, for example, the contribution from the coherent structures to the conventionally defined turbulent shear stress $\overline{u'v'}$ and the turbulent scalar transport $\overline{u'g'}$ and $\overline{v'g'}$ in the streamwise and normal direction respectively. During a coherent event, the instantaneous velocity fluctuations u' and v' with respect to the long-time average velocity $\overline{U}$ and $\overline{V}$, and the instantaneous scalar concentration fluctuation g' with respect to to the long-time averaged scalar concentration $\overline{G}$ can respectively be written as

$$u' = < U > + u_s \tag{1}$$

$$v' = < V > + v_s \tag{2}$$

$$g' = < G > + g_s \tag{3}$$

where the sign <> denotes ensemble-averaged fluctuations with respect to the corresponding long-time average value and the subscript 's' denotes the random departure of the instantaneous value from the ensemble average. The latter can be regarded as 'turbulence' superposed on the deterministic fluctuations. The instantaneous products $u'v', u'g'$ and $v'g'$ can then be ensemble averaged for each nondimensional time τ/t_i within the typical coherent event and subsequently averaged over the entire duration of the event to obtain

$$\overline{< u'v' >} = \overline{< U >< V >} + \overline{< u_s v_s >} \tag{4}$$

$$\overline{< u'g' >} = \overline{< U >< G >} + \overline{< u_s g_s >} \tag{5}$$

$$\overline{< v'g' >} = \overline{< V >< G >} + \overline{< v_s g_s >} \tag{6}$$

The left hand side of the above equations represent the contribution from a typical coherent event to the time-average transport. The two terms on the right hand side represent the contributions respectively from the deterministic and the random part of the fluctuations associated with this typical event.

Typical results for the station $x = 78$ are shown in Figs. 5 and 6 for the shear stress and the scalar transport in the normal direction respectively. It is seen that the superposed turbulence (which can be regarded as representing the jitter associated with the process of ensemble averaging) is as large as the organized component in the case of the shear stress but is less significant in the case of the scalar flux. However, at $x = 137$, the level of the superposed shear stress also was found to have a relatively small magnitude. In any case, the *total* contribution from the typical coherent event, given by the sum of the two components is seen to be about 60 % of the time-mean value. Similarly, at $x = 137$ this contribution was found to be approximately equal in magnitude to the time-mean value. Figure 10 shows similar results for the scalar transport. Results for the streamwise scalar transport also showed a similar trend. It is thus concluded that the typical coherent

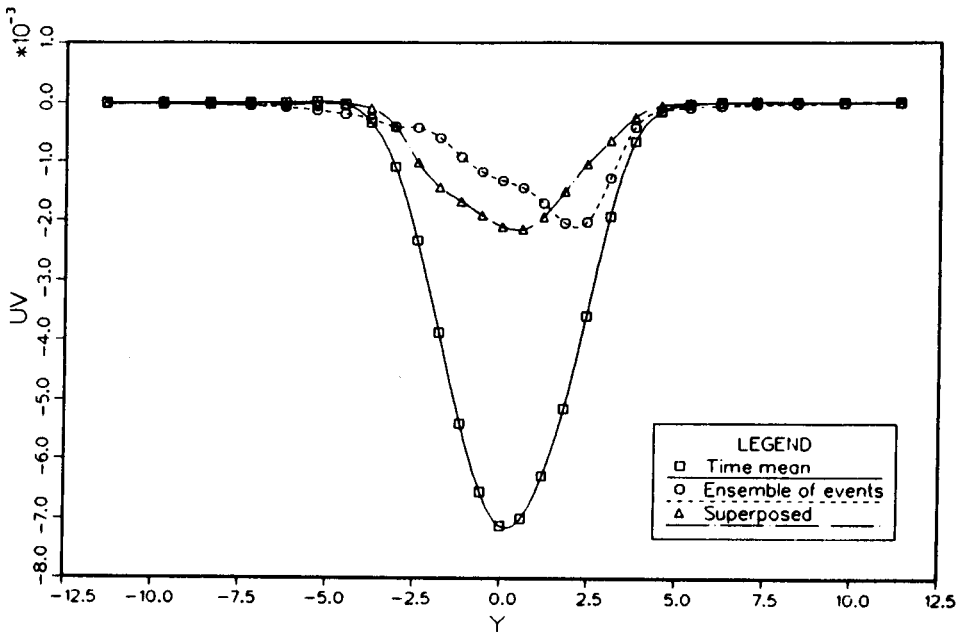

FIGURE 5. Contribution from the typical coherent event to turbulent shear stress. Station $x = 137$.

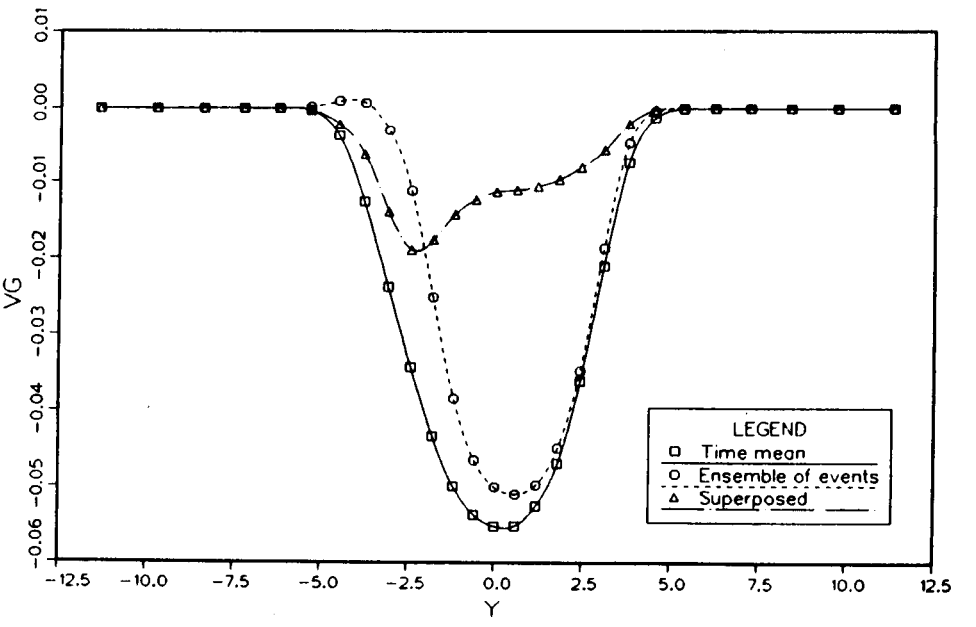

FIGURE 6. Contribution from the typical coherent event to turbulent transport of scalar in the normal direction. Station $x = 137$.

events carry shear stress and heat flux of approximately similar magnitude as the corresponding time-mean values. Hence, these typical coherent events are perhaps as significant as the rest of the events in the flow (but not necessarily the most significant) from the point of view of turbulent transport. The result, however, differs from the experimental results for the wake obtained in Jovic and Ramaprian [1986] which indicated that the shear stress associated with the coherent motion was 2 to 3 times larger than the time-mean value. This difference in the results must be due to the fundamental differences between the dynamics of the mixing layer and the far-wake, though effects of three-dimensionality and contamination with atypical events during eduction in the experiments might have contributed somewhat to the observed differences.

5. Results for a Pairing Event

The above results correspond to the so called typical coherent event observed at a given x-location. The mixing layer, however, is characterized by pairings of the coherent structures, which occur at random streamwise locations. However, it is likely that at any x-location, a pairing event can be observed if one waits for a long enough time. The rather restricted space-time domain of the present numerical simulation did not allow a large enough number of such pairing events to be sampled and ensemble averaged. However, individual pairing events were isolated and studied. The results for one such event, corresponding to the completion of a pairing at x=137 are discussed here. The results shown are expected to be typical of this phase of the pairing process.

Figures 7 and 8 show the scalar concentration and vorticity contours for the pairing event. Once again, overall topological similarity can be observed between the scalar and vorticity fields. However, the scalar gradients in the interior of the event are less strong than those of vorticity, which shows a nearly uniform variation from the center to the outer edge of the structure. Figures 9 and 10 show the cross-stream distribution of the transport terms for momentum and scalar. The same nomenclature as was used in Fig.5 and 6 has been retained even though the ensemble 'average' has been obtained over only *one* realization and hence the superposed component is zero. It is seen that the organized motion associated with the pairing event carries nearly eight times the value of the time-mean maximum shear stress in the mixing layer. On the other hand, the contribution from the pairing event to the scalar transport is of the same order as the time-mean value. Comparing these results with those for the typical coherent event, one can conclude that pairing events are responsible for bringing about a significant amount of turbulent transport. The contribution to transport of momentum is indeed spectacular during pairing, while the contribution to scalar transport is only moderate. Browand & Weidman [1976] have shown experimentally that single events lead to Reynolds stresses that are comparable to the time average, while pairing events are very significant with respect to Reynolds stress production; results that are consistent with our findings. The results shown in Figs. 9 and 10 may be slightly modified if ensemble averages are obtained over a large number of realizations. However, the events are so strongly

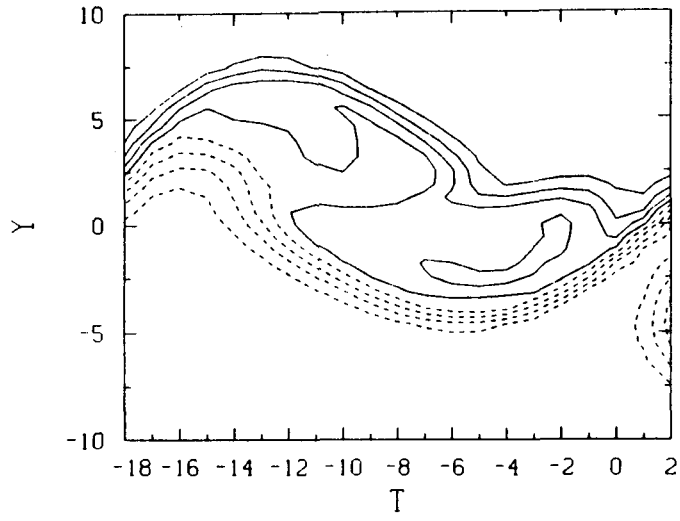

FIGURE 7. Contours of scalar concentration for a pairing event. Station $x = 137$.

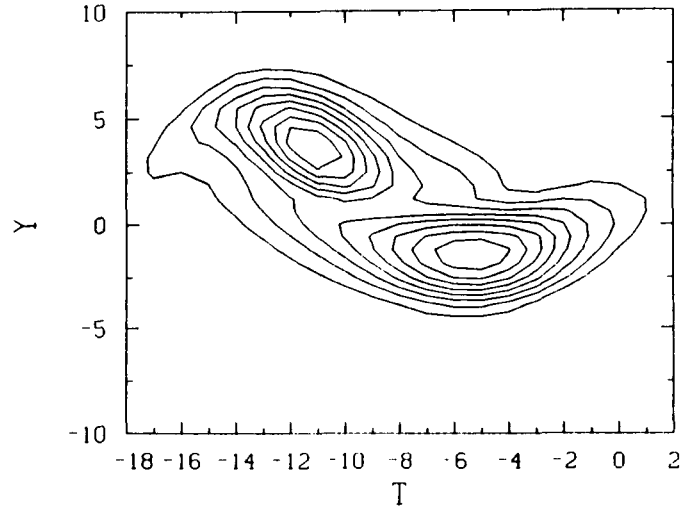

FIGURE 8. Contours of vorticity for a pairing event. Station $x = 137$.

coherent that it is unlikely that a major departure from this trend would emerge from the study of a large number of realizations.

6. Comparison of Scalar Conditioning with Vorticity Conditioning

Finally, it is instructive to compare the present eduction technique based on scalar level conditioning with other techniques. Unfortunately, it was not possible to make extensive comparisons with several techniques due to time-constraint. However, comparisons of the present results were made with those obtained using vorticity

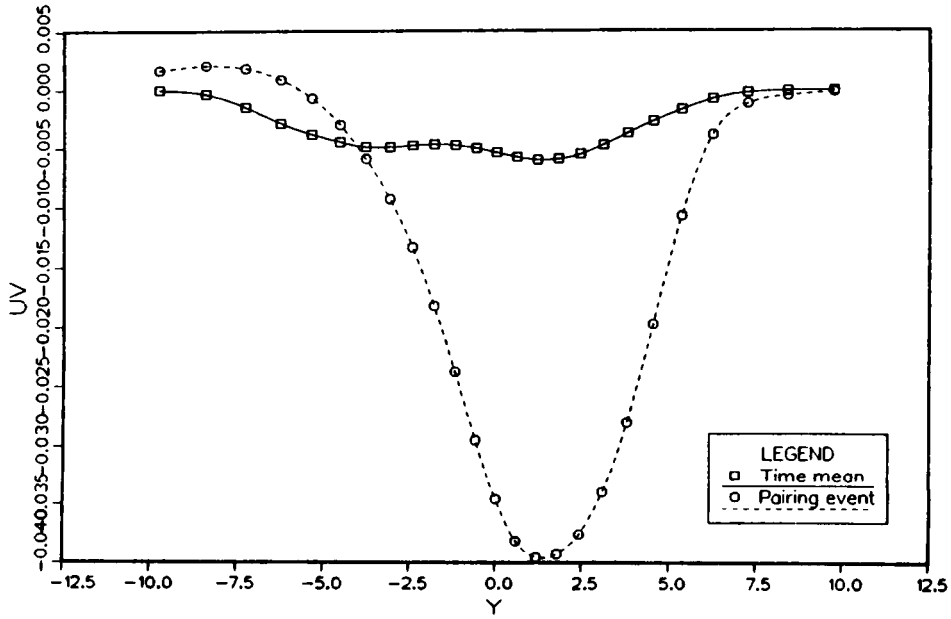

FIGURE 9. Contribution from the pairing event to the turbulent shear stress. Station $x = 137$

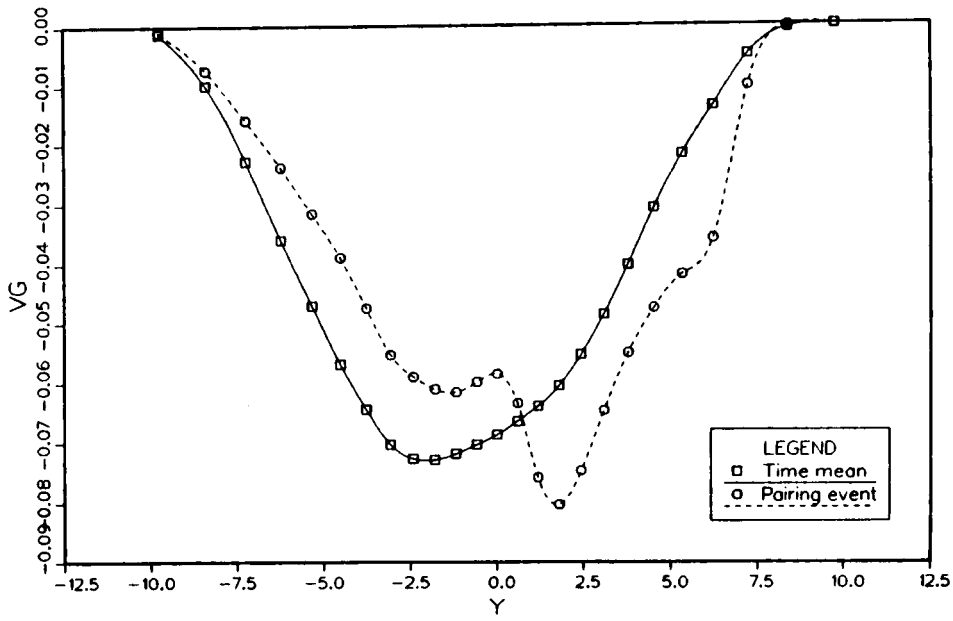

FIGURE 10. Contribution from the pairing event to the turbulent transport of the scalar in the normal direction. Station $x = 137$

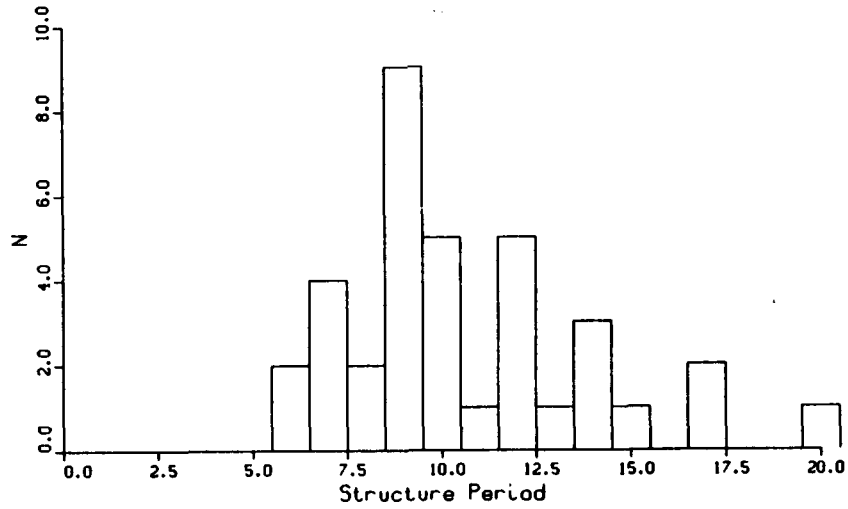

FIGURE 11. Histogram of event durations. Station $x = 78$, $y = 19$, vorticity threshold=0.04. Mean duration of events=10.6, $\sigma = 0.31$

level for the eduction of the coherent events. Vorticity is often regarded as the best criterion for the identification of the coherent structures. Instantaneous vorticity is, however, one of the most difficult quantities to monitor in an experiment. In the present numerically simulated mixing layer, however, instantaneous vorticity values were readily available. The eduction procedure used was analogous to that used with the scalar. Thus, a suitable y-location and a vorticity threshold level are selected by trial and error. Crossings of this level by the vorticity values in the increasing direction from zero are assumed to be associated with the passage of the coherent (vortical) events. Optimized histogram and ensemble averages are then obtained as in the case of scalar conditioning. Figure 11 shows the histogram of the duration of the coherent events. This can be compared with Figure 2. It is seen that while there are some differences in detail, the two histograms are quite similar. The mean duration of the events was nearly the same in the two cases. So also are the durations of the most frequent events. In fact, the contours of ensemble averaged scalar concentration and vorticity were found to be indistinguishable from those shown in Figs. 2 and 3 and are not therefore presented separately. The contours of ensemble-averaged shear stress $< U >< V >$ (corresponding to the organized motion) obtained with the two techniques are compared in Fig.12. It is seen that there are only very small differences between the two results. For example, there is only a 4% difference in the maximum values (and also minimum values) for the two cases. A somewhat larger difference (about 15%) was found in the value of the total shear stress carried by the coherent event. Even this difference is well within the uncertainties to be expected in a study such as this, especially when a small number of realizations are used to obtain the ensemble averages. It appears reasonable to conclude that with scalar tagging and conditioning, it is possible to

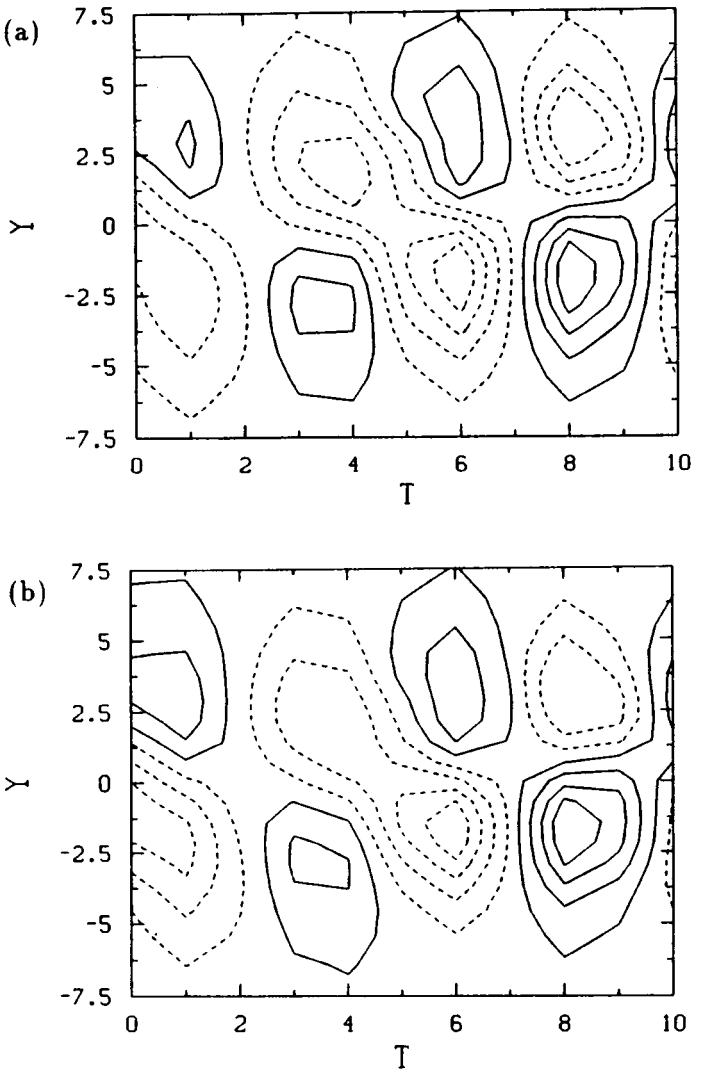

FIGURE 12. Contours of the ensemble-averaged shear stress $< U >< V >$ in the typical coherent event. Station $x = 78$. (a) from scalar conditioning (b) from vorticity conditioning.

isolate the typical coherent structures as reliably as with the more difficult vorticity conditioning technique.

7. Concluding Remarks

The present study, though limited in scope by time constraints, has led to some interesting observations and useful results. The study has demonstrated that, if properly used, passive scalar conditioning can prove to be a simple and effective

technique for the eduction and analysis of large-scale coherent structures in turbulent shear flows. The reason for its success is the fact that the scalar field under such conditions closely resembles the vortical field in respect of overall features like topology and large-scale structure. There are however differences between the two fields in respect of finer details within the structure. But, these latter differences do not affect the eduction process significantly. In fact, eduction based on scalar conditioning captures more or less the *same* structures as those captured by an alternate technique such as vorticity conditioning. The key requirements for the success of the scalar conditioning technique, however, are that the *entire stream* on one side of the mixing layer is maintained at a uniform scalar concentration and that the Schmidt number of the scalar is close to unity.

The study of the ensemble averaged properties associated with the coherent events was also very useful, in spite of the several restrictive test conditions, such as the use of two-dimensional simulation, low Reynolds number, arbitrary (though reasonable) initial forcing and downstream boundary conditions, and the small number of realizations under which it was conducted. This study showed that typical coherent events carry a significant amount of 'turbulence' and can therefore affect the overall transport of momentum and scalar in a significant manner. However, even more significant are the pairing events in affecting these transport phenomena. Particularly spectacular is the role of these events in the transport of momentum, which reaches several times the time-mean value. Scalar transport is not significantly increased during these events.

REFERENCES

JOVIC, S. AND RAMAPRIAN, B.R. IIHR Report 298, University of Iowa, Iowa City (1986).

BROWNE, L.W.B., ANTONIA, R.A. AND BISSET, D.K. 1986 . *Phys. Fluids.* **29**, 3612.

HUSSAIN, A.K.M.F. AND HAYAKAWA, M.J. 1987 . *J. Fluid Mech.* **180**, 193.

CIMBALA, J.M., NAGIB, H. M. AND ROSHKO, A. 1988 . *J. Fluid Mech.* **190**, 295-298.

SANDHAM, N.D. AND REYNOLDS, W.C. Proceedings of the Sixth Symposium on Turbulent Shear Flows , Toulouse, France. (1987).

BERNAL, L.P. 1988 . *Phys. Fluids.* **31**, (4), Sept. 1988, 2533.

BROWAND, F.K. & WEIDMAN, P.D. 1976 . *J. Fluid Mech.* **76**, 127-144.

Page intentionally left blank

Center for Turbulence Research
Proceedings of the Summer Program 1988

Sensitivity of mixing layers to three-dimensional forcing

By J. J. Riley[1], P. D. Mourad[1], R. D. Moser[2] AND M. M. Rogers[2]

1. Introduction

It is well-known that turbulent mixing layers are dominated by large-scale, fairly coherent structures, and that these structures are related to the stability characteristics of the flow (see, for example, Ho & Huerre 1984, for an excellent review of this subject). These facts have led researchers to attempt controlling such flows by selectively forcing certain unstable modes, which can in addition have the effect of suppressing other modes. For example Oster & Wygnanski (1982) and Ho & Huang (1982) found that, by subjecting the mixing layer to oscillatory disturbances upstream of the splitter plate at frequencies related to unstable modes, the growth of the layer could be significantly inhibited. Similarly it has been found (Husain & Hussain 1986) that forcing at certain frequencies and their subharmonics can enhance the growth of the mixing layer.

Much of the work on controlling the mixing layer has relied on forcing two-dimensional instabilities. In this study we address the results of forcing three-dimensional instabilities. The objectives of our work are twofold: (1) to understand how a mixing layer responds to three-dimensional perturbations, and (2) to test the validity of an amplitude expansion in predicting the mixing layer development. The amplitude expansion could be very useful in understanding and predicting the three-dimensional response of the flow to a variety of initial conditions.

The mixing layer is sensitive to several aspects of the imposed perturbations, including their wavelength or frequency (see, *e.g.*, Michalke, 1964), the relative phases of the disturbances if more than one are used (*e.g.*, Patnaik, Sherman & Corcos 1976), the relative amplitudes of the disturbances (Metcalfe *et al.* 1987), and their shape (*e.g.*, eigenfunctions of the Orr-Sommerfeld equation, etc.). The approach we would like to take is to systematically explore the sensitivity of the mixing layer to various types of three-dimensional perturbations, using both direct numerical simulations and amplitude expansions. However, the potential parameter space to explore is very large. In this preliminary study we begin by selecting several different conditions for simulation and examining the behavior of the computed flow fields. In order to test the amplitude expansion technique, we compare previous simulation results with predictions from the theory for cases where the simulations and theory treat similar initial conditions. In this preliminary study, we limit the application of the expansion technique to two-dimensional mixing layers.

1 University of Washington
2 NASA Ames Research Center

C-2

2. Mathematical description

Consider a temporally evolving mixing layer with a Cartesian coordinate system oriented with x in the mean flow direction, y in the direction of the variation of the mean velocity, and z in the transverse direction.

It is both convenient and natural to consider initial perturbations of the form

$$u_i(x,y,z) = \tilde{u}_i(\alpha,y,\gamma)e^{i(\alpha x+\gamma z)}$$

since this is the form of the stability eigenfunctions. The simulations and analysis were performed using initial conditions consisting of the sum of a few perturbations of this form. Consider first the two-dimensional modes, where $\gamma = 0$. If the simulations were initialized at a very low level with broad-banded noise, then the first significant disturbance would appear at approximately $(\alpha_F, 0)$, where α_F is the wave number of the most unstable mode based upon linear stability theory ($\alpha_F \approx 0.8892\delta$, where δ is the initial vorticity thickness, Michalke, 1964). Initialization of this mode causes roll up to occur (Patnaik, Sherman & Corcos 1976; Riley & Metcalfe, 1980), and the development of higher harmonics (*e.g.*, $(2\alpha_F, 0)$). If the initial field is broad-banded, then the subharmonic $(1/2\,\alpha_F, 0)$ will also show significant growth, both due to its own inherent instability and also to nonlinear interaction with the fundamental. Vortex pairing will eventually occur. The behavior of these two-dimensional disturbances is well-documented by laboratory experiments, numerical simulations, and theory.

Next consider three-dimensional disturbances ($\gamma \neq 0$). In laboratory experiments used to study the mixing layer downstream of a splitter plate, it is observed that the initial primary three-dimensional disturbance consists of streamwise vortices of a particular wavelength (approximately $\gamma_F = 1.5\alpha_F$) that appear locked in phase (Bernal, 1981; Ho & Huang, 1982). In the current nomenclature, these modes are the points $(0, \gamma_F)$ in the (α, γ) plane. Initial disturbances of this type were considered by Pierrehumbert & Widnall (1982), and their growth termed translative instability. It was found that, based upon linear stability theory, these translative modes are weakly algebraically unstable. However, in the presence of a finite amplitude, two-dimensional disturbance, the translative modes become highly unstable.

Another mode that has received some previous attention is the oblique mode at (α_F, γ_F), which was addressed theoretically by Pierrehumbert & Widnall (1982) and Corcos & Lin (1984), and numerically by Metcalfe *et al.* (1987). The latter work showed that initializing these modes along with the fundamental results in streamwise disturbances very similar to those observed in the laboratory. This mode is unstable according to linear stability theory, but the quoted previous work shows that it is much more unstable in the presence of finite amplitude, two-dimensional disturbances.

At this point it is important to mention certain differences between the spatially-evolving and temporally-evolving mixing layers. The former is what is usually studied in laboratory experiments, and is a more realistic approximation to many flows encountered in technology, *e.g.*, in mixing regions in reaction chambers. The

temporally-evolving mixing layer is probably a better model for geophysical situations, *e.g.*, mixing layers in the atmosphere or oceans. It has been studied more often numerically because of the significant numerical advantages in avoiding inflow/outflow boundary conditions. Some laboratory experiments have been conducted for the temporally-evolving case (see, *e.g.*, Thorpe, 1985) using salt-stratified water in a tilting tank.

The temporal mixing layer studied in the tilting tank experiments shows little evidence of the strong streamwise vortices which are commonly observed in spatially-evolving mixing layers (Thorpe 1985). This is perhaps due to the fact that the $(0, \gamma_F)$ mode would not be preferentially excited in these experiments. In spatially-evolving mixing layer experiments, streamwise vortices are often present at the edge of the splitter plate, and are probably related to features of the particular experimental facility (Ho, 1988). Although the temporally-evolving flow exhibits the same qualitative two-dimensional features as the spatially-evolving mixing layer, *e.g.*, rollup and pairing, it appears that the development of the three-dimensional disturbances may be significantly different, due to differences in the nature of the disturbances. In the numerical simulations presented in §4, initial disturbances which would produce streamwise vortices similar to those observed in *spatially* developing mixing layers were selected.

To address the problem of the sensitivity of the mixing layer to three-dimensional disturbances, we consider the constant density Navier-Stokes equations:

$$\frac{\partial \mathbf{u}}{\partial t} + \mathbf{u} \cdot \nabla \mathbf{u} = -\nabla p + R^{-1} \nabla^2 \mathbf{u} \tag{2.1}$$

$$\nabla \cdot \mathbf{u} = 0 \tag{2.2}$$

Here $\mathbf{u} = (u, v, w)$ is the velocity vector and p is the pressure. The equations have been nondimensionalized using the velocity scale $\Delta U/2$, half the mean velocity difference across the layer; the length scale $\delta = \Delta U / U_y(y = 0)$ (initial vorticity thickness) and the time scale $2\delta/\Delta U$. The Reynolds number R is defined $R = \Delta U \delta / 2\nu$.

The initial velocity field consists of an initial mean velocity U plus an initial perturbation $\mathbf{u}'$. U is taken to be an error function, $(U(y) = \mathrm{erf}(\sqrt{\pi} y))$ For boundary conditions we assume periodicity in the x and z directions, and assume that all perturbations decay as $|y| \to \infty$.

3 Amplitude expansion technique

We have extended a procedure for theoretical analysis of two-dimensional wave-wave interactions in unstable shear flows (Mourad, 1987; Mourad & Brown, 1988) to the case of two- and three-dimensional waves, here applied to the temporal mixing layer. The details of this derivation and results are in the Appendix. As a first application to the mixing layer, we will consider the classic problem of the interaction of a two-dimensional wave with its two-dimensional subharmonic, to determine if we can reproduce the phase-dependency of their evolution, as described in Patnaik, Sherman & Corcos (1976), Riley & Metcalfe (1980) and Ho and Huerre (1984); see also Mansour *et al.* in this volume.

3.1 Two-dimensional amplitude expansions

We begin by listing the equations governing the temporal evolution for the stream function of the two dimensional fundamental, with amplitude and phase $A(t)$ and $\theta_A(t)$, respectively, and of the subharmonic, with amplitude and phase $B(t)$ and $\theta_B(t)$, respectively.

$$\frac{1}{A}\frac{dA}{dt} - i\frac{d}{dt}\theta_A = a_0 + a_1\frac{B^2}{A}e^{-i(2\theta_B-\theta_A)} + a_3A^2 + a_4B^2 \tag{2.3}$$

$$\begin{aligned}\frac{1}{B}\frac{dB}{dt} - i\frac{d}{dt}\theta_B = {} & b_0 + b_1Ae^{-i(\theta_A-2\theta_B)} + b_3A^2 + b_4B_2 \\ & + b_7A^2e^{-2i(\theta_A-2\theta_B)} + b_8A^2e^{-i(\theta_A-2\theta_B)}\cos(\theta_A-2\theta_B) \\ & + b_9A^2e^{-i(\theta_A-2\theta_B)}\sin(\theta_A-2\theta_B)\end{aligned} \tag{2.4}$$

As discussed in detail in the Appendix, the rational for these equations is similar to that of Lorenz, or of Stuart's energy method (Ho & Huerre, 1984). Like them, we derive Equations (2.3) and (2.4) without benefit of asymptotic analysis, which would ordinarily allow for an ordering of the weights of the various physical processes in the mixing layer. We forgo asymptotics, because a reasonable small parameter is not available for our use in supercritical mixing layers. Instead, the expansions are truncated based on the physical processes we wish to include or remove from the model. Finally, like Lorenz and Stuart, we hope that the results lend at least qualitative insight into the true physical processes. We do, however, include more detail in the expansions than these other theories.

In 2.3 and 2.4, a_0 and b_0 govern the linear growth of their respective disturbances. They are complex constants of the form $\sigma_p - \omega_p i$, where σ_p is the growth rate and ω_p is the linear frequency of each of the waves.

The terms beginning with a_1 and b_1 represent the effects of the changes induced by each wave on the other. This direct interaction was the focus of the asymptotic study of Monkewitz (1988), who used an expansion near the critical Reynolds number (≈ 0) to define a small parameter. However, for supercritical flows, other nonlinear effects are also important (see Ho & Huerre 1984). Only a_1 and b_1 terms are included by Monkewitz and others, because they show that when the flow is near critical the return-feedback effects discussed below occur on a much longer time scale than the initial interaction.

Next, the term with coefficient a_3 represents the affects on the fundamental wave of the modified mean flow and the first harmonic $(2\alpha_F, 0)$. Both the modified mean and the first harmonic are forced by the fundamental. This term generally acts to check the unbridled growth of the wave in a supercritical flow.

The term with a_4 represents a variety of physical effects. These include the effect on the fundamental of (1) the modification to the mean flow induced by the subharmonic wave; (2) the distortion of the subharmonic induced by the fundamental (as represented by the b_1 term). The energy methods would have a term like a_4 in their evolution equations which would not include the second contribution.

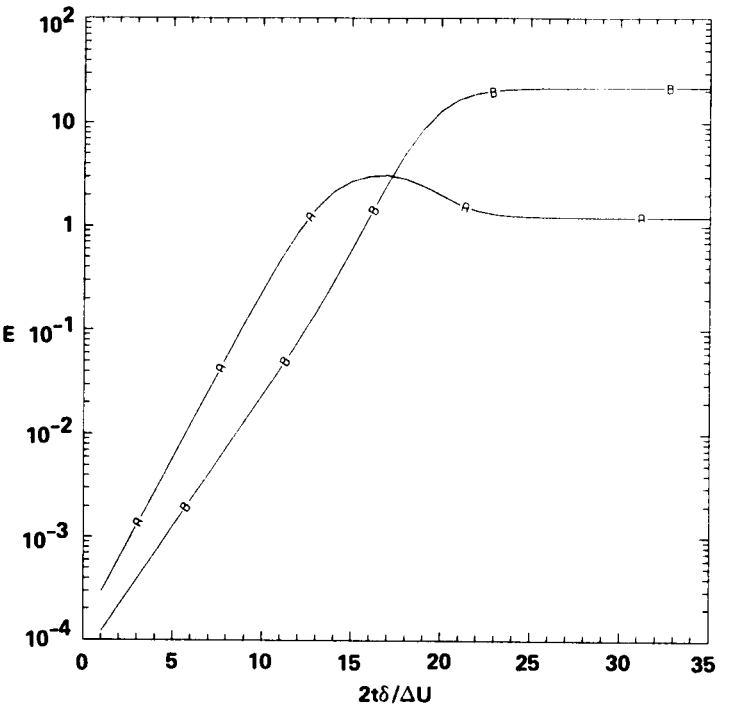

FIGURE 1. Evolution of the energy in the (A) fundamental ($E_{(\alpha_F,0)}$) and (B) subharmonic as predicted by equations (2.3) and (2.4).

The term beginning with b_3 represents the effects on the subharmonic of the changes in the mean flow induced by the fundamental, and the b_4 term is analogous to the a_3 term. In addition, b_4 includes additional effects due to the direct interaction of the fundamental and subharmonic, as in the a_4 term.

The more exotic looking terms with b_7, b_8 and b_9 are all due to the impact of the direct interaction of $(\alpha_F, 0)$ and $(\alpha_F/2, 0)$ on the subharmonic.

3.2 Two-dimensional amplitude expansion results

For this report, we will not consider a detailed discussion of the roles played by the various terms in the calculations; though this is of great interest, it is left for future work. Here we will verify the effect on the interactions of changing the initial phase difference between the fundamental and subharmonic. The importance of the relative phase is well documented (Husain & Hussain 1986, Patnaik, Sherman & Corcos 1976, and Riley & Metcalfe 1980). Following the definitions used in the numerical simulations, the fundamental and subharmonic are *in-phase* if alternate cores of the fundamental modes are aligned with the cores of the subharmonic modes. They are *out-of-phase* if the cores of the subharmonic are between the cores of the fundamental. (This is apparently opposite to the definition used in the review article of Ho & Huerre, 1984.) An operational definition like that above is important, since the linear stability eigenfunctions have an arbitrary phase.

Figure 1 shows a typical result of integrating the evolution equations (2.3 and

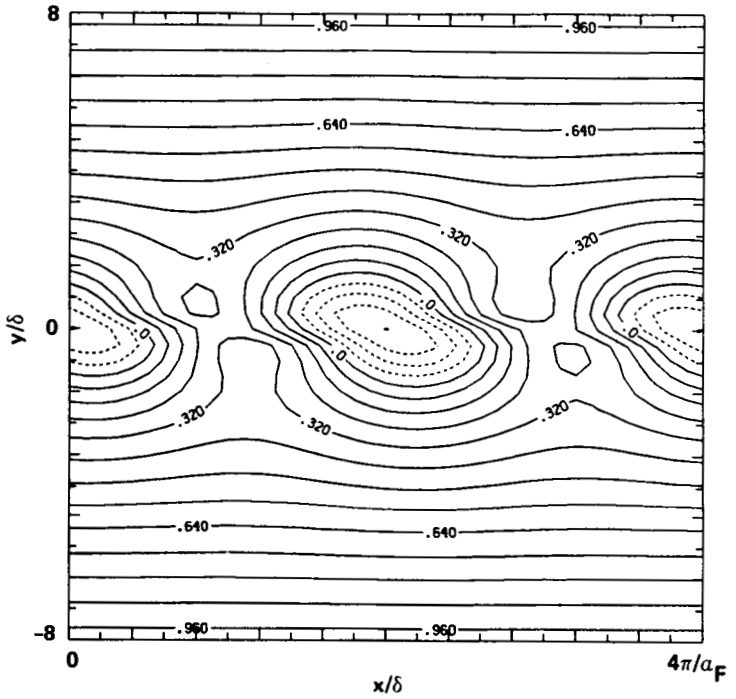

FIGURE 2. Contours of the stream function at time 13 as computed using the amplitude expansion for disturbances which are in-phase.

2.4). What is plotted is an approximation to the energy ($E_{(p,q)}$) in the fundamental and subharmonic modes, as given by;

$$E_{(\alpha_F,0)} = A^2(t) \int_{-\infty}^{\infty} [u^2_{0,(\alpha_F,0)} + v^2_{0,(\alpha_F,0)}]\, dy$$
$$E_{(\alpha_F/2,0)} = B^2(t) \int_{-\infty}^{\infty} [u^2_{0,(\alpha_F/2,0)} + w^2_{0,(\alpha_F/2,0)}]\, dy \qquad (3.1)$$

Note that these are unnormalized energies. The theory is also capable of generating a more complete energy integral, with the total nonlinear form $u_{(\alpha_F,0)}$, rather than the structurally linear form $u_{0,(\alpha_F,0)}$ (see the appendix for an explanation of the notation). This is a matter for future work.

The linear growth of each of the waves (the straight lines on this log-linear graph) is followed by the weak acceleration of the subharmonic (between nondimensional times 13 and 16) due to the effects of the b_1 term. The fundamental then equilibrates due to the action of a_3, while B keeps growing due to the forcing of A, as well as its own ability to extract energy from the mean flow. Once the subharmonic amplitude reaches a critical value, the fundamental is reduced, and the subharmonic equilibrates due to the action of b_4 and a_4. (Note that the final state as predicted here is suspect, since we have discovered that b_4 and a_4 are incomplete as currently calculated. This will be amended in future work.) This graph is representative of

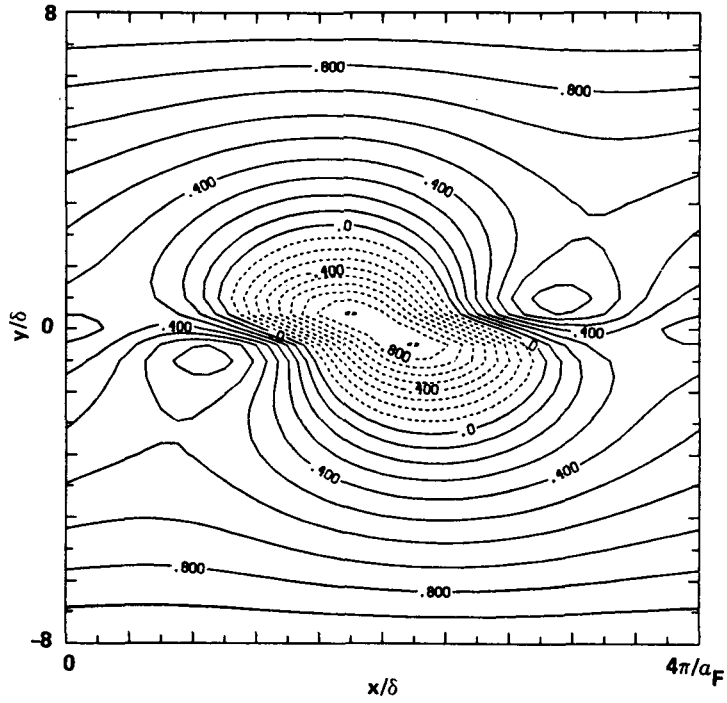

FIGURE 3. Contours of the stream function at time 18 as computed using the amplitude expansion for disturbances which are in-phase.

both the in-phase and out-of-phase calculations, at least qualitatively, and is similar to that in Riley & Metcalfe (1980).

During the linear portion of the evolution, the total stream function field (Figure 2) shows the characteristic scales associated with the fundamental mode, here at time 13 for the in-phase case. The subharmonic is there, with its core at the center of the plot underneath that of the fundamental. However, the subharmonic makes a negligible contribution to the field at this time. The stream function field for the out-of-phase case is the same. Note that this and all the following plots have streamwise domain lengths which equal the wavelength of the subharmonic: therefore, two fundamental vortices and one subharmonic vortex can fit into the domain.

Once the nonlinear interactions become important (nondimensional time of about 18), the flow patterns for the in-phase and out-of-phase cases become different. The total stream function field for the in-phase case (Figure 3) shows an *enhancement* of the original, central, fundamental vortex, at the expense of the vortices to either side, whose torn remnants are at the edge of the graph. This is the 'tearing' mode discussed in Patnaik, Sherman & Corcos (1976). Note that the mixing region, as well as the vortex itself, is smaller here than for the out-of-phase case at the same time (Figure 4). There the subharmonic vortex, made up of two paired, fundamental vortices, fills the graph, showing an increase in the mixing region.

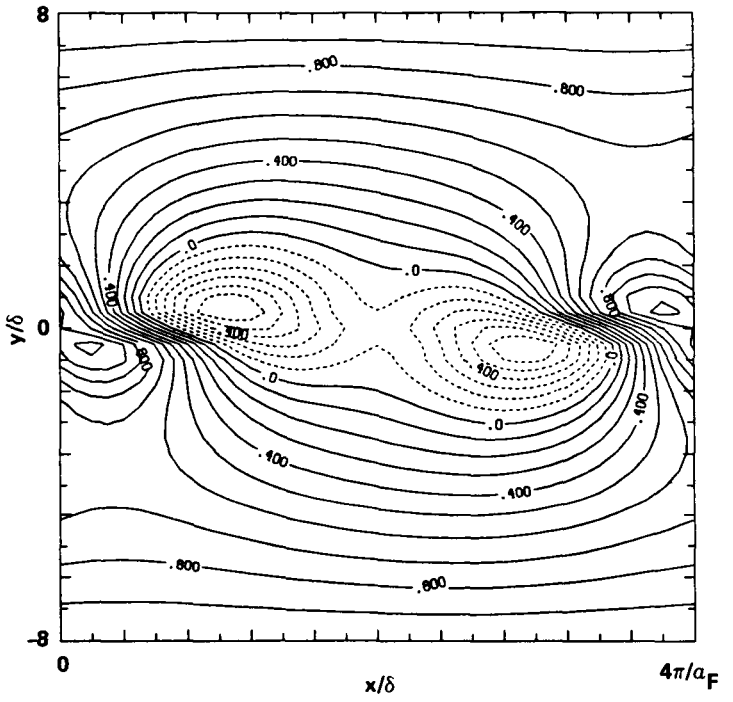

FIGURE 4. Contours of the stream function at time 18 as computed using the amplitude expansion for disturbances which are out-of-phase.

In this application of the amplitude theory, an important experimental and numerical result is reproduced: the effect of the relative phases of the waves. This is an important validation of the approach for this flow which provides encouragement for future applications of the theory. Future applications should include detailed analysis of the role played by each term in the expansion, and should include three-dimensionality as laid out in the appendix. Three-dimensional predictions can be compared to three-dimensional numerical simulations as described in §4 below.

4. Direct numerical simulations

In the numerical simulations, the Navier-Stokes equations (2.2) are solved using a spectral numerical method based on the expansions discussed by Cain, Ferziger & Reynolds (1984). Grid resolutions up to 64^3 were used for the results presented below.

In these preliminary studies, we present results for four different simulations. In the first two cases (Case I and Case II), the fundamental $(\alpha_F, 0)$ as well as the translational mode $(0, \gamma_F)$are initially nonzero. The fundamental mode is taken to be the solution to the Rayleigh equation at $\alpha = \alpha_F$, while the mathematical form

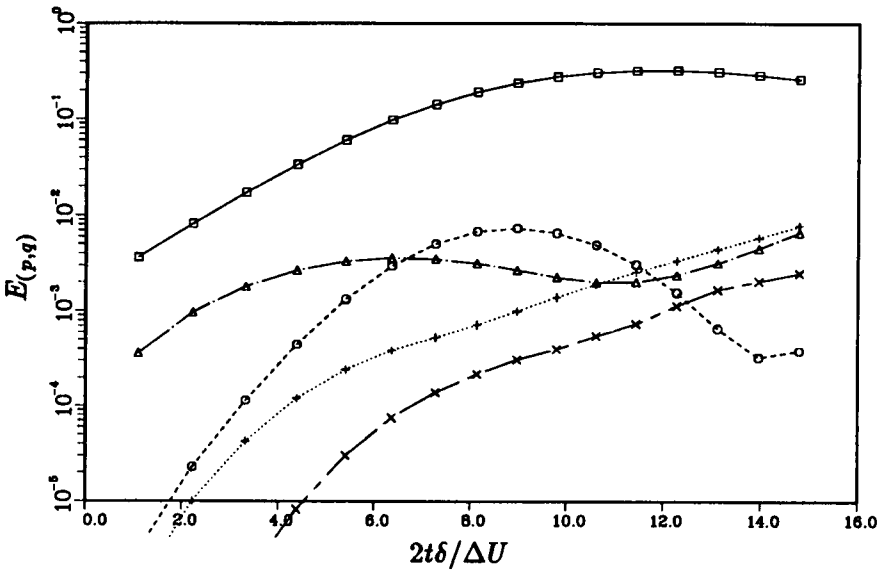

FIGURE 5. Evolution of model energies for CASE I, for the modes: □ , $(\alpha_F, 0)$; ○ , $(2\alpha_F, 0)$; △ , $(0, \gamma_F)$; + (α_F, γ_F); and × $(\alpha_F, 2\gamma_F)$. Modes $(\alpha_F, 0)$ and $(0, \gamma_F)$ were initially excited with energies 2×10^{-3} and 1.5×10^{-4} respectively.

for the translational mode is chosen to be

$$u(x, y, z, 0) = 0,$$
$$v(x, y, z, 0) = Ae^{-2y^2} \cos(\gamma_F z),$$
$$w(x, y, z, 0) = -\frac{4Ay}{\gamma_f} e^{-2y^2} \sin(\gamma_F z).$$

The difference in the two cases is the amplitude A. In Case I it is set to 0.025, while in Case II it is 0.05. In the latter two cases (Case III and Case IV), the fundamental plus the oblique modes (α_F, γ_F) and $(\alpha_F, -\gamma_F)$ are initially nonzero. The normal velocity v for the oblique modes is initially as given above, the other velocity components are such that continuity is satisfied and $\gamma_F u - \alpha_F w = 0$. In Case III the oblique mode is approximately out-of-phase with the fundamental, i. e., it is symmetric about the core of the two-dimensional vortex, while in Case IV the oblique wave is in-phase.

A plot of modal energies versus time for case I is shown in figure 5. In this and in the following, the modal energy is defined by

$$E(\alpha, \gamma, t) = \frac{1}{2} \Sigma_{\alpha,\gamma} \int |\tilde{u}_i(\alpha, y, \gamma, t)|^2 \, dy. \tag{3.2}$$

Here summation over i is implied, and $\tilde{u}_i(\alpha, y, \gamma, t)$ is the Fourier transform of $u_i(x, y, z, t)$ in the (x, z) plane. The summation sign denotes a sum over the modes (α, γ), $(\alpha, -\gamma)$, $(-\alpha, \gamma)$, and $(-\alpha, -\gamma)$.

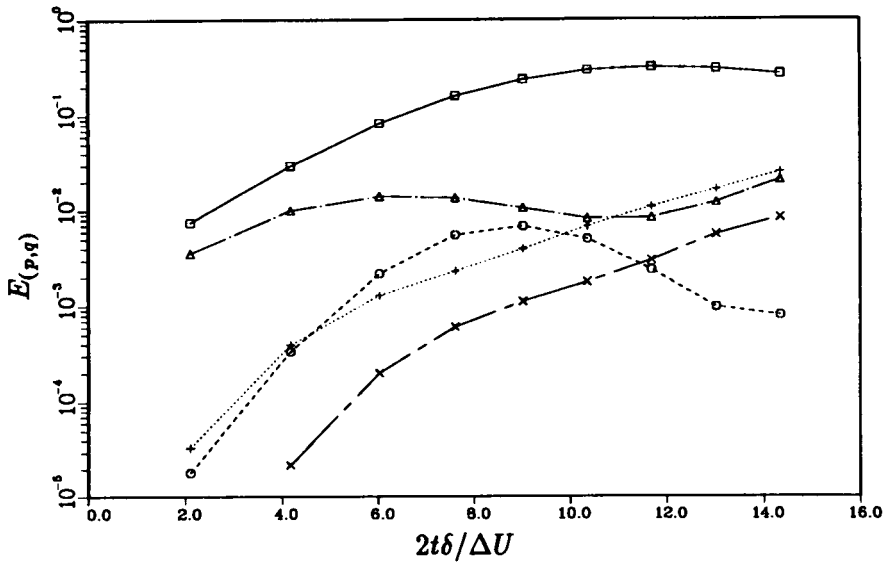

FIGURE 6. Evolution of model energies for CASE II, for the modes: □ , $(\alpha_F, 0)$; ○ , $(2\alpha_F, 0)$; △ , $(0, \gamma_F)$; + (α_F, γ_F); and × $(\alpha_F, 2\gamma_F)$. Modes $(\alpha_F, 0)$ and $(0, \gamma_F)$ were initially excited with energies 2×10^{-3} and 6×10^{-4} respectively.

In Figure 5 we see that the energy in the fundamental mode grows, at first exponentially, then more gradually, and finally levels off at time 12, which corresponds approximately to vortex rollup. At the same time the harmonic $(2\alpha, 0)$ grows very rapidly, peaking at about $t = 9$, and then decays as rollup is completed.

The translative mode, which is only algebraically unstable without the finite amplitude, two-dimensional mode, initially grows very rapidly. Further analysis of the results showed that this growth is initially mainly in the u-component, and is due to the streamwise vortices inducing motion in the y-direction, along the gradient of the mean velocity (Squire mode). As the mixing layer rolls up, vortex stretching occurs along the layer, resulting in further increase in this translative mode. We see that subsequently the oblique mode begins to grow rapidly, and ultimately overtakes the translative mode. Analysis of visualizations (see below) suggests that this growth is due both to the tilting of the streamwise vortices and the distortion of the main spanwise rollers by the the streamwise vortices.

Figure 6 gives the modal energies versus time for Case II, which has the same initial conditions as for Case I except that the translative mode amplitude is increased by a factor of 2. Comparing Figures 5 and 6, we see that the energies in the fundamental mode and its harmonic are essentially the same for the two cases. From an energetics point of view the two-dimensional rollup is totally unaffected by the three-dimensional motions, even though in this latter case the energy in the translative mode is within a factor of two of that in the fundamental mode (at about $t = 2$). Previously Metcalfe *et al.* (1987) observed that, in the interaction of an oblique mode with the fundamental, the fundamental mode played a catalytic

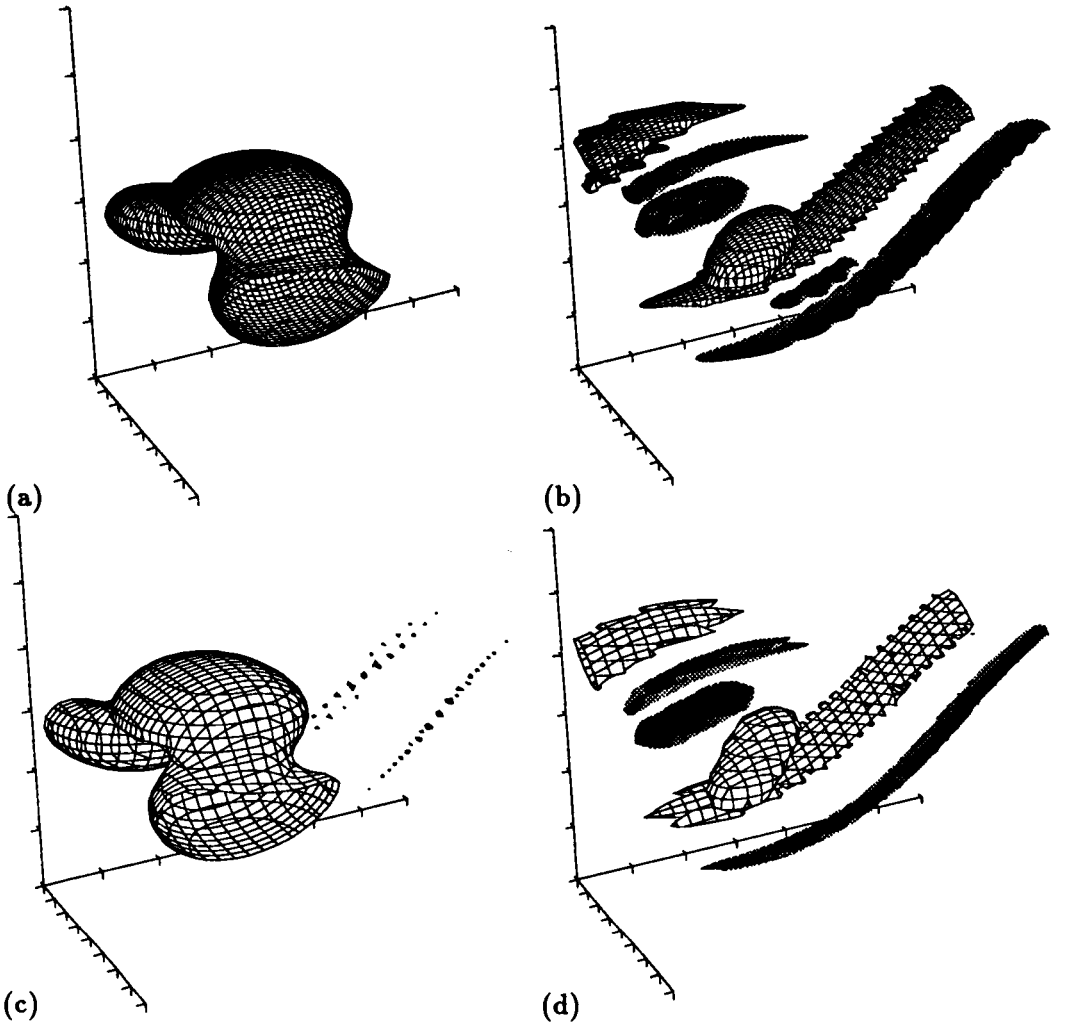

FIGURE 7. Iso-level surfaces of enstrophy *(a,c)* and ω_x *(b,d)* for CASE I *(a,b)* and CASE II *(c,d)*. Solid surfaces represent negative values. Contour levels are 1.5 in *(a,c)*, −0.3 and 0.3 in *(b)* and −0.6 and 0.6 in *(d)*.

role. Its presence was required for the enhanced growth of the oblique mode, but its energy was unchanged by the interaction. The increased energy in the oblique mode came from the mean flow. Our results indicate that this catalytic trait holds for both the fundamental and its harmonic interacting with the translative mode.

The total energy in the three-dimensional modes is significantly different for the two cases. However, examining the results more closely we find that the total energy in a particular three-dimensional mode for Case II is almost exactly four times the corresponding value for Case I. Since the initial amplitude for Case II is exactly twice that for Case I, this is consistent with the interpretation that the development of the three-dimensional dynamics is linear. This result gives some indirect support

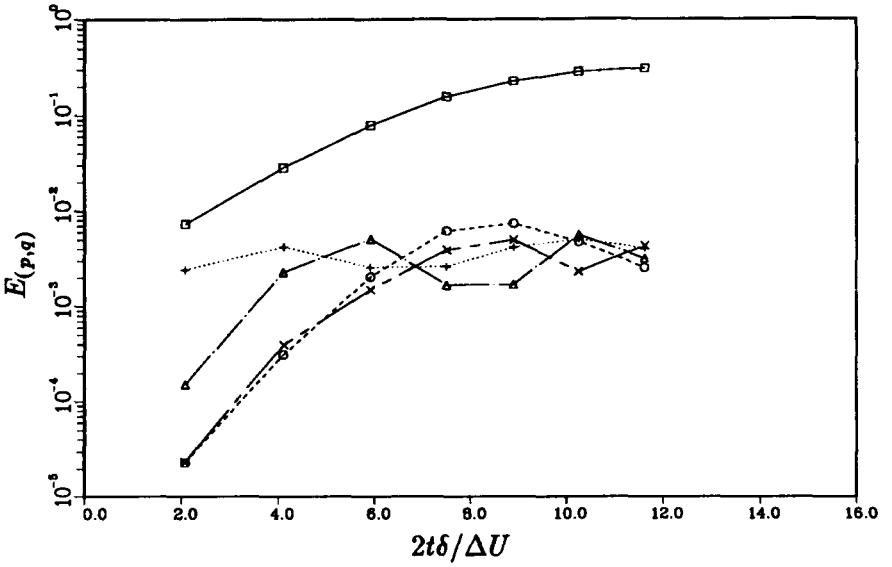

FIGURE 8. Evolution of model energies for CASE III, for the modes: □ , $(\alpha_F, 0)$; o , $(2\alpha_F, 0)$; △ , $(0, \gamma_F)$; + (α_F, γ_F); and × $(\alpha_F, 2\gamma_F)$. Modes $(\alpha_F, 0)$ and (α_F, γ_F) were initially excited with energies 2×10^{-3} and 10^{-3} respectively.

to the model of Corcos & Lin (1984) who, although studying the interaction of the fundamental mode with an oblique mode, assumed that the dynamics of the oblique mode were linear.

Perspective plots of iso-value surfaces of both streamwise vorticity (ω_x) and the norm of the vorticity ($\omega = \sqrt{\omega_i \omega_i}$) for these two cases are shown in figure 7. Note that in the plot of ω_x, the contour level for Case II was chosen to be twice that of the level for Case I. We see the development of the streamwise vorticity along the braids, and also these vortices being wrapped into the large-scale vortex core. Note that the streamwise vortices appear to be somewhat flat due to the straining field of the two-dimensional vortices. Also note the appearance of counter-rotating vortices in the core, probably due to the bending of the large-scale vortices by the streamwise vortices. It is interesting to note that the streamwise vorticity plots for the two cases are almost the same, lending strong support to the interpretation that the three-dimensional dynamics are essentially linear. This is surprising in view of the large distortions observed in the flow field. The plots of ω indicate the distortion of the large-scale vortices by the streamwise vortices.

We next discuss the results for the oblique wave cases: Case III, in which the oblique wave disturbance was initially approximately out-of-phase with respect to the vortex core, and Case IV, in which it was in-phase. Plots of the modal energy versus time for Cases III and IV appear in Figures 8 and 9, respectively. First note that in both cases the behavior of the energy in the two-dimensional modes is essentially identical to that for Cases I and II. This is further evidence that the

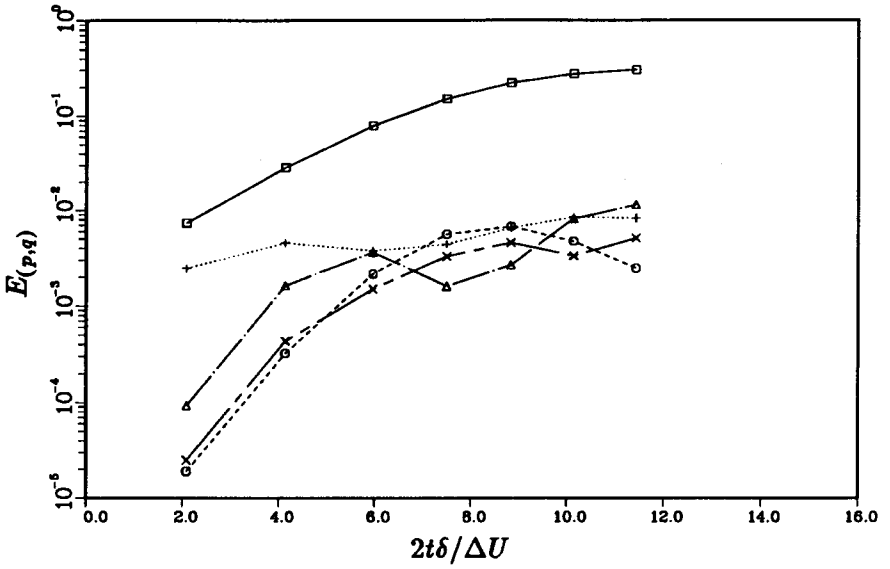

FIGURE 9. Evolution of model energies for CASE I, for the modes: □ , $(\alpha_F, 0)$; ○ , $(2\alpha_F, 0)$; △ , $(0, \gamma_F)$; + (α_F, γ_F); and × $(\alpha_F, 2\gamma_F)$. Modes $(\alpha_F, 0)$ and (α_F, γ_F) were initially excited with energies 2×10^{-3} and 10^{-3} respectively.

two-dimensional modes are unaffected by the three-dimensional motions, and is consistent with the catalytic character of the fundamental mode observed by Metcalfe *et al.* (1987). We further note that in both cases the oblique mode (α_F, γ_F) grows, but not as rapidly as the translational modes in the previous cases. Furthermore, in these cases the translational mode quickly grows from zero to be the same order as the oblique mode.

Though the energetics of the modes are unaffected by the phases, examination of the flow fields reveals that the details of the fields are quite different. Perspective plots of ω_x and ω for both cases appear in Figure 10. The time selected is $t = 10$, when rollup is almost complete. In Case III there is very little evidence of streamwise vorticity in the braid region; it has mainly been rolled into the vortex core. This is due to the fact that, initially, the stagnation point in the braids was near the zero in the streamwise vorticity. In Case IV streamwise vortices are evident, similar to those in Cases I and II. Comparing the plots of ω we see that the flow in the rollup regions is very different for the two cases.

5. Conclusions

From this preliminary study of the sensitivity of the mixing layer to three-dimensional disturbances, we draw a number of tentative conclusions. First it is clear that the mixing layer is sensitive to the wavelength of the disturbances (or frequency in the spatially-developing flow), the relative phases and amplitudes of the disturbances, and to the form of the disturbances. Clearly the disturbance needs to be well-defined in order to predict its behavior.

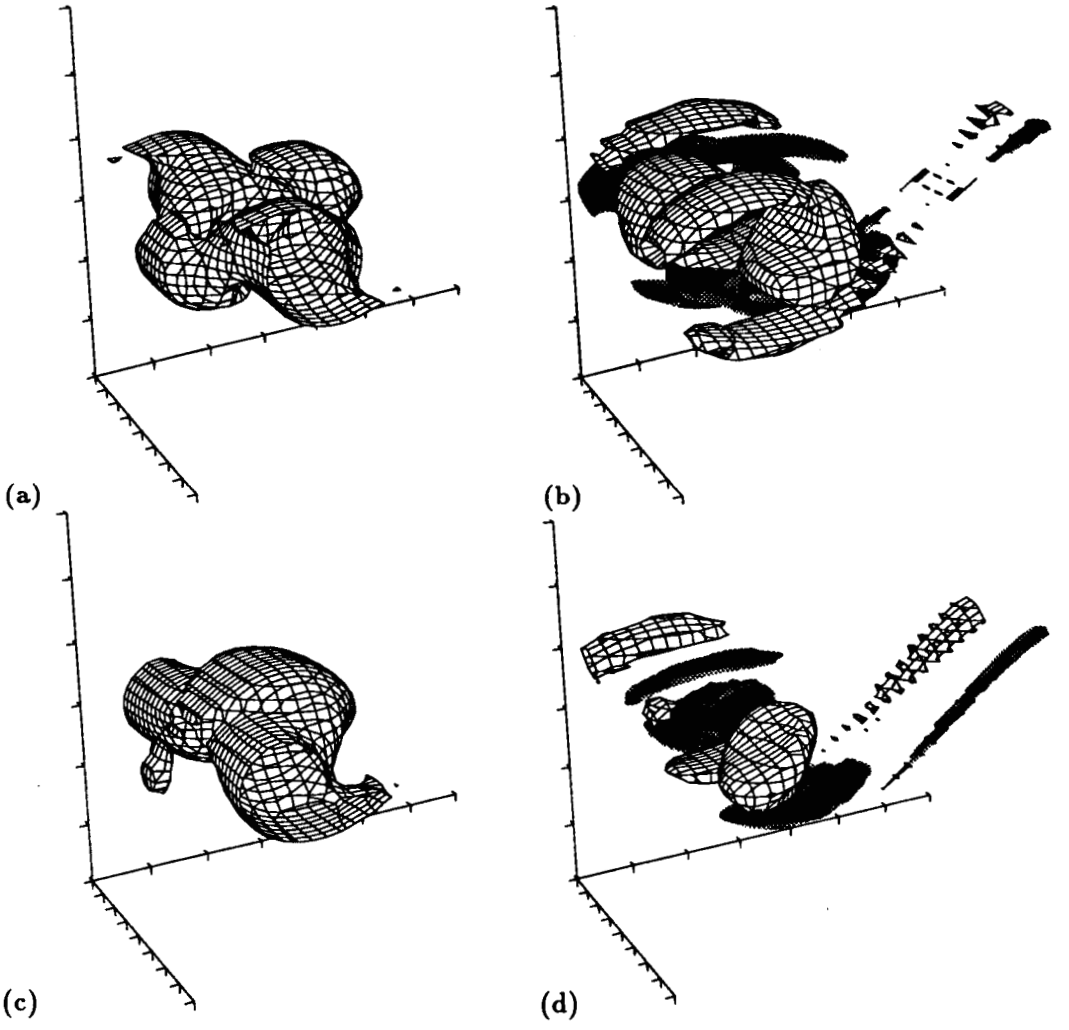

FIGURE 10. Iso-level surfaces of enstrophy *(a,c)* and ω_x *(b,d)* for CASE III *(a,b)* and CASE IV *(c,d)*. Solid surfaces represent negative values. Contour levels are 1.5 in *(a,c)*, −0.25 and 0.25 in *(b)* and −0.5 and 0.5 in *(d)*.

Secondly, it is important to realize that naturally-occurring temporally-evolving mixing layers may develop very different three-dimensional disturbances from those of spatially-evolving mixing layers. The principal initial three-dimensional disturbances in the spatial layer are fairly narrow-banded streamwise vortices, whose development and breakdown appear to be a principal factor in the transition to turbulence of the mixing layer. Their initiation appears to be related to features of the experimental facility. In the temporal layer it is unlikely that this mode is initially excited, and laboratory experiments do not show evidence of these vortices in the braid regions.

Third, at least during vortex rollup, the two-dimensional modes appear to be

almost totally unaffected by the three-dimensional disturbances. In addition, the three-dimensional disturbances behave in an almost linear fashion, being only affected by the two-dimensional rollup and not by their own interactions. This is true even though their energy levels are large, of the order of the energy in the two-dimensional modes.

Fourth, the translative instability appears to be faster growing than that of the oblique modes. This appears to be due to the growth of streamwise velocity fluctuations (the Squire mode). Fifth, the relative phase of the oblique mode perturbation with respect to the fundamental mode is not important in the energetics, but is important in the resulting flow pattern. And sixth, the successful preliminary work with the amplitude expansions suggests that they may be a useful quantitative tool for future research.

Finally, this preliminary study suggests additional simulations and mathematical analysis. For example, it would be useful to more carefully test the amplitude expansion technique by comparing its predictions with the results of direct numerical simulations for cases, both two- and three-dimensional, that treat the exact same initial conditions. If the theory appears to be adequate, then it could be used to better understand the interactions occurring in the simulations, and to determine what combinations of initial conditions might lead to desired features of the mixing layer behavior. With regard to the numerical simulations, there are a large variety of initial conditions which should be explored. Further simulations to determine the range of possible outcomes would be useful.

REFERENCES

BERNAL, L. P. 1981 The coherent structure of turbulent mixing layers. Ph.D. Thesis, California Institute of Technology.

CORCOS, G. M. & LIN, S.-J. 1984 The mixing layer: deterministic models of a turbulent flow. Part 2. The origin of three-dimensional motion. *J. Fluid Mech.* **139**, 67-95.

HERBERT, T. 1983 On perturbation methods in non-linear stability theory. *J. Fluid Mech.* **126**, 167-186.

HO, C.-M. 1988 Private Communication.

HO, C.-M. & HUANG, L.-S. 1982 Subharmonics and vortex merging in mixing layers. *J. Fluid Mech.* **119**, 443-473.

HO, C.-M. & HUERRE, P. 1984 Perturbed free shear layers. *Ann. Rev. Fluid Mech.* **16**, 365-424.

HO, C.-M. & GUTMARK, E. 1987 Vortex induction and mass entrainment in a small-aspect ratio elliptic jet. *J. Fluid Mech.* **179**, 383-405.

HUSAIN, H. S. & HUSSAIN, F. 1986 *Bull. of Am. Phys. Soc.* **31**, 1696.

METCALFE, R. W., ORSZAG, S. A., BRACHET, M. E., MENON, S. & RILEY, J. J. 1987 Secondary instability of a temporally-growing mixing layer. *J. Fluid Mech.* **184**, 207-243.

MICHALKE, A. 1964 On the inviscid instability of the hyperbolic tangent velocity profile. *J. Fluid Mech.* **19**, 543-556.

MONKEWITZ, P. A. 1988 Subharmonic resonance, pairing and shredding in the mixing layer. *J. Fluid Mech.* **188**, 223.

MOURAD, P. D. 1987 A nonlinear wave-wave interaction theory for the generation of multiscale large eddies in the atmospheric boundary layer. Ph.D. Thesis, University of Washington.

MOURAD, P. D. & BROWN R. A. 1988 On multiscale large eddy states in weakly stratified atmospheric boundary layers. submitted to the J. Atmos. Sci.

OSTER, D., & WYGNANSKI I. 1982 The forced mixing layer between parallel streams. *J. Fluid Mech.* **123**, 91-130.

PATNAIK, P. C., SHERMAN, F. S. & CORCOS, G. M. 1976 A numerical simulation of Kelvin-Helmholtz waves of finite amplitude. *J. Fluid Mech.* **73**, 215-240.

PIERREHUMBERT, R. T. & WIDNALL, S. E. 1982 The two- and three-dimensional instabilities of a spatially periodic shear layer. *J. Fluid Mech.* **114**, 59-82.

RILEY, J. J. & METCALFE, R. W. 1980 Direct numerical simulation of a perturbed turbulent mixing layer. *AIAA Paper No. 80-0274.*

THORPE, S. A. 1985 Laboratory observations of secondary structures in Kelvin-Helmholtz billows and consequences for ocean mixing. *Geophys. Astrophys. Fluid Dyn.* **34**, 175-199.

APPENDIX

In this appendix, we develop a theory for wave-wave interactions between oblique waves in supercritical shear flows. A more limited set of theoretical equations based upon the same procedure is used in the body of the text to study the interactions of a fundamental wave and its subharmonic. The more complete equations discussed here were developed during the summer workshop, and will be used in future studies.

The heart of the theory is a set of nonlinear evolution equations which govern the temporal history of the amplitudes of interacting waves. The theory is similar to Stuart's energy integral method, and Lorenz's derivation of his famous amplitude equations for convection. As in these other methods, we manipulate the Navier-Stokes equations in a formal way, without benefit of asymptotic arguments and with severe Fourier, Orr-Sommerfeld and amplitude truncations. Also like them, we hope that these truncations are a good approximation of the full series solution, and that they lend at least a qualitative insight into the physics of the problem. If we had recourse to asymptotically small parameters, a perturbation formalism would determine the relative weights of different physical effects. However, since the flow in question is supercritical, one cannot create a small parameter out of the governing Reynolds number. Neither has the relative energy of the disturbance to the mean flow proven useful as a small parameter. The subsequent evolution of the waves in the presence of the mean flow is governed by the ability of the waves and mean flow to exchange energy with each other, which, even in an initially linear regime, is independent of this parameter. With these obvious choices removed for supercritical flows there are no readily apparent small parameters that we can use. Supercritical flows generally evolve quickly away from any given initial state to a relatively remote state – a process which is not usually amenable to asymptotic analysis. With the formalism developed here, we can build tools which are simpler to use than the full Navier-Stokes equations, as well as lay bare the underlying physical processes. It becomes a powerful tool of analysis when used in tandem with experimental observations and/or direct numerical simulations.

The theory starts with the fully nonlinear, nondimensional Navier-Stokes equations, in the coordinate system used in the text. Separate the mean flow (a function of y and t alone) from the wavelike part (oscillatory in x and z) of the dependent variables, with the following notation:

$$\mathbf{U}(x,y,z,t) = \mathbf{U}_0(y) + \overline{\mathbf{U}}(y,t) + \mathbf{u}(x,y,z,t) \tag{A1.1}$$

$$P = \overline{P}(y,t) + p(x,y,z,t) \tag{A1.2}$$

The vector $\mathbf{U}_0 \equiv (U_0, 0, 0)$ defines the original flow field which will house the interacting waves. We have chosen:

$$U_0 \equiv \mathrm{erf}(\sqrt{\pi}y) \tag{A1.3}$$

where y is nondimensionalized by the initial vorticity thickness δ. This profile is selected because it is the self-similar laminar profile for a temporally-evolving mixing

layer. The mean pressure field will remain unspecified, as it does not enter into the problem. The vector $\overline{\mathbf{U}} \equiv (\overline{U}, 0, \overline{W})$ represents a time-dependent modification to the initial mean flow caused by nonlinear feedback from the spatially oscillating part of the field. It is calculated as part of the solution, as well as the modified mean pressure, given by $\overline{P}$.

Substituting the expansion (A1) into the Navier-Stokes equations one obtains the following:

$$u_t + U_0 u_x + v\frac{\partial}{\partial y}U_0 - \frac{1}{Re}\Delta u + p_x = -(\mathbf{u} + \overline{\mathbf{U}}) \cdot \nabla(u + \overline{U}) + \overline{\mathbf{u} \cdot \nabla u} \quad (A2.1)$$

$$v_t + U_0 v_x - \frac{1}{Re}\Delta v + p_y = -(\mathbf{u} + \overline{\mathbf{U}}) \cdot \nabla(v) + \overline{\mathbf{u} \cdot \nabla v} \quad (A2.2)$$

$$w_t + U_0 w_x - \frac{1}{Re}\Delta w + p_z = -(\mathbf{u} + \overline{\mathbf{U}}) \cdot \nabla(w + \overline{W}) + \overline{\mathbf{u} \cdot \nabla w} \quad (A2.3)$$

$$\overline{U}_t - \frac{1}{Re}\overline{U}_{yy} = -\overline{\mathbf{u} \cdot \nabla u} \quad (A2.4)$$

$$\overline{W}_t - \frac{1}{Re}\overline{W}_{yy} = -\overline{\mathbf{u} \cdot \nabla w} \quad (A2.5)$$

with:

$$\Delta \equiv \frac{\partial^2}{\partial x^2} + \frac{\partial^2}{\partial y^2} + \frac{\partial^2}{\partial z^2},$$

and the bar over the non-linear terms indicates the average in x and z (but not time) of each term.

A.1 Fourier expansions

The next step is to write the spatially oscillating components of the flow in a highly-truncated Fourier series in x and z. This series is truncated at the beginning so that the smallest number of Fourier components need be considered.

The collective nonlinear behavior of the primary waves with wavenumber vectors $(\alpha, 0)$, $(\alpha/2, 0)$, $(\alpha/2, \gamma)$ and (α, γ) is the main focus of this study. (Note that, for notational simplicity in this Appendix, we are dropping the subscript F, which denotes the fundamental mode in the main body of this paper.) This theory describes the evolution of a flow field by studying components of the Fourier transform of the velocity fields. The choice of the primary waves is motivated by the *observation* that these are significant waves: with this theory we will only attempt to explain their behavior, and can only suggest why these should be the waves of choice. According to linear theory, $(\alpha, 0)$ (also called the fundamental mode) initially grows most quickly, and $(\alpha/2, 0)$ is its subharmonic. The subharmonic is significant because after the roll-up of the initial vortices (equilibration of the fundamental wave), the subharmonic is observed to grow resulting in the pairing of the two-dimensional vortices. The pairing process is dependent upon the relative phases of $(\alpha, 0)$ and $(\alpha/2, 0)$, among other things. Observations show that the pairing is followed by, and sometimes concurrent with, the development of three-dimensionality in the

originally two-dimensional flow. Spectrally, this is represented by the inclusion of oblique waves (α,γ) and $(\alpha/2,\gamma)$.

Other waves could also be chosen as primary: for example, an interesting choice is the wavenumber vector $(0,\gamma)$, which denotes a system of longitudinal vortices. The formalism would proceed in the same fashion if these were included, with different evolution equations as the result. However, since this is as yet only a temporal theory, and $(0,\gamma)$ seems to be more relevant for spatially developing flow fields, we ignore this mode for now.

There is another class of waves which are included here, because they are forced by various combinations of the primary waves and their complex conjugates. For short times, these waves are observed to be slaved to the primary ones, that is the dynamics of these modes are dominated by the forcing. Their intrinsic dynamics are considered insignificant so no extra degrees of freedom will be required to account for their effects. For this limited study, we only include the first harmonic of $(\alpha,0)$, given by wavenumber vector $(2\alpha,0)$ because it is important for the interaction between $(\alpha,0)$ and (α,γ). We also assume that the modification to the mean and the so called Squire modes (see below) remain slaved to the primary waves.

Which waves to include, and whether they are included as free or forced waves, are subtle, contentious, important and open questions. They represent large areas of possible improvement as well as additional complexity.

Finally note that while we have only been discussing modes of the form (p,q), with p and q positive, all the modes $(\pm p,\pm q)$ are important. However, the velocity fields are real, which implies that two of these modes are not independent due to conjugate symmetry. In addition, we will require that the velocity be mirror symmetric in the z direction, which will eliminate the independence of another mode. This is a symmetry which is preserved by the Navier-Stokes equations so that with an initial condition satisfying this symmetry the solution will remain symmetric. Thus with the reality of the velocity and the mirror symmetry, only the modes (p,q) with p and q positive are independent.

For each Fourier mode (p,q) the y-dependence of the three velocity components must be represented. However, the constraint of continuity eliminates a degree of freedom so that only two y functions need be considered. To do this we define two new functions of y:

$$\psi \equiv \frac{i\hat{v}}{\delta}; \qquad \omega \equiv p\hat{w} - q\hat{u}, \tag{A3}$$

where $\hat{u}$, $\hat{v}$ and $\hat{w}$ represent the Fourier coefficients of the velocity components for the given wave number and $\delta = \sqrt{p^2+q^2}$. This notation is chosen because ψ can be interpreted as a stream function and ω is proportional to the y component of the vorticity; ω is also referred to as the Squire mode. Given ψ and ω for a particular Fourier mode, the velocity components can be recovered as follows:

$$\hat{u} = \frac{\delta p\frac{\partial\psi}{\partial y} - q\omega}{\delta^2}; \qquad \hat{v} = -i\delta\psi; \qquad \hat{w} = \frac{\delta q\frac{\partial\psi}{\partial y} + p\omega}{\delta^2}. \tag{A4}$$

The equations for ψ and ω for our Fourier mode (p,q) can easily be derived from the Navier-Stokes equations, with the result;

$$\left[\frac{\partial}{\partial t}+ipU_0\right]\hat{\Delta}\psi - ip\psi\frac{d^2U_0}{dy^2} - \frac{1}{\mathrm{Re}}\hat{\Delta}^2\psi = \frac{i}{\delta}\left[\frac{\partial(ip\Gamma_x+iq\Gamma_z)}{\partial y}+\delta^2\Gamma_y\right]_{(p,q)} \quad (A5.1)$$

$$\left[\frac{\partial}{\partial t}+ipU_0\right]\omega - i\delta q\psi\frac{dU_0}{dy} - \frac{1}{Re}\nabla^2\omega = [q\Gamma_x - p\Gamma_z]_{(p,q)}\,; \quad (A5.2)$$

where, $\Gamma = (\overline{\mathbf{U}}+\mathbf{u})\cdot\nabla(\overline{\mathbf{U}}+\mathbf{u})$, the subscript on Γ refers to the vector component, $\hat{\Delta}$ is the Fourier transformed Laplacian ($\hat{\Delta} = \partial^2/\partial y^2 - p^2 - q^2$) and $\delta^2 = p^2+q^2$. The notation $[\cdot]_{(p,q)}$ indicates the (p,q) Fourier mode of the quantity in brackets. The above equations are valid for all wave number pairs except $(0,0)$. The Fourier transformed Navier-Stokes equations for $\overline{U}$ and $\overline{W}$ are used directly for this mode.

We now introduce real amplitudes $A(t)$, $B(t)$, $C(t)$, $D(t)$ and phase functions $\theta_A(t)$, $\theta_B(t)$, $\theta_C(t)$, $\theta_D(t)$, one for each of the primary waves. The ultimate goal is to derive ordinary differential equations which govern the evolution of these functions. The forced first harmonic of $(\alpha,0)$, the forced modifications to the mean flow due to the various waves and the Squire modes do not have independent amplitudes. Rather, they are functions of the amplitudes of the forcing waves. This is consistent with the equations, and is as described in Herbert (1983). The expansion for u is given below. Those for v and w are similar in form. Note that the Fourier mode $(2\alpha,0)$ is especially busy, with two contributions. The functions $\hat{u}_{A,(2\alpha,0)}$ and $\hat{u}_{C,(2\alpha,0)}$ represent the response of the $(2\alpha,0)$ mode to forcing by the $(\alpha,0)$ mode and (α,γ) mode respectively.

$$\begin{aligned} u(x,y,z,t) = 2\mathrm{Real}\Big\{ & A(t)\hat{u}_{(\alpha,0)}e^{i(\alpha x-\theta_A(t))} + B(t)\hat{u}_{(\alpha/2,0)}e^{i(\alpha x/2-\theta_B(t))} \\ & + \left[A^2(t)\hat{u}_{A,(2\alpha,0)}e^{-2i\theta_A(t)} + C^2(t)\hat{u}_{C,(2\alpha,0)}e^{-2i\theta_C(t)}\right]e^{2i\alpha x}\Big\} \\ & + 4C(t)\mathrm{Real}\left\{\hat{u}_{(\alpha,\gamma)}e^{i(\alpha x-\theta_C(t))}\right\}\cos(\gamma z) \\ & + 4D(t)\mathrm{Real}\left\{\hat{u}_{(\alpha/2,\gamma)}e^{i(\alpha x/2-\theta_D(t))}\right\}\cos(\gamma z) \\ & + A^2(t)\overline{U}_A + B^2(t)\overline{U}_B + C^2(t)\overline{U}_C + D^2(t)\overline{U}_D, \end{aligned} \quad (A6)$$

where the dependence of $\hat{u}$ and $\overline{U}$ on y and t is understood.

A.2 Streamfunction equations

By substituting expansions like (A6) into the Navier-Stokes equations and converting to ψ and ω as in (A5) we can write the truncated modal equations governing each Fourier mode. In writing these equations we will make use of the following operators:

$$M_{(p,q)} \equiv \frac{\partial^2}{\partial y^2} - (p^2+q^2) \quad (A7.1)$$

$$L_{(p,q)} \equiv i(p^2+q^2)^{1/2}U_0 M_{(p,q)} - i(p^2+q^2)^{1/2}\frac{\partial^2 U_0}{\partial y^2} - \frac{1}{Re}M^2_{(p,q)} \tag{A7.2}$$

$$\Omega(\psi_{(p,q)},\psi_{(\pi,\rho)}) \equiv ip\left[\psi_{(p,q)}\frac{\partial}{\partial y}M_{(\pi,\rho)}\psi_{(\pi,\rho)} - \left(\frac{\partial}{\partial y}\psi_{(\pi,\rho)}\right)M_{(p,q)}\psi_{(p,q)}\right] \tag{A7.3}$$

$$N(p,q;\pi,\rho) \equiv i(p+\pi)\left(i\pi\hat{u}_{(p,q)}\hat{w}_{(\pi,\rho)} + \hat{v}_{(p,q)}\frac{\partial}{\partial y}\hat{w}_{(\pi,\rho)} + i\rho\hat{w}_{(p,q)}\hat{w}_{(\pi,\rho)}\right) - \frac{\partial}{\partial y}\left(i\pi\hat{u}_{(p,q)}\hat{u}_{(\pi,\rho)} + \hat{v}_{(p,q)}\frac{\partial}{\partial y}\hat{u}_{(\pi,\rho)} + i\rho\hat{w}_{(p,q)}\hat{u}_{(\pi,\rho)}\right) \tag{A7.4}$$

Below are examples of the resulting equations governing the stream-functions ψ. Equations for the Squire modes ω are similar. Note that the non-linear terms are expressed (using the above operators) in terms of the stream function whenever possible, but that the terms involving the N operator require the velocity components, which are found using (A4). Also note that these are partial differential equations in y and t. First is the equation for the stream function of the fundamental wave.

$$\begin{aligned}\left(\frac{\partial}{\partial t}+a(t)\right)M_{(\alpha,0)}\psi_{(\alpha,0)} + L_{(\alpha,0)}\psi_{(\alpha,0)} &= \frac{B^2}{A}e^{-i(2\theta_B-\theta_A)}\Omega(\psi_{(\alpha/2,0)},\ \psi_{(\alpha/2,0)}) \\ &+ \frac{D^2}{A}e^{-i(2\theta_D-\theta_A)}\left[N(\alpha/2,\gamma;\alpha/2,-\gamma)+N(\alpha/2,-\gamma;\alpha/2,\gamma)\right] \\ &+ A^2\left[\left\{\Omega(\psi^*_{(\alpha,0)},\psi_{A,(2\alpha,0)})+\Omega(\psi_{A,(2\alpha,0)},\psi^*_{(\alpha,0)})\right\}+\Omega(\psi_{(\alpha,0)},\psi_{A,(0,0)})\right] \\ &+ C^2\left[\left\{\Omega(\psi^*_{(\alpha,0)},\psi_{C,(2\alpha,0)})+\Omega(\psi_{C,(2\alpha,0)},\psi^*_{(\alpha,0)})\right\}+\Omega(\psi_{(\alpha,0)},\psi_{C,(0,0)})\right] \\ &+ \left[B^2\Omega(\psi_{(\alpha,0)},\psi_{B,(0,0)})+D^2\Omega(\psi_{(\alpha,0)},\psi_{D,(0,0)})\right].\end{aligned} \tag{A8.1}$$

Where $\psi_{(0,0)} = \int \overline{U}(y')\,dy'$ and the subscript letter on $\psi_{(0,0)}$ and $\psi_{(2\alpha,0)}$ indicate which primary mode is providing the forcing. The five different terms on the right-hand side of (A8.1) represent the following effects on the fundamental (in order): 1) the effects of the subharmonic 2) the influence of the oblique subharmonic, 3) the combined influence of those parts of the forced first harmonic and the modification of the mean flow which are caused by the fundamental wave, 4) the combined influence of those parts of the first harmonic and the modification of the mean flow which are forced by (α,γ), and 5) the influence of those modifications to the mean flow which are induced by the other waves. Next are the equations for the two parts of the forced first harmonic,

$$\left(\frac{\partial}{\partial t}+2a(t)\right)M_{(2\alpha,0)}\psi_{A,(2\alpha,0)} + L_{(2\alpha,0)}\psi_{A,(2\alpha,0)} = \Omega(\psi_{(\alpha,0)},\psi_{(\alpha,0)}) \tag{A8.2}$$

$$\left(\frac{\partial}{\partial t}+2c(t)\right)M_{(2\alpha,0)}\psi_{C,(2\alpha,0)} + L_{(2\alpha,0)}\psi_{C,(2\alpha,0)} = N(\alpha,\gamma;\alpha,-\gamma)+N(\alpha,-\gamma;\alpha,\gamma) \tag{A8.3}$$

The first equation (A8.2) describes the part forced by the fundamental $(\alpha, 0)$, while the second equation (A8.3) describes the part forced by the oblique fundamental (α, γ). Finally, we present the equation for the modification of the mean flow by the fundamental mode.

$$\left(\frac{\partial}{\partial t} + \frac{2}{A}\frac{\partial A}{\partial t}\right)\frac{\partial^2}{\partial y^2}\overline{U}_A + L_{(0,0)}\overline{U}_A = \frac{\partial}{\partial y}\left[\Omega(\psi_{(\alpha,0)}, \psi^*_{(\alpha,0)}) + \Omega(\psi^*_{(\alpha,0)}, \psi_{(\alpha,0)})\right] \tag{A8.4}$$

For equations (A8.2,A8.3 and A8.4) we are only interested in particular solutions since these are modes which are slaved to the primary modes. Equations for modes not presented above and equations for ω have similar form.

Functions a, b, c and d which appear in the above equations are defined below. They are the left-hand sides of what will become coupled Landau equations, which will give temporal development of the amplitudes and phases of the disturbances.

$$a(t) \equiv \frac{1}{A}\frac{dA}{dt} - i\frac{d}{dt}\theta_A \tag{A9.1}$$

$$b(t) \equiv \frac{1}{B}\frac{dB}{dt} - i\frac{d}{dt}\theta_B \tag{A9.2}$$

$$c(t) \equiv \frac{1}{C}\frac{dC}{dt} - i\frac{d}{dt}\theta_C \tag{A9.3}$$

$$d(t) \equiv \frac{1}{D}\frac{dD}{dt} - i\frac{d}{dt}\theta_D \tag{A9.4}$$

A.2 The amplitude expansion

The next step in the development of the theory is to develop expansions to describe the time and y dependence of the ψ's and the time dependence of the functions a, b, c and d. In choosing these expansions we arrange the terms so that the dependence on the amplitude and phase functions A, B, C, D, θ_A, θ_B, θ_C and θ_D, of the left and right hand sides of equations like (A8.1) will match. Thus the expansion for $\psi_{(\alpha,0)}$ is

$$\begin{aligned}\psi_{(\alpha,0)}(y,t) = {} & \phi_{0,(\alpha,0)} + \phi_{1,(\alpha,0)}\frac{B^2}{A}e^{-i(2\theta_B-\theta_A)} + \phi_{2,(\alpha,0)}\frac{D^2}{A}e^{-i(2\theta_D-\theta_A)} \\ & + \left[A^2\phi_{3,(\alpha,0)} + B^2\phi_{4,(\alpha,0)} + C^2\phi_{5,(\alpha,0)} + D^2\phi_{6,(\alpha,0)}\right] \\ & + \frac{BCD}{A}\left[\phi_{7,(\alpha,0)}e^{i(\theta_A-\theta_B-\theta_C+\theta_D)} + \phi_{8,(\alpha,0)}e^{i(\theta_A+\theta_B-\theta_C+\theta_D)}\right. \\ & \left. + \phi_{9,(\alpha,0)}e^{i(\theta_A-3\theta_B-\theta_C+\theta_D)}\right] + \ldots,\end{aligned} \tag{A11}$$

where it is understood that the ϕ_j are functions of y. Note that the amplitude and phase dependence of the first several terms is the same as the coefficients appearing on the right hand side of (A8.1). In addition there are the terms with coefficient

BCD/A, these terms arise because of the time derivative operator on the left side of (A8.1), that is the term

$$\left(\frac{\partial}{\partial t} + a(t)\right) M_{(p,q)}\psi_{(p,q)}.$$

If we had used the 'shape' assumption of Stuart or Lorenz, (A11.1) would consist of only the first term in this expansion, which is the solution to the Orr-Sommerfeld equation (see below). The current expansions retain more of the relevant physical processes. Similarly we obtain expansions for the time functions which have amplitude and phase dependencies dictated by the form of the equations like (A8.1). For example compare (A11) above with (A12.1) below. In the following equations the coefficients a_i, b_i, c_i, and d_i (Landau constants) are complex constants.

$$\begin{aligned} a(t) = a_0 &+ a_1\frac{B^2}{A}e^{-i(2\theta_B-\theta_A)} + a_2\frac{D^2}{A}e^{-i(2\theta_D-\theta_A)} + \left[a_3A^2 + a_4B^2 + a_5C^2 + a_6D^2\right] \\ &+ \frac{BCD}{A}\left[a_7e^{i(\theta_A-\theta_B-\theta_C+\theta_D)} + a_8e^{i(\theta_A+\theta_B-\theta_C+\theta_D)}\right. \\ &\left.+a_9e^{i(\theta_A-3\theta_B-\theta_C+\theta_D)}\right] + \ldots \end{aligned} \tag{A12.1}$$

$$\begin{aligned} b(t) = b_0 &+ b_1Ae^{-i(\theta_A-2\theta_B)} + b_2\frac{CD}{B}e^{-i(\theta_C-\theta_D-\theta_B)} + \left[b_3A^2 + b_4B^2 + b_5C^2 + b_6D^2\right] \\ &+ b_7A^2e^{-2i(\theta_A-2\theta_B)} + b_8D^2e^{-2i(\theta_D-\theta_B)} \\ &+ A^2e^{-i(\theta_A-2\theta_B)}\left[b_9\cos(\theta_A-2\theta_B) + b_{10}\sin(\theta_A-2\theta_B)\right] \\ &+ \frac{ACD}{B}\left[b_{11}e^{-i(\theta_A-3\theta_B+\theta_C-\theta_D)} + b_{12}e^{i(\theta_A+\theta_B-\theta_C-\theta_D)}\right. \\ &+ b_{13}e^{-i(\theta_A-\theta_B-\theta_C+\theta_D)} + e^{-i(\theta_A-2\theta_B)}\left\{b_{14}\cos(\theta_B-\theta_C+\theta_D)\right. \\ &\left.\left.+b_{15}\sin(\theta_B-\theta_C+\theta_D)\right\}\right] + \ldots \end{aligned} \tag{A12.2}$$

$$\begin{aligned} c(t) = c_0 &+ c_1A^2e^{-2i(\theta_A-\theta_B)} + c_2\frac{BD}{C}e^{-i(\theta_B+\theta_D-\theta_C)} + \left[c_3A^2 + c_4B^2 + c_5C^2 + c_6D^2\right] \\ &+ \frac{ABD}{C}\left[c_7e^{-i(\theta_A-\theta_B-\theta_C+\theta_D)} + c_8e^{-i(\theta_A+\theta_B-\theta_C-\theta_D)}\right] + \ldots \end{aligned} \tag{A12.3}$$

$$\begin{aligned} d(t) = d_0 &+ d_1Ae^{-i(\theta_A-2\theta_D)} + d_2\frac{BC}{D}e^{-i(\theta_C-\theta_B-\theta_D)} + \left[d_3A^2 + d_4B^2 + d_5C^2 + d_6D^2\right] \\ &+ d_7A^2e^{-2i(\theta_A-2\theta_D)} + d_8B^2e^{-2i(\theta_B-\theta_D)} + d_9\frac{ACD}{B}e^{-i(\theta_A-3\theta_B+\theta_C-\theta_D)} \\ &+ \frac{ABC}{D}\left[d_{10}e^{-i(\theta_A-\theta_B+\theta_C-3\theta_D)} + d_{11}e^{i(\theta_A-\theta_B-\theta_C+\theta_D)}\right. \\ &\left.+d_{12}e^{-i(\theta_A+\theta_B-\theta_C-\theta_D)}\right] + \ldots \end{aligned} \tag{A12.4}$$

Combining equations (A9) and (A12), ordinary differential equations for the amplitude and phase functions are obtained. It is these evolution equations that must be solved to obtain the time dependence of the desired solution. All that remains

is to compute the evolution coefficients a_i etc. The methodology for computing them is discussed below; however, they have not yet been computed for this three-dimensional case. Still, we can make some qualitative inferences from the form of these equations. Consider (12), in the form of $Aa(t)$, $Bb(t)$, etc., so that one can consider $dA/dt\ldots$ If $A(0) \neq 0$ while $B(0)$, $C(0)$, $D(0) = 0$, only the fundamental mode will evolve, since the other modes will remain zero. Their initially zero growth rate ($dB/dt(t = 0) = 0$, etc.) will remain zero ($dB/dt = 0$, etc. $\forall t$). Eventually, the fundamental will equilibrate due to the feedback from the modification to the mean flow and forced first harmonic, embodied in a_3A^3. This agrees with observations and the numerical simulations of Metcalfe, *et al.* (1988) among others. If only the fundamental and subharmonic have nonzero initial amplitudes, they will interact, causing pairing; however, the three-dimensional modes will remain zero, again because their forcing requires that at least one of them be nonzero in the initial conditions to get a nonzero time rate of change. Consider the case of nonzero initial amplitudes, save for the oblique subharmonic $(\alpha/2, \gamma)$. The fundamental and subharmonic will interact as before, while the more slowly growing, or even decaying oblique fundamental (α, γ) is initially of little consequence. The oblique subharmonic will remain negligible, because it requires the combined effort of the two-dimensional subharmonic and oblique fundamental to stimulate it into growth, represented mathematically by the d_2 term in (A12.4). When the fundamental gets large enough, its forced first harmonic will stimulate the oblique fundamental into accelerated growth (represented mathematically by the c_1 term in (A12.3)). This should occur at least simultaneously with, if not after pairing, because the a_1 and b_1 expressions which govern pairing are larger than the c_1 term, assuming comparable sizes of these coefficients. Finally, after the oblique fundamental mode reaches a size of some consequence, the oblique subharmonic will appear, driven by the two-dimensional subharmonic and the oblique fundamental via at least the d_2 term. It is too difficult to judge what happens beyond this. This scenario, suggested by the equations, is similar to numerical simulations and observations. Actual integration of the evolution equations is required to verify these conjectures.

One can test the individual effects and hence the importance of each of these terms through a series of integrations of the equations with and without the expression of interest. This will allow the analysis of the roles played by the various interactions. Comparisons with Corcos and Lin (1984) would be interesting, since they considered a partially linearized form of the Navier-Stokes equations, which contain, some, but not all of the interactions built into our equations. Future work will consider such a program of experimental mathematics.

Evaluating the expansion coefficients

Substituting expansions like (A11) and (A12) in (A8) and equating like terms in the amplitude and phase functions results in a series of linear equations for the expansion functions ϕ_i. The equations for ϕ_0 are Orr-Sommerfeld equations. For example, the $(\alpha, 0)$ equation is

$$a_0 M_{(\alpha,0)}\phi_{0,(\alpha,0)} + L_{(\alpha,0)}\phi_{0,(\alpha,0)} = 0, \qquad (A13.1)$$

where a_0 is the Orr-Sommerfeld eigenvalue and ϕ_0 is the eigenfunction. We will take as the solution the first (most unstable) eigenfunction and eigenvalue. The rest of the equations are linear, inhomogeneous and of the form

$$(\eta_j + a_0)M_{(\alpha,0)}\phi_{j,(\alpha,0)} + L_{(\alpha,0)}\phi_{j,(\alpha,0)} = Y_j - a_j M_{(\alpha,0)}\phi_{0,(\alpha,0)}, \qquad (A13.2)$$

where the η_j are nonzero complex numbers, and the Y_j are functions of y. Both η_j and Y_j can be determined from the solutions already obtained for a_i, b_i etc. and ϕ_i for $i < j$. As an example, the remainder of the analysis will be done for the fundamental mode $(\alpha, 0)$; the analysis for the other modes is similar.

Since the functions ψ are only defined to within a multiplicative constant, a normalization condition is necessary to obtain a solution to these equations. Also, since the linear solution $\phi_{0,(\alpha,0)}(y)$ has an arbitrary magnitude, so will the corrections (ϕ_j). It is convenient to choose a linear norm, and apply it in a way which allows the determination of the Landau coefficients. Herbert (1983) chooses a linear normalization, (designated by $\{\cdot\}$), such that the following normalization condition is satisfied:

$$\{\psi_{(\alpha,0)}(y,t)\} = 1 \quad \text{for all time.}$$

We use $\{\psi_{(\alpha,0)}(y,t)\} = \int_{-\infty}^{\infty} \psi_{(\alpha,0)}(y,t)dy$, although any linear norm which is not zero for ψ and ϕ_0 would do. Note that this condition is not simply $\{\phi_{0,(\alpha,0)}\} = 1$. This unusual choice of normalization places conditions on all of the $\phi_{n,(\alpha,0)}$, namely:

$$\{\psi_{(\alpha,0)}(y,t)\} = \left\{\sum_{n=0}^{\infty} F_n(t)\phi_{n,(\alpha,0)}(y)\right\} = \sum_{n=0}^{\infty} F_n(t)\left\{\phi_{n,(\alpha,0)}(y)\right\} = 1 \qquad (A14)$$

Since the $F_n(t)$ are functions of time (dependent on the amplitude and phase functions, see equation A11) and $F_0 = 1$, this condition is satisfied by requiring

$$\{\phi_{j,(\alpha,0)}\} = \begin{cases} 1, & j = 0; \\ 0, & j > 0. \end{cases} \qquad A15$$

Setting the right side of (A13.2) to zero produces the Orr-Sommerfeld equation with a parameter different from the first eigenvalue ($\eta_j \neq 0$); therefore, equation (A13.2) does not have homogeneous solutions (unless $\eta_j + a_0$ happens to also be an eigenvalue). The solution to (A13.2) is therefore just the sum of the responses to the individual inhomogeneous terms:

$$\phi_{j,(\alpha,0)} = \Upsilon_j - \frac{a_j}{\eta_j}\phi_{0,(\alpha,0)}, \qquad (A16)$$

where Υ_j is the solution to Equation (A13) corresponding to Y_j, and $a_j/\eta_j\phi_{0,(\alpha,0)}$ is the solution corresponding to the ϕ_0 term on the right side of (A13.2). Applying the normalization condition to (A16) and using (A15) the value for the Landau constant a_j is obtained,

$$a_j = \{\Upsilon_j\}\eta_j. \qquad (A18)$$

Thus we have found both the Landau constants and the expansion functions ϕ. In principle this procedure could be carried out to infinity, but in practice a severe truncation would again be applied. With the Landau constants, the ordinary differential equations for the amplitudes and phases can be integrated, and used to construct the velocity field in space and time.

Sampling inhomogeneous turbulent fields

By R. J. Adrian[1], P. Moin[2,3], & R. D. Moser[2]

1. Background

Consider a real random process $U(y)$ whose statistical properties vary inhomogeneously in the y-direction on an interval I. The Karhunen-Loeve expansion of the process is

$$U(y) = \sum_{m=1}^{\infty} a_m \phi_m(y), \tag{1}$$

where the expansion coefficients are

$$a_m = \int_I u(y)\phi_m(y)\, dy \tag{2}$$

and the expansion functions ϕ_m are eigen-solutions of

$$\int_I R(y,y')\phi_m(y')dy' = \lambda_m \phi_m(y). \tag{3}$$

In (3), $R(y,y')$ is the two-point correlation of of the process $U(y)$. The eigenfunctions are orthogonal on the interval I, that is

$$\int_I \phi_m(y)\phi_m(y')dy = \delta_{mn}. \tag{4}$$

Also, the expansion coefficients are related to the eigenvalues (λ) by

$$< a_m a_n >= \lambda_m \delta_{mn}, \tag{5}$$

thus they are statistically orthogonal.

The KL functions provide the "best" orthonormal set of functions in the sense that the expansion converges faster than expansions in terms of any other orthonormal set, as measured in the L_2 norm. These eigenfunctions reduce to the trigonometric functions if $U(y)$ is statistically homogeneous, so the primary significance of the KL expansion lies in its ability to efficiently represent statistically inhomogeneous processes.

1 University of Illinois
2 NASA/Ames Research Center
3 Stanford University

Shannon's Sampling Theorem provides a method for representing a homogeneous (i.e. stationary) band-limited continuous random process in terms of its samples at a finite number of points whose spacing is determined by the Nyquist criterion. In this case, the best representation of the process is an expansion in terms of a finite sum of trigonometric functions, and the samples must be taken periodically at a rate exceeding two times the maximum frequency in the signal spectrum. The question arises as to whether a similar result pertains to inhomogeneous random process and how such a result might be related to the KL expansion.

An inhomogeneous process that is band limited in the generalized sense that it can be represented by a KL expansion with M modes with zero mean square error, can also be represented by a sum of the form

$$U(y) = \sum_{\alpha=1}^{M} A_\alpha(y) U(y_\alpha), \tag{6}$$

where $y_\alpha, (\alpha = 1, \ldots, M)$ are a set of M sample points, and the interpolating functions are solutions of

$$\sum_{\alpha=1}^{M} A_\alpha(y)\phi_m(y_\alpha) = \phi_m(y), \qquad m = 1, \ldots, M \tag{7}$$

By analogy to Shannon's sampling theorem, we are particularly interested in the zeros of ϕ (*i.e.* $\phi(y_\alpha) = 0$) as sample points.

2. Computations for turbulent channel flow

The relevance of the foregoing to numerical computation of turbulence was explored by examining the spectrum of eigenvalues and the eigenfunctions of the one-dimensional process $U(y)$ in the turbulent channel flow data base. Inspection of the eigenvalue spectrum for the case of KL expansion over the wall layer domain $0 \leq y^+ \leq 40$ shows that the first eigenmode contains 73% of the total energy, and the first two eigenmodes contain 92% of the total (Moin and Moser 1989). Clearly the eigenfunction spectrum is rapidly decreasing, and there is some order M beyond which it is not necessary to include additional terms. The selection of M is somewhat arbitrary, but by $M = 10$, we find that the energy of the tenth mode relative to that of the first mode is 0.6×10^{-4}, so $M = 10$ is a reasonable cutoff.

Figure 1 shows $\phi_1(y)$ and $\phi_{10}(y)$ for KL expansion on $0 \leq y^+ \leq 40$. It should be possible to reconstruct $U(y)$ from its samples taken at the zeros of ϕ_{10}. There are nine zeroes (the zero at the wall is not counted because $U(y) = 0$ is a boundary condition). For comparison, the Chebychev polynomial grid points used in the direct numerical simulation are indicated by the squares. There are twenty-nine of these points. It is interesting to note that the spacings of KL sampling points are nearly equal (see Figure 1*b*. It appears that for sampling in the direction of flow inhomogeneity in boundary layers one does not have to use numerous points in the vicinity of the walls. This is because the KL eigenfunctions carry with them much

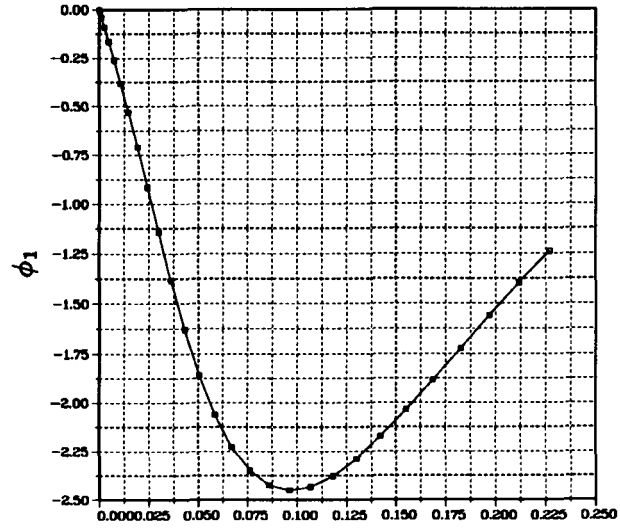

(a)

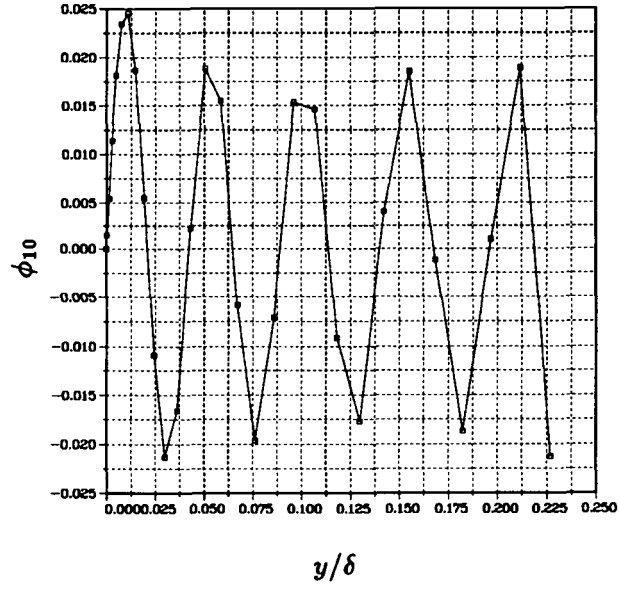

(b)

FIGURE 1. Eigenfunctions of the Karhunen-Loeve expansion for u over the interval $0 \leq y^+ \leq 40$. The sample points y_α are at the intersection of the solid lines and the horizontal line through zero. The open symbols are chebychev points. (a) $\phi_1(y)$, (b)$\phi_{10}(y)$.

of the rapidly varying parts of $U(y)$. Note, for example, the rapid variation of $\phi_1(y)$ close to the wall.

Computations for KL expansion on the full domain $0 \leq y^+ \leq 180$ reveals some interesting consequences of varying the domain (see Moin & Moser 1989). The eigenvalue spectrum is wider than that of the wall layer expansion. The bandwidth required to reach 0.27×10^{-4} of the energy in the first mode is $M = 30$, compared to $M = 11$ for the wall layers. However, the extent of the domain is over four times as large as the wall layer, so many of the additional modes are actually slowly varying functions needed to represent the longer fluctuations that occur in the wider layer.

The first and thirtieth eigenfunctions for the full channel width are shown in Figure 2. There are 64 Chebychev points on this interval (not counting $y = 0$) and 29 KL points

In contrast to the wall layer the spacing of sample points for expansion over the full layer increases by more than a factor of 2.5 from the wall to the centerline. This is presumably due to milder variation of the eigenfunctions in the vicinity of the walls. The spacing of the sample points may be related to the variation of turbulent length scale as one moves away from the wall.

3. Conclusions

The reconstruction of an inhomogeneous random process from a finite number of discrete samples can be performed in terms of the Karhunen- Loeve expansion for that process. The n^{th} eigenfunction has $n - 1$ zero crossings which are the sampling points for the inhomogeneous process. The rapid variation of the KL eigenfunctions makes it unnecessary to have a high density of sampling (or grid points) near the wall. However, this result should not be construed as to indicate that with spectral simulations significantly fewer grid points are required with the KL expansion as compared to other orthogonal expansions. Moin & Moser (1989) have shown that the the advantage of the KL expansion over Chebychev expansion rapidly diminishes when high percentage (say 90%) energy recovery is demanded.

Acknowledgement

RJA wishes to acknowledge the generous support of the Center for Turbulence Research. Portions of this work were supported by Grant NSF ATM 86-00509.

REFERENCES

MOIN, P. & MOSER, R. D. 1989 Characteristic eddy decomposition of turbulence. To appear in *J. Fluid Mech.*

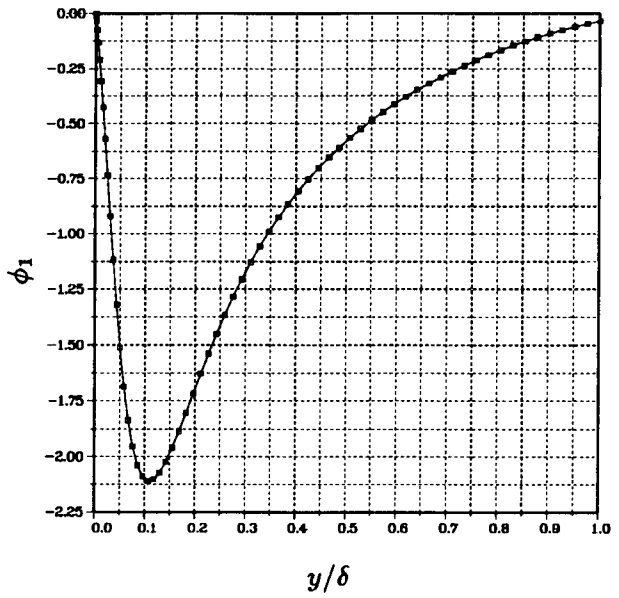

(a)

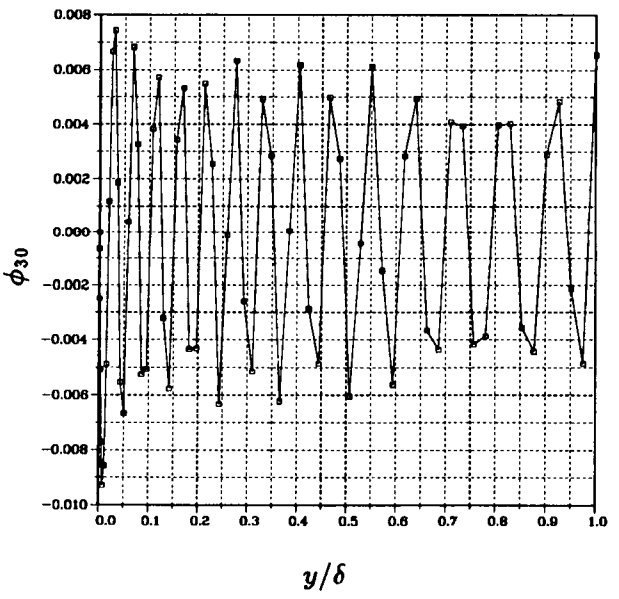

(b)

FIGURE 2. Eigenfunctions of the Karhunen-Loeve expansion for U over the interval $0 \leq y/\delta \leq 1$. The sample points y_α are at the intersetion of the solid lines and the horizontal line through zero. The open symbols are Chebychev points. (a) $\phi_1(y)$, (b)$\phi_{30}(y)$.

Page intentionally left blank

Dynamical interpretation of conditional patterns

By R. J. Adrian[1], & R. D. Moser[2], P. Moin[2,3]

1. Background

While great progress is being made in characterizing the three-dimensional structure of organized turbulent motions using conditional averaging analysis, there is a lack of theoretical guidance regarding the interpretation and utilization of such information. Questions concerning the significance of the structures, their contributions to various transport properties, and their dynamics cannot be answered without recourse to appropriate dynamical governing equations. One approach which addresses some of these questions uses the conditional fields as initial conditions and calculates their evolution from the Navier-Stokes equations, yielding valuable information about stability, growth, and longevity of the mean structure. To interpret *statistical* aspects of the structures, we need a different type of theory which deals with the structures in the context of their contributions to the statistics of the flow. As a first step toward this end, an effort has been made to integrate the structural information from the study of organized structures with a suitable statistical theory. This is done along the lines of Adrian (1977) by stochastically estimating the two-point conditional averages that appear in the equation for the one-point probability density function, and relating the structures to the conditional stresses. Salient features of the estimates are identified, and the structure of the one-point estimates in channel flow is defined.

2. One-point probability density

The equation governing f, the probability density function defined by

$$f_1(\mathbf{v},\mathbf{x},t)d\mathbf{v} = \text{Prob} \quad \mathbf{v} \le \tilde{\mathbf{u}}(\mathbf{x},t) < \mathbf{v} + \mathbf{dv} \tag{1}$$

is

$$\frac{\partial f_1}{\partial t} = -\frac{\partial}{\partial v_i}\left\{\left\langle \frac{\partial \tilde{u}_i}{\partial t}\middle| \mathbf{v}\right\rangle f_1(\mathbf{v},\mathbf{x},t)\right\} \tag{2}$$

where

$$\tilde{\mathbf{u}} = \mathbf{U} + \mathbf{u}, \quad <\tilde{\mathbf{u}}> = \mathbf{U} \tag{3}$$

1 University of Illinois
2 NASA/Ames Research Center
3 Stanford University

and **u** are respectively the total, mean, and fluctuating velocities, and **v** is a dummy variable for the p.d.f. (Lundgren 1967). The fluid dynamics is contained entirely within the conditional average of the time derivative which is given in terms of the Navier-Stokes equations by

$$\left\langle \frac{\partial \tilde{u}_i}{\partial t} \middle| \mathbf{v} \right\rangle = -\left\langle \tilde{u}_j \frac{\partial \tilde{u}_i}{\partial x_j} \middle| \mathbf{v} \right\rangle - \left\langle \frac{1}{\rho} \frac{\partial \tilde{p}}{\partial x_i} \middle| \mathbf{v} \right\rangle + \nu \left\langle \frac{\partial^2 \tilde{u}_i}{\partial x_l \partial x_l} \middle| \mathbf{v} \right\rangle \tag{4}$$

We can relate the p.d.f. equation to organized structures by observing that the two-point conditional average

$$< \tilde{\mathbf{u}}(x',t) | \tilde{\mathbf{u}}(x,t) = \mathbf{v} > = < \mathbf{u}' | \mathbf{v} > \tag{5}$$

is a good descriptor of organized structure, coinciding in most cases with structures found by other methods of conditional analysis and flow visualization (Adrian and Moin 1988), and that we can rewrite (4) in terms of $< \mathbf{u}' | \mathbf{v} >$ as follows:

$$\left\langle \frac{\partial \tilde{u}_i}{\partial t} \middle| \mathbf{v} \right\rangle = \lim_{x' \to x} \left\{ -v_j \frac{\partial}{\partial x_{j'}} < u_i' | \mathbf{v} > - \frac{1}{\rho} \frac{\partial}{\partial x_{i'}} < \tilde{p}' | \mathbf{v} > + \nu \frac{\partial^2}{\partial x_l' \partial x_l'} < \tilde{u}_i' | \mathbf{v} > \right\} \tag{6}$$

where $< \tilde{p}' | v >$ satisfies a Poisson equation:

$$\begin{aligned} \nabla'^2 < \tilde{p}' | \mathbf{v} > &= -\rho \frac{\partial^2}{\partial x_i' \partial x_j'} < \tilde{u}_i' \tilde{u}_j' | \mathbf{v} > \\ &= -\rho \frac{\partial^2}{\partial x_i' \partial x_j'} \{ U_i' U_j' + U_i' < u_j' | \mathbf{c} > + U_j' < u_i' | \mathbf{c} > + < u_i' u_j' | \mathbf{c} > \} \end{aligned} \tag{7}$$

In (6) $< \mathbf{u}' | \mathbf{v} >$ has been decomposed into the mean plus the conditional average of the fluctuation:

$$< \tilde{\mathbf{u}}' | \mathbf{v} > = \mathbf{U}' + < \mathbf{u}' | \mathbf{c} > \tag{8}$$

where $\mathbf{c} = \mathbf{v} - \mathbf{U}$ is a dummy fluctuation variable. Equations (6) and (7) show that the conditional eddy $< \mathbf{u}' | \mathbf{c} >$ enters each stress term of the Navier-Stokes equations and the convective term.

Let us approximate $< \mathbf{u}' | \mathbf{c} >$ by a linear stochastic estimate (Adrian 1977):

$$< u_i' | \mathbf{c} > = L_{ij}(\mathbf{x}, \mathbf{x}') c_j \tag{9}$$

where L_{ij} is found from (Adrian, Moin & Moser 1987)

$$< u_l u_j > L_{ij} = < u_i' u_l >, \quad l = 1,2,3 \tag{10}$$

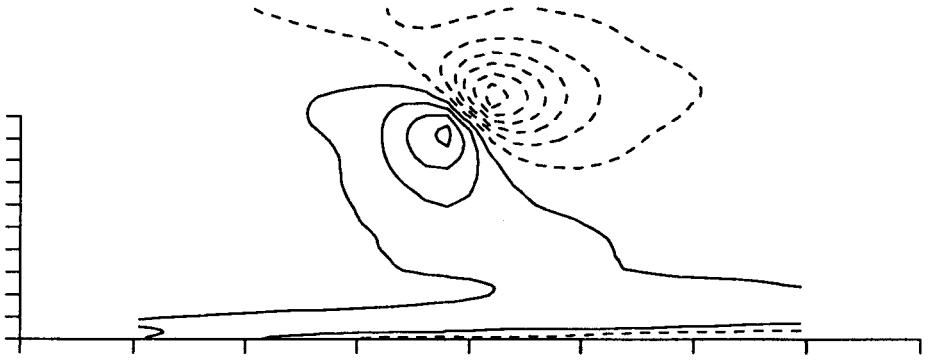

(a) FIGURE 1. Spanwise vorticity in the x-y plane of the stochastic estimate given a Q2 Reynolds stress event at $y^+ = 180$ (centerline) of the turbulent channel flow. The vertical axis is y and the end of the axis corresponds to the channel centerline. The contour increment is 1, and negative contours are dashed.

Substitution of (9) into the convective and viscous terms of (6) shows that the structure enters the dynamical statement in (6) through the following quantities:

$$L_{ij,k}(\mathbf{x},\mathbf{x}) = \lim_{\mathbf{x}'\to\mathbf{x}} \frac{\partial}{\partial x'_k} L_{ij}(\mathbf{x},\mathbf{x}') \tag{11}$$

$$L_{ij,kk}(\mathbf{x},\mathbf{x}) = \lim_{\mathbf{x}'\to\mathbf{x}} \frac{\partial^2}{\partial x'_k \partial x'_k} L_{ij}(\mathbf{x},\mathbf{x}') \tag{12}$$

These variables depend upon gradients of the two-point spatial correlation, $< u'_i u_l >$ which are *local* in nature ($\mathbf{x}' \to \mathbf{x}$). Thus, the only important feature of the coherent structure, in this approximation, is the gradient close to the center of the structure. We propose in future to study the behavior of $L_{ij,k}$ and $L_{ij,kk}$ for channel flow.

The *non-local* structure of $< \mathbf{u}'|\mathbf{c} >$ appears in (7), showing that the geometry and size of coherent structures will be important in determining closure approximation of the fast pressure-strain terms. The conditional Reynolds stress term in (7) determines the slow pressure component. It constitutes a separate closure problem for the p.d.f. equation.

3. Structure of the one-point conditional eddy

The structure of the linearly estimated conditional eddy $\tilde{u}'_i = L_{ij} u_j(\mathbf{x})$ has been determined from the channel flow data base of Kim, Moin & Moser (1987), using the R_{ij} tensor computer by Moin & Moser (1989). The conditional velocity, $\mathbf{u}(\mathbf{x})$, was prescribed at $y^+ = 5, 20, 30, 49, 103$, and 180 for the maximum Reynolds stress events defined by Moin, Adrian, and Kim (1987). The flow patterns for the second quadrant event at three levels are shown in Figures 1-3. Note that the mean velocity and vorticity are *not* included in these figures. For the conditions prescribed far

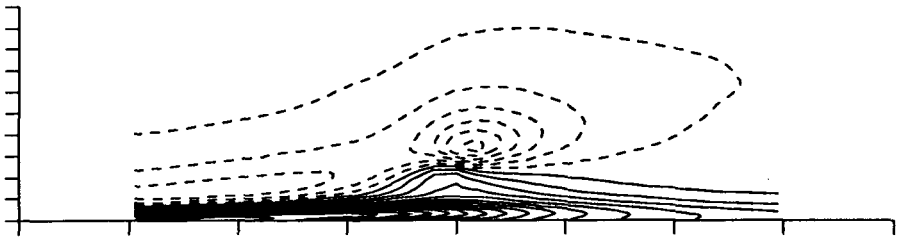

(a)

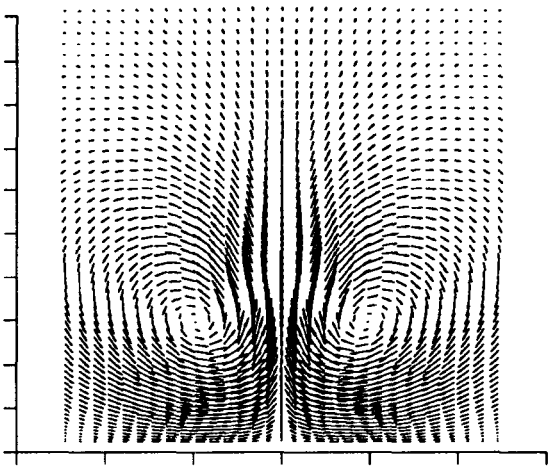

(b)

FIGURE 2. Spanwise vorticity (a) in the x-y plane and velocity vectors (b) in the z-y plane of the stochastic estimate given a Q2 Reynolds stress event at $y^+ = 49$ of the turbulent channel flow. The vertical axis is y and the end of the axis corresponds to the channel centerline. In (a) the contour increment is 2, and negative contours are dashed.

above the wall ($y^+ = 180$) the eddy is nearly a vortex ring inclined at an angle of approximately 45° to the flow, as determined by the direction of $\mathbf{u}(\mathbf{x})$. The ring is centered on $\mathbf{x}$ and it pumps fluid through its center so as to create large positive v and negative u, as explained in Adrian and Moin (1988). Note that addition of the mean velocity to the fluctuating field in Figure 1 may result in a structure resembling a hairpin vortex rather than a ring.

When the conditions are prescribed closer to the wall, $y^+ = 49$, the fluctuating flow pattern looks more like a hairpin vortex (Figure 2). The head of this hairpin is similar to the top half of the vortex ring in Figure 1, but the bottom looks like two streamwise oriented vortices. Their circulations are shown clearly in Figure 2(b), whose plane passes through the conditional point $\mathbf{x}$.

When the conditions are prescribed very close to the wall, $y^+ = 5$, the v-component of velocity is strongly suppressed, and the flow of the conditional eddy is essentially two streamwise vortices, c.f. Figure 3(b). These vortices lift low speed fluid up from the wall and bring it back down toward the wall, as shown by the v-contours in Figure 3(c). They are elongated in the x-direction, but not so much as to be two-dimensional.

It must be emphasized that the structure described above should not be construed as the structure of the instantaneous flow. Certainly it possesses many features of the organized structures in the flow field, but it is a smoothed picture which is also symmetrized due to the symmetries of the spatial correlation function. There is no implication, for example, that the instantaneous structures always occur with pairs of streamwise vortices, and, in fact, observations of instantaneous events suggest that double vortices are more rare than singles. However, the symmetry and smoothness of the conditional eddy is acceptable if it is interpreted in the context of the f_1-equation, since this equation deals, inherently, with the conditional field, and it does not require that they be perfectly faithful reproductions of the instantaneous realizations.

4. Conclusions

Coherent structures, as described by the conditional averages $< \mathbf{u}'|\mathbf{c} >$, contain structural information needed to close the p.d.f. equations. The form of the structure is expected to influence the behavior of the p.d.f., and hence the behavior of moment equation models that are derivable, in principle, from the solutions of the p.d.f. equation. Ultimately, this structure must be manifested in the values of coefficients that appear in closure models of the moment equations. More work is needed to assess the details of the way that structure feeds into the p.d.f. equations.

Acknowledgement

The first author (RJA) wishes to acknowledge the generous support of the Center for Turbulence Research. Portions of this research were also supported by Grant NSF ATM 86-00509

REFERENCES

ADRIAN, R. J. 1979 Conditional Eddies in Isotropic Turbulence. *Phys. Fluids.* **22,** 2065-2070.

ADRIAN, R. J., & MOIN, P. 1988 Stochastic Estimation of Organized turbulence Structure: Homogeneous Shear Flow. *J. Fluid Mech.* **190,** 531-559.

MOIN, P., ADRIAN, R.J., & KIM, J. 1987 Stochastic Estimation of Organized Structures in Turbulent Channel Flow. *6th Turbulent Shear Flow Symposium, Toulouse, France, Sept. 7-9, 1987.*

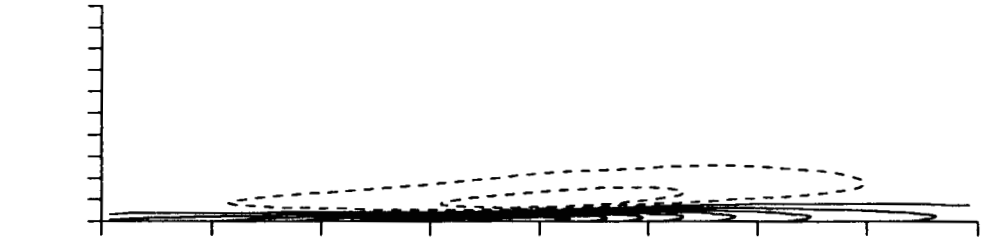

(a)

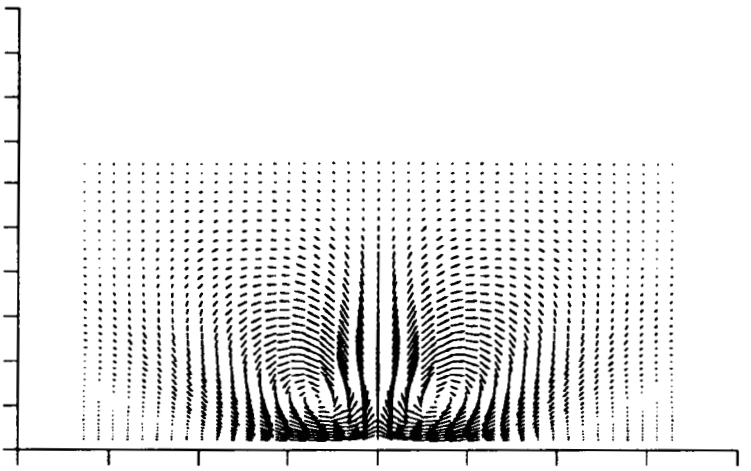

(b)

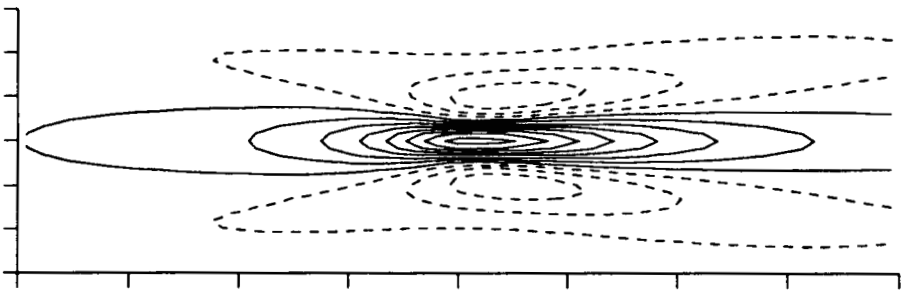

(c)

FIGURE 3. Spanwise vorticity (a) in the x-y plane, velocity vectors (b) in the z-y plane and normal velocity in the x-z plane of the stochastic estimate given a Q2 Reynolds stress event at $y^+ = 5$ of the turbulent channel flow. The vertical axis is y in (a) and (b), and the end of the axis corresponds to the channel centerline. The vertical axis is z in (c). The contour increment is 10 in (a) and 0.01 in (c), and negative contours are dashed.

MOIN, P. & MOSER, R. D. 1989 Characteristic eddy decomposition of turbulence. To appear in *J. Fluid Mech.*

ADRIAN, R. J., MOSER, R. D., & MOIN, P 1987 Stochastic Estimation of Conditional Eddies, Center for Turbulence Research Report, *CTR-S87.*

LUNDGREN, T. S. 1967 Distribution Functions in the Statistical Theory of Turbulence. *Phys. Fluids.* **10**, 969.

Page intentionally left blank

Center for Turbulence Research
Proceedings of the Summer Program 1988

Turbulence production near walls: the role of flow structures with spanwise asymmetry

By P. Henrik Alfredsson[1], Arne V. Johansson[1] and John Kim[2]

Space-time evolution of near-wall flow structures is described by conditional sampling methods, in which conditional averages are formed at various stages of development of shear-layer structures. The development of spanwise asymmetry of the structures was found to be important in the creation of the structures and for the process of turbulence production.

1. Introduction

Over the past two decades, the results from the pioneering flow visualization studies of the near-wall structure (e.g. Kline et al., 1967; Kim, Kline & Reynolds, 1971) and the resulting conceptual model of the various stages of the 'bursting' process has has remained as a cornerstone in our views of turbulence production in boundary layers. A central part of the model is the localized lift-up of low-speed fluid from the viscous sublayer into the buffer region, which creates strong, more or less symmetric (with respect to the spanwise center of the low-speed region) internal shear layers coupled to a velocity profile with inflectional character. The flow-visualization results indicated that a major portion of the turbulence production occurs during violent break-up of the flow structure into small scales, which was believed to originate from an inflectional instability giving rise to a growing oscillation of the lifted low-speed region. The conceptual model does not, however, account for regeneration of the low-speed regions in the viscous sublayer.

From flow-visualization studies and subsequent probe measurements it was concluded that a great portion of the turbulence production occurs during highly intermittent events. A mean time between consecutive events could be determined, and was found to be much larger than their duration. Hence, turbulence production was concluded to be strongly intermittent both in time and space. One should note, however, the inherent difficulty in flow visualization, using hydrogen bubble, dye or other techniques, to follow a specific structure or process for long times, because all path lines diverge rapidly in a turbulent flow. Also, structures need not be simply advected, but may propagate in somewhat of a wave-like manner through the action of pressure. The conditionally-averaged data indicate that there is no apparent sign of the break-up stage with associated small-scale motions. This is, however,

1 Royal Institute of Technology
2 NASA Ames Research Center

somewhat inherent in the conditional averaging methods, because motions of small or large scale that are weakly correlated or uncorrelated with the primary feature, on which the detection is focused, will be averaged out in the ensemble-averaging process. Large contributions to the Reynolds stress have mainly been found directly associated with the lift-up of low speed fluid, i.e. on the downstream side of the shear layer (Johansson et al. 1988).

Probe methods have been used to map some of the spatial features of the structures. For instance, Johansson et al. (1987a) analyzed two-probe measurements from the Göttingen oil-channel with the VITA-technique, which focused on the shear-layer structure of a certain size and strength. Information from only one xy-plane was available from the experiment. Obtaining a complete space-time mapping in three dimensions experimentally would be an extremely difficult task, but can in principle easily be done with the use of numerical data bases obtained from simulations. Johansson et al. (1988) used the NASA Ames computer-generated numerical data bases of turbulent channel flow, which has a spatial resolution of 17.7 and 5.9 viscous units in the streamwise (x) and spanwise (z) directions, respectively, to do space-time mapping of the shear-layer structures detected by the spatial counterpart of VITA. The Reynolds number based on friction velocity (u_τ), channel half-height (b) and kinematic viscosity (ν) is 180 close to that in the Göttingen oil-channel data, and excellent agreement with the measured data was obtained.

In the present study the NASA Ames numerical data bases are further utilized for space-time mapping of the near-wall structures. For this purpose 47 flow fields separated by three viscous time units were used. The present results shed new light on the near-wall structure of turbulent flows, and show that several of the long-lived views based on early flow visualization and probe measurements may need to be modified. It is also shown that the turbulence production is less intermittent in time than previously believed. Asymmetry of the structures is also found to be an important aspect of the whole process.

2. Results

2.1 Space-time evolution of the structures

Shear-layer structures were detected with the VISA method as follows. First, 'islands' of high local variance in the xz- plane at $y^+ = 15$ were identified. Then, the maximum within each island was used as the detection point. In this way the events were aligned in the streamwise and spanwise directions before ensemble averaging. The evolution of the structures was studied by tracking the islands of high local variance between consecutive flow fields. The structures were found to be quite persistent and could often be followed over streamwise distances of the order of 1000 viscous units (see Johansson et al. 1988).

All structures detected† at a chosen time were tracked forward as well as backward in time to locate the space-time position of maximum shear-layer strength

† with a VISA-threshold of $1.0u^2_{rms}$ and an averaging length of 200 viscous units.

(here taken as the maximum local variance) for each event. These space-time positions were then used to construct a conditionally averaged structure at 'maximum strength'. Similarly, conditional averages could be constructed at other stages of development. The events were tracked back to an 'early' stage, which we took to be the instant when the variance just exceeded $0.7u_{rms}^2$, and similarly for a late stage. The streamwise velocity patterns in the xy-midplane at these three stages of development clearly show the strong variation in strength of the velocity pattern on the upstream, 'sweep-side' of the shear-layer (figure 1). At late stages this part becomes quite weak, whereas the downstream, 'ejection-side' retains an almost constant strength over the observed evolution. This is true, not only for the streamwise velocity disturbance, but also for the associated uv-pattern. Indeed, the uv-contribution on the upstream (sweep-type) side of the shear-layer was found to be almost negligible in comparison with that on the ejection side.

The slope of the shear-layer at the detection point can be related to the 'age' of the structure. The angle of inclination decreased from a value of 17° at the early stage to 15° and 12° at maximum strength and the late stage, respectively. This is a manifestation of the stretching and tilting of the structure by the mean shear. The corresponding angles from the v-patterns show a similar evolution (although more accentuated), in which the 'early'-stage angle is as large as about 45°.

No signs of small scale oscillatory motions (or violent break-up) were found in conjunction with the late stages of development of the main structure; we confirmed this conclusion by following several individual events. Instead, the dominating part of the associated uv-contribution resulted from the persistent uv-peak on the downstream side of the shear-layer in the Lagrangian frame of reference, which is in contrast to the above-mentioned conceptual picture of the 'bursting' process.

The pressure patterns associated with the structure are shown in figure 2 for the three stages of development described above. It can be seen that an intense localized high-pressure region develops around and beneath the centre of the shear-layer. At maximum strength the maximum amplitude (deviation from the mean pressure) is about $2.9\tau_w$, or about $2p_{rms}$. These strong localized high-pressure regions could be of significant importance for boundary-layer noise generation. One should note that the actual amplitude is affected by 'phase jitter' in the conditional averaging process, i.e. the variation in the pressure-peak position relative to the detection position, determined from the maximum in local variance.

2.2 Removal of phase jitter

There are several types of difficulties in obtaining quantitatively accurate conditional averages of the various flow variables associated with the structure. The problem of phase jitter in the conditional averaging of quantities other than that on which the actual detection algorithm is applied has, for instance, been addressed by Blackwelder (1977). Johansson et al. (1987b) used a cross-correlation technique between the individual events and the ensemble average, which was shown to be quite effective in removing the phase jitter. It resulted in, among other things, a substantially increased amplitude of the wall-pressure peak associated with the structure.

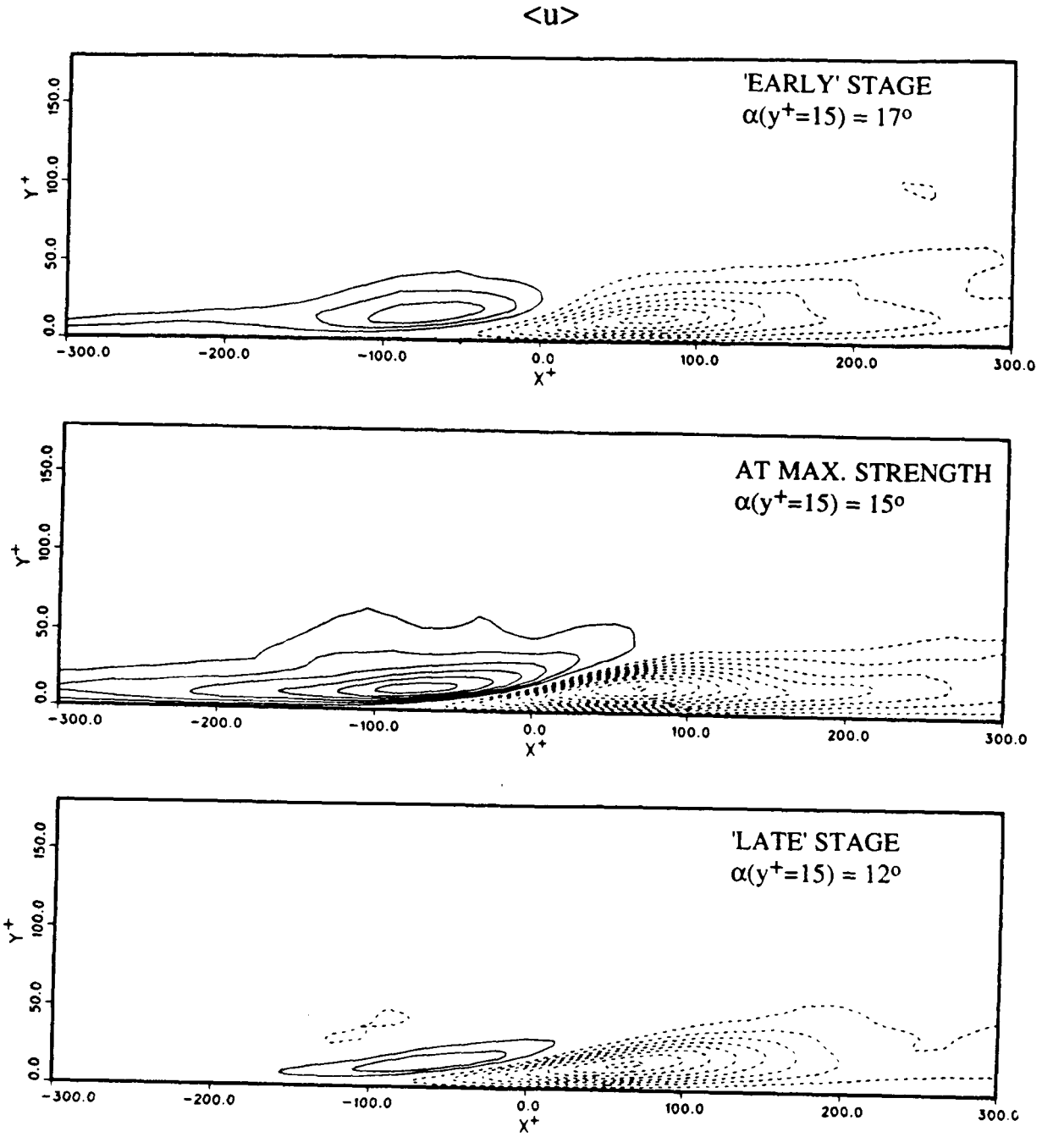

FIGURE 1. VISA-educed conditional averages of the fluctuating part of the streamwise velocity in the xy-midplane of the structure at three stages of development. Contour increment is $0.5u_\tau$, and dashed curves represent negative values.

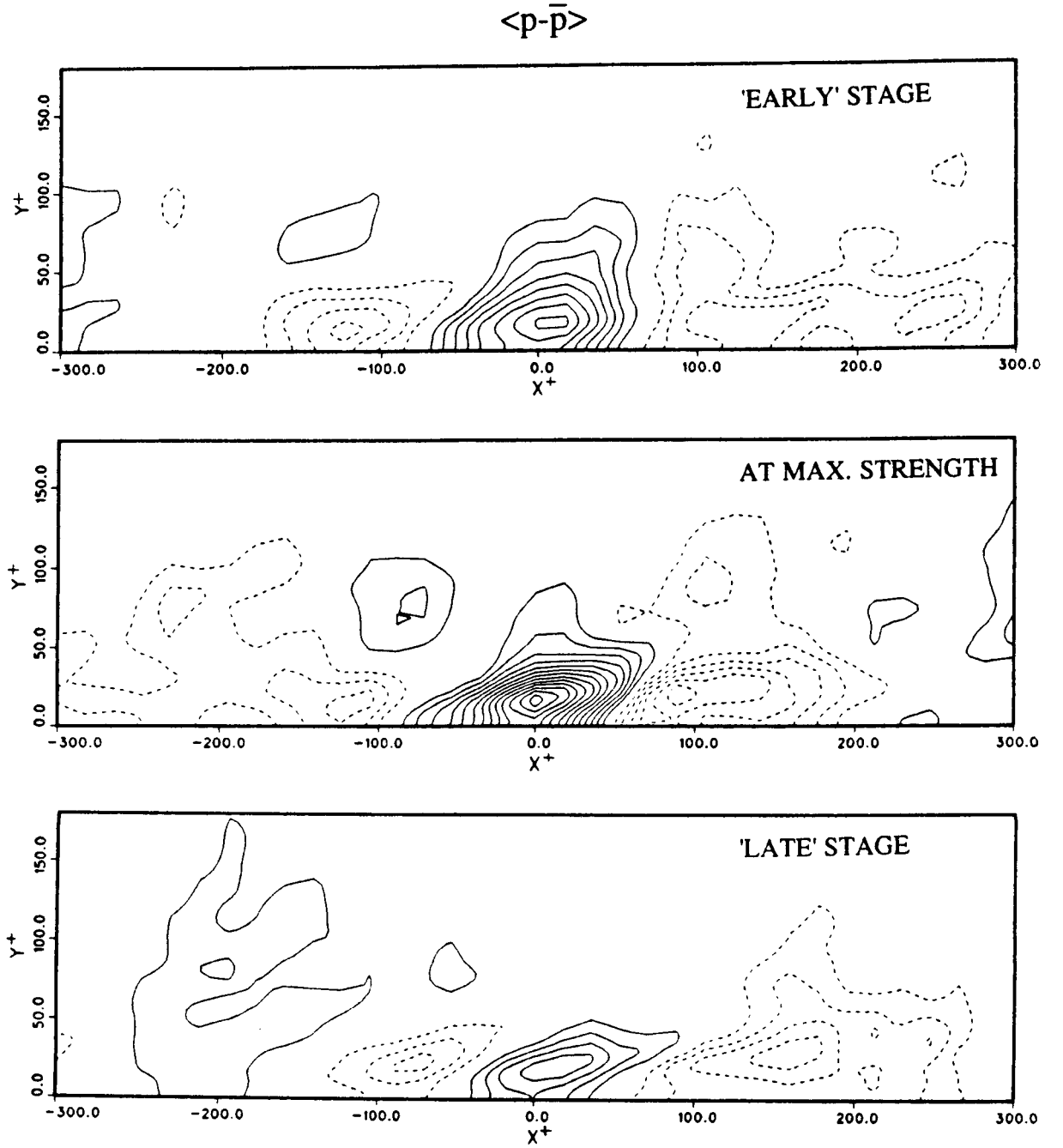

FIGURE 2. Conditional averages of the fluctuating part of the pressure ($< p - \overline{p} >$) in the xy-midplane of the structure at three stages of development. Contour increment is $0.2\tau_w$, and dashed curves represent negative values.

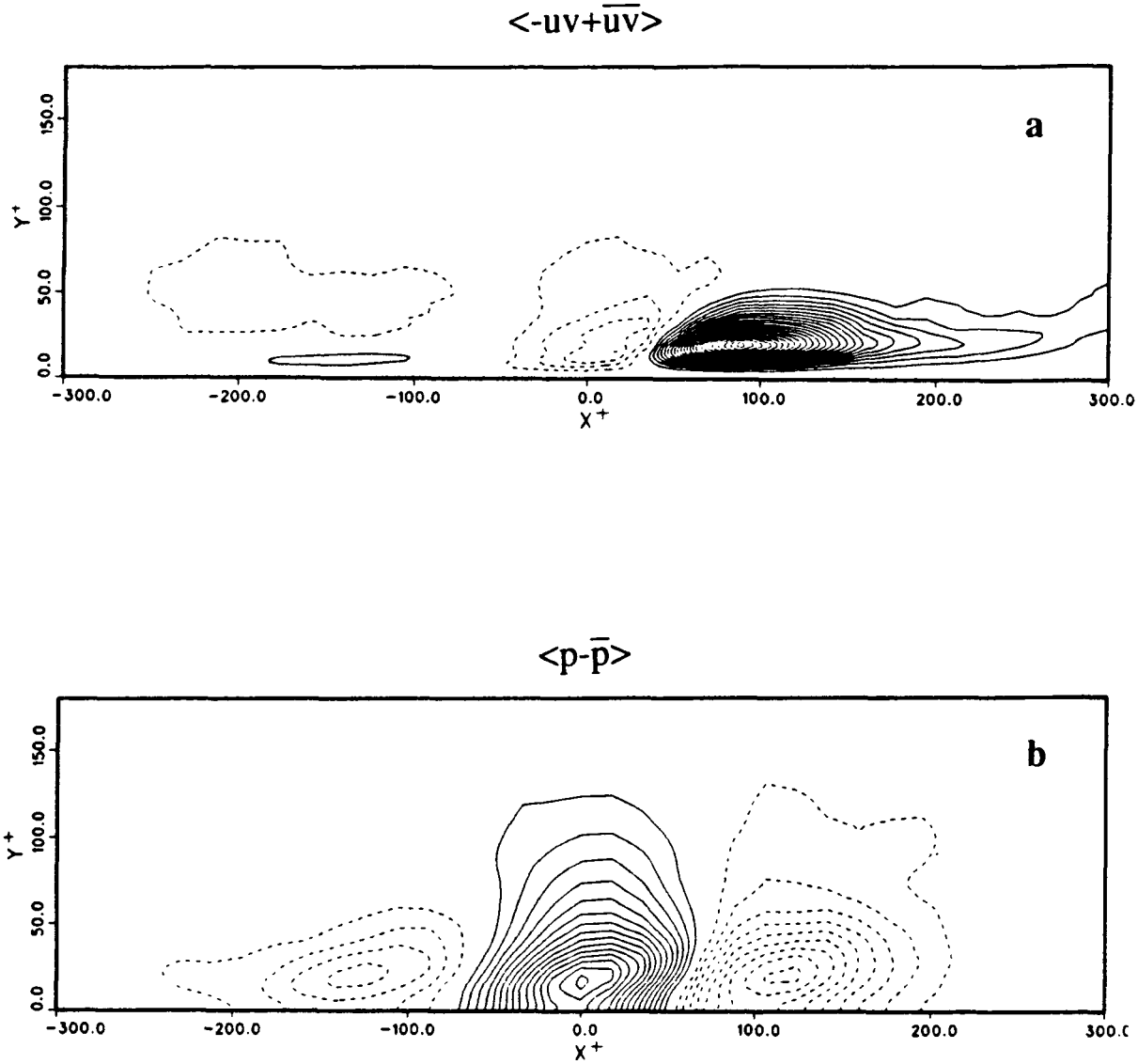

FIGURE 3. Phase-aligned conditional averages of a) $< -uv+\overline{uv} >$ and b) $< p-\overline{p} >$ in the xy-midplane of the structure for all events detected at a chosen time. Contour increments are $0.2u_\tau^2$ and $0.2\tau_w$, respectively.

A cross-correlation technique was applied for 'phase-alignment' of the Reynolds shear stress and pressure patterns (figure 3). For the conditional average of all events detected at a chosen time, the maximum amplitude of the uv pattern (i.e. $< uv - \overline{uv} >$) increased by 35% to $4.2u_\tau^2$ as a result of the alignment. Similarly, the maximum pressure-amplitude increased by 37% to $2.7\tau_w$ after the alignment. Also the spatial coherence in the direction normal to the wall increased somewhat.

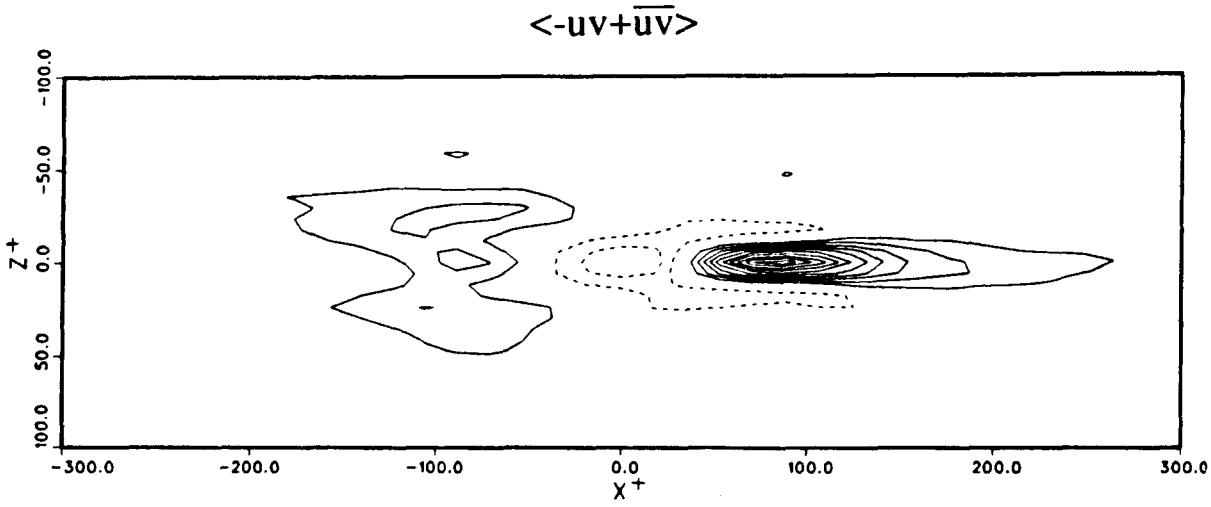

FIGURE 4. Conditional average of $< -uv + \overline{uv} >$ in the xz- plane of the structure at $y^+ = 15$ for all events detected at a chosen time. Contour increment is $0.2u_\tau^2$.

2.3 The role of spanwise asymmetry

Conventional conditional averaging schemes based on one-point detection yield averaged structures symmetric with respect to the xy- midplane when applied to flows with spanwise homogeneity. The conditional average of uv in a horizontal xz-plane at $y^+ = 15$, however, exhibits some interesting features, which indicate that the underlying individual realizations may perhaps not be symmetric (figure 4). The pattern has one lobe on each side of the $z = 0$ plane on the upstream side of the detection point, indicating that the the individual structures are predominantly asymmetric with respect to this plane. To test this hypothesis individual structures were followed in time. It was found that the strong shear often developed in a process where neighbouring elongated high- and low-speed regions interact through a localized spanwise motion, thus generating a flow structure with strong spanwise asymmetry.

In order to preserve this asymmetry in the construction of conditional averages a special scheme was devised, in which the individual structures were switched with respect to the xy-mid-plane (and reversing the sign of w) according to the sign of the spanwise derivative of u at the detection point. The resulting u-patterns in the $y^+ = 15$ plane, for the three stages of development described above, are shown in figure 5. The asymmetry is strongest at the stage of maximum strength of the shear-layer. This is indicative of the importance of spanwise asymmetry in the turbulence production processes, and it suggests that the evolution of near-wall flow structures is quite different from the generally accepted picture as of today.

A measure of the spanwise asymmetry can be obtained by examining the probability density distribution of $\partial u/\partial z$ at the detection point, i.e. at the position where $\partial u/\partial x$ is close to its maximum. In figure 6, the probability distribution of

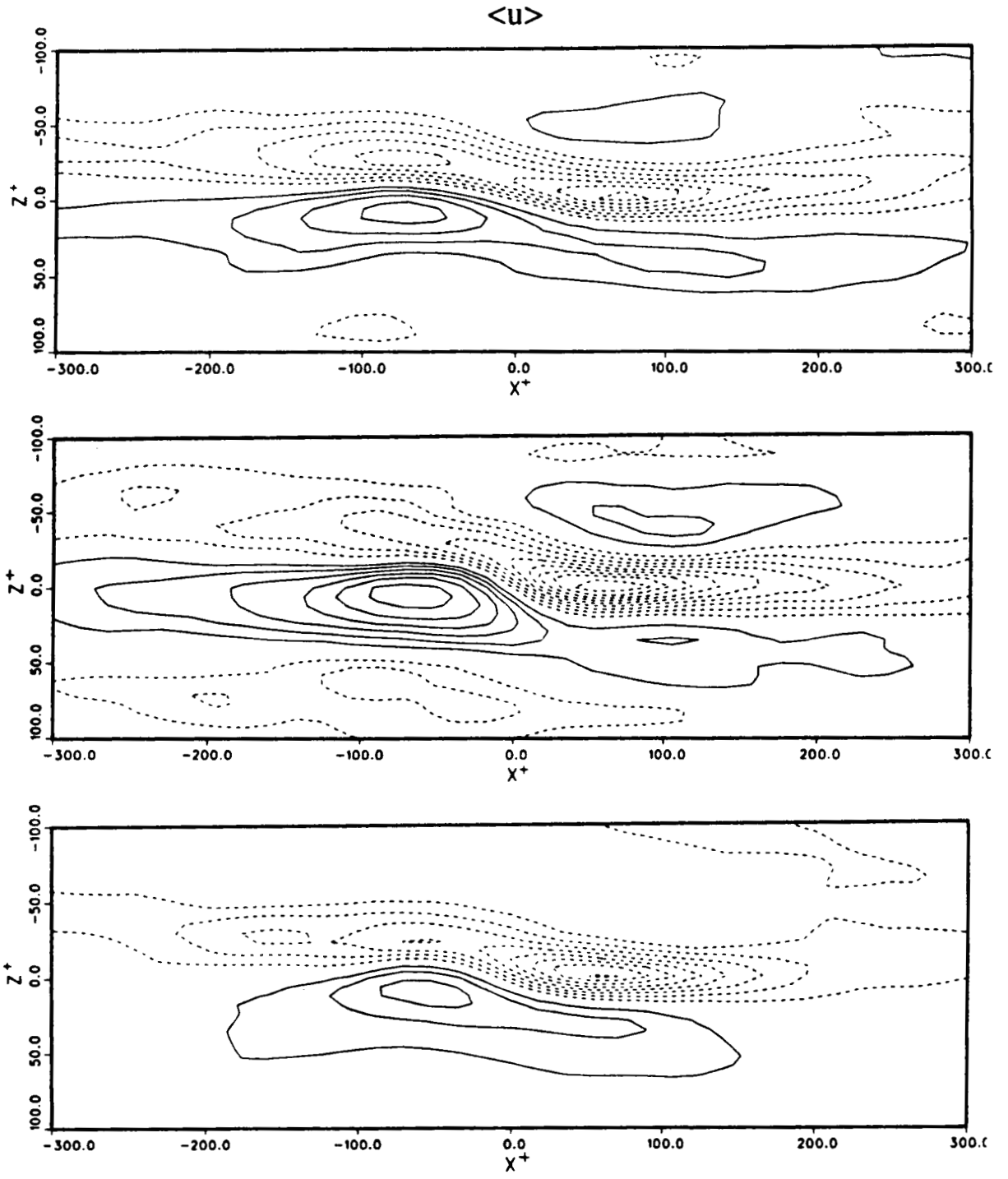

FIGURE 5. Conditional averages obtained with the modified VISA-method preserving spanwise asymmetry. Patterns for the fluctuating part of the streamwise velocity in the xz-plane of the structure at $y^+ = 15$ are shown at three stages of development. Contour increment is $0.5u_\tau$.

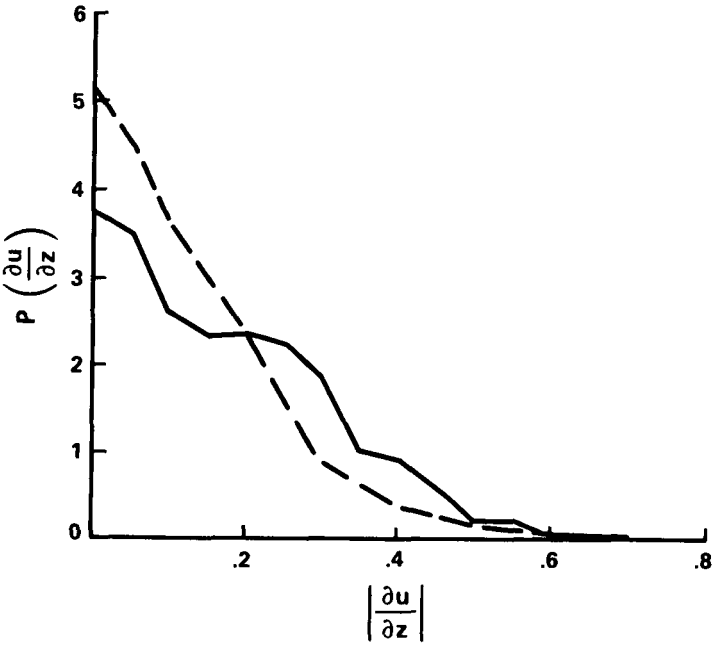

FIGURE 6. Probability density distribution of $|\partial u/\partial z|$: ---- , normal probability density with mean value of 0.11; ——— , conditional probability density at VISA detection point with mean value of 0.20.

$\partial u/\partial z$ at the detection point obtained from twelve different velocity fields (about 700 events were detected in these fields) is compared with the overall probability density for the $y^+ = 15$ plane. The distribution of $|\partial u/\partial z|$ at the detection point is significantly wider than the normal one, illustrating the fact that large $\partial u/\partial z$ often are associated with the shear layers. The average value of $|\partial u/\partial z|$ at the detection point is about twice the overall-average value at $y^+ = 15$. The average value of $|\partial u/\partial z|$ at the detection point was found to be as large as 60% of the mean velocity gradient at $y^+ = 15$.

From the evolution of the asymmetric structures (figure 5), we note that the streaky pattern remains more or less intact throughout the process, indicating that there may not be a need for a further regeneration process for the low- and high-speed streaks.

2.4 Tracking of large-amplitude uv-peaks

The above results suggest a picture of the near-wall turbulence production process in which an important role is played by large- amplitude Reynolds stress peaks that are quite persistent in time in the Lagrangian frame of reference. Large uv-peaks were therefore tracked in space and time in a similar manner to that described for the tracking of shear-layers. We followed second quadrant uv-peaks with an amplitude larger than $4u_{rms}v_{rms}$ at a chosen time both forward and backward in time from that instant. The mean 'survival time' over which the amplitude exceeds

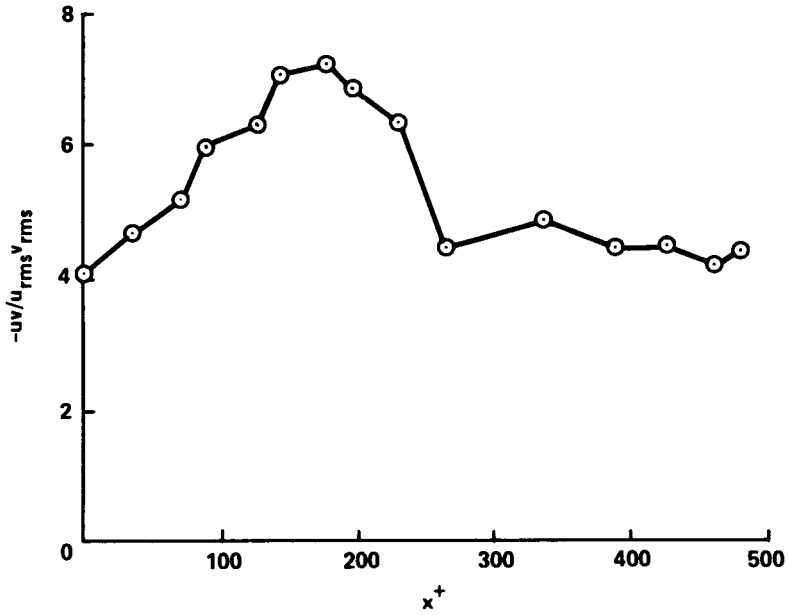

FIGURE 7. The amplitude of a second-quadrant uv-peak as it is followed over the period (45 viscous time units in this case) during which it has an amplitude larger than 4.0 $u_{rms}v_{rms}$.

the $4u_{rms}v_{rms}$ level was found to be more than 30 viscous time units. During this time the flow structure associated with this uv-peak has travelled more than 300 viscous length units (or 1.7 half channel heights). The example shown in figure 7 illustrates a uv-peak with an nondimensional amplitude above 4 over an interval of 45 viscous time units, during which it travelled nearly 500 viscous length units. In the Lagrangian reference frame the appearance of uv-peaks is spatially 'spotty', but certainly not intermittent in time. The average propagation velocity of the uv-peaks was found to be $9.9u_\tau$, comparable to that of the shear layer ($10.6u_\tau$).

3. Concluding remarks

The use of the NASA Ames numerical data bases has resulted in new insights into turbulence producing mechanisms in the near-wall region. The present study indicates that the commonly-held description of the turbulence production process needs some modification. The creation of small scales does not appear to be the major source of Reynolds stress or turbulent energy production; instead, a major source seems to be the persistent movement of low speed fluid out from the wall in front of the shear layer, which is a dominating feature of the flow in the near-wall region. The development of asymmetry in the spanwise direction seems to be an important component in shear-layer evolution, and suggests that an instability may take place between the high and low speed regions.

REFERENCES

BLACKWELDER, R.F. 1977 On the role of phase information in conditional sampling. *Phys. Fluids.* **20,** S232.

JOHANSSON, A.V., ALFREDSSON, P.H. & ECKELMANN, H. 1987a On the evolution of shear-layer structures in near-wall turbulence. In *Advances in Turbulence*, pp. 383-389, Proc. First European Turbulence Conference, Lyon, July 1986.

JOHANSSON, A.V., HER, A.V. & HARITONIDIS, J.H. 1987b On the generation of high amplitude pressure peaks in turbulent boundary layers and spots. *J. Fluid Mech.* **175,** 119.

JOHANSSON, A.V., ALFREDSSON, P.H. & KIM, J. 1988 Velocity and pressure fields associated with near-wall turbulence structures. In Proc. of the Zoran Zaric Memorial International Seminar on Near-Wall Turbulence, May 1988 Dubrovnik, Springer.

KIM, H.T., KLINE, S.J. & REYNOLDS, W.C. 1971 The production of turbulence near a smooth wall in a turbulent boundary layer. *J. Fluid Mech.* **50,** 133.

KLINE, S.J., REYNOLDS, W.C., SCHRAUB, F.A. & RUNSTADLER, P.W. 1967 The structure of turbulent boundary layers. *J. Fluid Mech.* **30,** 74.

Page intentionally left blank

Pressure–strain-rate events in homogeneous turbulent shear flow

By JAMES G. BRASSEUR† AND MOON J. LEE‡

A detailed study of the intercomponent energy transfer processes by the pressure–strain-rate in homogeneous turbulent shear flow is presented. Probability density functions (pdf's) and contour plots of the rapid and slow pressure–strain-rate (π_{ij} and ϕ_{ij}) show that the energy transfer processes are extremely peaky, with high-magnitude events dominating low-magnitude fluctuations, as reflected by very high flatness factors (30–40) of the pressure–strain-rate.

The concept of the energy transfer class defined as

$$\mathbf{C}^{\pm\pm\pm} = \{\phi_{ij}(\mathbf{x},t)\,|\,\phi_{11} \gtrless 0, \phi_{22} \gtrless 0, \phi_{33} \gtrless 0\}$$

has been applied to investigate details of the direction as well as magnitude of the energy transfer processes. In incompressible flow, six disjoint energy transfer classes exist. Examination of contours in instantaneous fields, pdf's and weighted pdf's of the pressure–strain-rate indicates that in the low-magnitude regions (roughly $|\phi_{\alpha\alpha}| < 1.5$ r.m.s. $\phi_{\alpha\alpha}$) all six classes play an important role, but in the high-magnitude regions four classes of transfer processes, $\mathbf{C}^{++-}$, $\mathbf{C}^{-++}$, $\mathbf{C}^{-+-}$ and $\mathbf{C}^{--+}$, dominate. The contribution to the average slow pressure–strain-rate from the high-magnitude fluctuations is only 50% or less. The relative significance of high- and low-magnitude transfer events is discussed.

1. Introduction

We continue the analysis of the local intercomponent energy transfer process associated with the pressure–strain-rate correlation terms in the dynamic equation for the Reynolds-stress tensor, initiated in Brasseur & Lee (1987, hereafter referred to as BL). The work continues a program of enquiry into the kinematic structure and dynamic processes associated with local, random events underlying statistical quantities modeled in second-order closures. *Event* refers to a local concentration of the quantity in an instantaneous turbulent field. The aim is to describe classes of local events with similar characteristics, their interrelationships, and their relative kinematic and dynamic *significance*. Of particular interest is the structure and overall contribution of the most *powerful* events relative to the underlying low-level turbulent field.

The pressure–strain-rate term is the most controversial and least-understood term modeled in Reynolds-stress transport closures. Direct numerical simulations are

† The Pennsylvania State University
‡ Center for Turbulence Research

ideally suited to its study. The analysis begins with homogeneous turbulence in which pressure-induced intercomponent energy transfer may be unambiguously described by the correlation between fluctuating pressure p and strain-rate tensor $s_{ij} = \frac{1}{2}(u_{i,j} + u_{j,i})$. Homogeneous turbulent shear flow is analysed as a prototypical shear flow with turbulence production by mean shear. Significant structural and statistical similarities have been found between homogeneous shear flow and inhomogeneous wall-bounded flows (Kim *et al.* 1987; Lee *et al.* 1987; Rogers & Moin 1987).

Pressure (and accordingly pressure–strain-rate) is commonly decomposed into 'slow' and 'rapid' parts (see §2.1). In BL, both rapid and slow parts are discussed. Here, we shall concentrate on *slow pressure–strain-rate* events, and on a single realization in the asymptotic development of the flow.

2. Preliminary considerations

2.1. *Homogeneous turbulent shear flow*

The transport equation for the Reynolds stresses $R_{ij} = \overline{u_i u_j}$ in homogeneous turbulence may be written as

$$\frac{dR_{ij}}{dt} = P_{ij} + O_{ij} + T_{ij} - D_{ij}, \tag{1}$$

where $P_{ij} = -(S_{ik}R_{jk} + S_{jk}R_{ik})$ is the production rate, $O_{ij} = -(\Omega_{ik}R_{jk} + \Omega_{jk}R_{ik})$ the kinematic-rotation term and $D_{ij} = 2\nu\,\overline{u_{i,k}u_{j,k}}$ the (homogeneous) dissipation rate (see Lee & Reynolds 1985, §2.2 for a discussion). The pressure–strain-rate tensor $T_{ij} = \frac{2}{\rho}\,\overline{ps_{ij}}$ is the average value of the local product of fluctuating pressure and strain rate. Since the trace of the *instantaneous* pressure–strain-rate product ps_{ij} is zero in incompressible flow, ps_{ij} does not contribute to the production of turbulent energy. Thus, ps_{ij} may be interpreted as transferring turbulent energy locally, as well as globally, among components.

Our coordinate system for homogeneous turbulent shear flow with mean velocity $\mathbf{U} = (Sy, 0, 0)$ is sketched in figure 1 ($S = dU/dy$ is the mean shear rate). Turbulent shear flow with unidirectional mean velocity has the characteristic that the sum of turbulent energy production and energy transfer by mean rotation ($P_{ij} + O_{ij}$ in Eq. 1) increases component energy in the flow direction $\overline{u^2}$. Experimental measurements (Harris *et al.* 1977; Tavoularis & Corrsin 1981) and numerical simulations (Rogallo 1981; Rogers *et al.* 1986; Lee *et al.* 1987) suggest that homogeneous shear flow approaches an asymptotic-growth state in which the streamwise component $\overline{u^2}$ contains the most energy, followed by the spanwise component $\overline{w^2}$, then the normal component $\overline{v^2}$.

The present investigation makes use of the full simulation data of homogeneous shear flow (Rogers *et al.* 1986). The simulation was carried out by using the pseudospectral code developed by Rogallo (1981) with periodic boundary conditions on a deforming grid of $128 \times 128 \times 128$ nodes. Run R128 is analysed at total shear $St = 4$ and 8 (the largest scales approach the size of the computational domain

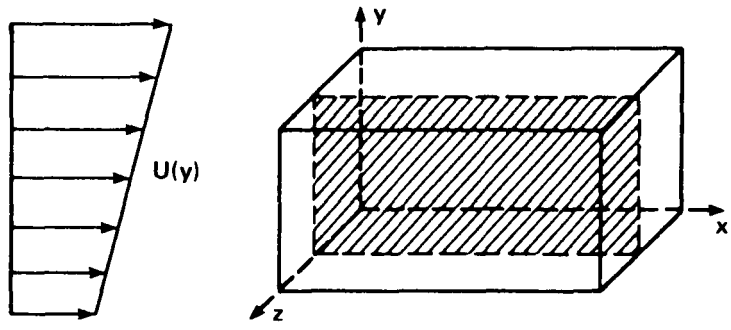

FIGURE 1. The subset of the computational domain and the xy-plane (hatched) over which the contours in figures 2 and 6 are shown. The spanwise location of the plane was arbitrarily chosen at the middle of the domain.

near $St = 16$). At $St = 8$, the Taylor-microscale Reynolds number is 74 and the dimensionless shear rate is $Sq^2/\epsilon = 8.8$ (where $q^2 = R_{ii}$ and $\epsilon = \frac{1}{2}D_{ii}$).

Corresponding to the two terms on the right hand side of the equation for fluctuating pressure in homogeneous shear flow

$$\frac{1}{\rho}\nabla^2 p = -2Su_{2,1} - u_{i,j}u_{j,i}, \tag{2}$$

pressure may be decomposed into two parts: $p = p_r + p_s$. The *rapid* pressure p_r responds directly to the mean shear, whereas the *slow* pressure p_s changes indirectly by the fluctuating velocities. *Instantaneous pressure–strain-rate* is accordingly separated into the rapid and slow parts:

$$\pi_{ij} = \frac{2}{\rho}p_r s_{ij} \quad \text{and} \quad \phi_{ij} = \frac{2}{\rho}p_s s_{ij}. \tag{3}$$

In BL, it was found that r.m.s. rapid pressure is approximately twice r.m.s. slow pressure from $St = 4$ to 8. The correlation coefficient between p_r and p_s, however, is very small, providing strong support for the modeling of the rapid and slow pressure–strain-rate terms separately (e.g. Lumley 1978). The lack of correlation between rapid and slow pressure is associated with a large difference in scale; p_r is contained within a very-large-scale, plane-wave-like structure, whereas p_s is concentrated in scales roughly corresponding to the 'energy-containing' eddies. Rapid and slow pressure–strain-rate, however, are only a factor of two different in scale, residing roughly within the 'energy-containing' range (vid. BL).

2.2. *Classes of the intercomponent energy transfer*

In order to explore the details of the physical processes in which turbulent kinetic energy is exchanged among components, we introduce the concept of *class* of the energy transfer processes. We discuss here only the slow pressure–strain-rate ϕ_{ij}, but the same technique has also been applied to the rapid term.

A *class of the intercomponent energy transfer* $\mathbf{C}^{s_1 s_2 s_3}$ is defined as the set of $\phi_{ij}(\mathbf{x}, t)$ with the same 'sign triplet' $(s_1 s_2 s_3)$ that are the signs of the intercomponent energy exchange, ϕ_{11}, ϕ_{22} and ϕ_{33}. There are six possible classes of the intercomponent energy transfer:†

$$\mathbf{C}^{\pm\pm\pm} = \{\phi_{ij}(\mathbf{x}, t) \,|\, \phi_{11} \gtrless 0, \phi_{22} \gtrless 0, \phi_{33} \gtrless 0\}. \tag{4}$$

For example, $\mathbf{C}^{-++}$ denotes the class of ϕ_{ij} in which energy leaves u ($\phi_{11} < 0$) and enters v and w ($\phi_{22} > 0$, $\phi_{33} > 0$). It may be noted that this classification is unique and the six classes are disjoint (or mutually exclusive).

The classification is used to quantify the contribution from each class to the average pressure–strain-rate. For this purpose, let $\phi_{ij}^{s_1 s_2 s_3}$ denote the values of the components of the instantaneous ϕ_{ij} that belong to class $\mathbf{C}^{s_1 s_2 s_3}$. Since the classes are disjoint, the average value of a pressure–strain-rate component is the sum of the contributions from the six classes for that component:

$$\Phi_{ij} = \overline{\phi_{ij}} = \sum_{s_1, s_2, s_3 = \pm} \Phi_{ij}^{s_1 s_2 s_3}, \tag{5}$$

where

$$\Phi_{ij}^{s_1 s_2 s_3} = \overline{\phi_{ij}^{s_1 s_2 s_3}}. \tag{6}$$

For example, Φ_{11}^{-++} represents the average value of all ϕ_{11}'s that belong to class $\mathbf{C}^{-++}$ ($\phi_{11} < 0$, $\phi_{22} > 0$ and $\phi_{33} > 0$).

By definition, Φ_{11}^{+++}, Φ_{11}^{++-} and Φ_{11}^{+--} are positive, and hence each represents energy transfer into u. The sum of these three positive parts represents the *total* energy transfer into u. The converse is true of the three negative contributions Φ_{11}^{-++}, Φ_{11}^{-+-} and Φ_{11}^{--+}. Thus, the average energy transfer rate in u may be decomposed as follows:

$$\Phi_{11} = \Phi_{11}^{+} + \Phi_{11}^{-}, \tag{7}$$

where

$$\Phi_{11}^{+} = \sum_{s_2, s_3 = \pm} \Phi_{11}^{+ s_2 s_3} = \Phi_{11}^{+++} + \Phi_{11}^{++-} + \Phi_{11}^{+--}, \tag{8a}$$

$$\Phi_{11}^{-} = \sum_{s_2, s_3 = \pm} \Phi_{11}^{- s_2 s_3} = \Phi_{11}^{-++} + \Phi_{11}^{-+-} + \Phi_{11}^{--+}. \tag{8b}$$

A similar decomposition can be obtained for the other components by appropriate permutation of the indices and sign triplets.

† (i) Classes $\mathbf{C}^{+++}$ and $\mathbf{C}^{---}$ are impossible in incompressible flow since $s_{ii} = 0$. (ii) The special cases with zero energy transfer in one, two or all components are ignored, since these occur very rarely in practice.

3. The local process of intercomponent energy transfer: slow term

3.1. *Spatial distribution of pressure–strain-rate*

Statistical averages of the instantaneous pressure–strain-rate terms π_{ij} and ϕ_{ij} show that energy is transferred out of the streamwise component u into the normal and spanwise components v and w, with w receiving the greater amount. At $St = 8$, the rapid and slow terms remove energy from u at the same rate. However, the *rapid* term transfers energy from u (and a lesser amount from v) into the *spanwise* component w, whereas the *slow* term transfers energy from u almost entirely into the *normal* component v (see BL).

As discussed in BL, however, analysis of the concentration of pressure–strain-rate events suggests a different, more complex process. We shall restrict the discussion to the slow term. Figure 2 shows contours of constant ϕ_{11}, ϕ_{22} and ϕ_{33} on the xy-plane shown in figure 1 (a 64×64 subset of the computational domain). The negative (solid) and positive (dashed) contours displayed are for $|\phi_{\alpha\alpha}| \geq 100$ (corresponding to 1.2–16.0 times the r.m.s. values). In this range, $\phi_{\alpha\alpha}$ is highly concentrated in relatively few (perhaps 30–40) powerful events over the computational domain.

The event labeled Ⓐ is the most powerful event in the computational domain (see BL for details). Here, it may be observed by overlaying the contours that energy is transferred locally from u, primarily to w and a little to v (small region of $\phi_{22} > 0$), and that w receives from v also. A similar process occurs in event Ⓑ. In event Ⓒ, energy leaves w to enter v; and in some parts of Ⓓ, energy is transferred from v to w, but from w to v in other parts.

In figure 3, a schematic is shown of the local energy transfer processes estimated by overlaying the contours in figure 2 and by classifying them into the six disjoint classes described in §2.2. Notice that the 'net' effect of energy transfer in the powerful events obtained by adding the contributions from the six classes is such that energy leaves u and enters v, consistent with the statistical averages. However, actual transfer processes are quite different. Among the possible six classes four classes of energy transfer are dominant (i.e. are associated with greatest amount of the energy transfer):

$$\mathbf{C}^{++-}, \quad \mathbf{C}^{-++}, \quad \mathbf{C}^{-+-}, \quad \mathbf{C}^{--+}. \tag{9}$$

Hence, the detailed processes underlying the net transfer (out of u into v) are such that energy is transferred from u primarily into w ($\mathbf{C}^{-++}$ and $\mathbf{C}^{--+}$), with v receiving most of its energy from w rather than from u ($\mathbf{C}^{-+-}$ and $\mathbf{C}^{++-}$).

3.2. *Probability density functions (pdf's)*

To characterize more quantitatively the local pressure–strain-rate events, a wide range of pdf's have been calculated. Comparison of pressure pdf's (not shown) with those in the log layer of a turbulent channel flow (J. Kim 1988, private communication) shows remarkable correspondence.

Pdf's $\mathsf{P}(\phi_{\alpha\alpha})$ of the diagonal components of ϕ_{ij} in standard form (scaled by the respective r.m.s. values ϕ'_{11}, ϕ'_{22}, ϕ'_{33}) are shown in figure 4; a Gaussian distribution is also plotted as a dotted line for reference. The flatness factors of ϕ_{11}, ϕ_{22}

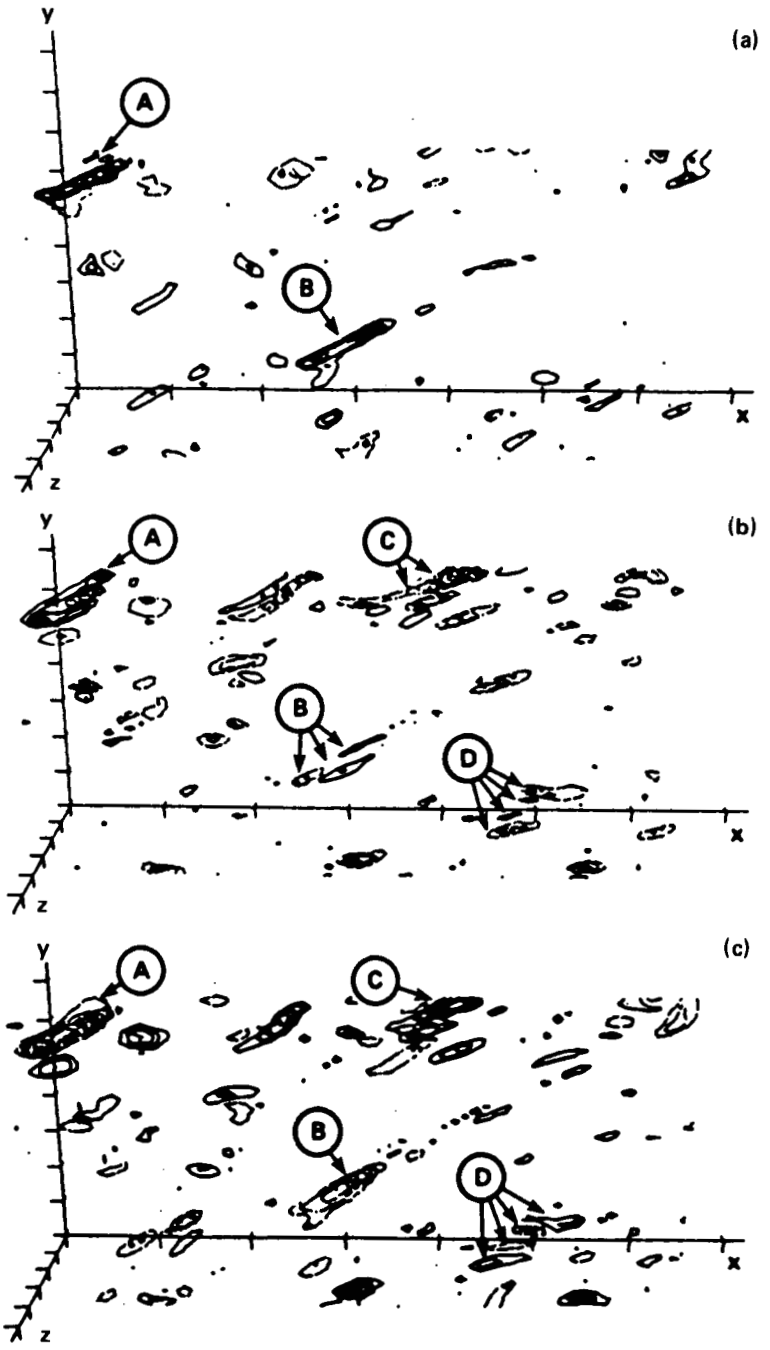

FIGURE 2. Contours of slow pressure–strain-rate on the xy-plane shown in figure 1 at $St = 8$: (*a*) ϕ_{11}; (*b*) ϕ_{22}; (*c*) ϕ_{33}. ——, negative; ----, positive. Four significant events are labeled (A), (B), (C) and (D).

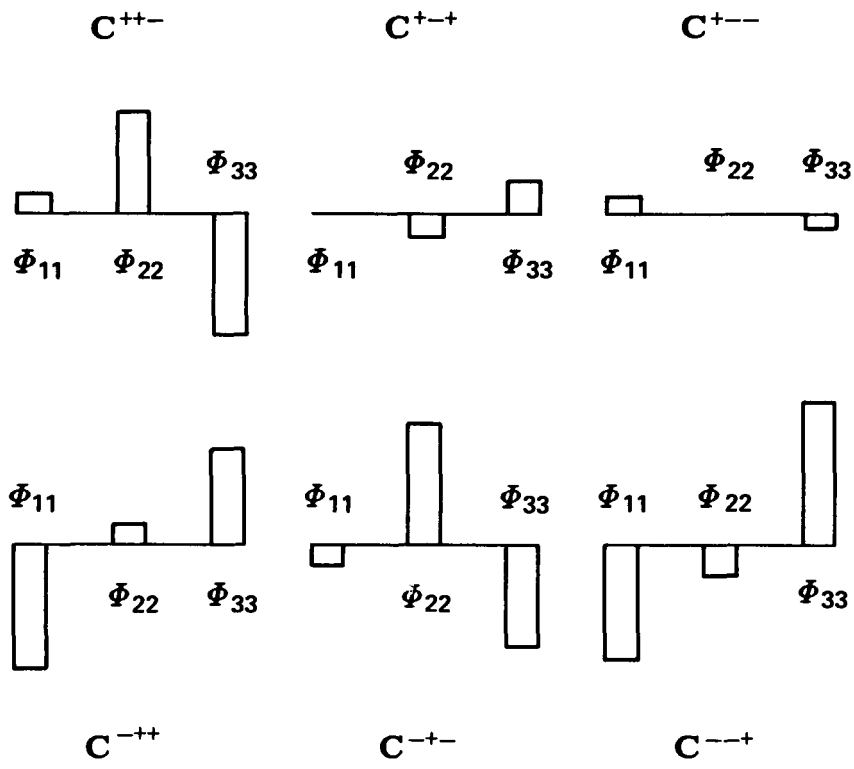

FIGURE 3. Schematic of the intercomponent energy transfer process, as deduced from contours of $\phi_{\alpha\alpha}$ in figure 2, shows that four transfer classes C^{++-}, C^{-++}, C^{-+-} and C^{--+} are dominant.

and ϕ_{33} are 41, 39 and 27, respectively. The high flatness factors, with the spikes in the pdf's near zero (see figure 4), are a reflection of the spottiness of the distribution of ϕ_{ij} with concentrated, high-magnitude events towering over a 'sea' of low-magnitude fluctuations. The skewness factors of ϕ_{11}, ϕ_{22} and ϕ_{33} are -3.9, 3.3 and 0.3, respectively. The high negative skewness factor of ϕ_{11} is indicative of dominance of negative events in the high-magnitude region; and the converse is true of ϕ_{22}. However, combination of the low skewness factor and high flatness factor of ϕ_{33} implies that high-level fluctuations of ϕ_{33} are relatively equally distributed on the both sides (figure 4*c*). These results are consistent with the deductions illustrated in figure 3.

The statistical average of the nth moment of a random variable ϕ is obtained by

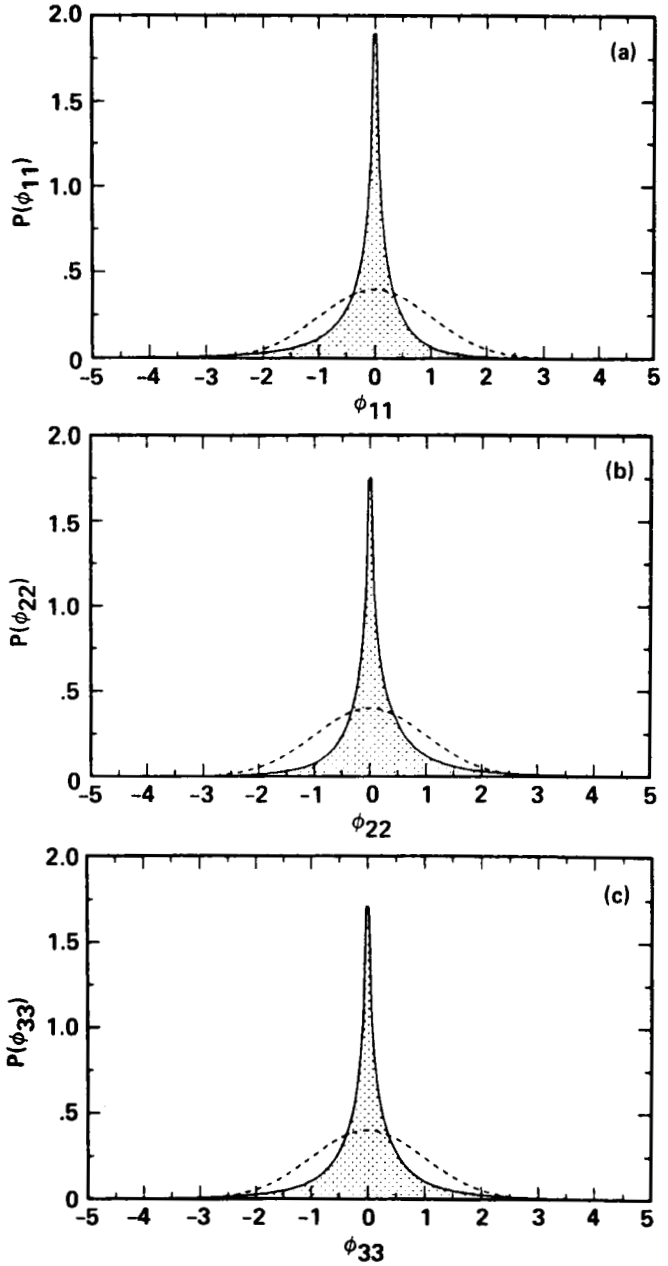

FIGURE 4. Pdf's of the diagonal elements of ϕ_{ij}: (*a*) $P(\phi_{11})$; (*b*) $P(\phi_{22})$; (*c*) $P(\phi_{33})$. ----, Gaussian distribution.

integrating the pdf of ϕ weighted by nth power of ϕ:

$$\overline{\phi^n} = \int_{-\infty}^{\infty} \phi^n \mathsf{P}(\phi)\, d\phi. \tag{10}$$

In order to evaluate the relative contributions to the mean value $\Phi_{\alpha\alpha} = \overline{\phi_{\alpha\alpha}}$ from different ranges of $\phi_{\alpha\alpha}$, the *weighted pdf* defined as $\phi_{\alpha\alpha}\mathsf{P}(\phi_{\alpha\alpha})$ is shown in figure 5 (the subdivisions are discussed below). The long tail in the *negative* ϕ_{11} region (ϕ_{11}^-) in figure 5(a) indicates that there is a substantial amount of energy leaving u in high-magnitude events, say, $\phi_{11}/\phi'_{11} < -1.5$ (see also figure 4a). On the other hand, figure 5(b) indicates that events with high-magnitude *positive* ϕ_{22} (ϕ_{22}^+) dominate in transferring energy into v (say $\phi_{22}/\phi'_{22} > 1.5$). However, both positive and negative ϕ_{33} events (ϕ_{33}^+, ϕ_{33}^-) equally contribute to the average Φ_{33} in the high-magnitude regions (say $|\phi_{33}/\phi'_{33}| > 1.5$, figure 5$c$). Also note that a considerable contribution to the statistical averages comes from low-magnitude events, $|\phi_{\alpha\alpha}/\phi'_{\alpha\alpha}| < 1.5$ (see §3.3 for a discussion).

The decomposition of the pressure–strain-rate introduced in §2.2 is applied to the weighted pdf. In figure 5, the height within each band denoted by a sign triplet shows the weighted pdf of $\phi_{\alpha\alpha}$ belonging to the corresponding class, and the area in that band represents contribution to the average from the class. For example, in figure 5(a), the area in the band $(-++)$ represents Φ_{11}^{-++} from class $\mathbf{C}^{-++}$ (in which $\phi_{11} < 0$, $\phi_{22} > 0$, $\phi_{33} > 0$):

$$\Phi_{11}^{-++} = \int_{-\infty}^{\infty} \phi_{11}\mathsf{P}(\phi_{11}^{-++})\, d\phi_{11}. \tag{11}$$

It is apparent that, in the low-magnitude regions, all the six classes of intercomponent energy transfer events play a significant role. However, high-magnitude portions (the tails of the weighted pdf's) are always dominated by only one class of events. In all, four classes of events dominate at high magnitudes — the same four classes listed in (9) on the basis of high-magnitude $\phi_{\alpha\alpha}$ contours.

Close agreement can be found between the high-magnitude portions of the pdf's and the local processes shown in figures 2 and 3. In the ϕ_{11}^- tail (figure 5a), for example, $\mathbf{C}^{-++}$ events are the major contributor. Similarly, the $\mathbf{C}^{-+-}$ events dominate in the ϕ_{22}^+ tail of figure 5(b), and $\mathbf{C}^{++-}$ and $\mathbf{C}^{--+}$ events, respectively, in the ϕ_{33}^- and ϕ_{33}^+ tails of figure 5(c).

3.3. *Relative significance of high- and low-magnitude events*

In contrast with the concentration of pressure–strain-rate events with high magnitude in figure 2, it is clear from the weighted pdf's (figure 5) that the net contribution of these powerful events to the statistical average is not necessarily dominant. This is because these events are concentrated in regions of very small volume and tower over a vast 'sea' of low-magnitude fluctuations whose total contribution to the average is as significant (figure 4). It is also clear from the previous discussions that the character of the high- and low-magnitude events is quite different. Indeed,

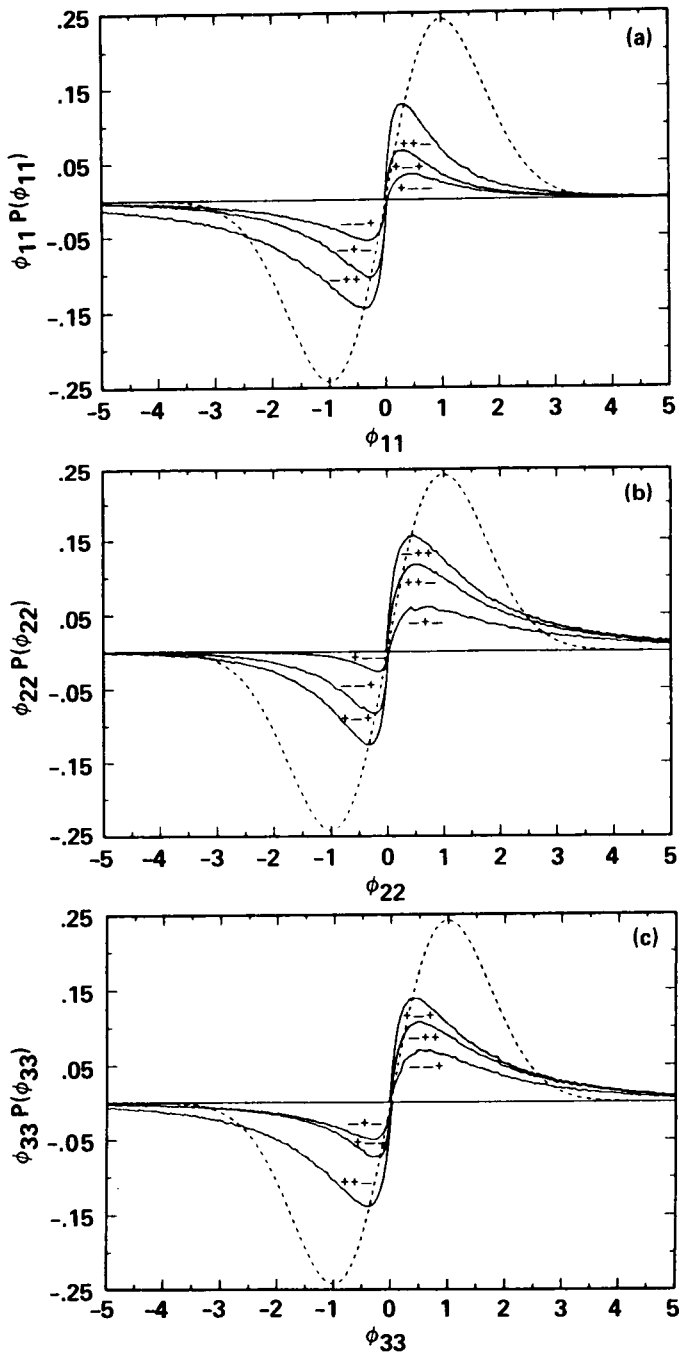

FIGURE 5. Weighted pdf's of the diagonal elements of ϕ_{ij}: (*a*) $\phi_{11}\mathsf{P}(\phi_{11})$; (*b*) $\phi_{22}\mathsf{P}(\phi_{22})$; (*c*) $\phi_{33}\mathsf{P}(\phi_{33})$. ----, weighted pdf for Gaussian distribution. The height within each band denoted by a sign triplet shows the weighted pdf of $\phi_{\alpha\alpha}$ belonging to the corresponding class, and the area in that band represents contribution to the average from the class.

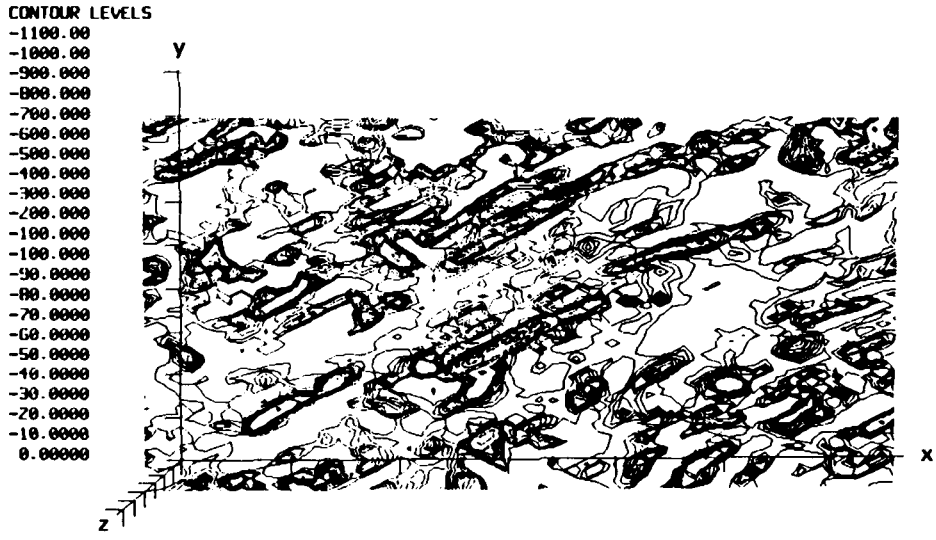

FIGURE 6. Contours of ϕ_{11} as in figure 2(a) with contours below $\phi_{11} = 100$ added. Note that countour increments below $\phi_{11} = 100$ are one-tenth of those above 100.

there is evidence that the powerful events are associated with the local coherent structure of the vorticity field (see BL).

Figure 6 shows contours of constant ϕ_{11} as in figure 2(a), but includes low-level contours below 100 (1.5 r.m.s.), the lowest level in figure 2(a). Note that the contour increment is 10 times smaller below $|\phi_{11}| = 100$ than above 100. Clearly, there is a great deal of low-magnitude activity which does not appear in figure 2(a). It turns out that the relative contribution to the average of the high-magnitude events (arbitrarily defined by the cutoff at 1.5 r.m.s) in each of the four dominant classes discussed above is roughly 50%. In other words, the high- and low-magnitude events contribute almost equally to the averages.

The statistical averages within each class of events, calculated by integrating the weighted pdf's in each band *over all magnitudes* of ϕ_{ij}, are schematically shown in figure 7. The same characteristics as in figure 3 can be found in this figure, i.e. most of energy transfer is carried out within the same four classes of events. Differences in detail, we speculate, are associated with the contributions of the low-magnitude ϕ_{ij} fluctuations to the averages.

Inspection of the energy transfer patterns in figure 7 poses an interesting question about the kinematic structure of the flow regimes involving intercomponent energy transfer. It appears that there is a common pattern of energy exchange in the all classes: the dominant energy transfer to or from one component is provided equally by the other two components. Does this mean that energy is exchanged axisymmetrically? If the off-diagonal terms in ϕ_{ij} (equivalently, s_{ij}) are negligible,

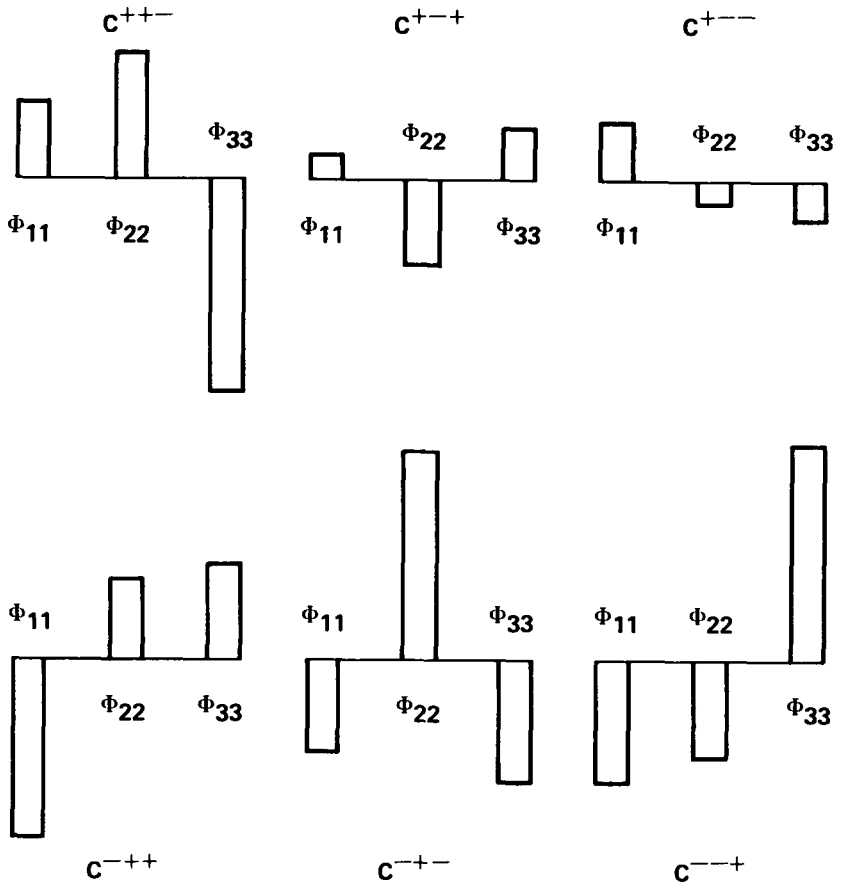

FIGURE 7. Schematic of the intercomponent energy transfer processes, representing the contributions from all magnitudes of ϕ_{ij} events, i.e. integration of the weighted pdf's in figure 5. The schematic also shows that the four classes C^{++-}, C^{-++}, C^{-+-} and C^{--+} are dominant (see figure 3).

then most of the energy transfer takes place within axisymmetric flow regimes, either 'rod-like' or 'disk-like' type. The answer awaits invariant analysis of the tensorial characteristics of the pressure–strain-rate (and strain rate).

4. Concluding remarks

Although a great deal has been learned about the process of intercomponent energy transfer as described by pressure–strain-rate correlations, many questions await further analysis. The most nagging of these questions regards the determination of 'significance.' It is clear, for example, that powerful pressure–strain-rate

events in which a great deal of energy transfer takes place locally in space exist; the pdf's of ϕ_{11}, ϕ_{22} and ϕ_{33} are extremely peaked around zero and possess very high flatness factors. It is because these events are so sparse that the net contributions to the statistical averages from the high-magnitude fluctuations are only 50% or less.

The *significance* of these powerful events in the evolution of the intercomponent energy transfer process, however, may be only partially related to their contribution to the statistical average. Indeed, the description of the qualitative features of the intercomponent energy transfer process as a whole by the high-magnitude events alone suggests that these powerful events may provide a major influence to the pressure–strain-rate fluctuations at all magnitudes. Currently in process is the development of schemes for isolation of the powerful events from the datasets through objective criteria, and further analysis of the separated datasets for determination of 'significance.'

Detailed analyses into the structure of powerful intercomponent energy transfer events, and their structural interrelationships with the local vorticity field are described in BL. We found that the energy transfer event Ⓐ in figure 2 is associated with a local stagnation point of high strain-rate and zero vorticity, apparently induced by a hairpin-vortex-type structure surrounding it. This event occurs in a region of *positive* slow pressure. Another powerful event with similar energy transfer characteristics was since found, which is associated with *negative* slow pressure. This event lies embedded within the legs of a hairpin vortex, suggesting that both events are associated with a vortical structure.

We briefly mention that the same analyses as described above have been applied to the rapid pressure–strain-rate term π_{ij} and results qualitatively similar to those for ϕ_{ij} have been found.

The authors wish to thank R. J. Adrian, J. C. R. Hunt, J. Kim, S. K. Lele, N. N. Mansour, P. Moin, R. S. Rogallo and M. M. Rogers for many helpful discussions during the 1988 Summer Program of the Center for Turbulence Research. J.G.B. gratefully acknowledges support from the Center for Turbulence Research and AFOSR.

REFERENCES

BRASSEUR, J. G. & LEE, M. J. 1987 Local structure of intercomponent energy transfer in homogeneous turbulent shear flow. In *Proc. 1987 Summer Program*, Center for Turbulence Research Report CTR–S87, NASA-Ames Research Center, pp. 165–178. [Referred to as BL in the text.]

HARRIS, V. G., GRAHAM, J. A. H. & CORRSIN, S. 1977 Further experiments in nearly homogeneous turbulent shear flow. *J. Fluid Mech.* **81**, 657–687.

KIM, J., MOIN, P. & MOSER, R. D. 1987 Turbulence statistics in fully-developed channel flow at low Reynolds number. *J. Fluid Mech.* **177**, 133–166.

LEE, M. J., KIM, J. & MOIN, P. 1987 Turbulence structure at high shear rate.

Sixth Symp. on Turb. Shear Flows, Toulouse, France, Sept 7-9, 1987, pp. 22.6.1–22.6.6.

LEE, M. J. & REYNOLDS, W. C. 1985 Numerical experiments on the structure of homogeneous turbulence. *Dept. Mech. Engng. Rep.* TF–24, Stanford University: Stanford, California.

LUMLEY, J. L. 1978 Computational modeling of turbulent flows. *Adv. Appl. Mech.* **18**, 123–176.

ROGALLO, R. S. 1981 Numerical experiments in homogeneous turbulence. NASA *Tech. Memo.* 81315.

ROGERS, M. M. & MOIN, P. 1987 The structure of the velocity field in homogeneous turbulent flows. *J. Fluid Mech.* **176**, 33–66.

ROGERS, M. M., MOIN, P. & REYNOLDS, W. C. 1986 The structure and modeling of the hydrodynamic and passive scalar fields in homogeneous turbulent shear flow. *Dept. Mech. Engng. Rep.* TF–25, Stanford University: Stanford, California.

TAVOULARIS, S. & CORRSIN, S. 1981 Experiments in nearly homogeneous turbulent shear flow with uniform mean temperature gradient. *J. Fluid Mech.* **104**, 311–347.

Center for Turbulence Research
Proceedings of the Summer Program 1988

Multifractal spectra in homogeneous shear flow

By A. E. Deane[1] and L. R. Keefe[2]

Employing numerical simulations of three–dimensional homogeneous shear flow we have calculated the associated multifractal spectra of the energy dissipation, scalar dissipation and vorticity fields. Our results for $(128)^3$ simulations of this flow, and those obtained in recent experiments that analyzed 1– and 2–dimensional intersections of atmospheric and laboratory flows, are in some agreement. A two–scale Cantor set model of the energy cascade process which describes the experimental results from one-dimensional intersections quite well, describes the three–dimensional results only marginally.

1. Introduction

Despite the usefulness of traditional statistical methods (*pdf's*, spectra etc.) for describing many features of turbulent flow, they do poorly when applied to phenomena such as energy dissipation that are intermittent in space or time. Then many higher moments of the *pdf* must be known for an adequate description. Traditional measures also fail to make full use of the self–similarity over length scales known to be characteristic of processes associated with the inertial range. Description of such phenomena as multifractals combines both their intermittent and self–similar character in a unified way. In this paper we go beyond the one– and two–dimensional limitations of experiments and obtain, for the first time, multifractal spectra that make full use of the three–dimensional character of a flow field of engineering interest.

Kolmogorov (1941) introduced the notion of inertial range by making powerful use of self–similarity, and later introduced a correction to account for intermittency of the energy dissipation (Kolmogorov 1962). Mandelbrot (1974) was the first to suggest that the dissipation field might be a fractal — a set of noninteger (Hausdorf) dimension. Frisch and Parisi (1985) elaborated this idea, introducing the term multifractal to denote a set upon which the scaling properties(such as exponents) of measures are not uniform over their support. Subsets of the support over which scaling properties are uniform are homogeneous fractals, and a multifractal may be thought of as a union of interleaved homogeneous fractals, each of which possesses different scaling properties and fractal dimension. The relation between the dimension of these homogeneous fractals and their scaling exponents is termed the multifractal spectrum. Later works by others(Halsey *et al.* 1986) showed practical methods of obtaining the multifractal spectrum from a particular distribution. A

1 Brown University
2 Center for Turbulence Research

number of recent experiments, and the results of this paper, support a multifractal model of energy dissipation. In addition, the scalar dissipation and vorticity fields are also found to be multifractal.

In the high Reynolds number limit the locally averaged energy dissipation, ϵ, can be shown to scale as (Meneveau and Sreenivasan 1987)

$$\epsilon \sim r^{\alpha-1} \tag{1}$$

where r is the extent of the averaging domain (Kolmogorov's original formulation assumes $\alpha = 1$). In the multifractal model each iso–α set has a different fractal dimension, denoted by $f(\alpha)$, whose determination is the objective of this work. A theoretical idea, supported by some experimental evidence, is that the multifractal spectrum, $f(\alpha)$, is a universal property of a given turbulent quantity, and so remains unchanged between different flows.

In a number of recent experiments Sreenivasan and his co–workers have obtained multifractal spectra of energy dissipation and passive scalar dissipation from different flows. While experimental measures of the dissipation field are likely to remain far more highly resolved than in numerically calculated fields, their three-dimensional character is inaccessible in experiments. This necessitates the use of one–(hot–wire), or two–dimensional(laser sheet visualization) "cross–sections" as the base data, and, consequently, assumptions regarding the sub–space structure of the fractals becomes unavoidable. In this paper we obtain spectra from a numerically calculated flow which is three–dimensional, and thus free from the experimental limitations. The field is from a homogeneous shear flow, a choice dictated by the $(128)^3$ resolution of the data and the fact that its homogeneity allows us to analyze the entire field, unlike wall–bounded flows where near–wall regions must be excluded.

We organize this paper as follows. In §II we describe the computations which produced the data set we have analysed. In §III we describe the multifractal model and our methodology for obtaining the spectra. The results are described in §IV and we conclude the paper in §V.

2. Homogeneous shear flow

Approximately homogeneous shear flow has been studied extensively. The imposition of uniform shear causes homogeneous isotropic turbulence to lose its isotropy and allows turbulence to be maintained by the transfer of energy from the mean–field. Thus homogeneous shear flow turbulence is non–decaying. Rose (1966) and Champagne *et al.* (1970) performed experiments on homogeneous shear flow, and Tavoularis and Corrsin (1981) added a passive scalar (temperature) by heating the generating rods. The experiments find a continuous growth of turbulent kinetic energy and its components, as well as a growth in the integral– and micro–scales. There is also a continuous departure from isotropy. The numerical simulations of Rogallo (1981) are true homogeneous shear, but are subject to problems associated with limitations on resolving the flow. As time evolves the energy transferred from the mean–field tends to accumulate in the small wavenumbers. This produces

anomalous behavior in the evolution of integral scales and other measures based on the large–scales of motion. Small–scale measures such as microscales are unaffected. The simulations show a continuous growth in turbulent kinetic energy, but a decrease in component energies in the transverse and spanwise directions, counter to experimental finding.

Rogers *et al.* (1986) and Rogers *et al.* (1987) have used the numerical scheme developed by Rogallo to obtain a clearer understanding of the dynamics of the flow. They find that the flow possesses coherent structures in the form of hairpin–like vortices. While we are unable here to make a connection between these organized structures and the multifractal spectrum of the vorticity, we note that phase coherent vorticity, which is often used as identifier of coherent structures, appears to be a feature of all high Reynolds number flow.

For the study described in this paper we have used a $(128)^3$ realization of this flow due to Rogers *et al.* (1986), designated C128U12 in the NASA Ames data base. The parameters of the simulation are: Taylor microscale Reynolds number, $Re_\lambda = 108$; viscosity, $\nu = 0.01$; and Prandtl number $\mathrm{Pr} = 0.7$. The simulation began from a field which had constant energy for $16k_0 \leq k \leq 32k_0$, where k_0 is the fundamental streamwise wavenumber. The chosen realization is at a time when a power law decay in the spectrum at high k can be observed, but the degradation at low–wavenumbers has not begun. The power law exponent is –3, not –5/3, so the flow does not attain an inertial range.

3. Multifractal model

Our analysis is based on the works of Hentschel and Proccacia (1983), Benzi *et al.* (1984), Frisch and Parisi (1985), Halsey *et al.* (1986) and Meneveau and Sreenivasan (1987a). Consider the kinetic energy dissipation field

$$\epsilon = \nu(\partial u_i/\partial x_j + \partial u_j/\partial x_i)^2 \tag{2}$$

Here u_i is the i–th component of the velocity, $i, j = 1, 2, 3$ such that x_i are the Cartesian coordinates and ν is the kinematic viscosity. The energy dissipation in a box of size r is

$$E_r \sim \epsilon r^3 \tag{3}$$

The theory of generalized dimensions considers the dimensions D_q of a set to be defined by

$$D_q = \frac{1}{(q-1)} \lim_{r \to 0} \frac{\log \sum p_m^q}{\log r} \tag{4}$$

where the sum is over all the boxes and p_m is the probability of finding a member of the set in the m–th box. For integer values of positive q the moments p_m^q correspond to finding q–tuple members of the set within a distance r. Here the set is the dissipation field, and we make the assumption

$$Z = \sum E_r^q \sim r^{(q-1)D_q}. \tag{5}$$

We take r to range from the mesh size to the size of the computational domain. This relation determines D_q from E_r. If the scaling (1) holds, then the sum in (5) can be represented in terms of r. This leads to an integral relation between D_q and α, which in the limit $r \to 0$ can be shown to lead to the relations (Meneveau and Sreenivasan 1987a, Halsey *et al.* 1986)

$$\alpha = \frac{d}{dq}[(q-1)(D_q + 1 - d)] \tag{6}$$

$$f(\alpha) = q\alpha - (q-1)(D_q + 1 - d) + d - 1. \tag{7}$$

Here d is the dimension of the embedding space and for our 3–dimensional field $d = 3$.

The dissipation of passive scalars

$$\chi_i = \gamma(\partial\theta/\partial x_i)^2, \tag{8}$$

where θ is concentration or temperature, and γ is molecular diffusivity, can be treated analogously. In experiments this quantity is easier to determine, since it involves no cross terms. The homogeneous shear flow that we have analyzed includes three scalar fields corresponding to imposed gradients in the three directions. We have performed the multifractal analysis on all three of these fields.

4. Results

Figure 1 shows the energy dissipation field from the simulation and serves to focus our ideas. For purposes of illustration only ($32 \times 32 \times 32$) points, corresponding to a 1/64th corner portion of the entire computational domain is shown. The intermittent nature of this quantity is evident and we wish to determine if it is self–similar over a range of length scales. By examining the data we have determined that the dissipation field tends to align itself along the direction of the mean shear much in the way that the vortices identified by Rogers (1986) do. While this does not affect our present analysis, an account of nonisotropic effects might be an extension of this and other works.

Given this field we calculate the generalized dimensions by obtaining Z as a function of r from Eqn. 5. Figure 2 shows the result where $Z^{1/q-1}$ versus r is plotted for different values of q. Nonextremal points appear to lie very nearly on a straight line. Hence we find least squares fit for each q value and determine $D_q(q)$ as the slopes of these lines. In calculating the slopes we have excluded the smallest value and the largest two values of r. The former we exclude because linear behavior is not evident here. We exclude the largest values of r because these scales are the size of the computational domain and we are interested in probing behavior for $r \to 0$. Note that the Kolmogorov microscale $\eta = 0.012$, which is smaller than the smallest value of $r = 0.049$. This means that in the numerical simulation the smallest scales are not quite resolved. Some of the departure from linearity observed in Fig. 2 is likely due to this lack of resolution.

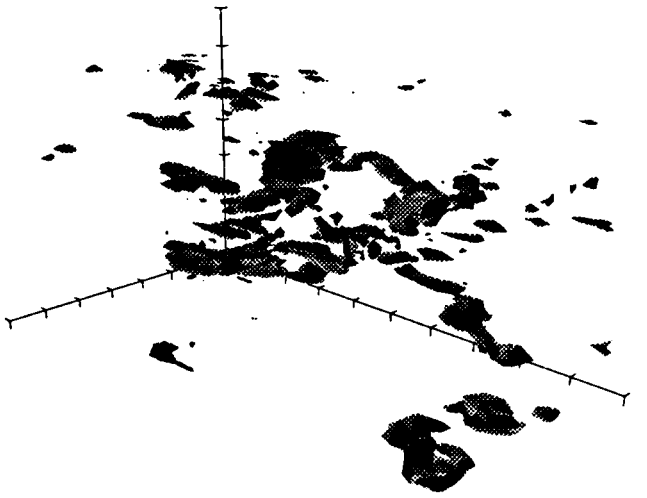

FIGURE 1. The three–dimensional contour surface $\epsilon = 200$, of the energy dissipation field.

Figure 3 shows the result of finding the slopes of the straight line fits to the data shown in the previous figure. Shown is D_q as a function of q. The nature of the curve is such that for large negative values of the moment q the curve asymptotes to a value that is larger than the value obtained asymptotically for large positive q. The intermediate values represent the range of (generalized) dimensions of the energy dissipation field. We find that $D_{-\infty} = 3.85$ and $D_{\infty} = 2.25$. We note that $D_0 = 3$, from Fig. 3, implying that the dissipation is space–filling.

Having obtained the D_q variation with q we can now use Eqns. 6,7 to determine the multifractal spectrum. We have used central differences to approximate the slope of the D_q curve in Fig. 3. The result of applying the transformations are shown in Fig. 4., which shows $f(\alpha)$ vs. α for the energy dissipation. Since we had found $D_0 = 3$, which from Eqn. 8 gives $f(\alpha_0)$, the data has a maximum at this value. We find that $f(1) = 2.97$ and $\alpha_0 = 1.12$.

We have carried out similar calculations for the scalar dissipation fields χ_1, χ_2 and χ_3. We omit presentation of intermediate results and show in Fig. 5 the $f(\alpha)$ curves for the three scalar fields. While there are differences between the spectra of these fields, these differences are small when compared to those with the $f(\alpha)$ for energy dissipation. The scalar field spectra are all broader. This is in accord with experimental finding. The result implies that the so–called intermittency exponent (see Meneveau and Sreenivasan 1987a) is larger for scalar dissipation fields.

The multifractal approach currently applies only to positive quantities. In order to apply the method to the vorticity field we consider the magnitude of the vorticity

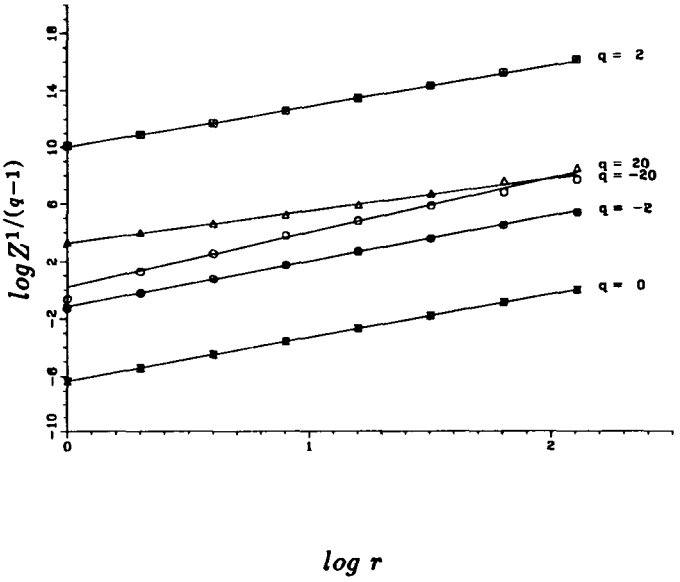

FIGURE 2. Results of applying eq. 5 to the dissipation field. The symbols are the calculated values. Lines are least-squares fits to the data with first point and last two points excluded.

$|\omega|$. Fig. 6 shows the $f(\alpha)$ curve for this field. Of more general interest than ω is ω^2, the enstrophy density. We have not calculated its $f(\alpha)$ curve, but it can be obtained from that of ω(Meneveau and Sreenivasan 1988).

Numerical simulations require initial conditions on velocity, and this implies a certain dissipation and vorticity field as well. The initial conditions used for the shear flow calculation did have a multifractal structure, as can be seen from the $f(\alpha)$ curves for the initial energy dissipation and initial vorticity magnitude fields in Figure 7. A purely random field $\zeta(x, y, z)$ yields the single point $f(0) = 3$ in Fig. 7. While the initial dissipation multifractal structure covers relatively more scales than the vorticity magnitude, it covers relatively fewer when the flow is developed (Fig. 3). For both quantities the expected increase in scaling range under the action of the Navier–Stokes equations is found. A strict inertial range may not have developed yet, but self–similarity is increasing at higher wavenumbers.

Having obtained $f(\alpha)$ curves for the various dissipation fields we now compare our findings with those obtained experimentally by Sreenivasan and his co–workers (Meneveau and Sreenivasan 1987a, Prasad *et al.* 1988). Shown in Fig. 3 as a dashed curve is their data for D_q vs. q. For $-10 < q < 10$ our data falls close to their curve, obtained by averaging over a number of developed laboratory and atmospheric flows. Our data is within their error bars. For large $|q|$ there are significant differences between our finding and theirs, some of them attributable to

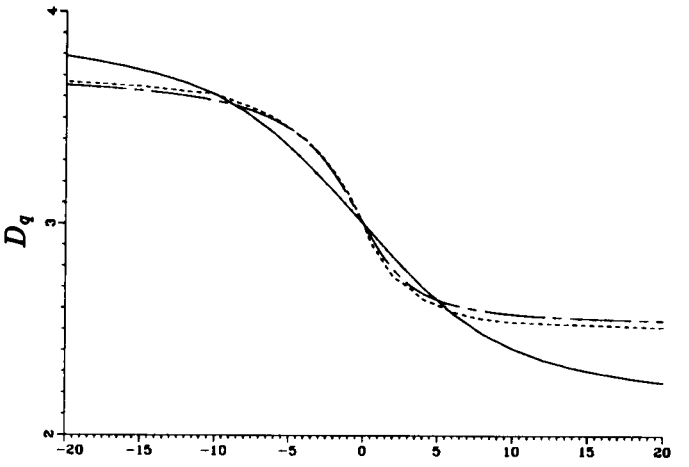

FIGURE 3. Variation of D_q with q. Solid line: our calculations; Dashed line: data of Meneveau and Sreenivasan(1987a); Chain dash: p–model with $p_1 = .7$.

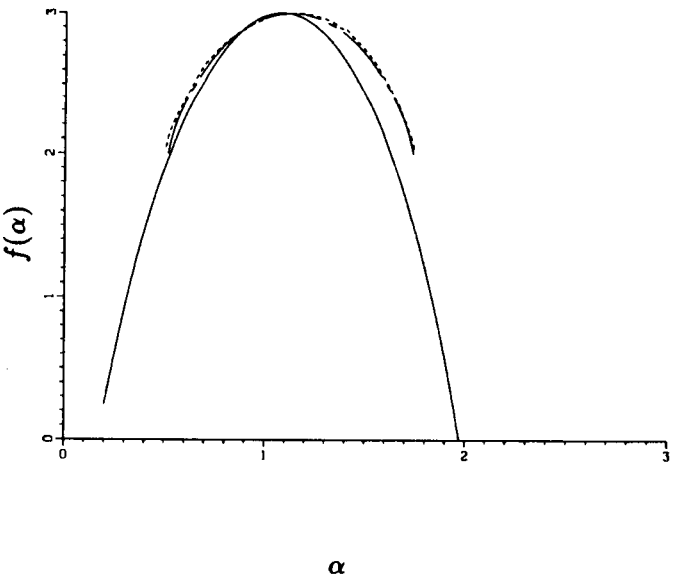

FIGURE 4. The multifractal spectrum $f(\alpha)$ of the dissipation field. Lines as in Figure 3.

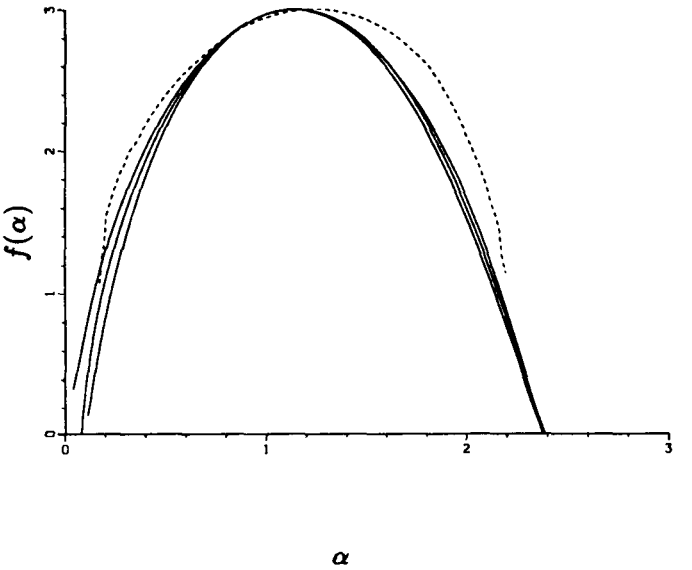

FIGURE 5. Multifractal spectra of the scalar dissipation fields, χ_i. Solid lines are our data, the dashed line is data from Prasad, Meneveau, and Sreenivasan(1988).

the general inaccuracy of the curves at large q, where small errors are compounded. In Figs. 4 and 5 the dashed curve shows their $f(\alpha)$ curves for energy and scalar dissipation. Although differences are exaggerated(by differentiation) when going from the D_q vs. q to the associated $f(\alpha)$ curves, the agreement is still fair. Note that since their data considered a one–dimensional (two–dimensional) intersection of the flow their data does not extend below $f(\alpha) < 2$ ($f(\alpha) < 1$). We conclude that our findings are in broad agreement with the experimental results. Like Meneveau and Sreenivasan we find that the energy and scalar dissipation fields are space–filling and $D_0 = 3$; that $\alpha_0 > 1$; that the $f(\alpha)$ curve is nearly symmetric and that spectrum for the scalar dissipation $f(\alpha)$ is broader than that for energy dissipation.

Since the energy dissipation field possesses multifractal scaling properties it might be possible to determine the general class of multifractal models to which it belongs. This prompted Meneveau and Sreenivasan (1987b) to investigate a Cantor–set model of the energy cascade process. Their so–called p–model envisions that the energy cascade in a turbulent flow may be modelled by the breakdown of an eddy into two smaller eddies of the *same* size, but with energies distributed in the ratio $p_1 : p_2$. This process, *ad infinitum*, results in a Cantor–set like structure for the kinetic energy that is a multifractal. A closed form solution relates D_q to q.

$$D_q = \log_2\{p_1^q + p_2^q\}^{1/(1-q)} \tag{9}$$

Meneveau and Sreenivasan found that their data was well approximated by taking $p_1 = 1 - p_2 = 0.7$. Following their work we perform a similar analysis to see if a

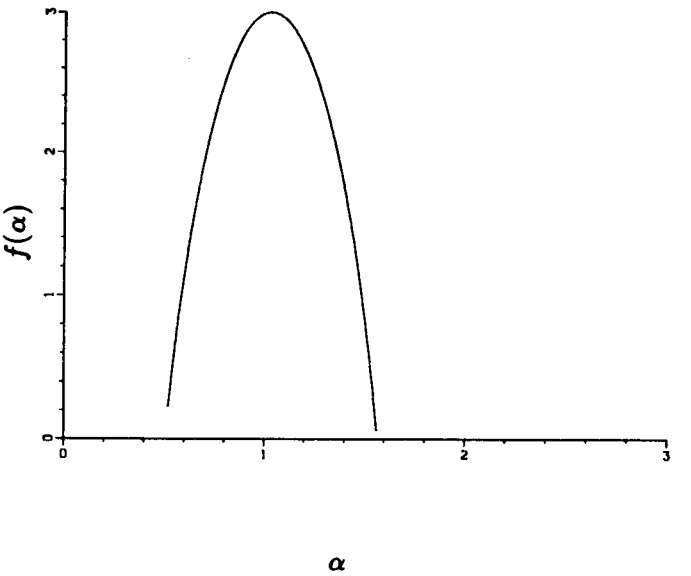

FIGURE 6. Multifractal spectra of the vorticity magnitude field, $|\omega|$.

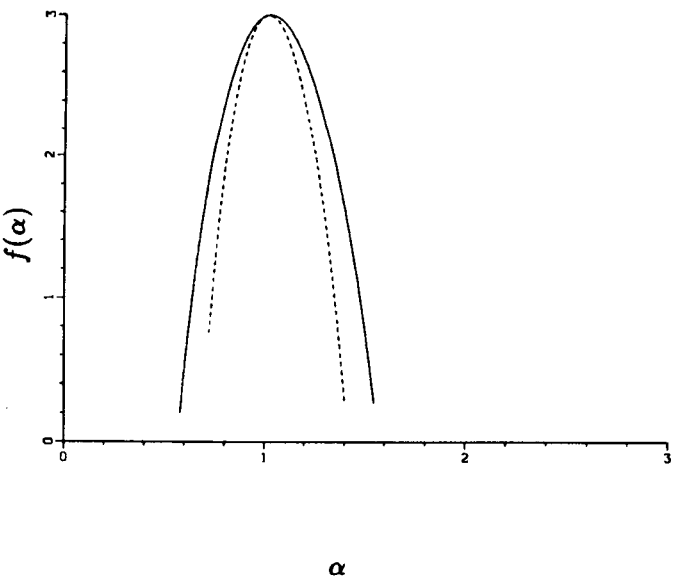

FIGURE 7. Multifractal spectra of the initial ϵ and $|\omega|$ fields. Solid line: ϵ; Dashed line: $|\omega|$.

two–scale Cantor set model fits our data. We do not find a satisfactory combination of values that fits our data even with nonequal eddies and energy partitions. The chain–dashed curve shown in Figs. 2–5 are from the p–model of Meneveau and Sreenivasan (1987b).

5. Conclusion

We have obtained first results for the multifractal spectra of several three–dimensional fields. Although these have been made for one realization of a specific flow — homogeneous shear flow — the multifractal spectra for a given field are thought to be a universal property for sufficiently high Reynolds number flows. Even though the flow we have examined is not at the asymptotically large Reynolds number where the multifractal formulation applies strictly, we find that a range of scales can be found in the flow that are self–similar. This self–similarity cannot be ascribed to the presence of an inertial range, but the multifractal model takes into account both the intermittent nature of the fields and the self–similarity in a unified way. Other available flow–fields are currently being examined in an on–going effort to understand multifractal structure in turbulent flow. The results are of value in modeling turbulent flow and energy cascade processes. Models which possess multifractal structure for the appropriate variables might more successfully predict quantities of engineering interest. Our study is a step in that direction.

We have made comparisons with results obtained from experimental studies. The conditions of the experiments differ from our conditions in three ways: the experiments are at higher Reynolds number; they use intersections of the fields; and the results represent an averaging over a number of realizations and flows. Thus, while we find broad agreement with experimental results, there are numerous differences in detail. It is not possible to ascribe the differences in the results to a particular difference in condition. However, such an evaluation will be possible with the availabilty of more data. The concurrence of experimental and numerical findings is of great importance in the justification of key assumptions made in the experiments. Conversely the analysis of intersections of flows, if justified, greatly increases the geometries and Reynolds numbers of flows which can be analysed for multifractal structure through experiments, but which are beyond practical numerical simulation.

Acknowledgments

This work was done as part of the 1988 Summer Program at the Center for Turbulence Research. AED would like to acknowledge the support and hospitality of the Center during the program. The authors gratefully acknowledge the invaluable help of Mike Rogers, who generated the data set we analyzed, and brought the data into a form usable by us. We thank him and Parvis Moin for discussions. AED would like to thank K. R. Sreenivasan and Charles Meneveau for discussions and their hospitality during visits to Yale University. They are also thanked for making their experimental data available for comparison.

References

Benzi, R., Paladin, G., Parisi, G. and Vulpiani, A., 1984, J. Phys. **A17**, 3521.

Champagne, F. H., Harris, V. G. and Corrsin, S., 1970, J. Fluid Mech. **41**, 81.

Frisch, U. and Parisi, G., 1985, in *Turbulence and Predictability in Geophysical Fluid Dynamics and Climate Dynamics*, (eds. M. Ghil, R. Benzi and G. Parisi, North–Holland, New York).

Hentschel, H. G. E. and Procaccia, I., 1983, Physica **8D**, 435.

Halsey, T. C., Jensen, M. H., Kadanoff, L. P., Procaccia, I. and Shraiman, B. I., 1986, Phys. Rev. A **33**, 1141.

Kolmogorov, A. N., 1941, C.R. Acad. Sci. USSR **30**, 301, 538.

Kolmogorov, A.N., 1962, J. Fluid Mech. **13**, 82.

Mandelbrot, B.B., 1974, J. Fluid Mech. **62**, 331.

Meneveau, C. and Sreenivasan, K. R., 1987a, Nuc. Phys. B (Proc. Suppl.) **2**.

Meneveau, C. and Sreenivasan, K. R., 1987b, Phys. Rev. Lett. **59**, 1424.

Prasad, R. R., Meneveau, C. and Sreenivasan, K. R., 1988, Phys. Rev. Lett. (to appear).

Rogallo, R.S., 1981, NASA Tech. Mem, 81315.

Rogers, M., Moin, P., and Reynolds, W., 1986, Rept. TF-25, Mech. Eng. Dept, Stanford Univ.

Rogers, M. and Moin, P., 1987, J. Fluid Mech. **176**, 33.

Rose, W. G., 1966, J. Fluid Mech. **25**, 97.

Sreenivasan, K.R. and Meneveau, C., 1986, J. Fluid Mech. **173**, 357.

Sreenivasan, K.R. and Meneveau, C., 1988, Phys. Rev. A (to appear).

Tavoularis, S. and Corrsin, S., 1981, J. Fluid Mech. **104**, 311.

Energy Transfer in Isotropic Turbulence at Low Reynolds Numbers

By J. A. Domaradzki[1], and R. S. Rogallo[2]

Detailed measurements were made of energy transfer among the scales of motion in incompressible turbulent fields at low Reynolds numbers generated by direct numerical simulation. It was observed that although the transfer resulted from triad interactions that were non-local in k space, the energy always transferred locally. The results are consistent with the notion of non-uniform advection of small weak eddies by larger and stronger ones, similar to transfer processes in the far dissipation range at high Reynolds numbers.

1. Introduction

Our goal was to analyze velocity fields generated by direct numerical simulations of homogeneous, isotropic turbulence to better understand how energy is transferred among different scales of motion in such flows. At the present time there is some controversy concerning the importance of local versus nonlocal energy transfer processes. A number of theoretical works (Deissler 1978, Kraichnan 1971, 1976, and Dannevik 1987) and one experimental work (Lii et. al. 1976) predict relatively large energy transfer between eddies of disparate sizes (nonlocal energy transfer). On the other hand the classical argument of Kolmogoroff stresses a local energy cascade as a leading cause of the universal subrange. The numerical work of Domaradzki et al. (1987), Domaradzki (1988), Brasseur and Corrsin (1987), and Kerr (1988) indicates that at low Reynolds number very little energy is transfered between distant wavenumbers; the energy transfer occurs between similar wavenumbers. The resolution of these contradictions is needed since essentially all turbulence theories and models rely on assumptions about the energy transfer and those assumptions are tested only indirectly by comparing predictions of the models with available experimental data.

2. The computed velocity fields

We have used velocity fields generated by numerical simulations initialized with three different energy spectra. All simulations were run for sufficiently long times to establish nonlinear interactions and the energy spectra decreased by at least three orders of magnitude between the energy peak and the maximum resolved

1 University of Southern California
2 NASA Ames Research Center

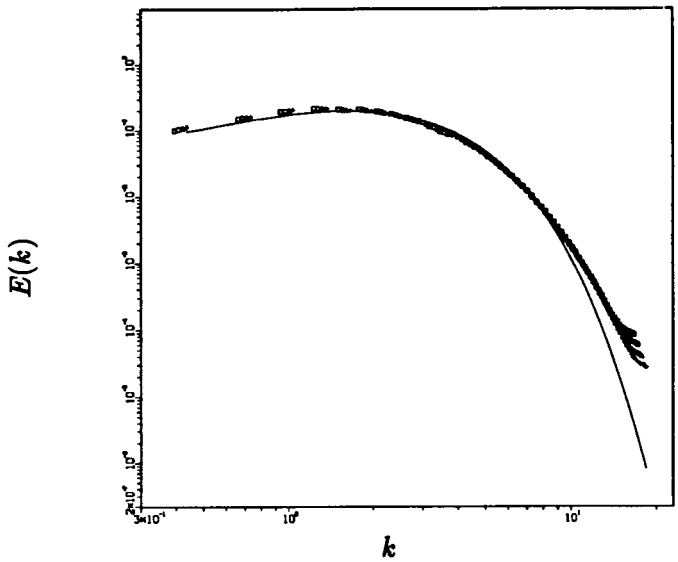

FIGURE 1. Three-dimensional energy spectra, normalized by total energy and Taylor microscale. —— data of Ling & Huang (1970), □ ○ △ + simulation I128D2 at several times.

wavenumber. The transfer spectra are well resolved and approach zero at the largest wavenumber. More detailed information about these fields is given in Table I.

The computed case I128D2D attempts to match the experimental results of Ling and Huang (1970) who found turbulence decay between microscale Reynolds numbers 30 and 3 to be self-similar. At this low Reynolds number the energy and dissipation ranges coincide, and there is only a single length scale. Use of the Taylor microscale collapses the results of the numerical simulations at different times (see figure 1) as it does the experimental data, and for this reason we consider the simulated velocity fields to be a fair model of laboratory, isotropic turbulence at low Reynolds numbers.

The case HIE24 was obtained from simulations of Lee and Reynolds (1985) that were initialized with an energy spectrum decreasing as $exp(-\alpha k^2)$ for large wavenumbers k. Such spectra are commonly used as initial conditions in direct numerical simulations of turbulence even though they decrease much faster than experimental spectra which behave as $exp(-\alpha k)$ for large wavenumbers.

The case F64DR is a result of simulations of turbulence forced in a manner suggested by Yakhot and Orszag (1986). Such forcing is used in the Renormalization Group (RNG) theory to generate a velocity field with a Kolmogoroff $k^{-5/3}$ spectrum that is stationary in time. Forcing of this type was used recently in simulations by Yakhot et al. (1988) to test numerically some predictions of the RNG theory. We were unable to obtain a significant inertial subrange in our forced simulations, the spectrum had a k^{-1} range at low wavenumber and decayed exponentially at higher wavenumbers. Nevertheless this velocity field is an important example of simulated

Table 1. Summary of computed cases

Case	N	k_{max}	k_{peak}	ν	R_λ	S
I128D2D	128^3	60.34	5	0.065	13.6	-0.44
HIE24	128^3	60.34	2	0.01377	20.4	-0.48
F64DR	64^3	30.16	1	0.1	46.0	-0.45

N = computational grid size
k_{max} = maximum resolved wavenumber
k_{peak} = location of maximum of energy spectrum
ν = molecular kinematic viscosity
R_λ = Reynolds number based on v_{rms} and Taylor microscale
S = velocity derivative skewness

turbulence that contains a range of wavenumbers k in which the energy spectrum decays algebraically. Such dependence is characteristic of high Reynolds number turbulence.

3. Basic measured quantities

The quantity of principal interest here is the energy exchange between a given mode $\mathbf{k}$ and all pairs of modes $\mathbf{p}$ and $\mathbf{q} = \mathbf{k} - \mathbf{p}$ that form a triangle with $\mathbf{k}$ as one of the legs and where $\mathbf{p}$ and $\mathbf{q}$ lie in some prescribed regions, $\mathcal{P}$ and $\mathcal{Q}$ respectively of the spectral space. For isotropic fields it is natural to choose $\mathcal{P}$ and $\mathcal{Q}$ as spherical shells $k - \frac{1}{2}\Delta k < |\mathbf{k}| < k + \frac{1}{2}\Delta k$ in the wave space with a shell thickness Δk. In addition to the velocity field $u_n(\mathbf{k})$ given on the entire Fourier mesh we define a truncated velocity field

$$u_n^{(\mathcal{PQ})}(\mathbf{k}) = \begin{cases} u_n(\mathbf{k}), & \text{if } \mathbf{k} \in \mathcal{P} \text{ or } \mathbf{k} \in \mathcal{Q}; \\ 0, & \text{otherwise.} \end{cases} \tag{1}$$

The transfer for the truncated field is then

$$T_{\mathcal{PQ}}(\mathbf{k}) = Im\{u_n^*(\mathbf{k}) P_{new}(\mathbf{k}) \int u_e^{(\mathcal{PQ})}(\mathbf{p}) u_w^{(\mathcal{PQ})}(\mathbf{k}-\mathbf{p}) d^3p\}, \tag{2}$$

where

$$P_{new}(\mathbf{k}) = k_w(\delta_{ne} - k_n k_e/k^2) + k_e(\delta_{nw} - k_n k_w/k^2), \tag{3}$$

the asterisk denotes complex conjugate, and the summation convention is assumed. We take regions $\mathcal{P}$ and $\mathcal{Q}$ to be spherical shells of radius p and q, and average over a spherical shell of radius k giving

$$T(k|p,q) = \begin{cases} 4\pi k^2 < T_{\mathcal{PQ}}(\mathbf{k}) >, & \mathcal{P} \equiv \mathcal{Q} \\ 4\pi k^2 < T_{\mathcal{PQ}}(\mathbf{k}) - T_{\mathcal{PP}}(\mathbf{k}) - T_{\mathcal{QQ}}(\mathbf{k}) >, & \mathcal{P} \not\equiv \mathcal{Q} \end{cases}$$

Here $< \ldots >$ denotes the spherical averaging over $\mathbf{k}$. Note that $T(k|p,q)$ is the transfer into band k resulting from all triads having one leg in p, one in q, and one

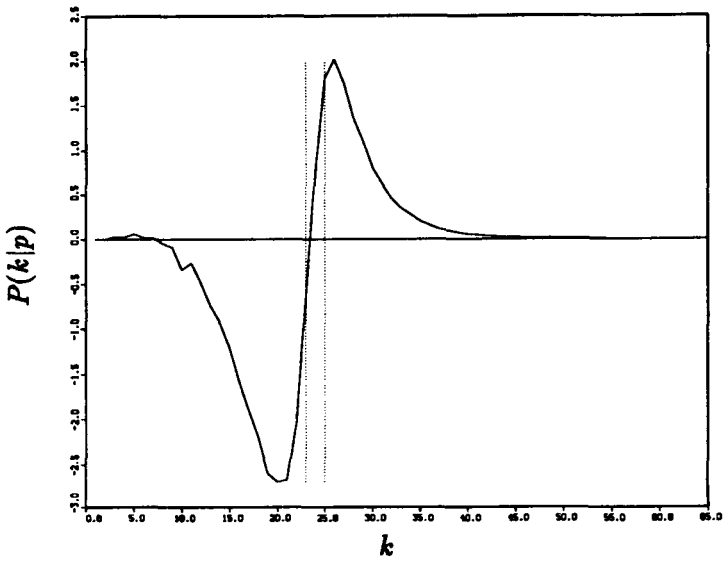

FIGURE 2. Energy transfer contributed by a single band. The total energy transferred by all triads having at least one leg in $23 < p < 25$ is shown.

in k. If the wave space is divided into distinct shells and $T(k|p,q)$ is summed over q for fixed p one obtains

$$P(k|p) = \sum_q T(k|p,q). \tag{4}$$

The function $P(k|p)$ calculated by Domaradzki (1988) by a different method was used to validate the calculations in this work. Finally, summing $P(k|p)$ over all shells p gives the total energy transfer to wavenumber k

$$T(k) = \sum_p P(k|p). \tag{5}$$

Functions $T(k), P(k|p)$, and $T(k|p,q)$ give progressively more detailed information about the energy transfer between different scales of motion.

4. Analysis of the function $P(k|p)$

Deissler (1978) estimated the energy transfer function $P(k|p)$ from the experimental data of Ling and Huang (1970) and concluded that their experimental data supports the notion of nonlocal energy transfer. Specifically, the calculated function $P(k|p)$ indicated that a wavenumber band k loses most of its energy to a band at wavenumber p that is about an order of magnitude greater than k.

In view of our results we believe that Deissler's analysis is in error. As Deissler points out, it is not possible to solve (5) uniquely for $P(k|p)$ because any function having zero sum may be added to the solution. Our measured function $P(k|p)$, for the same conditions as in figure 2a of Deissler, is shown in our figure 2 with

wavenumber band p indicated by the two dotted vertical lines. The peaks in the transfer are close to this band $23 < p < 25$ indicating that the energy is transferred among wavenumbers k that are comparable to p, and moreover, energy is transfered from smaller to larger wavenumbers i.e. from larger to smaller scales of motion. In figure 2 the function $P(k|p)$ is negligible for k outside the interval $\frac{1}{2}p < k < 2p$, and we conclude that most of the energy is transfered between modes with wavenumber ratios not exceeding two.

The shape of the function $P(k|p)$ for a fixed p shown in figure 2 is typical for all values of p beyond the energy peak and for all velocity fields considered in our work. When the wavenumber band p is near the peak of the energy spectrum the function $P(k|p)$ still has two peaks for k close to the band p but they are broader, and values of $P(k|p)$ for $k > 2p$ are significant.

The function $P(k|p)$ does not provide information about the third leg of the wavevector triad, two legs of which have lengths k and p respectively. That information is provided by the function $T(k|p,q)$.

5. Analysis of the function $T(k|p,q)$

For the velocity field I128D2D we have divided Fourier space into 13 spherical shells of thickness $\Delta k = 5$. In figure 3a we show the decomposition of the function $P(k|p)$ into functions $T(k|p,q)$ for p fixed in the wavenumber band $35 < p < 40$. The solid line represents $P(k|p)$ and the lines with symbols represent the individual contributions $T(k|p,q)$ of wavenumber bands q to the sum (4). Even though there is a total of thirteen bands q in the sum (4), only three or four contribute significantly. Those with the largest contributions are wavenumbers $q < 15$.

The total transfer $P(k|p)$ is mostly local since the peaks in the curve $P(k|p)$ are in the vicinity of the prescribed band p. Therefore, as explained in the previous section, the energy is transfered between two wavenumbers k of comparable magnitude to p, in this case $30 < k < 45$ and $35 < p < 40$. However, the decomposition (4) indicates that of all the triangles satisfying this condition only triangles with a *significantly smaller* third leg $q < 15$ contribute to the transfer. Similar behaviour was observed for other velocity fields considered in this work. The transfer curves for case HIE24 shown in figure 3b and for case F64DR shown in figure 4 exhibit the same qualitative behaviour as those in figure 3a. In all cases the transferring triads had a leg near the peak of the energy spectrum.

We conclude from this analysis that at low Reynolds numbers the *local energy transfer* between similar wavenumbers located beyond the energy containing range is due to *nonlocal wavevector triads* that have one leg much shorter than the other two.

It is interesting to note in the figures 3 and 4 that the effect of such nonlocal interactions on the smallest leg of the triad (large scale) is a small increase in its energy as represented by the positive values for $k < 15$ (figure 3), and for $k < 7$ (figure 4). This means that small (and less energetic) scales of motion transfer a small amount of energy to large (and more energetic) scales. This is a surprising result since the generally accepted models of energy transfer in turbulence assume

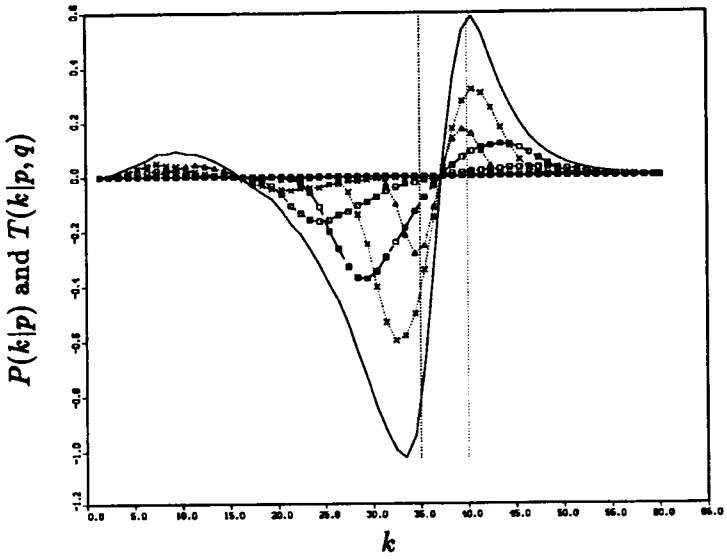

(a)

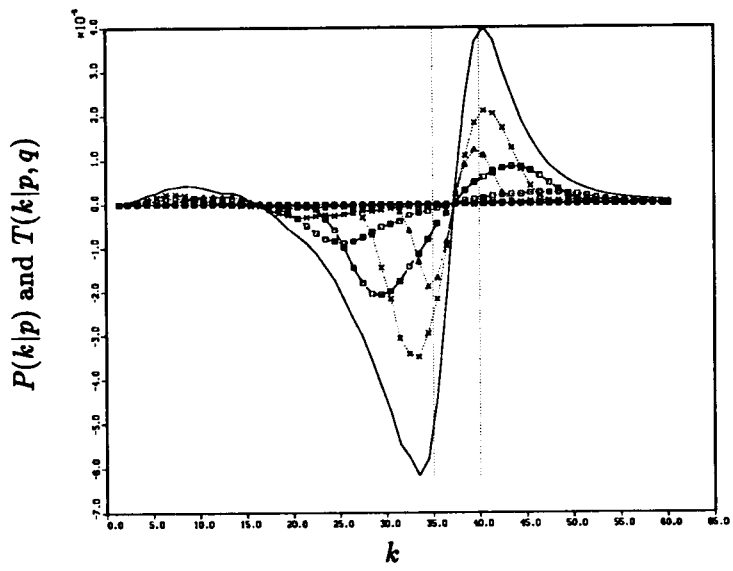

(b)

FIGURE 3. Detailed triad contributions to energy transfer: (a) case I128D2D, (b) case HIE24. The transfer spectra $T(k|p,q)$ are shown for band $35 < p < 40$, and all bands q that make a significant contribution to $P(k|p)$. $\triangle$ ····· $0 < q < 5$, $\times$····· $5 < q < 10$, $\square$ — — — $10 < q < 15$, $\square$ - - - - $15 < q < 20$, $\times$ — · — $20 < q < 25$, $\triangle$ — · — $25 < q < 30$, $\times$ - - - - $30 < q < 35$, ——— $P(k|p)$.

that energy is transferred from large to small scales by nonlocal interactions i.e. one small wavenumber transfering large amounts of energy to two large wavenumbers,

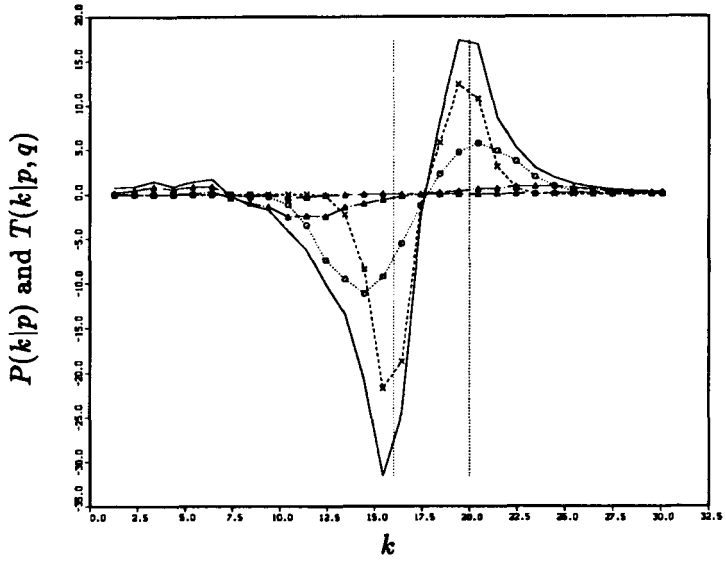

FIGURE 4. Detailed triad contributions to energy transfer for case F64DR. The transfer spectra $T(k|p,q)$ are shown for band $16 < p < 20$, and all bands q that make a significant contribution to $P(k|p)$. ×---- $0 < q < 4$, o ····· $4 < q < 8$, △ —·— $8 < q < 12$, —— $P(k,p)$.

and that eddy viscosity concepts provide an appropriate model.

6. Linear theory

The behavior, at high Reynolds numbers, of the turbulent energy spectrum in the far dissipation range, and the scalar spectrum in the viscous-convection range at high Prandtl number, have been predicted using assumptions about the structure of the velocity field at scales smaller than the Kolmogorov length. See Monin & Yaglom (1975), and the works cited there. The velocity field is assumed to contain small material regions, intermittent in space, in which the strain rate is high and spatially uniform. In addition to the assumption of disparate space scales, the time scales must also be assumed disparate to linearize the equation for vorticity. With these assumptions, the problem becomes a simple convection and decay problem in wave space with a spatially linear velocity field, and the general solution can be written explicitly (Saffman 1963). The interaction between scales is explicitly non-local with the larger scales, given by the Kolmogorov length, straining the smaller scales of the far dissipation range. Batchelor (1958) assumes the strain rates are constant in time, but Kraichnan (1968) points out that a rapidly varying strain rate would alter the solution significantly at high wavenumber.

We propose a similar situation at low Reynolds number, where the straining scales are again the dissipation scales, but now the energy and dissipation ranges are one and the same. It still seems reasonable to consider the interaction of disparate length and time scales and to linearize the vorticity equation, and we are led to the same

convection-decay equation in wave space encountered by Batchelor and Kraichnan at high Reynolds numbers. However, we can no longer assume that dissipation (straining) occurs in distinct material regions, intermittent in space and constant in time, and we must account for the energy decay and the increasing length and time scales of the straining scales. Therefore it seems natural to consider the unsteady initial-value problem of Kraichnan rather than the steady boundary-value problem of Batchelor. Kraichnan's approach leads to an energy spectrum with a $exp(-\alpha k)$ form at high wavenumber that is closer to the experimental measurements of Ling & Huang (1970) than is the $exp(-\alpha k^2)$ form predicted by Batchelor.

7. Conclusions

The major conclusion from this work is that the energy transfer in low Reynolds number turbulence is due to triad interactions that involve one short and two long legs of comparable lengths.

The energy is transfered mainly between the pair of large wavenumbers i.e. between comparable small scales, with one small eddy losing energy to a somewhat smaller one. In that sense the energy transfer is predominantly *local* since the eddies exchanging energy are of similar size. However, the triads responsible for such transfer are *nonlocal* since in addition to two small scales, one large scale of motion (small wavenumber) is involved.

Interactions of this type seem to be inconsistent with the older as well as modern (RNG) concepts of eddy viscosity that postulate nonlocal interactions moving energy from one large scale to two small ones. In that context it is important to distinguish between local (nonlocal) *energy transfer* and local (nonlocal) *triad interactions*. Energy transfer is often implicitly assumed to involve only two scales of motion: if they are similar,the transfer is local, if they are disparate the transfer is nonlocal. Triad interactions are local if all three legs of the triad are of comparable lengths and nonlocal if one of the legs is much shorter than the other two. With this distinction the eddy viscosity notion is based on the assumption that both the energy transfer and the triad interactions are nonlocal. The results of our work point toward *local energy transfer* that is caused by *nonlocal triad interactions*.

It seems possible that this transfer process can be described by a linear theory similiar to that of the far dissipation range at high Reynolds numbers, but first it is necessary to inquire in more detail about the space-time structure of the dissipation scales.

REFERENCES

BATCHELOR, G.K. 1958, *J. Fluid Mech.*, **5**, 113.

BRASSEUR, J.G., & CORRSIN, S. 1987, in *Advances in Turbulence*, Springer-Verlag, Berlin p.152.

DANNEVIK, W.P., YAKHOT, V., & ORSZAG, S.A. 1987, *Phys. Fluids*, **30**, 2021.

DEISSLER, R.G. 1978, *Appl. Sci. Res.*, **34**, 379.

DOMARADZKI, J.A., METCALFE, R.W., ROGALLO, R.S. & RILEY, J.J. 1987, *Phys. Rev. Lett.*, **58**, 547.

DOMARADZKI, J.A. 1988, to appear in*Phys. Fluids*, Oct. 1988.

KERR, R.M. 1988, submitted to *J. Fluid Mech.*.

KRAICHNAN, R.H. 1968, *Phys. Fluids.*, **11**, 945.

KRAICHNAN, R.H. 1971, *J. Fluid Mech.*, **47**, 525.

KRAICHNAN, R.H. 1976, *J. Atmos. Sci.*, **33**, 1521.

LEE, M.J. & REYNOLDS, W.C. 1985, *Report No. TF-24, Dept. of Mech. Eng., Stanford University.*

LII, K.S., ROSENBLATT, M. & VAN ATTA, C. 1976, *J. Fluid Mech.*, **77**, 45.

LING, S.C. & HUANG, T.T. 1970, *Phys. Fluids*, **13**, 2912.

MONIN, A.S. & YAGLOM, A.M. 1975, *Statistical Fluid Mechanics: Mechanics of Turbulence*, Vol. 2. The MIT Press.

SAFFMAN, P.G. 1963, *J. Fluid Mech.*, **16**, 545.

YAKHOT, V. & ORSZAG, S.A. 1986, *J. Sci. Comput.*, **1**, 3.

YAKHOT, V., ORSZAG, S.A. & PANDA, R. 1988, to appear*J. Sci. Comp.*.

Center for Turbulence Research
Proceedings of the Summer Program 1988

Turbulence characteristics inside a turbulent spot in plane Poiseuille flow

By D.S. Henningson[1], J. Kim[2], & P. H. Alfredsson[3]

1. Introduction

In wall-bounded shear flows the transition to turbulence through localized disturbances goes through a pattern starting with a development of shear layers. The localized normal velocity fluctuations induce normal vorticity through the lift-up effect (Gustavsson, 1978; Henningson, 1988; Landahl, 1975). These shear layers become unstable to secondary disturbances (Breuer, 1988), and if the amplitudes of the disturbances are large enough, a turbulent spot develops (Chambers & Thomas, 1983). The spot develops in approximately a self-similar manner with an average spreading angle of about 10° for most wall-bounded shear flows (Riley & Gad-el-Hak,1985). In plane Poiseuille flow spanwise wingtips of a spot consist of large-amplitude wave packets that breakdown as they propagate into the spot. The breakdown of the wave packets has been observed both in experiments (Henningson & Alfredsson, 1987) and in a numerical simulation (Henningson et al.,1987). The experiments have shown that the wave packets consist of the least stable Tollmien-Schlichting (T-S) mode. Analysis of the simulation data using kinematic wave theory has also shown that the wave breakdown is closely related to the spot spreading (Henningson,1988).

Investigations of the spot in boundary layers has shown that the turbulent part of the spot is very similar to fully-developed boundary layer. Wygnanski et al. (1976) showed that the mean profile at the center-symmetry plane has a logarithmic region and Johansson et al. (1987) showed that both the higher-order statistics and flow structures in the spot were the same as in the corresponding fully-developed flow. The aim of the present investigation is to study in what respects the turbulence inside the Poiseuille spot is similar to fully developed turbulent channel flow. The numerically simulated spot (Henningson et al. 1987) will be used in the present investigation, where the characteristics inside the spot will be compared to those of the wave packet in the wingtip area. A recent experimental investigation of the velocity field associated with the Poiseuille spot by Klingmann et al. (1988) will be used for comparison.

2. Eduction of Mean Velocity

1 Massachusetts Institute of Technology
2 NASA Ames Research Center
3 Royal Institute of Technology

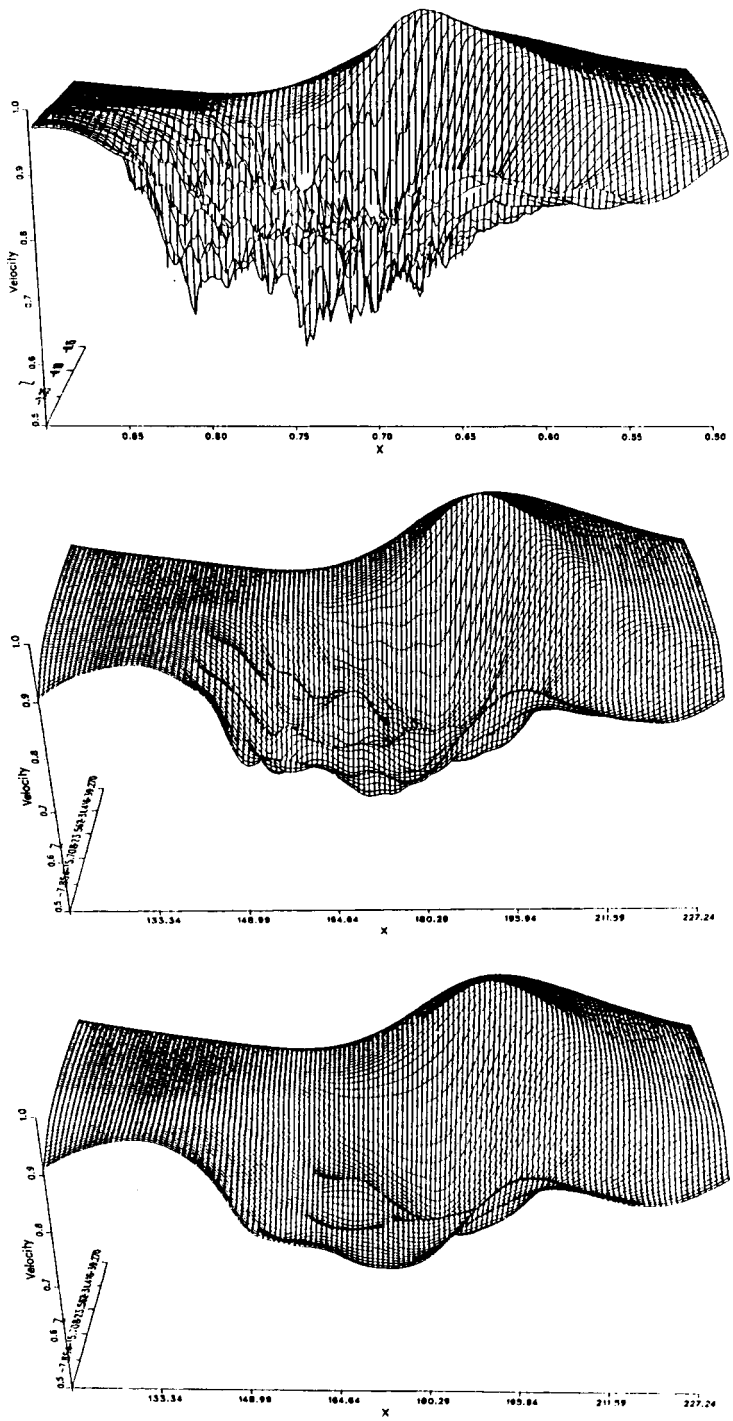

FIGURE 1. Surfaces of streamwise mean velocity at the centerline, a) conical averaging, b) and c) Gaussian filters with different filter widths at t=258. Note that only half the spot is shown.

The numerical simulation of a turbulent spot in plane channel was performed at Reynolds number of 1500 based on the centerline velocity (U_c) and the channel half-width (h). The reader is referred to Henningson et al. (1987) for details regarding the simulation. Because of its enormous cost of computation, no attempt was made to run several cases to obtain ensemble-averaged statistics. In order to compare the simulation results from this single realization to the ensemble-averaged results obtained from experiments, a mean velocity has to be defined. Analysis of the fluctuating components also requires a well defined mean. Since the spot is approximately self similar, a conical averaging procedure was tried first. One hundred and twenty velocity fields between $t = 222$ and $t = 258$ were interpolated into a conical coordinate system and added together. The horizontal conical coordinates were defined as $\xi = x/t$ and $\zeta = z/t$. The mean velocity obtained from this procedure was not smooth enough to be regarded as a mean as shown in Fig. 1a, where the surface representing the streamwise velocity at the centerline ($y = 0$) is plotted. The conical average of the normal velocity revealed more small-scale structures that survived the averaging process. Spatial averaging was also tried using Gaussian filters. Figures 1b and 1c show the results obtained by using two different filter widths. The Gaussian-filtered velocity field shown in Fig. 1c was chosen to represent the mean because the velocity fluctuations from the other two averages were judged to be too large in the turbulent area of the spot. The problem with a fairly wide Gaussian-filter function (in physical space) is that sharp gradients in the mean flow are smoothed out as well when the small scales are removed. This was observed at the transition region where sharp gradients exist.

The ensemble-averaged results from Klingmann et al. (1988) and those obtained from the procedure mentioned above are shown in Figs. 2 and 3, respectively. Agreement between the two results are remarkable: the sharp transition region with the dip in the velocity, the arrow head front part of the disturbance, and the speed-up of the laminar fluid around the spot. One may conclude from this comparison that the spatial average can reasonably well represent the true ensemble average. The spanwise mean velocity at the centerline is shown in Fig. 3c. Most of the fluid inside the spot can be seen to move outward while the laminar fluid in the front and back of the spot is directed towards the spanwise symmetry line, $z = 0$.

The fluctuating components can be defined as the full simulated velocities with the spatially averaged mean subtracted. Fig. 4 shows contours of streamwise and normal components. In Fig. 4a, we notice an artificial oblique structure at the spanwise wingtip of the spot, resulting from too much smoothing in the sharp gradient between the laminar and turbulent part. The streamwise fluctuating component closer to the wall is shown in Fig. 4b. The long streaky structure typical of near-wall turbulent flows can be seen inside the spot. The wingtip wave packet is discernible at this position, but it can be more clearly seen in the normal velocity at the centerline as shown in Fig. 4c.

The rms fluctuations are also computed from the fluctuating components. Contours of the rms fluctuation of streamwise velocity at the centerline are shown in

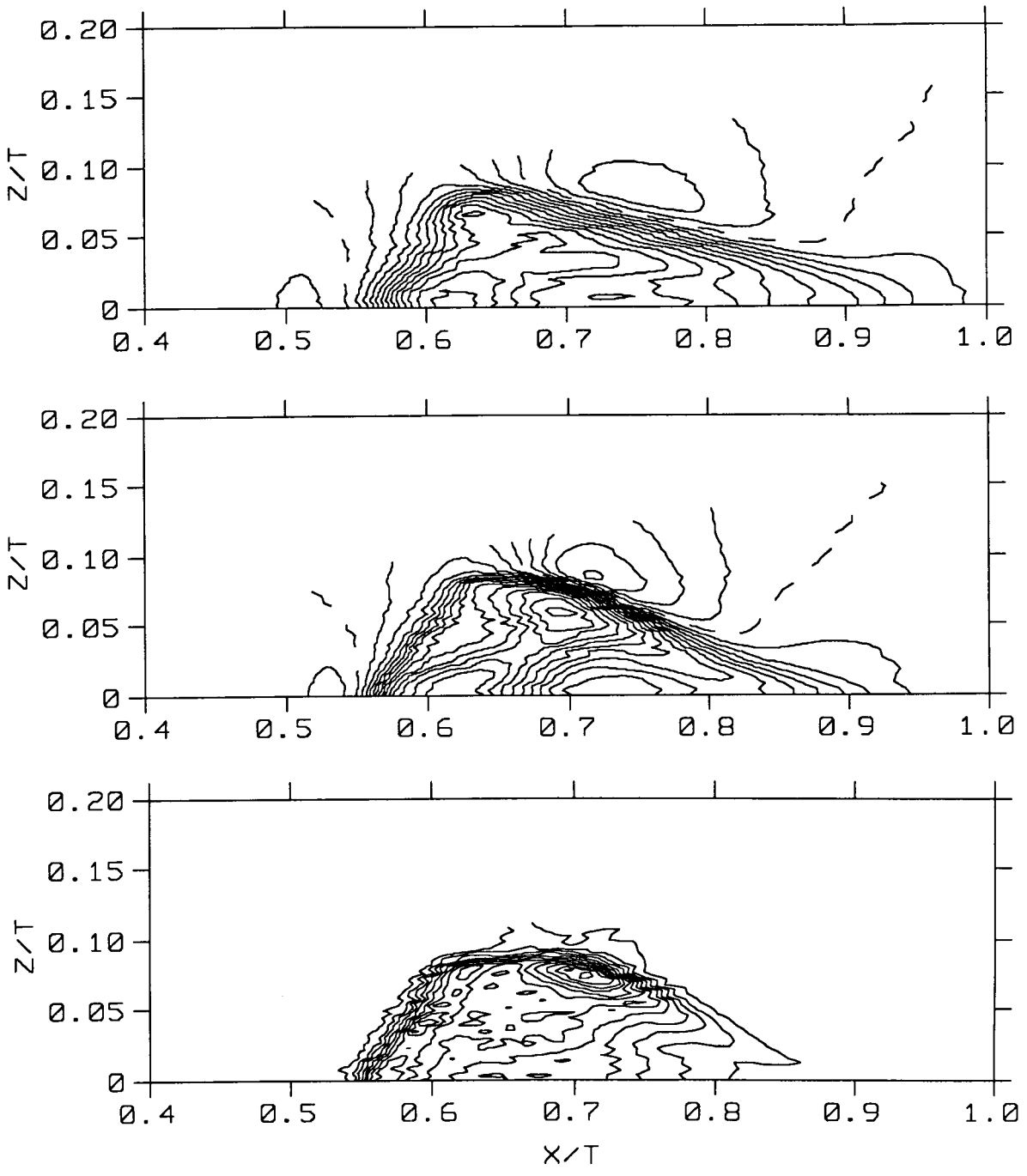

at the centerline (in conical coordinates), a) mean velocity measured at $x = 100$, b) mean velocity measured at $x = 200$, c) rms velocity measured at $x = 200$. Contour spacing is 0.02 in a) and b) and 0.01 in c).

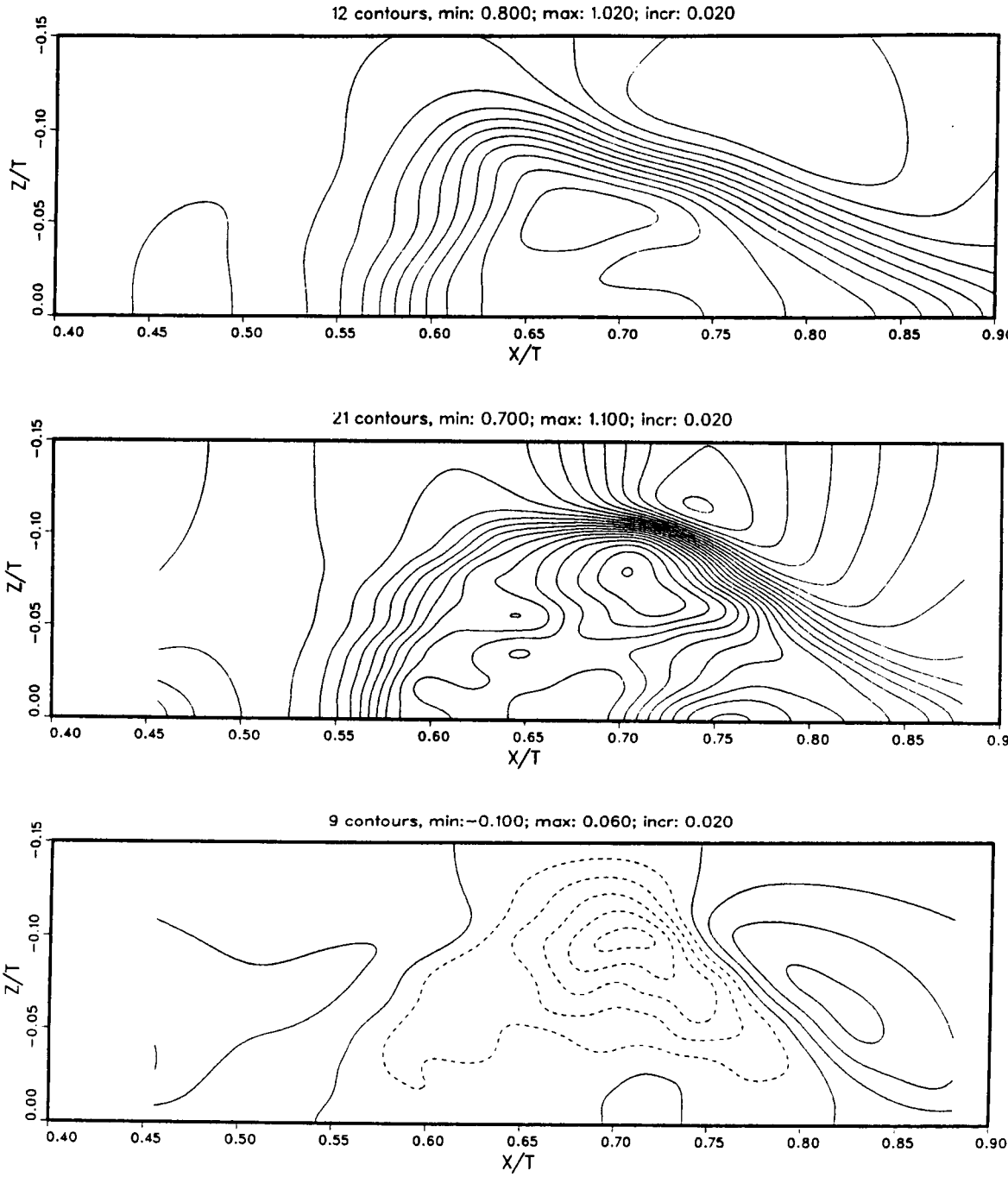

FIGURE 3. Contours of mean Gaussian filtered velocity at centerline, a) streamwise velocity for $t = 138$, b) streamwise velocity for $t = 258$, c) spanwise velocity for $t = 258$.

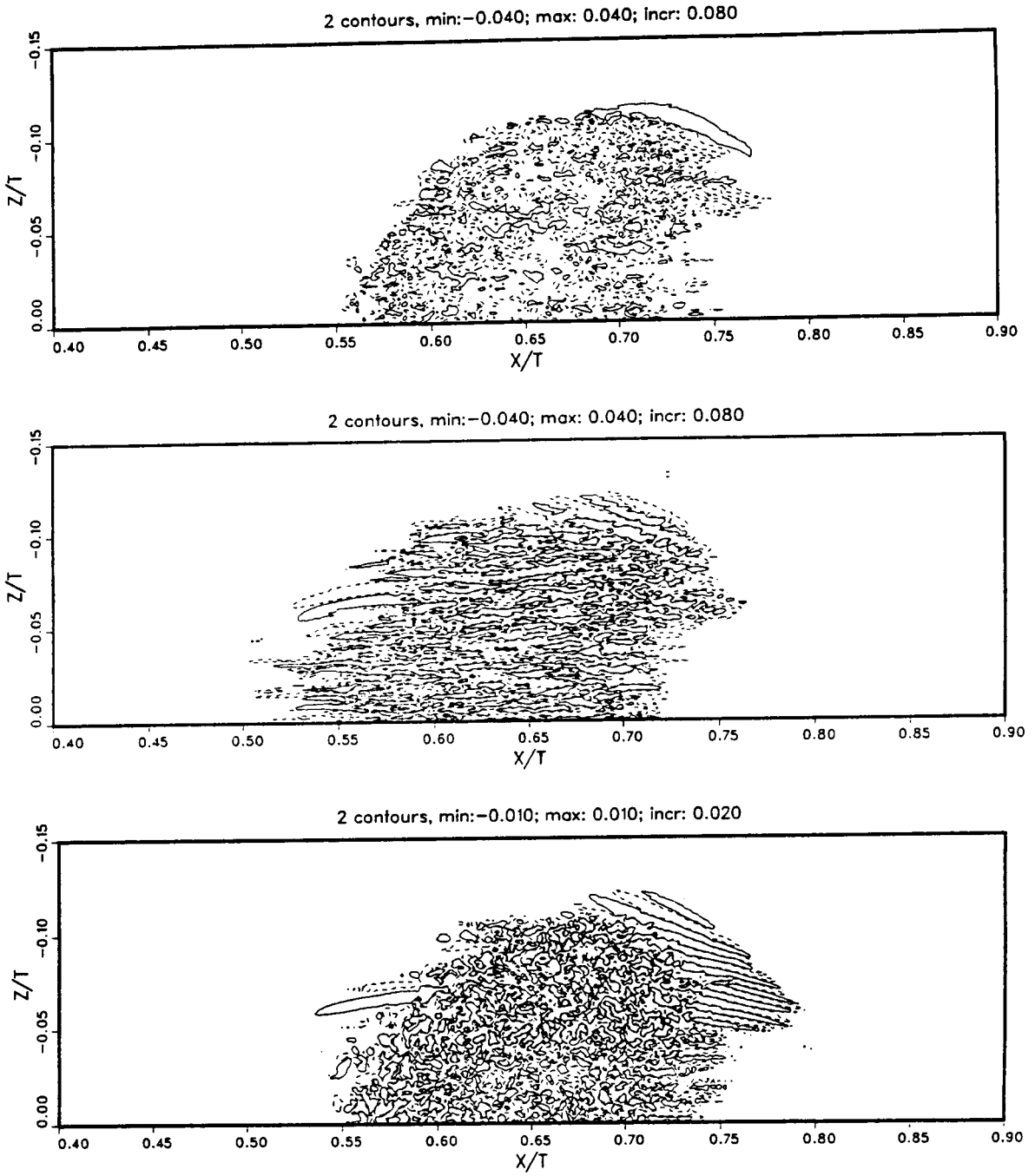

FIGURE 4. Contours of disturbance velocities for $t = 258$, a) streamwise velocity at $y = 0$, b) streamwise velocity at $y = -0.83$, c) normal velocity at $y = 0$. Dashed lines in this and following figures indicate negative contour levels unless stated otherwise.

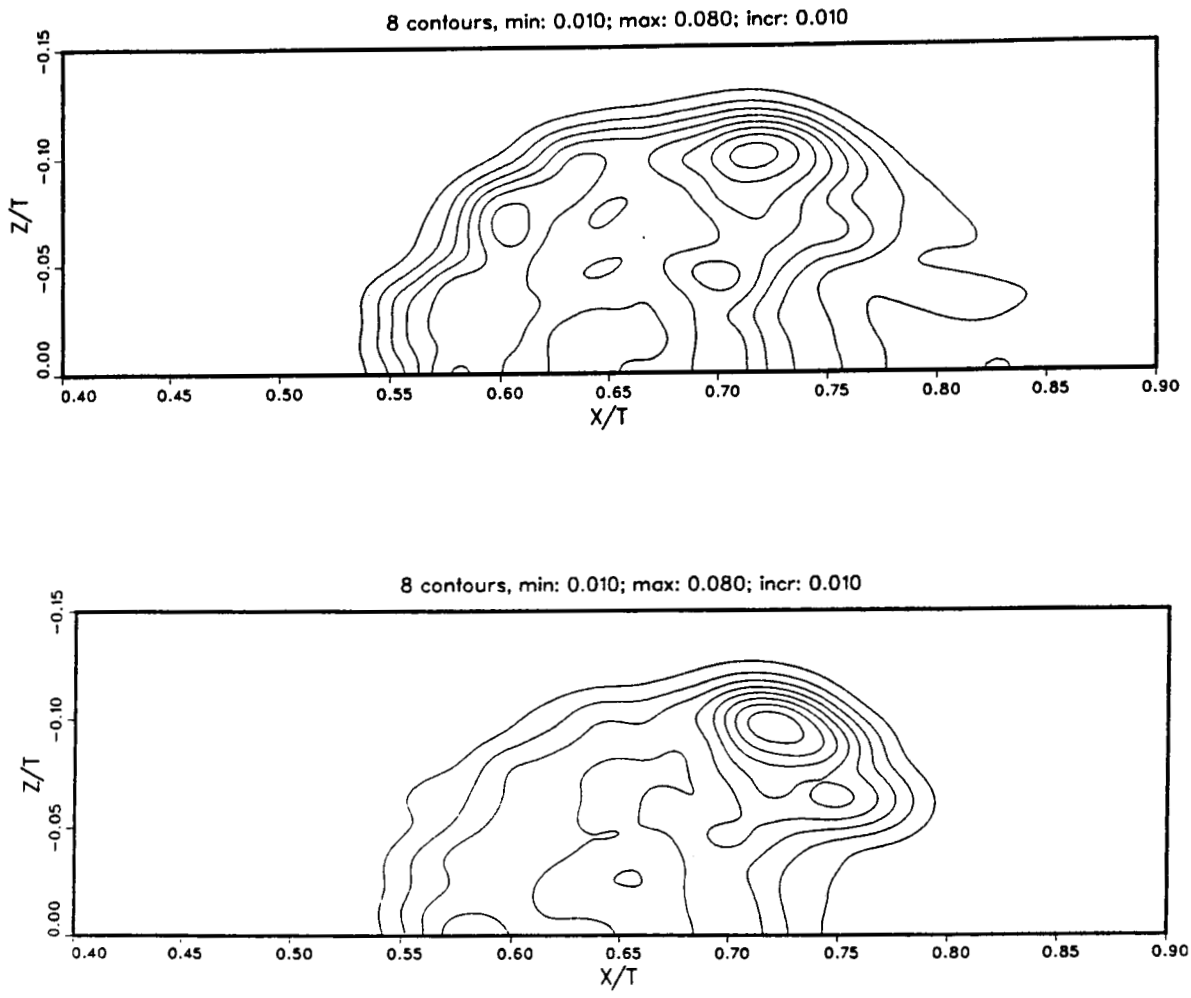

FIGURE 5. Contours of rms velocities for $t = 258$ at $y = 0$, a) streamwise and b) normal velocities.

Fig. 5a. It increases substantially high inside the turbulent part. The corresponding rms fluctuation obtained from experiments by Klingmann et al. is shown in Fig. 2c. They are in good agreement with each other, including the small peak in the wingtip region. This indicates that the peak is not due to the excess disturbance velocity induced by the Gaussian smoothing of the sharp transition gradient. The rms fluctuation of normal velocity at the the centerline is shown in Fig. 5b. It is also substantially larger in the turbulent area, but it rises to twice that value in the spanwise wave region. This is a consequence of the high amplitude T-S waves present at the wingtip.

3. Comparison with fully-developed turbulent channel flow

In order to compare turbulence characteristics inside the spot with those in fully developed channel flow turbulence, one would like to scale the flow variables with

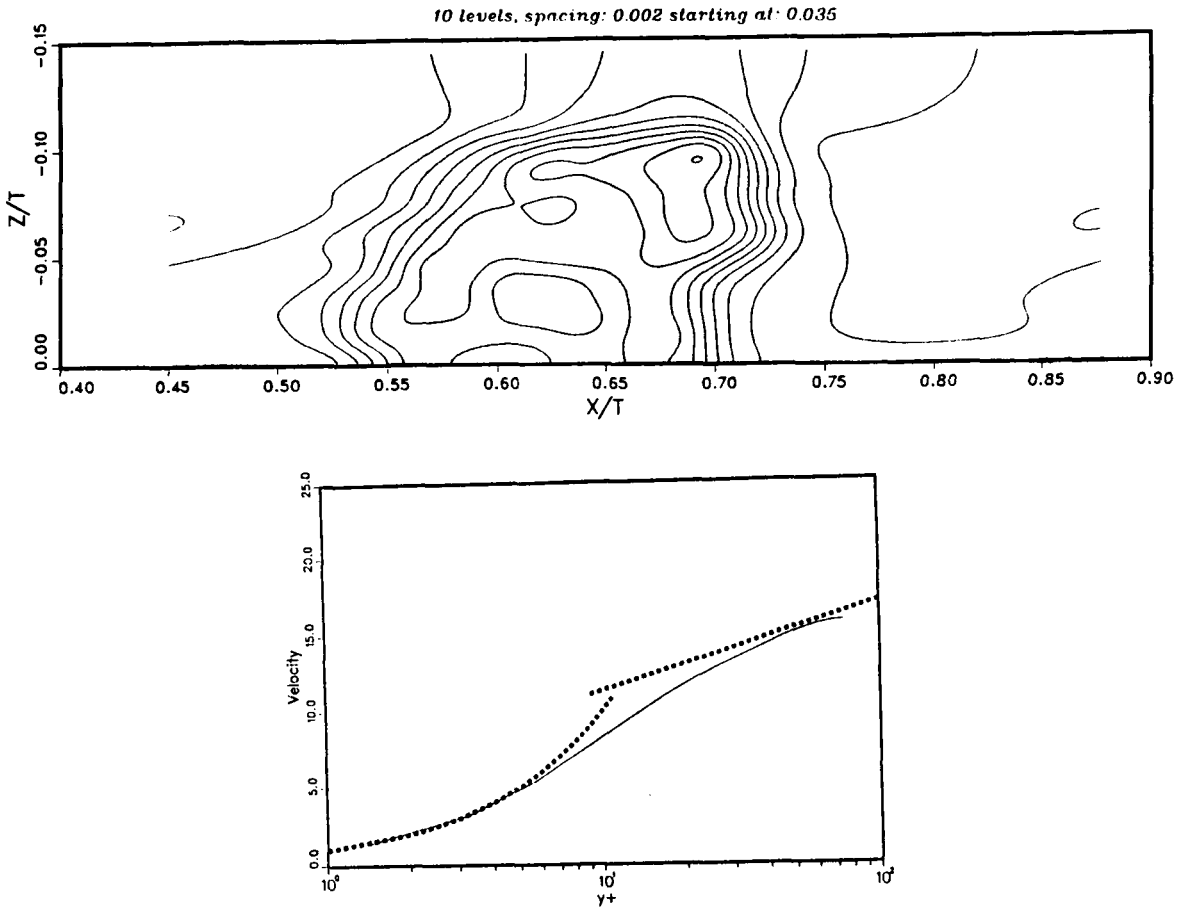

FIGURE 6. a) Contours of u_τ at lower channel wall, b) mean velocity in the lower channel half averaged over the turbulent area compared with the law of the wall and the log-law. Dashed curves are $u^+ = y^+$ and $u^+ = 2.5 \ln y^+ + 5.5$.

the inner-wall scaling, i.e., with the friction velocity $u_\tau^* = \sqrt{\nu dU/dy|_{wall}}$ and the kinematic viscosity ν. Contours of $u_\tau = u_\tau^*/U_{CL}$ are shown in Fig. 6a. A mean value of u_τ inside the spot was obtained by averaging it in the area $0.58 < \xi < 0.70$ and $-0.08 < \zeta < 0.0$ to yield about 0.05. (The above designated area will in the following be referred to as the turbulent area). The y-dependence of the mean streamwise velocity in the turbulent area is shown in Fig. 6b. The dotted curve is $u^+ = y^+$ and the line $u^+ = 2.5ln(y^+) + 5.5$, where the superscript $^+$ denotes a quantity scaled by the inner-wall scaling. The log-region is very small since the Reynolds number is low ($Re_\tau = u_\tau h/\nu \approx 70$). Considering the low Reynolds number the shape is in good agreement with other simulation and experimental results (Kim et al.,1987). The y-dependence of the rms values of three velocity components averaged over the turbulent area are shown in Fig. 7a. They are in good agreement with those corresponding to the fully-developed turbulent channel flow, except that the peak in the streamwise velocity close to the wall appears to

be a bit low. To contrast the findings in the turbulent area, a wave area is defined as $0.70 < \xi < 0.74$ and $-0.12 < \zeta < -0.08$. The y-dependence of the rms values in the wave area is shown in Fig. 7b. All of the fluctuating components are larger in the wave area, and the normal velocity has a different shape, which is somewhat similar to the mode shape of the least stable T-S wave. The Reynolds shear stress both in the turbulent and the wave area is shown in Fig. 7c. In the turbulent area it shows the behavior expected from a fully developed channel flow; in the wave area it is substantially higher, indicating higher turbulence production.

Another characteristic of wall-bounded turbulent shear flows is the sharp shear-layer structures found in the near-wall region. In order to examine the structure of the shear layers, the VISA (Variable-Time Space-Average) technique was used to detect them. This technique has been used by Kim (1985) and Johansson, Alfredsson & Kim (1987) to detect the shear layers in fully-developed turbulent channel flow. Islands of high variance of streamwise velocity were identified for a given flow field, and an ensemble average was obtained by aligning the maximum local variance in the islands for every individual event detected. The results obtained from this procedure is given in Figs. 8 and 9. They appear to be in good agreement with those obtained from the full turbulent simulation. Figures 8a and 8b show the typical inclined shear-layer structure associated with the lift-up of low speed fluid in the downstream and the downward sweep in the upstream. The spanwise structure of the shear layer is shown in Fig. 8c. The spanwise distance between the outer loops is slightly above 100 viscous units, indicating that the average spacing between the low- and high-speed streaks are captured correctly (Kim et al.,1987). The ensemble average of the shear-layer structure in the wave area shows a similar behavior in the normal plane (Fig. 9a), but the horizontal structure clearly reflects the wave-like characteristics (Fig. 9b). The oblique character of the waves can be seen, and more importantly a structure of peaks and valleys in the cross wave direction. This is typical of the secondary breakdown seen in vibrating-ribbon experiments, (Klebanoff et al., 1962; Nishioka et al., 1976). This supports the idea that the secondary instability is responsible for the breakdown of the large-amplitude waves and the subsequent rapid transition to turbulence.

4. Summary and discussion

Using a horizontal Gaussian-filter function a mean and fluctuating components were computed from instantaneous velocity fields obtained from a single realization. The streamwise component of the mean was in good agreement with the ensemble-averaged velocity field obtained from the experiments by Klingmann et al. (1988). The contours of streamwise rms fluctuation also showed a good agreement between the experimental and simulated results.

In the turbulent part of the spot the velocity field was very similar to that of fully-developed turbulent channel flow. The mean velocity and the rms fluctuations as well as the Reynolds shear-stress profiles all showed good agreements. The shear-layer structure obtained from the VISA technique also revealed similar behavior, indicating that the turbulence inside the spot behaves as if it were a fully-developed turbulent channel flow.

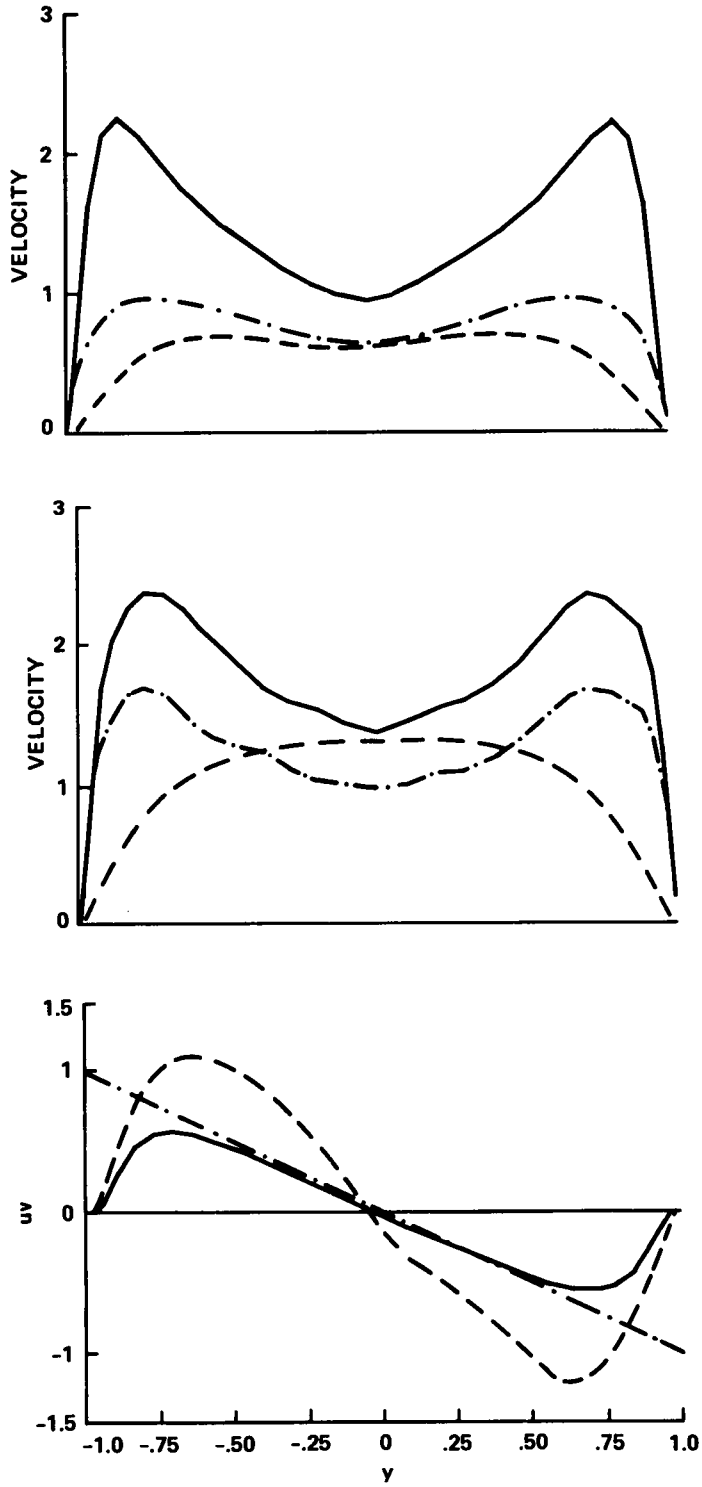

FIGURE 7. a) Rms velocities averged over the turbulent part, b) rms velocities averaged over the wave area (rms velocities are scaled with mean u_τ^* from the turbulent area: ——— , u_{rms}; - - - - , v_{rms}; ····· , w_{rms}. c) ——— , Reynolds shear stress in turbulent area; - - - - , wave area; ····· , $uv = -y$.

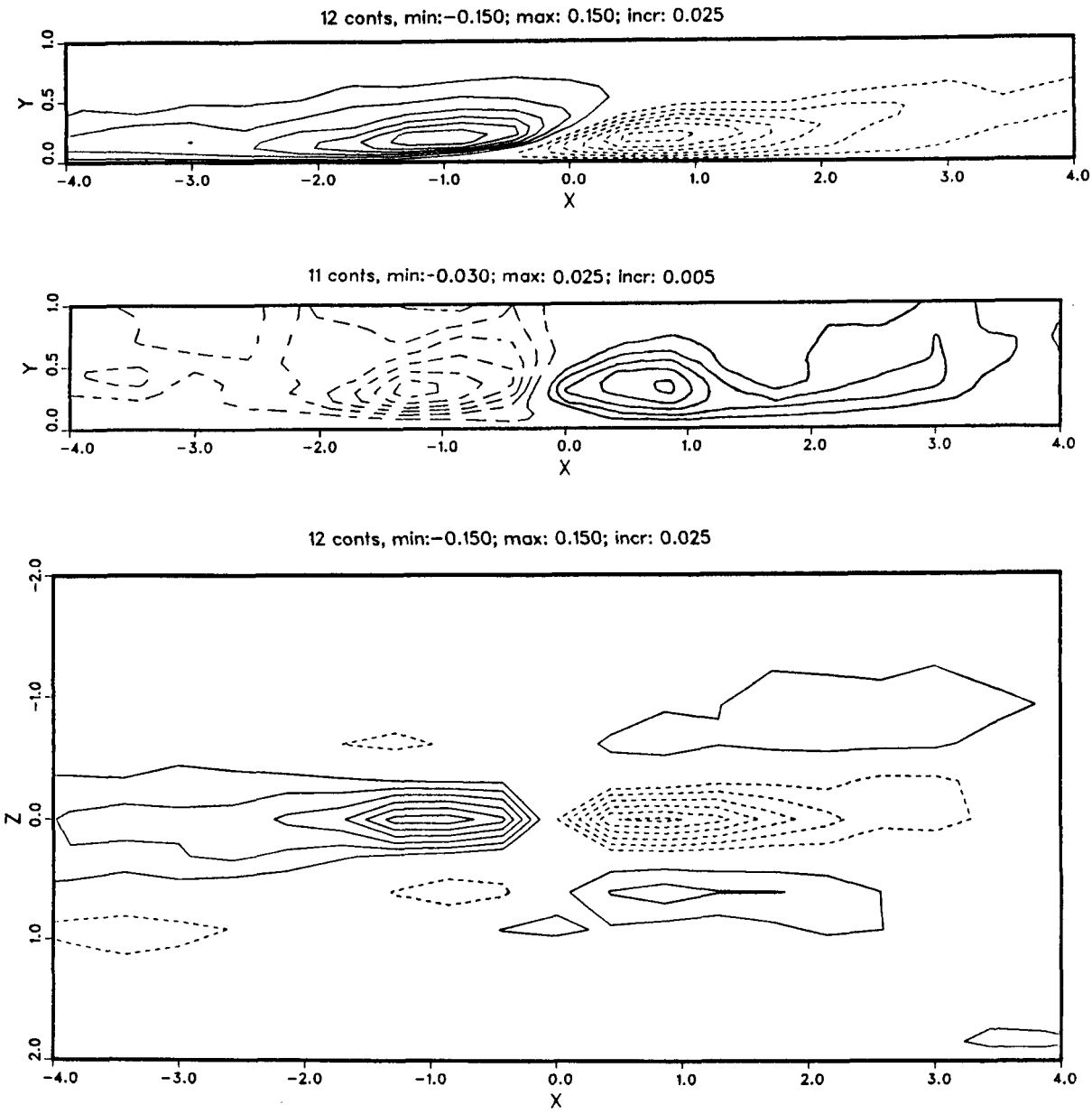

FIGURE 8. Contours of conditionally averaged velocities: a) streamwise velocity in the xy-plane along the center of the shear layer; b) normal velocity in the xy-plane; c) streamwise velocity in the xz-plane at $y = 0.22$. Note that y is measured from the bottom of the channel, and the tick marks denote 70 wall units.

The results from the wave area were somewhat different. The fluctuating components were larger, and the profile of rms fluctuations indicated the typical shape of the least stable T-S wave profile. The Reynolds stress was much higher in the wave area than inside the turbulent part, indicating high turbulence production in the

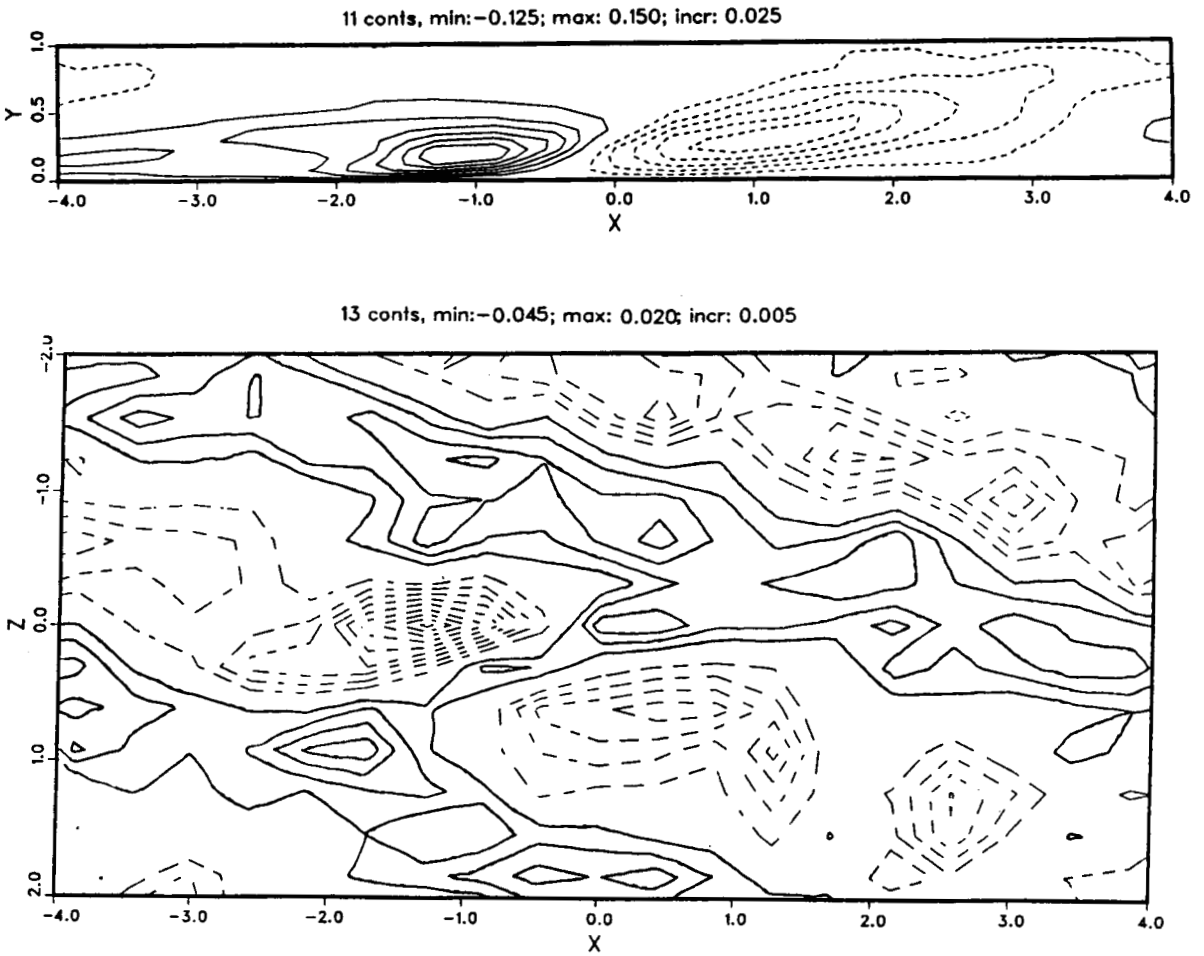

FIGURE 9. Contours of conditionally averaged velocities: a) streamwise velocity in the xy-plane; b) normal velocity in the xy-plane; c) streamwise velocity in the xz-plane at $y = 0.22$.

wave area. This is a property in common to T-S wave transition, and has been observed both in experiments (Klebanoff et al.,1962) and simulation (Gilbert,1988). The appearance of shear layers in the wave area is also typical of the T-S wave transition. The small-scale structure in the cross wave direction captured by the conditional averaging procedure is typical of secondary instability associated with T-S wave breakdown. Thus the transition from laminar to turbulent flow seems to follow a similar pattern in the wingtip area of the spot as in the 2D vibrating ribbon experiments.

Acknowledgment

We would like to thank Arne Johansson for many fruitful discussions.

REFERENCES

BREUER, K. S. 1988 The development of a localized disturbance in a boundary layer. FDRL Report No. 88-1, Dept. Aero. & Astro., MIT

CHAMBERS, F. W. & THOMAS, A.S.W. 1983 Turbulent spots, wave packets and growth.. *Phys. Fluids.* **26**, 1160.

GILBERT, N. 1988 Numerische simulation der transition von der laminaren in die turbulente kanalstromung. Ph.D. Thesis, Fakultat fur Maschinenbau der Universitat Karlsruhe.

GUSTAVSSON, L. H. 1978 On the evolution of disturbances in boundary layer flows.. Ph.D. Thesis, Dept. of Mech., R. Inst. Tech., Stockholm, Sweden.

HENNINGSON, D. S. 1988 The inviscid initial value problem for a piecewise linear mean flow.. *Stud. Appl. Math..* **78**, 31.

HENNINGSON, D. S. 1988 On the spreading mechanism of a turbulent spot in plane Poiseuille flow. 2nd Europ. Turb. Conf., Berlin.

HENNINGSON, D. S. & ALFREDSSON, P. H. 1987 The wave structure of turbulent spots in plane Poiseuille flow. *J. Fluid Mech.* **178**, 405.

HENNINGSON, D. S., SPALART, P. R. & J. KIM 1987 Numerical simulations of turbulent spots in plane Poiseuille and boundary layer flows. *Phys. Fluids.* **30**, 2914.

JOHANSSON, A. V., ALFREDSSON, P. H. & J. KIM 1987 Shear-layer structure in near-wall turbulence. Proc. of CTR summer program, NASA Ames - Stanford, 237.

JOHANSSON, A. V., HER, J. Y. & J.H. HARITONIDIS 1987 On the generation of high-amplitude wall-pressure peaks in turbulent boundary layers and spots. *J. Fluid Mech.* **175**, 119.

KLEBANOFF, P. S., TIDSTROM, K. D. & SARGENT, L. M. 1962 The three dimensional nature of boundary layer transition. *J. Fluid Mech.* **12**, 1.

KIM, J. 1985 Turbulence structure associated with the bursting event. *Phys. Fluids.* **28**, 52.

KIM, J., MOIN, P. & MOSER, R. D. 1987 Turbulence statistics in fully developed channel flow at low Reynolds number. *J. Fluid Mech177.* **133.**

KLINGMANN, B., ALFREDSSON, P. H. & HENNINGSON, D. S. 1988 An experimental study of the velocity field of turbulent spots in plane Poiseuille flow. 2nd Europ. Turb. Conf., Berlin.

LANDAHL, M. T. 1975 Wave breakdown and turbulence. *SIAM J. Appl. Math..* **28**, 735.

NISHIOKA, M., IIDA, S. & ICHIKAWA, Y. 1976 An experimental investigation of the stability of plane Poiseuille flow.. *J. Fluid Mech.* **72**, 731.

RILEY, J. J. & GAD-EL-HAK, M. 1985 The dynamics of turbulent spots. *Frontiers of Fluid Mechanics* (Eds. Davis & Lumley), Springer, 123.

WYGNANSKI, I., SOKOLOV, N. & D. FRIEDMAN 1976 On a turbulent spot in a laminar boundary layer. *J. Fluid Mech.* **78**, 785.

Center for Turbulence Research
Proceedings of the Summer Program 1988

Eddies, Streams, and Convergence Zones in Turbulent Flows

By J.C.R. Hunt[1], A.A. Wray[2], and P. Moin[3]

1. Introduction

Recent studies of turbulent shear flows have shown that many of their important kinematical and dynamical properties can be more clearly understood by describing the flows in terms of individual 'events' or streamline patterns. Examples of such events might be high values of filtered vorticity (Hussain 1986) or high velocity, perhaps in combination with straining (Adrian & Moin 1988), or high Reynolds stress (Blackwelder & Kaplan 1976).

These events or flow regions are studied because they are associated with relatively large contributions to certain average properties of the flow, for example kinetic energy, Reynolds stress, or to particular processes in the flow, such as mixing and chemical reactions, which may be concentrated at locations where streamlines converge (Leonard & Hill 1988) for fast chemical reactions (which we shall refer to as convergence or C regions), or in recirculating eddying regions for slow chemical reactions (Broadwell & Breidenthal 1982); figure 1a). These vortical regions (which we refer to as eddy or E regions) are also of importance in certain flame and combustion problems (Peters 1988) where turbulent flows transport bubbles or particles. Recent experimental and computational research (e.g. Hunt et al. 1988; Maxey 1987; Chung & Troutt 1988; Fung & Perkins 1989) has shown that bubbles (or other low-density fluid such as reactants) tend to concentrate in low-pressure regions, while denser particles, especially if buoyancy forces are important, tend to concentrate in the streaming or S regions between eddies (figure 1b). But those particles that are entrained into eddying regions can remain for long periods; in fact, the control of eddying regions forms the basis of a recently-patented metallurgical purification process.

Many authors have recognised that models for reactions and particles and bubbles require some assumption about the kinematics of the flow, for example, as a distribution of vortices of given life time (Brown & Hutchinson 1979; Picart et al 1986) or of vortices separated by stagnation points (Broadwell & Breidenthal 1982). Another approach following Kraichnan (1970) is to model the kinematics of the turbulent flow field by random Fourier space and time modes with the appropriate amplitudes and relations between space and time behavior (Fung et al. 1989). This 'kinematic simulation' is a 'cheap' enough way of representing different

1 University of Cambridge
2 NASA Ames Research Center
3 NASA Ames Research Center and Stanford University

kinds of turbulent flow field that it is then more feasible to compute reaction and combustion processes or particle and bubble motions.

However at present there is no generally agreed way of assessing the accuracy or appropriateness of a representation of turbulent flow fields. How much of the space should be occupied by eddy, convergence, or streaming zones? How strong should they be? And so on. Answering such questions is one of the main objectives of this research project.

Usually the diffusion and mixing problems for non-reacting and non-dynamical particles are discussed qualitatively in terms of how individual fluid particles move, and are analyzed quantitatively in terms of the statistics of the velocity and displacement of fluid particles (e.g. Monin & Yaglom (1971), vol. 1). The key parameters are the rms velocity fluctuations u_0 and the Lagrangian integral time scale T_L. The value of u_0 is the same (or similar) at a fixed measuring point and for a moving particle (Lumley 1961, a point that has been verified by the kinematic simulations). But T_L cannot be defined in terms of simple Eulerian statistics because it depends on how a particle moves through the flow field. Therefore it must depend, given the length and velocity scales (L, u_0), on the *nature* of the flow pattern and therefore on certain aspects of E, C, and S zones. It is also interesting to compare T_L with the time T_E over which the velocity at a point changes for an observer moving with the mean flow.

As an example, in figure 2 (a) the flow largely consists of streaming zones which of course change with time. Then the particle *trajectories* are rather straight, but the length scale over which the velocity is decorrelated is smaller, so in this case $T_L >> L/u_0$ and $T_L > T_E$.

On the other hand, if the flow consists largely of eddy zones (E) the velocity of a particle would keep changing on a time scale L/u_0. So $T_L \sim L/u_0$ (figure 2 (b)). The comparison between T_L and T_E depends on how slowly the eddies move. If $\langle u \rangle_E$ is the bulk velocity of the eddies, then $T_E \sim L/\langle u \rangle_E$ and $T_L > T_E$ if $\langle u \rangle_E > u_0$.

This information about T_L is useful for computing mean concentrations, but it does not tell us about the overall shape of a dye cloud (such as that depicted by Corrsin, quoted by Monin & Yaglom (1971)). This typical shape has been described as tendrils and 'whirls' by Berry (1978). It can be explained by rapid motion along the streaming (S) regions forming the 'tendrils' and then slow motion into the eddy (E) regions forming the 'whirls' of the dye clouds.

Also, other important statistics of clouds such as mean-square displacement $|\mathbf{x}|^2$ or width of the dye cloud L_c^2 and the mean shape of a contaminant cloud are not defined uniquely by u_0 and T_L; rather they depend sensitively on the kinematics of the flow field.

The identification of certain significant regions in a flow can also provide an important method for analyzing the dynamics of the flow. Recent computations for two-dimensional flows have established that significant vortical eddy regions interact with each other as if they are equivalent point vortices with the same circulation (McWilliams 1984). This then makes the computation of development of the whole flow much simpler, because the analysis of a set of point vortices is much simpler

computationally and conceptually than that for the whole flow field.

In other words, the whole dynamical evolution of the flow has in this case been reduced to a low-order system. It is not yet by any means clear whether a comparable simplification would be possible for a global analysis of a three-dimensional flow. But if the significant vortical regions and their detailed flow structure can be evaluated, certain *local* analyses may become possible, for example, the interaction of the eddy with its surrounding flow or with other eddies (Moin, Leonard, Kim 1986; Hunt 1987), or in high Reynolds numbers flows the interaction between the eddying and small-scale turbulence within the eddy (e.g. Kida & Hunt 1988) (or the interactions between 'coherent' and 'incoherent' motion (Hussain 1986)).

In a three-dimensional turbulent flow there are large coherent eddies or vortices, but because vorticity diffuses out of these regions or because vorticity is torn off the eddies when they interact, there has to be much smaller-scale chaotic vorticity in the flow between the large vortices. This small-scale chaotic vorticity can be significantly amplified and dissipation increased in *convergence zones* outside the eddy regions. The nature of this amplification changes depending on whether the convergence is flattening or elongating a material sphere. So for the dynamical analysis it is also important to define these convergence zones and to quantify the *magnitude* of the straining, defined by $E_{ij}E_{ji}$ where E_{ij} is the symmetric stress tensor $\frac{1}{2}(\partial u_i/\partial x_j + \partial u_j/\partial x_i)$, and its *nature*, by $III = E_{ij}E_{jk}E_{ki}$: $III > 0$ for elongating and $III < 0$ for flattening.

This approach to the dynamical analysis, conditionally sampling the flow and then considering the dynamical equations governing these regions, differs from analyzing the *whole* flow into eigenmodes (Fourier modes for homogeneous flows or Karhuen-Loeve modes for inhomogeneous flows) and then computing the interactions between the modes. The latter classical approach (described at length by Batchelor (1953) and under investigation at CTR by Rogallo & Domaradzki (1988)) is straightforward to understand for a few interacting *wave* modes which pervade a whole flow. But it is impossible conceptually when the significant dynamics is localized. Imagine trying to analyze the interaction of point vortices using Fourier methods!

Many other investigators have been and are currently engaged in identifying strong eddying or vortical regions using various criteria for these regions, such as low pressure; strong rotational motions defined by the local deformation tensor $\partial u_i/\partial x_j$, where $u_i(\mathbf{x}, t)$ is the velocity field (Herring 1988; Perry & Chong 1987); or regions where the vorticity of the filtered velocity field is large (Hussain 1986).

The aim of this project is to use the numerical simulations at CTR to develop suitable criteria for defining these eddying or vortical zones. But in this study we are also interested in defining the convergence (C) and streaming (S) zones, in order to define the whole flow field, for all the reasons given here.

2. Defining S, E, C zones in velocity fields

2.1 Qualitative and mathematical criteria

(i) Eddy zones (E)

These zones are approximately defined as strong swirling zones with vorticity. Irrotational swirling motion outside the zones is excluded. Also excluded are nearly straight shear layers on the edges of streaming zones.

In general in a turbulent flow the swirling rotational zones are also being stretched by larger-scale irrotational straining, which helps maintain their vorticity (e.g. in mixing layers the cores of spanwise 'rollers' are strained by the longitudinal 'braid' vortices).

We apply two criteria to define E zones, (a) and (b) below.

(a) the irrotational straining is small compared with the vorticity, i.e. the second invariant of the deformation tensor is less than a negative threshold value $-II_E$:

$$II < -II_E \tag{2.1a}$$

where

$$II = \frac{\partial u_i}{\partial x_j}\frac{\partial u_j}{\partial x_i} = E_{ij}^2 - \frac{1}{2}\omega_i^2 \tag{2.1b}$$

and E_{ij} is the symmetric strain tensor $\frac{1}{2}(\partial u_i/\partial x_j + \partial u_j/\partial x_i)$ and ω_i is the vorticity $\epsilon_{ijk}\partial u_k/\partial x_j$.

(b) If the pressure tends to a minimum somewhere in the zone, there is a pressure gradient across the streamline, i.e. $\frac{1}{\rho}\partial p/\partial r \approx +u_S^2/R$ where R is the radius of curvature. A criterion that is independent of the pressure field *outside* the eddy zone would be

$$p_{\mathbf{edge}} - p_{\mathbf{int}} > p_E, \quad \text{or} \quad p_{\mathbf{int}} < p_{\mathbf{edge}} - p_E \tag{2.2a}$$

where $p_{\mathbf{int}}$ is in the interior of the E region, $p_{\mathbf{edge}}$ is on the edge, and p_E is a threshold value. As a working approximation, we first try

$$p_{\mathbf{int}} < -p_E \tag{2.2b}$$

For most vortices, the criterion (a) is equivalent to the criterion suggested by Perry & Chong (1987) that eddies are where the eigenvalues of the deformation tensor $\partial u_i/\partial x_j$ are complex. It would *not* be exactly the same as (2.1a) in a case where a vortex was being strained (figure 3) parallel to itself. But if the straining is weak compared with the rotation, Perry's criterion is equivalent.

The reason why the pressure criterion (b) needs to be added to the vorticity criterion of (a) is that it ensures that, if the flow is rotational, then the streamlines are curved. In a shear flow with straight streamlines $II = 0$. But because II and p are non-linear quantities different kinds of flow fields, when added together, can satisfy the criteria. Consider a diffuse double vortex sheet or jet of scale ℓ:

$$u_3 = U_0 \mathrm{e}^{-(x_1^2+x_2^2)/\ell^2} \tag{2.3a}$$

embedded in a large, weak-motion vortex

$$u_1 = \Omega x_3, \quad u_3 = -\Omega(x_1 - R) \tag{2.3b}$$

For the flow (2.3a), $II = 0$, $\nabla p = 0$, but the addition of (2.3a) and (2.3b) leads to

$$II \approx -\frac{4x_1 U_0 \Omega}{\ell^2} e^{-(x_1^2+x_2^2)/\ell^2} - 2\Omega^2, \tag{2.3c}$$

while

$$\frac{\partial p}{\partial x_1} = \Omega U_0 e^{-(x_1^2+x_2^2)/\ell^2} - \Omega^2(R - x_1) \tag{2.3d}$$

Note how, if $U_0/\ell >> \Omega$, the addition of a straight shear layer increases the value of $|II|$ and $|\nabla p|$.

Also, note how II rapidly changes sign across the jet. Depending on the background value of pressure, (2.2b) might or might not be satisfied. However, (2.2a) would not be satisfied, if $|\Omega U_0 \ell| < p_E$. Clearly this is *not* an eddy in the sense we know.

So it suggests that an eddy zone on a scale ℓ_e should be defined by averaging II over ℓ_e; in our computations II is in fact computed from the unfiltered velocity field. Small eddies could be defined by considering frames of reference moving mainly with the large eddies; then fluctuations can appear as local 'cat's eyes'. We are not attempting to describe such rather artificial constructs.

(ii) Convergence zones (C)

These zones are approximately defined as regions where there is *irrotational* straining motion *and* where there is strong convergence and divergence of streamlines. There will be a stagnation point in such a region (defined in a suitable frame of reference).

The criteria for the C zones must be such as to avoid the irrotational swirling flow around vortices. Therefore we adopt two conditions: (a) the irrotational straining is large compared with the vorticity, so for some threshold value II_C,

$$II > II_C \tag{2.4}$$

and (b) the pressure rises in the interior of the C zone so

$$p_{\text{int}} - p_{\text{edge}} > p_C \tag{2.5a}$$

Or, more simply but less generally,

$$p_{\text{int}} > p_C \tag{2.5b}$$

The pressure criterion avoids the possibility of irrotational swirl and also the possibility of a jet or rotating flow. (In general, the large-scale C zones are most appropriately defined by averaging the criterion (2.4) over a scale ℓ_c (say, $1/4L$)).

(iii) Streaming zones

In these zones the flow is relatively fast, not very curved, and not diverging or converging strongly. These zones are the main 'highways' for fluid or marked particles to be transported across the flow. The suggested criteria are

$$\text{(a)} \quad u_i^2 > u_0^2 \qquad \text{for speed, and} \tag{2.6}$$

$$\text{(b)} \quad |II| < II_S \qquad \text{for weak curvature and convergence} \tag{2.7}$$

It is important to use the *unfiltered* velocity field because the vorticity and the value of $|II|$ may be high on the sides of these zones and filtering can 'smear' these values of II over the S zone, causing the criterion (2.7) to be not satisfied.

The criteria given above are such that not every point in the flow field is in an S, E, or C. But the conditions on II are made such that no point can belong to more than one type of zone, by choosing $II_S = \min(II_E, II_C)$.

2.2 Critical computations to be performed

(i) Diagnostic tests

The algorithms for S, E, C zones should be used to define these zones for a number of flows where direct simulations have been performed. A number of diagnostic tests should first be run to evaluate the significance and usefulness of the algorithms:

(a) Do the computed S,E,C zones correspond to the expected streamline patterns for these zones?

(b) What is the improvement in using the double (II, pressure) criteria over other criteria?

(c) How sensitive are the definitions of the zones to the magnitudes of II_E, II_C, p_E, p_C, u_0?

(d) Are the same criteria applicable to different types of turbulent flows?

(ii) Comparison with other investigations

(a) It would be desirable to compare our criteria with those suggested by Perry & Chong (1987).

(b) How do the 'eddy' zones defined by our criteria compare with the space occupied by 'coherent structures' as defined by other investigators, e.g. by Adrian & Moin (1988), for the channel flow (using conditional sampling to define the structure), and by Hussain, Jeong & Kim (1987) for homogeneous flow (using 'eduction' techniques), and Moser & Moin (1988) for the channel flow (using orthogonal eigenmode expansion).

(iii) To define kinematics

(a) The geometrical and topographic properties of the zones need to be defined, for example the relative volumes occupied by the S, E, C zones $V^{(S,E,C)}$, their typical extent $L^{(S,E,C)}$, and their spacing $D^{(S,E,C)}$.

(b) The movement of the eddy and convergence zones, or mobility (to help understand the Lagrangian time scale T_L), defined as the average velocity across such

a zone $\mu^{(E,C)} = |\langle \mathbf{v} \rangle|$, averaged across an E or C zone. The normalized value of $\hat{\mu}^{(E,C)} = \mu^{(E,C)}/|II|$ would be of interest.

(iv) To test and develop fluid mechanical concepts

(a) Processes of reaction and vorticity dynamics depend on the *nature* of irrotational straining in the C and E zones. So it is important to compute the third invariant of the rate of strain tensor E_{ij}:

$$III = E_{ij}E_{jk}E_{ki} \tag{2.9}$$

Peak and average values of $III^{(C,E)}$ within C and E zones need to be known. A correlation between $III^{(E)}$ and $II^{(E)}$ in the eddy zones would indicate how localized the formation of vorticity really is.

(b) As in previous 'coherent-structure' analysis, it might be interesting to compute the relative contribution to various global statistics by the S,E,C zones, e.g. $\overline{\omega_i^2}$ by E zones, $\overline{u_i^2}$ by S zones, $\overline{E_{ij}^2}$ by C zones. The typical helicity of the E zones chould be computed by $|\langle \mathbf{u} \cdot \omega \rangle|$ averaged over the E zone.

(c) For Lagrangian statistics, it would be interesting to know how long an average particle spent in the different zones.

3. Results and discussion

(i) Simulations for testing the concept of flow zones.

The first simulation used was homogeneous stationary turbulence driven by a stationary random force field. There are mean field and fluctuating components $(\overline{u}(\mathbf{x}), u(\mathbf{x}, t))$ of the velocity field. The emphasis of our study was to examine the fluctuating component $u(\mathbf{x}, t)$, which was of course strongly affected by the mean component (see Hunt, Wray & Buell 1987). The characteristic Reynolds number for u is about 20. No strong coherent structures were observed in the previous study.

The second simulation was the turbulent channel flow computed by Moin & Moser (1987), with a characteristic Reynolds number of the turbulence of about 100. In this case, strong streamwise vortices are formed, but a number of weaker 'structures' or eddies also exist in the flow which need identifying.

(ii) Checking and 'tuning' the algorithm

The algorithm for the E,C,S zones defined by (2.1a) and (2.2b), (2.4) and (2.5b), (2.6), and (2.7) were used to compute the areas occupied by these zones in the two flows. The magnitudes taken for the criteria were: (a) $II_C = (\overline{II^2})^{1/2}$, i.e. the rms value of II over the whole flow, with $II_E = 2II_C$, (b) $p_C = (\overline{p^2})^{1/2}$, the r.m.s value of p over the flow, with $p_E = 0.2p_C$, and (c) $u_0 = (\overline{|\mathbf{u}|^2})^{1/2}$, the rms value of the speed of the fluctuating component.

These values were computed, and the criteria were tested by comparing the indicated zones with the patterns formed by computed velocity vectors plotted onto the zones, for many realizations of the flow. The vectors were in one plane, e.g. (u_1, u_2), but the criteria were defined for the full three-dimensional flow field. As

shown in figure 4, it is clear that where (u_1, u_2) vectors circled round a region, the zone identification using the algorithms above indicated on eddy, E, region; where there was a local stagnation point, the zone computations indicated a convergence, C, region. Where vectors indicated high speed regions with low curvature, the zone computations indicated streaming, S, regions.

In the initial stages, a spatially filtered velocity field was used to calculate the quantities in the different zone algorithms. However, we found that in the indicated E,C,S zone areas, the flow structure did not correspond to swirling, coverging, or streaming motion. The explanation was probably that the spatial filtering smeared the vorticity over the zones, so that their definition was effectively changed. Consequently spatial filtering was abandoned. Some examples of bad disagreement between the indicated zones and the actual patterns are shown in figure 5.

The same algorithm and the same parameters developed for homogeneous turbulence were then applied to channel flow. The agreement between expected flow structure in the different flow zones and the actual flow structure was even more satisfactory than for homogeneous turbulence.

The general features found for the flow zones were:

(i) Eddy zones

These zones were isolated and distributed uniformly over the flow. Across any section of these zones the 'swirl' velocity is in one direction, and the vorticity, on the scale of the zone, is in one direction. The swirl velocity of the vorticity, on the scale of the zone, is maximum around the circumference of the zones. The typical diameter of these zones using our criteria is about $L/4$ where the spacing between them is about L. Not all eddy zones were circular in cross section, a few were quite elongated in the plane being examined, but in that case the vorticity was approximately parallel to the elongation. By examining the eddy zones intersecting a plane at different times, it was clear that some eddy zones move around (usually the weaker vortices) while others move very little (usually the stronger zones). This random movement of vortical regions under the action of larger scales had been studied by Hunt, Wray & Buell (1987).

(ii) Convergence zones

The C zones were also isolated, generally round or square shaped regions. Across a section of any zone there appeared to be a single large-scale straining motion, usually with a stagnation point in the zone somewhere (i.e. the principal axes of the strain did not change direction significantly). Their length scale and distribution was similar to that of E zones.

(iii) Streaming zones

The S zones are elongated and sometimes filamentary regions leading into C zones. The curvature is small. They do not generally lead into E zones. Their longest extend is about L to $1.5L$, while their width is typically $0.5L$. The maximum velocity in these regions (which must be greater than u_0), is generally less the

maximum velocity on the edge of the E zones.

(iv) Straining processes in the flow zones.

The third invariant III of the deformation tensor $\partial u_i/\partial x_j$, defined by (2.9), was computed over the flow. Regions where III was positive and negative are indicated by different contours, on a background of the indicated flow zones in figure 6.

It was found that, in the convergence C zones, more than 3/4 of the area has $III < 0$, while in the eddy zones more than about 3/4 of the area has $III > 0$. Also, the maximum positive and negative values of III were located in these zones.

4. Discussion and conclusions

(i) The main conclusion is that homogeneous and sheared turbulent flow fields are made up of characteristic flow zones — eddy, convergence, and streaming zones. A set of objective criteria have been found to describe regions in which the streamlines circulate, converge or diverge, and form streams of high velocity flow. Previous investigations to identify characteristic regions or coherent structures seem to have been less successful in selecting criteria that define the zones in a way that accords with the qualitative kinematical definition of the regions.

(ii) The most interesting question arising from this study is: What is the characteristic three-dimensional eddy structure that is consistent with these flow zones, and with the values of the third invariant III? From the fact that the eddy zones are approximately vortex tubes, it is likely that the main structure is one of vortex lines concentrating in smaller regions into vortex tubes. These vortices induce motion in each other and can produce strong stream zones between them, and C zones where they meet other S zones.

In turbulent flow, especially at higher Reynolds number, smaller eddy structures can appear, especially at the edges of the E zones and in the C zones. The vorticity of these eddies is strained by the flow around the E zones and by the converging/diverging streams in the C zones. This leads (see figure 7) to elongating straining ($III > 0$) around the edges of the E zones and to flattening straining ($III < 0$) within the C zones.

(iii) As Leonard & Hill (1987,8) have pointed out, flame or reaction fronts are likely to occur in the C zones and that the fronts must tend to lie parallel to the plane normal to the principal direction of compressive strain of $\partial u_i/\partial x_j$. (Since $III < 0$, the other two directions are elongational.)

(iv) It would of course be interesting to compute different statistics for the C zones to provide a good basis for an objective description of each of the key flow structures.

REFERENCES

ADRIAN, R.J. & MOIN, P. 1988, *J. Fluid Mech.*, **190**, 531-559.

BATCHELOR, G.K. 1953, *Homogeneous Turbulence*, Cambridge University Press.

BERRY, M.V. 1978, *Institute of Phys. Conf. Proc. No. 46*, 16-120.

BLACKWELDER, R.F. & KAPLAN, R.E. 1979, *J. Fluid Mech.*, **76**, 89-112.

BROADWELL, J.R. & BREIDENTHAL, R.E. 1982, *J. Fluid Mech.*, **125**, 397-410.

BROWN, D.G. & HUTCHINSON, P. 1979, *J. Fluids Eng.*, **101**, 265-269.

CHUNG, J.N. & TROUTT, T.R. 1988, *J. Fluid Mech.*, **186**, 199-222.

FUNG, J. & PERKINS, R.J. 1989, *Proc. 2nd European Turbl. Conference*, Springer-Verlag, Berlin .

HERRING, J. 1988, *Proc. 17th Int. Cong. Theor. Appl. Mech.*, Grenoble.

HUNT, J.C.R. 1987, *Trans. Can. Soc. Mech. Eng.*, **11**, 21-35.

HUNT, J.C.R., WRAY, A.A., & BUELL, J. 1987, *Proc. CTR Summer Program*, 77-94.

HUNT, J.C.R. & AUTON, T.R., SENE, K., THOMAS, N.H. & KOWE, R. 1988, *Proc. Conf. Transient Phenomena in Multiphase Flow*, Hemisphere (in press).

HUSSAIN, A.K.M.F. 1986, *J. Fluid Mech.*, **173**, 303-356.

HUSSAIN, A.K.M.F., JEONG, J. & KIM, J. 1987, *Proc. CTR Summer Program*, 273-290.

KIDA, S. & HUNT, J.C.R. 1988, *J. Fluid Mech.*, accepted.

KRAICHNAN, R.H. (1970) *Phys. Fluids.*, **13**, 22-31.

LEONARD, A.D. & HILL, J.C. 1987, *Proc. CTR Summer Program*, 141-146.

LEONARD, A.D. & HILL, J.C. 1988, *Proc. CTR Summer Program.*

LUMLEY, J.L. 1962, *Mechanique de la Turbulence*, Paris ed. CNRS.

MCWILLIAMS, J.C. 1984, *J. Fluid Mech.*, **146**, 21-43.

MAXEY, M.R. 1987, *J. Fluid Mech.*, **174**, 441-465.

MOIN, P., LEONARD, A. & KIM, J. 1986, *Phys. Fluids.*, **29**, 955-963.

MONIN, A.S. & YAGLOM, A. 1971, *Statistical Fluid Mechanics. Vol. 1*, M.I.T. Press.

MOSER, R.D. & MOIN, P. 1988, *J. Fluid Mech.*, submitted.

PERRY, A.E. & CHONG, M.S. 1987, *Ann. Rev. Fluid Mech.*, 125-155.

PETERS, N. & WILLIAMS, F.A. 1988, *22nd Symposium on Combustion*, Seattle.

PICART, A., BERLEMONT, A. & GOUESBET, G. 1986, *Int. J. Multiphase Flow*, **12**,No. 2, 237-261.

ROGALLO, R.S. & DOMARADZKI, J.A. 1988, *Proc. CTR Summer Program.*

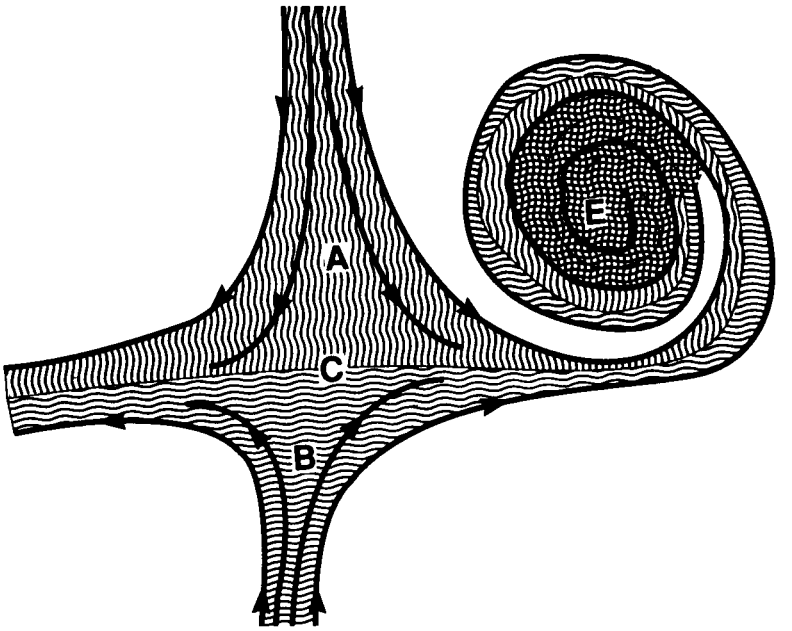

FIGURE 1A. Showing how reacting species (A,B) tend to react in C zones for fast or E zones for slow reactions.

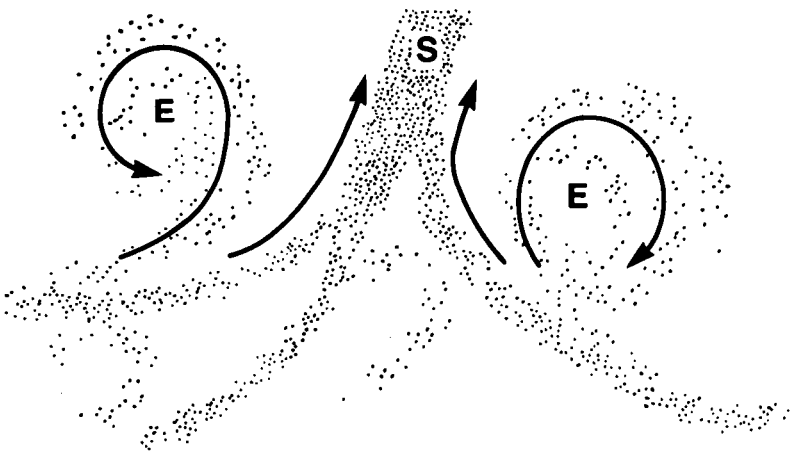

FIGURE 1B. Showing how particles tend to concentrate in the streaming S zones.

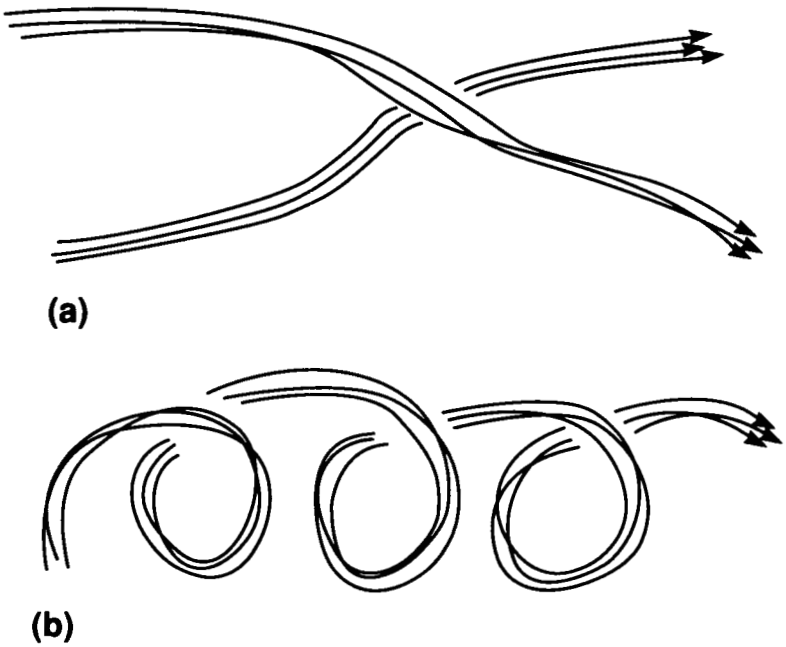

FIGURE 2. Typical trajectories: (a) for particles mainly in S zones, $T_E << T_L$; (b) for particles mainly in E zones so that $T_E \sim T_L$.

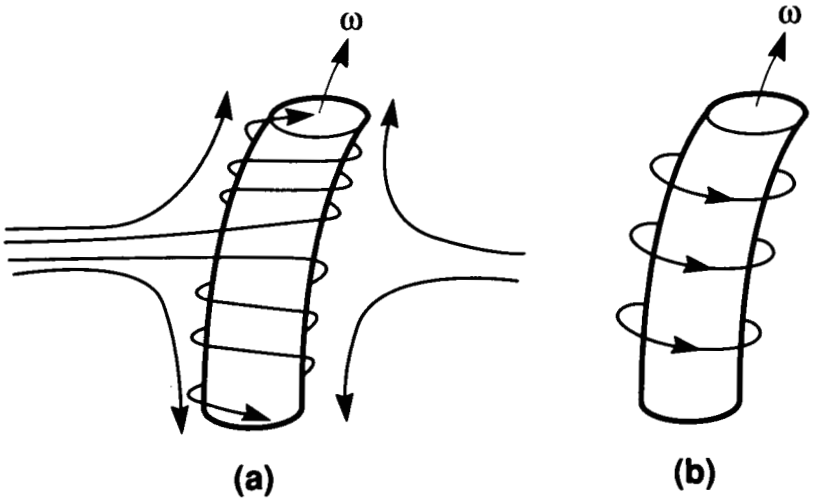

FIGURE 3. Choice of criteria: in (a) there is straining and vorticity, and in (b) pure vortical motion; if the straining is strong enough, case (a) is not counted as an eddy!

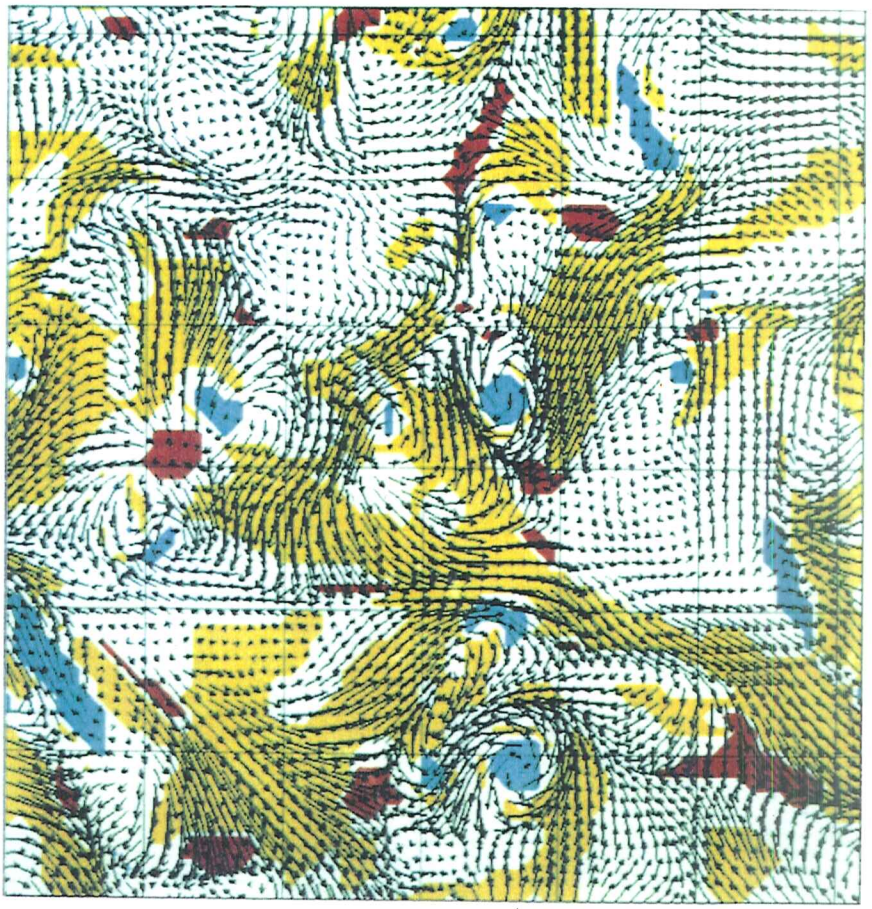

FIGURE 4. S,E,C zones with the full velocity field used in the criteria. Cyan: Eddies ($p < -p_E$; $II < -II_E$); Yellow: Streams ($u^2 > u^2_{\rm rms}$; $|II| < II_S$); Red: Convergence zones ($p > p_C$; $II > II_C$); White: Unclassified zones.

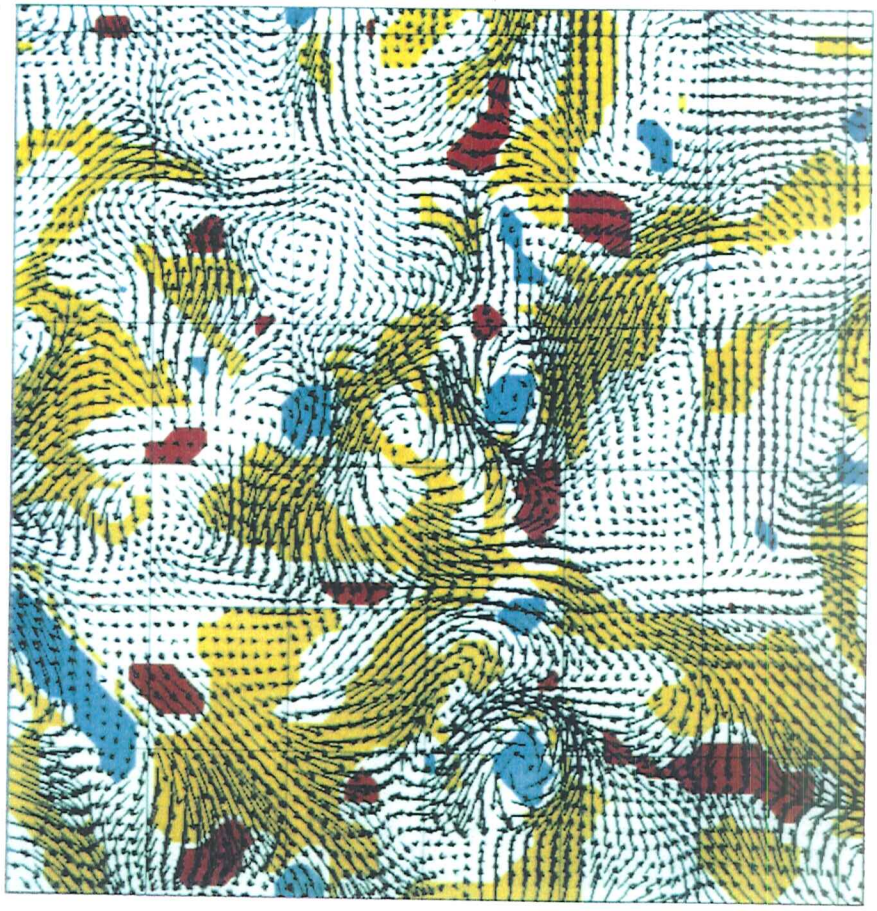

FIGURE 5. S,E,C zones with the filtered velocity field used in the criteria. Cyan: Eddies ($p < -p_E$; $II < -II_E$); Yellow: Streams ($u^2 > u^2_{\rm rms}$; $|II| < II_S$); Red: Convergence zones ($p > p_C$; $II > II_C$); White: Unclassified zones.

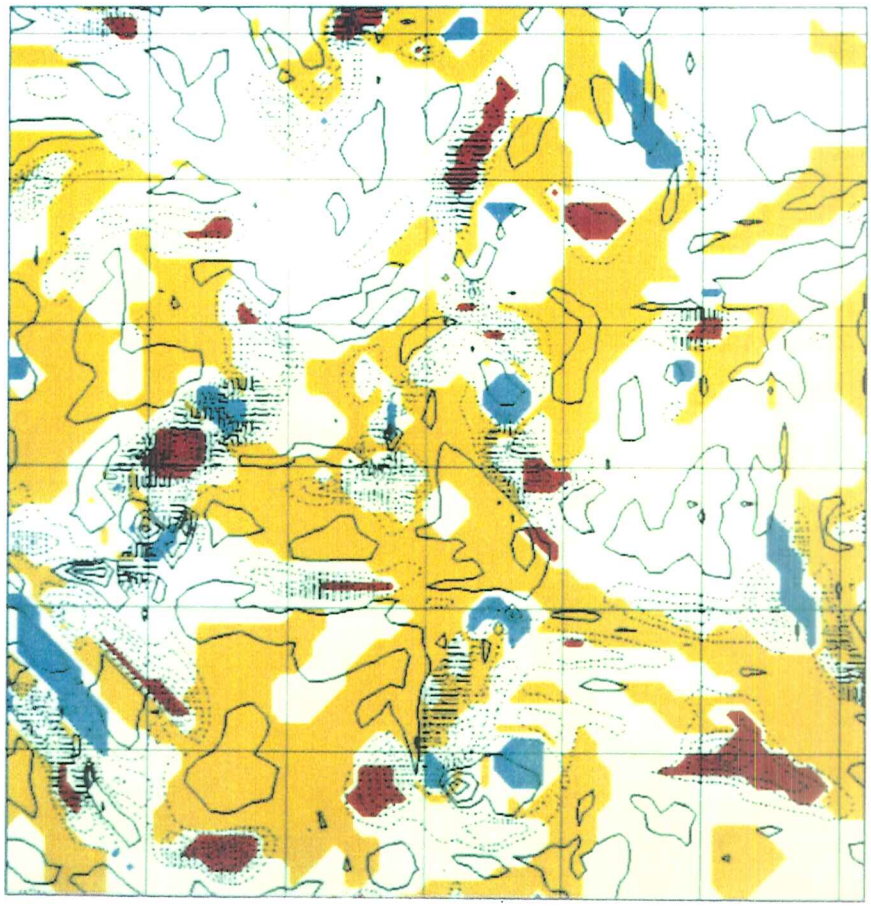

FIGURE 6. S,E,C zones shown with contours of III. Solid contours are positive and dashed negative. Cyan: Eddies ($p < -p_E$; $II < -II_E$); Yellow: Streams ($u^2 > u^2_{\rm rms}$; $|II| < II_S$); Red: Convergence zones ($p > p_C$; $II > II_C$); White: Unclassified zones.

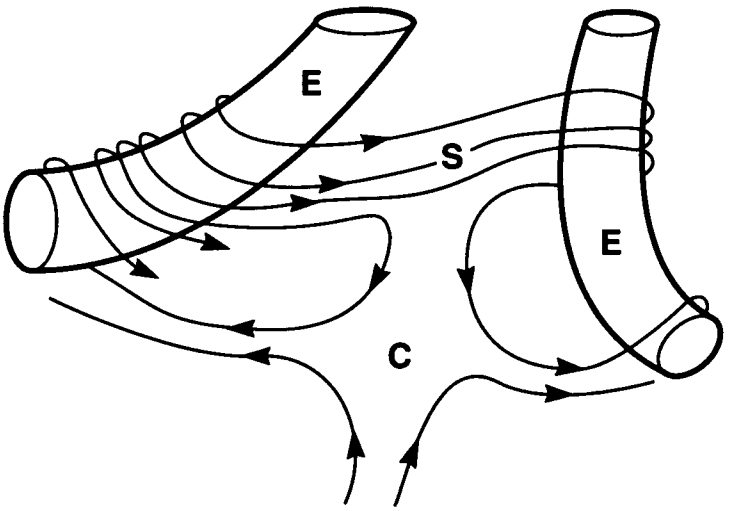

FIGURE 7. An interpretation of the characteristic flow zones in homogeneous turbulence in terms of vortex tubes at an angle to each other. Note the narrow streaming region between them. In the C region small vortices normal to the large-scale flow are stretched (and 'piled up'), and in the S region these are compressed (and 'spaced out'). These effects lead to $III > 0$ near E and $III < 0$ in C.

Center for Turbulence Research
Proceedings of the Summer Program 1988

Theoretical model for VITA-educed coherent structures in the wall region of a turbulent boundary layer

By Marten T. Landahl[1]

1 Introduction

Experiments on wall-bounded shear flows (channel flows and boundary layers) have indicated that the turbulence in the region close to the wall exhibits a characteristic pattern of intermittently formed coherent structures. This was first clearly demonstrated in the visualization experiments of Kline et al.(1967), in which it was seen that most of the turbulence generation takes place during randomly recurring, comparatively short-time, bursting events in the near-wall region (in the viscous and buffer layers) separated by periods of unsteady, but basically inactive, quasi-laminar motion. The coherent structures have been found to carry a major portion of the turbulent stress.

For a quantitative study of coherent structures it is necessary to make use of conditional sampling. One particularly successful sampling technique is the Variable Integration Time Averaging technique (VITA) first explored by Blackwelder and Kaplan (1976). In this, an event is assumed to occur when the short-time variance exceeds a certain threshold multiple of the mean square signal. This sampling technique has been found to bring out structures characterized by a low-speed (downstream) region and a high-speed (upstream) one separated by a thin, inclined shear layer. The measurements by Johansson and Alfredsson (1982) showed that the rate of occurrence of such structures ("bursting rate") varies with the integration time and threshold parameter selected. The most frequently found structures have streamwise lengths of the order of a few hundred viscous wall units. In the original work on the modelling of the VITA structures (Landahl, 1984a; 1984b) the structure was assumed to be initiated by a local inflectional type instability producing a transient disturbance, localized in space and time, the evolution of which was then followed by application of an approximate linear theory in which the effects due to viscosity and streamwise pressure gradient were neglected. This theory was found to give results for the sampled velocity signatures in good qualitative agreement with the experiments.

The analysis presented here removes some of the assumptions in the earlier models in that the effects of pressure and viscosity are taken into account in an approximation based on the assumption that the near- wall structures are highly elongated in the streamwise direction. The appropriateness of this is suggested by the observations but is also self consistent with the results of the model which show that the

1 Massachusetts Institute of Technology

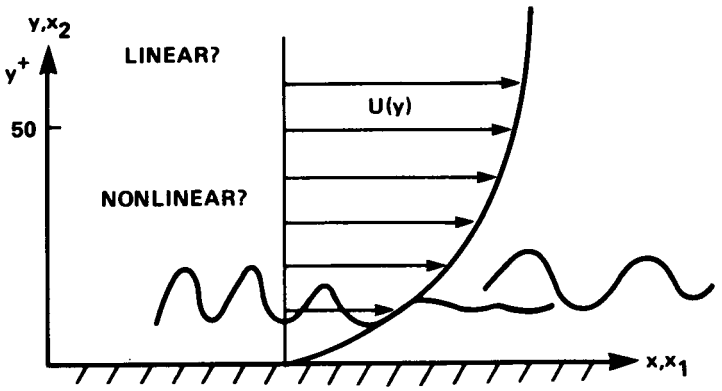

FIGURE 1. Coordinate system and definitions.

streamwise dimension of the structure grows with time, so that the approximation should improve with the age of the structure.

2. Analysis

Basic assumptions in the analysis are that the mean flow is parallel and that the nonlinearity is intermittent. Denoting by $U(x_2)(x_2 = y)$ the mean velocity, by $u_i(x_j, t)$ the fluctuating velocity, and by p the fluctuating part of the pressure (see Figure 1). Navier-Stokes equations give the following set of equations for the fluctuating velocity field

$$\frac{Du_j}{Dt} - vU'\delta_{i1} = -\frac{\partial p}{\partial x_i} + \nu\nabla^2 v + T_i \tag{1}$$

where

$$Ti = \frac{\partial \tau_{ij}}{\partial x_j} \tag{2}$$

and where

$$\tau_{ij} = -\rho(u_i u_j - \overline{u_i u_j}) \tag{3}$$

are the "fluctuating Reynolds stresses", overbar denoting average.

Elimination of the pressure with the aid of the continuity equation,

$$\frac{\partial u_i}{\partial x_i} = 0 \tag{4}$$

gives the following equation for the vertical velocity component:

$$D(\nabla^2 v)/Dt - \frac{\partial v}{\partial x}U'' - \nu\nabla^4 v = q \tag{5}$$

where

$$q = \nabla^2 T_2 - \frac{\partial^2 T_i}{\partial x_i \partial x_2} \tag{6}$$

and where

$$T_i = \frac{\partial \tau_{ij}}{\partial x_j} \tag{7}$$

For infinitesimal fluctuating velocity amplitudes the right-hand side of (7) may be neglected, and one recovers the Orr-Sommerfeld equation (in physical space) for the v-component.

On the anticipation that the structures to be analyzed have a boundary layer character in the sense that their vertical dimensions are much smaller than their horizontal ones, the dominating terms in the expression for q would be those having the highest-order y- derivatives, namely

$$< q > \cong -(\frac{\partial^2}{\partial y^2})[\frac{\partial(uv)}{\partial x} - \frac{\partial(vw)}{\partial z}] \quad + \quad \text{higher order horiz. derivatives} \tag{8}$$

For such eddies, we will determine an approximate inviscid solution valid for small y (i.e., small compared to the largest horizontal dimensions of the eddy). We write the equation as follows:

$$\frac{D\phi}{Dt} - \nu\nabla^2\phi = q_1 \tag{9}$$

where

$$\phi = \nabla^2 v \tag{10}$$

$$q_1 = q + U''\frac{\partial v}{\partial x} \tag{11}$$

In the inviscid limit ($\nu = 0$) the formal solution of (9) is given by

$$\phi = \int_{-\infty}^{t} q_1(\xi_1; y; z, t_1)dt_1 \tag{12}$$

where

$$\xi_1 = x - U(y)(t - t_1) \tag{13}$$

On the anticipation that most of the structures of special interest are highly elongated in the streamwise direction and thus vary slowly in the x-direction, we will, for simplicity in the analysis, include only the terms originating from the lowest-order x-derivatives. Hence, the term on the right-hand side of (11) proportional to U'' will be neglected in the following. Of course, this is only allowed if U'' does not change sign anywhere, because then an inflectional-type instability may produce an exponentially growing wave for which the term is essential. The inviscid solution (12) then simplifies to

$$\phi = \int_{-\infty}^{t} q(\xi_1; y; z, t_1)dt_1 \tag{14}$$

The solution for v is obtained by solving the Poisson equation (10). Application of Fourier transform in the x, z-plane gives, with 'tilde' denoting transformed quantities, $k = \alpha^2 + \beta^2$, α and β being the transform variables in x and z, respectively,

$$\tilde{v} = -\frac{1}{2k}\int_0^\infty [e^{-k|y-y_1|} - e^{-k(y+y_1)}]\tilde{\phi}(y_1)dy_1 \tag{15}$$

where the second term under the integral sign is selected so as to give $\tilde{v} = 0$ on the wing. For values of y that are small compared to the horizontal dimensions of the structure, and for a structure with a small vertical extent compared to its horizontal dimensions ("flat eddy"), (14) may be expanded to yield, to lowest order in y,

$$\tilde{v} \cong \frac{1}{2}\int_0^\infty (|y - y_1| - y - y_1)\tilde{\phi}(\xi, y_1; z, t_1)dy_1 \equiv \tilde{v}_f \tag{16}$$

or, in the physical plane,

$$v_f = \frac{1}{2}\int_0^\infty (|y - y_1| - y - y_1)\phi(\xi_1, y_1; z, t_1)dy_1 \tag{17}$$

It follows from (17) that the streamwise size of the disturbed region from an initial disturbance grows linearly in time at a rate $U_{\max} - U_{\min}$, where $U_{\max}$ and $U_{\min}$ are, respectively, the maximum and the minimum velocities of the mean flow.

For a structure with vertical and spanwise dimensions both small compared to the streamwise dimension ("sausage eddy") the appropriate approximation is found by replacing k by $|\beta|$ in (15). Upon inversion this yields

$$v = \frac{1}{2\pi}\int_0^\infty dy_1 \int_{-\infty}^\infty \phi(\xi_1, y_1, z_1, t_1)\log(\frac{r_1}{r_2})dz_1 \equiv v_s \tag{18}$$

If q is intermittent so that it is zero for $t > t_o$, say, then for the flat-eddy approximation (17) for $t > t_o$,

$$v_f = \frac{1}{2}\int_0^\infty (|y - y_1| - y - y_1)\phi_o(\xi, y_1; z)dy_1 \tag{19}$$

where $\xi = x - (t - t_o)U(y_1)$ and where

$$\phi_o(\xi, y; z) = \nabla^2 v_o = \int_{-\infty}^{t_o} q(\xi'; y; z, t_1)dt_1 \tag{20}$$

where $\xi' = \xi + U(y)(t_1 - t_o)$. Similarly, for the "sausage" approximation (18)

$$v_s = \frac{1}{2\pi}\int_0^\infty dy_1 \int_{-\infty}^\infty \phi_o(\xi, y_1, z_1, t_1)\log(\frac{r_1}{r_2})dz_1 \tag{21}$$

It follows from (19)-(21) that, for any smooth function ϕ_o, the vertical velocity will decay like t^{-1} as $t \to \infty$ when q is intermittent.

The streamwise component u satisfies

$$\frac{Du}{Dt} = -\frac{\partial p}{\partial x} - vU' - \nu\nabla^2 u + q_u \tag{22}$$

where q_u stands for the nonlinear terms. In accordance with the intermittency assumption of the nonlinear terms, we assume that q_u is negligible for $t > t_o$. At large times the coherent structure becomes highly elongated so that $\partial p/\partial x$, as well, becomes negligible. With the additional assumptions that $u = 0$ for $t = t_o$, the inviscid solution for u then becomes

$$u = -U'(y)lm \tag{23}$$

where

$$l_m = \int_{-\infty}^{t} v(\xi_1; y; z, t_1)dt_1 \tag{24}$$

is the vertical displacement (in linearized approximation) of the fluid element from its initial undisturbed position at $t = -\infty$. This result is equivalent to that proposed Prandtl (1925) in his mixing- length theory, see Landahl (1984b).

After application of conditional sampling to the above equations they may then be used for the study of coherent structures. For this purpose it is necessary to select a suitable model for the the nonlinear driving terms represented by q.

3. Statistical model for the nonlinear driving term

Since the coherent structures are intermittent, and hence well separated in time and space, they may be regarded as statistically independent. Upon application of conditional sampling to the nonlinear terms one could therefore expect the sampled stress term $< q >$ (angular brackets denoting conditionally sampled quantities) to give results varying with time and horizontal distances like a Gaussian "hat". For a coherent structure which is symmetrical in the z-direction, one would expect $< vw >$ to be zero. Thus, the term involving $< vw >$ may be neglected and from (7) it follows that an expression of the form

$$< \tau_{11} >= f(y)[1 - 2(\frac{z}{l_3})^2]\exp[-(\frac{x}{l_1})^2 - (\frac{z}{l_3})^2 - (\frac{\tau}{t_b})^2] \tag{25}$$

where l_1 ,l_3, and t_b are, respectively, the streamwise, spanwise, and time scales of the burst, and where $\tau = t - t_o$, would give an appropriate representation of the nonlinear driving term. The function of z multiplying the exponential is selected so as to make

$$\int_{-\infty}^{\infty} < \tau_{11} > dz_1 = 0 \tag{26}$$

since otherwise the resulting disturbance will not vanish for large $|z|$, i.e., will not be a localized one.

The dependence on y cannot be found by such simple reasoning; therefore, we make use here of the model proposed by Bark (1975),

$$f(y) = C(\frac{y}{l_2})^3\exp[-(\frac{y}{l_2})^2] \tag{27}$$

C being a constant (not needed, see below), which, with the vertical scale l_2 chosen to be 15 in viscous wall units, gives a good fit to the Reynolds stress distribution during bursting found in the measurements by Kim et al. (1972). In the following treatment we shall adopt the simple model that the nonlinear terms are highly intermittent so that we set $t_b \approx 0$. Thus, upon insertion in (20) we find

$$\phi_o = K[1 - 2(\frac{z}{l_3})^2](\frac{\partial}{\partial \xi})\exp[-(\frac{\xi}{l_1})^2 - (\frac{y}{l_2})^2 - (\frac{z}{l_3})^2] \tag{28}$$

where K is a numerical constant measuring the integrated strength of the nonlinear driving term.

4. Correction for long-time viscous effects

From (22) we have for long times when $v \to 0$ and the nonlinear and viscous effects are negligible

$$\frac{Du}{Dt} \approx 0 \tag{29}$$

Thus, as $t \to \infty$

$$u(x, y, z, t) \to u_\infty(\xi; y; z) \tag{30}$$

where $\xi = x - (t - t_o)U(y)$. However, viscous diffusion will become important for large times when u must satisfy

$$\frac{Du}{Dt} - \nu \nabla^2 u = 0 \tag{31}$$

By introducing the convected coordinate ξ by setting

$$u = u(\xi, y, z, t) \tag{32}$$

one finds that

$$\nabla^2 u = t^2[U'(y)]^2 \frac{\partial^2 u}{\partial \xi^2} - 2tU'(y)\frac{\partial^2 u}{\partial \xi \partial y} - tU''(y)\frac{\partial u}{\partial \xi} \tag{33}$$

Hence, as t becomes large,

$$\frac{\partial u}{\partial t} - vt^2[U'(y)]^2 \frac{\partial^2 u}{\partial \xi^2} + (\text{higher order terms in } t^{-1}) = 0 \tag{34}$$

Upon neglecting the terms of higher order in t^{-1} and introducing the new time variable $T = \nu t^3[U'(y)]^{2/3}$ we may cast (34) in the standard diffusion equation form

$$\frac{\partial u}{\partial T} - \frac{\partial^2 u}{\partial \xi^2} = 0 \tag{35}$$

with the initial condition for $T = 0$

$$u = u_\infty(\xi, y, z) \tag{36}$$

which may be easily solved using standard methods. For a nonlinear source of the form (28) one obtains the simple result that the same functional behavior with ξ remains, except that l_1 is replaced by L_1, everywhere, where

$$L_1 = \sqrt{l_1^2 + 4t^3[U'(y_1)]^{2/3}} \tag{37}$$

and ϕ_o is multiplied by l_1/L_1. Thus, the long-time effect of viscosity is to make the disturbed region extend even further in the streamwise direction and to weaken the disturbance.

5. Vita-educed coherent structures

In the VITA method one averages over events for which the short-time variance

$$\mathrm{var}(u,T) = \frac{1}{T}\int_{t_e-T/2}^{t_e+T/2} u^2(t)dt - [\frac{1}{T}\int_{t_e-T/2}^{t_e+T/2} u(t)dt]^2 \tag{38}$$

exceeds a pre-selected threshold value ku_{rms}^2, where T is the integration time, k is the threshold level, selected to be typically $k \approx 1$, u_{rms}^2 is the mean-square fluctuating velocity, and where $t = t_e$ is the centered time of the event. The conditionally sampled u velocity is then usually presented as a function of the time $\tau = t - t_e$ relative to the event. The experiments show that, for a given integration time T, the normalized conditionally sampled value

$$< u >^* = < u > / \sqrt{ku_{rms}^2} \tag{39}$$

is approximately independent of the threshold parameter k and a function only of the time τ relative to the event. On the assumption that the theoretical model for the "typical" sampled event represents most of the fluctuation energy, a procedure for the model VITA event may then be outlined as follows: First, the model for the typical event is used to find the streamwise length scale, l_1, and location x behind the initial onset point which gives the maximum of the variance, var_{max}, for a given T. Then

$$< u >^* = < u > / \sqrt{var_{max} u_{rms}^2} \tag{40}$$

where $u_{rms}^2 = < u^2 >$ for the structure.

An analogous procedure can be followed for space-averaged (VISA) structures, but for the present work only VITA results were worked out.

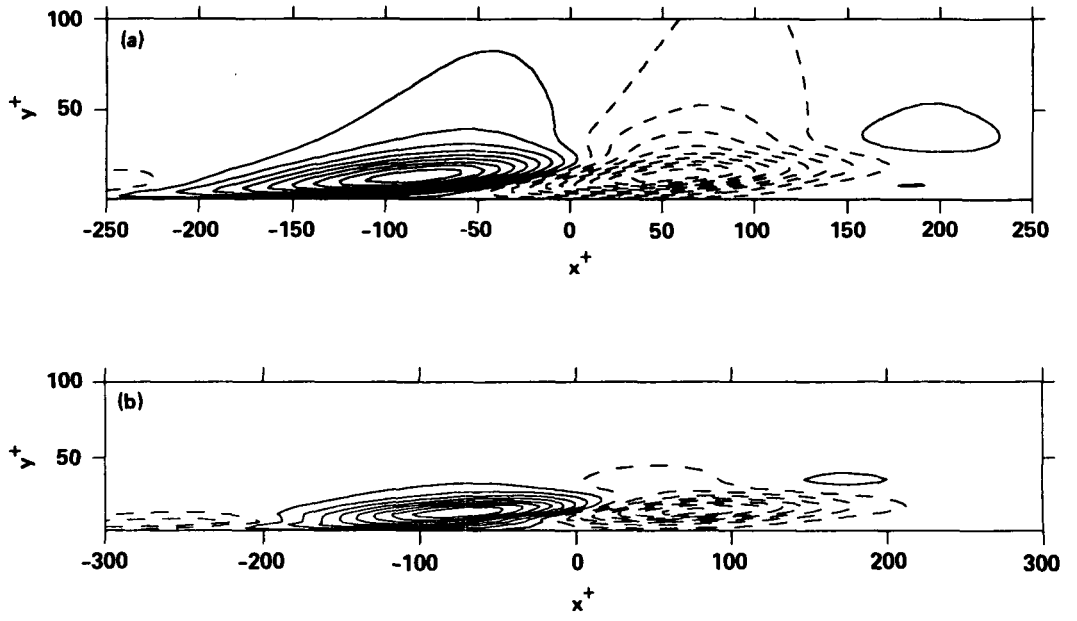

FIGURE 2. Contours of streamwise perturbation velocities in the plane $z = 0$ for model VITA-educed coherent structure at $\tau = 0$ ($t^+ = 24$) for a variance integration time of $T^+ = 20$, with $l_1 = 95$, $l_2 = 15$, $l_3 = 35$. a) Flat-eddy approximation. b)"Sausage" approximation.

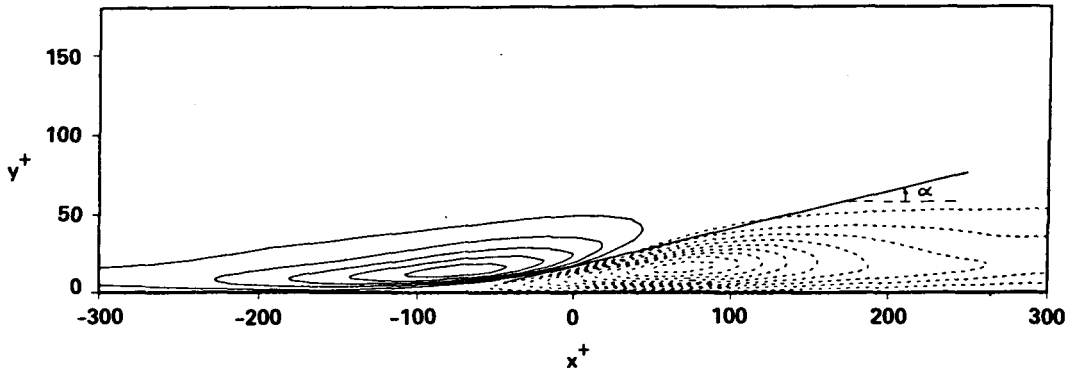

FIGURE 3. Contours of VISA-educed coherent structures with integration distance of $X^+ = 200$ obtained from numerical simulations for channel flow (from Alfredsson et al., 1988)

6. Numerical results for VITA structures

The procedure outlined above to find l_1 and x producing the highest variance for the selected integration time could be accomplished in a small numbers of trials by first selecting an initial guess of l_1 and determine for this the value of x, and the corresponding value of the integration time $T = T_m$, which yields the highest value

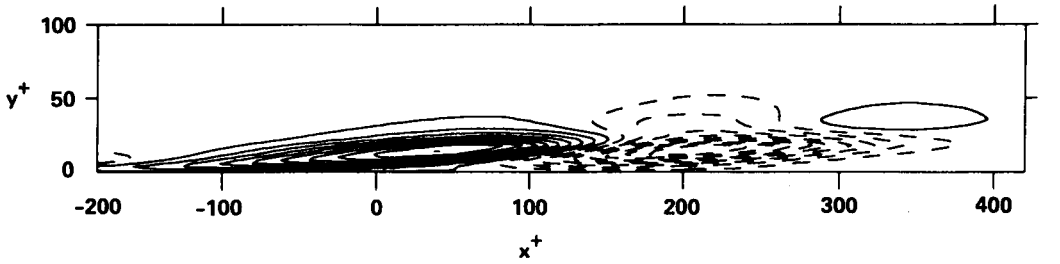

FIGURE 4. Contours of streamwise velocity perturbation at $\tau^+ = 12$ $(t^+ = 36)$ for VITA-educed eddy considered in Figure 2. "Sausage" approximation.

of the variance for the velocity scaled according to (39). A close approximation to the value of l_1 required to give the maximum for a particular desired integration time T, and the corresponding x, can then be determined simply by multiplying the original values of these quantities by T/T_m. It follows from the theory that, if viscosity is neglected, this procedure should give the correct parameter combination yielding the greatest variance for that value of the chosen averaging time. For the viscous case some small additional adjustments of the parameter values were found to be required in order to arrive at the maximum.

For the numerical evaluation of the integrals in (19) - (21), Simpson's rule was used with 20 points in the y-interval $0 - 3l_2$. The contribution from the region $y > 3l_2$ was found to be negligible. For the mean velocity distribution Reichardt's (1951) expression was employed.

Calculations were carried out for a VITA averaging time of $T^+ = 20$, applied at $y^+ = 15$, which should correspond approximately to VISA- structures obtained for an averaging streamwise distance of $X^+ = 200$, the mean velocity U at that distance from the wall being approximately 10 in viscous units. This choice was made in order to compare the results with the VISA-educed structures obtained by Alfredsson et al. (1988) from the numerical simulations for a channel flow. The procedure outlined above gave that the maximum of the normalized variance occurred at $x^+ = 225$ for $l_1^+ = 95$ at the time $t^+ = 24$ after the onset of the structure. In the calculations were used $l_2^+ = 15$ and $l_3^+ = 30$, the latter found to give a spanwise scale close to that found from the numerical simulations.

In Figure 2 the contours of constant streamwise fluctuation velocity for the coherent structure thus found in the x, y-plane are shown, both for the flat-eddy (Figure 2a) and the sausage (Figure 2b) approximations. The main qualitative difference between the two shows up for large values of y^+, which is as expected, since both approximations should hold for $y^+ \to 0$. The comparison with the VISA-structure obtained by Johansson et al (1988), see Figure 3, demonstrates that the model captures correctly the qualitative features seen in the numerical results. Thus, it shows the appearance of a high-speed upstream region separated from a low-speed downstream region by a tilted shear layer. The results for a later time, for $t^+ = 36$ (Figure 4), demonstrates that the shear layer tilts over more and more in the streamwise direction as time advances, as would indeed be the expected effect of the deformation

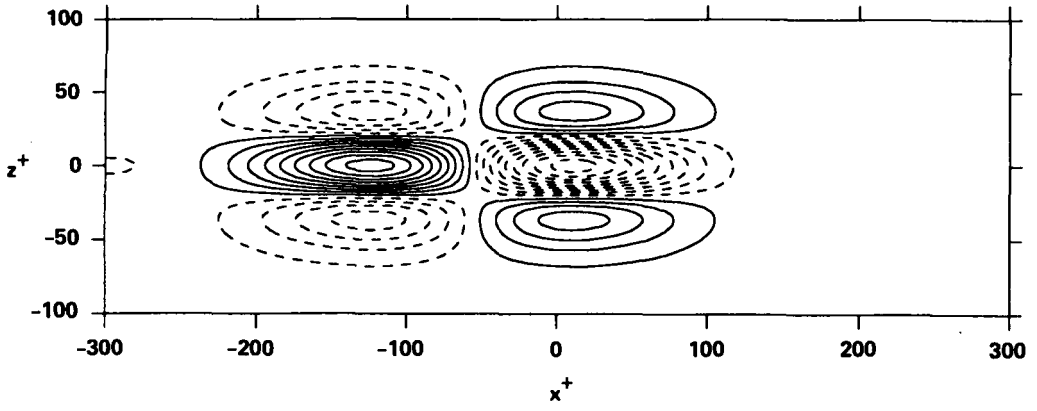

FIGURE 5. Contours at $y^+ = 15$ of streamwise velocity perturbations at $\tau^+ = 0$ according to theoretical model of Figure 2.

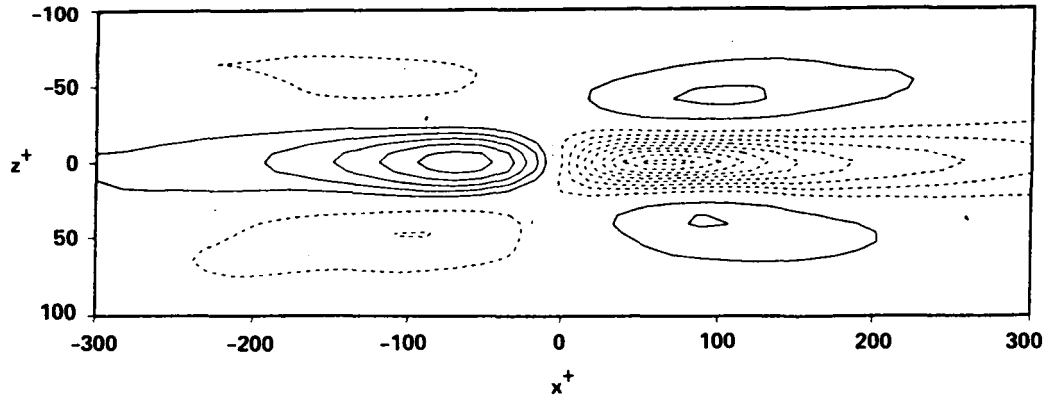

FIGURE 6. Contours at $y^+ = 15$ for VISA-educed structure from numerical simulations (from Alfredsson et al., see Figure3).

by the mean shear. The u-velocity contours in the x, z-plane for $y^+ = 15$ (Figure 5) show spanwise lobes of low velocity outside the high-velocity region and high-speed lobes outside the low-speed region, again in qualitative agreement with the results found from the numerical simulations (Figure 6). The streaky structure becomes more pronounced as time increases, as illustrated in Figure 7.

The major shortcoming of the model appears to be that it underpredicts the length of the downstream low-speed region. This could be a consequence of the assumption of an instantaneous onset of the structure. The results from the numerical simulations indicate that the onset of the bursting motion is not as abrupt as was believed earlier from the results by Kline et al. (1967), but is instead a more gradual process. Such a process, extended in time, would indeed tend to lengthen the downstream region more than the upstream one, as can be seen from (17),(18).

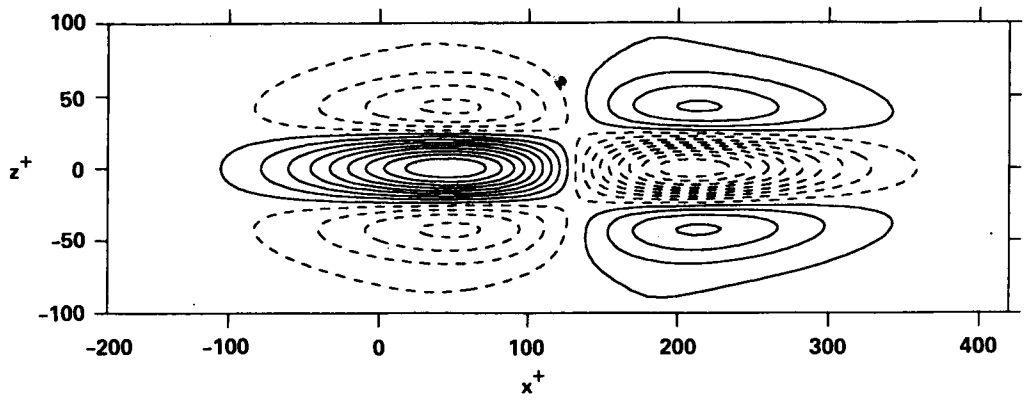

FIGURE 7. Contours of streamwise perturbation velocity for model VITA eddy (see Figure 2) at $\tau^+ = 12$.

7. Discussion and conclusions

The characteristic behavior of the VITA-educed coherent structure may be partly explained on basis of the concept of algebraic instability. From linear inviscid theory one can show (Landahl, 1980) that the kinetic energy of a localized three-dimensional initial disturbances in a parallel shear flow without any inflection point (thus being stable to wave-like disturbances according to the Rayleigh criterion) will, for a broad class of disturbances, increase linearly in time indefinitely after the onset. In the long-time behavior of the disturbance, the streamwise perturbation velocity will eventually reach a finite value, but the streamwise extent of the disturbed region will grow linearly with time, thus making the total kinetic energy, integrated over the streamwise direction, continue to grow linearly for indefinite times. Viscosity will eventually make the disturbance decay, but will take a comparatively long time to make itself felt, so that the early evolution period of the structure is likely to be dominated by inviscid mechanisms.

Further work is needed to clarify the nature of the nonlinear excitation sources. A preliminary analysis of the NASA/Ames numerical simulation data indicates (Landahl, et al. 1987) that the nonlinearity is indeed strongest in the immediate neigborhood of the wall, but the low Reynolds numbers data available to date give information only for a small range of y^+-values outside the near-wall region so that it is difficult to draw any conclusions about the behavior in the outside inviscid region.

REFERENCES

ALFREDSSON, P.H., JOHANSSON, A.V. & KIM, J. 1988 Turbulence production near walls: the role of flow structures with spanwise asymmetry. Proceedings, 2nd Summer Program of the Center for Turbulence Research. NASA Ames/Stanford University.

BLACKWELDER, R.F. & KAPLAN, R.E. 1976 On the wall structure of the turbulent boundary layer. *J. Fluid Mech.* **76**, 89.

BARK, F.H. 1975 On the wave structure of the wall region of a turbulent boundary layer. *J. Fluid Mech70.* **229.**

BREUER, K.S. 1988 The Development of a Localized Disturbance in a Boundary Layer. Mass. Inst. Tech. FDRL Report 88-1.

JOHANSSON, A.J & ALFREDSSON, P.H. 1982 On the structure of turbulent channel flow. *J. Fluid Mech.* **122**, 295.

JOHANSSON, A.V., ALFREDSSON, P.H., & ECKELMANN, H. 1987 On the evolution of shear-layer structures in near-wall turbulence. In *Advances in Turbulence* (eds. Comte-Bellot & Mathieu), Springer, 383.

KIM, H.T., KLINE, S.J. & REYNOLDS, W.C. 1972 The production of turbulence near a smooth wall in a turbulent boundary layer. *J. Fluid Mech.* **50**, 133.

KLINE, S.J, REYNOLDS, W.C., SCHRAUB, F.A. & RUNSTADLER, P.W. 1967 The structure of turbulent boundary layers. *J. Fluid Mech.* **30**, 741.

LANDAHL, M.T. 1967 A wave-guide model for turbulent shear flow. *J. Fluid Mech.* **27**, 443.

LANDAHL, M.T. 1980 A note on algebraic instability of inviscid parallel shear flows. *J. Fluid Mech98.* **243.**

LANDAHL, M.T. 1984a On the dynamics of large eddies in the wall region of a turbulent boundary layer. In *Turbulence and Chaotic Phenomena in Fluids* (ed. T. Tatsumi), Elsevier, 467.

LANDAHL, M.T. 1984b Coherent structures in turbulence and Prandtl's mixing-length theory. Z. Flugwiss. Weltraumforsch. **8**, 233.

LANDAHL, M.T., KIM, J. & SPALART, P.R. 1987 An active-layer model for wall-bounded turbulent shear flows. In *Studying Turbulence Using Numerical Simulation Databases*, NASA Report CTR-S87, 297.

LIGHTHILL, M.J. 1952 On sound generated aerodynamically. I General theory. Proc. R. Soc. London, Ser. **A211 (1107)**, 564.

PRANDTL, L. 1925 Bericht uber Untersuchungen zur ausgebildeten Turbulenz. Z. angew. Math. Mech. **5**, 136.

REICHARDT, H. 1951 Z. angew. Math. Mech. **31**, 208.

RUSSELL, J.M. & LANDAHL, M.T. 1984 The evolution of a flat eddy near a wall in an inviscid shear flow. *Phys. Fluids,27, 557.*

Center for Turbulence Research
Proceedings of the Summer Program 1988

The structure of sheared turbulence near a plane boundary

By MOON J. LEE† AND J. C. R. HUNT‡

An analysis is presented of how a plane boundary affects the structure of turbulence in a sheared free stream. A uniform-shear boundary layer (USBL) is formulated with slip velocity condition at the surface, and inhomogeneous rapid distortion theory is applied. The effects of 'blocking' by the surface on the turbulence structure in USBL is compared with those in the shear-free boundary layer (SFBL).

Shear produces highly anisotropic eddies elongated in the flow direction. The spanwise spectra of the streamwise velocity $\Theta_{11}(\kappa_3; y)$ suggest the existence of the streaky structures in the flow. The mean streak spacing estimated from the energy spectra increases with the distance from the surface, in qualitative agreement with previous measurements and computations.

The vertical velocity variance $\overline{v^2}$ is reduced with shear at all heights, roughly in proportion to the reduction in the homogeneous value, but the shape of the profile remains unchanged only near the surface: $\overline{v^2}/\overline{v^2}^{(H)} \sim y^{2/3}$. The turbulent shear stress $-\overline{uv}$ increases with total shear at all distances from the boundary. Scaled with the homogeneous value, the profile of the shear stress does not vary with time. The universal profile near the surface is $\overline{uv}/\overline{uv}^{(H)} \sim y^{2/3}$, similar to the vertical variance profile.

The streamwise integral scales increase with shear, indicating elongation of the streamwise extent of eddies. It is shown that, at given total shear, the spanwise extent of the streaks determined from $L_{uu}^{(z)}$ widens as the boundary is approached. The smallest of the integral scales, $L_{vv}^{(z)}$, is a measure of the dissipation scale, and decreases with shear in a self-similar way: $L_{vv}^{(z)} \sim y$.

1. Introduction

1.1. *Motivation and background*

In most models of sheared turbulent flows near plane boundaries, it is assumed that the mean 'shear rate' $S = dU/dy$ controls the structure of turbulence, especially the relation between the Reynolds shear stress $-\overline{uv}$ and the energy of the turbulence $q^2 = \overline{u_i u_i}$. There is some support for this assumption when calculations for $\overline{u^2}$ and $-\overline{uv}$ and the cross-correlations $R_{ij}(\mathbf{r})$ in *homogeneous* uniform-shear flows $U = U_0 + Sy$ are compared with computations and measurements in turbulent boundary layers where S is not uniform (Lee, Kim & Moin 1987; Townsend

† Center for Turbulence Research
‡ University of Cambridge

1976). For close agreement between the two situations at a given height y, it was found necessary that the homogeneous shear and the boundary layer should have the same dimensionless shear rate $S^* = SL/q$ (L is an appropriate length scale), and that total shear $\beta = St$ should be chosen appropriately. This homogeneous-shear assumption is the basis of Reynolds-stress transport modelling as explained by Lumley (1978).

However, it is also known that the larger scales of motion (defined as greater than y at a height y) are affected by the boundary, because vertical motions are *blocked* at $y = 0$ (Bradshaw 1967; Townsend 1961). In turbulent flows, *without* shear near a *rigid* boundary or density interfaces, previous investigations (experimental, theoretical and computational) have shown that the blocking effect changes the variances of the different turbulence components $\overline{u^2}$, $\overline{v^2}$, $\overline{w^2}$, and the length scales. The largest effect is on the variance and the streamwise integral scale $L_{22}^{(x)}$ of the normal component $\overline{v^2}$; near the boundary, $\overline{v^2} \sim y^{2/3}$ and $L_{22}^{(x)} \sim y$ (Hunt & Graham 1978; Hunt 1984).

Since there are many interesting and important turbulent flows near flat boundaries in which there are quite different shear rates, it is important to understand and quantify the effect of blocking by a surface in the presence of shear.

There have been previous unpublished studies using rapid distortion theory by Maxey (1978) and Durbin (1979).

Hunt, Moin, Moser & Spalart (1987*a*) analysed the correlations between two points y and y_0 ($y \leq y_0$) of the normal velocity component, $\widetilde{R}_{22}(y_0, y)$ using direct numerical simulations. It was found that the two-point correlation is, as hypothesised, a function of y/y_0, but the form differs from the linear profile in shear-free boundary layers (Hunt 1984), and is less than y/y_0 (figure 1).

Hunt, Spalart & Mansour (1987*b*) examined the variation of the *dissipation length* L_ϵ defined as $\epsilon/\overline{v^2}^{3/2}$. They compared computations in the boundary layer and channel flow with a simple model $L_\epsilon^{-1} = A_B/y + A_S\,(dU/dy)/\overline{v^2}^{1/2}$ (Hunt, Stretch & Britter 1988). The two terms represent the effect of blocking and shear, respectively. Good agreement was found except at the outer edge of the boundary layer. The *sensitivity* to shear of the *dissipation scale* is clearly much greater than for the cross-correlations $\widetilde{R}_{22}$ and $\widetilde{R}_{12}$, which are dominated by blocking. An important aim of the present work is to explain this difference by looking closely at different length scales.

1.2. *Uniform-shear boundary layer*

It is possible to use Rapid Distortion Theory (RDT) to study how homogeneous turbulence in a uniform shear is deformed when a plate is suddenly introduced into the flow at time $t = 0$. The analysis is *inviscid* so the only effect of the plate is to block velocity fluctuations normal to itself. In addition, the *mean* velocity profile is not changed. Because the mean vorticity remains *uniform*, this leads to a great simplification in the analysis. In reality, the presence of the wall leads to Reynolds stress gradients, which would over a long period affect the mean velocity profile; this is the effect we ignore here.

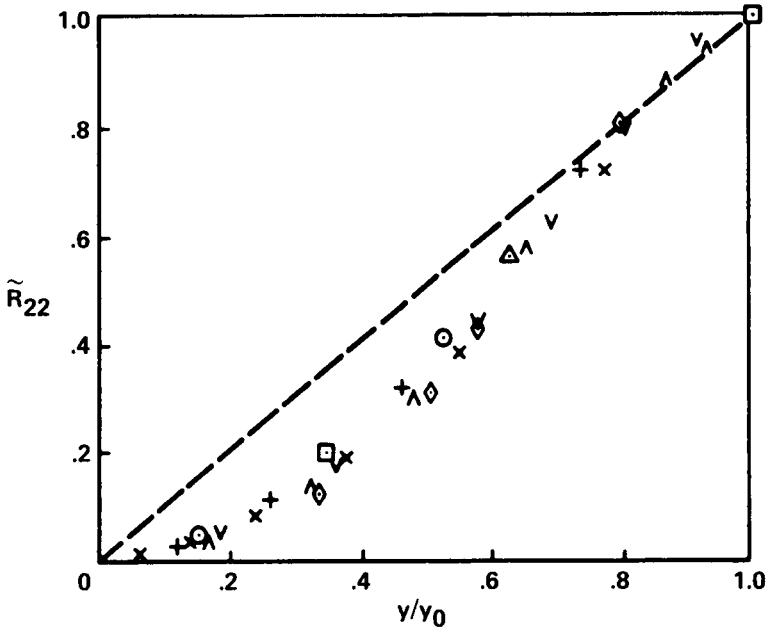

FIGURE 1. Cross-correlation of v at heights y_0 and y, normalized by $\overline{v^2}(y_0)$ computed from numerical simulations (turbulent boundary layer, Spalart 1987; plane channel flow, Kim, Moin & Moser 1987). Symbols, data from numerical simulation; — — — —, theoretical prediction and data for SFBL (Hunt 1984): $\widetilde{R}_{22} \simeq y/y_0$. [From Hunt *et al.* (1987*a*).]

The detailed aspect of the analysis that needs considering is the difference between the blocking effect of the boundary on the sheared turbulence compared with unsheared turbulence. In a shear-free boundary layer (SFBL), there is *isotropic* turbulence in the free stream, which leads to both horizontal components $\overline{u^2}$ and $\overline{w^2}$ increasing equally near the wall as a result of the irrotational fluctuation being axisymmetric about the y-axis. However, in a uniform-shear boundary layer (USBL), the turbulence in the free stream above the surface is quite *anisotropic*. This leads to a different redistribution of energy between u and w at the surface (Wong 1987) and a change in the interaction with the mean shear. This question has not been analysed in detail before.

The particular computations that are presented here are: (i) the variation with y of the one-dimensional spectra $\Theta_{ij}(\kappa_1; y)$ and $\Theta_{ij}(\kappa_3; y)$ at different total shear $\beta = St$; (ii) the Reynolds stresses $\overline{u_i u_j}$ as a function of y; and (iii) the variation with y of the integral length scales in the homogeneous directions (x, z) of the different velocity components $L_{ij}^{(x_k)}$. The smallest of these integral scales is usually a good indicator of the dissipation scale L_ϵ, though this point has not been investigated systematically!

2. Analysis

2.1. *Formulation of the problem*

We summarize here the assumptions, equations and boundary conditions governing the linearised (RDT) analysis of a turbulent velocity field $\mathbf{u}(\mathbf{x},t)$ in a uniform shear flow $\mathbf{U} = (U_0 + Sy, 0, 0)$ (see figure 2).

The condition for ignoring the nonlinear inertial terms over the period of the distortion is that the shear is strong enough for the straining terms to dominate over nonlinear inertial terms, that is

$$S^* = SL/q \gg 1. \tag{2.1}$$

Over a period of time, the small nonlinear terms affect the redistribution of turbulence energy and momentum between different components. If $S^* \sim 1$, this relaxation time t_r is of order L/q, so the criterion for importance of nonlinear terms is that

$$t > t_r \sim L/q \tag{2.2}$$

(Gartshore, Durbin & Hunt 1983; Bertoglio 1986).

But if S^* is large, the rate at which the anisotropy is growing by linear processes is so much greater than by nonlinear processes that, as Lee *et al.* (1987) have shown, the nonlinear redistributive processes are negligible (especially for $\overline{u^2}$ and $\overline{uv}$) even when $t \geq t_r$.

For the linearised analysis of the USBL, it is also necessary to assume that the gradient of the Reynolds stress has a weak effect on the mean velocity profile over the time T_D of distortion:

$$T_D \left| -\frac{\partial^2 \overline{uv}}{\partial y^2} \right| \ll S \tag{2.3a}$$

or

$$S^* = SL/q \gg qT_D/L. \tag{2.3b}$$

The inviscid analysis used here can only correspond to physical experiments involving a real viscous fluid, if the viscous stresses are negligible within the flow for energy-containing eddies and if the no-slip boundary condition can be neglected (see figure 2). Hunt & Graham's (1978) detailed analysis of both these effects led to the following conditions for neglecting them:

$$qL/\nu \gg 1, \tag{2.4}$$

$$\sqrt{\nu T_D} \ll L \quad \text{and} \quad \delta_v \ll L, \tag{2.5a,b}$$

where δ_v is the thickness of the viscous layer on the surface, which must exist if the velocity U_0 of the free stream at $y = 0$ is not equal to the velocity of the surface U_b (figure 2*b*-i). If $U_b = U_0$, as in the moving-belt experiment of Uzkan & Reynolds (1967) and Thomas & Hancock (1977), there is no *mean* boundary layer, but the

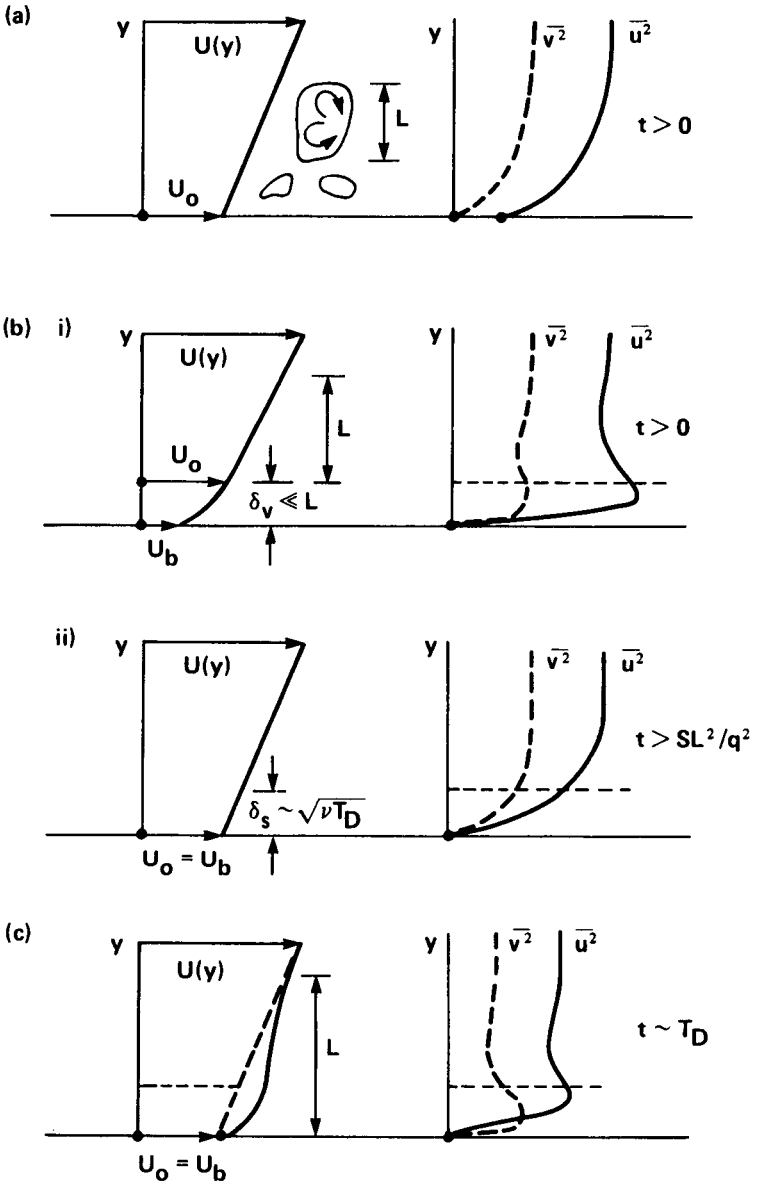

FIGURE 2. Schematic diagram of a uniform-shear boundary layer (USBL), showing (*a*) the ideal problem; (*b*) the experimental reality: (i) if $U_b \neq U_0$, theory requires $\delta_v \ll L$, (ii) if $U_b = U_0$, theory requires $\delta_s \sim \sqrt{\nu T_D} \ll L$; (*c*) the slow distortion of the mean velocity profile ($t \sim T_D$) because of the Reynolds-shear-stress gradient.

fluctuating velocity must still be zero. This thin surface layer affected by this no-slip fluctuating condition is of order $\sqrt{\nu T_D}$ (figure 2*b*-ii).

Given the assumptions (2.1) to (2.5), the equations for the linearised problem are

$$\frac{\overline{D}\mathbf{u}}{Dt} = -\nabla p - Sv\mathbf{i}, \tag{2.6}$$

$$\nabla \cdot \mathbf{u} = 0, \tag{2.7}$$

where $\overline{D}/Dt = \partial/\partial t + U\partial/\partial x$, $\mathbf{U} = (U_0 + Sy, 0, 0)$ and p is the kinematic pressure fluctuation. The initial and boundary conditions are given by

$$\mathbf{u}(\mathbf{x}, t) = \mathbf{u}^{(\mathrm{H})}(\mathbf{x}, t) \quad \text{at} \quad t = 0, \tag{2.8a}$$

where $\mathbf{u}^{(\mathrm{H})}$ is a prescribed random velocity field, and

$$v(x, y = 0, z, t) = 0 \quad \text{for} \quad t > 0. \tag{2.8b}$$

The analytical solution is obtained as a sum of the homogeneous flow field, $\{\mathbf{u}^{(\mathrm{H})}, p^{(\mathrm{H})}\}(\mathbf{x}, t)$, subject to uniform shear, and the blocking flow field induced by the surface, $\{\mathbf{u}^{(\mathrm{B})}, p^{(\mathrm{B})}\}(\mathbf{x}, t)$:

$$\mathbf{u}(\mathbf{x}, t) = \mathbf{u}^{(\mathrm{H})}(\mathbf{x}, t) + \mathbf{u}^{(\mathrm{B})}(\mathbf{x}, t), \tag{2.9a}$$

$$p(\mathbf{x}, t) = p^{(\mathrm{H})}(\mathbf{x}, t) + p^{(\mathrm{B})}(\mathbf{x}, t). \tag{2.9b}$$

Then, $\mathbf{u}^{(\mathrm{H})}(\mathbf{x}, t)$ satisfies (2.6) subject to (2.8*a*) at $t = 0$; it does *not* satisfy (2.8*b*). But $\mathbf{u}^{(\mathrm{B})}(\mathbf{x}, t)$ satisfies (2.6) subject to

$$v^{(\mathrm{B})}(\mathbf{x}, t) = 0 \quad \text{at} \quad t = 0. \tag{2.10a}$$

From (2.8) and (2.9), it can be shown that

$$v^{(\mathrm{B})}(x, y = 0, z, t) = -v^{(\mathrm{H})}(x, y = 0, z, t) \quad \text{for} \quad t > 0, \tag{2.10b}$$

and

$$\mathbf{u}^{(\mathrm{B})}(\mathbf{x}, t) \to 0 \quad \text{as} \quad y \to \infty. \tag{2.10c}$$

By taking the curl of (2.6), it follows that

$$\frac{\overline{D}}{Dt}\nabla^2 v^{(\mathrm{B})} = 0. \tag{2.11}$$

So from (2.10*a*), one finds that this equation for $v^{(\mathrm{B})}(\mathbf{x}, t)$ reduces to Laplace's equation: $\nabla^2 v^{(\mathrm{B})} = 0$. Once $v^{(\mathrm{B})}(\mathbf{x}, t)$ is obtained, $p^{(\mathrm{B})}(\mathbf{x}, t)$ is obtained from

$$\nabla^2 p^{(\mathrm{B})} = -2S\frac{\partial v^{(\mathrm{B})}}{\partial x}. \tag{2.12}$$

Thence from (2.6), $w^{(\mathrm{B})}(\mathbf{x}, t)$ and $u^{(\mathrm{B})}(\mathbf{x}, t)$ are calculated.

The statistical and Fourier analyses are similar to the method for *inhomogeneous* RDT developed by Hunt (1973), and used for SFBL by Hunt & Graham (1978) and for a uniform-shear layer by Gartshore, Durbin & Hunt (1983).

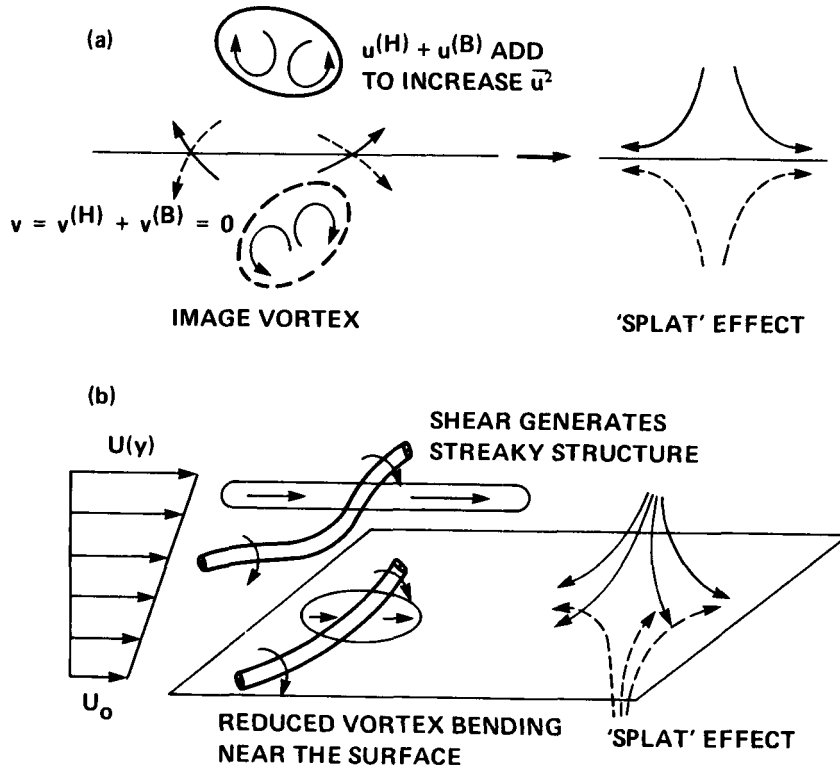

FIGURE 3. Schematic diagram to show difference between the mechanisms for shear-free boundary layer (SFBL) and for uniform-shear boundary layer (USBL): (*a*) SFBL, image vortex below $y = 0$ induces irrotational velocity $\mathbf{u}^{(B)}$ above $y = 0$; (*b*) USBL, reduced vortex bending near the surface reduces $\overline{u^2}$ while the splat effect increases $\overline{u^2}$.

2.2. *Physical interpretation*

The difference in their mechanics between a shear-free boundary layer (SFBL) and a uniform-shear boundary layer (USBL) can be understood from the linearised vorticity equation obtained by taking the curl of (2.6):

$$\frac{\overline{D}\boldsymbol{\omega}}{\overline{D}t} = (\boldsymbol{\omega}\cdot\nabla)\mathbf{U} + (\boldsymbol{\Omega}\cdot\nabla)\mathbf{u}. \tag{2.13}$$

In a SFBL where $\nabla\mathbf{U} = 0$ and $\boldsymbol{\Omega} = 0$, this equation reduces to

$$\frac{\overline{D}\boldsymbol{\omega}}{\overline{D}t} = 0. \tag{2.14}$$

The effect of the boundary is simply to introduce an *irrotational* velocity field, so the vorticity is not affected by the boundary, i.e.

$$\mathbf{u}^{(B)}(\mathbf{x},t) = \nabla\phi(\mathbf{x},t), \qquad \boldsymbol{\omega}(\mathbf{x},t) = \boldsymbol{\omega}^{(H)}(\mathbf{x},t). \tag{2.15}$$

This irrotational velocity field induced by image vorticity below $y = 0$ produces the *splat* effect: the vertical component $v^{(B)}$ blocks $v^{(H)}$ so that $v = 0$ at $y = 0$, while the horizontal components add to increase $\overline{u^2}$ and $\overline{w^2}$ (figure 3*a*).

But in a USBL the addition of the blocking velocity field $\mathbf{u}^{(B)}(\mathbf{x}, t)$ affects $\boldsymbol{\omega}$ because of the term $(\boldsymbol{\Omega}\cdot\nabla)\mathbf{u}$, which is the effect of velocity perturbations distorting the vorticity $\boldsymbol{\Omega} = (0, 0, \Omega_z)$ of the mean shear. The terms $\Omega_z \partial v/\partial z$ and $\Omega_z \partial w/\partial z$ primarily determine ω_y and ω_z, and u has contributions from $\Omega_z \int_0^z \omega_y \, dz \sim \Omega_z v$ and $\Omega_z \int_0^y \omega_z \, dy \sim \Omega_z \int \partial v/\partial y \, dy \sim \Omega_z v$. (Note that in a shear flow the eddies are elongated in the flow direction, so $\partial u/\partial x \ll \partial v/\partial y$.) Thus, near the boundary, as v decreases, $\overline{u^2}$ and $-\overline{uv}$ also decreases. However, in the USBL, there is also a tendency of $\overline{u^2}$ and $\overline{w^2}$ to *increase* because of the impacting (or splatting) of the normal fluctuations at the boundary. The analysis shows the different contributions by these two mechanisms.

3. Results and discussion

We assume here that the initially homogeneous turbulence is isotropic and has the von Kármán spectrum of the dimensionless form

$$E^{(H)}(\kappa) = \frac{A\kappa^4}{(c_K + \kappa^2)^{2+\mu}} \tag{3.1}$$

where $\mu = \frac{5}{6}$, $A = \frac{55}{9\pi} c_K^{\mu}$ and $c_K = 0.558$. Note that this spectrum behaves as κ^4 in low-wavenumber region ($\kappa \ll 1$) and has the $\kappa^{-5/3}$ Kolmorogov form at high wavenumbers ($\kappa \gg 1$). All the quantities are made dimensionless by the initial r.m.s. velocity u_0 and integral length scale L_0. Note that in USBL the turbulence quantities change with total shear $\beta = St$. In order to highlight the effects of shear on turbulence structure near a boundary, comparison is made with the results for SFBL ($\beta = 0$) (for details, see Hunt & Graham 1978; Hunt 1984).

3.1. *Energy spectra*

In figure 4, the one-dimensional energy spectra $\Theta_{ij}(\kappa_1; y)$ are plotted for SFBL. When the turbulence is unsheared, the near-wall behavior of the spectra is such that there is no variation in $\Theta_{11}(\kappa_1 \to 0; y)$, but the increase in $\Theta_{33}(\kappa_1 \to 0; y)$ exactly balances the reduction in $\Theta_{22}(\kappa_1 \to 0; y)$, viz.

$$\Theta_{11}^{SFBL}(\kappa_1 \to 0; y) = \Theta_{11}^{(H)}(\kappa_1 \to 0) = 1/\pi, \tag{3.2}$$

$$\Theta_{22}^{SFBL}(\kappa_1 \to 0; y \to 0) + \Theta_{33}^{SFBL}(\kappa_1 \to 0; y \to 0) = 1/\pi, \tag{3.3}$$

where $\Theta_{ij}^{(H)}(\kappa_1)$ are the one-dimensional energy spectra of the initially homogeneous, isotropic turbulence, i.e. $\Theta_{ij}(\kappa_1; y \to \infty, t = 0)$. Similar results can be found by a symmetry consideration: $\Theta_{33}^{SFBL}(\kappa_3 \to 0; y) = \Theta_{33}^{(H)}(\kappa_3 \to 0) = 1/\pi$, $\Theta_{11}^{SFBL}(\kappa_3 \to 0; y \to 0) + \Theta_{22}^{SFBL}(\kappa_3 \to 0; y \to 0) = 1/\pi$. Asymptotic analysis (Hunt & Graham 1978) shows that near the surface

$$\Theta_{22}^{SFBL}(\kappa_1 \to 0; y \to 0) = \Theta_{22}^{SFBL}(\kappa_3 \to 0; y \to 0) \sim y^{5/3}. \tag{3.4}$$

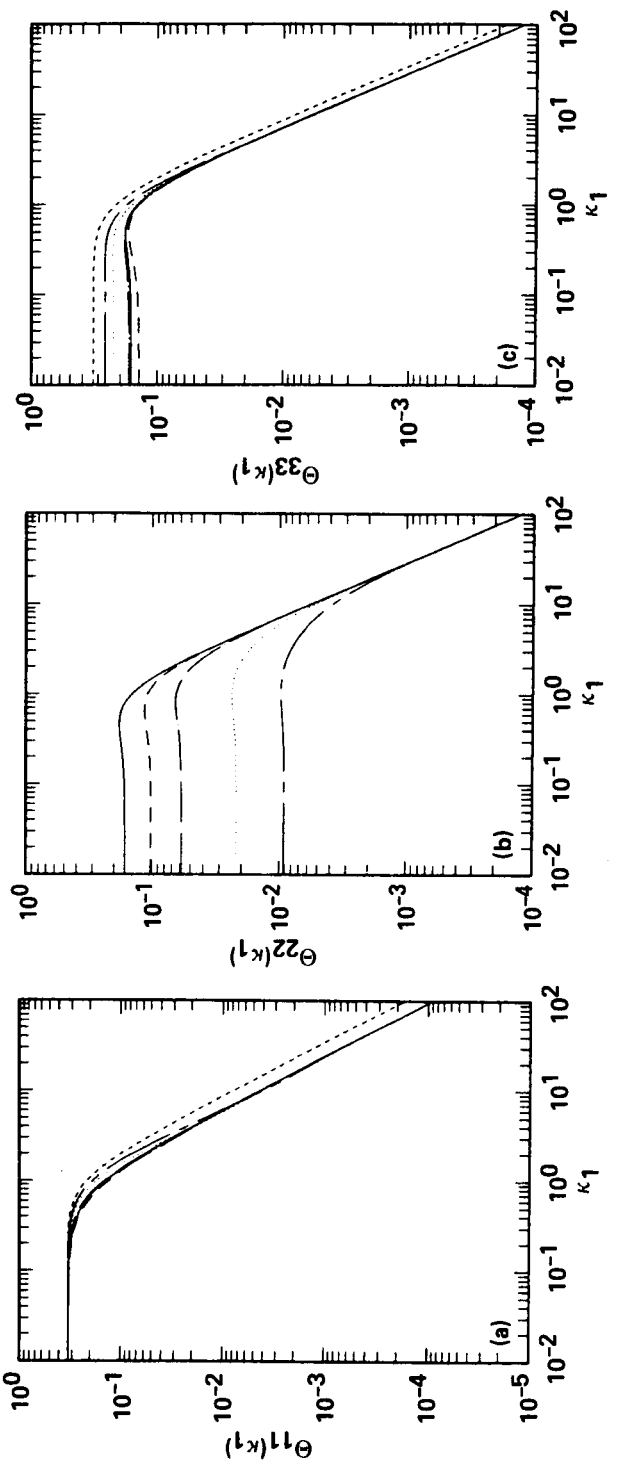

FIGURE 4. The one-dimensional energy spectra in SFBL ($\beta = 0$): (*a*) $\Theta_{11}(\kappa_1; y)$; (*b*) $\Theta_{22}(\kappa_1; y)$; (*c*) $\Theta_{33}(\kappa_1; y)$. - - -, $y = 0$; ——, $y = 0.1$; ....., $y = 0.2$; —·—, $y = 0.5$; — — —, $y = 1$; ——, $y = 5$.

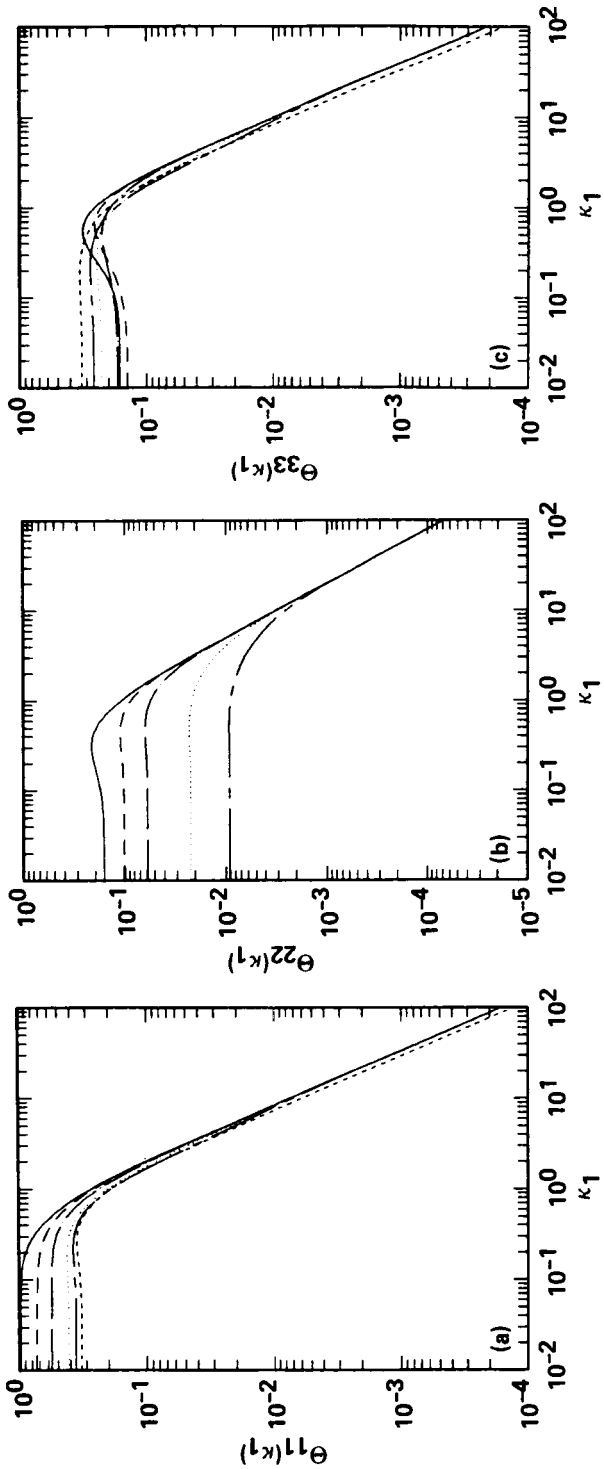

FIGURE 5. The one-dimensional energy spectra in USBL ($\beta = 2$): (*a*) $\Theta_{11}(\kappa_1; y)$; (*b*) $\Theta_{22}(\kappa_1; y)$; (*c*) $\Theta_{33}(\kappa_1; y)$. ----, $y = 0$; — — —, $y = 0.1$; ....., $y = 0.2$; —·—, $y = 0.5$; — — — —, $y = 1$; ———, $y = 5$.

In order to examine the effect of shear on the energy spectra, the results for USBL (when $\beta = 2$) are shown in figure 5. The most salient feature is that, as $\kappa_1 \to 0$, there is a dramatic increase with shear in the spectrum $\Theta_{11}(\kappa_1; y)$ of the streamwise velocity at distances away from the surface (cf. figures 4*a* and 5*a*). However, near the surface the spectrum is *not* affected by shear

$$\Theta_{11}^{\text{USBL}}(\kappa_1 \to 0; y \to 0) = \Theta_{11}^{\text{SFBL}}(\kappa_1 \to 0; y) = 1/\pi. \tag{3.5}$$

That is, very close to the surface, the streamwise motion of large-scale eddies is dominated by the induced image vortices as shown in figure 3(*a*), independent of shearing in the free stream. In contrast, shear does not change the values of $\Theta_{22}(\kappa_1 \to 0; y)$ and $\Theta_{33}(\kappa_1 \to 0; y)$ for *all* y:

$$\Theta_{22}^{\text{USBL}}(\kappa_1 \to 0; y) = \Theta_{22}^{\text{SFBL}}(\kappa_1 \to 0; y), \tag{3.6a}$$

$$\Theta_{33}^{\text{USBL}}(\kappa_1 \to 0; y) = \Theta_{33}^{\text{SFBL}}(\kappa_1 \to 0; y). \tag{3.6b}$$

At high wavenumbers, however, the spectrum $\Theta_{22}(\kappa_1; y)$ of the component normal to the boundary is significantly reduced by shear for all y (cf. figures 4*b* and 5*b*), which implies that the vertical motion of small-scale eddies is sensitive to shear. Interestingly enough, $\Theta_{11}(\kappa_1; y \to 0)$ is reduced much more in the high-wavenumber region ($\kappa_1 > 1$) than it is enhanced at low wavenumbers ($\kappa_1 < 1$); in fact, $\overline{u^2}$ on the surface in the USBL is lower than the SFBL value: $\overline{u^2}(y = 0) < \frac{3}{2}$.

It is of fundamental importance to observe the peaks in the spanwise spectrum $\Theta_{11}(\kappa_3; y)$ of the streamwise velocity (figure 6*a*), which implies the existence of eddies at the corresponding spanwise scales. The peaks in $\Theta_{11}(\kappa_3; y)$ at distances away from the wall and the high streamwise velocity variance (see figure 9) are direct evidence of the presence of *streaky structures* in the flow (see Kline *et al.* 1967). Notice that the peaks are much more discernible in the spectra at heights away from the wall, consistent with the earlier observation of the low- and high-speed streaks in homogeneous shear flow where there is no boundary (Lee *et al.* 1987). The fact that the streaks exist in sheared turbulence, independent of the presence of the boundary, but not in the SFBL strongly supports the assertion put forward by Lee *et al.* that the main mechanism of generating the streaks is the mean shear but not the wall blocking. This is supported also by the experiment of Uzkan & Reynolds (1967).

As shear increases, the peak in the spectrum (or streaks) is discernible at heights closer to the wall (e.g. for $\beta = 4$, see figure 6*b*). This means that, as shear is prolonged, the lateral extent of the streaks are mainly controlled by the effect of shear rather than by the blocking effect. Note that other aspects of the turbulence (e.g. $\overline{v^2}$ and $-\overline{uv}$) remain affected by the blocking whatever the total shear.

It is of interest to examine how the mean spacing λ_z between the streaks varies with the distance from the surface. The mean streak spacing is determined from the wavenumber $\kappa_3^{(s)}$ at which $\Theta_{11}(\kappa_3; y)$ peaks, i.e. $\lambda_z = 1/\kappa_3^{(s)}$. It is clear from figure 7 that λ_z increases with y, in qualitative agreement with measurements and computations in turbulent boundary layers (Kline *et al.* 1967; Kim *et al.* 1987).

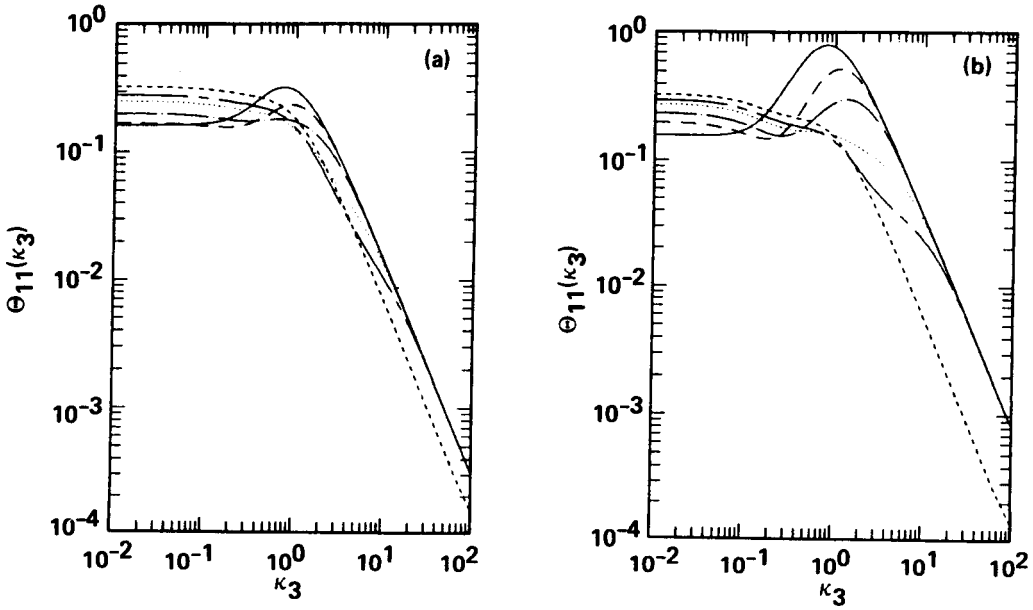

FIGURE 6. The one-dimensional energy spectra $\Theta_{11}(\kappa_3; y)$ in USBL: (*a*) $\beta = 2$; (*b*) $\beta = 4$. ----, $y = 0$; — — —, $y = 0.1$; ·····, $y = 0.2$; —·—, $y = 0.5$; — — — —, $y = 1$; ——, $y = 5$.

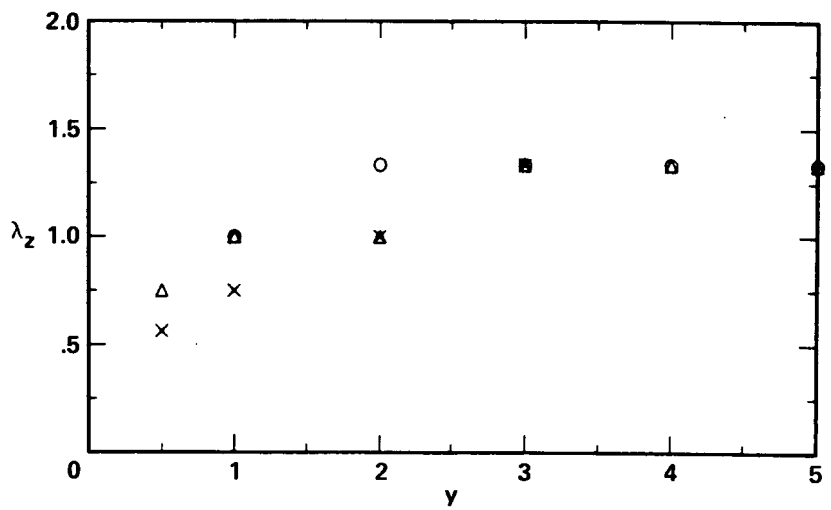

FIGURE 7. Variation with the distance from the boundary of the mean streak spacing, λ_z, determined from the wavenumber at which $\Theta_{11}(\kappa_3; y)$ peaks. ○, $\beta = 2$; △, $\beta = 4$; ×, $\beta = 8$.

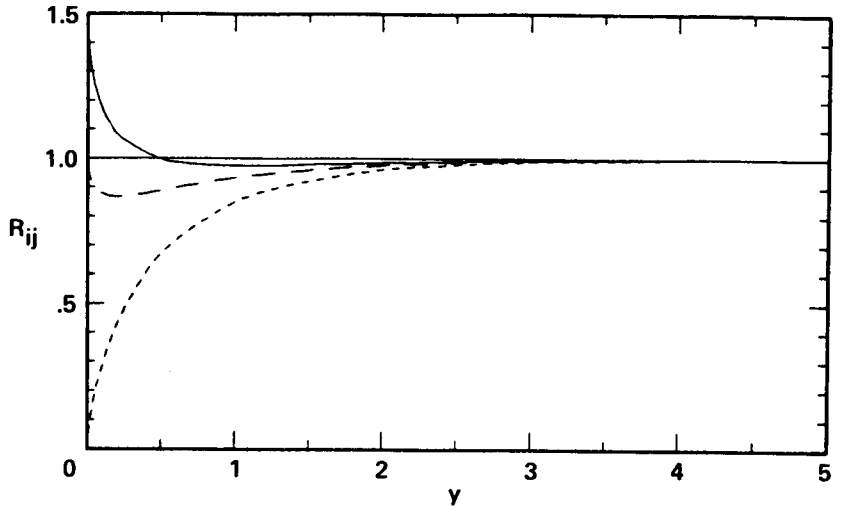

FIGURE 8. Profile of the Reynolds stresses in SFBL ($\beta = 0$). ——— , $\frac{1}{3}\overline{u_i u_i}$; ——— , $\overline{u^2} = \overline{w^2}$; ---- , $\overline{v^2}$.

The spanwise spectrum $\Theta_{33}(\kappa_3; y)$ of the spanwise velocity fluctuation as $\kappa_3 \to 0$ is unchanged for *all* y:

$$\Theta_{33}^{\text{USBL}}(\kappa_3 \to 0; y) = \Theta_{33}^{\text{SFBL}}(\kappa_3 \to 0; y) = \Theta_{33}^{(\text{H})}(\kappa_3 \to 0) = 1/\pi. \tag{3.7}$$

Thus, (3.7) and (3.6*b*) indicate that in this flow the large-scale spanwise fluctuation is not affected by shear (cf. figs. 4*c* and 5*c*). Also note that

$$\Theta_{11}^{\text{USBL}}(\kappa_3 \to 0; y \to 0) = \Theta_{11}^{\text{SFBL}}(\kappa_3 \to 0; y \to 0) = 1/\pi. \tag{3.8}$$

3.2. *Reynolds stresses*

In figure 8, the Reynolds stresses $\overline{u_i u_j}$ are shown as functions of y for SFBL. In SFBL, if the homogeneous field is isotropic, the horizontal variances are equal, $\overline{u^2} = \overline{w^2}$, for all y. Near the surface, the splat effect results in transfer of energy from the vertical component to the horizontal components:

$$\left.\begin{aligned} &\overline{u^2}(y \to 0) = \overline{w^2}(y \to 0) = \tfrac{3}{2} - O(y^{2/3}), \\ &\overline{v^2}(y \to 0) \sim y^{2/3} \end{aligned}\right\} \quad \text{in SFBL.} \tag{3.9a,b}$$

The horizontal variances are decreased from the wall value to the homogeneous value of unity within about $y = 0.5$ from the wall. The vertical variance $\overline{v^2}$ shows

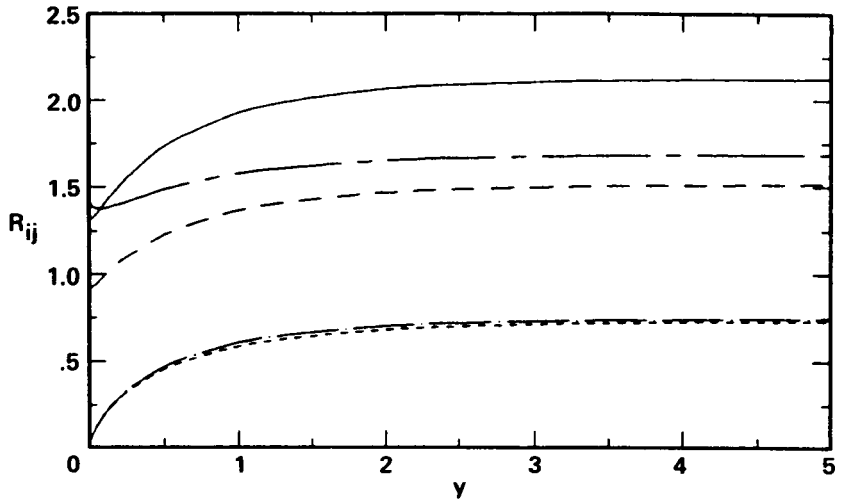

FIGURE 9. Profile of the Reynolds stresses in USBL ($\beta = 2$). ————, $\frac{1}{3}\overline{u_i u_i}$; ——, $\overline{u^2}$; ----, $\overline{v^2}$; — — —, $\overline{w^2}$; —·—, $-\overline{uv}$.

monotonic increase from zero at the wall to 95% of its homogeneous value (unity) over a distance of about 2.

Variation of the kinetic energy in SFBL is not monotonic. Except at the surface where $q^2/q_0^2 = 1$, the kinetic energy is less than its homogeneous value; the ratio q^2/q_0^2 attains its minimum value of about 0.85 at $y \simeq 0.2$.

Figure 9 shows the profile of the Reynolds stresses in USBL ($\beta = 2$). An important aspect of USBL is the increase of the turbulent kinetic energy by the transfer from the mean flow to turbulence (i.e. turbulence production). Therefore, the kinetic energy is much larger in USBL than in SFBL (except in the vicinity of the surface), e.g. 50% increase in the homogeneous value when $\beta = 2$ (cf. figues 8 and 9). The dip near the surface (at $y \simeq 0.2$ when $\beta = 2$) is a direct consequence of the reduction of the horizontal variances there, as explained below. Note that in USBL the turbulent kinetic energy at the surface is not equal to the homogeneous value, unlike in SFBL.

In USBL the horizontal variances $\overline{u^2}$ and $\overline{w^2}$ are markedly enhanced by shear except very close to the wall. The reduction of these variances can be explained by the effect of the reduced bending of vortex filaments (see figure 3*b*); the spanwise variance $\overline{w^2}$ is less reduced than the streamwise variance $\overline{u^2}$.

Comparison of the vertical variance $\overline{v^2}$ in figures 8 and 9 shows that there is a substantial reduction with shear at all heights. [The apparently coincidental profiles of $\overline{v^2}$ and $-\overline{uv}$ in the figure 9 is incidental at this particular time ($\beta = 2$).] It is interesting to consider how $\overline{v^2}$ in the vicinity of the boundary changes with shear.

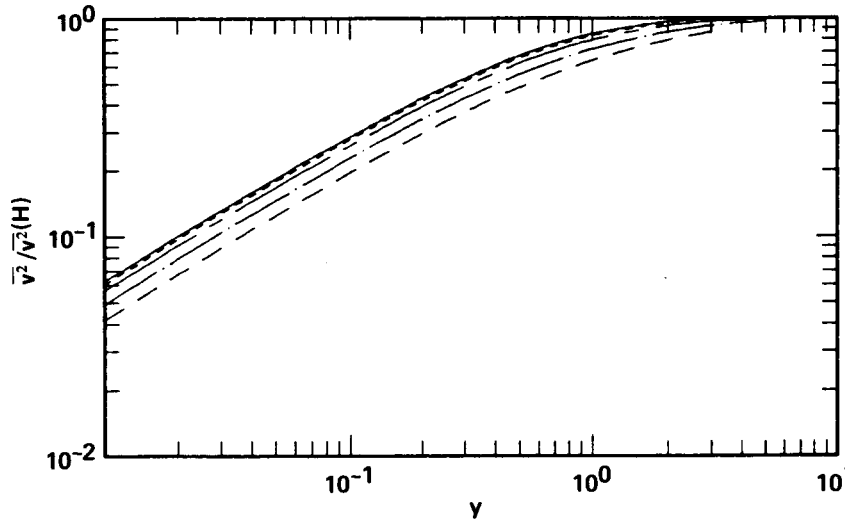

FIGURE 10. Variation of the vertical variance profile with total shear: $\overline{v^2}/\overline{v^2}^{(H)}$ *vs.* y. ——, $\beta = 0$; - - - -, $\beta = 1$; — - —, $\beta = 2$; — · —, $\beta = 4$; — — — —, $\beta = 8$.

When scaled by the homogeneous value $\overline{v^2}^{(H)}$, the profiles of $\overline{v^2}$ at different values of β show (figure 10) that as $y \to 0$

$$\overline{v^2}(y \to 0, \beta) \sim \overline{v^2}^{(H)}(\beta)\, y^{2/3} \quad \text{in USBL.} \tag{3.10}$$

Another important difference in USBL is the development of the turbulent shear stress $-\overline{uv}$ with shear. Note that the shear stress is also subject to reduction by the wall blocking. The profile of the shear stress exhibits a monotonic increase from zero at the wall towards the homogeneous value that increases with shear. Thus, the same scaling used for $\overline{v^2}$ is used for the shear stress: as $y \to 0$,

$$\overline{uv}(y \to 0, \beta) \sim \overline{uv}^{(H)}(\beta)\, y^{2/3} \quad \text{in USBL.} \tag{3.11}$$

Figure 11 shows $\overline{uv}/\overline{uv}^{(H)}$ as a function of y at different times. This function does not change with total shear. It is within 20% of the value of $\overline{v^2}/\overline{v^2}^{(H)}$ at $\beta = 0$.

3.3. *Integral length scales*

Integral length scales in the x_m-direction of the correlations between the velocity components u_i and u_j at y are defined as

$$L_{ij}^{(x_m)}(y) = \frac{\pi \Theta_{ij}(\kappa_m = 0; y)}{\overline{u_i u_j}(y)} \quad \text{(no sum on } i \text{ and } j\text{)}. \tag{3.12}$$

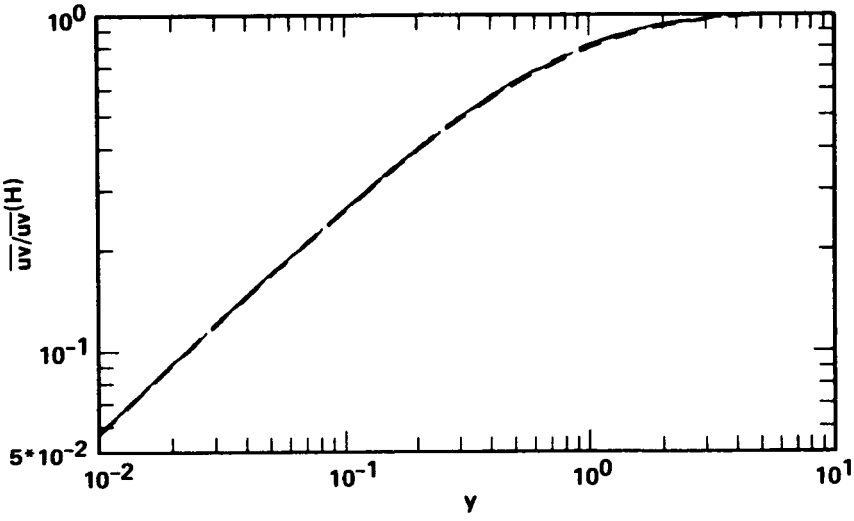

FIGURE 11. Variation of the turbulent shear-stress profile with total shear: $\overline{uv}/\overline{uv}^{(H)}$ *vs.* y. ----, $\beta = 1$; — — —, $\beta = 2$; — · —, $\beta = 4$; — — — —, $\beta = 8$.

Profiles of the streamwise integral scales $L_{uu}^{(x)}$, $L_{vv}^{(x)}$ and $L_{ww}^{(x)}$ in SFBL are shown in figure 12. Very close to the wall, the streamwise scale of the vertical velocity grows faster than that of the streamwise velocity; from (3.2), (3.4) and (3.9*a*,*b*), one finds

$$L_{uu}^{(x)}(y \to 0) = \tfrac{2}{3} + O(y^{2/3}), \quad L_{vv}^{(x)}(y \to 0) \sim y \quad \text{in SFBL.} \tag{3.13a,b}$$

However, over a distance until $L_{uu}^{(x)}$ reaches the homogeneous value of unity ($0.1 < y < 0.5$, say), the growth rate of $L_{uu}^{(x)}$ is higher. The integral scale of the spanwise velocity $L_{ww}^{(x)}$ exhibits a monotonic decrease.

Profiles of the streamwise integral length scales in USBL are plotted in figure 13. The effect of shear is to increase the streamwise scales of the streamwise and vertical velocity fluctuations, $L_{uu}^{(x)}$ and $L_{vv}^{(x)}$, and to reduce the scale of the spanwise fluctuation, $L_{ww}^{(x)}$, for all heights from the boundary. The increase of $L_{uu}^{(x)}$ indicates elongation with shear of the streamwise extent of the streaks. The near-wall behavior of the integral length scales can be found from (3.5)–(3.8) and (3.10):

$$\left.\begin{aligned} &L_{uu}^{(x)}(y \to 0) = L_{uu}^{(x)}(y \to 0) = 1/\overline{u^2}, \\ &L_{vv}^{(x)}(y \to 0) \sim y/\overline{v^2}^{(H)}, \\ &L_{ww}^{(x)}(y \to 0) = L_{ww}^{(x)}(y \to 0) = 1/\overline{w^2} \end{aligned}\right\} \quad \text{in USBL.} \tag{3.14a,b,c}$$

Near the boundary the scales of the horizontal components decrease with shear, but $L_{vv}^{(x)}$ increases with shear.

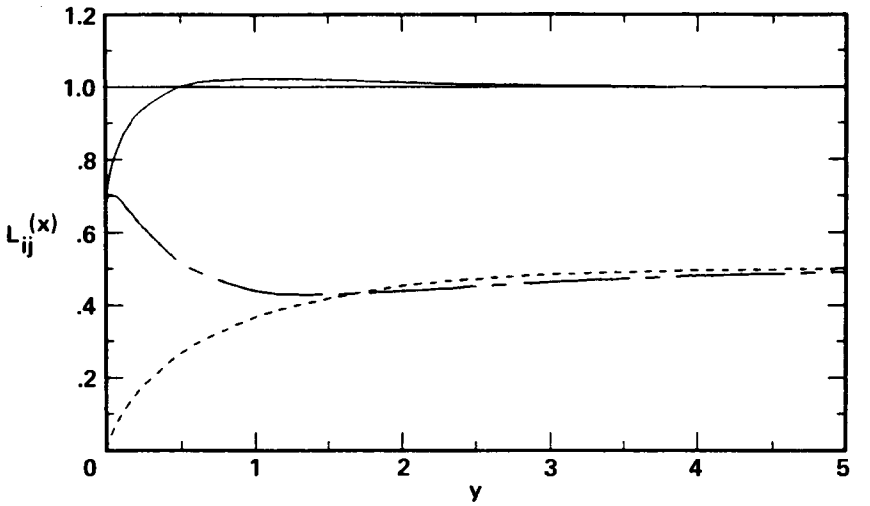

FIGURE 12. Profile of the streamwise integral scales $L_{ij}^{(x)}(y)$ for SFBL ($\beta = 0$). ——, $L_{uu}^{(x)} = L_{ww}^{(z)}$; - - - -, $L_{vv}^{(x)} = L_{vv}^{(z)}$; — - —, $L_{ww}^{(x)} = L_{uu}^{(z)}$.

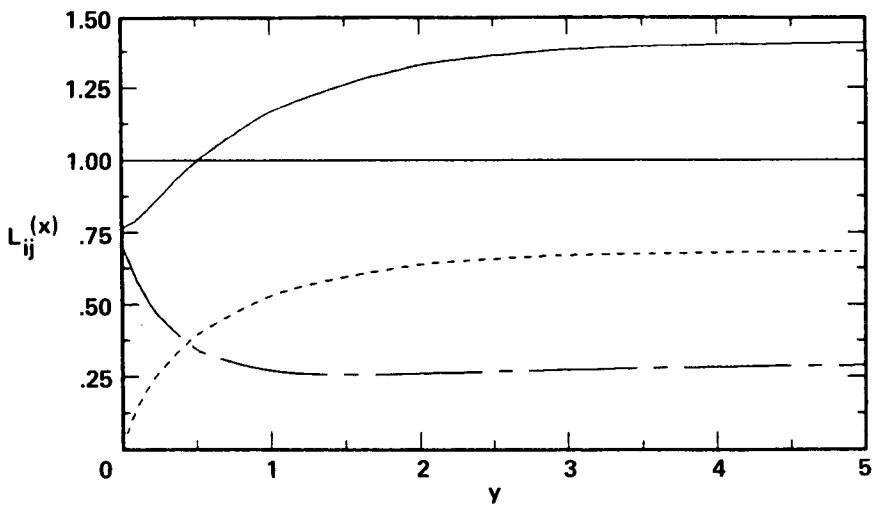

FIGURE 13. Profile of the streamwise integral scales $L_{ij}^{(x)}(y)$ for USBL ($\beta = 2$). ——, $L_{uu}^{(x)}$; - - - -, $L_{vv}^{(x)}$; — - —, $L_{ww}^{(x)}$.

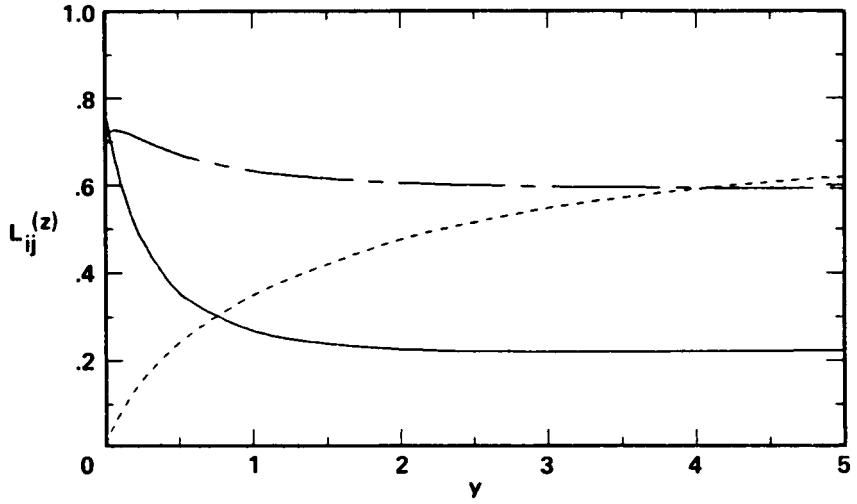

FIGURE 14. Profile of the spanwise integral scales $L_{ij}^{(z)}(y)$ for USBL ($\beta = 2$). ——, $L_{uu}^{(z)}$; - - - -, $L_{vv}^{(z)}$; — — —, $L_{ww}^{(z)}$.

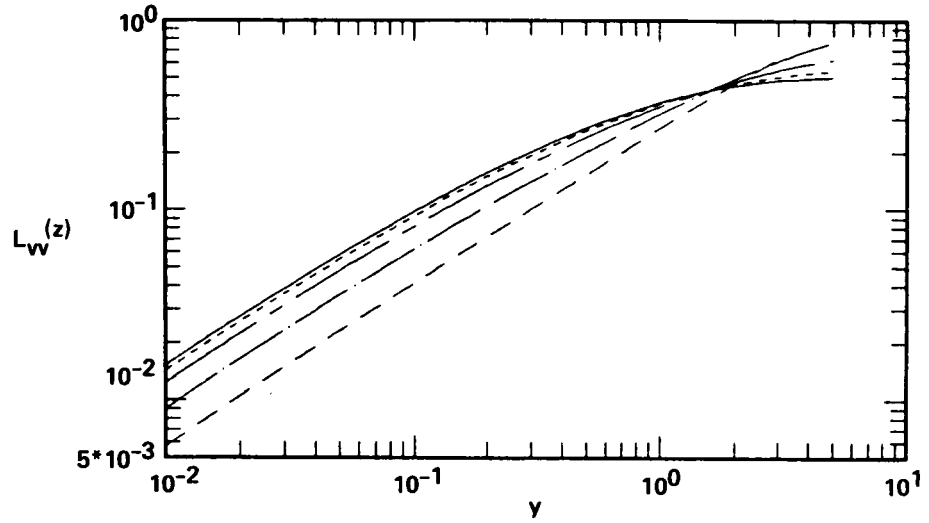

FIGURE 15. Variation with total shear of the profile of $L_{vv}^{(z)}$. ——, $\beta = 0$; - - - -, $\beta = 1$; — — —, $\beta = 2$; ····· , $\beta = 4$; — — — —, $\beta = 8$.

Figure 14 shows the profiles of the spanwise integral scales in USBL (for comparison with SFBL, see figure 12, where $L_{uu}^{(z)} = L_{ww}^{(z)}$, $L_{vv}^{(z)} = L_{vv}^{(z)}$, $L_{ww}^{(z)} = L_{uu}^{(z)}$). For heights away from the boundary, the scales of the streamwise velocity fluctuation, $L_{uu}^{(z)}$, and of the spanwise fluctuation, $L_{ww}^{(z)}$, are markedly decreased with shear, but the scale of the vertical motion, $L_{vv}^{(z)}$, is increased. Near the boundary, however, $L_{uu}^{(z)}$ (and $L_{ww}^{(z)}$) increases with shear from the unsheared value $\frac{2}{3}$. This means that since $L_{uu}^{(z)}$ may be interpreted as the characteristic scale for the spanwise extent of the streamwise eddies (streaks), at given total shear the spanwise extent of the streaky eddies widens as the boundary is approached, which is consistent with the reduced bending of vortex near the boundary (see figure 3*b*).

We note that $L_{vv}^{(z)}$ is the smallest of all the integral scales in the vicinity of the boundary, and thus it may be a good estimate for the dissipation scale L_ϵ. Figure 15 shows the profile of $L_{vv}^{(z)}$ at different values of total shear. The spanwise scale of the vertical fluctuation varies in a self-similar way near the boundary: $L_{vv}^{(z)} \sim A_\epsilon y$, where $A_\epsilon = A_\epsilon(\beta)$ decreases with shear.

4. Concluding Remarks

We have studied the effects of shear on turbulence structure near a plane boundary. It has been shown that the blocking of the vertical component of turbulence by the boundary is only slightly affected by the presence of shear (which is consistent with figure 1). However, the shear significantly changes the way in which the boundary affects the horizontal components $\overline{u^2}$, $\overline{w^2}$ and the Reynolds stress $-\overline{uv}$. In the SFBL the blocking (or splat) effect leads to the horizontal components being amplified. In a USBL the reduction in $\overline{v^2}$ near the boundary reduces the production of $-\overline{uv}$ and $\overline{u^2}$ by more than the splat effect increases $\overline{u^2}$. The physical explanation is given in §2.

We plan to look into other aspects of the surface blocking in sheared turbulence. In order to determine the relative effects of the wall blocking and shear on the vertical length scale, it would be of interest to examine the profiles of the two-point correlations of the vertical component of velocity at different distances from the surface and of the streamwise and vertical components.

A remarkable recent result has been the demonstration that applying the linear (RDT) distortion to an actual realisation of initially homogeneous isotropic velocity fields leads to velocity fields that contain many major large-scale coherent structures (Lee *et al.* 1987). These structures appear very *similar* in their scale, shape and distribution to structures that have been found in the direct simulations of homogeneous (uniform) shear flows and in the simulations and experiments of turbulent sheared boundary layers. This similarity implies that RDT is a useful way of computing the structures in shear flows. We intend to study the kinematical properties of the structures in uniform shear over a rigid surface to see how the structures are affected by the blocking effects.

REFERENCES

BERTOGLIO, J. P. 1986 Etude d'une turbulence anisotrope, modélisation de sous-maille et approche statistique. Thése de Doctorat d'État, Université Claude-Bernard Lyon: Lyon, France.

BRADSHAW, P. 1967 'Inactive' motion and pressure fluctuations in turbulent boundary layers. *J. Fluid Mech.* **30**, 241–258.

DURBIN, P. A. 1979 Rapid distortion theory of turbulent flows. Ph. D. Thesis, University of Cambridge: Cambridge, England.

GARTSHORE, I. S., DURBIN, P. A. & HUNT, J. C. R. 1983 The production of turbulent stress in a shear flow by irrotational fluctuations. *J. Fluid Mech.* **137**, 307–329.

HUNT, J. C. R. 1973 A theory of turbulent flow round two-dimensional bluff bodies. *J. Fluid Mech.* **61**, 625–706.

HUNT, J. C. R. 1984 Turbulence structure in thermal convection and shear-free boundary layers. *J. Fluid Mech.* **138**, 161–184.

HUNT, J. C. R. & GRAHAM, J. M. R. 1978 Free-stream turbulence near plane boundaries. *J. Fluid Mech.* **84**, 209–235.

HUNT, J. C. R., MOIN, P., MOSER, R. D. & SPALART, P. R. 1987*a* Self-similarity of two-point correlations in wall-bounded turbulent flows. *Proc. of the 1987 Summer Program*, Center for Turbulence Research, Stanford University and NASA-Ames Research Center, pp. 25–36.

HUNT, J. C. R., SPALART, P. R. & MANSOUR, N. N. 1987*b* A general form for the dissipation length scale in turbulent shear flows. *Proc. of the 1987 Summer Program*, Center for Turbulence Research, Stanford University and NASA-Ames Research Center, pp. 179–184.

HUNT, J. C. R., STRETCH, D. D. & BRITTER, R. E. 1988 Length scales in stably stratified turbulent flows and their use in turbulence models. In *Proc. IMA Conf. on Stably Stratified Flow and Dense Gas Dispersion* (ed. J. S. Puttock), Chester, England, April 1986, pp. 285–321, Clarendon Press: Oxford, England.

KIM, J., MOIN, P. & MOSER, R. D. 1987 Turbulence statistics in fully-developed channel flow at low Reynolds number. *J. Fluid Mech.* **177**, 133–166.

KLINE, S. J., REYNOLDS, W. C., SCHRAUB, F. A. & RUNSTADLER, P. W. 1967 The structure of turbulent boundary layers. *J. Fluid Mech.* **30**, 741–773.

LEE, M. J., KIM, J. & MOIN, P. 1987 Turbulence structure at high shear rate. In *Sixth Symp. on Turbulent Shear Flows*, Toulouse, France, Sept. 7–9, 1987 (ed. F. Durst *et al.*), pp. 22.6.1–22.6.6.

LUMLEY, J. L. 1978 Computational modeling of turbulent flows. *Adv. Appl. Mech.* **18**, 123–176.

MAXEY, M. R. 1978 Aspects of unsteady turbulent shear flow, turbulent diffu-

sion and tidal dispersion. Ph. D. Thesis, University of Cambridge: Cambridge, England.

SPALART, P. R. 1988 Direct simulation of a turbulent boundary layer up to $R_\theta = 1410$. *J. Fluid Mech.* **187**, 61–98.

THOMAS, N. H. & HANCOCK, P. E. 1977 Grid turbulence near a moving wall. *J. Fluid Mech.* **82**, 481–496.

TOWNSEND, A. A. 1961 Equilibrium layers and wall turbulence. *J. Fluid Mech.* **11**, 97–126.

TOWNSEND, A. A. 1976 *The structure of turbulent shear flow.* 2nd edn. Cambridge University Press: Cambridge, England.

UZKAN, T. & REYNOLDS, W. C. 1967 A shear-free turbulent boundary layers. *J. Fluid Mech.* **28**, 803–821.

WONG, H. 1987 Turbulence near angled and curved surfaces. Ph. D. Dissertation, University of Cambridge: Cambridge, England.

Analysis of homogeneous turbulent reacting flows

By A. D. Leonard[1], J. C. Hill[1], S. Mahalingam[2], AND J. H. Ferziger[2]

Full turbulence simulations at low Reynolds numbers were made for the single-step, irreversible, bimolecular reaction between non-premixed reactants in isochoric, decaying, homogeneous turbulence. Various initial conditions for the scalar field were used in the simulations to control the initial scalar dissipation length scale, and simulations were also made for temperature-dependent reaction rates and for non-stoichiometric and unequal diffusivity conditions. Joint probability density functions (pdf's), conditional pdf's, and various statistical quantities appearing in the moment equations were computed. Preliminary analysis of the results indicates that compressive strain-rate correlates better than other dynamical quantities with local reaction rate, and the locations of peak reaction rates seem to be insensitive to the scalar field initial conditions.

1. Background

Chemically reacting species that are not premixed are separated by a reaction zone, unless the time scale for mixing is much less than the time scale for reaction. The structure of the reaction zone is determined by interactions of the turbulent motion, molecular diffusion, and chemical kinetics. Molecular diffusion controls the rate of reaction when the kinetic rate is very fast and the reaction zone becomes a surface separating regions of reactants. This surface is typically a contour surface for a conserved scalar species. The reaction zone has a finite thickness for fast but finite rate kinetics. The reactants become completely mixed when the kinetic rate is very slow, and the classification of "non-premixed" is then irrelevant, because the kinetics, rather than transport processes, control the rate of reaction.

Previous simulations of inert scalars are useful in the study of reacting flows because an infinitely fast reaction can be described in terms of a conserved scalar species. Simulations of inert scalars in homogeneous turbulence show a tendency for the scalar gradient to align with the most compressive rate of strain of the velocity field and for the rate of scalar dissipation to be highest where the alignment of the scalar gradient and the direction of the compressive strain rate is greatest (Ashurst *et al.*, 1987). Previous work with reacting scalars (Leonard and Hill 1987, 1988; Hill, Leonard & Rogers 1987) show that the compressive strain rate direction tends to be perpendicular to the reaction zone, in agreement with the results of Ashurst *et al.*

1 University of Iowa
2 Stanford University

Probability density functions (pdf's) are frequently used in the statistical treatment of reacting turbulent flows, because the source terms do not need to be directly modeled. Mixing effects are seen in the statistical equations as conditional expectations of scalar dissipation. Eswaran and Pope (1988) have used direct numerical simulation to study the evolution of the pdf and the conditional scalar dissipation of an inert scalar species. The initial mixing rate was increased by a decrease in length scale, but evolution of the shape of the pdf of the scalar was not affected. The pdf was initially a "double delta" function, which would be appropriate for the conserved scalar of unmixed reactants. It evolved into a nearly Gaussian form. The conditional dissipation approached a self-similar value and became independent of the level of the scalar. The conditional dissipation needs to be modeled properly to give accurate mixing results, but current modeling efforts (*e.g.*, Pope, 1985; Kollmann, 1987) do not account for the effects of reaction rate on the mixing terms. The price to pay for treating the source terms exactly in reacting flows is the need to model all of the mixing effects, and this must be done in a higher dimensional system (Hill, 1988).

2. Problem Description

The specific problem under study is an irreversible reaction of two initially segregated species in homogeneous turbulence. The reaction mechanism can be expressed as

$$\mathrm{A} + \mathrm{B} \rightarrow \mathrm{P}.$$

Full turbulence simulations were performed for the evolution of the concentration and velocity fields, taking into account the advection and Fickian diffusion of species A, B, and P. The turbulence in most cases was isotropic and decaying. The velocity field was incompressible and not affected by the concentration fields, even in the studies using a temperature-dependent reaction rate. The governing equations for the study are

$$\frac{\partial A}{\partial t} + \mathbf{u} \cdot \nabla A = \mathcal{D}_A \nabla \diamond 2A + w_A,$$

with similar equations for the evolution of species B and P, and

$$\frac{\partial \mathbf{u}}{\partial t} + \mathbf{u} \cdot \nabla \mathbf{u} = -\frac{\nabla p}{\rho} + \nu \nabla \diamond 2\mathbf{u}.$$

The concentration of species A is denoted by A and the rate of change due to reaction by w_A. Two forms of the source terms were used in the studies,

$$w_A = -kAB$$
$$w_A = -k_0 e \diamond -T/T_a AB,$$

where the k's are reaction rate constants and T_a is the activation energy in the nonisothermal case.

The initial concentration distribution was one of two forms: alternating stripes of reactant species aligned perpendicular to one of the coordinate axes, or spatially

segregated species uniform on the largest scales of the domain. The second form of initial conditions was created using a procedure similar to that used by Eswaran and Pope (1988). The initial velocity field was chosen by randomly selecting Fourier coefficients and scaling them so the three dimensional energy spectrum fit a specified function. This initial velocity field was allowed to develop in a "pre-simulation" until the skewness of the velocity derivative had a value that agreed with experimentally measured conditions in turbulent flows.

The simulation method used an existing pseudospectral code (Rogallo, 1981) that was modified to include the rate of change of scalar values due to chemical reactions. The domain for most studies was $64 \diamond 3$ points. Three velocity components and eight scalar values were included in the numerical solutions.

One objective of the study was to determine the influence of local properties of the turbulence on the local reaction rate and structure of the reaction zone. This includes studies of the alignment of directions of strain rate and concentration gradients for reacting scalars for different speeds of reaction and of the influence of vorticity on reaction zone structure. The long-term goal of such a study is to model average reaction rate using strain-rate parameters.

A second objective was to determine the importance of the initial conditions in previous calculations (Leonard and Hill 1987). In these studies with a preferential alignment of the scalar fields and no variation in scalar length scales, globally-averaged scalar microscales showed little sensitivity to reaction rate.

A third objective was to determine if there is any effect of reaction rate on conditional expectations of molecular diffusion terms in a hierarchy of pdf equations. The modeling of these terms neglects any dependence on reaction rate, despite the fact that the pdf approach is widely used in the statistical treatment of reacting flows.

Additional questions concerned the behavior of reactions with non-stoichiometric conditions or with species having different mass diffusivities, as well as the local structure of the reaction zone for temperature-dependent kinetics.

2. Approach

The existing databases of homogeneous turbulent flows with chemical reaction were inadequate to answer the questions that had been raised, and so the emphasis was placed on the generation of new databases during the Summer Program, with careful consideration of physical parameters and initial conditions. Additional diagnostics were developed and added to the code to permit evaluation of the evolution of single point pdf's, single-point conditional expectations, and averages over two, rather than three, spatial dimensions during the course of the simulations.

The conditions of the studies made during the Summer Program are summarized in Tables I and II. Table I groups the simulations into 7 different studies, each study consisting of one or more simulations. Parameters for the scalar variables were varied within each study, as well as between different studies, in order to isolate effects such as initial conditions or kinetic mechanism.

Most studies have in common a decaying isotropic turbulent velocity field which has evolved from what will be called a "developed" initial field, isothermal reaction,

Table I. Summary of Studies◇a

Name of Study	Effects Studied	Initial Conditions	Comments
1. "Non-ideal" a) Non-stoichiometric b) Unequal diffusivity	Migration of reaction zone	Gaussian v-field (Same as '87 study) Scalar slabs	Reaction zone follows $X = 0$
2. "Slab"	Kinematics of reaction zone (Improved v-field)	Developed v-field Scalar slabs	Confirmed '87 results re: strain effects
3. "Flame"	Ignition and quenching	Developed v-field Scalar slabs Isothermal	Arrhenius rate expression Quenching not observed
4. "Stirred"	Effect of scalar field initial conditions	Developed v-field Prestirred scalar	Conditional scalar dissipation measured
5. "Stripes"	Effect of scalar dissipation scale	Developed v-field Scalar stripes (1,2,3,4)	Conditional scalar dissipation measured
6. "Forced"	Decouple reaction rate from turbulence decay	Developed v-field Scalar slabs or other	Incomplete (Compiled code untested)
7. "Shear"	Strain-rate dependence on reaction rate and scalar field structure	Top-hat v-spectrum Scalar slab in plane of shear	Incomplete (Excessive Gibbs' ringing for conditions used)

◇a All studies were for decaying homogeneous turbulence except for #6 and 7. The term "scalar slabs" denotes one stripe of one reactant centered in the domain of non-premixed reactants, hence there are two reaction zones initially. Improved diagnostics, including various joint-pdf's and planar averages, were used for all studies except #1.

equal mass diffusivities for all species, and stoichiometric proportions of reactant concentrations. The parameters and initial conditions shared by a majority of the simulations are given in Table II. The individual features of each study that were changed are discussed in the remainder of this section, using the informal names in Table I as convenient identifiers.

1. **"Non-ideal."** The non-ideal study examined the migration of the reaction zone for two different conditions. One simulation was made with stoichiometric coefficients (B_0/A_0) of 1 and 2 for two different reaction rates. The second simulation

Table II. Conditions for the Simulations

Physical parameters	
ν	0.02
$\mathcal{D}$ ◇ a	0.0286
k, k_0	various◇ b
Initial values◇ c	
u'	1.03
λ_g	0.381
Λ_f	0.844
$\bar{A}$, $\bar{B}$	1.0
λ_A	various

◇a $\mathcal{D}_A = \mathcal{D}_B = \mathcal{D}$ for all studies except #1b.

◇b The parameter was varied within some studies, as well as between studies.

◇c These initial conditions are for the "developed" velocity field used in studies #2–5, and for a stoichiometric proportion of reactant concentrations.

used a mass diffusivity ratio, $(\mathcal{D}_A/\mathcal{D}_B)$, of 1 and 3.5 for a stoichiometric ratio of 1. The initial reactant concentrations were the "scalar slabs," meaning one stripe of each reactant. The initial energy spectrum for the velocity field fit a Gaussian form, and the velocity field was allowed to develop for 100 time steps before the reaction began. The initial value of R_λ was about 20. The Damköhler numbers based on the diffusivity and initial mean concentration of species A and defined by

$$\mathrm{Da_I} = kA_0\Lambda_f/u'$$
$$\mathrm{Da_{II}} = kA_0\lambda_A \diamond 2/\mathcal{D}_A$$

were 0.8 and 4 for the first kind and 30 and 150 for the second kind.

2. **"Slab."** The slab study was aimed at repeating the results from the previous Summer Program with a different detailed velocity field. Fourier coefficients for the velocity field were chosen from a Gaussian distribution, subject to satisfying

the continuity equation and an initial energy spectrum $E(k) \propto k \diamond 4/(1 + (kL) \diamond 3) \diamond 2$, and allowed to develop for 100 time steps. This initial field had more energy at high wavenumbers than did the field used for the 1987 study, and so R_λ was smaller. The initial value of R_λ was 19.7. Two reactions were included in the simulation with different reaction rate coefficients. The Damköhler numbers for this study were 1.64 and 6.56 for the first kind and 62.8 and 251 for the second kind. Eight scalars were carried in the simulation: the reactant and product concentrations for each reaction and the concentrations of two inert species having different initial conditions.

3. **"Flame."** The "flame" study used the same initial conditions for the velocity and reactant species as in the slab case, but the reaction rate was temperature dependent, with an Arrhenius-type rate constant. For this case the temperature was calculated (actually, the fractional approach to the adiabatic flame temperature was used), rather than the product concentration. Simulations were performed for two different values of the Lewis number, in order to examine the possibility of strain-induced quenching, and also for two different values of the Zeldovich number. The Zeldovich number is defined here as the logarithm of the ratio of the reaction rate at the adiabatic flame temperature to the reaction rate at the initial temperature. Zeldovich numbers of 1 and 2 were used in the study. The Damköhler numbers based on the initial temperature and mean concentrations were the same as those used in the "slab" study.
4. **"Stirred."** Conditions for the "stirred" study were identical to the "slab" case, except for having different initial scalar distributions. A scalar field was defined in a manner similar to that for the velocity field, by scaling Fourier coefficients to fit an energy spectrum and advancing the coefficients in a "pre-simulation". In the case of the reactant concentrations, one reactant was set to be a (positive) initial value at the points were the initial scalar was positive and the other reactant was set to be a (positive) initial value at the points where the initial scalar was negative. The high wavenumbers were damped to eliminate Gibbs' ringing in the initial conditions. The reactant species were spatially segregated, but uniform on a large scale. The microscales for the reactants were much smaller than in the slab case, so mixing will tend to be faster. The Damköhler numbers of the second kind were 7.71 and 30.9, while the Damköhler numbers of the first kind were identical.
5. **"Stripes."** The initial values of reactant concentration in the slab and stirred cases differed both in orientation of the reaction zones and in the dissipation length-scale. The stripe study isolates the effect of the initial concentration scale from the orientation. One reaction rate coefficient is used for the calculation of reactant species for 4 reactions, each with different initial conditions. Damköhler numbers of the second kind were 13.7, 19.2, 30.4, and 62.8.
6. **"Forced."** Reactions in decaying homogeneous turbulence are unduly influenced by the amount of mixing in the early part of the simulation and controlled by diffusion in the later parts of the simulation. A forcing mechanism was devised to maintain a constant energy level but has not been implemented at this point.

7. **"Shear."** The same scalar field initial conditions of the "slab" case were used in the shear case, with the initial reaction zones lying in the plane of shear, but with a mean velocity gradient imposed on the flow. The initial velocity field was defined using the top-hat energy spectrum $E(k) =$ constant, for $k_1 < k < k_2$. The resolution was doubled in the direction of the mean flow, using a wavenumber grid $64 \times 64 \times 128$. A preliminary run was made—at too high a Damköhler number, apparently—but discontinued because of excessive Gibbs' ringing. Intensification of vorticity that occurs in the shear case clearly imposes limitations on the Damköhler number range that can be simulated.

3. Preliminary Results

Because most of the effort at the Workshop was spent in developing new databases for subsequent analysis, very little analysis was accomplished at the Workshop itself, and the preliminary results discussed here were obtained by cursory examination of some representative save-fields. Interpretation of the statistical results, especially the dependence of conditional expectations of scalar dissipation rate on the Damköhler number (dimensionless reaction rate constant), is still in progress, as is a more detailed examination of the saved fields. The principal results obtained so far deal with the kinematics of the reaction zone and with the influence of initial concentration length scales on the reaction (Hill & Leonard, 1988; Leonard *et al.*, 1988), and some of those results are summarized below.

The main observation from the **"Non-ideal"** study was the movement of the reaction zone for both the non-stoichiometric and the unequal diffusivity cases. The maximum reaction rate for the non-stoichiometric case occurred at the same point as the value of the conserved scalar corresponding to stoichiometric conditions ($X \equiv A - B = 0$). The conserved scalar treatment is not valid for the case of reactants with unequal diffusivities, but the behavior is qualitatively the same for the two cases. The mass flux of reactants to the reaction zone must be the same for both reactants, but the fluxes are unequal in the non-ideal cases, either because of a difference in diffusivity or in concentration gradient, and so the reaction front must move.

"Slab" initial conditions are used to study the structure of the reaction zone because two distinct fronts are present in the simulation. In the present study the initial reaction zones are perpendicular to the y axis and located at $y = \pi/2$ and $y = 3\pi/2$. The average positions of the fronts will not change in isotropic turbulence for reactions between stoichiometric proportions of reactants with equal diffusivities.

The scalar field has a preferential alignment with this initial condition. The gradients of reactant concentrations are in the direction of the y axis. The initial velocity condition is isotropic, so the probability of the cosine of the angle between concentration gradient and any of the eigenvectors of the rate of strain tensor is uniformly distributed. The concentration gradients become aligned with the direction of most compressive strain. Figure 1 shows the pdf's of the angles between the gradient of concentration for species A and eigenvectors of the rate of strain tensor for the slab

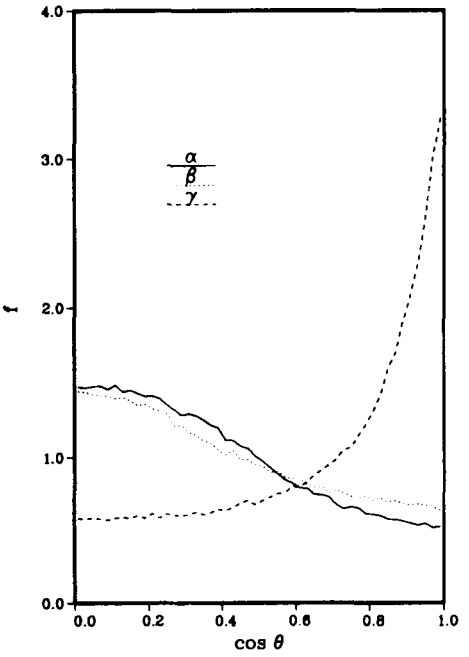

FIGURE 1. Probability density function $f(\cos\theta)$ of the alignment of the gradient of reactant species concentration and the eigenvalues of the strain-rate tensor, for a *slab* case at $t = 2.75$.

case at a dimensionless time of 2.75. The pdf is sharply peaked at $\cos\theta_\gamma = 1$ (where θ_γ is the angle between the gradient of species A and the eigenvector corresponding to the most compressive strain rate) after only 100 steps or $t = 0.4$. The alignment is in agreement with the results of Ashurst *et al.* (1987), but the present results show how rapidly it develops.

A cross section of the domain in the slab case, either in an $x-y$ or a $y-z$ plane, shows two distinct, distorted reaction zones, as seen in Figure 2. The degree of alignment with the eigenvector corresponding to γ, the least principal strain rate, is shown in Figure 3. Concentration gradient alignment with compressive strain is important because the strain increases the magnitude of the gradient, which increases the mass transport of reactant species to the reaction zone, which increases rate of reaction. This is shown by the set of equations developed from the conservation equations for the reactants in the case of an isothermal reaction,

$$\frac{d\bar{A}}{dt} = -k\overline{AB},$$

$$\frac{d\overline{AB}}{dt} = -2\mathcal{D}\overline{\nabla A\cdot\nabla B} - k\overline{AB(A+B)},$$

$$\frac{d\overline{\nabla A\cdot\nabla B}}{dt} = -2\mathcal{D}\overline{\nabla\nabla A:\nabla\nabla B} - 2\overline{\nabla A\cdot\mathbf{e}\cdot\nabla B} - k\left[\overline{(A+B)\nabla A\cdot\nabla B} + \overline{B\nabla A\cdot\nabla A} + \overline{A\nabla B\cdot\nabla B}\right].$$

We refer to the term $\nabla A \cdot \mathbf{e} \cdot \nabla B$ as "gradient compression", because the gradients are being amplified by the tendency of turbulence to move material surfaces together. When the scalar gradients are aligned with γ the gradient compression becomes $-\gamma|\nabla A||\nabla B|$. This term, which is positive because the gradients of A and B are in opposite directions and $\gamma < 0$, increases the magnitude of $\nabla A \cdot \nabla B$ at a rate $e \diamond -2\gamma t$ in the absence of diffusion or reaction. Contours of AB, $|\nabla A \cdot \nabla B|$, and $\nabla A \cdot \mathbf{e} \cdot \nabla B$ all show peak values in the same regions.

A second consequence of the scalar gradient alignment is that the location of peak reaction rates seems not to be very sensitive to the initial conditions of the scalar field. The initial values of the **"Stirred"** case were determined randomly, while the initial values of the "slab" case were chosen deterministically. The velocity field was the same for the two cases. A cross section of the slab case in a $x-z$ plane, as well as cross sections of the stirred case in any plane, show a more random structure than that in Figure 2. Regions of intense reaction rate for the slab and stirred cases coincide in a plane that was the center of one of the initial reaction zones for the slab case (Figs. 4 and 5), even though the initial concentration fields are different.

Since the reaction rate is high in the same locations for completely different initial conditions, it may be possible to predict the structure of the reaction zones from a knowledge of velocity field. One parameter that must be used is the rate of strain. Criteria were proposed by J. Hunt and A. Wray at the CTR Summer Program to determine kinematic structures of the flow field. These structures are identified as streams, eddies, and convergence zones, based on the strain rate invariants, vorticity, kinetic energy, and pressure. Hunt and Wray suggest that the reaction rate will be highest in the convergence zones. Simulation results, however, show that regions where the reaction rate is high are not necessarily convergence zones. The gradient compression term appears to be the best marker of regions of high reaction rate.

Only a few remarks will be made here about the remaining studies. First, the **"Flame"** study. The reaction rate has been found to be higher when the magnitude of γ is large, because of the gradient compression. Gradient compression is believed to be responsible for quenching in flames, because the transport of heat away from the reaction zone becomes more important than the transport of reactants to the reaction zone for Arrhenius kinetics. Simulations with temperature-dependent reaction rate do not show any reduction of reaction rate where the strain rates are high. The only qualitative difference between the temperature-dependent case and the isothermal case is that the reaction zones are initially thinner in the former case, an apparent ignition effect.

Comparison of results from the **"Stripes"** study with those of the "stirred" and "slab" studies shows that as one increases the scalar dissipation scale, mixing becomes more important, and the reactants decay faster. (The fraction of the domain occupied by scalar dissipation zones, and hence reaction zones, is increased.) In the case of several stripes, interference effects clearly become important after several hundred time steps, and the reaction zones lose their identity.

The studies of chemical reactions in **"Forced"** and **"Shear"** turbulence were not carried out during the Workshop (except for coding of the forcing algorithm in

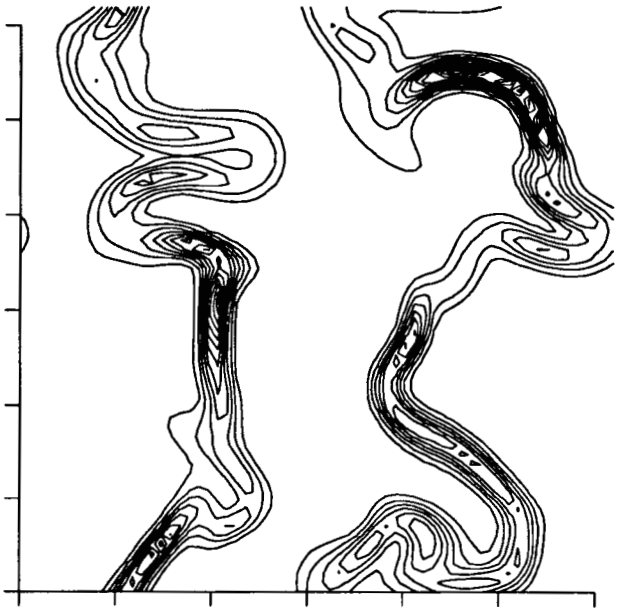

FIGURE 2. Contours of reaction rate, kAB, for a *slab* case at $t = 2.75$ in the plane $x = 0$.

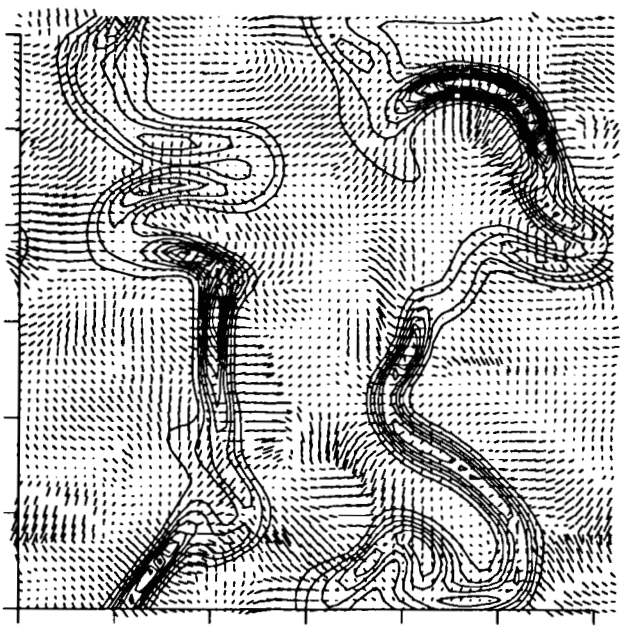

FIGURE 3. Eigenvectors of γ, the least principal strain rate, superimposed on the contours of reaction rate from Figure 2.

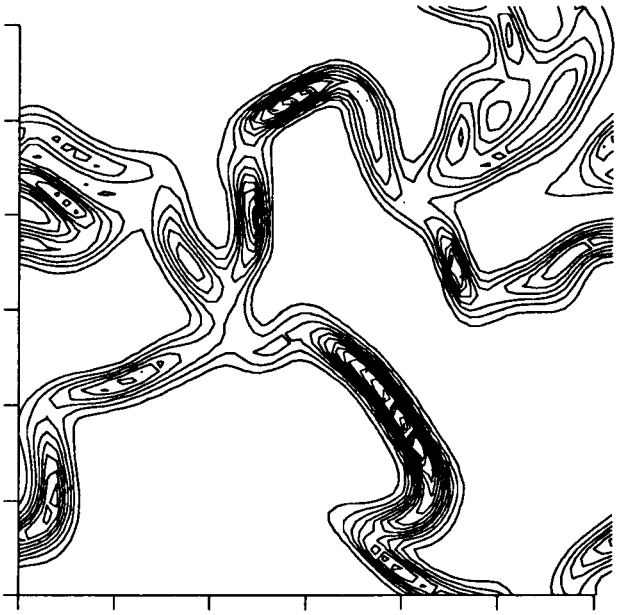

FIGURE 4. Contours of reaction rate, kAB, for a *slab* case at $t = 2.75$ in the plane of the original reaction zone, $y = \pi/2$. These data are for the same time and the same run as figure 3; only the planes observed are different.

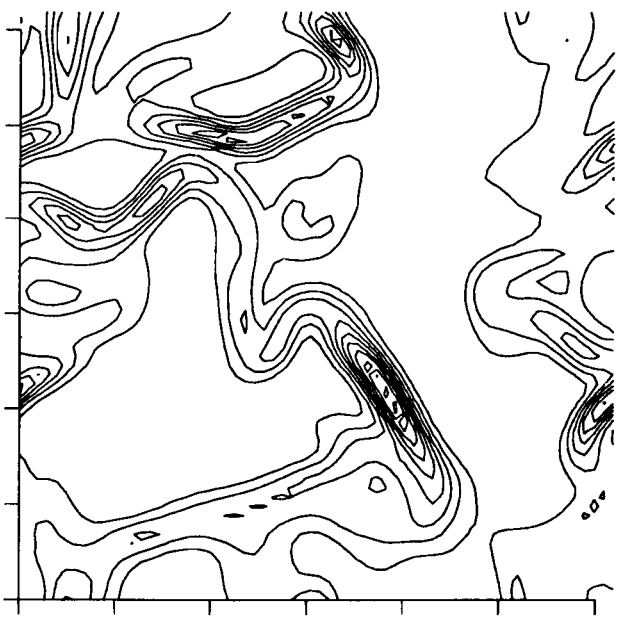

FIGURE 5. Contours of reaction rate, kAB, for a *stirred* case at $t = 3.12$ in the plane $y = \pi/2$. Coincidence, at nearly the same time, of the locations of the highest reaction rates as for the slab case in figure 4 should be noticed.

the former case and making a preliminary run at too high a Damköhler number in the latter), and those studies will be continued.

4. Conclusions

The local rate of strain in the fluid appears to be the feature of turbulence that has the most direct influence on the course of a chemical reaction, indicating that rate of strain should be incorporated into models for reacting flows. Reaction zones are aligned perpendicular to the direction of compressive strain rate, and the magnitude of the reaction rate is greatest when the magnitude of the strain rate is highest. The straining motion of the fluid compresses concentration gradients to enhance molecular diffusion, and thereby reaction rate. These observations support the simple one-dimensional model by Gibson and Libby (1972) of the reaction zone, in which the reaction surface is aligned with the most compressive strain rate, and the fluid motion is approximated by $u = -\gamma x$ in a coordinate system fixed to the reaction zone.

Preliminary examination of the saved fields suggests furthermore that the alignment of scalar gradient and strain rate directions is independent of initial conditions, and that the highest reaction rates tend to occur at the same points in the flow for reactions with different initial reactant distributions. Changing the initial scalar microscale, and hence changing the fraction of the domain occupied by reaction zones, affects the overall reaction rate and scalar dissipation rates.

The analysis of the data generated during the Summer Program is continuing, and additional simulations are being made where necessary. Further studies of non-isothermal cases are planned, as well as non-decaying turbulent flows.

Acknowledgments

The computer resources used in this study were provided by the Numerical Aerodynamical Simulation program of the NASA-Ames Research Center. The authors benefitted from discussions with W. T. Ashurst, J. C. R. Hunt, J. J. Riley, R. S. Rogallo, M. M. Rogers, and A. A. Wray, and appreciate the use of data analysis programs developed by A. Wray.

REFERENCES

ASHURST, W. T., KERSTEIN, A. R., KERR, R. M., & GIBSON, C. H. 1987 *Phys. Fluids* **30**, 2343–2353.

ESWARAN, V. & POPE, S. B. 1988 *Phys. Fluids* **31**, 506–520.

GIBSON, C. H. & LIBBY, P. A. 1972 *Combust. Sci. and Technol.* **6**, 29–35.

HILL, J. C. 1988 Tutorial, 1988 CTR Summer Program.

HILL, J. C. & LEONARD, A. D. 1988 *APS Bull.* **33**, 2256.

HILL, J. C., LEONARD, A. D., & ROGERS, M. M. 1987 *APS Bull.* **32**, 2120.

KOLLMAN, W. 1987 Tutorial, 1987 CTR Summer Program.

LEONARD, A. D. & HILL, J. C. 1987 *Proc. 1987 CTR Summer Program.*

LEONARD, A. D. & HILL, J. C. 1988 *J. Scient. Computing* **3**, 25–43.

LEONARD, A. D., HILL, J. C., MAHALINGAM, S., & FERZIGER, J. H. 1988 *APS Bull.* **33**, 2257.

POPE, S. B. 1985 *Prog. Energy Combust. Sci.* **11**, 119–92.

ROGALLO, R. S. 1981 *NASA TM 81315.*

Cut-and-connect of two antiparallel vortex tubes

By MOGENS V. MELANDER† AND FAZLE HUSSAIN‡

Motivated by our early conjecture that vortex cut-and-connect plays a key role in mixing and production of turbulence, helicity and aerodynamic noise, we have studied the cross-linking of two antiparallel viscous vortex tubes via direct numerical simulation. The Navier-Stokes equations are solved by a dealiased pseudo-spectral method with 64^3 grid points in a periodic domain for initial Reynolds numbers Re $(= \Gamma/\nu)$ up to 1000; Γ is the circulation and ν is the kinematic viscosity. The vortex tubes are given an initial sinusoidal perturbation to induce a collision and keep the two tubes pressed against each other as annihilation continues. Cross-sectional and wire plots of various properties depict three stages of evolution: (I) *Inviscid* induction causing vortex cores to first approach and form a contact zone with a dipole cross-section, and then to *flatten* and *stretch*. (II) Vorticity annihilation in the contact zone accompanied by *bridging* between the two vortices at both ends of the contact zone due to a collection of cross-linked vortex lines, now orthogonal to the initial vortex tubes. The direction of dipole advection in the contact zone reverses. (III) *Threading* of the remnants of the original vortices in between the bridges as they pull apart. We show the crucial stage II to be a simple consequence of vorticity annihilation in the contact zone, link-up of the un-annihilated parts of vortex lines, and stretching and advection by the vortex tube swirl of the cross-linked lines, which accumulate at stagnation points in front of the annihilating vortex dipole. We claim that bridging is the essence of any vorticity cross-linking and that annihilation is sustained by stretching of the dipole by the bridges.

Induction by the bridges reverses the curvature of the dipole vortices and the direction of their motion. This reversal would arrest annihilation, were it not for the fact that the stretching by the bridges sustains annihilation, albeit at a slower rate. The bridges pull away from each other by self induction while the stretched remnants (i.e. threads) of the initial vortex dipole decay. The threads decay very slowly both because of the balance between stretching and viscous diffusion, and because of the absence of induction pressing the threads against each other. Threading, in addition to bridging, is an integral part of reconnection contributing to mixing and enstrophy cascade.

Vortex reconnection details are found to be insensitive to asymmetry. Modeling of the reconnection process is briefly examined. We also examine the 3D spatial details of scalar transport (at unity Schmidt number), enstrophy production, dissipation and helicity.

---

† Southern Methodist University
‡ University of Houston

1. Introduction

Since turbulent flow can be viewed as a tangle of vortices, vortex dynamics is an attractive and tractable avenue for understanding fundamental turbulence mechanisms. The discovery of large-scale organized vortical motions, popularly called "coherent structures" (CS), in flows which were heretofore regarded as fully random (Cantwell 1981; Lumley 1981; Kim & Moin 1986), has fostered the concept that CS dominate turbulence phenomena such as transports of heat, mass and momentum, combustion and chemical reaction, and generation of drag and aerodynamic noise, and that these phenomena can be managed by active and passive manipulation of CS formation and interactions (Hussain & Husain 1987). Vortex dynamics can be an effective tool in understanding CS topology and dynamics in unexcited and excited flows, especially in the absence of any theoretical framework for CS.

Inviscid vortex dynamics is particularly suited for studying CS evolution and interaction as CS dynamics is essentially inviscid and we define CS in terms of vorticity (Hussain 1980, 1986). Inviscid vortex dynamics are governed by the conservation theorems of Kelvin and Helmholtz and the Biot-Savart induction equation. In the case of thin vortices with small curvature, the local induction approximation provides a considerable simplification in analysis and gathering intuition regarding the instantaneous self and mutual inductions of vortical structures. Two particular idealizations have found extensive use: filaments and point vortices. Representation of vortices by filaments is appropriate under some constraints and has been dealt with by many researchers (Leonard 1980; Siggia 1985; Schwarz 1985). For a discussion of motions of point vortices see Aref (1982). A generalized point vortex model for 2D vortex merger has been given by Melander *et al.* (1986, 1988). Many interesting phenomena have been studied by inviscid vortex dynamics: entanglement (Hopfinger *et al.* 1982; Takaki & Hussain 1984), short wave instability (Widnall *et al.* 1974; Saffman 1978), Tkachenko waves (Andreck & Glaberson 1982), for example.

Viscous vortex interactions can be classified into two categories: augmentation and annihilation of circulation. Pairing and entanglement usually produce accumulation of circulation due to merger of like-signed vortices, although pairing of opposite-signed vortices has been observed (Hussain 1983). Annihilation of circulation, for which viscosity is essential, can occur with and without reconnection. Head-on collision of viscous vortex rings (Kambe & Minota 1983) is an example of annihilation without reconnection and has been numerically simulated in a companion study (Stanaway *et al.* 1988). Examples of annihilation with reconnection include aircraft trailing vortices (Crow 1970), pinching-off in hairpin tips in boundary layers (Moin *et al.* 1986), fusion of two parallel adjacent vortex rings (Oshima & Asaka 1977; Kida *et al.* 1988), two colliding rings at arbitrary orientations (Schatzle 1987), splitting of an elliptic jet into two (Hussain & Husain 1987), collision of two antiparallel vortex filaments (Meiron *et al.* 1988), etc. Note that Meiron *et al.* use two zero-circulation vortices—an unnecesary complication not present in our study. The studies of a trefoil vortex (Kida & Takaoka 1987) and of two colliding orthogonal vortex tubes (Zabusky & Melander 1988) also fall in this general category; the motions in both these cases, however, are extremely complex and not

easily understood.

1.1. *Motivation*

The cut-and-connect process, also called cross-linking or reconnection, is of general interest as an example where topology is not preserved. However, there are particular motivations for the present study. Following Laufer's (1974) proposal that vortex pairing was the dominant factor in jet noise generation, we argued that pairing was an unlikely cause in practical jets, which involve very little pairing, and that it was the breakdown of vortical structures which produced most noise in jets. We then proposed cross-linking as the specific mechanism involved (Hussain 1983) and then further proposed it to be responsible for mixing, turbulence production and helicity generation (Hussain 1986). Although we had no measurements (of vorticity) to support our claim regarding the role of vortex cut-and-connect, we presented an idealized model which not only shed some light on the mechanism but also produced far-field jet noise predictions in qualitative agreement with experiments (Takaki & Hussain 1985).

The second motivation for a rigorous study of the cross-linking process is to obtain a clear understanding of the role of viscosity. In the absence of viscosity, vortex lines are material and thus cannot cut and connect, according to the theorems of Kelvin and Helmholtz. It is clear that viscosity is crucial to cross-linking, as emphasized in the analysis of Takaki & Hussain (1985). They coined the phrase 'cut and connect' to emphasize the topology-changing nature of the event, although the event, a consequence of viscous diffusion, obviously involves no cutting (or breaking) whatsoever of vortex lines. There are many who still feel viscous effects are irrelevant to cross-linking (Benjamin 1985). For example, Melander & Zabusky (1988) suggest that viscous effects are not operative at large Re during several convective intervals.

Different mechanisms of cross-linking are implied in different studies. Siggia & Pumir (1985) and Ashurst & Meiron (1987) proposed "tangling and collapse" of vortices. In their idealized analysis, Takaki & Hussain (1985) transformed the cut-and-connect problem into an equivalent problem where cross-linking occurs smoothly (but very rapidly) as a viscous diffusion phenomenon. Kida & Takaoka's (1987) simulation suggests that high-vorticity fingers ejected from the main vortices, get elongated and then connected with other fingers to form "bridges". (Note that this mechanism, despite the same name, is quite different from the bridging mechanism we discuss here). Melander & Zabusky's (1988) simulation suggests the formation of hairpin vortices, which are pulled out from the outer layer fluid of colliding vortices and then intensified, causing subsequent entanglement. As will be seen here, the mechanism we observe and analyze is indeed quite different—it is truly viscous. Viscous annihilation is a precondition for our bridging. Kida & Takaoka's 'bridging', as Melander & Zabusky's mechanism, is by mutual induction and does not require viscosity for initiation. Their mechanism may occur at high Re, but whether it will occur on an inviscid time scale at high Re is unclear.

Another aspect that remains unresolved is the characteristic time scale of the phenomenon. Takaki & Hussain (1985) emphasized that viscosity was crucial, yet

its effect was indirect. They claimed that the cut-and-connect happened rapidly in a time scale $\mathcal{O}(\sigma^2/\Gamma)$, where σ is the instantaneous core size. Based on his data, Schatzle (1987) proposed two time scales $\sigma/(e\nu)^{1/2}$ and $\sigma^2/(\Gamma\nu)^{1/2}$ in terms of strain rate e and circulation Γ. The strain rate is set by Γ in ways that remain unclear. He also quotes a time scale of $(1/2e)\log(\sigma^2 e/\nu)$ suggested to him by Saffman and Leonard. He was unable to indicate a clear preference between these three, as all three gave values comparable to those in his experiment. Meiron *et al.* (1988) have proposed a time scale of $\log(\Gamma/\nu)/2e$. Melander & Zabusky (1988) also suggest that if there is balance between strain and dissipation, then the time scale $\sim \log(\Gamma/\nu)$.

Singularity of the Navier-Stokes equation is another reason why cross-linking is particularly interesting. Do solutions of the incompressible Navier-Stokes equation (in the limit $\nu \to 0$) blow up in finite time? Recent studies by Siggia (1985) and Siggia & Pumir (1985) suggest singularity of the Euler solutions in finite time. (Also, Pumir & Siggia (1987) claim that there is a singularity in the Navier-Stokes equation at sufficiently high Re). However, their study involving inviscid vortex filaments cannot be viewed as conclusive as it is not clear if the solutions obtained by vortex filament simulations correspond to solutions of Euler equations near the time of singularity, including the fact that their simulations do not consider strong core deformation which, as we will see herein, is a crucial factor in cross-linking. The singularity issue is not addressed in the present paper but is discussed in a concurrent study elsewhere (Kerr & Hussain 1988).

1.2. *Objective*

It is clear from the above brief review that the cross-linking mechanism and the time scales involved are far from being understood. The need for modeling the event cannot be overemphasized. However, modeling should be based on carefully digested observations—not a popular practice! Schatzle (1987) proposed that further careful experiment and numerical simulation were needed. Meiron *et al.* (1988) also concluded, as we did, that the present state of understanding of cross-linking was extremely poor and that further study was warranted.

Before stating our objective, we must explain why we studied antiparallel vortices and why numerically.

In spite of numerous flow visualization studies of reconnection, especially in rings, there is practically no quantitative measurement, except the recent one by Schatzle (1987). Unfortunately, his measurements involve ensemble averaging, assuming identical details of the cross-linking process in space and time in successive runs of the same event by repeated experiments; in addition to the inherent smoothing in such ensemble averaging (along with spatial averaging used by him), his measurements are limited in resolution and also by the fact that data were taken in one plane only. This clearly misses 'bridging' which we claim here to be the essence of cross-linking. We need instantaneous data over the 3D field with adequate resolution. Pending further development in measurement technology (now in progress in our laboratory), experimental methods cannot now do much better. However, supercomputer simulation can provide time evolution of reconnection in 3D and with adequate resolution, especially at low Re.

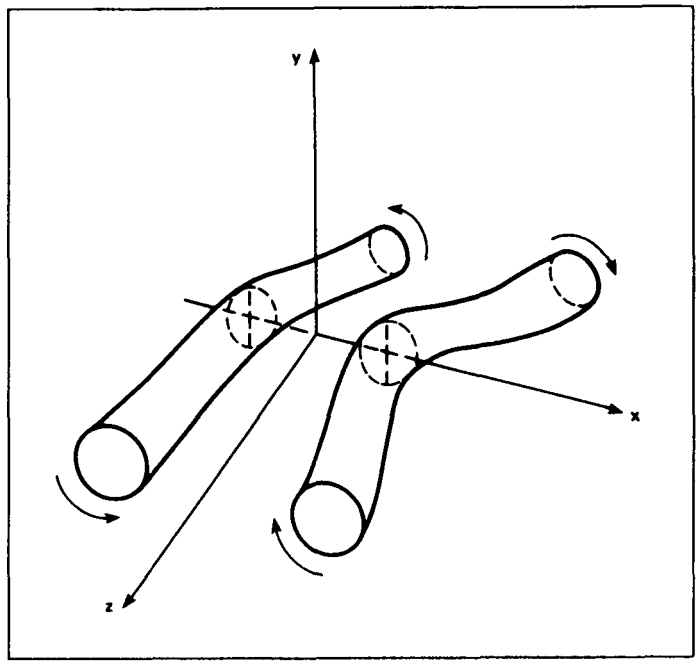

FIGURE 1. Schematic of the initial vortex tubes and coordinates.

The simulation of Kida & Takaoka (1987) of a trefoil and of Melander & Zabusky (1988) of two colliding orthogonal vortex tubes show that the local interaction, which involves entanglement and cross-linking, is extremely complex, even virtually intractable. However, we know that two vortex filaments of arbitrary orientations will tend to become antiparallel by mutual induction as they approach each other. This was also apparent in the simulations of Siggia (1985) and Pumir & Siggia (1987). Thus, one can focus on the details of cross-linking by considering the simple case of antiparallel vortex tubes. In order to aid the collision and annihilation, so that the two vortex tubes press against each other for sustained annihilation, they were given parallel sinusoidal perturbations, the planes of the two cosine waves being inclined to each other (figures 1 & 2).

The objectives of this study were to:

i) Obtain a clean simulation of two antiparallel vortex tubes with initially circular cross-section.

ii) Explain the detailed mechanism of cross-linking by examining the processes of annihilation, motion of dipole and bridging.

iii) Explain the origin and role of bridging.

iv) Identify the time scale of cross-linking.

v) Explain the final stage of cross-linking (that is, is reconnection complete or is there debris left?).

vi) Determine sensitivity of cross-linking to asymmetry.

vii) Study topology and dynamics of cross-linking by considering the 3D fields of properties, including enstrophy production, dissipation, helicity, scalar transport

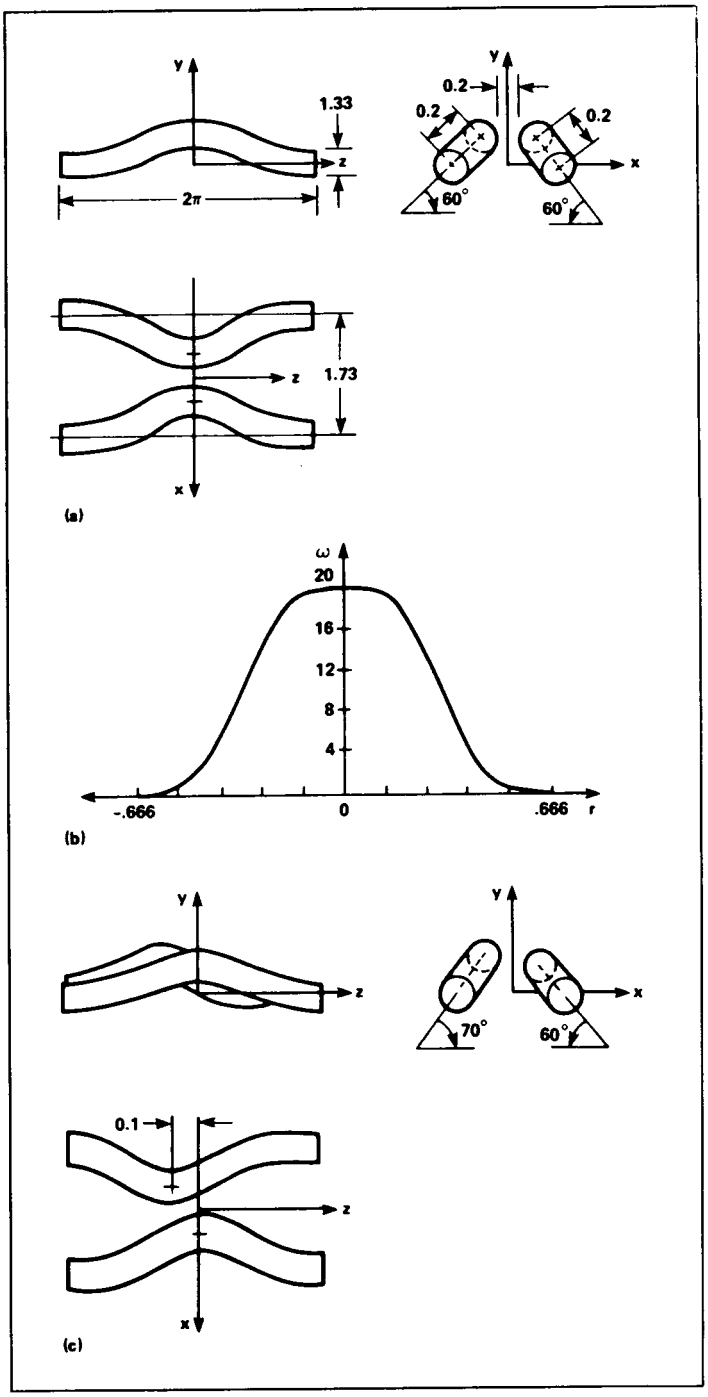

FIGURE 2. (a) Three views of the initial state for symmetric computation; (b) initial vorticity distribution within the core; (c) initial configuration for asymmetric computation.

etc.

viii) Suggest modeling of the cross-linking: core deformation and head-tail formation, bridging and threading.

2. Simulation method

Our numerical method, used for solving the Navier-Stokes equation in a cube with periodic boundary conditions, is a pseudo-spectral (Galerkin) method with a fourth-order, predictor-corrector for time stepping. Dealiasing is performed by a 2/3-spherical truncation in k-space. The choice of periodic boundary conditions is justified by the fact that cross-linking is a strong local vortex interaction, which is insensitive to weak nonlocal effects. In a different study by Melander & Zabusky (1988, and private communication) the influence of adjacent boxes was studied, and it was found that the effect is inconsequential.

The initial conditions consist of two antiparallel vortices with a sinusoidal perturbation as shown in figure 2. Each vortex (unperturbed) has a circular cross-section with an initial vorticity profile given by,

$$\omega(r) = \begin{cases} 20\,[1 - f(r/0.666)] & r < 0.666 \\ 0 & r \geq 0.666 \end{cases}, \qquad f(\eta) = \exp\left[-K\eta^{-1}\exp(1/(\eta-1))\right], \quad K = \frac{1}{2}\exp(2)\log(2). \tag{1}$$

After the perturbation is applied, this defines a vorticity field $\boldsymbol{\omega}_{\text{in}}$ which may not be divergence free. In order to ensure a divergence-free vorticity field we first calculated the curl of the specified initial vorticity field,

$$\boldsymbol{\eta} = \nabla \times \boldsymbol{\omega}_{\text{in}}, \tag{2}$$

and then find a modified vorticity field $\boldsymbol{\omega}$ by inverting the following two equations,

$$\boldsymbol{\eta} = \nabla \times \boldsymbol{\omega}, \qquad \nabla \cdot \boldsymbol{\omega} = 0, \tag{3}$$

which guarantee divergence-free vorticity field. This inversion makes a slight adjustment in $\boldsymbol{\omega}_{\text{in}}$ without introducing any noticeable vorticity away from the core (i.e., $r > 0.666$).

The total circulation in the box vanishes due to the symmetry in the initial condition. Therefore, there is no need to use vortices whose individual circulations vanish, as is the case in the initial conditions used by Meiron *et al.* (1988).

3. Observations

Figure 1 shows the schematic of the initial vortices along with the coordinates x, y, z. For the sake of clear identification let us distinguish the two planes of symmetry: we will call the xy-plane the *symmetric* plane and yz-plane the *dividing* plane. Figure 2(a) shows three views of the initial configuration of the vortex pair. Note that the computational domain contains one full wave with the cross-linking zone

at the center of the domain. The two sine waves are inclined to each other at 60° so that these two vortices move by self induction along the local binormal (Batchelor 1967; p. 510) to make contact at the center and that they remain pressed against each other as the annihilation continues. The initial inclination angle, the amplitude of the sine wave and the core separation were chosen to shorten the time required to make contact. The vortex cores of circular cross-section are centered along the sine wave. The vorticity distribution (figure 2b) has compact support so that, unlike the Gaussian distribution which has tails extending to infinity, there is no vorticity outside the core boundary (i.e. $r = 0.666$). This is somewhat of an artifact, but introduced to make the cross-linking process clean, focused at the contact zone, and tractable. Without this, vorticity cross-linking would occur everywhere along the dividing plane and would cloud the central issue. This initial configuration was obtained as the optimum after some iteration. Figure 2(c) shows the initial configuration used to determine the effects of asymmetry on the evolution of the cross-linking process. Note that this configuration is asymmetric in all directions. In this paper all figures will be for the symmetric simulation only. We will merely mention the effect of asymmetry.

The results will be discussed at the times $t = 0, 1, 2, 3, 3.75, 4.5$ and 6 where t is time t^* nondimensionalized by initial peak vorticity, i.e. $t = t^*|\omega|_{\max}(0)/20$.

Figures 3(a–g) show surfaces of $|\omega| = 0.3|\omega|_{\max}(0)$. The corresponding vorticity contours in the symmetric (xy) plane are shown in figures 4(a–g). Between the first two frames, self-induction brings the two cores closer and they deform from being circular. At $t = 2$ the cores are siginificantly flattened. The two vortices contact each other at some time between $t = 2$ and 3. Note that by $t = 3$ the formation of the characteristic head-tail structure of a vortex dipole is clear. Up to this point the vorticity distribution within each is not unlike that in the case of head-on collision of circular vortex rings studied by Stanaway *et al.* (reported herein). Note that the two cores move upward by mutual induction. Until this time, the vorticity in the dividing (yz) plane is zero, but not now. The vorticity contours in this plane at $t = 3, 3.75, 4.5$ and 6 are shown in figures 5 (a–d), respectively.

As will be discussed in the next section, annihilation of vorticity in the symmetric (xy) plane is accompanied by appearance of orthogonal vorticity in the dividing (yz) plane as a result of cross-linking. The amount of circulation lost by annihilation is precisely the amount of circulation appearing in the dividing (yz) plane. So the amount of circulation annihilated at $t = 3$ is apparent from that in figure 5(a).

The most dramatic change in the topology happens between $t = 3$ and 3.75. Between these two times significant annihilation has happened. There is also the appearance of two humps in figure 3(e) connecting the two vortex tubes across the initial contact point. These two, which we call "bridges", are direct consequences of annihilation and resulting reconnection, and will be discussed later.

The circulation Γ in one half of the xy plane is shown in figure 6 as a function of time. Note that most of the circulation decay by annihilation has already taken place by $t = 3.75$. The same amount of circulation has accumulated in the yz plane (figure 5b). By $t = 4.5$, 70% of the circulation has been annihilated. Because of

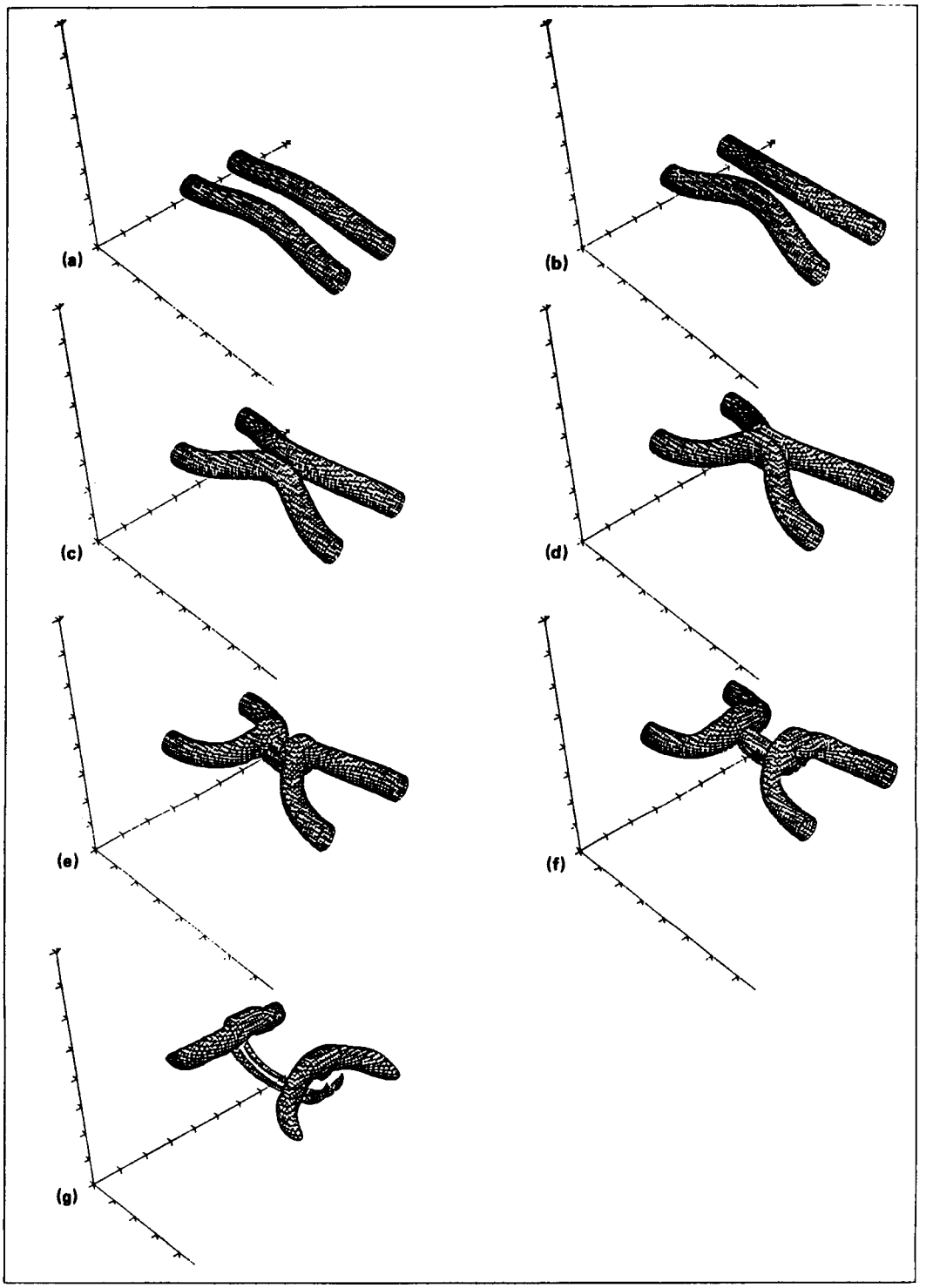

FIGURE 3. Wire plots of $|\omega|$ surface at 30% of initial peak vorticity. (a) $t = 0$; (b) $t = 1$; (c) $t = 2$; (d) $t = 3$; (e) $t = 3.75$; (f) $t = 4.5$; (g) $t = 6$.

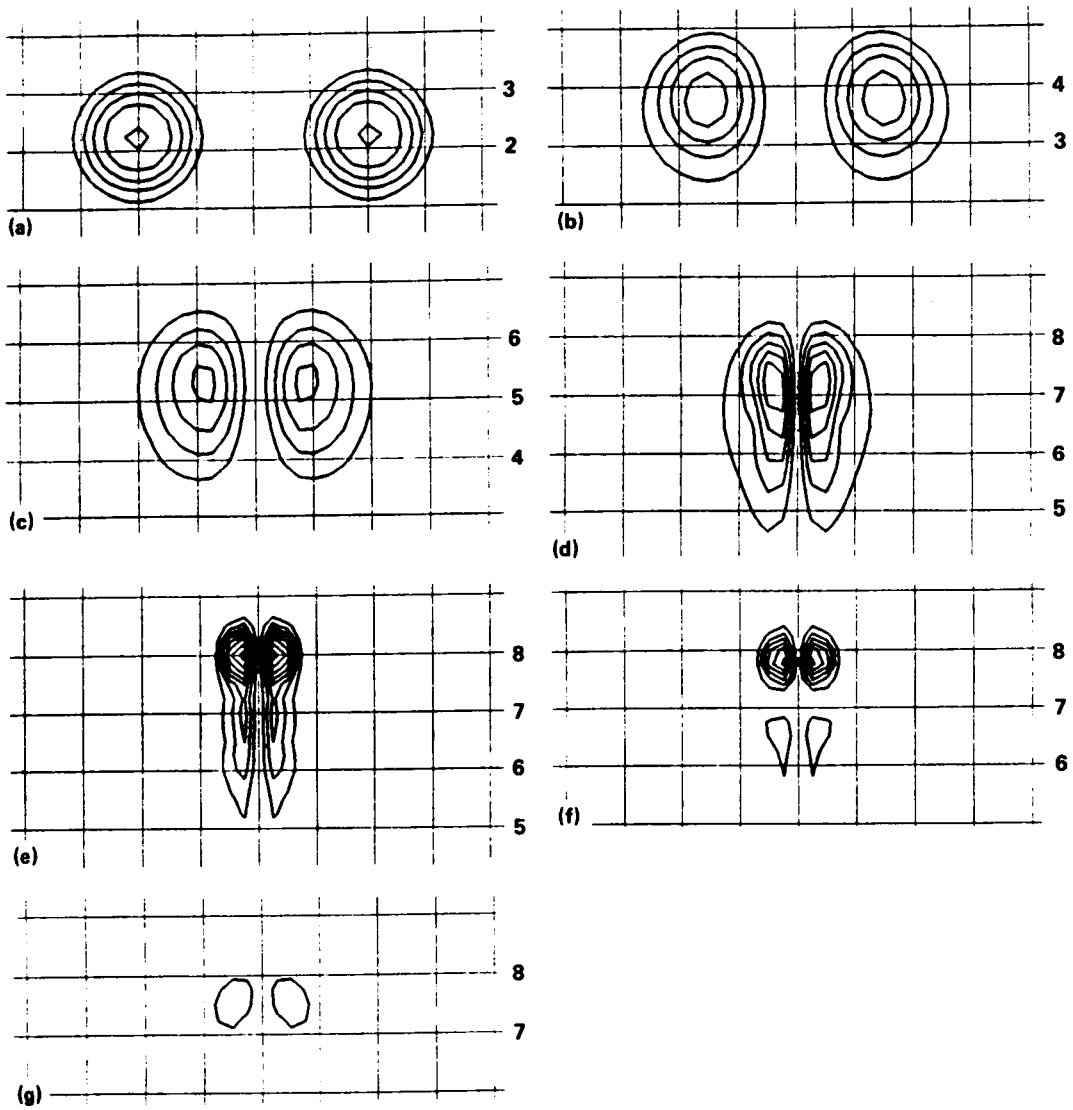

FIGURE 4. Contours of vorticity normal to the symmetric (xy) plane at times corresponding to figures 3(a–g). The grid is four times coarser than the computational mesh. The numbers on the right indicate the dipole motion in the y direction.

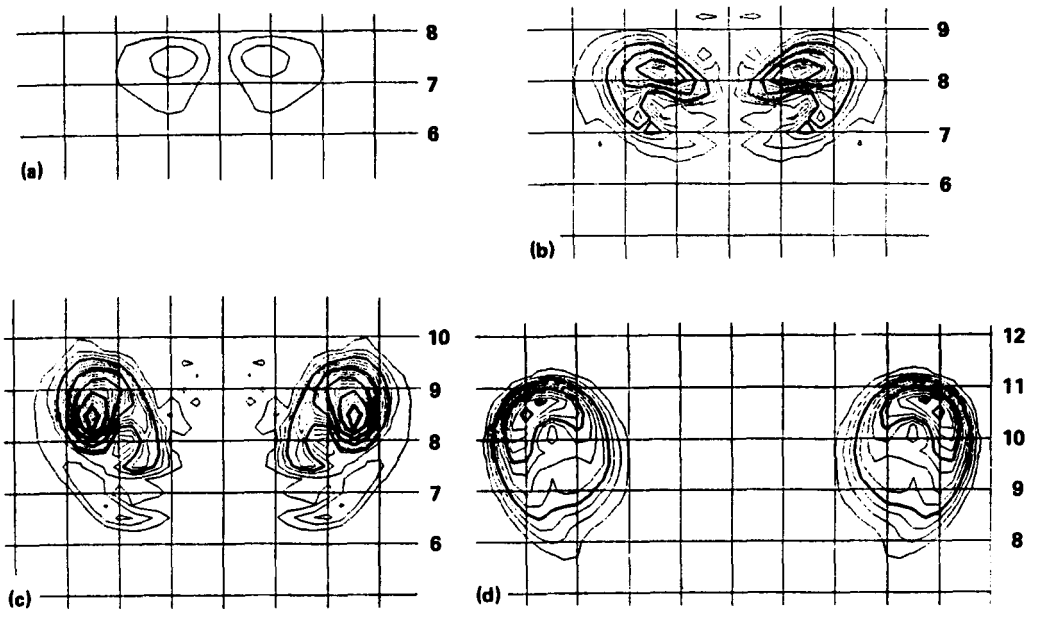

FIGURE 5. Contours of ω_x in the dividing (yz) plane. Contour spacing: thin lines, $\Delta\omega_x = 1$; thick lines, $\Delta\omega_x = 4$. (a) $t = 3$; (b) $t = 3.75$; (c) $t = 4.5$; (d) $t = 6$.

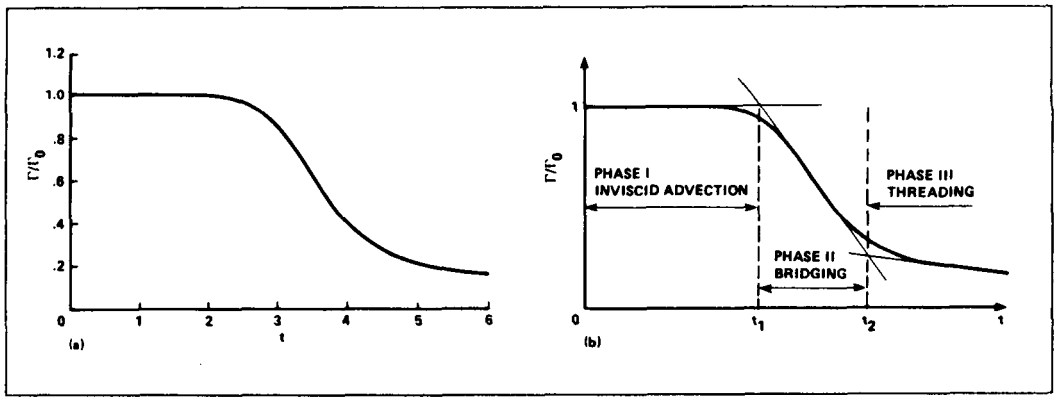

FIGURE 6. (a) Circulation as a function of time in one half of the symmetric (xy) plane; (b) Phases and time scales of reconnection.

higher vorticity concentration, the annihilation is much more between the heads than between the tails. The head moves ahead leaving the tail behind (figures 3f, 4f). The tail decays more by viscous diffusion than by annihilation. The reconnected vortex configuration at $t = 3.75$ is such that the bridges move apart by self-induction. An interesting point to observe is that the bridges pull apart much faster than the rate at which the vortices initially approach each other (compare figures 4 and 5). This is because the bridges, looking like curved hairpins, have much larger curvature and therefore higher self-induction velocities. The two bridges now induce a downwash in the contact zone which reverses the direction of motion of the vortex dipole. As the two bridges pull apart they stretch the dipole into two slender threads. The two threads now undergo annihilation at a slower pace (figure 6); because of reversal of the curvature of the threads their self-induction is not such as to keep them pressed against each other. In fact the two threads now move apart (compare figures 4f, 4g), their separation is smallest at the center where they are straight and larger near the ends where they are more curved (hence have higher self-induction away from each other). The reversal of the curvature of the threads and their moving apart would arrest annihilation, but the axial stretching of the threads intensifies their vorticity and thus sustains their annihilation by cross-diffusion, although at a slower pace. Note that at $t = 6$, the threads appear pinched off from the bridges. The picture is not totally clear; there appears to be complex entanglement of the thread ends around the bridges. The details of the entanglement are clearly not captured by the resolution in our simulation.

The simulation is terminated at $t = 6$ because beyond this time the vortices in the neighboring cubes start affecting the flow. Also, since the threads decay slowly at viscous time scales no further significant changes are expected. The two reconnected crescent-shaped vortices (essentially halves of vortex rings connecting across the boundary, which would evolve little from now on) taper off at the boundary at the $|\omega|$ level plotted, presumably because the vorticity is highly diffuse at the boundary; thus there is no vorticity at the level plotted.

While the threads are slowly decaying, there is a possibility that the thread pair may undergo a second-level cut-and-connect. This can happen if a perturbation reverses the dipole motion in the contact zone. It can also happen without a perturbation due to the fact that the middle portion of the threads can reverse curvature, once again, by mutual induction. Then self induction will pull the two threads closer to each other to enhance annihilation, reconnection and formation of "bridglets". Thus, this second cross-linking may constitute a second stage in a sequence of cut-and-connect interactions—a fascinating cascade mechanism!

The cut-and-connect generates orthogonal vorticity. The threading, or even successive cascade of cross-linking, would produce finer scales of vorticity with progressive increase of vorticity surface and decrease in scale. This may lead to enhanced mixing. The progressive fine scale generation would be a new and interesting enstrophy cascade mechanism. As we have claimed that cut-and-connect happens continually in all turbulent flows, we have here a non-statistical explanation for mixing and enstrophy cascade.

Figure 6(a) suggests three characteristic time scales of the phenomenon. Phase I: $0 < t < t_1$, where t_1 is the approach time during which circulation remains virtually constant while vorticity increases sharply. Phase II: $t_1 < t < t_2$, during which most annihilation takes place. Phase III: $t > t_2$, the period of decay of threads. These three phases can be identified by drawing a straight line tangent to the $\Gamma(t)$ curve through the point of inflection (figure 6b). The point where this tangent intersects the $\Gamma(0)$ line defines t_1. The determination of t_2, however, is not so precise as the decay curve slope is not well defined for the duration of the simulation. We estimate for this simulation $t_1 \approx 2.7$ and $t_2 \approx 4.3$. Using these two times, one can define the reconnection time as $t_r = t_2 - t_1 = 1.6$. This value compares favorably with Schatzle's (1987) time scale $\sigma^2/(\Gamma\nu)^{\frac{1}{2}} \approx 1.7$, while the time scale $\sigma^2/\Gamma \approx .05$ proposed by Takaki & Hussain (1985) is too fast. We also note that the viscous time scale $\sigma^2/\nu \approx 55$ is too long. We expect the reconnection time to decrease with Re; hence, the Takaki-Hussain time scale may be more appropriate at high Re.

We also followed the evolution of a passive scalar for the case of unit Schmidt number. This scalar was put in one vortex only, and in this vortex the scalar was set equal to the vorticity magnitude. At $t = 6$, we found virtually no scalar in the threads and very little in the bridges. Where vorticity is enhanced by stretching, markers are depleted; thus visualization may divert our attention away from most interesting points in a flow.

4. Discussion

4.1. *Bridging: the essence of vortex cross-linking*

We claim that bridging is the essence of cross-linking and is a simple consequence of vorticity annihilation. That is, all cross-linking must involve bridging. When vortices collide in a nonparallel manner other facets of interaction such as entanglement and filamentation may mask bridging, but it is the central mechanism by which vorticity cross-linking happens. Here we delineate the mechanism and suggest possible modeling of it.

Consider the two antiparallel vortex tubes (figure 7a) with three vortex lines each, emanating from three fluid particles in the main core. Viscous cross-diffusion annihilates the innermost vortex lines along the contact zone. This would leave the two innermost vortex lines devoid of their central parts, were it not the case that the remainder of these vortex lines link-up or connect near each end of the contact zone (figure 7b). The pumping (i.e. swirl) of the vortex tubes advects this reconnected vortex line upward, while simultaneously, vorticity diffusion across the tip of the narrow cusp (the reconnection point) makes the tip recede so that the tip radius of curvature increases from zero (figure 7c). The advection of the cusp is arrested as it approaches the stagnation point in front of the vortex dipole. In parallel, the swirl of the tubes stretch the vortex line and further increases the radius of curvature at the cusp (figures 7d,e). The continual stretching of the vortex line 'straightens out' the kink as the line is wrapped around the two tubes (figure 7f). Where the cusp disappears (i.e., whether the cusp disappears before arrival at the stagnation point) depends on the ratio of the advection time to diffusion time, hence

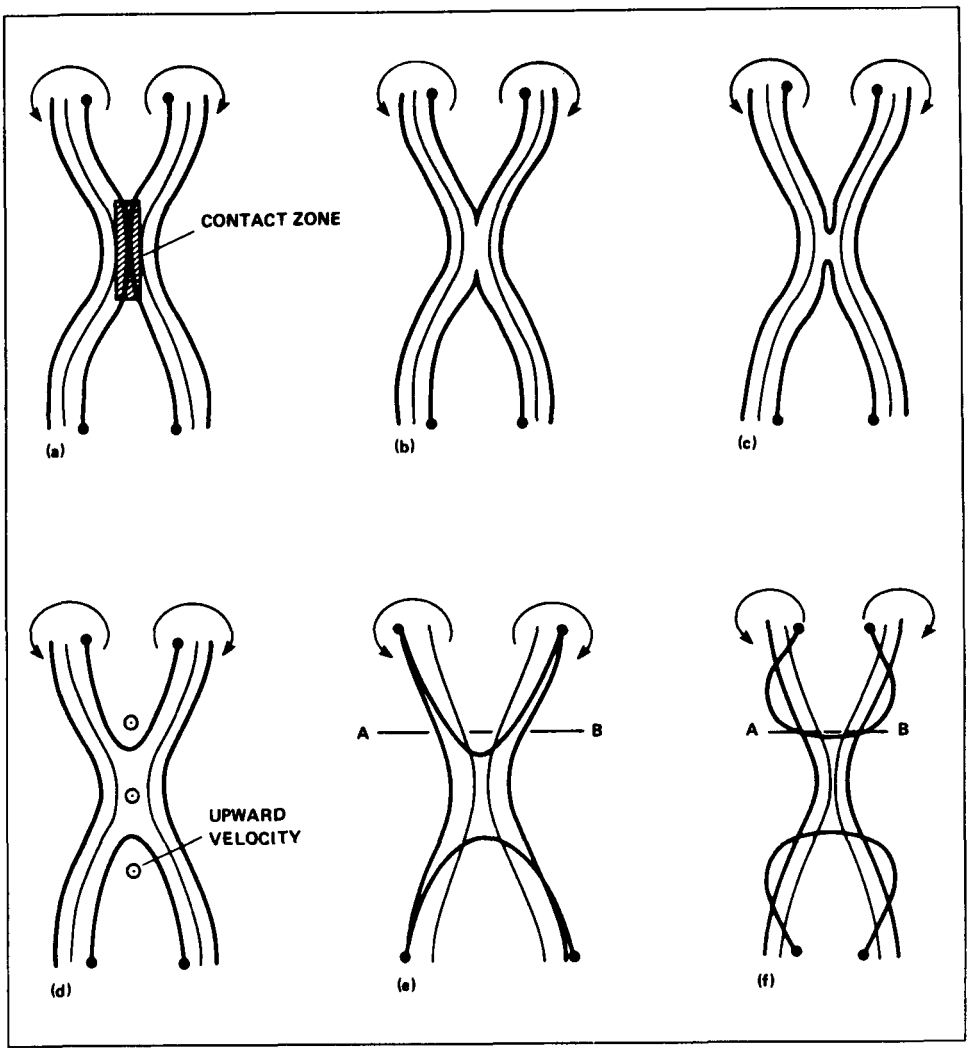

FIGURE 7. (a–f) schematic of annihilation and reconnection.

Re. This is how one sees *Re* entering directly into the discussion and modelling of the phenomenon. It should be obvious how successive reconnected vortex lines pile up at the stagnation points to form bridges.

To further understand the bridging mechanism, let us now consider the cross-section AB in figures 7(e) and 7(f). Drawn in figure 7(g), this cross-section shows the dipole structure of the antiparallel vortex tubes. In a reference frame moving with this dipole the streamline patterns have two stagnation points: S_T and S_B. It is now clear that our reconnected vortex line comes to a rest near the front stagnation point S_T. This point being a saddle, the vortex line is subject to continued stretching along the diverging separatrix a–a.

This scenario illustrates how reconnected vortex lines appear on the top of the

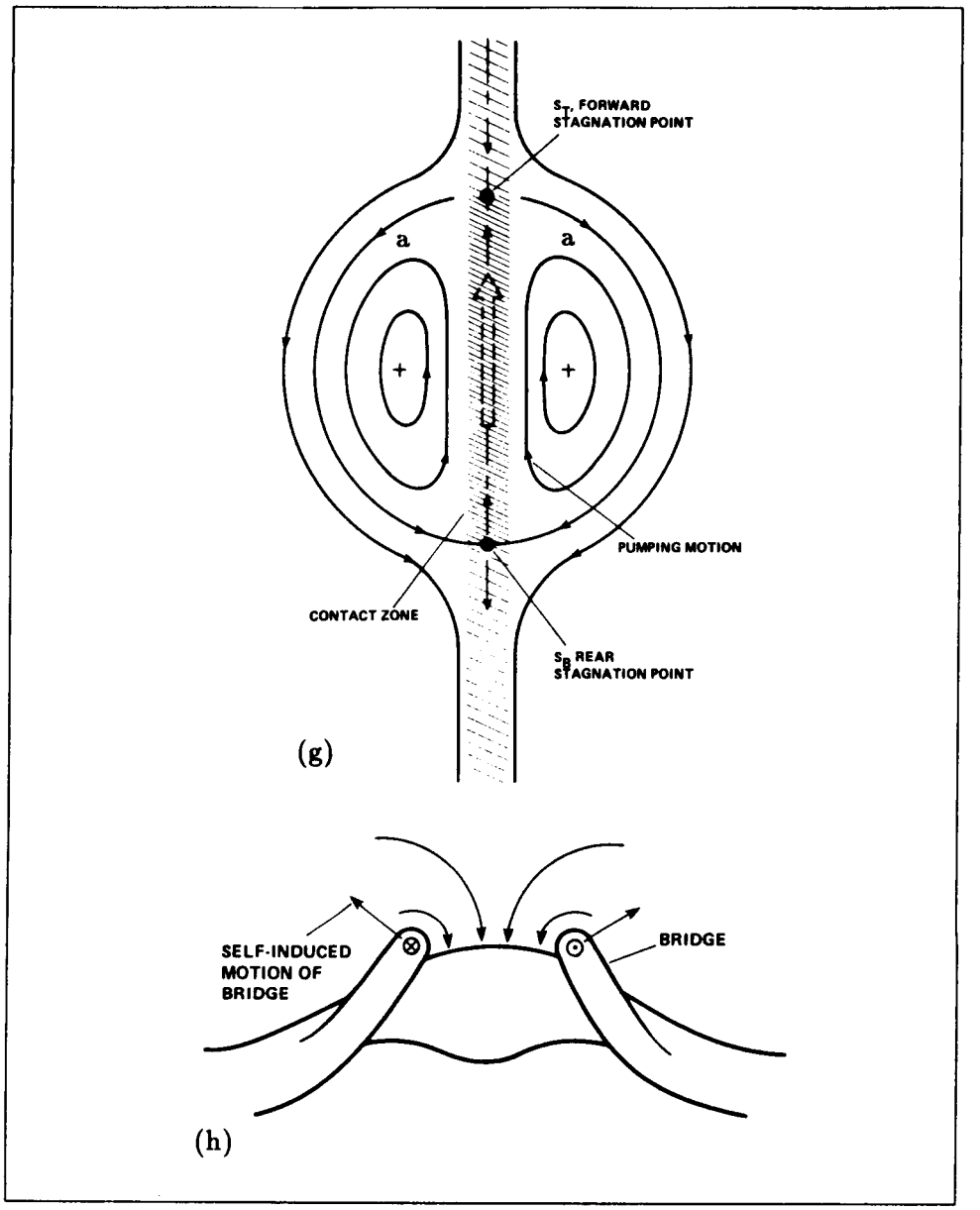

FIGURE 7. (g) streamline pattern in the xy-plane showing stagnation points S_T and S_B; (h) bridging showing self-induced motion of the bridge (straight arrows) and velocity induced on the threads (curved arrows).

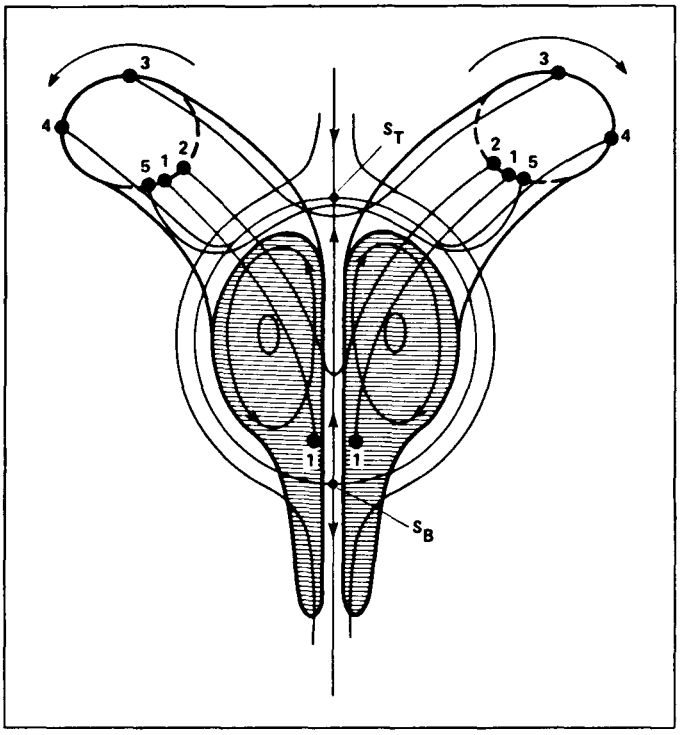

FIGURE 8. Advection and accumulation of reconnected vortex lines forming bridges. The streamline pattern of 7(g) is superimposed on the vorticity contours (hatched area). Lines 1-1, 2-2, 3-3, 4-4 and 5-5 represent successive positions of a vortex line.

antiparallel vortex tubes and get aligned orthogonally i.e. along a–a. Figure 7g also shows that as the reconnected vortex fluid is pumped to S_T, the contact zone (marked by hatches with intensity intended to denote local rate of annihilation) continuously gets supplied with fresh vortex lines starting essentially from near the back stagnation point S_B. The effect of this mechanism is an accumulation of the newly-linked vortex lines at S_T along a–a, thereby explaining the 'humps' we observe on top of the antiparallel vortices in the wire plots (figure 3e). The motion of the bridges due to self induction and the flow induced by them are illustrated in figure 7(h).

The process is schematically explained in the perspective view of one half of the two vortices in figure 8. The figure depicts vortex lines emanating from a fluid particle located at points numbered 1–5 at successive instants.

Figure 9 is a cross-sectional view of the dipole, showing both streamlines (in the frame advected with the dipole) and zones of vorticity. The streamlines show how fluid marked by annihilated vorticity (hence also the tips of the reconnected vortex lines) is advected away from in between the two vortices (dipole) to the stagnation point as the connection point recedes by both diffusion and stretching.

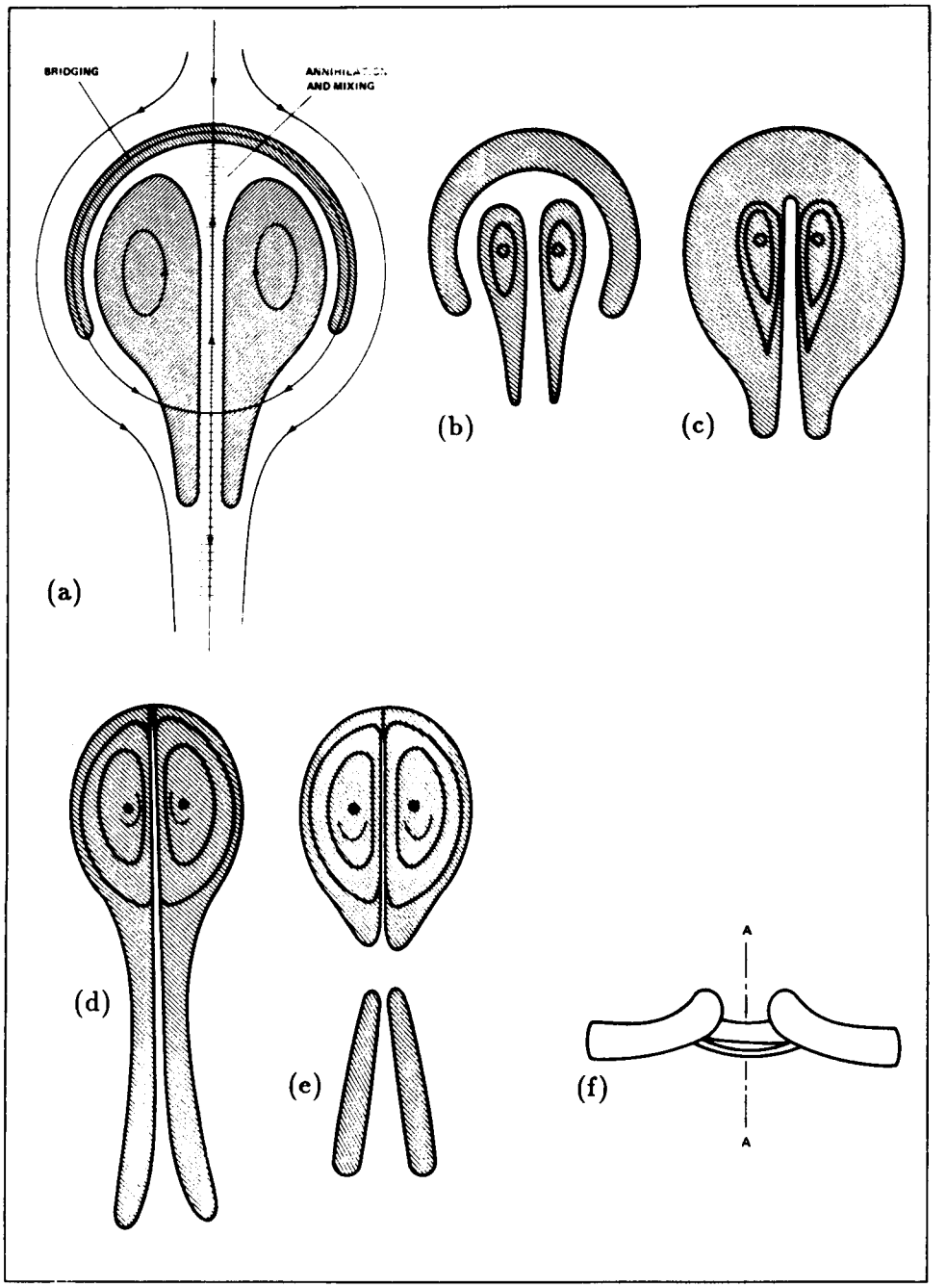

FIGURE 9. (a–f) Motion in dipole and vorticity field in a plane parellel to the xy-plane and passing through the bridges. The configuration (c) results from (b) after fusion of the shroud with the eyes. The head-tail structure is shown in (d) before the head detaches from the tail in (e), which is the cross-section A–A in (f).

The cross-section, as viewed in $|\omega|$ contours, then takes a shape shown in figure 9(b). The characteristic structure of a head-tail dipole with a top shroud (the shroud containing vorticity orthogonal to that of the two "eyes") undergoes changes as the "eyes" are continually depleted due to annihilation and the shroud, which represents a bridge, becomes heavier (due to accumulation of newer vortex lines). Simultaneously, as a result of viscous diffusion the shroud fuses with the dipole into a single structure (figure 9c).

As the reconnected vortex lines accumulate near S_T, so that the bridges acquire a circulation comparable to that of the antiparallel vortex tubes, a new phase of the evolution begins. The bridges (now looking like curved hairpins) begin to move away from each other by self-induction, and also initiate a downwash in the contact zone (figure 7h). This downwash soon becomes strong enough to dominate the upward motion of the dipole in the symmetry plane. There are two reasons for this; first, the circulation in the bridges grows; second, the dipole acquires a head-tail structure and only the vorticity in the head is responsible for the upward motion (figure 9d). Mutual induction causes the heads to move ahead leaving the tail behind to undergo uneventful viscous decay. This is shown in figure 9(e) which represents the section A–A in figure 9(f) representing the state at $t = 4.5$ (figures 3f, 4f). The downwash causes the curvature of the antiparallel vortices to reverse. The antiparallel vortices will therefore no longer be pushed towards each other by self-induction; on the contrary, self-induction will now tend to push the vortices apart. The primary cause of continued fast annihilation is therefore disappearing. This explains why the cut and connect is only partial. The slender threads, which are the remnants of the original vortex tubes, disappear on a longer and qualitatively different time scale.

Regarding accumulation of reconnected vortex lines, the vorticity contours in the yz plane show interesting features (figures 5a–d). As seen from figure 7, new (reconnected) vortex lines are drawn in the bridges from the contact zone, as the bridges continue their swirl. In figure 5b the right hand side bridge moves counterclockwise and the left hand side one moves clockwise. As more and more vortexlines are accumulated, the bridge core starts to become rounded. The peak vorticity is not at the center but toward the side to which the bridges are being advected by mutual and self induction.

4.2. *Modeling of cross-linking, bridging and threading*

In spite of extensive current interest in the cut-and-connect mechanism, its understanding is poor. Less satisfactory is its modeling. We emphasize that one must translate observations—numerical and experimental—into an analytical, at least conceptual, model. In this section we discuss how the insights that we have obtained may be used to construct a model for the crucial stage II, namely, bridging. We shall merely provide the conceptual framework of our model and hope to treat analysis in the future. We draw upon well-understood and simple vortex situations and try to keep the model two-dimensional, at least locally.

There are four principal ingredients of our qualitative description of the cross-linking mechanism in phase II. These are : (i) self-induction due to curvature, (ii)

stretching (by mutual induction) and core deformation, (iii) evolution of two orthogonal vortex dipoles: one in the symmetric plane and the other in the dividing plane, and (iv) annihilation of antiparallel vortex lines by cross-diffusion. Of these, core deformation and cross-diffusion seem to be most difficult to model accurately. Both effects are coupled to the details of the vorticity distribution within the cores: diffusion is the strongest in regions of large gradients and core deformations produce complicated regions of gradient intensification (Melander *et al.* 1987). We concentrate on adequately modeling these two effects, ignoring for the time being 3D details which we consider less important. In this framework, we limit our consideration to the two orthogonal planes—the symmetric and dividing planes—hoping to use the simple 2D evolution equations in each plane, that are coupled together to model 3D effects. The 3D effect is included by incorporating local curvature of the vortices. The bridges are nonplanar so that curvature varies continuously in direction and magnitude along the vortex. We shall make the assumption, however, that curvature is constant along a vortex, although a function of time.

At the end of phase I (inviscid advection), the two vortex tubes touch each other with a contact zone that extends from C_1 to C_2 as shown in two orthogonal views in figures 10(a) and 10(b) and perspective view in 10(c). The cross-linked vortex-lines $C_1'C_1''$ and $C_2'C_2''$ lying within the bridges have radius of curvature r_b at the intersection of the bridges with the dividing plane. Their binormals $\mathbf{b}_{C_1}$ and $\mathbf{b}_{C_2}$ at C_1 and C_2 are in the dividing (yz) plane, but parallel to neither the z nor y axis. In the symmetric plane (figure 10b), vortex tubes have a radius of curvature r_c and the binormal $\mathbf{b}_c$ is in the x direction. We assume for modeling purposes that r_b, r_c, $\mathbf{b}_{C_1}$, $\mathbf{b}_{C_2}$ depend only on time.

In our simplified model the interaction zone consists of two orthogonal dipoles. Let us call the dipole formed by the bridges as the *growing* dipole and the one formed by the initial annihilating vortex tubes as the *dying* dipole. The treatment of the dying dipole is 2D but allows for: i) curvature effects, ii) stretching in the z direction (figure 10d), and external velocity field $\mathbf{v}_b$ due to the bridges or growing dipole (figure 10c). The x-dependence of $\mathbf{v}_b$ is not strong near $x = 0$. Thus we can take the $\mathbf{v}_b$ field from the yz plane and assume it to be constant across the dying dipole. The axial stretching $S_z = \partial w_b/\partial z$ of the dying dipole can accordingly be assumed to be that in the yz plane. To consider the time evolution of the radius of curvature r_c, we assume that the tubes remain parallel (i.e., they remain pressed against each other) and their mutual induction is constant along the length, so that the change of curvature is only due to z-variation of $\mathbf{v}_b$. By symmetry $\partial v_b/\partial z = 0$. Hence r_c is determined by $\partial^2 v_b/\partial z^2$. However, since $\mathbf{v}_b$ is a function of z and y, assuming that we focus our attention on $z = 0$, we must specify the position along the y-axis where $\partial^2 v_b/\partial z^2$ should be evaluated. The centroid location of the decaying dipole is the clear choice. With these approximations we may write equations for the dying dipole; these equations depend only on the flow in the dividing (yz) plane.

How do we model the growing dipole? As vorticity is being annihilated (in the

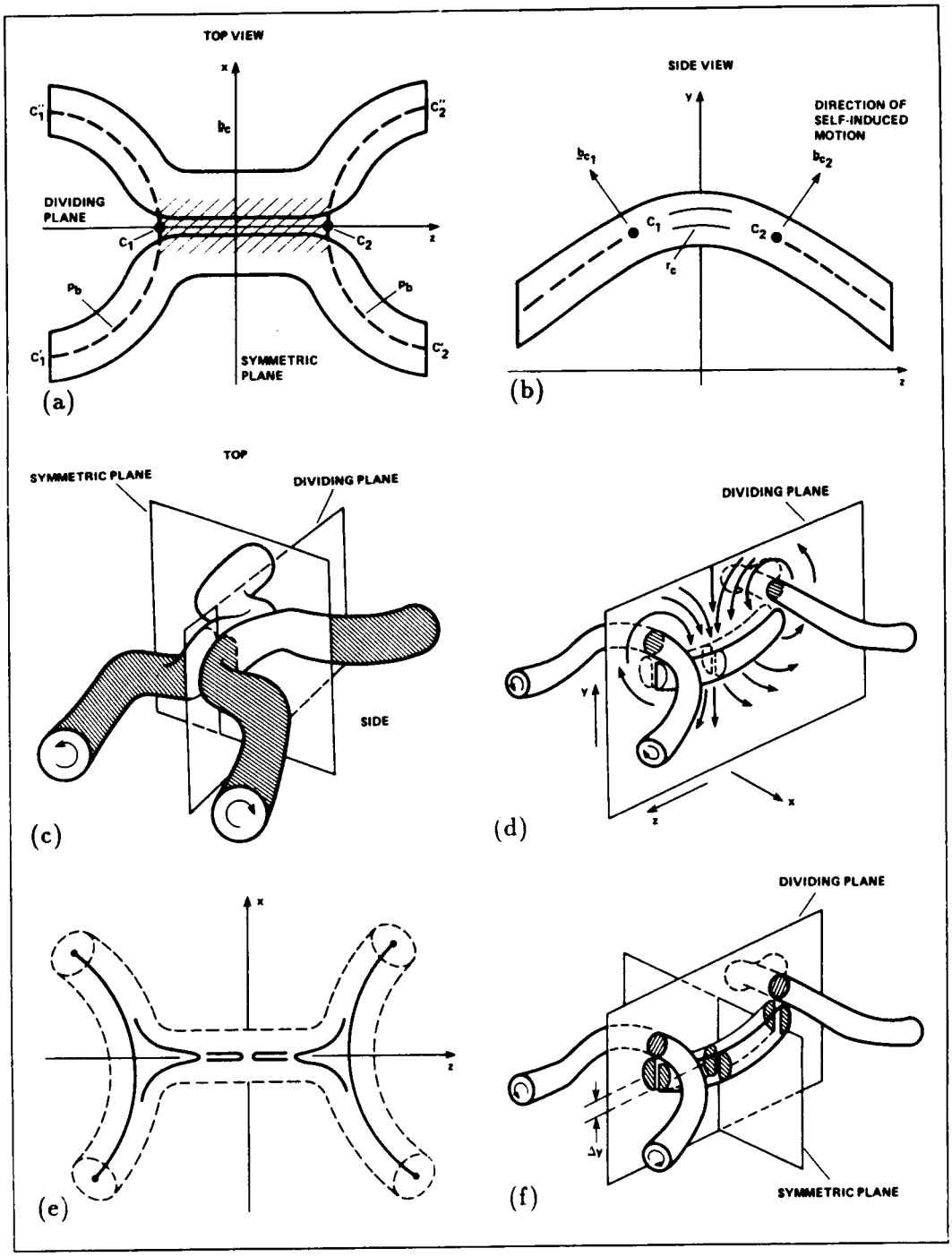

FIGURE 10. Modeling of the reconnection, bridging and threading. The cross-linking zone is shown is shown in top view (a), side view (b) and perspective view (c). The growing dipole is illustrated in (d). The receding of vortex lines during annihilation and cross-linking is shown in (e). The curvature of threads and their modeling is shown in (f).

dying dipole) by cross-diffusion, we immediately feed an equivalent amount of microcirculation into the growing dipole i.e. to the bridges. A crucial question is at what location should this microcirculation be added in the dividing plane. Since vortex lines in the contact zone are nearly antiparallel, we assume an instant annihilation throughout the entire length of the contact zone. In reality, the process is a progressive, though quick, retreat, as shown in figure 10(e). The z-coordinate for the addition of microcirculation is thus clear, namely, the end points C_1 and C_2 of the contact zone. At what y? Let us assume that the dying dipole under the bridges is exactly the same as in the symmetric plane (figure 10e) except that it is displaced in y by Δy due to curvature r_c (thus Δy is known when the distance between the bridges i.e. between C_1 and C_2 is known). The midpoint of this dipole (i.e. point d) denotes the y-location for addition of microcirculation. In other words, the y-location for addition of microcirculation equals the y-location for annihilation plus Δy. The advection of this microcirculation from d to C_1 depends on the strength of the dying dipole. Once again, C_1 and C_2 are the centroids of the bridges in the dividing plane. How the binormals $\mathbf{b}_{C_1}$ and $\mathbf{b}_{C_2}$ evolve is not clear to us yet, but we believe we have here an outline of a reasonable cross-linking model.

The model thus gives evolution equations for two 2D problems with initial conditions given by phase I. The advantage of this model is that we avoid making any assumption regarding core deformation and annihilation, which are two most crucial parts of the process. The disadvantage is that inaccuracies may result from the fact that we have made strong assumptions on the overall 3D structure of the process. However, these assumptions are motivated by our observations.

4.3. *Effect of asymmetry*

The simulation with initial asymmetries produced virtually the same pictures of vorticity wire plots as in figures 3(a–g). At $t = 6$, the plot is virtually indistinguishable from that shown in figure 3(g). We conclude that the phenomenon is insensitive to small asymmetries as long as the vortices are of equal circulations and the analysis (Takaki & Hussain 1985) and high-resolution simulation (Kerr & Hussain 1988) involving symmetry are appropriate for studying the phenomenon.

4.4. *Re dependence*

In order to obtain some idea of the dependence on Re, another simulation for $Re(= \Gamma/\nu) = 500$ was performed. Plots of $|\omega|$ are shown in figures 11(a–h). A similar evolution is seen as at $Re = 1000$ except that at $t = 6$ the reconnection is at an earlier stage. Note that the vorticity level in figures 11 (a–e) are those of figure 3 (i.e., 30% of the initial peak value). At this lower Re, vorticity diffuses more; thus a lower vorticity level is required for capturing the details.

See figures 11(f–h) for vorticity surfaces at the 15% level. We conclude that while time is not scaled properly (which is not unexpected) the mechanisms present are the same. It is particularly interesting to note that two orthogonal dipoles are clear in figures 11(d,e).

5. Other topological properties

The 3D direct simulation of the Navier-Stokes equation provides considerable

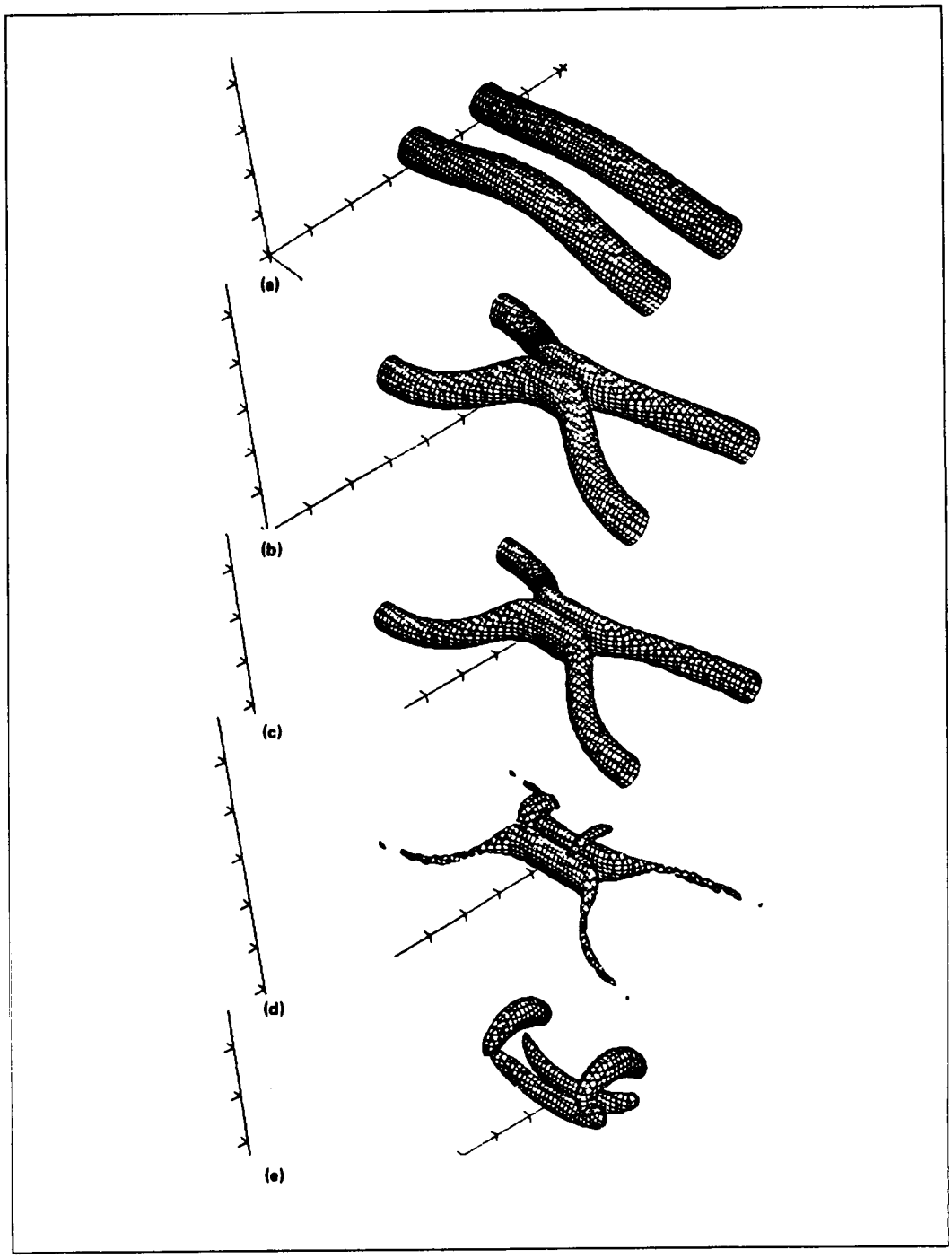

FIGURE 11. Wire plots of $|\omega|$ at 30% of initial peak vorticity at t =0,3,3.75,4.5 and 6, respectively.

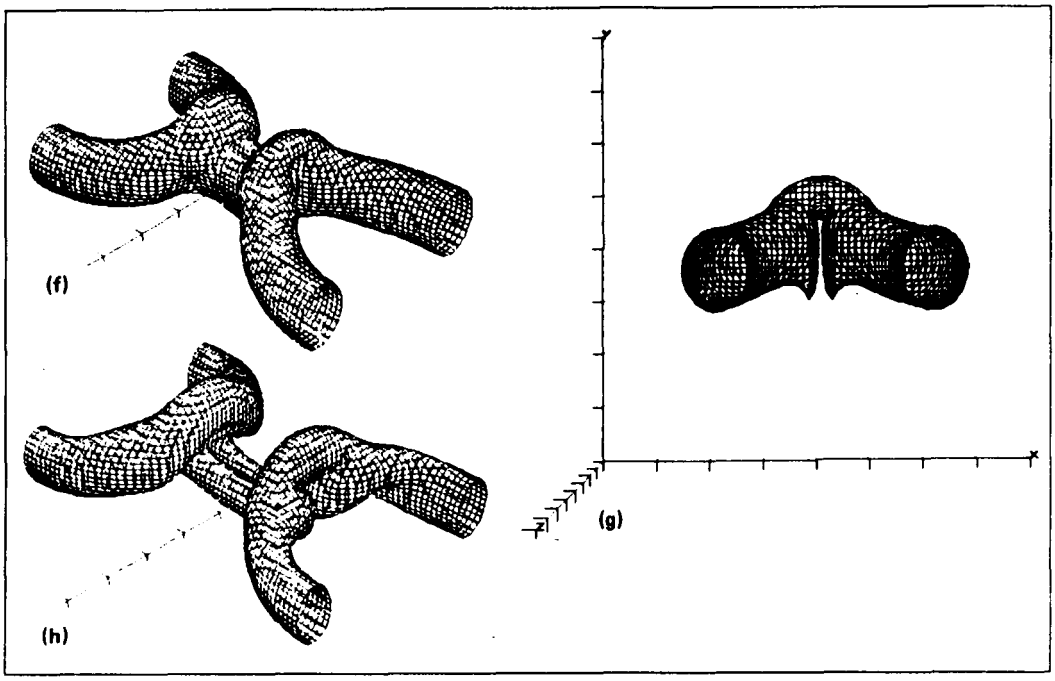

FIGURE 11. (f–g), two views of $|\omega|$ surface at 15% of initial peak vorticity at t =4.5; (h), same as (f) but at t =6.

amount of spatial data unavailable experimentally. These provide the researcher valuable information regarding the topology and dynamics of the interacting vortices. While post-processing and visual examination on graphic stations proves extremely illuminating, information gathered visually is typically overwhelming and has to be properly synthesized and interpreted. More challenging is the selection of appropriate flow fields, the inspection plane or view, property of interest and contour levels to optimally capture a time-changing dynamical event in a turbulent flow. We did not have adequate time for this phase and thus present here a few select examples of topological properties during the reconnection process.

The approach undertaken here is similar to the ones employed by us for the study of coherent structures in turbulent shear flows (See for example Hussain 1980, 1983, 1986). Of the variety of properties that can be useful in studying the topology and dynamics, we limit our attention to scalar intensity c, enstrophy production $P_s = \omega_i s_{ij} \omega_j$, dissipation $\epsilon = 2\nu s_{ij} s_{ij}$ and helicity density $h = u_i \omega_i$. We will present here only a few examples. The contours of dissipation are shown for the symmetry (xy) plane in figure 12(a–e) for $t = 2, 3, 3.75, 4.5$ and 6, and for the dividing (yz) plane in figure 12(f–i) for $t = 2, 3, 3.75$ and 4.5, respectively.

In order to focus on specific details, we choose one instant, namely, $t = 4.5$. Figure 13 shows enstrophy production.

Dissipation and helicity are shown in figures 14 and 15 at 20% and 50% of their peaks values. The perception of the details depends considerably on the contour

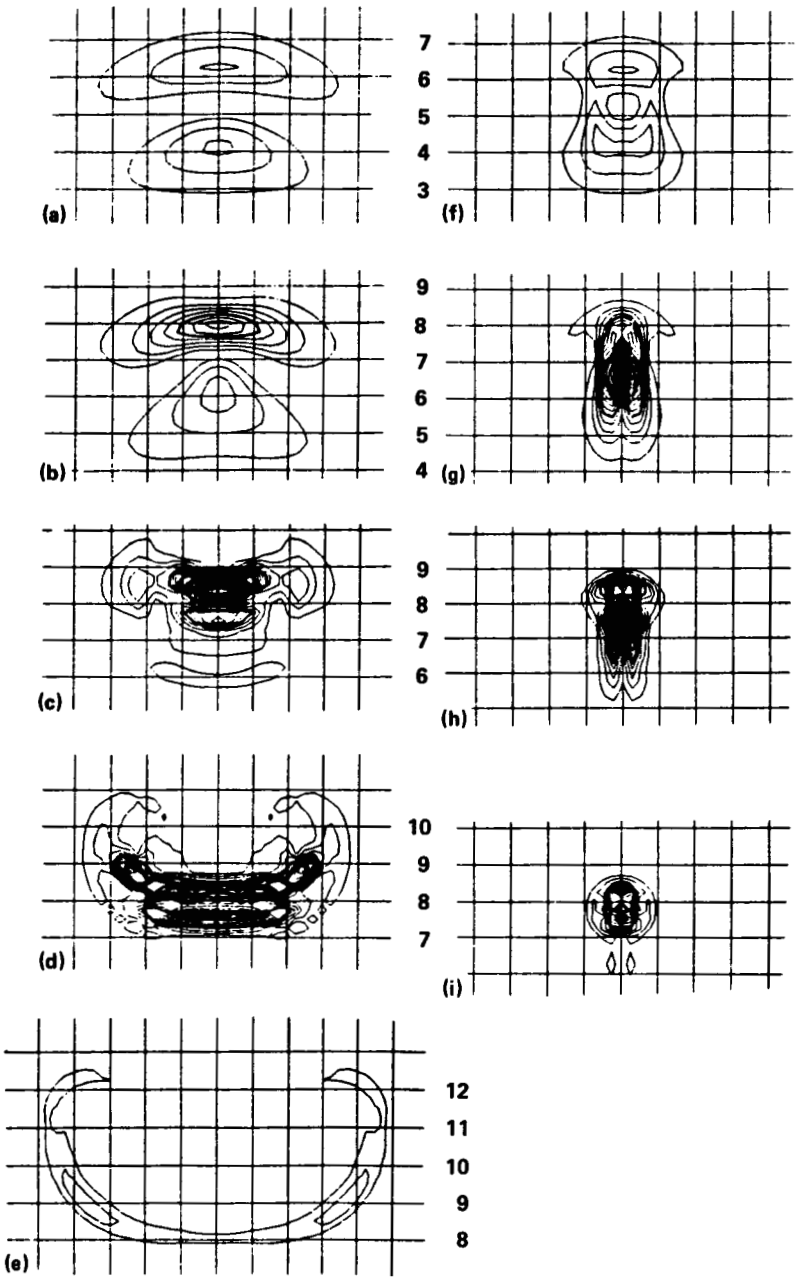

FIGURE 12. Contours of kinetic energy dissipation rate. (a–e), yz-plane at t =2,3,3.75,4.5 and 6, respectively; (f–i), xy-plane at t =2,3,3.75, and 4.5, respectively. The grid is four times coarser than the computational mesh. The numbers on the right serve to indicate the y locations.

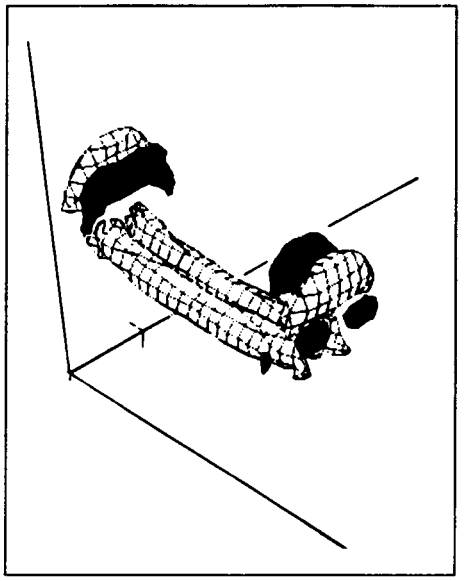

FIGURE 13. Surface contours of enstrophy production at $t = 4.5$. Black, negative production at 20% of the peak negative value; hatched, positive production at 20% of the peak positive value. The magnitude of the positive peak is about twice as large as the negative peak.

level. The correspondence between cross-sectional and projected views (for example, compare 12d and 14) is not obvious. One must examine the entire flow field; however, space does not permit comprehensive documentation. Below, we only summarize our observations without including additional figures.

Not surprisingly, enstrophy production occurs mostly in the contact zone and threads and somewhat in the bridges but in complicated way. For instance figure 13 shows that in the bridges there is both positive and negative production corresponding to vorticity stretching and compression, respectively. For most of the remaining regions, there is very little production, except that there are large regions of low-level *negative* production. This is because self induction produces slight compression and fattening of the vortices (see figure 3). This is consistent with the observed accumulation of scalar, as well as progressive fattening of the scalar domain, in the same regions.

Within the dipole, dissipation mostly occurs in a small region containing the contact plane (figures 12f–i) but significant dissipation is also present above the contact zone around the forward stagnation point. We find the peak to lie near the intersection of the two symmetry planes. Since helicity density vanishes in these planes by symmetry, the peaks of dissipation and helicity density are mutually exclusive. There is significant helicity generation where the threads wrap around the bridges (figure 15). The high helicity density in the threads (figure 15b) suggests long life—consistent with our observation that the threads decay very slowly.

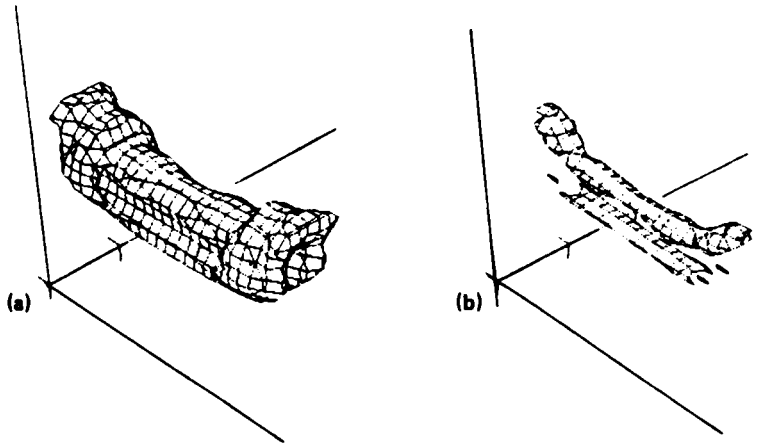

FIGURE 14. Surface contours of dissipation at $t = 4.5$. (a) 20% level; (b) 50% level.

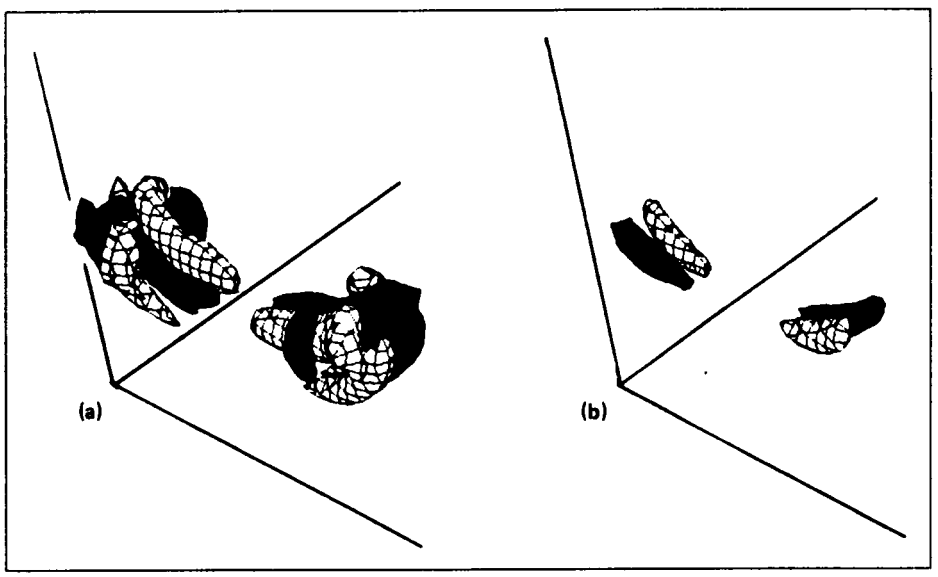

FIGURE 15. Contours of helicity density at $t = 4.5$. (a), 20% of peak negative (black) and positive (hatched); (b) 50% levels as in (a).

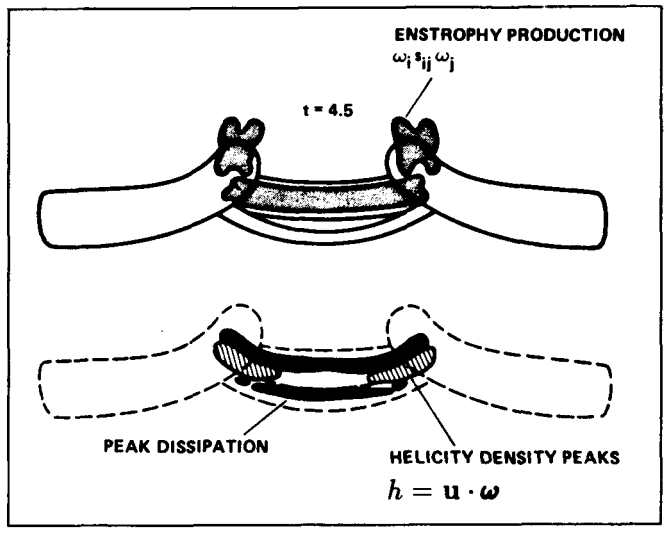

FIGURE 16. Comparison between regions of large enstrophy production, helicity density and dissipation at $t = 4.5$.

The possible correspondence between dissipation and helicity has been of particular interest in studies of turbulent flow. Hussain (1986) suggested that contrary to claims elsewhere (Moffatt 1985; Tsinober & Levich 1983) the domains of helicity and dissipation cannot be spatially independent even though the peaks may be. The present data are consistent with this view (see figure 16).

When we compare the scalar field with vorticity (for computation with unit Schmidt number) we find that they are rather different. In particular, the bridges have no scalar. This can be explained by the fact that vorticity stretching is accompanied by corresponding decrease of specie concentration. We have persistently warned against the use of flow visualization for study of coherent structures and vorticity field in turbulent or unsteady flow and warned that the difference is not due to non-unity Schmidt number alone (Hussain 1980, 1983). The present simulation clearly supports our warning.

6. Concluding remarks

Vortex interactions involving cross-linking consist of four phases: (0) antiparellelization, (i) core flattening and stretching, (ii) bridging, and (iii) threading. Since the first was observed in various numerical simulations and is consistent with Biot-Savart induction, we focused on the latter three phases. The choice of antiparallel vortices has eliminated distracting complexities that result in the case of collision at arbitrary orientations. The simulation not only has shed considerable light on the heretofore unknown details of the mechanism but also helped us provide a conceptual model. The most significant outcomes of this study are the discovery and explanation of the bridging process and the fact that cross-linking is incomplete. The formation of long-lived threads clearly play some role in enstrophy cascade and

mixing. These threads decay at viscous time scale due to the formation of head-tail structure and the reversal, induced by the bridges, of the curvature of the vortex dipole. The simulation has also vividly demonstrated that vorticity field can be different from scalar field even in the case of unity Schmidt number. The phenomenon is clearly the same at different Re while the reconnection time is *Re* dependent.

This simulation is a first attempt at understanding the reconnection mechanism. But more information is needed regarding the details of the topology change and *Re* effect. We need higher *Re* simulations with finer resolution before finer analysis can be attempted. Considering inherent limitation of even the supercomputer capability, invoking symmetry seems unavoidable. Simulations and analysis invoking symmetries, which were viewed with skepticism by many researchers, are now vindicated.

As hard as it is, we must obtain detailed 3D experimental data, beyond those provided by Schatzle's experiments. It is through a close collaboration between experiments and simulation that a clearer understanding and modeling of this phenomenon will emerge. We are planning such collaborative research involving high-resolution simulation and experiments.

This research was mostly performed during the 1988 summer term of the CTR. We are thankful to K. Shariff and P. Moin for illuminating discussions. In addition, F.H. acknowledges the support of ONR Grant N00014-87-K-0126.

REFERENCES

ANDRECK & GLABERSON 1982 Tkachenko waves. *J. Low Temp. Phys.* **48**, 257–296.

AREF, H. 1982 Integrable, chaotic, and turbulent vortex-motion in two-dimensional flows. *Ann. Rev. Fluid Mech.* **15**, 345–389.

ASHURST, W.T. & MEIRON, D.I. 1987 Numerical study of vortex reconnection. *Phys. Rev. Lett.* **58**, 1632–1635.

BATCHELOR, G.K. 1967 *An Introduction to Fluid Dynamics*.Cambridge University Press: Cambridge, England.

BENJAMIN, T.B. 1985 Private communication.

CANTWELL, B.J. 1981 Organized motion in turbulent flow. *Ann. Rev. Fluid Mech.* **13**, 457–515.

CROW, S.C. 1970 Stability theory for a pair of trailing vortices. *AIAA J.* **8**, 2172–2179.

HOPFINGER, E., BROWAND, F.K. & GAGNE, Y. Turbulence and waves in a rotating tank. 1982 *J. Fluid Mech.* **125**, 505–534.

HUSSAIN, F. & HUSAIN, H. 1987 Passive and active control of jet turbulence. In *Turbulence Management and Relaminarization* (ed. H. Liepman & R. Narasimha), pp. 445–457, Springer Verlag: New-York, Heidelberg, Berlin.

HUSSAIN, A.K.M.F. 1980 Coherent structures and studies of perturbed and unperturbed jets. In *The Role of Coherent Structures in Modelling Turbulence and Mixing* (ed. J. Jimenez), Lecture Notes in Physics, vol. 136, pp. 252–291, Springer Verlag: New-York, Heidelberg, Berlin.

HUSSAIN, A.K.M.F. 1983 Coherent structures–reality and myth. *Phys. Fluids* **26**, 2816–2850.

HUSSAIN, A.K.M.F. 1986 Coherent structures and turbulence. *J. Fluid. Mech.* **173**, 303–356.

KAMBE, T. & MINOTA, T. 1983 Acoustic wave radiated by head-on collision of two vortex rings. *Proc. R. Soc. Lond.* A **386**, 277–308.

KERR, R.M. & HUSSAIN, F. 1988 Simulation of vortex reconnection. *Physica* D, Submitted.

KIDA, S. & TAKAOKA, M. 1987 Bridging in vortex reconnection. *Phys. Fluids* **30**, 2911–2914.

KIDA, S., TAKAOKA, M. & HUSSAIN, F. 1988 Reconnection of two vortex rings. *Phys. Fluids*, Submitted.

KIM, J. & MOIN, P. 1986 The structure of the vorticity field in turbulent channel flow. Part 2. Study of ensemble averaged fields. *J. Fluid Mech.* **162**, 339–363.

LAUFER, J. 1974 On the mechanism of noise generation by turbulence. In *Omaggio a Carlo Ferrari*, Liberia editrice universitaria levrotto & bella Torino, 451–464.

LEONARD, A. 1980 Vortex methods for flow simulation. *J. Comp. Phys.* **37**, 289–335.

LUMLEY, J. 1981 Coherent structures in turbulence. In *Transition and Turbulence* (ed. R.E. Meyer), pp. 215–242, Academic Press: New York.

MEIRON, D.I., SHELLEY, M.J., ASHURST, W.T. & ORSZAG, S.A. 1988 Numerical study of vortex reconnection. *Physica D*, Submitted.

MELANDER, M.V., ZABUSKY, N.J. & STYCZEK, A.S. 1986 A moment model for vortex interactions of the two-dimensional Euler equations. Part 1. Computational validation of a Hamiltonian elliptical representation. *J. Fluid Mech.* **167**, 95–115.

MELANDER, M.V., MCWILLIAMS, J.C. & ZABUSKY, N.J. 1987 Axisymmetrization and vorticity-gradient intensification of an isolated two-dimensional vortex through filamentation. *J. Fluid Mech.* **178**, 137–159.

MELANDER, M.V. & ZABUSKY, N.J. 1988 Entanglement produces an apparent reconnection of 3D vortex tubes. *Phys. Rev. Lett.*, Submitted.

MELANDER, M.V., ZABUSKY, N.J. & MCWILLIAMS, 1988 Symmetric vortex merger in two dimensions: causes and conditions. *J. Fluid Mech.* **195**, To appear.

MOFFATT, H.K. 1985 Magnetostatic equilibria and analogous Euler flows of arbitrarily complex topology. Part 1. Fundamentals. *J. Fluid Mech.* **159**, 359–378.

MOIN, P., LEONARD, A. & KIM, J. 1986 Evolution of a curved vortex filament into a vortex ring. *Phys. Fluids* **29**, 955–963.

OSHIMA, Y. & ASAKA, S. 1977 Interaction of two vortex rings along parallel axes in air. *J. Phys. Soc. Jap.* **42**, 708–713.

PUMIR, A. & SIGGIA, E.D. 1987 Vortex dynamics and the existence of solutions to the Navier-Stokes equations. *Phys. Fluids* **30**, 1606–1626.

SAFFMAN, P.G. 1978 The number of waves on unstable vortex rings. *J. Fluid Mech.* **84**, 625–639.

SCHATZLE, P.R. 1987 An experimental study of fusion of vortex rings. Ph.D. Thesis, Graduate Aeronautical Laboratories, Calif. Inst. Tech.

SCHWARZ, K. 1985 Three-dimensional vortex dynamics in superfluid ^{4}He: Line-line and line-boundary interactions. *Phys. Rev.* B **31**, 5782–5804.

SIGGIA, E.D. 1985 Collapse and amplification of a vortex filament. *Phys. Fluids* **28**, 794–805.

SIGGIA, E.D. & PUMIR, A. 1985 Incipient singularities in the Navier-Stokes equations. *Phys. Rev. Lett.* **55**, 1749–1752.

STANAWAY, S.K., SHARIFF, K. & HUSSAIN, F. 1988 Head-on collision of viscous vortex rings. In Proceedings of the 1988 Summer Program, Center for Turbulence Research.

TAKAKI, R. & HUSSAIN, F. 1984 On the dynamics of entangled vortex filaments. *Phys. Fluids* **27**, 761–763.

TAKAKI, R. & HUSSAIN, A.K.M.F. 1985 Recombination of vortex filaments and its role in aerodynamic noise. In *Proc. Fifth Symposium on Turbulent Shear Flows*, pp. 3.19–3.25.

TSINOBER, A. & LEVICH, E. 1983 On the helical nature of three-dimensional coherent structures in turbulent flows. *Phys. Lett.* A **99**, 321–324.

WIDNALL, S.E., BLISS, D.B. & TSAI, C.-Y. 1974 The instability of short waves on a vortex ring. *J. Fluid. Mech.* **66**, 35–47.

ZABUSKY, N.J. & MELANDER, M.V. 1988 Three dimensional vortex tube reconnection: morphology of orthogonally-offset tubes. *Physica* D, Submitted.

Head-on collision of viscous vortex rings

By S. STANAWAY[1], K. SHARIFF[2], AND F. HUSSAIN[3]

The head-on collision of two identical axisymmetric viscous vortex rings is studied through direct simulations of the incompressible Navier-Stokes equations. The initial vorticity distributions considered are those of Hill's spherical vortex and of rings with circular Gaussian cores, each at Reynolds numbers of about 350 and 1000. The Reynolds number is defined by Γ/ν, the ratio of circulation to viscosity. As the vortices approach each other by self-induction, the radii increase by mutual induction, and vorticity cancels through viscous cross-diffusion across the collision plane. Following contact, the vorticity distribution in the core forms a head-tail structure (for the cases considered here), a behavior which has also been observed in inviscid calculations (Shariff *et al.* 1988), 3D viscous calculations (Melander & Hussain 1988, MH), and experiments (Oshima 1978). The characteristic time of vorticity annihilation is compared with that of a 3D collision experiment (Schatzle 1987) and 3D numerical simulations (MH). It is found that the annihilation time is somewhat longer in our axisymmetric case than it is in the symmetry plane of the experiment and 3D numerical simulation. Furthermore, by comparing the annihilation time with a viscous timescale and a circulation timescale, we deduce that both the strain-rate due to local effects and that due to 3D vorticity realignment are important. The flow is computed to the large time Stokes flow limit where the circulation decays as $t^{-3/2}$ and the vorticity distribution agrees with the self-similar solution of the Stokes equations. In this limit, the self-annihilation is exactly twice the mutual annihilation. For one of the cases computed, the far-field quadrupole sound is compared with the experimental results of Kambe & Minota (1983). The agreement is quite good even though the two *Re*'s are very different.

1. Introduction

Organized vortex structures are seen in many turbulent flows (Cantwell 1981). Their interactions may involve a change in topology through reconnection. For example, trailing vortices of an aircraft cross link to form vortex rings (Crow 1970), or an elliptic jet may bifurcate by splitting of elliptic rings thus significantly enhancing mixing (Hussain & Husain 1987). This is an important process in turbulence since reconnection is likely to involve significant mixing, cascade of energy, dissipation, and helicity generation (Hussain 1986). Studying annihilation and reconnection may also benefit vortex filament methods which currently model such processes

1 NASA/Stanford Center for Turbulence Research
2 NASA Ames Research Center
3 University of Houston, Dept. of Mechanical Engineering

with *ad hoc* approaches (Leonard 1975). Another motivation for the study of reconnection is to determine its role in jet noise (Hussain 1983; Bridges & Hussain 1987).

Many vortex reconnection situations have been studied experimentally and numerically: two rings colliding at an angle (Schatzle 1987; Ashurst & Meiron 1987), two or more rings initially in the same plane (Oshima & Asaka 1977), hairpin vortex evolving into a vortex ring (Moin *et al.* 1986), and two sinusoidal vortex tubes of opposite circulations (MH, in this volume). For clarity of discussion, consider the case of MH shown in figure 1. As in all of the 3D situations, portions of the two vortices approach each another (figure 1a) and upon "contact" (figure 1b), vorticity is annihilated across the collision plane (plane yz). In 3D flow, annihilation is accompanied by vorticity realignment or *reconnection* (in the x direction). In contrast, an axisymmetric vortex ring collision (shown schematically in figure 2) contains only annihilation. It is useful, however, to consider annihilation alone since this process is kinematically related to reconnection. A cartoon of figure 1, shown by figure 3a, illustrates that because circulation is constant along vortex tubes, the rate-of-decrease of circulation in the *annihilating* region (plane xy) is equal to the rate-of-increase of circulation in the *connecting* region (plane yz). One objective of this work is to compute the annihilation time for the axisymmetric collision and compare this to experiments of rings colliding at an angle (Schatzle 1987) and to a numerical simulation of cross linking vortex tubes (MH) to determine the role of the three dimensionality of the vorticity field in annihilation.

More precisely, we are comparing the axisymmetric case to a plane in the 3D collision, specifically, to symmetry plane xy in figure 3. The vorticity contours in this plane, given by figures 4a-4d, correspond to figures 1a-1d. In the 3D problem the characteristics of the vorticity distribution affecting annihilation such as core size and shape, and the local radius of curvature of vortex filaments, referred to as *local effects*, are supplemented by non-local influences from the bridges which arise from vorticity realignment (for a discussion of bridging, see MH). The objective of this work is to quantify these local effects, which entirely compose the axisymmetric case, and determine their relevance to three dimensional reconnection.

2. Problem Description

The time-dependent annihilation of axisymmetric vortex rings is entirely governed by the local character of the vorticity (i.e. core shape, size, strength and curvature). General trends of this process can be understood by considering the velocity induced by these local effects, referred to as the *local induction* approximation (Batchelor 1973, p.510).

Because the domain is unbounded and does not contain any bodies, the only mechanism permitting the circulation of a vortex ring (i.e. defined by the circuit of figure 5) to change, is diffusion of vorticity across the axis of symmetry and the collision plane. We refer to diffusion across the symmetry axis as self annihilation, and across the collision plane as mutual annihilation. The rate-of-change of circulation

about a material circuit is given by

$$\frac{d\Gamma}{dt} = -\nu \oint (\nabla \times \boldsymbol{\omega}) \cdot d\mathbf{l}. \tag{1}$$

Applying equation (1) to a quarter plane shown in figure 5 gives

$$\oint (\nabla \times \boldsymbol{\omega}) \cdot d\mathbf{l} = \int_0^\infty \frac{1}{\sigma} \frac{\partial(\sigma\omega)}{\partial\sigma} dx - \int_\infty^0 \frac{\partial\omega}{\partial x} d\sigma \tag{2}$$

with the terms on the right hand side giving the contributions from segments 1 and 3 of figure 5; the contribution from segment 2 is zero. From this, we see that larger normal derivatives of vorticity along the x and σ axes result in greater rate-of-loss of circulation.

The effects that influence the gradients can be seen by the local induction approximation (Batchelor, p.519). Consider the induced velocity field resulting from line elements (length $= 2L$) of two curved filaments (radius of curvature $= R$) which are in close proximity (separation distance $= b$) (figure 6). The induced velocity from a line element is resolved into its circumferential and binormal components. The circumferential component,

$$du_\phi(x,y) = \frac{\omega(x',y')\,dx'dy'}{2\pi\Delta}, \tag{3}$$

upon integration, represents the limit of a 2D vortex pair (i.e. dipole). Here, Δ is the distance between x,y and x',y', the point where the line element intersects the xy plane. The binormal component,

$$du_b(x,y) = \frac{1}{4\pi R(x',y')} \omega(x',y')\,dx'\,dy' \log\left(\frac{L}{\Delta}\right) + \mathcal{O}(1) \tag{4}$$

gives the *self-induction* which presses the cores against each other and increases the gradients, and hence the circulation decay. Note that this analysis is valid only when b and the core size are much smaller than R and $2L$. The velocity field found from the integral of equation (3) causes the cores to translate and to subject each other to a strain rate that scales as $e \sim \Gamma/b^2$. As the cores approach, e increases.

Now for each instantaneous form of the velocity induced by one vortex on the other (characterized by e), there will be an equilibrium configuration in which the motion induced by one vortex on itself, is balanced by the flow induced by the other vortex. In other words if the self-induced motion were suppressed (thus fixing e) the locally two-dimensional flow would be steadily translating in the absence of viscosity. Such equilibrium shapes are well known and include a family of 2D translating pairs for uniform vorticity (Pierrehumbert 1980, among others) and the single solution for peaked vorticity (Batchelor 1973, p.535). If e changes slowly compared with the vorticity, adiabatic invariance will hold (Neu 1984, p.2400) and the cores will migrate through the equilibrium shapes as they approach each other.

In this case, core deformation will be modest. In the cases considered here, the cores flatten considerably more indicating a loss of adiabatic invariance. The parameter governing this, α, is the ratio of how fast e changes compared to the time scale of internal rotation:

$$\alpha \sim \frac{\frac{d}{dt}\left(\frac{e}{\omega}\right)}{1/T_{\text{rot}}}, \tag{5}$$

or,

$$\alpha \sim \frac{\delta^3}{b^3}\frac{\delta}{R}\log\left(\frac{R}{\delta}\right). \tag{6}$$

Thus, given the same core size to separation ratio (δ/b), cores that are thin compared to the radius of curvature are more resistant to distortion. Equations (3) and (4) give the qualitative behavior of the core approach and flattening in the limiting case of thin cores.

For the head-on collision the combined circulation of the two rings is zero ($\Gamma = 0$), and the term proportional to $\log L$ from self-induction vanishes upon integration. Furthermore, since $\log \Delta$ is the Green's function for the streamfunction (say Ψ_{2D}) of the locally 2D flow, one obtains upon integration

$$u_b(x, y, t) = \frac{\Psi_{2D}(x, y, t)}{R}. \tag{7}$$

Now, given an equilibrium 2D flow at each instant, on each streamline of the vortex

$$\Psi_{2D} = \Psi_o(t) - V(t)x, \tag{8}$$

where $\Psi_o(t)$ is the value of the streamfunction on the streamline in a reference frame translating with the dipole at velocity $V(t)$. Since $\Psi_o(t)$ is a function that decreases as the cores come together, the first term in equation (8) provides a *rigid* motion of the cores towards each other with an ever decreasing velocity while the second term provides a linear flattening in x (Shariff 1988).

3. Review of Earlier Work in Axisymmetric Vortex Ring Collisions

The problem of the collision of two axisymmetric vortex rings is classical and is described in the very first paper dealing with vortex motion (Helmholtz 1858) where it is assumed that the fluid is inviscid, and the cores sufficiently thin that they do not deform. In 1893 Dyson considered the case of a constant vorticity distribution in a circular core, rotating as a solid body and assumed large separations compared to core size. He found that the cores unphysically overlap when the rings have stretched by an amount

$$\frac{R}{R_o} = 1.06\left[\log\left(\frac{8R_o}{\delta_o}\right) - \frac{7}{4}\right]. \tag{9}$$

Shariff *et al.* (1988) numerically solved a 1D evolution equation for the shape of the core boundary to investigate deviations from Dyson's solution for small separations.

They found that until the time when the radius has stretched approximately twice as far as indicated in equation (9) (2.49 instead of 1.06) the cores deform very little and instead follow the shapes of the steady 2D translating pairs computed by Pierrehumbert (1980).

Oshima (1978) conducted a smoke visualization study with Re_D ranging between 133 and 1865, based on initial propagation speed and exit diameter. Her photographs will be presented for comparison. Kambe & Minota (1983) studied the acoustic wave radiated when two shock-tube generated rings ($Re_D = 42,000$) collide. We shall provide comparison with the quadrupole part of the measured acoustic far-field signal. Considering the widely different Reynolds numbers of the experiment and simulation, the agreement is surprising. Kambe & Minota also develop a simple model for the trajectory of the vortices and decay of circulation. The model is based on an exact 1D solution of the Navier-Stokes equations for two layers of vorticity of opposite signs that are pressed together by an externally imposed plane strain.

After the present work was completed it came to our attention that Kambe & Mya Oo (1984) have studied the axisymmetric collision with a finite difference method in a bounded domain at Reynolds numbers (Γ/ν) from 140–1400 which are comparable to those of the present study. Liu & Ting (1982) employed a finite-difference scheme with boundary conditions specified using far-field expansions. They consider a vortex ring collision with $\Gamma/\nu = 201$, a very small initial separation equal to 0.20 of the toroidal radius and a core radius of 0.05 times the toroidal radius. Results are presented for a short time during which the the rings have stretched to only $R/R_o = 1.6$.

4. Methods

The Navier-Stokes equations are solved in an unbounded domain using a spectral code developed by Stanaway, Cantwell & Spalart (1988). The method relies on divergence-free basis functions, with the result that continuity is inherently satisfied and the pressure does not appear in the working equations. In particular, the basis functions are composed of Legendre polynomials in the polar direction and Jacobi polynomials matched to an algebraic mapping of the radial coordinate. Time advancement is second order accurate, implicit for the linear terms (Adams Bashforth), and explicit for the nonlinear term (Crank-Nicolson). The code has been tested using a comprehensive set of diagnostics (rate of convergence, stability at high Reynolds numbers, conservation of impulse, rate of energy decay etc.).

Given the dynamic solution, the quadrupole part of the acoustic signal is computed using the theory of vortex sound developed by Möhring (1978). It assumes that the sound source is compact. This means that if u and l are characteristic velocity and lengths of a vortical region and c_o is the speed of sound of the undisturbed medium, then the wavelength $c_o l/u$ of the radiation should be much larger than l, or, the eddy Mach number $M = u/c_o \ll 1$. The final working expression for

the far-field acoustic pressure p is

$$p(\mathbf{x},t) = \frac{\rho_o}{c_o^2}\frac{x_i x_j}{|\mathbf{x}|^3} Q'''_{ij}(t_r),$$
$$Q'''_{ij}(t) = \frac{1}{12\pi}\frac{\partial^3}{\partial t^3}\int y_i(\mathbf{y}\times\boldsymbol{\omega})_j \, d\mathbf{y}, \tag{10}$$
$$t_r = t - |\mathbf{x}|/c_o.$$

The novelty and usefulness of this expression lies in the fact that it relates the far-field acoustic pressure directly to the unsteadiness of the incompressible vorticity field via the third derivative of its second moment. Equation (10) represents the quadrupole part of the signal; a more complete theory by Kambe & Minota (1983) shows that in the presence of viscosity there is also a monopole whose time behavior is proportional to the second time derivative of the kinetic energy. We restrict attention here to just the quadrupole. For the axisymmetric case, equation (10) becomes

$$p(r,\theta,t) = \frac{\rho_o}{4rc_o^2}\left(\cos^2\theta - \frac{1}{3}\right) Q'''(t - r/c_o),$$
$$Q'''(r) \equiv \int x\sigma^2\omega(x,\sigma)\,dx\,d\sigma. \tag{11}$$

5. Results

Results are presented in figures 7-10 for initial conditions of thin and thick core rings at low and high Reynolds numbers. The parameters for each case are as follows:

CASE No. (FIGURE No.)		$(\Gamma/\nu)_o$	DESCRIPTION	PARAMETERS	
1	(7)	350	Thin core	$a_o/R_o = 0.35$	$X_o/R_o = 3$
2	(8)	1000	"	"	"
3	(9)	357	Smoothed Hill's vortex	$r_i = 0.8$, $r_o = 1.3$	$X_o/R_o = 2$
4	(10)	1073	"	"	"

For all of the cases shown, the resolution was fixed at 65 × 65 modes. For the thin core cases (1 & 2) the initial vorticity distributions in the cores are Gaussian (centered at X_o, R_o) with an "image" at $(X_o, -R_o)$ in order to ensure zero vorticity along the axis. The core radius, a_o, is defined as as the distance from the center of the core to where the maximum velocity occurs in two-dimensions.

The initial vorticity profile for the thick core cases (3 & 4) is that of Hill's spherical vortex (Batchelor 1973 p.526). The abrupt jump in vorticity is replaced by a smooth transition between a specified inner radius, r_i, and an outer radius, r_o:

$$\omega = Ar\sin\theta \begin{cases} 1 & r \le r_i \\ 1 - f(\xi) & r_i < r < r_o \\ 0 & r \ge r_o \end{cases} \tag{12}$$

where

$$f(\xi) = \exp[-K\xi^{-1}\exp(1/(\xi-1))] \quad 0 \le \xi \le 1$$

$$\xi = \frac{r - r_i}{r_o - r_i} \qquad K = 1/2(\exp 2)(\log 2).$$

following Melander *et al.* (1987).

For each of the cases presented, vorticity contours are shown at several instants (figures 7a-d, 8a-d, 9a-d, 10a-d), followed by time-dependent diagnostics. These instants (i.e. $t_1, t_2, t_3, \ldots$) are marked on the curve, $\Gamma(t)$, by solid dots. Let us first consider the thin ring cases (figures 7 and 8). Driven by self-induction, the two vortex rings propagate toward each other. The core shapes begin to immediately adjust from the initial profile to a characteristic oblong shape shown by the vorticity contours of figures 7b and 8b. The peak vorticity, ω_p, initially decreases due to viscous diffusion (figures 7g, 8g) while the circulation remains constant (since a significant amount of vorticity has not yet reached either the collision plane or the axis of symmetry). The curve of ω_p is ragged because it is the maximum value of the vorticity on the grid points instead of the maximum value of the smooth function. As the rings get closer, the ring radii increase due to mutual induction, and neglecting viscosity this means that the vorticity of a vortex filament will increases like σ. These two effects are opposing each other, and their relative importance determines whether the peak vorticity will increase or decrease. For the high Re case (figure 8), stretching is more dominant as seen by the larger percentage increase of peak vorticity throughout the calculation. As the interaction proceeds, vorticity gradients steepen along the collision plane, and vorticity annihilation is enhanced. The cores do not continue to flatten uniformly but clump at the top forming a head-tail structure. Note that this head-tail structure is remarkably similar to figure 4 of the 3D collision. As the circulation decreases, mutual induction and stretching decrease and at some point, viscous diffusion dominates.

The stages are very similar for the Hill's vortex cases. One difference is that vorticity begins to annihilate across the axis of symmetry as the rings approach since the vorticity extends to the symmetry axis. From equation (2), we see the the vorticity will initially decay like

$$\left(\frac{d\Gamma}{dt}\right)_0 = -\frac{6\nu\Gamma_o}{R_H^2}, \tag{12}$$

where R_H is the radius of the vortex boundary. This behavior persists through t_2 in figure 9e and 10e.

Dissipation and rate-of-change of energy are plotted in figures 7f, 8f, 9f, 10f as solid and dashed lines, respectively. The curves of these two independently evaluated measures agree within plotting error, indicating that the viscous term is well resolved. The minima and maxima of the dissipation show very similar trends to ω_p in all of the cases.

The lower Re cases (figure 7, $Re = 350$ and figure 9, $Re = 357$) have essentially stopped stretching at the final time shown, while the higher Re cases (figure 8, $Re = 1000$ and figure 10, $Re = 1073$) are still stretching when the computation is stopped.

In the present version of the code, the rings are not able to be resolved for longer times than shown for figures 8 and 10. It is likely that the apparent oscillations in the tail in both cases are due to insufficient resolution. In future work, the code could either be tailored to compute this flow for longer times or run on a machine with more core memory than is allowed on the CRAY-XMP.

To summarize our observations, we define four phases of the collision of axisymmetric vortex rings: phase I – approach, where the only means of annihilation is diffusion across the axis of symmetry; phase II – collision and annihilation, where a characteristic head-tail structure is observed; phase III – arresting of vortex radius increase, where viscous diffusion dominates; phase IV – self-similar solution of the axisymmetric Stokes equations (i.e. the Stokes quadrupole solution).

The next issue is whether the annihilation time of the axisymmetric problem, t_{ann}, is of the same order as the circulation timescale, $T_c \equiv a_o^2/(\Gamma_o \nu)^{1/2}$, or the viscous timescale, $T_\nu \equiv a_o^2/\nu$ (note that $T_\nu = (\Gamma_o/\nu)^{1/2}\, T_c$). It was found in the symmetry plane of 3D problems (i.e. Schatzle 1987, and MH 1988) that the annihilation time was nearly equal to the circulation timescale. Furthermore, Schatzle suggested that out-of-plane strain enhances the rate of annihilation. Since the axisymmetric collision removes the out-of-plane strain while retaining the strain rate induced by local effects, a comparison of time scales is a first step in deducing the relative importance of the local and nonlocal effects.

The ratio of the annihilation time to circulation timescale in terms of the input parameters is

$$\frac{t_{\text{ann}}}{T_c} = \frac{\bar{t}_{\text{ann}}}{\bar{t}_o} \left(\frac{\Gamma_o}{\nu}\right)^{1/2} \left(\frac{R_o}{a_o}\right)^2 \frac{1}{\tilde{R}_o} \tag{14}$$

where $\tilde{R}_o = 3.0$, $\Gamma/\nu = 350$, $a_o/R_o = 0.25$, and from figure 7h, $\bar{t}_o = 1.0 \times 10^{-4}$, $\bar{t}_{\text{ann}} \approx 0.2 \times 10^{-4}$ (consult Stanaway (1988) for details of the normalization). Substituting these numbers into equation 14, we get $t_{\text{ann}}/T_c = 3.4$ and $t_{\text{ann}}/T_\nu = 0.18$. Therefore, the annihilation timescale for the axisymmetric collision is faster than the viscous timescale and slower than the timescale set by the circulation. This indicates the local effects are important in enhancing annihilation, however, nonlocal effects such as vorticity realignment are also important in 3D. In a 3D situation, one might expect that during the initial stages of the the collision, local effects are dominant, and as the circulation in the symmetry plane weakens, the bridges strengthen and the out-of-plane stain becomes the more important effect.

To understand 3D effects on annihilation, consider for example, the simulation of MH. Those portions of the tubes that develop vorticity mainly in the x direction induce a strain that is out of the xy symmetry plane. If this induced flow could be modeled as an axisymmetric strain (radially inward in the xy plane and outward along z) then the effect on the locally two-dimensional solution is merely a rescaling of time and spatial coordinates. See for example Lundgren (1982, p.2194) who shows how one can generate an axially strained solution from a two-dimensional one. We do not yet have quantitative information about the type of strain present in the MH database, however, examination of the diagonal components of the strain-rate tensor in the detailed experimental measurements of Schatzle (1987) does suggest

axisymmetric strain in the symmetry plane at the location where the vorticity is the highest (From frame 16: pp. 114, 135, 142, 149 of his thesis). The non-locally induced flow can alter the sense of curvature of vortex lines through the xy section thus halting annihilation whereas in the axisymmetric case the curvature remains of one sign.

Another issue addressed with case 1 (figure 7) is the local contributions to annihilation and the final period of decay. The rate of change of circulation is shown in figure 7h with inlays of the vorticity distributions at particular times. Figures 7i, 7j, and 7k then show a plot of the integrand contributing to $\frac{d\Gamma}{dt}$ along the collision axis at three instants. Note that the tail does contribute significantly, indicating that a model of this process cannot neglect this region. Figure 7h shows the circulation on a log-log plot until very late times where it is seen to asymptote to $\Gamma \sim t^{-3/2}$. This behavior can be understood from a solution obtained by Phillips (1956) for the final period of decay of an inhomogeneous patch of turbulence. Basically the idea is to consider the evolution of the Fourier transform of the velocity expanded in the powers of the wavenumber κ. We write the expansion cryptically as

$$\hat{\mathbf{u}} \sim I + (Q + A)\kappa + \ldots. \tag{15}$$

Here I and A are the conserved linear and angular impulse, respectively, both of which are zero in the present situation, and, Q is the quadrupole moment. At late times the nonlinear terms in the Navier-Stokes equation will be small and the high wavenumber parts of the transform will decay. Phillips shows that, to the extent that the nonlinear terms can be neglected, Q is constant. Hence at large times the only relevant parameters are Q and ν from which the behavior of Γ follows dimensionally. The explicit form for the quadrupole solution (Cantwell, private communication) is

$$\bar{\omega} = \frac{K}{\bar{t}^{\,5/2}}\, \eta^2\, e^{-\eta^2}\, \sin(2\theta) \tag{16}$$

where K = constant, $\eta = \frac{r}{\sqrt{4\nu t}}$, $\bar{\omega} = \frac{\omega}{(I/\rho)}$, and θ is the polar angle (figure 2). The computed large time solution (figure 7k) is in agreement with this Stokes solution (equation 16). By substituting equation (16) into equation (2), it is found that for the asymptotic solution the contribution to circulation decay from the symmetry axis is exactly twice that from the collision line. In other words, in the asymptotic decay state, self-annihilation of the circulation is exactly twice mutual-annihilation.

Another issue studied with this case is that of noise generation. Kambe & Minota (1983) have measured the quadrupole part of the acoustic signal when high-speed rings ($Re_D = 42{,}000$) collide. Figure 12 compares the computed time factor $Q'''(t)$ (solid) with the measured value (dotted), the time origin being shifted to make the zero crossings coincide. The initial transient of the simulation is due to relaxation of the core shapes to equilibrium and may be remedied in the future by increasing the intial separation. The overall agreement at two widely different Re suggests that a certain integral measure of the two flows is insensitive to Re. Observing the relationship between the acoustic quadrupole, Q_{ij}, and Phillips' quadrupole

moment (for which he provides an evolution equation) we obtain

$$Q''_{ij}(t) = 2\pi^2 \frac{d^2}{dt^2} \int (u_i u_j - 1/3\ \delta_{ij} u^2)\ d\mathbf{x}, \tag{17}$$

i.e. the strength and directivity of the quadrupole measures changes in the overall anisotropy of the velocity field and this appears to be insensitive to Re.

Figure 11 shows a comparison of the viscous calculation (case 4) with results obtained using the inviscid code of Shariff *et al.* (1988). The solid line is the boundary of the vortex across which ω/σ jumps from being constant to zero. The viscous vortices stretch less rapidly but in both cases the core shapes evolve similarly; they do not flatten uniformly but fill out and develop a tube-like head and a sheet-like tail similar to the 3D simulation of MH. The experimental photograph (figure 12a) from Oshima (1978) shows a similar structure. In the experiments the smoke in the head pinches and leaves the tail behind. This is shown in figure 12b which shows an oblique view at 30° from the plane of collision at a later instant. The inner disk is the tail and the outer circle is the head. The head-tail split is also clear in the MH simulation.

It is interesting that, in the inviscid calculation, while the head region at the final instant shown contains only 46% of the circulation, its self-energy is 88% of the total.

5. Conclusion

The head-tail structure has been observed in the viscous simulation of axisymmetric colliding vortex rings. Inviscid and viscous collision calculations show qualitatively the same head-tail core structure with the major difference that annihilation causes the vortex to slow down and to travel a finite distance. Among the time-dependent diagnostics computed were circulation, rate-of-change of energy, dissipation, peak vorticity, and impulse. The peaks in dissipation and maximum vorticity occur concurrently for all of the cases. The large time behavior was shown to be the quadrupole solution of the Stokes equations with the character that the self-annihilation due to diffusion of vorticity across the centerline of the vortex gives twice the annihilation as that of the vorticity across the collision plane in this limit. The time scale associated with one case was compared to the time scale observed in a 3D experiment and 3D simulation. It indicated that in 3D, both the out-of-plane strain and the strain-rate due to local effects are important.

Future work recommended includes increased resolution, further investigation of the noise generated at higher Reynolds numbers, and extension of these studies to three dimensions.

Acknowlegements

We would like to thank M.V. Melander for sharing with us his database and thoughts and P.R. Spalart for many useful discussions. F.H. gratefully acknowledges

support from the Center for Turbulence Research and ONR Grant N00014-87-K-0670.

REFERENCES

ASHURST, W.T. & MEIRON, D.I. 1987 Numerical study of vortex reconnection. *Phys. Rev. Lett.* **58**, 1632–1635

BATCHELOR, G.K. 1973 *An Introduction to Fluid Dynamics*. First paperback edition. Cambridge University Press.

BRIDGES, J.E. & HUSSAIN F. 1987 Roles of initial condition and vortex pairing in jet noise. *J. Sound Vib.* **117**, 289–312.

CANTWELL, B.J. 1981 Organized motion in turbulent flow. *Ann. Rev. Fluid Mech.* **13**, 457–515.

CROW, S.C. 1970 Stability theory of a pair of trailing vortices. *A.I.A.A. J.* **8**, 2172–2179.

DYSON, F.W. 1893 The potential of an anchor ring.— Part II. *Phil. Trans. Roy. Soc. London A* **184**, 1041–1106.

HELMHOLTZ, H. VON 1858 On integrals of the hydrodynamical equations which express vortex motion. Transl. Tait, P.G., 1867 *Phil. Mag.* Series 4 **33**, 485–512.

HUSSAIN, A.K.M.F. 1983 Coherent Structures – Reality and Myth. *Phys. Fluids* **26**, 2816–2850.

HUSSAIN, F. 1986 Coherent Stuctures and Turbulence. *J. Fluid Mech.* **173**, 303–356.

HUSSAIN, F. & HUSAIN, H.S. 1987 Passive and active control of jet turbulence. In *Turbulence Management and Relaminarization* (ed. Liepman, H. & Narasimha, R.) Springer, 445–457.

KAMBE, T. & MINOTA, T. 1983 Acoustic wave radiated by head-on collision of two vortex rings. *Proc. R. Soc. Lond. A* **386**, 277–308.

LEONARD, A. 1975 Numerical simulation of interacting, three-dimensional vortex filaments. In *Fourth International Conference on Numerical Methods in Fluid Mechanics*, Springer, 245–250.

LIU, C.H. & TING, L. 1982 Numerical solution of viscous flow in unbounded fluid. In *Eighth International Conference on Numerical Methods in Fluid Dynamics* (ed. Krause, E.) Lecture Notes in Physics **170**, Springer, 357–363.

LUNDGREN, T.S. 1982 Strained spiral vortex model for turbulent fine structure. *Phys. Fluids* **25**, 2193-2203.

MELANDER, M.V., MCWILLIAMS, J.C. & ZABUSKY, N.J. 1987 Axisymmetrization and vorticity gradient intensification of an isolated two-dimensional vortex through filamentation. *J. Fluid Mech.* **178**, 137–159.

MELANDER, M.V. & HUSSAIN, F. 1988 Cut-and-connect of two antiparallel vortex tubes. In *CTR Proc. of the Summer Prog. 1988.*

MÖHRING, W. 1978 On vortex sound at low Mach number. *J. Fluid Mech.* **85**, 685–691.

MOIN, P., LEONARD, A., & KIM, J. 1986 Evolution of a curved vortex filament into a vortex ring. *Phys. Fluids* **29** , 995.

MOORE, D.W. & SAFFMAN, P.G. 1975 The instability of a straight vortex filament in a strain field. *Proc. R. Soc. Lond. A.* **346**, 413–425.

NEU, J. 1984 The dynamics of a columnar vortex in an imposed strain. *Phys. Fluids* **27**, 2397–2402.

OSHIMA, Y. & ASAKA, S. 1977 Interaction of two vortex rings along parallel axes in air. *J. Phys. Soc. Jap.* **42**, 708–713.

OSHIMA, Y. 1978 Head-on collision of two vortex rings. *J. Phys. Soc. Jap.* **44**, 328–331.

PHILLIPS, O.M. 1956 The final period of decay of non-homogeneous turbulence. *Proc. Camb. Phil. Soc.* **52**, 135–151.

PIERREHUMBERT, R.T. 1980 A family of steady, translating vortex pairs with distributed vorticity. *J. Fluid Mech.* **99**, 129–144.

SADOVSKII, V.S. 1970 Vortex regions in a potential stream with a jump of Bernoulli's constant at the boundary. *Prikladnaia matematika i mekhanika* **35**, 729–735.

SCHATZLE, P.R. 1987 An experimental study of fusion of vortex rings. Ph.D. Thesis, Graduate Aeronautical Laboratories, Caltech.

SHARIFF, K., LEONARD, A., ZABUSKY, N., FERZIGER, J. 1988 Acoustics and dynamics of coaxial interacting vortex rings. *Fluid Dyn. Res.* **3**, 337-343.

SHARIFF, K. 1988 Dynamics of a class of vortex rings. Ph.D. Thesis, Thermosciences division of Mechanical Eng. Dept., Stanford Univ. (to be submitted).

SIGGIA, E.D. 1987 Vortex dynamics and the existence of solutions to the Navier-Stokes equations. *Phys. Fluids* **30**, 1606–1626.

STANAWAY, S.K., CANTWELL, B.J. & SPALART, P.R. 1988 Navier-Stokes simulations of axisymmetric vortex rings. A.I.A.A. Paper 88-0318.

STANAWAY, S.K. 1988 A numerical study of viscous vortex rings using a spectral method. Ph.D. Thesis, Aeronautics and Astronautics Dept., Stanford Univ., Also NASA TM 101041.

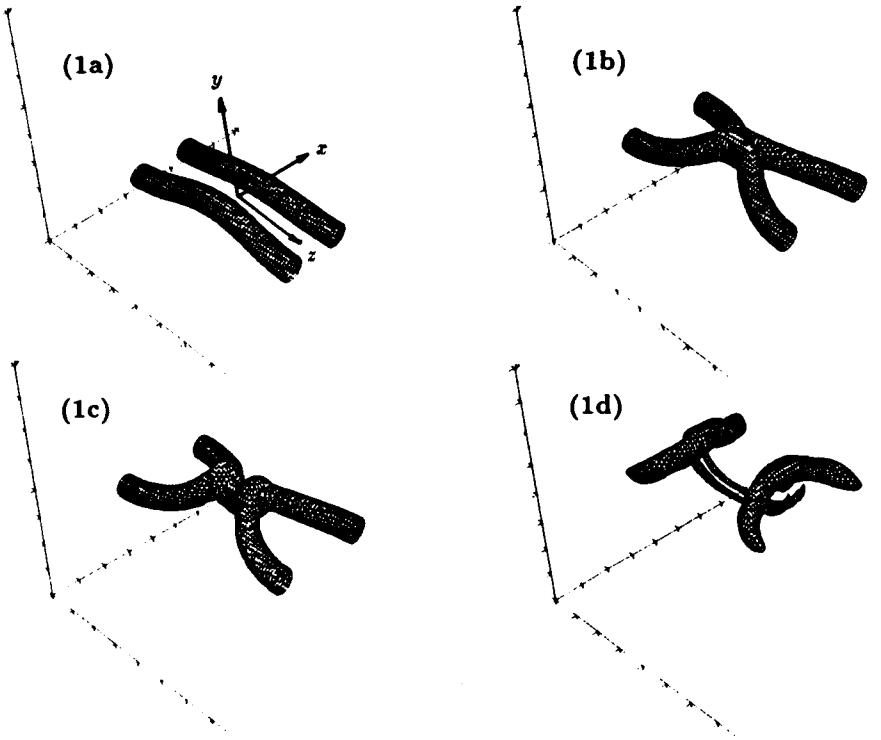

Figure 1. Numerical simulation of cross linking vortex tubes (figure courtesy of Melander & Hussain 1988). Surfaces correspond to a constant level of vorticity magnitude.

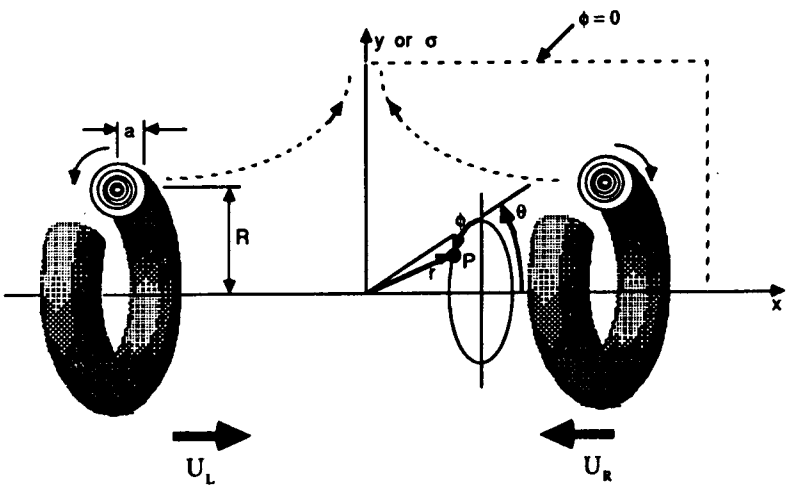

Figure 2. Schematic of axisymmetric vortex ring configuration used to study collision and annihilation.

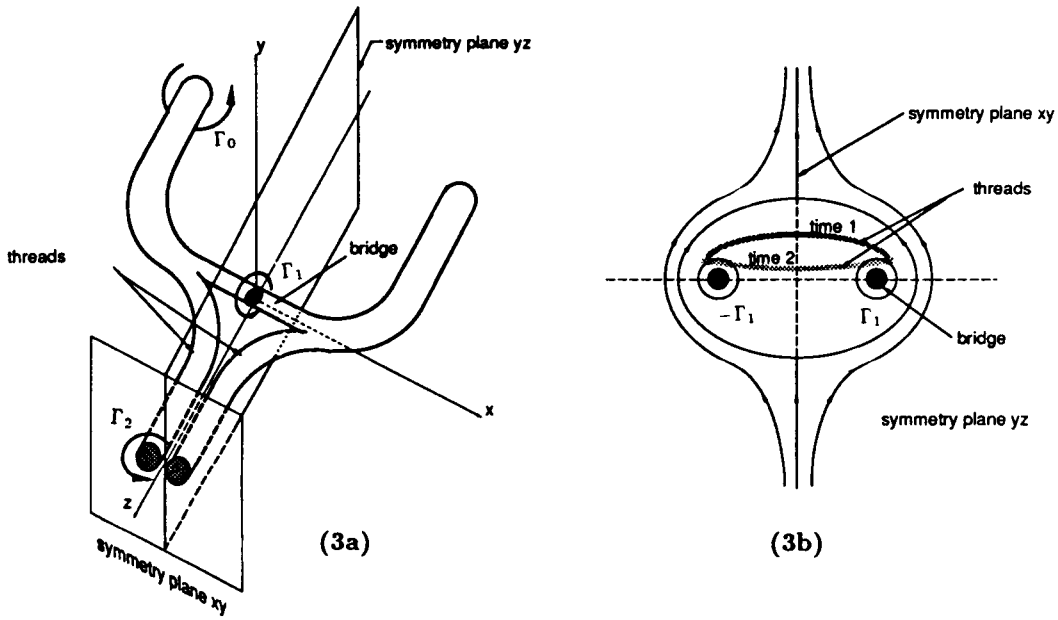

Figure 3. Schematic of cross linking vortex tubes (figure 1). (a) Showing bridges and threads. (b) Symmetry plane yz showing reversal of thread curvature from one time to the next.

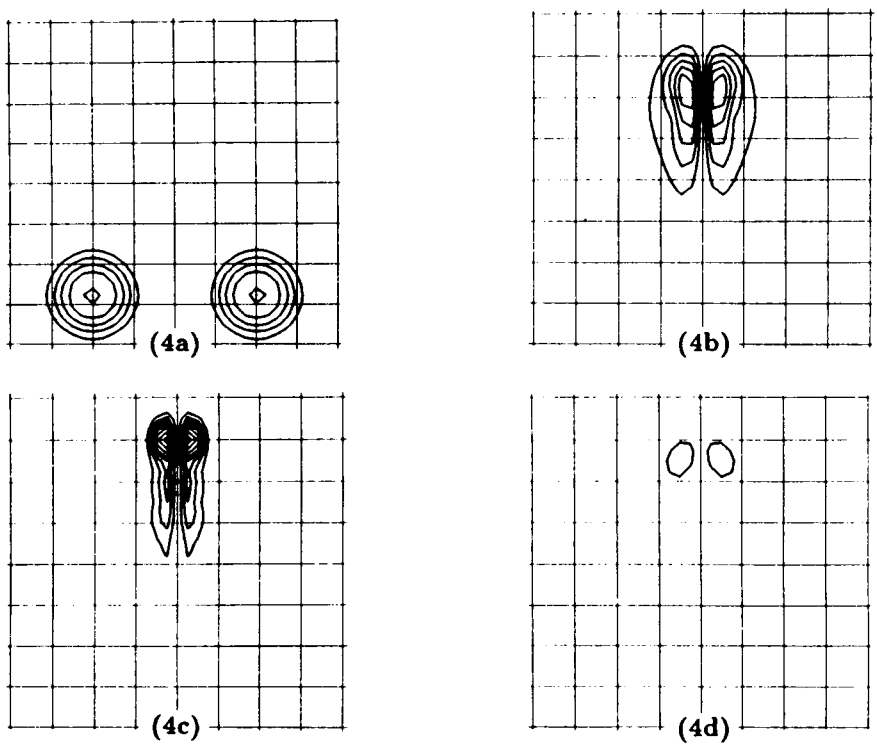

Figure 4. Vorticity contours in symmetry plane xy at times corresponding to figures 1a-1d (figure courtesy of Melander & Hussain 1988).

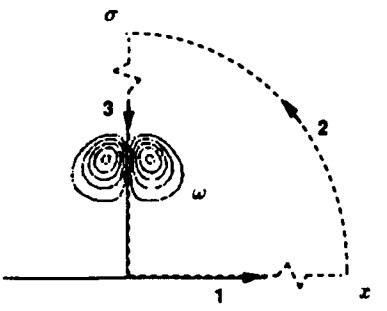

Figure 5. Schematic showing the definition of circulation in the collision of axisymmetric vortex rings of the same strength.

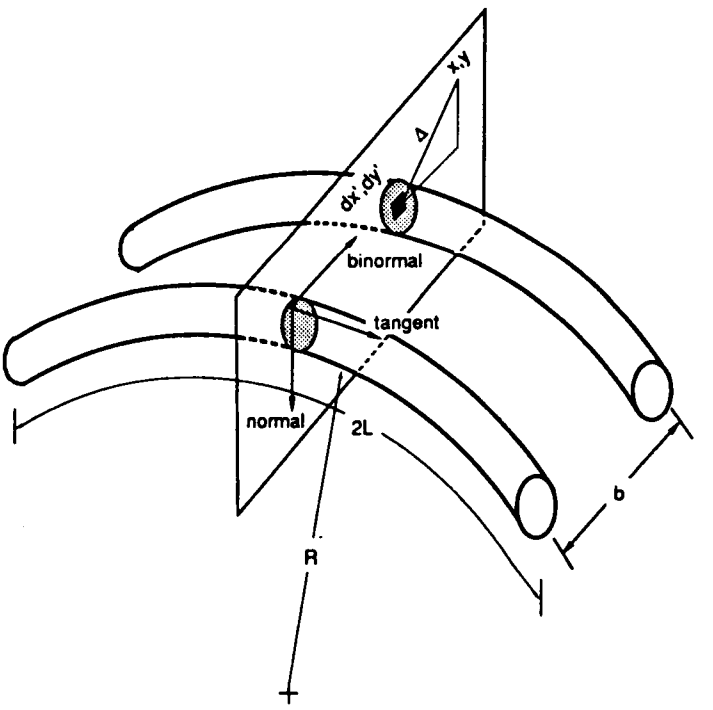

Figure 6. Local induction approximation of two curved vortex filaments of infinitesimal cross section.

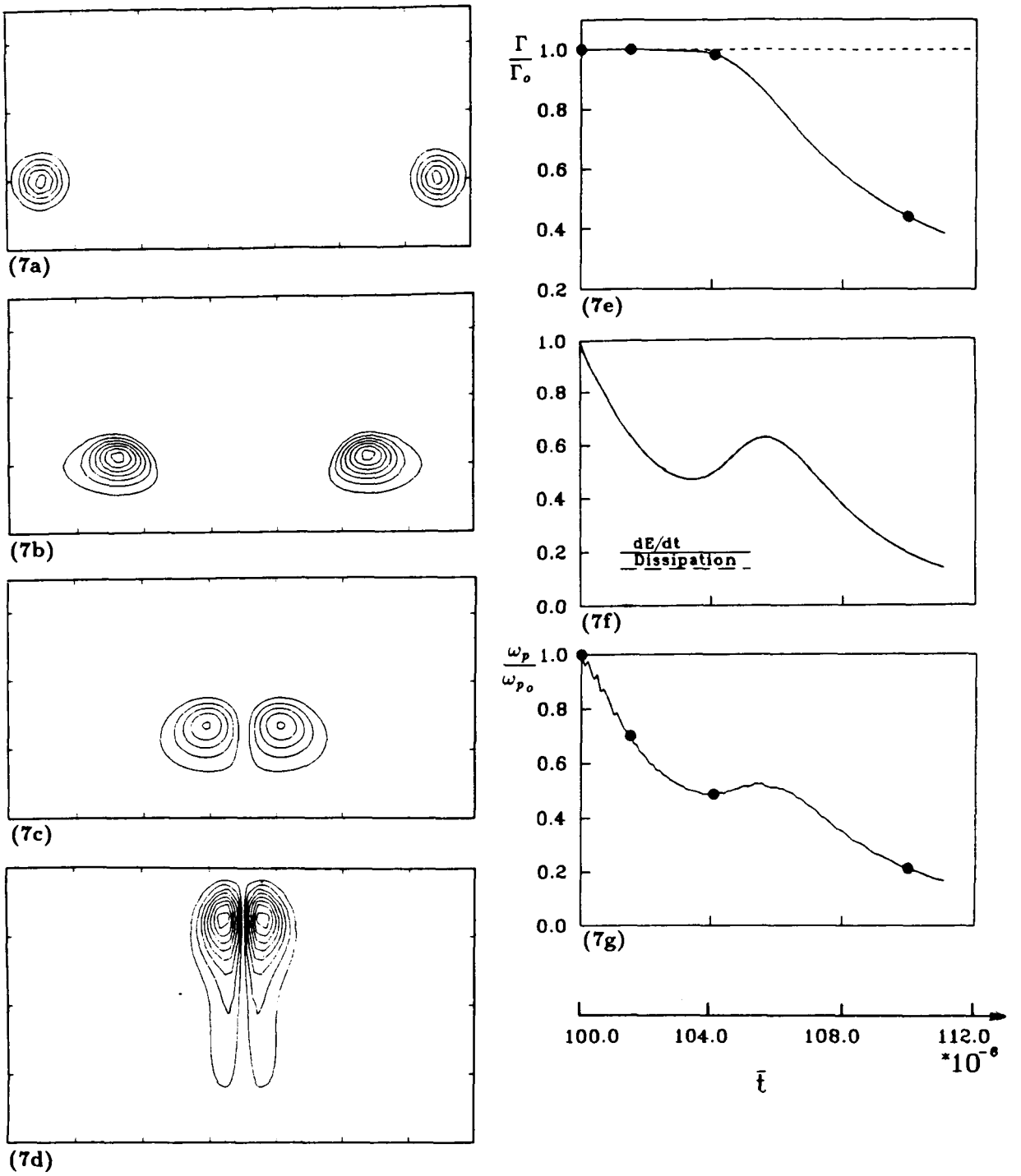

Figure 7. Axisymmetric collision, $(\Gamma/\nu)_o = 350$, $(a/R)_o = 0.35$: (a)–(d) vorticity contours; (e) circulation; (f) rate-of-change of energy and dissipation (relative to initial value); (g) peak vorticity (h) rate-of-change of circulation; (i)–(k) local contribution of vorticity annihilation along the collision plane; (l) log-log plot of circulation versus time; (m) time factor of the acoustic pressure.

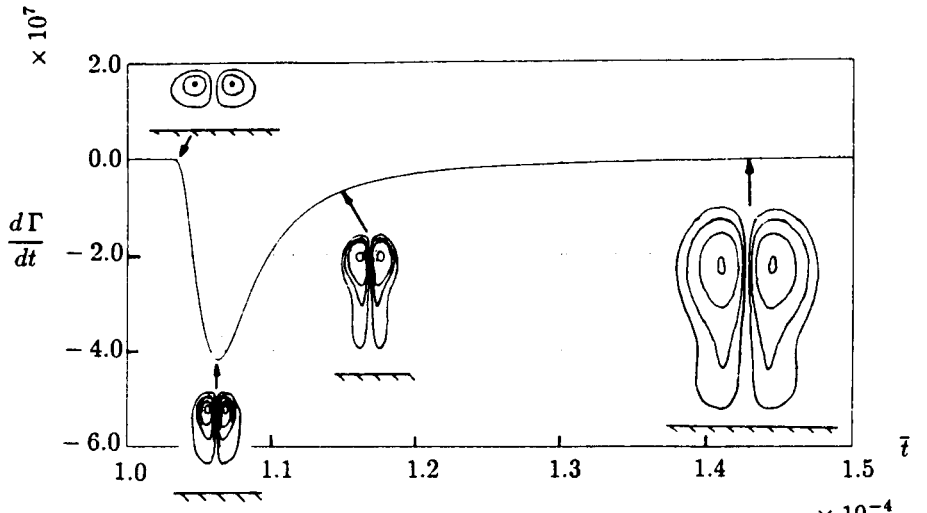

Figure 7h

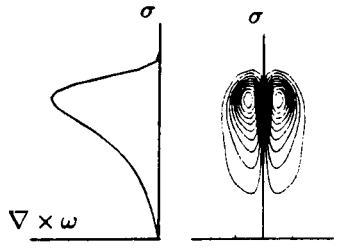

Figure 7i

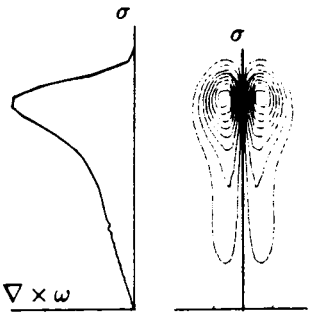

Figure 7j

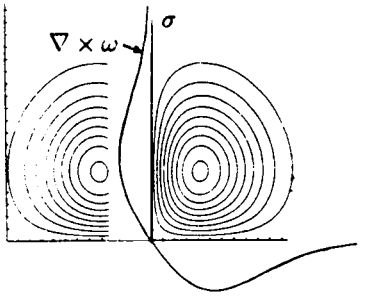

Figure 7k

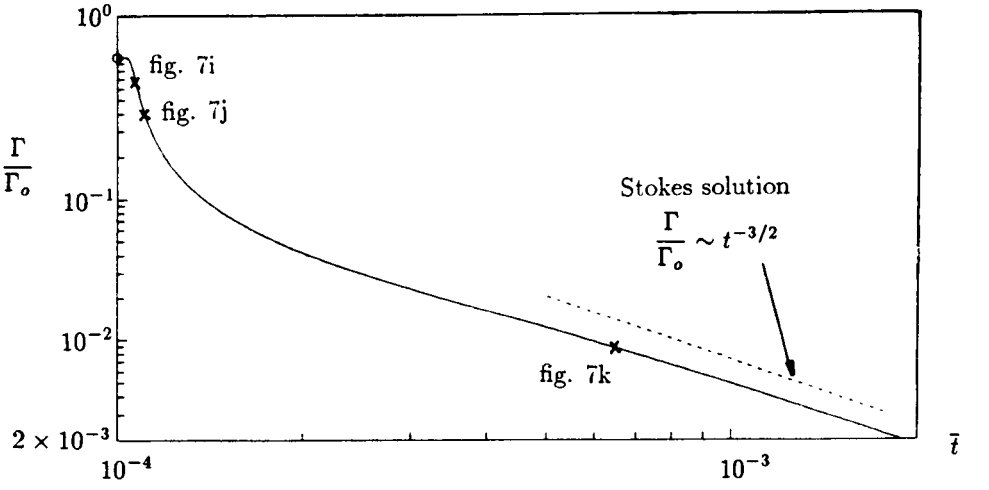

Figure 7ℓ

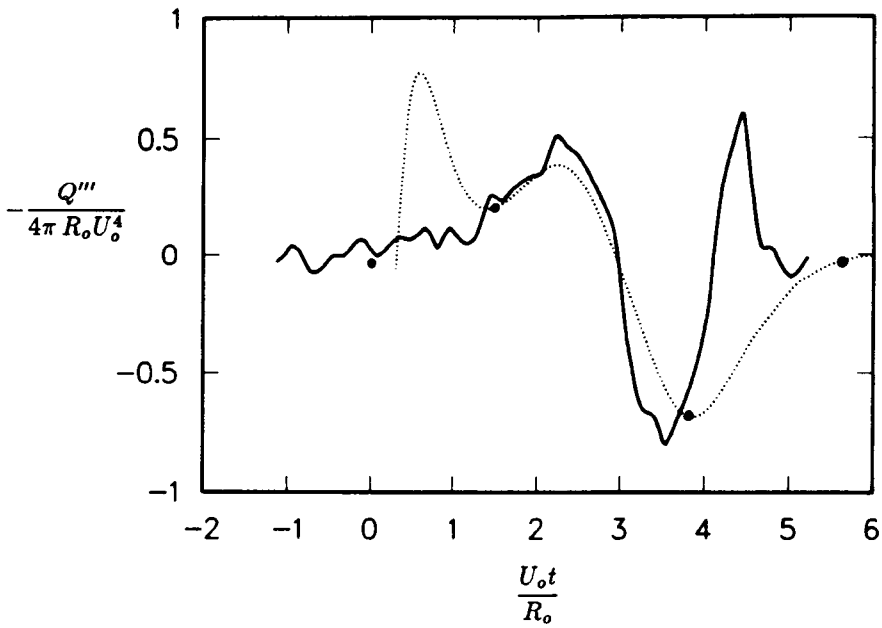

Figure 7m. Time factor of the acoustic pressure. ··· Navier-Stokes simulation; — experiment (Kambe & Minota 1983); • instants corresponding to figures 7a–7d.

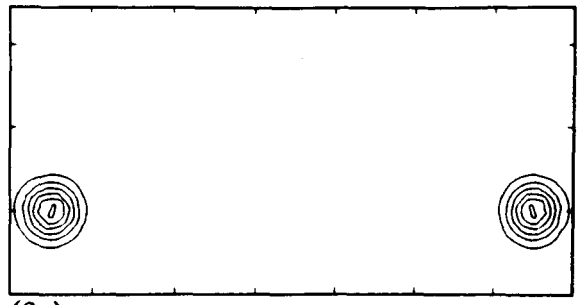

(8a)

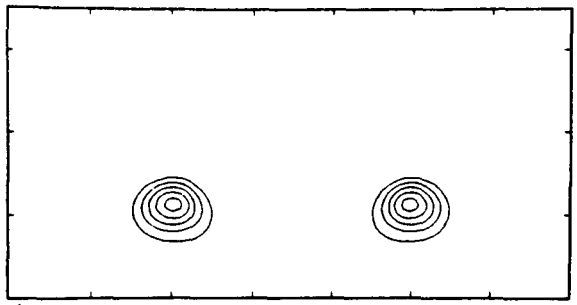

(8b)

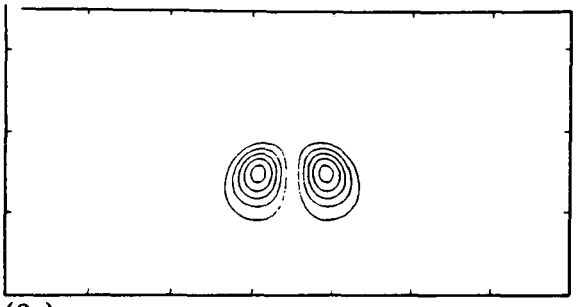

(8c)

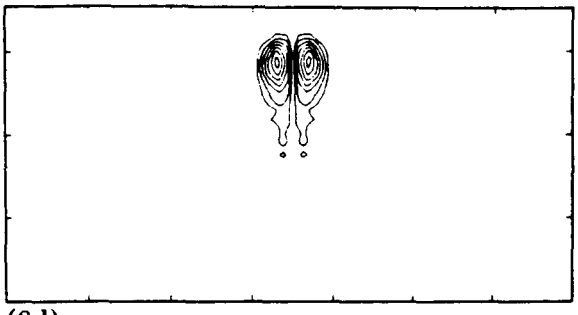

(8d)

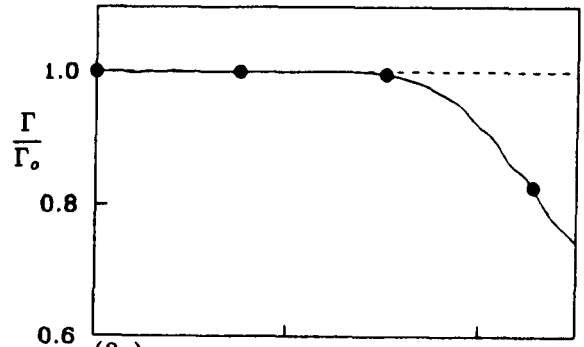

(8e)

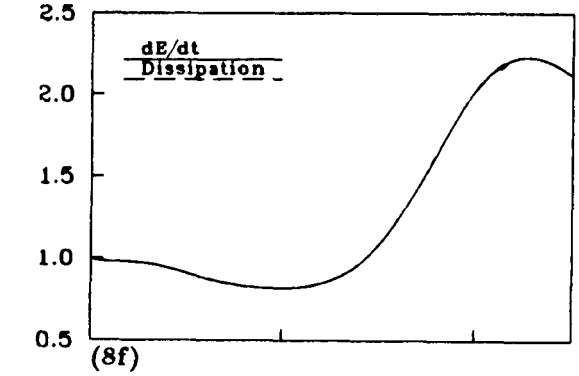

(8f)

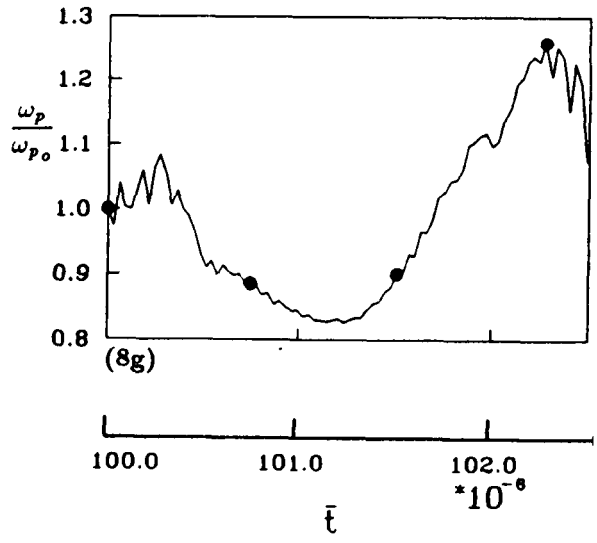

(8g)

Figure 8. Axisymmetric collision, $(\Gamma/\nu)_o = 1000$, $(a/R)_o = 0.35$. (a)–(d) vorticity contours. (e) circulation (f) rate-of-change of energy and dissipation (relative to initial value); (g) peak vorticity.

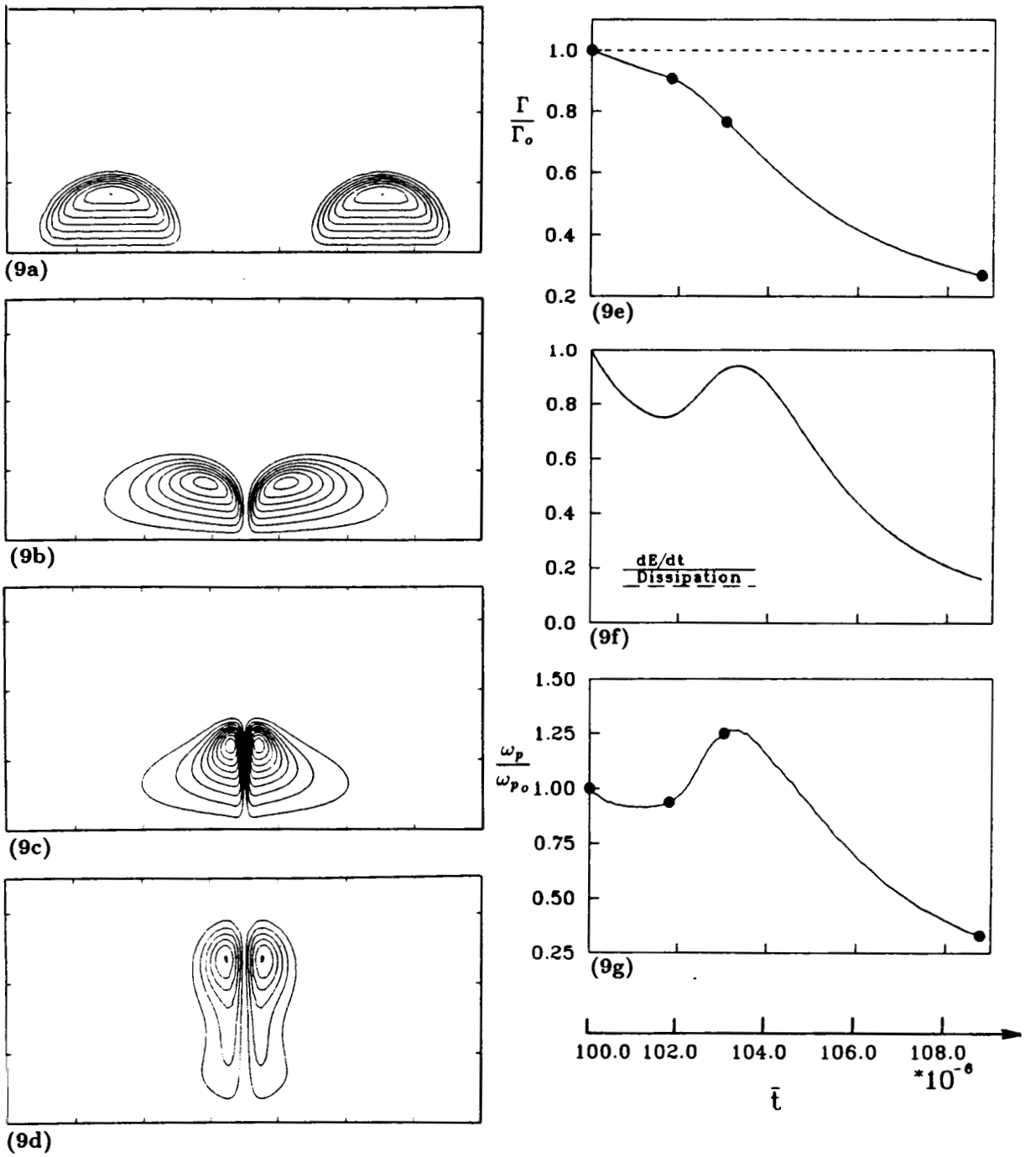

Figure 9. Axisymmetric collision, $(\Gamma/\nu)_o = 357$, initial condition of Hill's spherical vortices. (a)–(d) vorticity contours. (e) circulation (f) rate-of-change of energy and dissipation (relative to initial value); (g) peak vorticity.

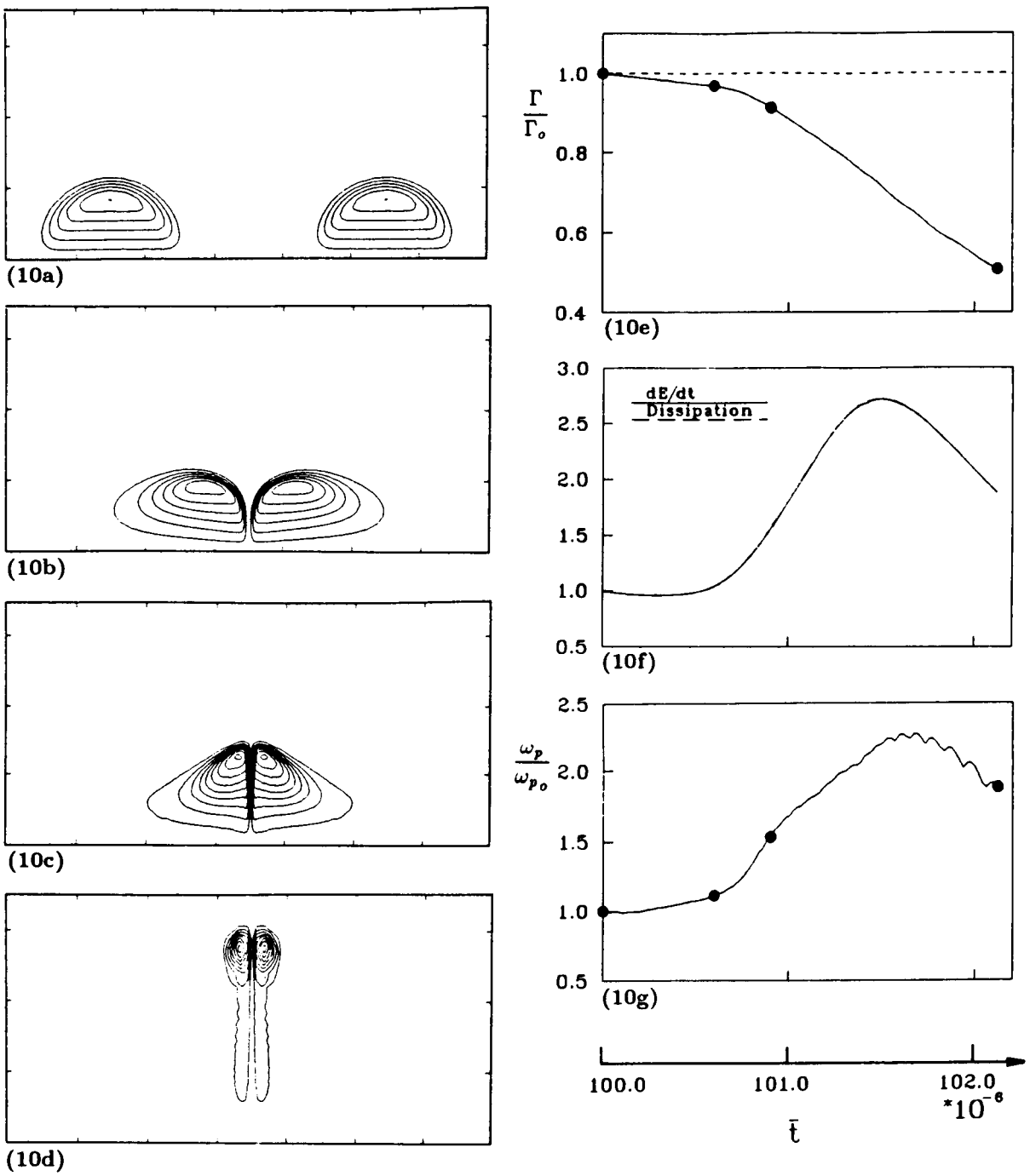

Figure 10. Axisymmetric collision, $(\Gamma/\nu)_o = 1073$, initial condition of Hill's spherical vortices. (a)–(d) vorticity contours. (e) circulation (f) rate-of-change of energy and dissipation (relative to initial value); (g) peak vorticity.

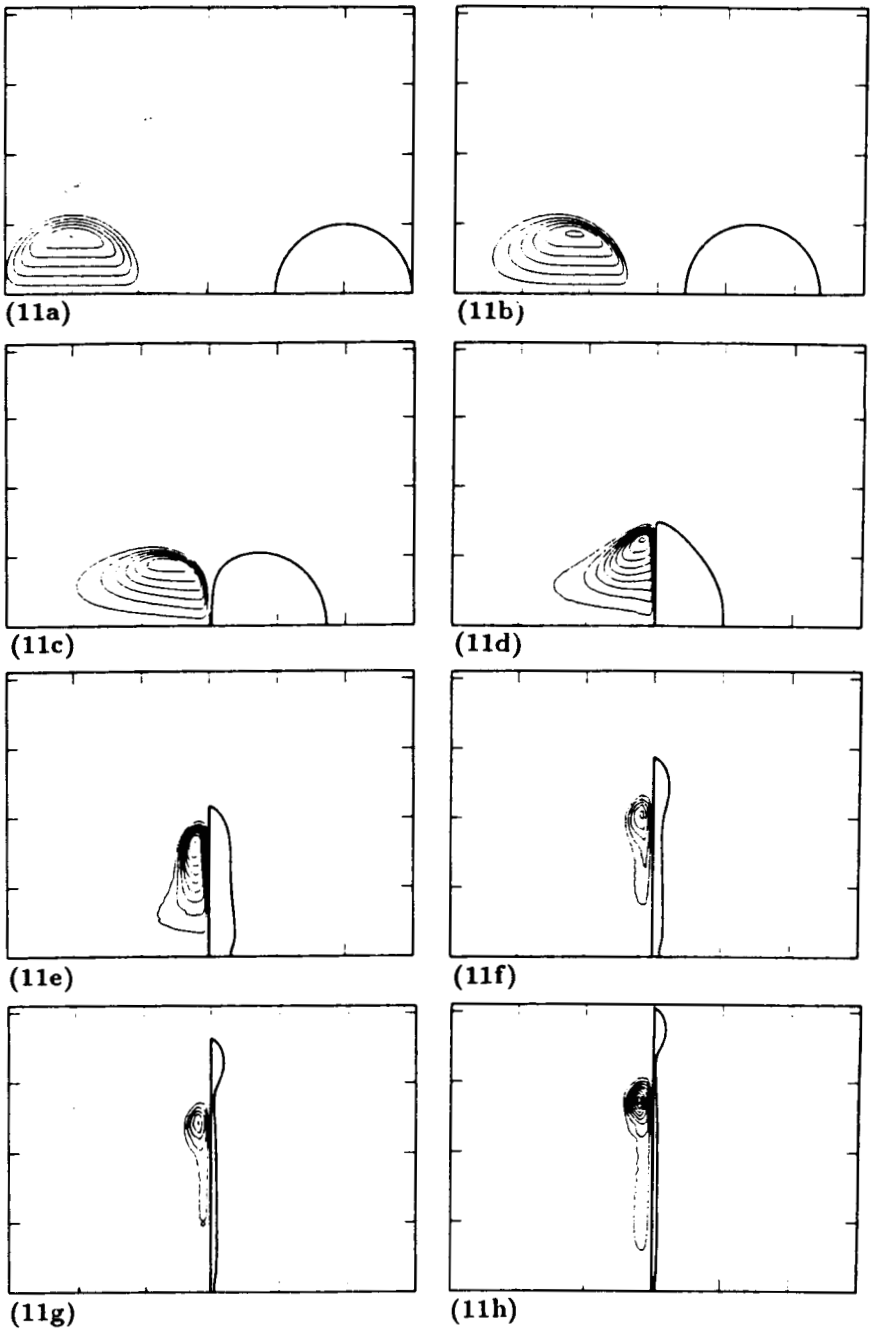

Figure 11. Comparison of viscous calculation of figure 10 (left half) and inviscid calculation using contour dynamics (right half).

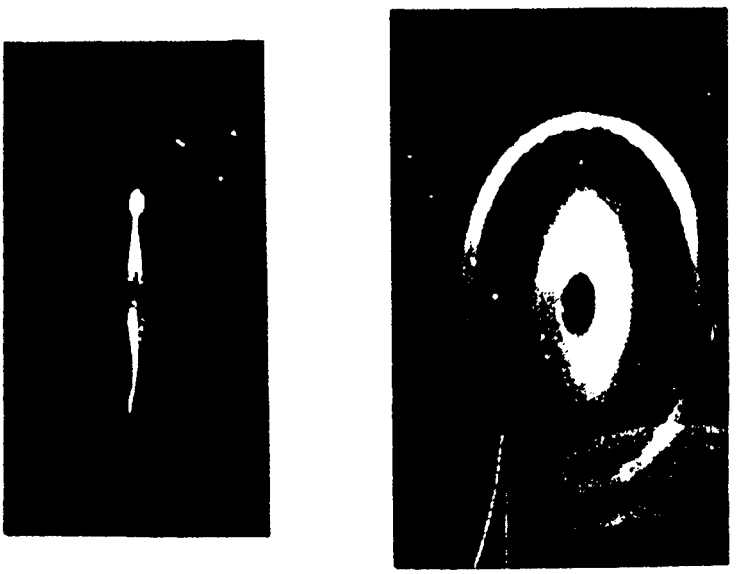

Figure 12. Experiment (Oshima 1978) showing core shape of colliding axisymmetric vortex rings: (a) side view; (b) oblique view at 30° from the plane of collision at a slightly later time.

Optical propagation through a homogeneous turbulent shear flow

By C. RANDALL TRUMAN† AND MOON J. LEE‡

Effects of organized turbulent structures on the propagation of an optical beam in a homogeneous shear flow have been studied. A passive-scalar field in a computed turbulent shear flow is used to represent index-of-refraction fluctuations, and phase errors induced in a coherent optical beam by turbulent fluctuations are computed. The organized vortical structures produce a scalar distribution with elongated regions of intense fluctuations which have an inclination with respect to the mean flow similar to that of the characteristic hairpin eddies. It is found that r.m.s. phase error is minimized by propagating approximately normal to the inclined vortical structures. Two-point correlations of vorticity and scalar fluctuation suggest that the regions of intense scalar fluctuation are produced primarily by the hairpin eddies.

1. Introduction

The passage of coherent electromagnetic beams through turbulent flow fields results in degradation of optical quality. Distortions in phase by index-of-refraction fluctuations reduce beam intensity in the far field. Propagation of wave in atmospheric situations has been studied extensively (see Tatarskii 1971, Chapter 4). The present study, however, is motivated by the need to understand (and predict) losses in optical quality induced by thin shear layers through which a beam must pass. These include, for example, a mixing layer at the exit cavity of a laser (see Baxter, Truman & Masson 1988).

The physical problem of interest in the present study is a coherent optical beam in the visible range, whose width is large compared to the length scales of turbulence in the shear layer through which it passes. The beam width is assumed to be the same order as the size of the computational flow field, which is about ten times the largest length scale of turbulence. The beam wavelength selected was 4×10^{-7} m with flow field dimensions on the order of 0.1 m.

The effect of turbulent fluctuations upon optical quality is commonly modeled assuming isotropic, homogeneous turbulence with a Gaussian distribution (e.g. Tatarskii 1971, §§47–49). As noted by Liepmann (1979), however, "the theory of homogeneous [and isotropic] turbulence does not lead to decisive progress in coping with the shear flow and general mixing problems." Current understanding of turbulent shear flow shows the statistical theories, including models of optical

† University of New Mexico
‡ Center for Turbulence Research

degradation (see Sutton 1969), to be inadequate. Thus successful predictions of beam degradation must account for instantaneous turbulence structures of both the large- and small-scale eddies.

This work has been undertaken to gain an understanding of the relative importance of the large- and small-scale turbulent fluctuations in optical propagation. A passive-scalar field in a homogeneous shear flow computed by Rogers, Moin & Reynolds (1986) is used to represent an instantaneous index-of-refraction field. It is our primary interest to explore the effects of organized turbulence structures in turbulent shear flow on the propagation of a coherent optical beam. The basis for computing phase error induced by turbulent fluctuations is discussed first.

2. Wave propagation in a turbulent medium

2.1. *Parabolic wave equation*

Maxwell's equations govern the behavior of an electromagnetic beam propagating through a turbulent medium. The magnetic permeability is assumed to be constant while the dielectric constant (and thus the refractive index) is assumed to be space-variant (Goodman 1985, pp. 393–399), and the effects of depolarization are negligible (Monin & Yaglom 1975, Chapter 9). We neglect the time-dependence of the refractive index, since the time scale for propagation of light through a flow field is much smaller than that of turbulent fluctuations.

A scalar electric field $E(\mathbf{x}_*)$ may be considered and the transformation $E = ue^{iKx_*}$ yields

$$2iK\frac{\partial u}{\partial x_*} + \nabla_*^2 u + K^2(n^2 - 1)u = 0, \tag{1}$$

where x_* is the distance in the direction of propagation, $\nabla_*^2 = \partial^2/\partial x_*^2 + \partial^2/\partial y_*^2 + \partial^2/\partial z_*^2$, K is the wavenumber of the coherent optical beam and $n(\mathbf{x}_*)$ is the index of refraction. The complex function $u(\mathbf{x}_*)$, which represents the *amplitude* and the *phase* of the electric field, is then slowly varying in the propagation direction.

In practice, the time-averaged spatial variation in index of refraction is ignored. Such variations may displace the beam focus (e.g. beam steering), but induce no loss in far-field intensity (Born & Wolf 1975, pp. 462–463). Moreover, the effect of these variations can be treated by conventional optical techniques.

Since the effects of turbulent structures are of primary interest, a fluctuating wave equation is described. The instantaneous index of refraction is written as

$$n = 1 + n', \tag{2}$$

where n', typically of order $O(10^{-6})$, is understood to be the fluctuation with respect to the spatial distribution of index of refraction.

If backscatter is not important, one may neglect the second derivative with respect to x_* in (1). Then, after neglecting the term quadratic in n', one obtains the parabolized Helmholtz equation:

$$2iK\frac{\partial u}{\partial x_*} + \frac{\partial^2 u}{\partial y_*^2} + \frac{\partial^2 u}{\partial z_*^2} + 2K^2 n' u = 0. \tag{3}$$

A pseudospectral method was developed by Clark, Truman & Masson (1988) to solve (3) for the phase and amplitude of a coherent optical beam which propagates through a turbulent medium with a deterministic index-of-refraction field.

2.2. *Optical path difference*

When diffraction of the optical beam is significant, the parabolized Helmholtz equation (3) must be solved. For the present study, however, the selected parameters ensure that diffraction is negligible, and the restrictions of geometric optics (or acoustics) hold (Keller 1954). With the second derivatives representing diffraction neglected, the parabolic equation (3) reduces to an ordinary differential equation with a variable coefficient $n'(\mathbf{x}_*)$. Since changes in beam amplitude are negligible over a short propagation distance, only changes in phase need to be considered.

In this case, the phase error can be determined by

$$\Delta\phi = K \int_0^s n' \, dx_*, \tag{4}$$

where s is the distance along the propagation path. This integral, known as the *optical path difference*, multiplied by the wavenumber of the beam yields the phase error induced by variations in the index of refraction. The use of the optical path difference to compute phase errors along arbitrary paths allows the use of the full numerical database, which is beneficial in analyzing statistical quantities and associated instantaneous turbulence structures.

3. Results and discussion

A flow field in a homogeneous turbulent shear flow computed on a $128 \times 128 \times 128$ grid by Rogers, Moin & Reynolds (1986) has been analyzed to provide 'data' for the present study. We have chosen a flow field (C128U12 in Rogers *et al.*'s notation) at dimensionless time $St = 12$ (S is the shear rate), in which most turbulence statistical correlations are 'fully-developed.' Here, (x, y, z) denote the coordinates in the streamwise, transverse and spanwise directions, respectively.

3.1. *Passive-scalar field*

The instantaneous passive scalar θ (θ_2 in Rogers *et al.*'s notation) subjected to uniform mean velocity and scalar gradients transverse to the mean flow, dU/dy and $d\Theta/dy$, is used to represent the index-of-refraction fluctuations n'; the passive scalar is scaled to an r.m.s. value of 10^{-6}. As discussed in §2.1, the mean scalar gradient is neglected, since only phase distortions due to turbulent fluctuations are of interest. The phase errors are computed based on the instantaneous index of refraction as determined from the passive scalar distribution.

In order to examine the spatial distribution, contours of the scalar fluctuations are shown on a vertical xy-plane in figure 1. It is clearly shown that the scalar field consists of regions of intense fluctuation which have an orientation similar to the structures of the vorticity field, i.e. the hairpin vortices (Rogers & Moin 1987). Notice that regions in which scalar fluctuations are two or even three times as large

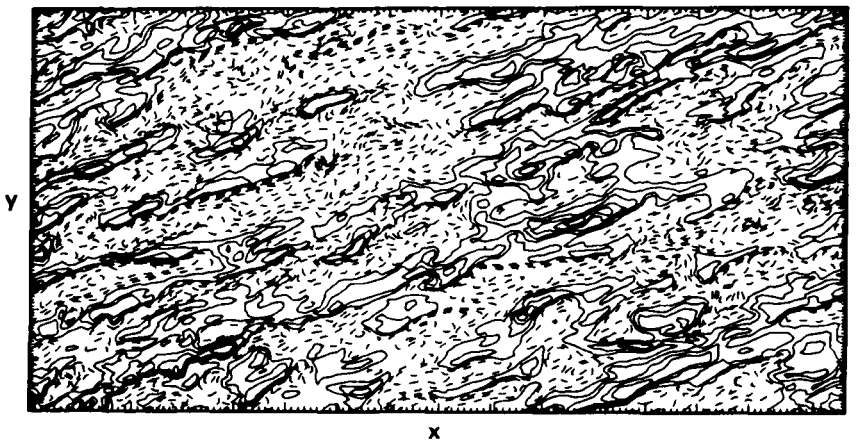

FIGURE 1. Contours of constant scalar fluctuation θ on an xy-plane in homogeneous turbulent shear flow (Rogers *et al.* 1986). The scalar field is elongated in the flow direction due to applied shear, similar to the vorticity field.

as the r.m.s. value are inclined at approximately 45° from the gradient direction and are elongated along the direction of inclination. This result suggests that the large-scale vortical structures strongly influence the scalar distribution.

3.2. *Effect of propagation angle on phase error*

The nonisotropic nature of the scalar distribution immediately leads to a hypothesis that the phase errors depend on the direction of propagation through the turbulent field. In order to verify this hypothesis, phase errors have been computed by using (4) for propagation along several directions in the computed flow field. [For the present problem, solutions from (3) are almost identical to those from (4).] The angle of the beam propagation α is measured counter-clockwise from the flow direction (x-axis); for example, propagation in the direction of the mean scalar gradient (y-axis) has an angle $\alpha = 90°$. Note that propagation at $\alpha - 180°$ and α are identical.

Figures 2(a–d) show contours of the phase error for propagation between the top and bottom xz-planes of the computational domain at $\alpha = 45°$, 90°, 135° and 153.4°, respectively. Data in each case has been scaled to account for the different propagation path lengths so that contour increments are the same in each figure. The distribution of phase error for propagation at $\alpha = 45°$ (fig. 2a) is highly localized and shows the largest phase errors, while the cases at $\alpha = 135°$, 153.4° (figs. 2c, d) show distributions somewhat elongated in the flow direction and much less phase errors (see also figure 3).

The (spatial) r.m.s. phase error normalized by the value for the vertical propagation ($\alpha = 90°$) is plotted in figure 3. In accord with the above qualitative indications, the r.m.s. phase error attains a maximum for the propagation along the vortical structures ($\alpha_{\max} \simeq 45°$ or $-135°$) and a minimum at an angle approx-

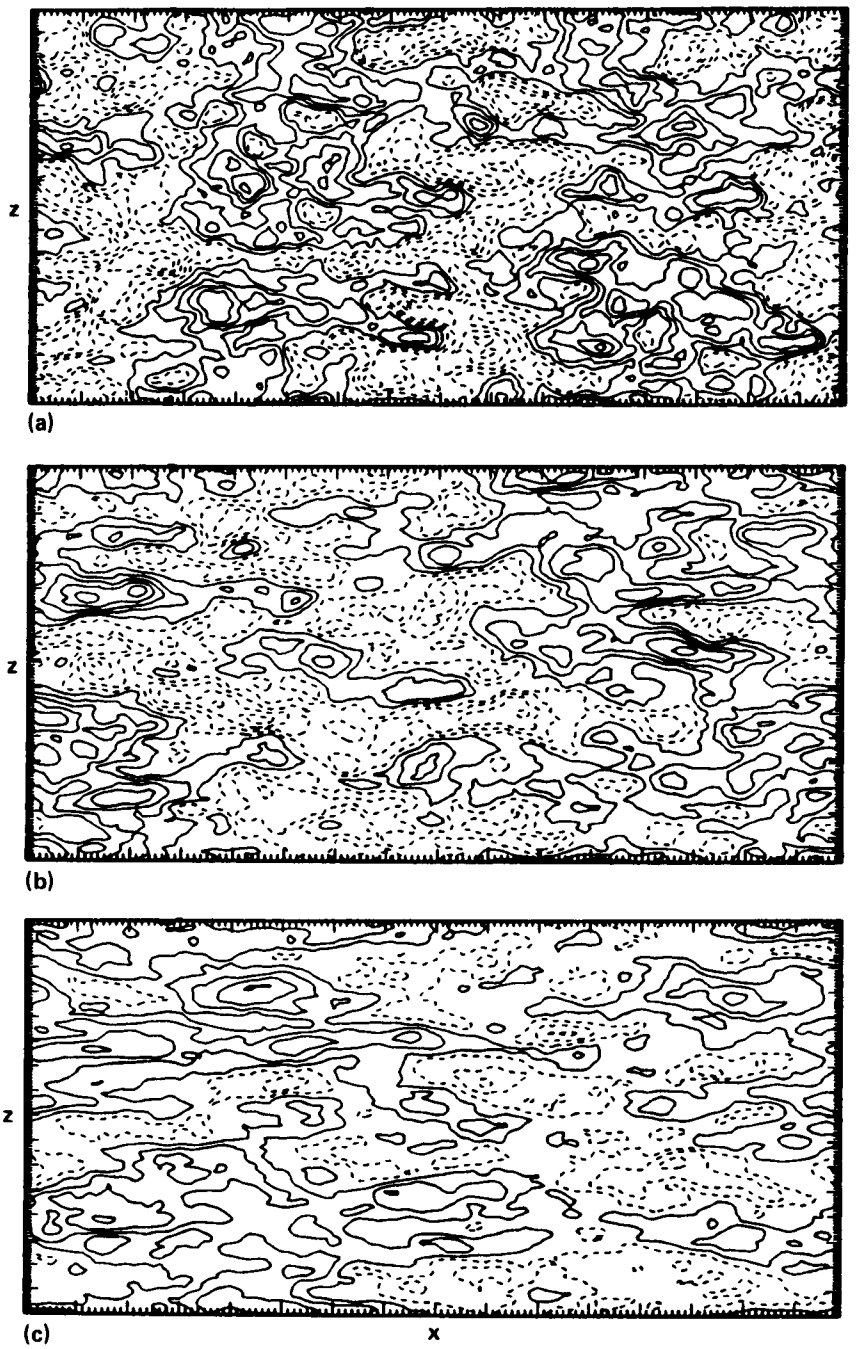

FIGURE 2(*a–c*). For caption see next page.

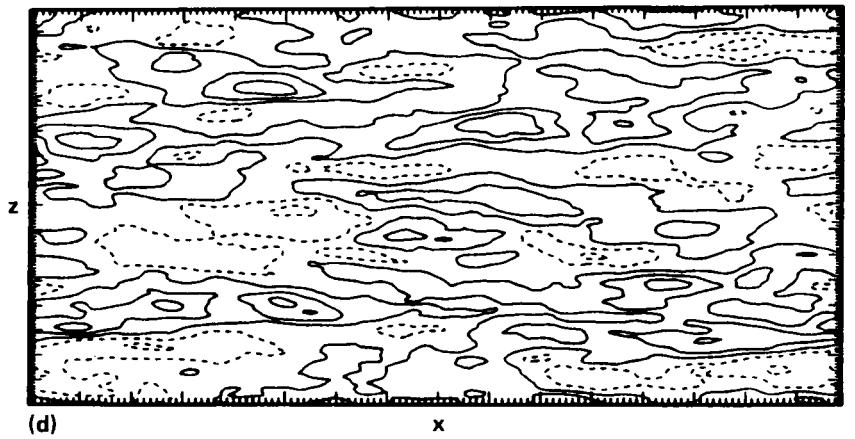

FIGURE 2. Contours of the phase error $\Delta\phi$ on the horizontal xz-plane for propagation through homogeneous shear flow at various angles α: (*a*) 45°; (*b*) 90°; (*c*) 135°; (*d*) 153.4°.

imately normal to them ($\alpha_{\min} \simeq 150°$ or $-30°$). The maximum r.m.s. phase error at $\alpha_{\max}$ is about twice the minimum value at $\alpha_{\min}$. Consequently, these results confirm that the scalar fluctuations are concentrated in regions aligned with the vortical structures and are elongated in that direction.

3.3. *Physical model for scalar fluctuations*

The above results indicate that the distribution of scalar fluctuations is directly influenced by the vortical structures, namely the numerous hairpin vortices (Rogers & Moin 1987). A simple model relating scalar fluctuations to the vortical structures is shown in figure 4. The flow induced by an 'upright' hairpin has a region of $n' < 0$ between and above its legs, and regions of $n' > 0$ outside and below its legs. This is a direct consequence of the dominant role of the hairpin vortices in inducing the scalar fluctuations: 'cold' fluid ($n' < 0$) is brought up between the hairpin legs, while 'hot' fluid ($n' > 0$) is pulled down outside the legs. Conversely, an 'inverted' hairpin has a region of $n' > 0$ between and below its legs and regions of $n' < 0$ outside and above its legs. The importance of this scalar transport by vortical structures to the scalar flux was discussed by Rogers *et al.* (1986).

3.4. *Two-point correlations*

The feasibility of the above model for scalar fluctuations induced by vortical structures can be tested by examining the two-point cross-correlations of scalar and vorticity fluctuations. It is suggested from the conceptual model for generation of scalar fluctuation shown in figure 4 that there should be a strong correlation between vorticity and scalar fluctuation at a separation in the spanwise direction r_z of about half the average spacing Λ_z of the hairpin legs.

In figures 5 and 6, the spanwise cross-correlations of vorticity and scalar made

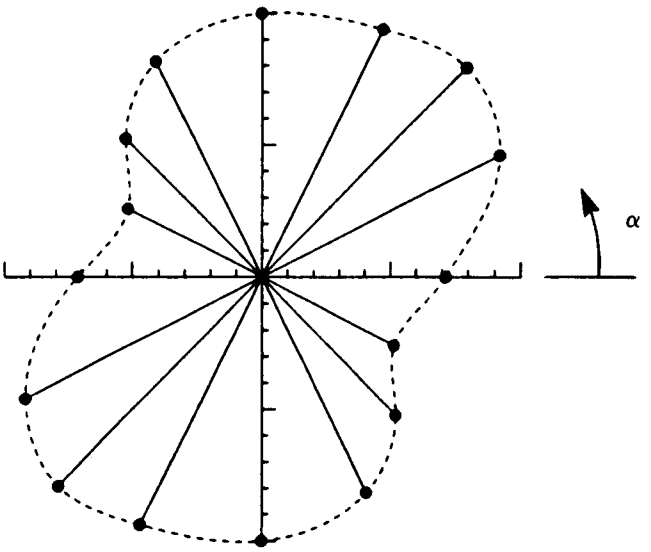

FIGURE 3. Dependence of r.m.s. phase error on the angle of beam propagation. The r.m.s. values are normalized by the value for the vertical propagation ($\alpha = 90°$).

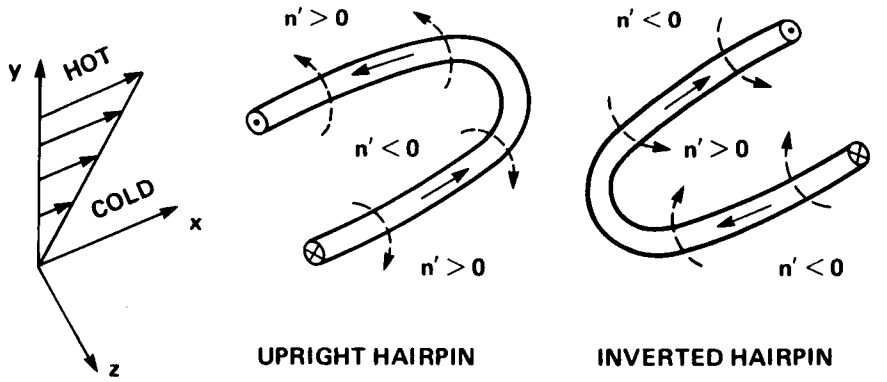

FIGURE 4. Schematic of a conceptual picture showing the scalar fluctuations induced by the 'upright' and 'inverted' hairpin vortices. The arrows with solid line indicate vorticity and the arrows with broken line describe how the induced flow field transports passive scalar.

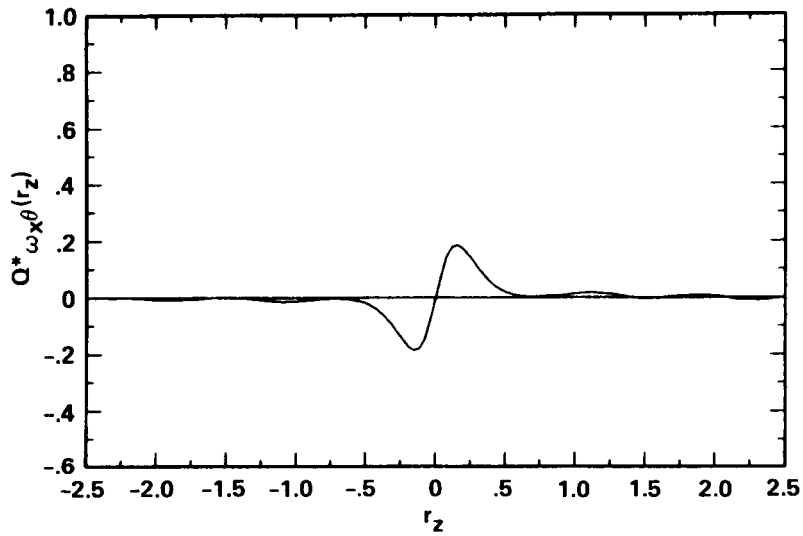

FIGURE 5. Two-point spanwise correlation $Q^*_{\omega_x\theta}(r_z)$ of ω_x and θ, showing a pair of peak and valley at distances half the hairpin-leg spacing: $|r_z| \simeq \frac{1}{2}\Lambda_z$.

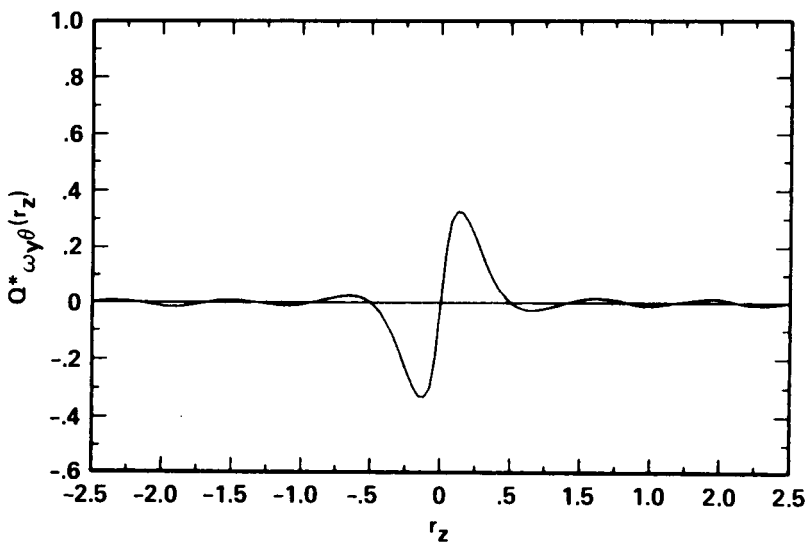

FIGURE 6. Two-point spanwise correlation $Q^*_{\omega_y\theta}(r_z)$ of ω_y and θ, showing a pair of peak and valley at distances half the hairpin-leg spacing: $|r_z| \simeq \frac{1}{2}\Lambda_z$.

dimensionless by the respective r.m.s. values ω_i' and θ' are shown:

$$Q^*_{\omega_i\theta}(\mathbf{r}) = \frac{\overline{\omega_i(\mathbf{x})\,\theta(\mathbf{x}+\mathbf{r})}}{\omega_i'\,\theta'} \qquad \text{(no sum on } i\text{)}, \tag{5}$$

where the overbar denotes the statistical average taken over the three-dimensional space. It is evident that there exists a fair amount of correlation between the scalar and vorticity fluctuations. Because the hairpins are oriented (on the average) at 45° in the xy-plane, both ω_x and ω_y correlate well with θ. For positive spanwise separations ($r_z > 0$) the correlation is positive $Q^*_{\omega_i\theta}(r_z) > 0$, whereas for negative spanwise separations ($r_z < 0$) the correlation is negative $Q^*_{\omega_i\theta}(r_z) < 0$. Notice that each leg of the upright as well as inverted hairpins contributes to the correlations in the same manner.

The two-point spanwise correlations $Q^*_{\omega_x\theta}(r_z)$ and $Q^*_{\omega_y\theta}(r_z)$ in the figures indeed show a pair of distinctive peak and valley antisymmetrically. The distance between the peak and valley corresponds to the average spacing between the hairpin legs $\Lambda_z \simeq 0.23$, estimated from the two-point auto-correlation of vorticity. This is entirely consistent with the physical picture of scalar-fluctuation generation sketched in figure 4. The correlations computed for a field at an earlier time, $St = 8$ (not shown), are nearly identical.

4. Conclusions

The phase distortion induced in a coherent optical beam by turbulent fluctuations in a homogeneus shear flow is highly anisotropic, i.e. sensitive to the direction of propagation. This is a result of intense scalar (i.e. index-of-refraction) fluctuations in elongated regions which are inclined to the mean flow similar to the vortical structures (hairpin vortices). A conceptual model is proposed for scalar fluctuations produced by the hairpin eddies, which are characteristic of homogeneous shear flow. This concept is supported by the two-point vorticity-scalar correlations which show a pair of maximum and minimum at spanwise distances which correspond to one-half the spacing between the hairpin legs.

The importance of large-scale vortical structures and the associated scalar distribution to optical distortion has been established. It would be of fundamental interest to investigate the relative importance of small- and large-scale turbulent structures to phase distortion in propagation through turbulent shear flow. A study of probability density functions of the phase error and two-point correlations of vorticity and scalar gradient would also be of interest. An examination of the effects of inhomogenity could be carried out by using databases from direct numerical simulation of turbulent boundary layers and mixing layers.

Helpful discussions were held with L. Hesselink, M. M. Rogers and S. K. Lele. Support by AFOSR Project 2307Y1, through the Air Force Weapons Laboratory, Albuquerque, New Mexico, is gratefully acknowledged.

REFERENCES

BAXTER, M. R., TRUMAN, C. R. & MASSON, B. S. 1988 Predicting the optical quality of supersonic shear layers. *AIAA Paper* 88–2771.

BORN, M. & WOLF, E. 1975 *Principles of Optics: Electromagnetic Theory of Propagation, Interference and Diffraction of Light.* 5th edn. Pergamon: Oxford, England.

CLARK, T. T., TRUMAN, C. R. & MASSON, B. S. 1988 Prediction of optical phase degradation through a turbulent shear flow. *AIAA Paper* 88–3664.

GOODMAN, J. W. 1985 *Statistical Optics.* Wiley-Interscience: New York.

KELLER, J. B. 1954 Geometrical acoustics. I. The theory of weak shock waves. *J. Appl. Phys.* **25**, 938–947.

LIEPMANN, H. W. 1979 The rise and fall of ideas in turbulence. *Amer. Sci.* **67**, 221–228.

MONIN, A. S. & YAGLOM, A. M. 1975 *Statistical Fluid Mechanics: Mechanics of Turbulence*, Vol. 2, MIT Press: Cambridge, Mass.

ROGERS, M. M. & MOIN, P. 1987 The structure of the vorticity field in homogeneous turbulent flows. *J. Fluid Mech.* **176**, 33–66.

ROGERS, M. M., MOIN, P. & REYNOLDS, W. C. 1986 The structure and modeling of the hydrodynamic and passive scalar fields in homogeneous turbulent shear flow. *Dept. Mech. Engng. Rep.* TF–25, Stanford University: Stanford, California.

SUTTON, G. W. 1969 Effect of turbulent fluctuations in an optically active fluid medium. *A.I.A.A. J.* **7**, 1737–1743.

TATARSKII, V. I. 1971 *The effects of the turbulent atmosphere on wave propagation. NSF Rep.* TT 68–50464, Nat. Tech. Info. Service (NTIS), U.S. Dept. of Commerce. [Translated from the Russian original (1967, ≪NAUKA≫: Moscow) by Israel Program for Scientific Translations (IPST) Staff.]